UNIVERSIDAD COMPLUTENSE DE MADRID

FACULTAD DE CIENCIAS QUÍMICAS
Departamento de Química Orgánica I

TESIS DOCTORAL

Diseño, síntesis y fotoquímica de complejos luminiscentes de Ru (II) con ligandos polyazaheteroaromáticos para aplicaciones como sensores medioambientales

MEMORIA PARA OPTAR AL GRADO DE DOCTOR

PRESENTADA POR

André Eduardo Pereira Guedes Ribeiro dos Santos

Director

Guillermo Orellana Moraleda

Madrid, 2014

UNIVERSIDAD COMPLUTENSE DE MADRID

FACULTAD DE CIENCIAS QUÍMICAS

Departamento de Química Orgánica I

DISEÑO, SÍNTESIS Y FOTOQUÍMICA DE COMPLEJOS LUMINISCENTES DE Ru(II) CON LIGANDOS POLIAZAHETEROAROMATICOS PARA APLICACIONES COMO SENSORES MEDIOAMBIENTALES

MEMORIA PARA OPTAR AL GRADO DE DOCTOR

PRESENTADA POR

André Eduardo Pereira Guedes Ribeiro dos Santos

Director

Prof. Guillermo Orellana Moraleda

Madrid, 2014

“The great tragedy of science - the slaying of a beautiful hypothesis by an ugly fact.”

Thomas Huxley

Para ti, Vicky.

Acknowledgments

To all of those who made this possible. Thank you.

Me gustaría comenzar por agradecer a mi amigo y orientador de tesis, el Profesor Dr. Guillermo Orellana, por todas las reuniones, revisiones, pistas y sugerencias. Juntamente con la Profesora Dra. Mª Cruz Moreno Bondi, me habéis permitido trabajar en el grupo GSOLFA y haber crecido gracias a él. Agradezco también toda la ayuda de los Profesores Dr. David Fresnadillo, Dr. Fernando Navarro y Dra. Mª Dolores Marazuela.

A la Profesora Dra. Leticia González y al Dr. Daniel Escudero por la supervisión y colaboración en todo mi trabajo de química computacional. Do mesmo modo, agradeço também a Tiago Silva pelas horas de CPU.

A Nuria Martín por haber estado siempre disponible, por toda la ayuda y amistad.

A Kassio y Klecia, por las horas que hemos trabajado juntos, de forma productiva y estimulante. A Yinay y Helena, por vuestro trabajo. A Elena, por haberme ayudado unas mil veces con el HPLC. A Bruno, Juan, Ana e Manoel, por vuestras sugerencias y enriquecedoras discusiones.

Obrigado Irene. Sempre optimista, feliz e com os pés na terra, fazes-me ser uma pessoa melhor. Sem a tua paciencia e apoio nunca teria conseguido, especialmente durante este ultimo ano. Obrigado por teres lido e revisto toda a minha tese, por todo o trabalho de proof reading. Te quiero! Mãe e pai, obrigado por todo o vosso esforço que me permitiu chegar até aqui, por serem meus amigos e me receberem sempre com carinho. Aos meus irmãos Sara, Ricardo, Raquel e Emanuel por toda a amizade. Quiero expresar mi profundo cariño a Paloma y Chema, por vuestra reconfortante figura de padres adoptivos.

A Artur Moro por me ter posto em contacto com o meu supervisor de tese. A Fausto Oliveira pela sua amizade e ajuda. A todos mis compañeros de laboratorio que aún no habia mencionado, Paco, David, Raquel, Clara, Alexandre, Irene, Victoria, Ruyman, Pili, Sergio, Aurelien, Nico, Manoel y Freda. Gracias a vosotros me senti como en casa desde el primer día. Muchas gracias, amigos.

A todos os "mil amigos", Matos, Raquel, Fade, Patrizia, Batatas, Galvão, Rosa, Mónica, Catarina, Vitória, Helder, Bruno, Bete. Passar meses sem vocês só se compensa pelo tempo de férias. Não há nada como ter amigos estarolas para levar umas quantas doses de "show no mercy" e humildade. Obrigado por serem o meu espelho de realidade e colchão de apoio.

Enfin un énorme merci à Mme Cornet, pour toutes les heures consacrées à Vicky. En réalité, vous êtes l'une des personnes qui m'ont le plus facilité la rédaction de ma thèse. Merci.

Table of contents

Glossary of acronyms

AA	Atomic Absorption
ACN	Acetonitrile
ACT	Acetone
AEE	Adiabatic Electronic Emission
ahb	5-Acetyl-2-hydroxybenzaldehyde
ap	1,10-Phenanthrolin-5-amine
bim	2,2'-Biimidazole
bpy	2,2'-Bipyridine
bpytym	*N,N'*-(2,2'-Bipyridine-4,4'-diyl)bis(2-(thymin-1-yl)acetamide
BuCN	Butyronitrile
CAS	Chemical Abstracts Service
cdi	1,1'-Carbonyldiimidazole
CHCA	α-Cyano-4-hydroxycinnamic acid
CPU	Central Processing Unit
CT	Charge Transfer
dab	2,2'-Bipyridine-4,4'-diamine
dcab	2,2'-Bipyridine-4,4'-dicarboxylic acid
DCM	Dichloromethane
DEPT	Distortionless Enhancement by Polarization Transfer
DFT	Density Functional Theory
DIEA	*N,N*-Diisopropylethylamine
DLR	Dual Lifetime Referencing
DMF	Dimethylformamide
DMSO	Dimethyl sulfoxide
dnob	4,4'-Dinitro-2,2'-bipyridine-*N,N'*-dioxide
dob	2,2'-Bipyridine-*N,N'*-dioxide
ECP	Effective Core Potential or pseudopotential
EPA	Environmental Protection Agency
ERG	Electron releasing Group
ESI-MS	Electron Spray Ionisation Mass Spectrometry
EWG	Electron Withdrawing Group
FAA	Furnace Atomic Absorption
FRET	Förster Resonance Energy Transfer
FT-IR	Fourier Transform Infrared spectroscopy
GM	Global Minimum
GS	Ground State
GTO	Gaussian Type Orbital
HAA	Hydride Atomic Absorption
haip	1-(4-Hydroxy-3-(1H-imidazo[4,5-*f*]-1,10-phenanthrolin-2-yl)phenyl)ethanone
HF	Hartree-Fock
hmba	2-Hydroxy-5-methoxybenzaldehyde
hmip	2-(1H-Imidazo[4,5-*f*]-1,10-phenanthrolin-2-yl)-4-methoxyphenol
HMQC	Heteronuclear Multiple-Quantum Correlation
HOMO	Highest Occupied Molecular Orbital

Glossary of acronyms (continued)

HPLC	High Performance Liquid Chromatography
IC	Internal Conversion
ica	2-Imidazolecarboxaldehyde
ICP-MS	Inductively Coupled Plasma Mass Spectrometry
ICT	Intramolecular Charge Transfer
iip	2-(1H-Imidazol-2-yl)-1H-imidazo[4,5-*f*]-1,10-phenanthroline
IL	Intraligand
im	Imidazole
IR	Infrared
ISC	Intersystem Crossing
ISE	Ion-Selective Electrode
IUPAC	International Union of Pure and Applied Chemistry
LLCT	Ligand-to-ligand Charge Transfer
LM	Local Minimum
LMCT	Ligand-to-metal Charge Transfer
LUMO	Lowest Unoccupied Molecular Orbital
MC	Metal-Centred
MCL	Maximum Contaminant Level
MECP	Minimum Energy Crossing Point
MLCT	Metal-to-ligand Charge Transfer
MMC	Metal-Metal-Centred
MMLCT	Metal-Metal-to-ligand Charge Transfer
MO	Molecular Orbital
MOT	Molecular Orbital Theory
nbpy	4,4′-Dinonyl-2,2′-dipyridyl
NMR	Nuclear Magnetic Resonance
nody	*N*⁴,*N*⁴'-Dioctadecyl-2,2'-bipyridine-4,4'-dicarboxamide
PAA	Platform Atomic Absorption
PBS	Phosphate Buffered Saline
PCM	Polarizable Continuum Model
PCT	Photoinduced Charge Transfer
pdo	1,10-Phenanthroline-5,6-dione
PES	Potential Energy Surface
PET	Photoinduced Electron Transfer
phen	1,10-Phenanthroline
PLC	Preparative Layer Chromatography
PVC	Poly(Vinyl Chloride)
S_0	Singlet ground state
SCF	Self-Consistent Field
SOC	Spin-Orbit Coupling
SOMO	Single Occupied Molecular Orbital
SPT	Single Photon Timing
STO	Slater Type Orbital
T_1	Lowest triplet excited state

Glossary of acronyms (continued)

TD-DFT	Time-Dependent Density Functional Theory
TFA	Trifluoroacetic acid
THF	Tetrahydrofuran
TICT	Twisted Intramolecular Charge Transfer
TLC	Thin Layer Chromatography
TMS	Tetramethylsilane
tyma	Thymine-1-acetic acid
tymim	2-(Thymin-1-yl)-1-(1H-imidazol-1-yl)ethanone
UV-Vis	Ultraviolet-Visible
ZPE	Zero-Point Energy

Glossary of mathematical terms

A	Absorbance
A	See section 1.10.2
B	See section 1.10.2
B_i	Pre-exponential factor
c	Concentration /mol dm^{-3}
c	Speed of light in vacuum (3×10^8 /m s^{-1})
G	Guest
I	Luminescence intensity
I_{exc}	Intensity of the excitation light
I_t	Emission decay profile (Eq. 2)
K_a	Association constant
k_q	Bi-molecular quenching constant
k_r	Radiative rate (Eq. 41)
k_{nr}	Non-radiative rate
l	Optical pathlength /cm
L	Ligand
pK_a	Logarithmic acid dissociation constant
pK_{ap}	Logarithmic apparent acid dissociation constant
R	Gas constant (8.314 J mol^{-1} K^{-1})
δ	NMR shift /ppm
Δf	Solvent-specific orientation polarizability term (Eq. 32)
ε	Molar absorption coefficient /dm^3 mol^{-1} cm^{-1}
h	Planck constant ($6.62606957(29) \times 10^{-34}$ /J s)
κ	Emission collection efficiency (Eq. 1)
λ	Wavelength /nm
ν_{abs}	Energy of the absorption maximum /cm^{-1}
ν_{em}	Energy of the emission maximum /cm^{-1}
τ	Luminescence lifetime (Eq. 2 and Eq. 40)
τ_M	Pre-exponential weighted mean lifetime (Eq. 3)
Φ_L, Φ_{em}	Luminescent quantum yield (Eq. 1, Eq. 38 and Eq. 39)
Φ_{ISC}	Intersystem crossing quantum yield

DESIGN, SYNTHESIS AND PHOTOCHEMISTRY OF LUMINESCENT Ru(II) COMPLEXES WITH POLYAZAHETEROAROMATIC LIGANDS FOR ENVIRONMENTAL SENSING APPLICATIONS

André Ribeiro dos Santos
Universidad Complutense de Madrid, 2014

Supervisor: Prof. Guillermo Orellana Moraleda

Abstract

Background

Nature abounds with examples of self-assembled chemical systems capable of specific analyte recognition. This capability stems from an overall stabilization of the system, either due to structural, electrostatic or entropic phenomena. In fact, the study of the phenomena that determine the stability of a ligand-substrate entity improves our capacity to design systems capable of specific molecular recognition.[1] The detection of waterborne analytes like heavy metals or hydrocarbons is of special interest when considering human health.

Waterborne heavy metals. Heavy metals are considered those elements weighting between 63.5 and 200.6 and with a specific density greater than 5 g cm^{-3},[2] i.e. all the elements between copper and mercury. Nevertheless, the term heavy metal is sometimes broadened to post-transition and transition metals like aluminium, cobalt or iron. The reason why heavy metals represent such threat lies in the fact that not only are they toxic but also non-biodegradable like other organic contaminants, so they tend to accumulate into high concentrations becoming persistent either in nature or living organisms.[3] For this reason the monitoring of heavy metals in water gains relevance, taking into consideration that the different analytes and concentrations depend on the origin and use of the aqueous source.

The work presented in this Thesis addresses mainly two divalent heavy metals, copper and mercury. Copper is known to have beneficial properties in animal metabolism at trace concentrations. Nevertheless, if present in high concentrations, it can cause gastrointestinal distress like vomiting after short term exposure but also liver or kidney damage if one is to be submitted to long term exposure, due to corrosion of old household plumbing systems.[3] Mercury, on the other hand, can also cause a variety of diseases like

kidney damage or neurological damage.[2b] It may originate from industrial wastewater discharges or landfills and croplands leakages. The primary source of human mercury ingestion is fish, in particular big fish (tuna, swordfish, etc) that have been exposed for longer periods of time to hazardous mercury ions. The European Commission under the *drinking water directive* states that the limit concentration for copper in drinking water is 2.0 mg L^{-1} and that for mercury is 1 μg L^{-1}.[4]

Chemical sensor. Currently, the most accepted definition for chemical sensor dates from 1996, where Wolfbeis made a slight modification to his first definition, which states *"Chemical sensors are miniaturised analytical devices that can deliver real-time and online information on the presence of specific compounds or ions in complex samples."* [5] A chemical sensor can be described in three components: i) the sample, which contains one or more analytes to be recognized; ii) a transducer, which accounts for the conversion of such recognition patterns into a measurable signal and iii) a signal-processor to relate the signal into analyte concentration.[5a, 6] The operating principle of the transducer is what usually defines the chemical sensor group, the two most common being the ones based on electrochemical and optical phenomena. These optical sensing devices, often called optodes, have been growing in importance for the last three decades greatly due to the use of optical fibres which allows by remote and distributed measurement.[7]

Luminescence detection. Luminescence is becoming one of the most commonly used tools for chemical sensing.[8] It describes the emission of UV-Vis light that takes place when an excited electron finds a radiative path towards deactivation. This process allows the researcher with direct visualization of what is happening at the molecular level,[9] where in some cases a *single* photon is the required energy for obtaining a signal.[10] In this sense, any fluorophore that suffers a change in its initial luminescence properties upon analyte addition is a potential molecular probe. Depending on the parameter to be detected, the mechanism behind the luminescence change will be different. Oxygen luminescent-based sensors for example, make use of the *energy transfer* after collisional quenching of triplet excited states that reduces both intensity and lifetime of ruthenium complexes due to dynamic quenching.[11] Other molecular probes with pre-determined receptors designed for specific binding display luminescence static quenching and for this reason no change in their lifetimes is observed. The intensity change in their luminescence is a well known process called *photoinduced electron transfer* (PET) and is often used for sensing of cations and anions (Figure 1). There are other transduction processes that lead to changes in the luminescence, for example, the excited state *proton transfer* allowing the development of pH sensors,[8, 10, 12] the *twisted intramolecular charge transfer* (TICT) which allows polarity probes that normally show significant emission wavelength shifts depending on the media (solvatochromism),[13]

or even the solvent stabilization of the molecular probe which then shows a dependence of the absorption, emission and the excited state lifetime with the solvent.[14]

Eq. 1 shows the mathematical interpretation of the luminescence intensity, I_L. It is seen that I_L is directly proportional to i) the intensity of the excitation light, I_{exc} ii) emission collection efficiency, κ, comprising all instrumental parameters and iii) the concentration of the fluorophore, *c*. One sees that luminescence intensity measurements are affected by the intensity of the excitation source and the sensitivity of the detector. These are known to lose efficiency upon extended use. Moreover, it is also directly proportional to the concentration of luminophore which can decrease with time. On the other hand, the use of luminescence lifetime as a transduction method does not depend on any of those factors, and even allow measurements through turbid samples as the excited state lifetime is an intrinsic property of every fluorophore. There is a technique that takes advantage of devices that rely on lifetime measurements to measure intensity changes in the emission of the fluorophore, called dual lifetime referencing (DLR) method.[6, 7b, 15]

State of the art. According to the EPA,[16] among the recommended techniques for waterborne heavy metal analysis are the Inductively Coupled Plasma Mass Spectrometry (ICP-MS) or the Atomic Absorption (AA), among others. These analytical procedures are usually tedious and expensive approaches, necessary to meet the detection limits defined by the environmental agencies. Nevertheless, there are already commercially available platforms that not only meet the detection limit requirements, but also provide *in-situ* online monitoring. When considering portable (and affordable) sensors, the most common sensing devices for waterborne ionic-species detection still lie on electrochemical processes for signal transduction. These are capable of multi-parameter detection.[17] On the other hand, it is expected that optical-based detection schemes become the best option in the future, due to the advantages that have already been discussed, in particular those relying on luminescence transduction. Yet, most of the commercially available optical devices for ion-sensing rely solely on UV-absorption techniques.[17c-e, 17h, i]

Luminescent ruthenium(II) complexes are excellent candidates for molecular probing. [11-12, 18] Among the advantageous characteristics that render polypyridyl complexes of ruthenium(II) suitable for sensor applications are: i) high luminescent quantum yields and molar absorption coefficients allow for cheaper detectors and excitation sources; ii) photostability; iii) Large stokes shifts (> 150 nm), which simplifies the sensor optical requirements by reducing interferences; iv) Long luminescent lifetimes (up to 10 μs) arising from triplet excited states which allow cheaper single-photon detectors and v) ligand tunability. The latter is responsible for the application of such indicator dyes to the detection of a wide variety of analytes. By modifying the structure of the ligands, a specific analyte

receptor may be devised, as well as different solubility properties. Ligand tunability may also alter the photophysical picture of the ruthenium complex by changing the nature of the emissive excited state.[18b, 19] Nonetheless, when narrowing the literature search to indicator dyes sensitive to either Cu(II) or Hg(II) ions, based on the luminescent properties of water soluble ruthenium(II) complexes there are only a handful of results.[20] Figure 4 shows an example of two Ru(II) complexes sensitive to Cu(II) and Hg(II).

Binding constants. If a luminescent molecular probe (ligand) is sensitive to an analyte (guest), it means that some change occurs to its photophysical properties upon recognition. The rationalization of such recognition process with mathematical equations that describe the system is of analytical interest, especially when anticipating sensor applications. From these binding isotherms one obtains an insight on how stable a supramolecular ligand-guest arrangement is (binding constants), and also its stoichiometry. When addressing the binding constants determination, the stoichiometry of the system is often an unknown parameter that the analyst must identify before any other calculation. There are two common experiments that may facilitate the determination of stoichiometry by spectroscopic data, the *method of continuous variations* also known as Job's method[21] and the *mole ratio method*. Both of these methods depend on how high the binding constants are since the lower the binding constant, the less pronounced a trend is, and more difficult it is to define the stoichiometry. Finally, another generalised method for determination of stoichiometry is the simple evaluation of the fitting quality of the data to specific equations that describe a specific stoichiometry. The equations that describe the intensity changes in both absorption and luminescence for a Ligand-to-Guest stoichiometry of 1:1, 1:2 and 2:1 are shown in sections 1.7.1, 1.7.2 and 1.7.3, respectively.

Computational chemistry. Thanks to fast computers and user-friendly software programs, one can peek inside molecules in both space and time dimensions, being capable of describing the structure of short-lived transition states, as well as the potential energy pathways that yield such transition states. It relies on theoretical approximations, or models, to describe the system under study. The theoretical approximations depend not only on the chosen model but also on the level of complexity applied to describe each system. Generally, increasing the complexity of such models leads to higher CPU time requirements and more precise results. One of the most common approaches to describe the electronic structure of large molecules is called density functional theory (DFT). This methodology was developed in the mid 1960s by P. Hohenberg, W. Kohn and L. J. Sham.[22] It is based on quantum mechanics ab initio iterative calculations and shows a good compromise between results and computational cost. A common gradient-corrected DFT method applied for Ru(II) complexes

is the B3LYP exchange-correlation functional.[23] A summary of the different job types performed in this work is shown in Figure 6.

Luminescent ruthenium(II) complexes. A great deal of information about the electronic structure of a ruthenium(II) complex can be extracted just by analyzing its absorption spectrum. Figure 8 shows the characteristic spectrum profile of aqueous solutions of both $Ru(bpy)_3Cl_2$ and $Ru(phen)_3Cl_2$. The vertical transitions that lead to the observed UV-Vis absorption spectrum are represented in Figure 7. The most energetic vertical transitions appear in the UV region and involve the ligands. They can either be *ligand-centred* transitions (LC), *intra-ligand* (IL) or *ligand-to-metal charge transfers* (LMCT), defined as **1** and **2** in Figure 7. The transitions associated with the metal atom are either *metal-centred* (MC) transitions (**4**, Figure 7) or *metal-to-ligand charge transfers* (MLCT) at around 450 nm (**3**, Figure 7). The broad emission band of polypyridyl Ru(II) complexes has a maximum at around 600 nm and is composed by a manifold of radiative decays from the triplet excited state ($\Phi_{ISC} = 1$).[24] This triplet excited state is responsible for large luminescence lifetimes (0.1 – 10μs).[19a] One last important deactivation pathway lies in the thermal population of a metal-centred excited state (^{3}MC), which if populated undergoes non-radiative *d-d* transition.[19b] This process is evidenced by a decrease in the luminescence lifetime as temperature increases. The fact that the photophysical properties of Ru(II) complexes depend not only on the medium but also on temperature allows their use in molecular probing of several parameters. These are used as pH sensors,[12] humidity,[25] solvents,[14] and naturally, temperature.[8]

Scope of the Thesis

The main objective of this Thesis has been to develop novel luminescent polypyridyl ruthenium(II) complexes for aqueous sensing applications. This was achieved by a judicious molecular design which led to the synthesis of polypyridyl ligands with specific receptor moieties and, ultimately, to their ruthenium(II) heteroleptic complexes. Moreover, two luminescent ruthenium(II) polypyridyl complexes functionalized with polyalkyl chains were also synthesised. Therefore, the work presented in this Thesis tackled four major areas: organic synthesis, analytical chemistry, photochemistry and computational chemistry.

Results

Synthesis of polypyridyl ligands. The presented chelating ligands were synthesised using the commercially available 1,10-phenanthroline (phen) and 2,2'-bipyridine (bpy) (Figure 10). The products were obtained by slight modifications to synthetic routes already

described in the literature. Moreover, some of these products were already described elsewhere, yet for different purposes than those of this work. These ligands are the following: 1,10-phenanthroline-5,6-dione (pdo);[26] 5-acetyl-2-hydroxybenzaldehyde (ahb);[27] 2,2'-bipyridine-4,4'-diamine (dab);[28] l2-(Thymin-1-yl)-1-(1H-imidazol-1-yl)ethanone;[29] and 1,10-phenanthrolin-5-amine.[19a] The remaining synthesised ligands were described here for the first time, three of them being imidazo[4,5-*f*]-1,10-phenanthroline derivatives (iip, hmip and haip) and two being bpy derivatives (bpytym and nody). All compounds were identified by proper characterization through standard techniques, for example, proton and carbon nuclear magnetic resonance (Table 1 and Table 2), infra-red spectroscopy, fusion point, elemental analysis and mass spectrometry (spectra show in section 6.1).

Synthesis of polyazaheterocyclic ruthenium(II) complexes. The synthetic procedure for obtaining heteroleptic and homoleptic Ru(II) complexes was described elsewhere.[30] In the case of the heteroleptic complexes, the bis-substituted Ru(II) based precursor was prepared using the commercially available 1,10-phenanthroline (phen) or 4,4′-dinonyl-2,2′-dipyridyl (nbpy) ligands. In this way, four heavy-metal sensing dyes were successfully synthesised, $[Ru(phen)_2(iip)](PF_6)_2$, $[Ru(phen)_2(hmip)](PF_6)_2$, $[Ru(phen)_2(haip)](PF_6)_2$ and $[Ru(phen)_2(bpytym)](PF_6)_2$. Two other Ru(II) dyes were also synthesised aiming hydrocarbon detection, one heteroleptic and one homoleptic, $[Ru(nbpy)_2(nody)](PF_6)_2$ and $[Ru(nody)_3]Cl_2$. It is worth mentioning that the $[Ru(phen)_2(iip)](PF_6)_2$ dye has been published in the form of an international patent (WO2011009981) submitted by our group.[31] The synthesised Ru(II) complexes were identified by similar characterization as that described for the ligands (chapter VI), but also by absorption, emission and lifetime spectroscopy.

Photochemistry of heavy-metal sensing Ru(II) dyes. The photochemistry chapter addresses the two types of dyes, the first part being those containing heavy-metal specific receptors. These four luminescent dyes (the iip, hmip, haip and bpytym complexes) were characterised in organic and aqueous solution at several pH values, and also under presence of 10 divalent heavy-metals (also at different pH values for optimum pH evaluation). It was observed that the emission profile of these dyes is quite insensitive to solvent changes, nonetheless the emission intensity is drastically quenched at high pH values. Using the commercially available HypSpec software, a global analysis of the absorption data was performed. This led to the determination of the acidity constants, pK_a and also binding constants, K_a.

In this way, four pK_a values were determined for $[Ru(phen)_2(iip)]^{2+}$, 3.35 ± 0.01, 5.02 ± 0.01, 8.35 ± 0.02 and 12.10 ± 0.05. At pH 7.5, the luminescence is quenched upon Cu(II) addition by 92%, while only 35% and 31% by Ni(II) and Hg(II), respectively. Lifetime

spectroscopy indicated that the quenching mechanism behind Cu(II) and Hg(II) addition is static quenching, while Ni(II) shows a purely dynamic quenching. The binding constants were determined in presence of Cu(II) and Hg(II), indicating a supramolecular Ru(II)-Metal(II) stoichiometry of 2:1. Their values are summarized in Table 6.

As for the similar $[Ru(phen)_2(hmip)]^{2+}$ and $[Ru(phen)_2(haip)]^{2+}$, which structure differs only in the *para* substitution of the phenol ring (methoxy and acetyl groups, respectively), three pK_a values were determined. The hmip complex shows pK_a values of 2.03 ± 0.06, 7.92 ± 0.03 and 10.36 ± 0.02 while the haip complex shows pK_a values of 4.29 ± 0.01, 6.56 ± 0.01 and 9.26 ± 0.03. The heavy-metal induced luminescence quenching studies showed that while the hmip complex is mildly quenched by all metals (copper being the highest at 45%), the haip complex shows a 83% luminescence quenching in presence of Cu(II), but also upon addition of Pb(II) (25%) and Hg(II) (14%) as shown in Figure 35 and Figure 42, respectively. Similarly to the iip complex, lifetime spectroscopy showed that Cu(II) ions also produce a static quenching of the luminescence of $[Ru(phen)_2(haip)]^{2+}$. The binding constants showed a 2:1 stoichiometry equilibrium between the haip complex and the copper(II) ions. The K_a values are summarized in Table 12.

Finally, the bpytym complex displays two pK_a values at 9.42 ± 0.01 and 11.92 ± 0.01 and its luminescence properties are insensitive to the addition of any of the 10 heavy-metals.

Photochemistry of hydrocarbon sensing Ru(II) dyes. The second part of this chapter addresses those ruthenium complexes that contained aliphatic chains in their ligands, the $[Ru(nody)_3]^{2+}$ and $[Ru(nbpy)_2(nody)]^{2+}$ complexes. Both complexes were characterised in solvents of different polarity by means of absorption, emission and lifetime spectroscopy (the latter also as a function of temperature). It was observed that by changing the polarity of the medium, both probes show hypsochromic and bathochromic shifts of their absorption and emission maximums, respectively. These results are similar to that obtained for a similar probe.[14] The luminescence lifetime spectroscopy study showed a smaller dependence of the lifetime with solvent polarity. Still, by increasing the polarity of the solvent, there is a decrease in the luminescence lifetime of the homoleptic complex, in contrast to the behaviour of the heteroleptic complex, which shows higher lifetimes with increasing polarity. The accessibility of the non-radiative ^{3}MC state of both complexes was evaluated by means of lifetime spectroscopy with varying temperature. The results show that this state is only accessible for the heteroleptic complex.

Computational study of heavy-metal sensing Ru(II) dyes. The computational chemistry study (by means of B3LYP/6-31G* DFT and TD-DFT) allowed the rationalization of some photophysical features of the iip, hmip, haip and bpytym complexes. The most stable geometries of both ground- and excited states were computed and corroborated by the

frequency studies, as no imaginary frequencies were found. The TD-DFT calculations on the ground-state structure yielded the vertical excitation energies (UV-Vis spectra) while the same calculations on the excited state structure (at singlet multiplicity) led to the emission maximum. The excited state of the iip and haip complexes is of metal-to-ligand ^{3}MLCT nature (metal towards the iip ligand), that of hmip is of intra-ligand ^{3}IL nature while that of bpytym is of metal-to-ligand ^{3}MLCT nature (metal towards the phen ligands). Despite their differences, the three iip, hmip and haip complexes display a change in their excited state upon pH increase, showing a ligand-to-ligand ^{3}LLCT excited state upon deprotonation. The study of heavy-metal addition was also studied for the iip and bpytym complexes. In the supramolecular 1:1 $[Ru(phen)_2(iip)]^{2+}$-Cu(II) case, the excited state is of ^{4}MMLCT character and is similar to the ^{3}MLCT state of the free dye. This leads to a similar emission maximum upon Cu(II) addition (results are 7% underestimated than the experimental value). Yet, another excited state was calculated which is lower in energy with regards to the ^{4}MMLCT and centred in the Cu(II) moiety, herein called $^2D_{twist}$. In contrast to the iip complex, calculations on the supramolecular $[Ru(phen)_2(bpytym)]^{2+}$-Hg(II) dyad show no change in the photophysical properties of the dye upon metal coordination.

Conclusions

Photochemistry. Table 19 gathers the relevant spectroscopic features of the heavy-metal probes. It was shown that the four dyes present similar spectroscopic properties both in the ground- and the excited states. However, the bpytym complex shows a slightly red-shifted emission maximum (20 nm), which arises probably due to the presence of the bpy scaffold.

In terms of Cu(II) binding affinity, it was shown that the haip complex has higher association constants which can justify its higher selectivity. Nonetheless, higher K_a values do not imply higher sensitivity since Cu(II) is responsible for 92% luminescence quenching of the iip complex, against the 83% of the haip complex.

Despite structurally similar, the hmip and haip complexes show significantly different Cu(II) sensitivity. The presence of the electron donating methoxy group against the electron withdrawing acetyl group of the hmip and haip complexes has a drastic effect on the acidity of the *p*-hydroxyl group. The pK_a value of this group changes from 7.9 to 6.6 when changing from methoxy (hmip) to acetyl (haip), respectively. Consequently it is the higher acidity of the OH group that increases the affinity of the haip complex towards Cu(II) ions.

The bpytym complex did not show any sensitivity towards Hg(II), neither towards any of the tested heavy-metals. The computational study suggests that the binding event between bpytym and Hg(II) is indeed possibly, but that this does not alter the electronic

structure of the dye hence no response is observed. Since the excited states of the free and supramolecular dyes are directed towards the ancillary phen ligands, it might be possible to activate the Hg(II) response by substituting the ancillary electron-rich phen ligands by bpy ligands.

The careful design and synthesis that led to the structures of $[Ru(phen)_2(iip)](PF_6)_2$, $[Ru(phen)_2(hmip)](PF_6)_2$ and $[Ru(phen)_2(haip)](PF_6)_2$ had the objective of developing Cu(II) sensitive dyes. Figure 83 shows the analytical response of these dyes towards heavy-metals. It is seen that such objective was achieved as Cu(II) is the heavy-metal that most changes produces in the luminescence properties of the Ru(II) complexes. The fact that such quenching occurs by means of static quenching indicates a pre-association of the analyte and ligand in the ground-state, allowed by the shape of the receptor.

The hydrocarbon sensing probes $[Ru(nbpy)_2(nody)](PF_6)_2$ and $[Ru(nody)_3]Cl_2$ display a higher stabilization with increasing polarity, as showed in Figure 84. It was concluded that the Lippert-Mataga model failed in predicting the behaviour of such cationic dyes in varying solvents, as some data points were scattered throughout the plot. This probably occurs due to the presence of the amide groups in the nody ligand, as they can play a role in specific solvent-probe interactions. Still, it was shown that the heteroleptic complex displays higher response to solvent polarity than its peer homoleptic compound and also higher than another homoleptic Ru(II) nbpy based luminescent probe.[14]

Computational study. In this study, it was shown that the B3LYP hybrid functional produces more accurate results than the CAM-B3LYP functional. In this way, the UV-Vis spectra were successfully reproduced for both neutral and acid/base species of the Ru(II) complexes. The luminescence emission maximum was predicted by two approaches, TD-DFT and Δ-SCF, the latter yielding slightly better results. The observed luminescence quenching at high pH values was rationalized by noting the change in the photophysical picture of the complexes, which changes from ^{3}MLCT (or ^{3}IL) at neutral charge to ^{3}LLCT upon deprotonation. Also, the luminescence quenching of $[Ru(phen)_2(iip)]^{2+}$ by Cu(II) was successfully explained by the appearance of a new deactivation pathway, through a low-energy excited state centred at the Cu(II) moiety.

DISEÑO, SÍNTESIS Y FOTOQUÍMICA DE COMPLEJOS LUMINISCENTES DE Ru(II) CON LIGANDOS POLYAZAHETEROAROMATICOS PARA APLICACIONES COMO SENSORES MEDIOAMBIENTALES

André Ribeiro dos Santos
Universidad Complutense de Madrid, 2014

Director: Prof. Guillermo Orellana Moraleda

Resumen

Introducción teórica

En la naturaleza pueden encontrarse múltiples ejemplos de sistemas químicos auto-ensamblados capaces de identificar moléculas específicas. Este proceso de reconocimiento selectivo resulta de la estabilización global del sistema, ya sea por fenómenos estructurales, electrostáticos o entrópicos. El estudio de estos fenómenos de estabilización permite el diseño racional de sistemas capaces de transmitir información al usuario sobre un analito específico.[1] De especial relevancia para el ser humano está la detección de analitos en medio acuoso tales como metales pesados o hidrocarburos.

Metales pesados en medio acuoso. Convencionalmente, se considera metal pesado todo elemento químico de masa atómica comprendida entre 63.5 y 200.6, con una densidad específica superior a 5 g cm^{-3},[2] es decir, todos los elementos comprendidos entre el cobre y el mercurio. Sin embargo, algunos metales de transición y postransición como el aluminio, cobalto o hierro también se incluyen en esta clasificación. Al contrario de los contaminantes orgánicos, que también son tóxicos, los metales pesados no son biodegradables, por lo que se pueden acumular y alcanzar altas concentraciones en el medio ambiente e incluso en los seres vivos.[3] Por ello, y teniendo en cuenta la salud pública, resulta imperativo monitorizar la concentración de metales pesados en medio acuoso.

El trabajo realizado en esta tesis se concentró esencialmente en dos metales bivalentes: cobre y mercurio. Aunque beneficioso a bajas concentraciones en el metabolismo de los animales, una exposición crónica al cobre – por ejemplo por corrosión de canalizaciones – puede producir daños hepáticos o renales.[3] Por otro lado, una exposición prolongada a mercurio puede causar daños hepáticos o neuronales.[2b] La primera causa de

exposición a mercurio es la ingesta de pescados de gran tamaño, los que a su vez, han sido expuestos a aguas contaminadas. Según la Directiva Marco del Agua de la Unión Europea (Directiva 98/83/EC sobre la calidad de agua para consumo humano), la concentración máxima de cobre permisible es de 2 mg L^{-1} mientras que la de mercurio es de 1 μg L^{-1}.[4]

Sensor químico. En 1996, Peter Wolfbeis definió los sensores químicos como dispositivos analíticos miniaturizados capaces de expresar, en tiempo real y de forma continua, información sobre compuestos específicos o iones en muestras complejas.[5] Un sensor químico puede describirse por tres componentes: i) la muestra, donde un sustrato es reconocido por un receptor; ii) el transductor, que convierte el proceso de reconocimiento en una señal y iii) un procesador que convierte esa señal en un valor distinguible de interés.[5a, 6] El principio de funcionamiento del transductor define el tipo de sensor, siendo los más comunes los electroquímicos y ópticos. Estos últimos han ganado importancia en los últimos 30 años, principalmente merced al uso de fibras ópticas que permiten monitorización a distancia y de forma distribuida.[7]

Detección por luminiscencia. Este método de transducción es uno de los más difundidos entre los sensores ópticos.[8] La luminiscencia es el fenómeno de emisión de luz UV-Vis que resulta del decaimiento radiativo de un electrón en un estado excitado. Este proceso permite observar directamente y con alta sensibilidad el mundo a escala molecular, muchas veces al coste energético de un solo fotón.[9-10] De este modo, todo fluoróforo que sufra un cambio en sus propiedades luminiscentes al entrar en contacto con un sustrato, puede considerarse una sonda molecular.

El mecanismo por el cual la luminiscencia se ve afectada varía en función del par receptor/sustrato. Por ejemplo, los sensores de oxígeno basados en complejos luminiscentes de rutenio(II) dependen de la supresión dinámica del estado excitado triplete a través de la transferencia de energía entre el complejo de Ru(II) y el oxígeno molecular.[11] La supresión dinámica reduce tanto el tiempo de vida del estado excitado como la intensidad de luminiscencia de la sonda, permitiendo así relacionar la reducción de la señal con la concentración de sustrato. Por otro lado, existen procesos de supresión estática de la luminiscencia, que se traducen en una reducción de su intensidad manteniendo el mismo tiempo de vida, independientemente de la concentración de analito. Un ejemplo de estos procesos se observa en sondas moleculares cuyos receptores son quelantes, con estructuras pre-determinadas para determinado analito. El cambio de intensidad tiene origen en el conocido proceso de transferencia de electrón foto-inducida, o PET (del inglés *Photoinduced Electron Transfer*), y se encuentra ilustrado en la Figura 1. Existen otros procesos detrás de los cambios de luminiscencia de un fluoróforo que permiten desarrollar sondas para diferentes analitos, como por ejemplo, la transferencia de protón en el estado excitado para

los sensores de pH,[8, 10, 12] el TICT (del inglés *twisted intramolecular charge transfer*) para sensores de polaridad del medio[13] o la estabilización de un fluoróforo en determinado medio, también para sensores de polaridad.[14]

La formulación matemática de la intensidad de luminiscencia, I_L, se define por la Eq. 1. Se observa que I_L depende de i) la intensidad de excitación o I_{exc}; ii) la sensibilidad del detector o κ y iii) la concentración de fluoróforo o *c*. Una pérdida de eficiencia de los componentes del dispositivo o una reducción de concentración del pigmento conllevan a una menor señal y, por consiguiente, a un falso resultado. Por este motivo, los sensores luminiscentes basados en tiempo de vida del estado excitado son más robustos que los dispositivos basados exclusivamente en intensidad. Además, como el tiempo de vida es una característica intrínseca al fluoróforo, esta técnica de bajo coste también permite monitorizaciones en medios turbios. Un método que permite utilizar las ventajas prácticas de registrar en tiempo de vida a luminóforos que sufren supresión estática de luminiscencia se denomina DLR (del inglés *Dual Lifetime Referencing*).[6, 7b, 15]

Situación actual. Los métodos de análisis recomendados por la agencia estadounidense EPA para determinar metales pesados y otras especies iónicas en aguas son invariablemente costosos, laboriosos y requieren técnicos especializados. Entre ellos se encuentran la espectrometría de masas con fuente de plasma de acoplamiento inductivo (ICP-MS) o la absorción atómica (AA). Sin embargo, existen actualmente dispositivos asequibles capaces no solo de cumplir los requisitos de límite de detección sino también de medir de forma continua y en campo. Muchos de los dispositivos portátiles para especies iónicas se basan en transductores electroquímicos, y son capaces de medir múltiples analitos simultáneamente.[17] Al mismo tiempo, los dispositivos basados en luminiscencia siguen ganando cuota de mercado por las razones antes mencionadas, si bien los dispositivos ópticos comercialmente más extendidos hoy en día son los basados en técnicas de absorción de luz UV.[17c-e, 17h, i]

Los complejos luminiscentes de rutenio(II) son candidatos ideales como luminóforos.[11-12, 18] El indicador ideal posee características que le hacen ser económico: i) elevado rendimiento cuántico y absortividad molar que permiten bajar el coste del detector y de la fuente de excitación; ii) fotoestabilidad; iii) valor elevado de su desplazamiento de Stokes (> 150 nm), lo que permite detectar la emisión con menos interferencias debido a fenómenos de dispersión; iv) largos tiempos de vida de luminiscencia y v) ligandos adaptables, lo que posibilita diseñar un receptor específico para un analito o incluso cambiar propiedades como la solubilidad o la fotofísica del complejo.[18b, 19] Sin embargo, la oferta bibliográfica de sensores de mercurio y cobre basados en cambios de la luminiscencia de complejos de rutenio(II) capaces de medir en medio acuoso es bastante limitada, ya que la mayoría ha sido

estudiada en medio orgánico.[20] La Figura 4 ilustra dos complejos de Ru(II) sensibles a Cu(II) y Hg(II).

Constantes de asociación. El estudio espectroscópico sobre las propiedades fotofísicas de un luminóforo en presencia de un analito permite obtener isotermas de absorción. Estas, a su vez, dan información sobre el equilibrio del sistema, como la estabilidad del complejo supramolecular o la estequiometría. Esta información es importante desde el punto de vista analítico, máxime considerando sus aplicaciones como sensor. Para identificar la estequiometría del sistema, muchas veces desconocida, se suele recurrir a uno de los dos siguientes métodos: el método de Job,[21] y el método de la relación molar; sin embargo, ambos métodos son poco fiables para casos donde la constante de equilibrio sea baja. Otra forma de obtener información sobre la estequiometría de determinado equilibrio es el ajuste de los resultados del estudio fotofísico a las ecuaciones que describen el comportamiento óptico de diferentes equilibrios. La situación que proporcione mejor ajuste es asumida como la real. El desarrollo matemático de las ecuaciones que describen la variación en absorción y emisión de un equilibrio ligando:sustrato 1:1, 2:1 y 1:2 puede encontrarse en las secciones 1.7.1, 1.7.2 y 1.7.3, respectivamente.

Química computacional. Gracias al desarrollo constante de la programación y los microprocesadores, la química computacional es hoy en día una técnica accesible y muy poderosa, con la que el químico puede obtener información a nivel molecular resuelta tanto en el espacio (estructura) como en el tiempo (estados de transición). Este área de la química recurre a aproximaciones, o modelos, para describir el sistema en estudio. La complejidad de los modelos utilizados es función directa del tiempo de CPU y de la calidad de resultados. Uno de los modelos más comunes para describir la estructura electrónica de la materia es el DFT (del inglés *Density Functional Theory*). Este modelo, publicado en los años 60 por P. Hohenberg, W. Kohn y L. J. Sham,[22] se basa en la mecánica cuántica y presenta un buen compromiso entre tiempo de procesamiento y exactitud de resultados. En cálculos sobre complejos de rutenio(II), se verificó que el funcional híbrido B3LYP permite la obtención de buenos resultados.[23] Un resumen de los diferentes tipos de cálculo que se hizo en este trabajo se puede encontrar en la Figura 6.

Complejos luminiscentes de rutenio(II). El análisis del espectro de absorción de un complejo de rutenio(II) permite obtener información sobre su estructura electrónica. En la Figura 8 se pueden observar los espectros de los complejos $Ru(bpy)_3Cl_2$ y $Ru(phen)_3Cl_2$ en medio acuoso. La asignación de las transiciones electrónicas responsables por el espectro de absorción se muestra en la Figura 7. En la región más energética, en el UV, se observan bandas intensas asociadas a los ligandos (LC, IL y LMCT, **1** y **2** en la Figura 7) mientras que las transiciones asociadas al centro metálico se dan a energías más bajas y son de menor

intensidad. Éstas pueden ser: centradas en el metal, a partir de 300 nm (MC, **4** en la Figura 7); o transferencias de carga metal-ligando en torno a 450 nm (MLCT, **3** en la Figura 7).

Considerando la emisión de los complejos de rutenio(II), ésta se da alrededor de 600 nm y resulta de la composición de múltiples decaimientos radiativos a partir del estado excitado triplete, originando así una banda de emisión ancha ($\Phi_{ISC} = 1$).[24] El mismo estado triplete es responsable de los largos tiempos de vida de emisión (0.1 – 10μs).[19a] A través de la absorción de un fotón, existe también la posibilidad de poblar un estado excitado no radiativo – importante en la fotofísica de estos complejos – denominado ^{3}MC (del inglés *Metal Centred*). Este estado, térmicamente alcanzable, es el responsable de la disminución de la luminiscencia cuando se aumenta la temperatura. [19b] El hecho de que las propiedades fotofísicas de los complejos de rutenio(II) dependan no solo del medio sino también de la temperatura permite su utilización más allá de los sensores de especies químicas: también son utilizados como sondas de pH,[12] humedad,[25] disolventes,[14] o temperatura.[8]

Objetivos y planteamiento

El objetivo principal de esta Tesis fue el desarrollo de nuevas sondas luminiscentes sensibles a metales pesados en medio acuoso. Para ello se llevó a cabo la síntesis y caracterización de compuestos de coordinación de rutenio(II) con ligandos heterocíclicos quelatantes diseñados específicamente para cobre(II) y mercurio(II). Igualmente, se sintetizaron y caracterizaron dos sondas de la misma familia funcionalizadas para detección de hidrocarburos en agua. De este modo, el trabajo desarrollado asienta en áreas de la química como la síntesis orgánica, la química analítica, la fotoquímica y la química computacional.

Resultados

Síntesis de ligandos polipiridínicos. Los ligandos quelantes presentados en este trabajo tienen como precursores comerciales la 1,10-fenantrolina (phen) y la 2,2'-bipiridina (bpy) (Figura 10). La síntesis de los ligandos se llevó a cabo mediante pequeñas variaciones sobre rutas sintéticas encontradas en la bibliografía. Algunos precursores y ligandos han sido descritos anteriormente, si bien no se les ha encontrado la aplicación planteada en este trabajo. Entre ellos se encuentran la 1,10-fenantrolina-5,6-diona (pdo),[26] el 5-acetil-2-hidroxi-benzaldeído (ahb),[27] la 4,4'-diamina-2,2'-bipiridina (dab),[28] la 2-(timina-1-il)-1-(1H-imidazol-1-il)etanona,[29] y la 5-amino-1,10-fenantrolina.[19a] De los restantes ligandos quelantes, tres son derivados de la imidazo[4,5-*f*]-1,10-fenantrolina (iip, hmip y haip) y dos son derivados de bpy (bpytym y nody), todos ellos descritos por primera vez en este trabajo.

Entre las técnicas utilizadas para caracterización e identificación de los compuestos heterocíclicos están la resonancia magnética nuclear de protón y carbón (Tablas 2 y 3), espectroscopia de absorción infrarroja, punto de fusión, microanálisis y espectrometría de masas (ver espectros en el capítulo VI).

Síntesis de quelatocomplejos de Ru(II). Para la obtención de los quelatocomplejos heterolépticos de Ru(II) se prepararon inicialmente los precursores bis-quelatocomplejos de Ru(II) con 1,10-fenantrolina o con el ligando comercial 4,4'-dinonil-2,2'-bipiridina. En el siguiente paso se introdujo el tercer ligando mediante el procedimiento de Sullivan.[30] De esta forma se obtuvieron 4 complejos diseñados para sensores de metales $[Ru(phen)_2(iip)](PF_6)_2$, $[Ru(phen)_2(hmip)](PF_6)_2$, $[Ru(phen)_2(haip)](PF_6)_2$ y $[Ru(phen)_2(bpytym)](PF_6)_2$. Se obtuvieron 2 quelatocomplejos de Ru(II) diseñados para sensor de hidrocarburos, un heteroléptico de formula $[Ru(nbpy)_2(nody)](PF_6)_2$ y un quelatocomplejo homoléptico de Ru(II) utilizando el ligando nody, el $[Ru(nody)_3]Cl_2$. Es importante resaltar que el quelatocomplejo $[Ru(phen)_2(iip)](PF_6)_2$ ha sido publicado por nuestro grupo mediante una patente internacional (WO2011009981).[31] Los complejos luminiscentes obtenidos han sido caracterizados de igual modo que los ligandos heterocíclicos (capítulo VI) y también mediante espectroscopia de absorción, emisión y tiempo de vida de luminiscencia.

Estudio fotoquímico de los complejos de Ru(II) sensibles a metales pesados. En la primera parte del trabajo se han caracterizado los complejos de Ru(II), en disolución orgánica y acuosa a diferentes valores de pH, y también en presencia de 10 metales bivalentes (también en disolución acuosa y a distintos valores de pH para identificar el pH óptimo de trabajo). Se observó que el perfil de emisión de las 4 sondas luminiscentes (los complejos iip, hmip, haip y bpytym) es bastante insensible al cambio de disolvente. Sin embargo, la intensidad de emisión se ve reducida al aumentar el pH. A través del programa informático HypSpec se hizo el análisis global a los espectros de absorción en función del pH para la determinación de los valores de pK_a y también en presencia de metales pesados para la determinación de los valores de las constantes de asociación, K_a.

De esta forma, se han determinado 4 valores de pK_a para el complejo $[Ru(phen)_2(iip)]^{2+}$: 3.35 ± 0.01, 5.02 ± 0.01, 8.35 ± 0.02 y 12.10 ± 0.05. La luminiscencia del complejo $[Ru(phen)_2(iip)]^{2+}$ se ve suprimida en un 92% al añadir 5 equivalentes de Cu(II), en un 35% por la presencia de Ni(II) y en un 31% por Hg(II) a pH 7.5. Mediante espectroscopia de tiempo de vida, se determinó la naturaleza de la supresión de luminiscencia observada. Así pues, el Cu(II) y el Hg(II) producen una supresión puramente estática sobre el compuesto $[Ru(phen)_2(iip)]^{2+}$, mientras que en el caso del Ni(II) la supresión es puramente dinámica. Se determinaron las contantes de asociación en presencia de Cu(II) y Hg(II), obteniendo una

estequiometría de 2:1 (complejo-analito). Los valores de K_a se encuentran resumidos en la Tabla 7.

En el caso de los complejos $[Ru(phen)_2(hmip)]^{2+}$ y $[Ru(phen)_2(haip)]^{2+}$ – cuya estructura apenas difiere en el grupo sustituyente en posición *para* de hidroxilo a acetilo respectivamente – se han determinado 3 constantes de protonación. El complejo hmip presenta los valores de pK_a de 2.03 ± 0.06, 7.92 ± 0.03 y 10.36 ± 0.02 mientras que el complejo haip presenta los valores de pK_a de 4.29 ± 0.01, 6.56 ± 0.01 y 9.26 ± 0.03. El estudio de supresión de luminiscencia en presencia de diferentes metales pesados indicó que, mientras la luminiscencia del complejo hmip se ve reducida de forma poco intensa por casi todos los metales (el Cu(II) produciendo una supresión del 45%), el complejo haip presenta una supresión de luminiscencia, en presencia de Cu(II), del 83%; pero también en presencia de Pb(II) (25%) y Hg(II) (14%) (Figuras 32 y 39, respectivamente). La naturaleza de la supresión causada por cobre fue estudiada mediante espectroscopia de emisión resuelta en el tiempo, que confirmó ser puramente estática – indicando una asociación en el estado fundamental entre el ligando haip y el Cu(II). Se determinaron las contantes de asociación en presencia de Cu(II), obteniendo una estequiometría de 2:1 (complejo:analito). Los valores de K_a se encuentran resumidos en la Tabla 10.

Por último se observó que el complejo bpytym presenta 2 valores de pK_a, a 9.42 ± 0.01 y 11.92 ± 0.01, y que sus propiedades espectroscópicas no se ven afectadas por la presencia de los metales estudiados.

Estudio fotoquímico de los complejos de Ru(II) sensibles a hidrocarburos. La segunda parte del trabajo fotoquímico se centró en los complejos cuyos ligandos contienen cadenas alifáticas $[Ru(nody)_3]^{2+}$ y $[Ru(nbpy)_2(nody)]^{2+}$. Para ello se han caracterizado los 2 complejos de Ru(II) en disolventes de distinta polaridad mediante espectroscopia de absorción, emisión y tiempo de vida, esta última variando la temperatura. Se observó que, al aumentar la polaridad del medio, ambas sondas presentan un desplazamiento hipsocrómico y batocrómico, en absorción y emisión, respectivamente. Este resultado está de acuerdo con lo observado para otra sonda luminiscente de Ru(II).[14] El estudio de espectroscopia resuelta en el tiempo demostró una menor relación entre el tiempo de vida de luminiscencia de las sondas y la polaridad del medio. Sin embargo, al aumentar la polaridad parece producirse una disminución del tiempo de vida de luminiscencia del complejo homoléptico, en contraste a lo observado para el complejo heteroléptico, cuyo tiempo de vida de luminiscencia aumenta. Se ha realizado un estudio de tiempo de vida en función de la temperatura para evaluar la accesibilidad térmica del estado excitado no-radiativo ^{3}MC en el caso de los 2 complejos. Los resultados parecen indicar que este estado solo es accesible para el caso del complejo heteroléptico.

Estudio computacional de los complejos de Ru(II) sensibles a metales pesados. El estudio de química computacional – mediante B3LYP/6-31G* DFT y TD-DFT – permitió la racionalización desde el punto de vista fotofísico de algunos de los resultados obtenidos para los complejos iip, hmip, haip y bpytym. Se encontraron así las geometrías de menor energía tanto para el estado fundamental como para el excitado. El estudio de frecuencias corroboró que las estructuras son mínimos reales debido a la ausencia de frecuencias imaginarias. Mediante TD-DFT, se calcularon las energías de las excitaciones verticales, tanto para el estado fundamental (espectro de absorción) como para el estado excitado en multiplicidad singlete (máximo de emisión). El estado excitado más estable de los complejos iip y haip es de naturaleza ^{3}MLCT (transferencia de carga rutenio-ligando funcional). Para el complejo hmip, el estado excitado de más baja energía es ^{3}IL (intra-ligando hmip), mientras que para el caso del complejo bpytym este estado es ^{3}MLCT (transferencia de carga rutenio-phen). Aunque la naturaleza del estado excitado de estos compuestos varíe con la estructura, se observó un cambio en la naturaleza del estado excitado de los 3 complejos iip, hmip y haip al pasar de pH neutro a alcalino, de tal modo que a pH alcalino el estado excitado es ^{3}LLCT. Además del estudio teórico ácido/base, se llevó a cabo también el estudio de las propiedades fotofísicas de los complejos iip y bpytym en presencia de Cu(II) y Hg(II), respectivamente. En el caso del complejo supramolecular 1:1 $[Ru(phen)_2(iip)]^{2+}$-Cu(II), el estado excitado de carácter ^{4}MMLCT es similar al ^{3}MLCT del complejo libre. Éste origina un máximo de emisión teórico un 7% menos energético que el observado experimentalmente. Además, se encontró también una estructura asociada a un estado excitado de más baja energía centrado en el Cu(II), denominado $^2D_{twist}$. No obstante, en el caso del complejo supramolecular $[Ru(phen)_2(bpytym)]^{2+}$-Hg(II) no se observa ningún cambio en la naturaleza del estado excitado ni en el máximo de emisión teórico respecto al complejo libre.

Conclusiones.

Fotoquímica. La Tabla 20 reúne algunas de las propiedades fotoquímicas de los complejos luminiscentes de Ru(II) diseñados como sondas de metales pesados. Se observó que todos presentan propiedades espectroscópicas similares, tanto en el estado fundamental como en el estado excitado. Sin embargo, el complejo $[Ru(phen)_2(bpytym)]^{2+}$, que contiene un ligando derivado de la 2,2'-bipiridina, presenta el máximo de emisión desplazado hacia el rojo (20 nm). Esto se debe posiblemente a la diferencia estructural entre los esqueletos bpy y phen.

Comparando la afinidad de los complejos iip y haip a Cu(II) mediante los valores de las constantes de asociación, se verifica que el complejo haip presenta mayor afinidad hacia el cobre, lo que puede justificar su mejor selectividad. Sin embargo, un valor de K_a superior no

implica mejor sensibilidad, ya que en el caso del complejo iip la luminiscencia se ve suprimida en 92%, mientras que la luminiscencia del complejo haip solo es suprimida en 83%.

Aunque los dos complejos hmip y haip tengan sitios de unión similares, ellos muestran respuestas significativamente diferentes frente a Cu(II). Se propone que la influencia del grupo sustituyente del fenol en posición *para* produce un cambio drástico en la acidez del grupo hidroxilo. El grupo donador metoxi, comparado con el grupo aceptor acetil, cambia el valor de pK_a del grupo hidroxilo de 7.9 a 6.6 en los complejos hmip y haip, respectivamente. De esta forma, la mayor acidez del ligando haip permite su acentuada afinidad por el catión cobre(II) al pH de trabajo.

El complejo bpytym no presentó algún tipo de sensibilidad ni a Hg(II) ni a los restantes metales estudiados. Los estudios de química computacional sugieren que el evento de unión entre el ligando bpytym y el Hg(II) es posible; pero que no altera la estructura electrónica del complejo, por lo que no hay señalización de tal evento. Como el estado excitado de los complejos libre y en presencia de Hg(II) se encuentra dirigido hacia el ligando espectador 1,10-fenantrolina, quizá se pudiera activar la respuesta de este complejo mediante la sustitución de los ligandos 1,10-fenantrolina, ricos en electrones, por 2,2'-bipiridina.

La estructura de los ligandos iip, hmip y haip fue diseñada teniendo como objetivo la afinidad hacia el cobre(II). La Figura 83 compara la respuesta a metales de estos tres complejos. Se observa que el objetivo fue conseguido, dado que el Cu(II) es el metal que más respuesta obtiene por parte de los complejos luminiscentes, y produce una supresión estática de la luminiscencia.

Las sondas luminiscentes sensibles al disolvente presentan mayor estabilización en medio polar, como queda demostrado en la Figura 84. Se verificó la insuficiencia del modelo (*Lippert-Mataga*) empleado para describir el comportamiento de los pigmentos catiónicos en los distintos disolventes, al observarse una notoria dispersión de algunos puntos respecto del comportamiento predicho por este modelo. Se consideró la posibilidad de que esto ocurra debido a la presencia de grupos amida en el ligando nody, que pueden ser responsables por interacciones especificas sonda-disolvente. Sin embargo, al despreciar los puntos de mayor dispersión, el modelo Lippert-Mataga indica que este complejo ostenta una mayor dependencia de la polaridad del medio que el complejo homoléptico, e incluso que otro complejo publicado anteriormente.[14]

Estudio computacional. En este estudio, se observó que el funcional hibrido B3LYP produce resultados más precisos que el funcional CAM-B3LYP. Los espectros de absorción fueron reproducidos con éxito, tanto para las especies neutras como para las distintas especies ácido/base de los complejos. El máximo de emisión se obtuvo mediante dos técnicas,

TD-DFT y Δ-SCF, donde la ultima produjo resultados con menor error respecto a los valores experimentales. La disminución de la intensidad de luminiscencia de los 3 complejos iip, hmip y haip en pH alcalino se justifica debido al cambio de la naturaleza del estado excitado, que pasa de ^{3}MLCT (o ^{3}IL) a ^{3}LLCT. La supresión de luminiscencia de $[Ru(phen)_2(iip)]^{2+}$ causada por Cu(II) fue justificada con éxito por la generación de una nueva vía de desactivación no radiativa al unirse el Cu(II), a través de un estado excitado de más baja energía centrado en Cu(II).

Como **aportaciones fundamentales de esta Tesis**, pueden destacarse: (i) en el campo de la *Química Orgánica* y de *Coordinación*, la preparación y caracterización estructural exhaustiva de nuevos ligandos heterocíclicos quelatantes de carácter *ditópico*, capaces de coordinar simultáneamente dos metales de transición, además de un nuevo ligando de carácter hidrófobo, así como de sus correspondientes complejos luminiscentes con Ru(II), como útiles sondas de metales de transición y polaridad de disolvente; (ii) en el campo de la *Fotoquímica* y de la *Química Computacional*, este trabajo supone un avance importante en la comprensión, racionalización y predicción de los procesos de desactivación de los estados excitados de complejos de Ru(II) con ligandos heterocíclicos de tipo α-diimina, inducidos tanto por la variación del pH del medio, como por la presencia de un metal de transición diferente, coordinado al ligando ditópico, o por la temperatura; (iii) desde el punto de vista de la *Química Analítica*, la Tesis representa una aportación significativa para el desarrollo de dispositivos sensores opto-electrónicos, capaces de monitorizar in situ y en continuo, la concentración en agua de iones de metales de transición como es el Cu(II) o de hidrocarburos, gracias al desarrollo ex-novo de indicadores específicos antes desconocidos, cuyas características fotoluminiscentes permiten la utilización de la tecnología comercial desarrollada para monitorizar el oxígeno disuelto en aguas (la patente PCT concedida WO2011009981 de los indicadores y películas sensoras así lo atestigua); (iv) en el área de la *Química Medioambiental*, este trabajo representa la posibilidad real de disponer de sensores para monitorizar la contaminación por cobre de las aguas superficiales y subterráneas, o detectar la presencia y el nivel de concentración de hidrocarburos en dichas aguas.

References/Referencias

[1] J.-M. Lehn in *Design of organic complexing agents. Strategies towards properties*, Alkali Metal Complexes with Organic Ligands, *Vol. 16,* Springer Berlin / Heidelberg, **1973**, pp. 1-69.
[2] a) N. K. Srivastava and C. B. Majumder, *J. Hazard. Mater.* **2008**, *151*, 1-8; b) L. Järup, *Brit. Med. Bull.* **2003**, *68*, 167-182.
[3] F. Fu and Q. Wang, *J. Environ. Manage.* **2011**, *92*, 407-418.
[4] in *Drinking Water Directive*, European Commission, **1998**.
[5] a) C. McDonagh, C. S. Burke and B. D. MacCraith, *Chem. Rev.* **2008**, *108*, 400-422; b) G. G. Cammann, E. A. Guilbault, H. Hal, R. Kellner and O. S. Wolfbeis in *Proceedings of the Cambridge Workshop on Chemical Sensors and Biosensors*, The Cambridge Definition of Chemical Sensors, *Vol. 1,* Cambridge University Press, New York, **1996**.
[6] T. Mayr in *Optical sensors for the determination of heavy metal ions*, *Ph.D. Thesis*, Regensburg, Regensburg, **2002**, p. 140.
[7] a) X.-D. Wang and O. S. Wolfbeis, *Anal. Chem.* **2012**, *85*, 487-508; b) G. Orellana and D. Haigh, *Curr. Anal. Chem.* **2008**, *4*, 273-295.
[8] G. Orellana, C. Cano-Raya, J. López-Gejo and A. R. Santos in *Online Monitoring Sensors*, (P. Wilderer), Treatise on Water Science, *Vol. 3,* Elsevier, Oxford: Academic Press, **2011**, pp. 221–262.
[9] R. A. Bissell, A. P. de Silva, H. Q. N. Gunaratne, P. L. M. Lynch, G. E. M. Maguire and K. R. A. S. Sandanayake, *Chem. Soc. Rev.* **1992**, *21*, 187.
[10] G. Orellana in *Fluorescence-based sensors*, (F. Baldini, A. N. Chester, J. Homola and S. Martellucci), Optical Chemical Sensors, *Vol. 224,* Springer Netherlands, **2006**, pp. 99-116.
[11] J. López-Gejo, D. Haigh and G. Orellana, *Langmuir* **2009**, *26*, 2144-2150.
[12] L. Tormo, N. Bustamante, G. Colmenarejo and G. Orellana, *Anal. Chem.* **2010**, *82*, 5195-5204.
[13] a) W. Rettig and R. Lapouyade in *Fluorescence probes based on twisted intramolecular charge transfer (TICT) states and other adiabatic photoreactions*, (J. R. Lakowicz), Topics in fluorescence spectroscopy, *Vol. 4,* Plenum Press, New York, **1994**, pp. 109-149; b) N. Ghoneim, *Spectrochim. Acta, Part A* **2000**, *56*, 1003-1010.
[14] A. M. Castro, J. Delgado and G. Orellana, *J. Mater. Chem.* **2005**, *15*, 2952-2958.
[15] T. Mayr, I. Klimant, O. S. Wolfbeis and T. Werner, *Anal. Chim. Acta* **2002**, *462*, 1-10.
[16] in *Technical Notes on Drinking Water Methods*, Environmental Protection Agency, **1994**, p. 112.
[17] a) http://www.astisensor.com; b) http://www.nexsens.com; c) https://www.ysi.com; d) http://www.hach.com; e) http://www.swan.ch; f) http://www.nico2000.net; g) http://www.in-situ.com; h) http://www.s-can.at; i) http://www.horiba.com; j) http://www.hannainst.com; k) http://www.environnement-sa.com
[18] a) M. Bedoya, M. T. Diez, M. C. Moreno-Bondi and G. Orellana, *Sens. Actuators, B* **2006**, *B113*, 573-581; b) E. N. Dixon, M. Z. Snow, J. L. Bon, A. M. Whitehurst, B. A. DeGraff, C. Trindle and J. N. Demas, *Inorg. Chem.* **2012**, *51*, 3355-3365; c) H. M. Rowe, W. Xu, J. N. Demas and B. A. DeGraff, *Appl. Spectrosc.* **2002**, *56*, 167-173.
[19] a) D. Garcia-Fresnadillo and G. Orellana, *Helv. Chim. Acta* **2001**, *84*, 2708-2730; b) S. Campagna, F. Puntoriero, F. Nastasi, G. Bergamini and V. Balzani in *Photochemistry and photophysics of coordination compounds: Ruthenium*, (S. Campagna and V. Balzani), Photochemistry and Photophysics of Coordination Compounds I, *Vol. 280,* Springer-Verlag Berlin, Berlin, **2007**, pp. 117-214.
[20] a) E. Coronado, J. R. Galan-Mascaros, C. Marti-Gastaldo, E. Palomares, J. R. Durrant, R. Vilar, M. Gratzel and M. K. Nazeeruddin, *J. Am. Chem. Soc.* **2005**, *127*, 12351-12356; b) X. Li, Y. Chen, J. Meng, K. Lü, A. Zhang and B. Zhang, *Chinese J. Chem.* **2011**, *29*, 1947-1950; c) P. Comba, R. Kramer, A. Mokhir, K. Naing and E. Schatz, *Eur. J. Inorg. Chem.* **2006**, 4442-4448; d) A. M. Josceanu, P. Moore, S. C. Rawle, P. Sheldon and S. M. Smith, *Inorg. Chim. Acta* **1995**, *240*, 159-168.
[21] A. Job, *Annales de Chimie* **1928**, *9*, 113-203.

[22] a) P. Hohenberg and W. Kohn, *Phys. Rev.* **1964**, *136*, B864-B871; b) W. Kohn and L. J. Sham, *Phys. Rev.* **1965**, *140*, A1133-A1138.
[23] a) A. D. Becke, *J. Chem. Phys.* **1993**, *98*, 1372-1377; b) C. Lee, W. Yang and R. G. Parr, *Phys. Rev. B* **1988**, *37*, 785-789.
[24] V. Balzani, G. Bergamini, F. Marchioni and P. Ceroni, *Coord. Chem. Rev.* **2006**, *250*, 1254-1266.
[25] M. C. Moreno-Bondi, G. Orellana and M. Bedoya in *Fibre optic sensors for humidity monitoring*, Springer Series on Chemical Sensors and Biosensors, *Vol. 1,* Springer-Verlag, **2004**, pp. 251-280.
[26] M. Yamada, Y. Tanaka, Y. Yoshimoto, S. Kuroda and I. Shimao, *Bull. Chem. Soc. Jpn.* **1992**, *65*, 1006-1011.
[27] a) N. U. Hofsløkken and L. Skattebøl, *Acta Chem. Scand.* **1999**, *53*, 258-262; b) A. Tromelin, P. Demerseman and R. Royer, *Synthesis* **1985**, *1985*, 1074-1076; c) P. Kahnberg, C. W. Lee, R. H. Grubbs and O. Sterner, *Tetrahedron* **2002**, *58*, 5203-5208.
[28] a) G. Maerker and F. H. Case, *J. Am. Chem. Soc.* **1958**, *80*, 2745-2748; b) P. Kavanagh and D. Leech, *Tetrahedron Lett.* **2004**, *45*, 121-123.
[29] Y. Inaki and H. Hiratsuka, *J. Photopolym. Sci. Technol.* **2000**, *13*, 739-744.
[30] B. P. Sullivan, D. J. Salmon and T. J. Meyer, *Inorg. Chem.* **1978**, *17*, 3334-3341.
[31] M. G. Orellana, R. J. L. Urraca and A. Ribeiro dos Santos, *Method for preparing thin films for chemical optical sensors*, Universidad Complutense de Madrid, Spain, **2011**, p. 19.

Chapter I

Background

1.1. Introduction

Nature abounds with examples of simple chemical species associating into supramolecular arrangements with higher functionality. This tendency to an increase in complexity plays a major role in evolution, as higher complexity brings more information into the system. The driving force of such association is controlled by thermodynamics meaning that a more stable supramolecular entity possesses less total energy than its separated chemical entities. The same principle applies to molecular selectivity, meaning that a particular ligand can better recognize a substrate over any other ligand. Better selectivity can arise from structure (molecular hindrance vs. matching shapes), bonding interactions (opposite charges vs. similar charges) or other factors that lower the system's total energy. In fact, the study of the phenomena that determine the stability of a ligand-substrate entity improves our capacity to design systems capable of specific molecular recognition.[1]

One of the many advantages of such smart design is to have molecules as building blocks for *chemical* sensors capable of providing us with information (through molecular recognition) about certain species relevant to industrial processes, aquatic life or the human health. Naturally, this bio-compatible media is mainly water, where several parameters are of great importance, e.g. glucose or other metabolites in blood, heavy metals in water, pH, dissolved oxygen or other gases, hydrocarbons, or temperature, to name a few.

1.2. Heavy metals in water

Since the beginning of the industrial revolution in Britain at the end of the XVIIIth century, industrial processes have been responsible for continuous wastewater discharges into the environment, often rich in toxic heavy metals like iron, cobalt, copper, zinc and tin, among others. Heavy metals are considered those elements weighting between 63.5 and 200.6 and with a specific density greater than 5 g cm^{-3},[2] i.e. all the elements between copper and mercury. Nevertheless, the term "heavy metal" is sometimes broadened to other metals like aluminium, cobalt or iron. Cadmium and lead ions, for instance, are common in battery production, and aluminium smelting is known to produce heavy-metal rich wastewaters. In addition to industrial processes, waterborne heavy metals may also originate from less massive production sources such as the use of aluminium as flocculating agent in swimming

pools.[3] The reason why heavy metals represent such threat lies in the fact that not only are they toxic but also non-biodegradable, so that they tend to accumulate in significant concentrations becoming persistent either in Nature or living organisms.[4]

By now, one should be concerned with the effects of such hazardous species in the ecosystem and, more importantly, in public health. Particular focus should be placed on the ones that are main threats to human health, namely lead, cadmium, mercury and arsenic.[2b] Despite the knowledge that heavy metals are hazardous to all forms of life (when in toxic concentrations), these are still present in many water sources around the globe, sometimes with increasing concentrations. For this reason, in situ monitoring of heavy metals in water gains relevance, taking into consideration that the different analytes and concentrations depend on the origin and use of the aqueous source. This fact is clearly exemplified by noting that, according to the US Environmental Protection Agency (EPA), the toxic concentration of arsenic to the aquatic community is 340 mg L^{-1} while the same parameter applied to drinking waters is reduced to 0.010 mg L^{-1}.[5]

The work presented in this Thesis deals mainly with two divalent heavy metals, copper and mercury. Copper is known to have beneficial properties in the animal metabolism at trace concentrations. Nevertheless, if present in high concentrations, it can cause gastrointestinal distress leading to vomiting after short term exposure, but also liver or kidney damage if the organism is subject to long term exposure e.g. due to corrosion of old household plumbing systems.[4] According to the EPA, the maximum contaminant level (MCL) for copper in drinking waters is 1.3 mg L^{-1}; however it also recommends reducing this value to 1.0 mg L^{-1} to avoid alterations such as colour or taste.[5] In contrast to the EPA, the European Commission *Drinking Water Directive* mandates that the limit concentration for copper in drinking water be below 2.0 mg L^{-1}.[6]

As far as toxic mercury ions is concerned, the MCL is 0.002 mg L^{-1} in the United States, while in the Europe Union this value is 0.001 mg L^{-1}.[5-6] Mercury can cause a variety of diseases like kidney or neurological damage.[2b] It may originate from industrial wastewater discharges, landfills of waste and croplands leakages. The primary source of human mercury ingestion is fish, in particular big fish (tuna, swordfish, etc.) that have been exposed for longer periods of time to hazardous mercury ions.

1.3. Definition of chemical sensor

The definition of chemical sensor has been somewhat dynamic throughout the last thirty years, being updated as necessary and also with several literature examples of its misuse. In 1990 Wolfbeis defined “chemical sensors” as:

(…) "small-sized devices comprising a recognition element, a transduction element, and a signal processor capable of continuously and reversibly reporting a chemical concentration."[7]

This interpretation states that if a device is to be considered as a chemical sensor it is mandatory that it functions in a *continuous and reversible* way, eliminating from such group all test strips and disposable sensing schemes ("dosimeters"). One year later, the International Union of Pure and Applied Chemistry (IUPAC) published a more extended definition for chemical sensor to satisfy a wider number of scientists:

"A device that transforms chemical information, ranging from the concentration of a specific sample component to total composition analysis, into an analytically useful signal. The chemical information, mentioned above, may originate from a chemical reaction of the analyte or from a physical property of the system investigated. Chemical sensors contain two basic functional units: a receptor and a transducer part. Some sensors may include a separator which is, for example a membrane."[8]

The document includes more details on the different types of chemical sensors, but its main definition lacks the above mentioned notion of reversibility. Currently, the most accepted definition of a chemical sensor dates from 1996, when Prof. Wolfbeis made a slight modification to his first definition, stating:

"Chemical sensors are miniaturised analytical devices that can deliver real-time and online information on the presence of specific compounds or ions in complex samples."[9]

Such statement is also known as the "Cambridge definition" and, although missing the term *reversible,* it states that a sensor must perform under *online* operation mode which implies it should work either reversibly, or be capable of (fast unattended) *in situ* regeneration.[3] This feature allows lower costs for sensing devices as they require less human intervention. In a recent publication, the authors show concern over the severe general misuse of the term chemical sensor in the last decade, justifying its use as the sole purpose of augmenting publication value.[10]

The chemical sensing device may be described by three separate components: the *sample* which contains one or more analytes to be recognized by the molecular "detector", a

transducer which accounts for the conversion of such recognition patterns into a measurable signal, and a *signal-processor* to relate the signal into analyte concentration.[9a, 11]

The first component is generally behind the sensor selectivity, involving molecular recognition in many cases. *Molecular recognition* is defined as "the energy and the information involved in the binding and selection of substrate(s) by a given receptor molecule; it may also involve a specific function".[12] Jean Marie Lehn emphasized the term recognition, defining it as binding with a purpose, involving a pattern detection process through a structurally well-defined set of intermolecular interactions. As pointed out in the Introduction section, binding of a guest and a host forms a complex characterised by its thermodynamic and kinetic stability and selectivity, that is the amount of information brought into operation.[13]

The *operating principle* of the transducer is what usually defines the chemical sensor group. Numerous literature reports describe the features of such groups, the two major ones being *electrochemical* and *optical*, but others are also identified such as electrical, mass-sensitive, magnetic and thermometric sensors.[3, 7-8, 10, 14] Electrical devices differ from the electrochemical ones in that the former do not measure a reaction as the signal is related to the change of (electrical) properties upon interaction with the analyte. Mass-sensitive devices include piezoelectric and acoustic wave phenomena, magnetic devices are based on paramagnetic effects, and thermometric devices measure the heat of a specific chemical reaction. Electrochemical devices include voltammetric, potentiometric (amperometric) and chemical sensitized field effect transistor (chemFETs) sensors. Finally, the optical sensors branch out in subgroups based on absorbance, reflectance, luminescence, fluorescence, refractive index, optothermal, light scattering and plasmonic resonance effects.

The third subset of an optical sensor comprises the light source, the detector, and signal-processing unit. In the optical sensors group there are also important components that have been introduced to improve sensing capabilities such as optical fibres, waveguides or integrating spheres. These optical sensing devices, often called *optodes*, have been growing in importance for the last three decades largely due to the use of optical fibres which allow for remote and distributed measurement, less interference from the environmental light, operation in hazardous sites for either human beings or the instrumentation, as they require only a small sensing layer on the tip or cladding of the fibre to be placed inside the sampled media (*in situ* measurement).[10, 15]

1.4. Luminescence detection

Fluorescence and phosphorescence are sub-classes of a more general process called luminescence. The latter can also be classified as chemiluminescence, electroluminescence, radioluminescence, sonoluminescence, etc., depending on the mode of the (electronic) excitation. Luminescence describes the emission of ultraviolet/visible/near infrared light that takes place when an excited electron finds a radiative path towards deactivation. This process allows the researcher a direct visualization of what is happening at the molecular level.[16] In fact, every light source we know being either our mid-aged sun's nuclear fusion, a light bulb or the beautiful glow worm, emits light as luminescence.[14b]

The difference between fluorescence and phosphorescence lies in the average time it takes the emitted light to fade out from the moment an "instant" excitation was made. Although there is no well-defined rate to separate fluorescence from phosphorescence, the accepted values are around 10^8 s^{-1} (lifetimes of ca. 10 ns) for fluorescence and slower rates of 10^3 s^{-1} (lifetimes around milliseconds or more) for phosphorescence processes.[17] The reason why fluorescence is a fast decaying process lies on the overall spin of the excited molecule, where the excited electron remains with opposite spin to the ground state electron in the transition-originating orbital. The decay from this singlet excited state is spin-allowed hence the high probability for the radiative emission to occur in competition with (fast) non-radiative processes such as *internal conversion*. On the other hand, if the excited electron finds its way towards a more stable triplet state, a process known as *intersystem crossing* (ISC) occurs. Emission from this triplet excited state is spin-forbidden and therefore, less probable (slower), leaving opportunity for other non-radiative decay processes to occur.

Nevertheless, there are some classes of compounds that exhibit hybrid behaviour, with excited state lifetimes in the interval between those of fluorescence and phosphorescence processes. These are preferably referred to as *luminescent* compounds, where metal-ligand complexes (either coordination or organometallic compounds) are the paradigm. The *heavy-atom* effect (acceleration of the ISC rate) is responsible in these cases for the "mixed" singlet-triplet spin system, particularly known for rhodium(II), ruthenium(II), osmium(II) and iridium(II) complexes.[17-18]

Luminescence is becoming one of the most commonly used tools for chemical sensing.[3] This is greatly due to miniaturization and efficiency developments of the optical platforms that improve their response in terms of sensitivity, selectivity, stability, robustness, and response time, among others. On the other hand, luminescence-based sensors still need perfection to overcome interferences such as temperature, turbidity, or even other analytes that yield false positives – especially in the case of molecular probes designed for analyte binding.[3, 14b, 19] Any fluorophore that undergoes a change in its initial luminescence

properties upon the analyte addition, *e.g.* quenching or increase of its emission ("turn-off" or "turn-on" sensing, respectively), emission wavelength shift or emission lifetime variations is a potential molecular probe. Depending on the parameter to be detected, the *mechanism* behind the observed luminescence change will be different. Luminescent-based molecular oxygen sensors, for example, make use of the *energy transfer* after collisional quenching of a triplet excited state, that reduces both the intensity and lifetime of photoexcited coordination complexes due to dynamic *quenching*.[20] Other molecular probes with pre-determined receptors designed for specific binding display static luminescence quenching and for this reason no change in their excited state lifetimes is observed. The change in the luminescence features of the latter occurs often by a well-known process called *photoinduced electron transfer* (PET) and is often used for cations and anions sensing. This quenching mechanism can also be used for "turn-on" probes if the quencher is part of the fluorophore (see section 1.6). Upon the analyte binding, usually ionic species, the orbitals in the moiety responsible for the quenching of the emission are no longer available and an increase of the luminescence intensity is observed. Since an excited molecule has higher oxidation and reduction potentials than its ground state, PET can occur when a molecular orbital (intramolecular or supramolecular) has a certain energy between the HOMO (highest occupied molecular orbital) and LUMO (lowest unoccupied molecular orbital) of the fluorophore (Figure 1). If this orbital is vacant, an electron transfer from the previous LUMO of the excited fluorophore can take place (Figure 1a) yielding a transient oxidized fluorophore species (F^+). In contrast, if the relevant orbital of the quencher species is occupied, an electron transfer from this orbital to the HOMO of the excited fluorophore can occur (Figure 1b) yielding a transient reduced fluorophore species (F^-). Both mechanisms are responsible for the recovery of the ground state of the fluorophore via a non-radiative decay of the emission.

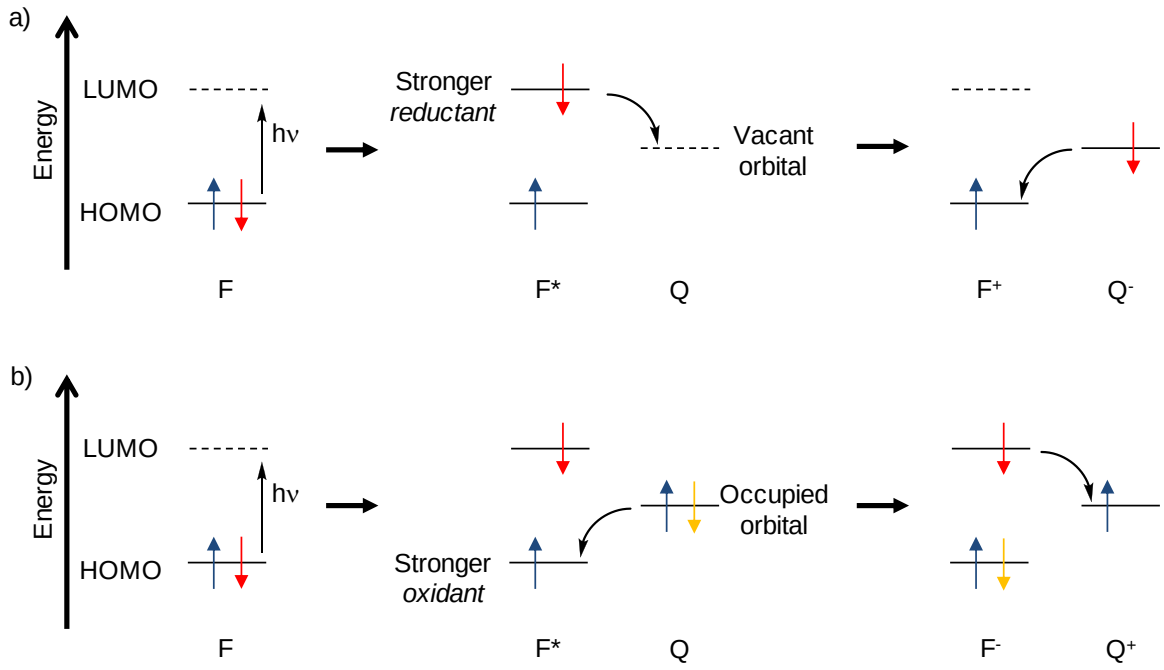

Figure 1. Simplified energy diagram for a fluorophore (F) and quencher (Q) involved in a photoinduced electron transfer (PET) quenching mechanism. Depending on the electron distribution the process can occur via a vacant or occupied orbital of the quencher (a) and (b), respectively.

The excited state fluorophore is considered as a different "compound" than its ground state counterpart, due to its different electronic distribution. For this reason, many compounds display different protonation constants in their ground and excited states. This excited state *proton transfer* to/from the photoexcited molecule is behind the mechanism of many pH sensors.[3, 14b, 21]

Compounds like Nile red, that undergo *twisted intramolecular charge transfer* (TICT) upon excitation are known to be good polarity probes, normally with significant emission wavelength shifts depending on the media (solvatochromism).[22] Another feature useful for polarity sensing takes advantage of solvent stabilization of the molecular probe, showing a dependence of the absorption, emission and the excited state lifetime with the solvent (see section 1.10).[23]

A mechanism that indirectly influences the luminescent properties of a fluorophore is known as *Förster resonance energy transfer* (FRET), sometimes incorrectly called *fluorescence* resonance energy transfer.[24] In this case, there is a spectral overlap between the absorption profile of an acceptor molecule or moiety and the emission band of the donor fluorophore. Upon analyte binding, the changes in the absorption of the acceptor affect the efficiency of the energy transfer process.[14b]

Under the purpose of a luminescent sensor design, *intensity-based* sensors have particular drawbacks when compared to *lifetime-based* devices. To better describe such limitations, it is useful to mathematically express the luminescence intensity as a function of all the relevant factors that determine its value in a luminophore:

$$I_L = I_{exc}\,\Phi_L\,\kappa\,\varepsilon_\lambda\,l\,c \qquad \text{Eq. 1}$$

where the luminescent intensity, I_L is directly proportional to i) the intensity of the excitation light, I_{exc}; ii) the emission quantum yield, Φ_L, which is given by the ratio of emitted vs. absorbed photons; iii) the emission collection efficiency, κ, comprising all instrumental parameters. The product $\varepsilon_\lambda lc$ describes the absorption of the fluorophore, according to the *Beer-Lambert-Bouguer law* in which ε_λ is the molar absorption coefficient at the excitation wavelength λ, given in $dm^3\ mol^{-1}\ cm^{-1}$; l is the optical pathlength in cm and c is the concentration of fluorophore in mol dm^{-3}.

The mentioned drawbacks lie in the fact that, from Eq. 1, it is evident that the luminescence intensity measurements are affected by the intensity of the excitation light source and the detector sensitivity. These are known to lose efficiency upon prolonged use. Moreover, it is also directly proportional to the concentration of luminophore, the level of which can decrease over time by leaching (insufficient membrane affinity), bleaching (photodegradation), or irreversible receptor-analyte associations.

On the other hand, the use of the emission lifetime as transduction method makes luminescence measurements immune to all of those factors, and even allows determinations through turbid samples as the excited state lifetime is an intrinsic property of every fluorophore. However, more than one emitting species are usually observed if the fluorophore finds itself in different environments, either due to heterogeneous immobilization sites or aggregates within the sensitive film. The mathematical expression that describes the emission decay profile, I_t is given by a sum of exponentials:

$$I_t = \sum_i I_i e^{\frac{-t}{\tau_i}} \qquad \text{Eq. 2}$$

where I_i is the intensity over time in the emission decay profile after the end of the excitation pulse, τ_i is the luminescence lifetime (reciprocal of the rate constant of the emission decay of the species i). If there is only one emitting species, then the profile becomes mono-exponential and Eq. 2 is simplified.

In the case where the profile requires a multi-exponential fit, then a *mean emission lifetime* value is used to describe the overall process, the most common of which is the pre-exponential weighted mean lifetime, τ_M:[25]

$$\tau_M = \frac{\sum_i I_i \tau_i}{\sum_i I_i} \qquad \text{Eq. 3}$$

Finding a good fit to a multiexponential function by no means indicates that an equal number of species of different emission lifetimes exists within the sensor film. It usually represents different populations of emissive species with similar lifetimes that cannot be resolved by the luminescence spectrometer.[26]

With cheaper, powerful, smaller light sources and faster electronics, sensing based on pump-probe lifetime measurements is gaining importance. Yet, an even cheaper method relies on *phase*-sensitive excited state lifetime determination methods, by measuring the modulated emission upon exciting the fluorophore with a modulated light source.[3]

There is a technique that takes advantage of devices that use phase-sensitive detection to measure intensity changes in the fluorophore emission. The dual lifetime referencing (DLR) method, requires two luminophore molecules with similar spectral characteristics (overlapping excitation and detection wavelengths) but quite different excited state lifetimes. The long-lived molecule acts as a reference while the short-lived is the actual analyte-sensitive fluorophore. The phase shift of the mixed modulated emission profile of the two dyes is related to the ratio of their intensities, so when the intensity changes upon analyte binding it gets reflected on the apparent emission lifetime measured.[11, 15, 27]

1.5. Current methods for ion detection

The report *Technical Notes on Drinking Water Methods* of the EPA,[28] contains a list with the water analysis methods to be used for several parameters, including heavy metals and other ionic species. Among the techniques mentioned therein, Inductively Coupled Plasma Mass Spectrometry (ICP-MS), Atomic Absorption (AA), Platform Atomic Absorption (PAA), Hydride Atomic Absorption (HAA) and Furnace Atomic Absorption (FAA) are found. Those analytical methods require several steps to be carried out by specialized personnel, such as field trips for regular sampling –which often needs pre-treatment–, as well as chemical analysis in expensive laboratory equipment. Such tedious expensive approaches are necessary to meet the detection limits defined by the environmental agencies.

Nevertheless, there are already commercially available platforms that not only meet the detection limit requirements, but also provide *in-situ* online monitoring. When

considering portable (and affordable) sensors, the most common sensing devices for waterborne ionic species detection still rely on electrochemical processes for signal transduction. Ion-selective electrodes (ISE) are available for a manifold of relevant ionic species such as ammonium, chloride, iodide, fluoride, nitrate, potassium, sodium and heavy metals.[29] There are many mechanisms behind the generation of a current that relates to the concentration of an analyte in ISE, an example being the calcium electrode. A poly(vinyl chloride) (PVC) membrane is functionalized with an organic receptor responsible for binding and transportation of calcium ions. The transport leads to a difference in the electrical potential between both sides of the membrane leading to a measurable current proportional to the concentration.[3]

It may be expected that optical detection schemes become the best option in the future for selected applications, due to the advantages that have already been discussed in section 1.3, in particular those relying on luminescence transduction. Yet, most of the commercially available optical devices for ion sensing employ UV *absorption* techniques.[29c-e, 29h, i] Some even offer multi-parameter sensing by adopting a chemometric approach, a powerful statistical method behind *optical noses*.[30] Included among the optical transduction methods are found many useful commercial products that do not display a reversible response (e.g. test strips or colorimetric solutions), and should not be considered *true* sensors but rather dosimeters.[3]

1.6. Luminescent ion sensors

Among the optical devices used for ion sensing, the best choice is probably those based on the changes in the luminescent properties of *indicator dyes*. This is due to the high *sensitivity* offered by supramolecular single receptor-analyte arrangements taking into account that sometimes a *single* photon is just the required energy for obtaining a signal.[14b] With regard to the sensor device, the indicator dye is placed in close contact with the sample of interest by immobilization in permeable polymer supports, or even on the optical fibre surface (either the tip or as cladding replacement). The sensor response rate depends on how long it takes for the waterborne analytes to diffuse into the sensing layer. It is clear that the thinner a film is, the faster the response rate but the lower amount of luminophore molecules it can bear. With this principle in mind, desirable characteristics for ion indicator dyes are high quantum yields and high molar absorption coefficients. It is also convenient that the excitation light sources are powerful enough for maximizing the electron excitation although, unfortunately, they lead to higher photobleaching through excited state intermediates, and ultimately to signal drift.[14b] Another issue related to polymer supports is the increase of

scattering effects due to the heterogeneity of the medium. In order to avoid interference from the scattered light, the detection wavelength should be red-shifted as much as possible from the excitation wavelength. For this reason, indicator molecules with a large *Stokes* shift (in rough terms, the energy difference between the lowest lying absorption and the emission wavelengths, see section 1.9.3), such as those displaying an *intramolecular charge transfer* (ICT) excited state (section 1.4) or metal-to-ligand charge transfers observed in metal complexes (see section 1.9), are preferable.[14b, 17]

Another driving force that warrants research in this field is the quest for *selectivity* improvement through smart molecular design, in order to obtain specific receptor moieties for particular analytes, avoiding the drawback of interfering ions. This is particularly true in the case of heavy metal sensing, where the analytes often present electronic similarities (ion radius, charge, coordination number, hardness) and, therefore, similar affinities towards the synthetic receptors.[19] This fact leads of course to false positives.

The previous two paragraphs discuss the importance of both sensitivity and selectivity in the design of indicator dyes. The first parameter is associated with *photophysics* while the latter is associated with *supramolecular* chemistry. In luminescent ion sensors, the indicator dye is normally composed of a **receptor** moiety linked to a **luminophore**, in close proximity or via a spacer chain. The assembly depends mainly on the analyte, which dictates the *signalling mechanism* (energy transfer, PET, PCT, etc.) and the *ligand topology*. As an example, small ions such as sodium or potassium show affinity for crown ethers containing heteroatoms like oxygen or nitrogen. Since nitrogen atoms in crown ethers possess a lone electron pair, a nearby fluorophore will not display emission due to a PET process from the nitrogen atom to the fluorophore moiety (Figure 1b). If the sodium (or potassium) ion is bound to the crown ether, the lone electron pair of the nitrogen atom is stabilised and can no longer undergo electron transfer towards the photoexcited fluorophore. In this way, the analyte binding leads to a significant increase in the luminescence, hence the name “turn-on” sensors. Figure 2 shows the first “turn-on” sensor based on a crown ether receptor and an anthracene signalling unit, which upon binding of the ion leads to a 47-fold enhancement of the indicator dye Φ_F.[19, 31]

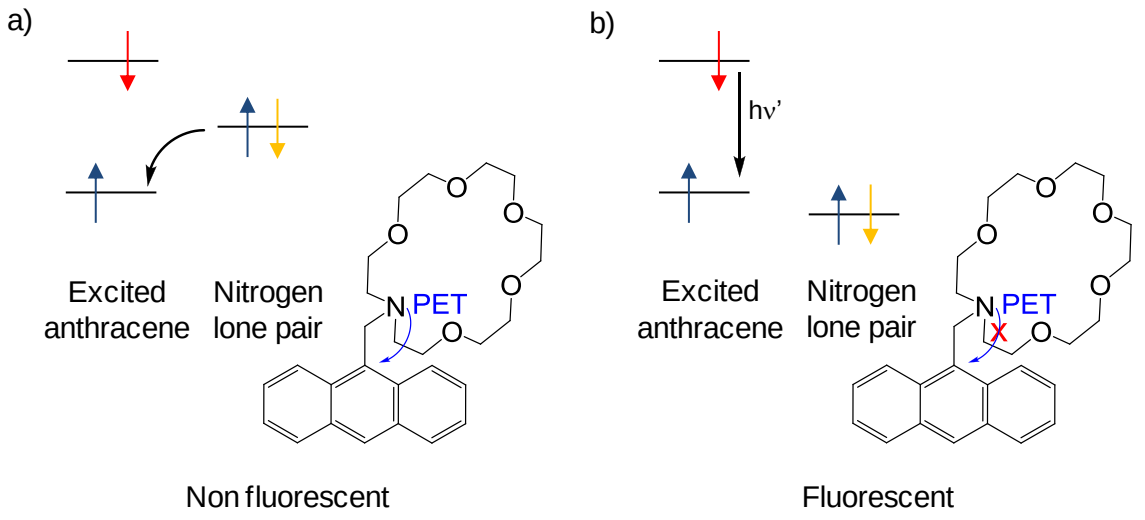

Figure 2. Example of a PET potassium and sodium "turn-on" sensor by de Silva et al.[31] The indicator dye was designed to display a minimum of fluorescence due to the nitrogen PET quenching of the anthracene moiety (a). Upon binding of the cation, the lone pair is stabilised so that no PET occurs leading to intense fluorescence (b).

An additional type of system that shows enhancement of its luminescent properties but is not rationalized as any type of energy transfer is showed in Figure 3. It is based on the energy changes of its LUMO orbital, modifying the emissive nature of the dye. This polyazaheterocyclic ligand,[32] is a faintly emissive organic ligand due to its nπ* transition nature.[33] However, after binding of Li^+ there is an increase in both the molar absorption coefficient and its luminescence intensity (12-fold). This indicates a change in the photophysical picture of the dye, where the emissive state changes from a nπ* in its *free* form to a ππ* transition after *complexation*.

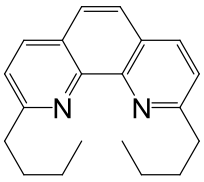

Figure 3. Example of a weakly emissive ligand that displays "turn-on" sensing features upon Li^+ binding.[32] See text for details.

There are many examples of waterborne Hg(II) sensors in the literature, the majority of them being of fluorescence turn-on type.[34] Nonetheless, this type of "turn-on" indicator dyes is not easily applicable for detection of heavier ions, as they display redox potentials so that the analyte can act as luminescence quencher. In this case, either PET or PCT, from the

fluorophore towards the analyte (or vice-versa) dominates the photophysical picture.[19] Considering real-world applications where the indicator dye is preferably immobilized on a (hydrophilic) polymer support or dissolved in water (in an adequate chamber), the examples showed henceforth operate strictly in aqueous media.[34a] Furthermore, narrowing the literature search to indicator dyes sensitive to either Cu(II) or Hg(II) ions, based on the luminescent properties of ruthenium(II) polyazaheterocyclic complexes yields a handful of results.[35] These dyes normally display a luminescence *turn-off* (**quenching**) upon the analyte binding. Figure 4a shows an example of a ruthenium dye that loses its emission upon Cu(II) binding in aqueous medium.[35c] The recognition moiety capitalizes on the electronic properties of the pyridine nitrogen atoms. In the case of Hg(II) recognition moieties, it is well known that the soft sulphur atom shows an important affinity for this ion, explaining the use of the thiocyanate moieties in the indicator dye depicted in Figure 4b.[35a]

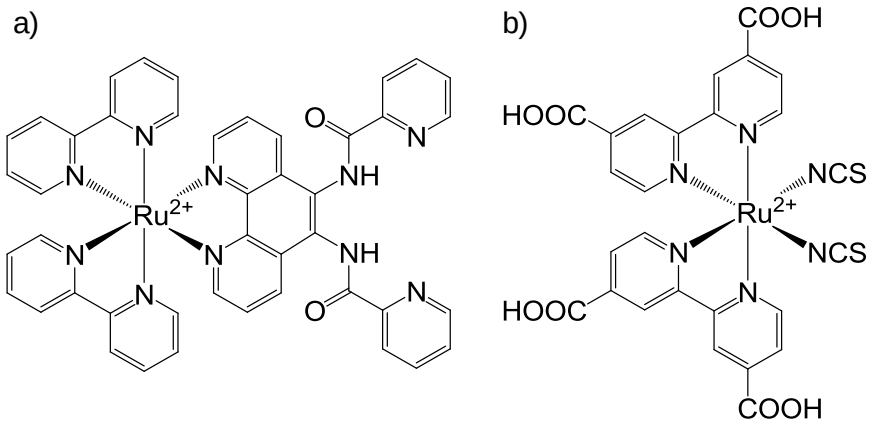

Figure 4. Structures of Ru(II) indicator dyes for Cu(II) (**a**) and Hg(II) (**b**) sensing. Both dyes display luminescence turn-off upon analyte binding.[35a, 35c]

In fact, the literature search for such ruthenium-based luminescent indicators that work in aqueous media demonstrates that most of the hits are not for aqueous purposes, but rather mixed organic/aqueous or purely organic solvents. In the words of Prof. Wolfbeis, "*who on Earth wants to sense (…) in acetonitrile*?"[10] This lack of reports reflects the fact that efficient ion probes do not normally work in purely aqueous media due to the strong ion solvating power of this solvent.

1.7. Binding constants

If a luminescent molecular probe (*ligand*) is to be sensitive to an analyte (*guest*), some sort of change must occur to its photophysical or photochemical properties upon the ligand-guest interaction. Depending on the system, this change may affect the host luminescence intensity (steady-state), excited state lifetime, spectral shifts or all of them. These changes may also affect the absorption spectrum, which might have an effect on the steady-state luminescence spectra (see Eq. 1, section 1.4). The rationalization of such recognition process with mathematical equations that describe the system is of analytical interest, especially when anticipating sensor applications. From the *binding isotherms* one obtains an insight on how stable a supramolecular ligand-guest arrangement is (binding constants), and also its stoichiometry.

When addressing the binding constants determination, the stoichiometry of the system is often an unknown parameter that the spectroscopist must identify beforehand. There are graphical evidences that may provide hints for the determination of the ligand–guest stoichiometry. A 1:1 equilibrium often leads to clearly defined isosbestic points although the opposite is not necessarily true: clear isosbestic points do not necessarily mean a 1:1 stoichiometry.[36] Certain linear plotting forms derived for 1:1 systems normally yield nonlinear plots when the system is of a more complex nature. The calculation of different K_1 values at different wavelengths is also evidence of a more complex equilibrium than 1:1 stoichiometry.[37] A very useful method is the measurement of the mass of the supramolecular complex by mass spectrometry, yet not always accessible.

There are two common experiments that facilitate determination of the stoichiometry by spectroscopic data, namely the *continuous variations method* (also known as Job's method[38]) and the *mole ratio method*.

The Job's method consists on measuring a property, which changes upon the complex formation, of different solutions in which the total concentration is maintained and the analyte-to-ligand mole ratio is raised from 0 to 1. For example, the absorbance variations at a certain wavelength are measured in the absence and in the presence of the analyte and plotted against the analyte ratio (that is, $0 < x < 1$). The maximum of the resulting concave curve yields the stoichiometry of the system.[36]

The *mole ratio method* represents a certain property that changes when increasing the analyte concentration at a constant ligand concentration. This should yield a plot that breaks when the equilibrium stoichiometry is reached, i.e. when the addition of more analyte does no longer affect the properties of the solution because all of the available ligand is bound to the analyte. Both of these methods depend on how high the binding constants are as the

lower the binding constant, the less pronounced a trend is, and more difficult it is to extract the stoichiometry from any of the above methods.

Finally, another general method for determination of the ligand–guest stoichiometry is the simple evaluation of the quality of the data fitting to the mathematical equations that describe a specific stoichiometry. The following equations describe the changes in both the absorption and the luminescence intensity for ligand-to-guest stoichiometries of 1:1, 1:2 and 2:1.

1.7.1. Ligand-to-guest 1:1 binding isotherm

Let us consider the simplest 1:1 case, in which one molecule of analyte (guest, G) binds to one molecule of the probe (ligand, L), being its equilibrium constant K_1:

$$L + G \rightleftharpoons LG \qquad K_1 = \frac{[LG]}{[L][G]} \qquad \text{Eq. 4}$$

Following the mass balance equation, the *total* concentration of ligand and the *total* concentration of guest can be defined as the sum of the *free* species as follows:

$$L_T = [L] + [LG] \qquad \text{Eq. 5}$$

$$G_T = [G] + [LG] \qquad \text{Eq. 6}$$

Choosing absorption as the spectroscopic parameter to be measured, it can be considered that the total absorbance (at a particular wavelength) of a solution A_T, is the sum of the individual absorption (at the same wavelength) of each species:

$$A_T = \varepsilon_L b[L] + \varepsilon_G b[G] + \varepsilon_{LG} b[LG] \qquad \text{Eq. 7}$$

By combining Eq. 7 with Eq. 5 and Eq. 6, after replacing all terms containing *free* concentrations it follows that:

$$\frac{\Delta A}{b} = \varepsilon_L[L]_T + \varepsilon_G[G]_T + [LG](\varepsilon_{LG} - \varepsilon_L - \varepsilon_G) \qquad \text{Eq. 8}$$

where $\Delta A = \Delta A_T - \Delta A_0$, and ΔA_0 is the absorbance at $[G]_T = 0$, that is, the changes in the absorbance after analyte addition. Eq. 8 can be further simplified taking into account that i) the optical pathlength b, is equal to 1; ii) the first term is the absorption without guest, i.e. A_0; iii) the second term refers to the absorption of the guest, which is assumed to be transparent at the analytical wavelength, so that it equals zero, and iv) defining the term ($\varepsilon_{LG} - \varepsilon_L - \varepsilon_G$) as $\Delta\varepsilon_{11}$ results:

$$\Delta A = \Delta\varepsilon_{11}[\mathrm{LG}] \qquad \text{Eq. 9}$$

The *free* concentration of the supramolecular Ligand-Guest complex [LG] can be expanded with the help of Eq. 4, and so it becomes:

$$\Delta A = \Delta\varepsilon_{11} K_1[\mathrm{L}][\mathrm{G}] \qquad \text{Eq. 10}$$

Using both equations Eq. 4 and Eq. 5, the term *free* ligand concentration [L], can be substituted by L_T / (1 + K_1[G]) and equation Eq. 10 can finally be modified to obtain the sought expression that yields the relationship between absorbance variation as a function of G:

$$\frac{\Delta A}{[\mathrm{L_T}]} = \frac{\Delta\varepsilon_{11} K_1[\mathrm{G}]}{1+K_1[\mathrm{G}]} \qquad \text{Eq. 11}$$

Therefore, by plotting the variation in the absorption of a ligand solution as a function of the *free* concentration of the added guest, and using Eq. 11 to fit the curve, both the binding constants K_1 and $\Delta\varepsilon_{11}$ are obtained

It must be again emphasised that the guest (analyte) concentration shown in Eq. 11 is the *free* concentration, a parameter that the analyst does not know in advance. To properly calculate the binding constant value, a set of iterative steps using Eq. 11 and Eq. 12 must be taken.

$$[\mathrm{G}]_\mathrm{T} = [\mathrm{G}] + \frac{[\mathrm{L}]_\mathrm{T} K_1[\mathrm{G}]}{1 + K_1[\mathrm{G}]} \qquad \text{Eq. 12}$$

The iterative steps go as follows. Consider *n* data points, each representing the resulting absorbance after addition of a *known total* concentration of the guest ion, $[\mathrm{G}]_\mathrm{T}$. The first step consists in assuming that the *free* guest concentration is given by $[\mathrm{G}] = [\mathrm{G}]_\mathrm{T}$, and using this data to calculate K_1 from Eq. 11. With the obtained binding constant value, Eq. 12 is used to calculate each *free* guest concentration that yields the correct *total* guest concentration for each *n* data point. The second step starts by using the calculated *free* guest concentration values in Eq. 11 to derive a new K_1 value. The iteration steps stop when the calculated parameters (K_1 and [G]) no longer vary.[36]

The set of Eq. 7 to Eq. 11 describes the changes in the absorption at a specific wavelength for a 1:1 equilibrium. Naturally, the same methodology can be applied to describe the changes in the emission intensity. In this case the total fluorescence, I_F of a solution is obtained by expanding Eq. 1 to include the fluorescence of all species:

$$I_F = (I_{exc}\Phi_F\kappa\varepsilon_\lambda l)_L[L] + (I_{exc}\Phi_F\kappa\varepsilon_\lambda l)_G[G] + (I_{exc}\Phi_F\kappa\varepsilon_\lambda l)_{LG}[LG] \qquad \text{Eq. 13}$$

The terms in brackets have already been described in Eq. 1, section 1.4. This equation can be simplified by noting that the initial fluorescence I_0, that is, the fluorescence prior to addition of the guest ion corresponds to the situation where $[L]_T = [L]_0$. It can also be simplified by assuming that the guest ion, G is non-fluorescent and therefore the second term is zero. Finally it is transformed by dividing it by I_0 and using Eq. 4 to yield Eq. 14.

$$\frac{I_F}{I_0} = \frac{(I_{exc}\Phi_F\kappa\varepsilon_\lambda l)_L[L]}{(I_{exc}\Phi_F\kappa\varepsilon_\lambda l)_L[L]_0} + \frac{(I_{exc}\Phi_F\kappa\varepsilon_\lambda l)_{LG}[LG]}{(I_{exc}\Phi_F\kappa\varepsilon_\lambda l)_L[L]_0} = \frac{[L] + \alpha[LG]}{[L]_0} =$$

$$= \frac{[L] + \alpha K_1[L][G]}{[L] + K_1[L][G]} = \frac{1 + \alpha K_1[G]}{1 + K_1[G]} \qquad \text{Eq. 14}$$

The term α is given by

$$\frac{(I_{exc}\Phi_F\kappa\varepsilon_\lambda l)_{LG}}{(I_{exc}\Phi_F\kappa\varepsilon_\lambda l)_L}$$

This relationship between luminescence intensity and *free* guest concentration allows the analyst to calculate the binding constant value K_1, a value that should be comparable to the one obtained with Eq. 11 from absorption measurements of the same system. It must be underlined again the need to carry out iteration steps between Eq. 12 and Eq. 14 to obtain the correct *free* concentration values and, consequently, the correct K_1.

The derived equation describes the changes in the luminescence intensity for a 1:1 ligand-to-guest stoichiometry. In the particular case where the guest produces a complete luminescence quenching of the ligand upon binding before the photoexcitation takes place (*static quenching*), then the term α is equal to zero and Eq. 14 becomes the inverse of the classical Stern-Volmer equation.

1.7.2. Ligand-to-Guest 2:1 binding isotherm

Increasing the complexity of the system, a supramolecular arrangement in which two molecules of ligand bind a guest ion may be found: for example two imidazole ligands binding a copper(II) atom in a square planar fashion.[39] This 2:1 system can be described as a second ligand molecule binding a previously formed LG 1:1 supramolecular arrangement:

$$L + G \rightleftharpoons LG \qquad K_1 = \frac{[LG]}{[L][G]} \qquad \text{Eq. 4}$$

$$LG + L \rightleftharpoons L_2G \qquad K_2 = \frac{[L_2G]}{[L][LG]} \qquad \text{Eq. 15}$$

being its equilibrium constant K_2 given by Eq. 15, which yields $[L_2G]$ as:

$$[L_2G] = K_1 K_2 [G][L]^2 \qquad \text{Eq. 16}$$

Following the mass balance equation, the *total* concentration of ligand and *total* concentration of guest can be defined as the sum of the *free* species as follows:

$$L_T = [L] + [LG] + 2[L_2G] \qquad \text{Eq. 17}$$

$$G_T = [G] + [LG] + [L_2G] \qquad \text{Eq. 18}$$

Choosing **absorption** as the spectroscopic parameter of interest, the overall absorbance can be defined according to Eq. 19:

$$A_T = \varepsilon_L b[L] + \varepsilon_G b[G] + \varepsilon_{LG} b[LG] + \varepsilon_{L_2G} b[L_2G] \qquad \text{Eq. 19}$$

Carrying out the same operations that were performed on Eq. 7, and simplifying in the same way as for Eq. 8 by defining the term ($\varepsilon_{L2G} - 2\varepsilon_L - \varepsilon_G$) as $\Delta\varepsilon_{21}$, it becomes:

$$\Delta A = \Delta\varepsilon_{11}[LG] + \Delta\varepsilon_{21}[L_2G] \qquad \text{Eq. 20}$$

Expanding the [LG] and $[L_2G]$ terms from equations Eq. 4 and Eq. 15, Eq. 20 can be represented as:

$$\Delta A = \Delta\varepsilon_{11} K_1 [L][G] + \Delta\varepsilon_{21} K_1 K_2 [L]^2[G] \qquad \text{Eq. 21}$$

Finally, by modifying [L] with equations Eq. 4, Eq. 15 and Eq. 17, it can be replaced by $L_T/(1 + K_1[G] + K_1K_2[G][L])$ and Eq. 21 becomes the final mathematical relationship that describes the dependence of the ligand absorbance on the concentration of both the analyte and ligand in a 1:1 + 2:1 equilibrium sequence (Eq 22).

$$\frac{\Delta A}{[\mathrm{L_T}]} = \frac{\Delta\varepsilon_{11}K_1[\mathrm{G}] + \Delta\varepsilon_{21}K_1K_2[\mathrm{G}][\mathrm{L}]}{1+K_1[\mathrm{G}] + 2K_1K_2[\mathrm{G}][\mathrm{L}]} \qquad \text{Eq. 22}$$

It is possible to find similarities between this equation and Eq. 11, where the only difference lies in the additional numerator and denominator terms to the right that account for the absorbance of the 2:1 species. Unlike the cases of stoichiometries 1:1 and 1:1 + 1:2 (see below), the determination of the *free* guest concentration in the case 1:1 + 2:1 is not as straightforward as an iterative process using Eq. 12 or Eq. 31, respectively. This is due to the fact that when deriving the equation that describes $[\mathrm{G}]_\mathrm{T}$ as a function of [G], the term *free* ligand concentration [L] is persistent and cannot be ignored.

In order to obtain the corresponding **luminescence** binding isotherm that describes the 1:1 + 2:1 equilibrium, a similar approach to what was taken for Eq. 14 is sufficient. To that end, Eq. 13 is expanded to include the term that accounts for the fluorescence of the L_2G species (for the sake of simplicity the guest ion G, is considered to be non-fluorescent and is not included).

$$I_\mathrm{F} = (I_\mathrm{exc}\Phi_\mathrm{F}\kappa\varepsilon_\lambda \mathrm{l})_\mathrm{L}[\mathrm{L}] + (I_\mathrm{exc}\Phi_\mathrm{F}\kappa\varepsilon_\lambda \mathrm{l})_\mathrm{LG}[\mathrm{LG}] + (I_\mathrm{exc}\Phi_\mathrm{F}\kappa\varepsilon_\lambda \mathrm{l})_{\mathrm{L_2G}}[\mathrm{L_2G}] \qquad \text{Eq. 23}$$

The following transformations are the same than for the 1:1 case, in which the desired equation is obtained upon dividing by I_0 and using Eq. 4, Eq. 15 and Eq. 17:

$$\frac{I_\mathrm{F}}{I_0} = \frac{[\mathrm{L}] + \alpha[\mathrm{LG}] + \gamma[\mathrm{L_2G}]}{[\mathrm{L}]_0} = \frac{[\mathrm{L}] + \alpha K_1[\mathrm{L}][\mathrm{G}] + \gamma K_1K_2[\mathrm{L}]^2[\mathrm{G}]}{[\mathrm{L}] + K_1[\mathrm{L}][\mathrm{G}] + 2K_1K_2[\mathrm{L}]^2[\mathrm{G}]}$$

$$= \frac{1 + \alpha K_1[\mathrm{G}] + \gamma K_1K_2[\mathrm{L}][\mathrm{G}]}{1 + K_1[\mathrm{G}] + 2K_1K_2[\mathrm{L}][\mathrm{G}]} \qquad \text{Eq. 24}$$

The term α has been defined in page 17, and γ is given by

$$\frac{(I_\mathrm{exc}\Phi_\mathrm{F}\kappa\varepsilon_\lambda \mathrm{l})_{\mathrm{L_2G}}}{(I_\mathrm{exc}\Phi_\mathrm{F}\kappa\varepsilon_\lambda \mathrm{l})_\mathrm{L}}$$

Eq. 22 and Eq. 24 were obtained considering that *two molecules of ligand* bind to the guest (metal ion). If we now consider that *two molecules of analyte* bind to one molecule of ligand, the mathematical expression derived is similar (but not identical!).

1.7.3. Ligand-to-Guest 1:2 binding isotherm

This type of arrangement is very common in the case where the ligand has two binding sites. In the following case, the two binding sites are considered equivalent so that the first associative step is independent on where the coordination is taking place. Such ditopic ligand can be exemplified by a biimidazole (or biimidazolate) ligand, which binds two ions of copper(II) via two nitrogen atoms on each side.[40]

Following the same procedure as that of previous systems described above, the binding isotherms that describe the changes in absorption and emission upon analyte addition can be obtained by considering that one molecule of the guest ion binds a previously formed LG 1:1 supramolecular complex, with its own binding constant K_2:

$$\mathrm{L} + \mathrm{G} \rightleftharpoons \mathrm{LG} \qquad K_1 = \frac{[\mathrm{LG}]}{[\mathrm{L}][\mathrm{G}]} \qquad \text{Eq. 4}$$

$$\mathrm{LG} + \mathrm{G} \rightleftharpoons \mathrm{LG_2} \qquad K_2 = \frac{[\mathrm{LG_2}]}{[\mathrm{G}][\mathrm{LG}]} \qquad \text{Eq. 25}$$

The binding constant K_2 yields $[\mathrm{LG_2}]$ as:

$$[\mathrm{LG_2}] = K_1 K_2 [\mathrm{L}][\mathrm{G}]^2 \qquad \text{Eq. 26}$$

As before, according to the mass balance equation, the *total* concentration of ligand and *total* concentration of guest can be defined as the sum of the *free* species as follows:

$$\mathrm{L_T} = [\mathrm{L}] + [\mathrm{LG}] + [\mathrm{LG_2}] \qquad \text{Eq. 27}$$

$$\mathrm{G_T} = [\mathrm{G}] + [\mathrm{LG}] + 2[\mathrm{LG_2}] \qquad \text{Eq. 28}$$

The binding isotherm that describes the changes in the **absorption** of a 1:1 + 1:2 system is obtained by carrying out the same reasoning as that leading to Eq. 19. Defining $\Delta\varepsilon_{12}$ as $\varepsilon_{LG2} - \varepsilon_L - 2\varepsilon_G$, Eq. 29 follows:

$$\frac{\Delta A}{[\mathrm{L_T}]} = \frac{\Delta\varepsilon_{11} K_1 [\mathrm{G}] + \Delta\varepsilon_{12} K_1 K_2 [\mathrm{G}]^2}{1 + K_1 [\mathrm{G}] + K_1 K_2 [\mathrm{G}]^2} \qquad \text{Eq. 29}$$

As expected, Eq. 29 is similar to the binding isotherm that describes a 1:1 + 2:1 system (Eq. 22). The difference lies in the terms that define the second binding step, which in this case do not depend on the concentration of the ligand species.

For the case of describing the changes in the **luminescence** intensity instead of the ligand absorption, the procedure is identical to the one discussed in the previous section. The binding isotherm for the 1:1 + 1:2 system is given by:

$$\frac{I_F}{I_0} = \frac{[L] + \alpha[LG] + \gamma[LG_2]}{[L]_0} = \frac{[L] + \alpha K_1[L][G] + \gamma K_1 K_2[G]^2}{[L] + K_1[L][G] + K_1 K_2[G]^2[L]}$$

$$= \frac{1 + \alpha K_1[G] + \gamma K_1 K_2[G]^2}{1 + K_1[G] + K_1 K_2[G]^2} \qquad \text{Eq. 30}$$

The term α has been defined in page 17, and γ is given by

$$\frac{(I_{exc}\,\Phi_F\,\kappa\,\varepsilon_\lambda\,l)_{LG_2}}{(I_{exc}\,\Phi_F\,\kappa\,\varepsilon_\lambda\,l)_L}$$

To obtain the equation that relates the *total* concentration of the guest ion with the concentration of its *free* form, the mass balance given by Eq. 28 must be transformed by substituting the terms [LG] and [LG_2] by their equivalents from Eq. 4 and Eq. 25, respectively. The last step consists in substituting the *free* ligand concentration by its equivalent from the mass balance Eq. 27 to yield Eq. 31:

$$[G]_T = [G] + \frac{[L_T]\left(K_1[G] + 2K_1K_2[G]^2\right)}{1 + K_1[G] + K_1K_2[G]^2} \qquad \text{Eq. 31}$$

As for the 1:1 case, this equation is necessary to carry out the iterative process that allows the correct determination of the binding constant values K_1 and K_2 in a 1:1 + 1:2 system.

1.8. Computational chemistry

This section tries to give a general overview of the theory behind the calculations involved in computational chemistry. It is not intended to dwell on the somewhat complex mathematical equations typical of quantum chemistry, but rather to make the reader familiar with the notions and terms that help to understand the applicability of the methods used. [41]

The previous section showed us equations that are used as models to describe certain chemical equilibriums. Several illustrative diagrams, like the Jablonski or the Franck-Condon principle ones are used on a regular basis as simplifications that help to describe photophysical processes. These interpretations or models can be compared to the plastic models used by chemistry students to better understand molecular structures. In either case, they all provide tools to describe the chemistry behind experimental observations.[41a]

Computer technology has undergone an exponential increase in processor speed since the second half of the last century. It was the necessary piece for generalization of the theory behind quantum chemistry as a tool to describe and understand chemical phenomena. Efficient software for electronic structure modelling such as Gaussian09 has also participated alongside.[42] Computational chemistry depends on the same fundamental laws of physics as other areas like photochemistry or organic chemistry. Yet, it allows us to peek inside molecules in both space and time dimensions, being capable of describing the structure of short-lived transition states, as well as the potential energy pathways that entail such transition states. Thanks to fast computers and user-friendly software, it is nowadays possible to run calculations to predict chemical properties *before* spending precious time and resources in laboratory synthetic procedures. It is also true that, as for most models, computational chemistry lacks the capability of describing the total system, resorting to theoretical approximations that lead to acceptable results. Although such models are under continuous improvement, the accuracy of a theoretical result ultimately lies in the experienced chemist assessment.

The theoretical approaches depend not only on the chosen model but also on the level of complexity used to describe the system under study. There are two types of approximations, one based on the laws of classical physics, called *molecular mechanics* and another one based on quantum mechanics, called *electronic structure theory*. The first involves less complex calculations due to the simplicity of the models used, and it is computationally inexpensive in terms of CPU time. Naturally, it yields less accurate results but, thanks to its simplicity and ubiquitous presence in most software packages, it is often used by chemists that work in other fields. Both theoretical approaches can perform calculations on finding the atomic arrangement that leads to the more stable geometry

(geometry optimization), determine the energy of such structure and calculate the interatomic vibrational frequencies as well.

1.8.1. Molecular mechanics

This method was once known as the Westheimer or the force-field method. It aimed to the determination of *molecular* equilibrium structures using classical *mechanics* that finally led to the term molecular mechanics (MM) in the 1970s.[41b]

These theoretical simulations based on classical physics have the advantage of yielding fast calculations, particularly important when dealing with large molecules such as proteins. This is achieved at the expense of certain approximations; a pictorial example would be the balls-and-springs model.[41b] MM performs calculations on the interactions between nuclei, while the electrons are not explicitly computed. Molecular mechanics are developed in different methods, each of them defined by a different *force field*. A force field is made up of three components: i) a set of **equations** that defines the potential energy of the molecule according to the relative position of its atoms; ii) a **description** of each *atom type*, including charge, hybridization and the effect that other bonded atoms produce on it, and iii) a set of **parameters** that include bond lengths and angles, called *force constants*.[41a] Several *force fields* exist that describe a particular group of molecules, with specific atoms that best describe each case. To name a few, the *Dreiding* force field describes most common atoms, the *MM1* and *MM2* force fields are useful for hydrocarbons, the *AMBER* and the *OPLS* force fields better describe proteins or nucleic acids and, finally, the *Unified Force Field* (UFF) includes parameters for all the elements of the Periodic Table.[41b]

Molecular mechanics can be useful for fast evaluation of certain molecular features, yet it cannot predict interesting properties based on electronic effects, such as calculations of electronically *excited* states. They also require that each molecule has its own model or force field so it cannot be applied on a general basis.

1.8.2. Electronic structure theory

Instead of considering molecules as balls on strings, this method is based on the fundamental laws of quantum mechanics. As its name stands for, it uses theory to describe not only the nuclei but also the electrons that "orbit" around it. To do so, it relies on the famous Schrödinger equation, which is known to lack an analytical solution for multi-electron atoms. This happens because of the recognized three-body problem, also common to the gravitational laws that limit the accurate trajectory calculation of three bodies in space.

At the atomic scale with more than one electron, the problem arises from the simultaneous Coulomb repulsion between electrons and the electron-proton attraction. The

solution lies once again in resorting to approximations that yield results in good agreement with the experimental data.

***Ab initio* Hartree-Fock.** The *orbital model* is a useful approximation to describe electronic interactions. In this case, the electron is treated as a single particle under the influence of a field caused by the other electrons. The latter simply occupy a particular region of space (orbital) with a given *probability*, and affect the electron of interest with an *averaged* repulsion. A well-known orbital model is the so-called Hartree-Fock (from the work of William and Douglas Hartree, later improved by Fock). The HF model requires iterative calculations at the level of each electron which is affected by the fields caused by other electrons in the molecule. This means that the field of all the electrons is the same as the total field, hence the term *self-consistent field* (SCF). Fock brought an improvement to the method by adapting the model to agree with the *Pauli exclusion principle*, where no two electrons in the same atom may be described by the same quantum state.

Orbital treatment. The shape of the orbital depends on the model, where two common types are used: the Slater type orbital (STO) and the Gaussian type orbital (GTO). The STO is named after John C. Slater who interpreted each electron in a multi-electron atom to adopt the shape of hydrogen-type orbitals and to have a determined shielding constant according to the group: 1s; 2s, 2p; 3s, 3p; 3d; 4s, 4p; 4d; 4f; and so forth.[43] The HF method using STOs suffers from a major drawback when dealing with molecules, as it generates an extensive number of integrals in six dimensions also known as *integral bottleneck*.[41b] The Gaussian type orbital is a description of atomic orbitals via Gaussian basis functions.[44] This has allowed overcoming the integral bottleneck problem thanks to the fact that Gaussian basis functions are much simpler to deal with, and the only mathematical difficulty is dealt by high CPU times. Nevertheless, comparing to STOs, GTOs fail to describe the electron spatial probability at the core of the atom. *Hehre et al.* came up with a practical solution by describing STOs as a sum of the necessary GTOs.[45] This approach brought together the real-world spatial description of molecular orbitals (STOs) with the mathematically practical GTOs. This expansion is represented as STO/*n*G where *n* represents the number of Gaussian functions in linear combination that fits a Slater type orbital. An improvement to this method consists in splitting the valence orbitals into outer and inner shells, so that a different number of Gaussian functions is used to describe each orbital.[46] As an example, a STO/6-31G calculation means that the inner STOs are described by one basis function composed of a linear combination of 6 Gaussians, while the split-valence STOs are described by two basis functions with different sizes: an inner shell STO described by a linear combination of 3 Gaussians and a similar outer shell described by 1 Gaussian.[41a]

A further improvement of the method involves adding *polarization* and *diffusion* functions. *Polarization* functions allow orbitals to change their shape by adding equations that describe orbitals of higher orbital quantum number. In other words and as an example, the first asterisk after the STO/6-31G** means that the basis set includes characteristics of d shape orbitals for (*n*s, *n*p) atoms, while the second asterisk means characteristics of *p* shape to *n*s atoms. This notation can also be represented by the letters d and p, respectively. This is useful for molecules, especially those containing heavy atoms in which the atomic orbitals may suffer from spherical distortion upon the molecule formation.[41b] The *diffusion* functions are useful to better describe molecules with "loose" electrons, namely negative charges or valence orbitals that lie far away from the nucleus either in atoms with lone-pairs or excited states. In this case, the diffusion applied to heavy atoms is represented by the first "+" sign while the second "+" sign refers to hydrogen atoms: STO/6-31++G.[41a]

When dealing with large molecules bearing heavy atoms such as metal complexes, calculations can be extremely time consuming due to the amount of integrals needed for the description of all electrons in all atoms. A simple way of reducing CPU time is considering that the electrons residing in inner orbitals (*core electrons*) do not play a significant role in determining molecular properties such as bond length or geometry. This assumption is similar to what is observed in atoms across the Periodic Table: each Group has similar reactivity due to the valence electronic configuration, independently of how many electrons constitute the core of the atom. Such core electrons are simply described by a repulsive potential that affects valence electrons. This mathematical "short-cut" is called *effective core potential* (ECP) or *pseudopotential* and it also includes relativistic effects for the inner core electrons of heavy atoms.[41c]

Density Functional Theory. The theory described so far consists in the HF model, where each electron is considered to be influenced by an averaged potential that derives from the other electrons. The advantageous simplification brought by this approach is at the same time its drawback, as no electron-electron interaction takes place, yielding inaccurate predictions due to the lack of the so-called *electron correlation*. A theoretical model that includes such interactions is the *density functional theory* (DFT). This useful methodology relies in *ab initio* iterative calculations, similar to Hartree-Fock SCF methods, but leads to improved results at a similar computational cost. Unlike HF, it avoids the use of molecular orbital wave functions by considering an overall electron density. The initial DFT was developed in the mid 1960s by P. Hohenberg, W. Kohn and L. J. Sham.[47]

In DFT methods, the electron correlation is treated by *functionals* of the electron density, where the mathematical term "functional" means function of a function. Such functionals utilize four separate energy components to describe the overall electronic energy:

i) kinetic energy; ii) electron-nucleus and nucleus-nucleus interactions; iii) Coulomb repulsion arising from electron-electron interactions, and iv) an *exchange-correlation* term that includes extra electron-electron interactions dependent on the electron density.[41a] The exchange-correlation term is itself divided in two functionals, as its name implies: the *exchange functionals* and *correlation functionals*. Each of these two functionals can be of two different types, either *local* (electron density dependent) or *gradient-corrected* (electron density and gradient dependent).

A manifold of functionals can be constructed by choosing different types of exchange and correlation functionals, each either local or gradient-corrected. A common gradient-corrected DFT method is the B3LYP exchange-correlation functional, where B3 stands for Becke three-parameter *exchange* functional and LYP stands for Lee-Yang-Parr *correlation* functional.[48] The B3LYP functional is in fact a *hybrid functional*, since it contains a mixture of HF-DFT exchange and DFT correlation functionals.

1.8.3. Gaussian computations

To finish this Introduction section, a quick overview of some useful calculations (jobs) is presented. The results presented in this Thesis were obtained by running four different job types: i) geometry optimizations; ii) single-point energy jobs; iii) frequency calculations, and iv) time-dependent DFT (TD-DFT) calculations. These calculations can be run in gas-phase or taking into account solvent effects. The solvent can be introduced in the calculations in several ways such as explicit solvent molecules that interact with moieties of the target molecule, periodic solvent boxes, or an external surface with a certain dielectric constant produced by the bulk solvent. The latter model is known as polarizable continuum model (PCM).

Geometry optimizations. The aim of a geometry optimization is to obtain a calculated geometry that provides a minimum in the energy of a molecule (or molecules). The program uses the first derivative of the energy (*gradient*) to evaluate the progress of small geometry changes. When the *gradient* is smaller than a certain threshold, the optimization stops and a minimum is output. The gradient can be thought of as the slope of the potential energy surface (PES) represented in Figure 5. Due to the methodology used, this minimum can be a *local minimum* rather than the *global minimum*. Under normal circumstances, the starting geometry is input from a careful selection based on data from analogous molecules such as bond lengths or dihedral angles. Figure 5 also shows a local maximum and a global maximum in the PES. These coordinates can be regarded as geometries associated to transition states.

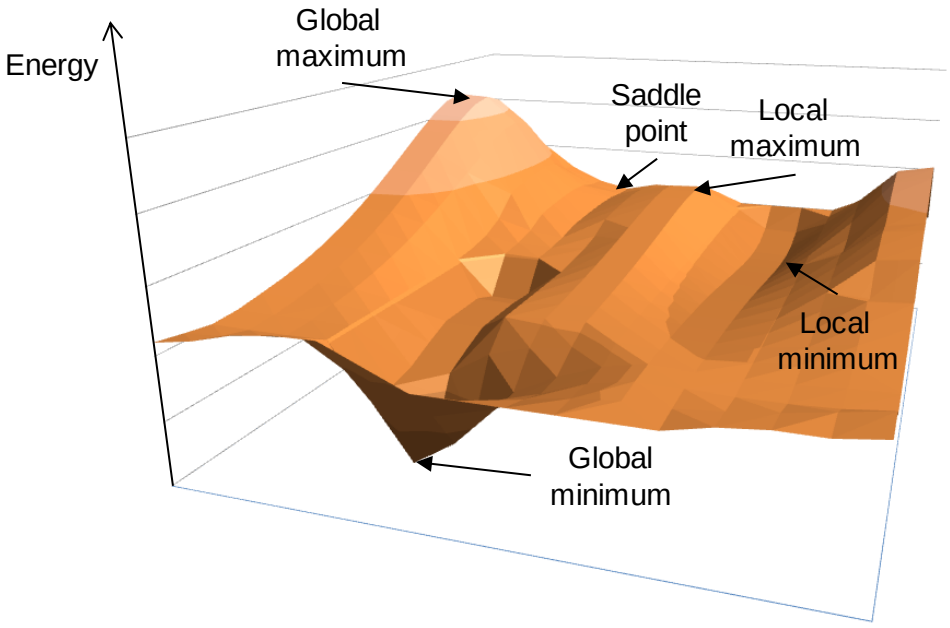

Figure 5. Potential energy surface plot of a hypothetical molecule. The *x* and *y* axis are two of the *n* degrees of freedom of the atoms in such molecule. See text for details.

Single-point energy calculations. This type of job can be described as determining the energy of a molecule (or molecules) at a given geometry. Relating this to the PES of Figure 5, it would correspond to the calculation of the energy at a specific single-point in the energy surface. Being a calculation that uses a single-geometry, it requires less CPU time. For this reason, it can provide more accurate energy results by adding solvent effects or by increasing the complexity of the basis set.

Frequency calculations. So far, the calculations described involve nuclei with no vibrational modes, as if they were fixed in space. This type of frequency calculations yield just the energy (and direction) associated to the vibration of the atomic nuclei within a molecule. This computational protocol yields information on the vibrational spectrum, which is comparable to the experimental infrared (IR) absorption spectrum. Another useful information is the nature of the structure obtained after a geometrical optimization computation. If the optimized structure is a transition state then it is characterized by being a minimum in one direction and a maximum in the other one. This type of stationary point is called *saddle point* (Figure 5) and presents at least one imaginary frequency. For this reason, all optimization jobs should be followed by a frequency calculation (at the same level of theory) to confirm that it is a true minimum. Frequency calculations also yield the *zero-point energy* (ZPE) of the optimized geometry which accounts for the necessary energy correction due to persistent vibration even at 0 K.

TD-DFT calculations. Time-dependent DFT calculations allow the determination of the one-photon excitation energies for a given structure with a given multiplicity. The same methodology can be applied for optimized excited state geometries, but at ground state multiplicity. This means that the calculated excitation energies for this structure will give a value of its emission energy. Another method that yields an approximate value for the emission energy is the Δ-SCF. In rough terms, this method consists in calculating the energy difference between the excited and ground states at the geometry of the optimized excited state.[49] Figure 6 depicts an energy diagram that summarizes the data given in each of the above calculations.

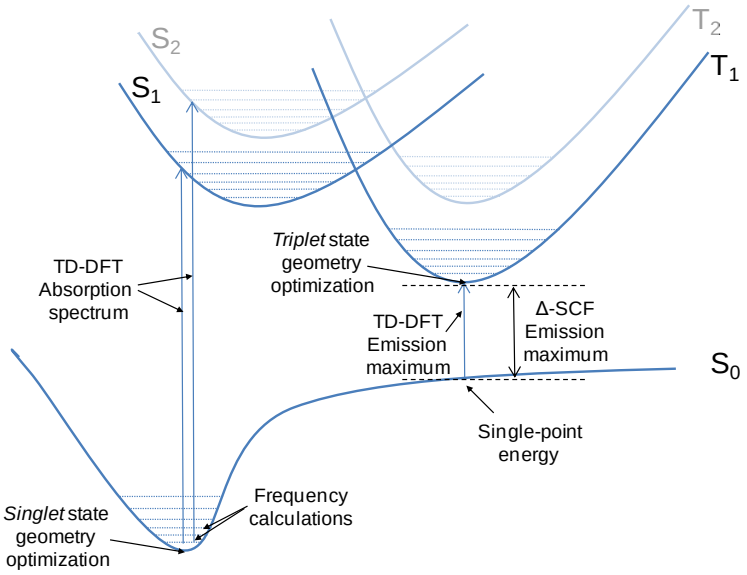

Figure 6. Energy diagram for a hypothetical molecule which can undergo ISC towards a stable triplet excited state. The labels refer to the calculations described in the text.

1.9. Luminescent ruthenium(II) complexes

Before plunging into the photophysical aspects that characterize ruthenium(II) complexes, a general introduction of its electronic structure is presented. Due to the nature of the Ru(II) coordination compounds included in this Thesis, the following paragraphs will be limited to metal complexes in octahedral symmetry.

1.9.1. Electronic Structure Theory

Among the different theories that describe the electronic structure of metal complexes, such as the crystal field theory (CFT), the ligand field theory (LFT) or the *molecular orbital theory* (MOT), the latter achieves a good balance between experimental observations and rationalization. In an octahedral field, the six coordination positions are aligned with the x-, y- and z-axis. The metal *d* orbitals that point to the ligands are, according to its symmetry, the $d_{x^2-y^2}$ and d_{z^2}. The remaining three *d* orbitals, the d_{xy}, d_{xz} and d_{yz} are positioned between each axis (or coordination bond). This orientation leads to an energy splitting of the orbitals in two sets: the higher in energy e_g set and the more stable t_{2g} set. According to the MOT, the formation of a metal complex consists essentially in the interaction of the nine valence orbitals of the metal, *d* (5), *s* (1) and *p* (3) with the σ and π orbitals of the ligands. If such interaction is to occur, an orbital overlap must take place; therefore, the metal and ligand orbitals that participate in the formation of the coordination complex must share the same symmetry.

The six metal orbitals responsible for σ-bonding are those oriented towards the ligands, namely, the orbitals e_g (2), *p* (3) and *s* (1). Similarly, the six metal orbitals that participate in the π-bonding are the t_{2g} (3) and the *p* (3). In the case of the ligands, the MOT requires a linear combination of the six ligand σ orbitals that generates orbitals with similar symmetry as the metal σ orbitals. The same method is used for the twelve π ligand orbitals, in this case generating six symmetry orbitals that interact with the six π metal orbitals and another set of six orbitals that do not interact and are *non-bonding* orbitals.

Figure 7 shows a simplified energy distribution diagram of a hypothetical octahedral coordination complex, as predicted by the MOT. It also shows the vertical excitations, which will be explained in section 1.9.2. The molecular orbital (MO) placing depends on the energy of the participating orbitals of the metal and the ligand. Also, the newly formed MOs that constitute the metal-ligand complex adopt the orbital character of either metal or ligand, depending on which one is the closest in energy. As shown in Figure 7, the character of each molecular orbital is shown by its colour, green for predominantly ligand-type and blue for metal-type. The dashed bonds represent vacant, anti-bonding molecular orbitals. As the energy of the σ orbitals of the ligands is lower in energy than any of the metal valence

orbitals, the six σ-bonding MOs are of ligand character, σ_L. In the presented example, the π orbitals of the ligands are higher in energy than the metal *d* orbitals. This leads to a stabilised t_{2g} π orbital set of metal character. In the particular case of octahedral polypyridine ruthenium(II) complexes, the metal electronic configuration is d^6 and each of the three ligands provides four unshared electrons from the two pyridine nitrogen atoms. Ligands and metal combined sum 18 valence electrons, which fill the first nine MOs of Figure 7.

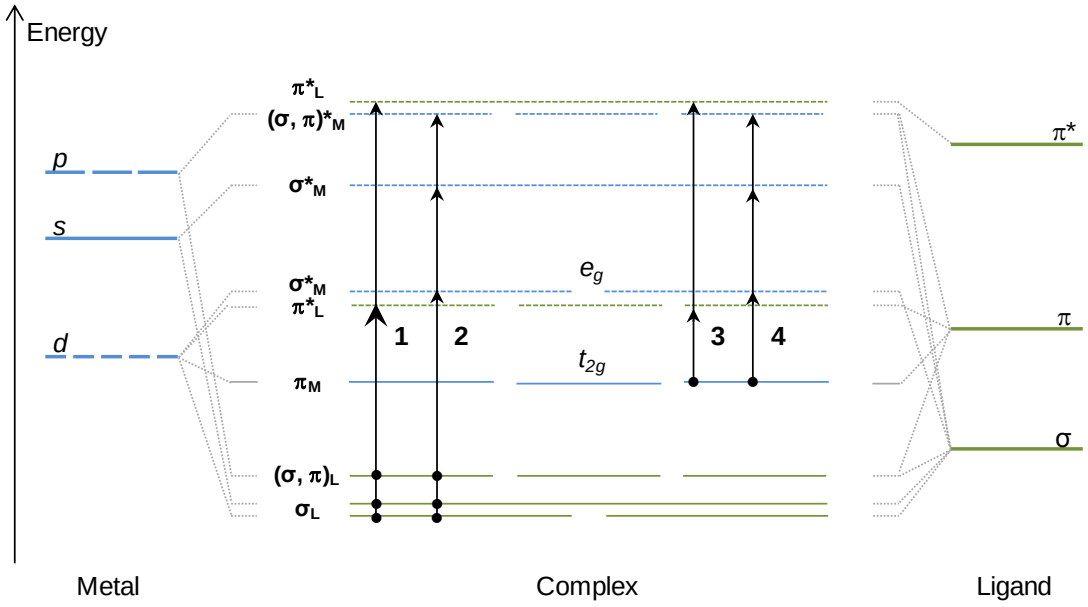

Figure 7. Electronic energy diagram based on the molecular orbital theory for a metal complex of octahedral symmetry.[50] The metal orbitals (blue) interact with symmetry orbitals of the ligand (green) to generate bonding (solid line) and anti-bonding (dashed lines) molecular orbitals. The arrows represent types of vertical excitations where (1) LC, (2) LMCT, (3) MLCT and (4) MC. See text for details.

1.9.2. Electronic absorption spectrum

A great deal of information about the electronic structure of a ruthenium(II) polypyridyl complex can be extracted just by analysing its absorption spectrum. Figure 8 shows the characteristic spectrum of 2,2'-bipyridine (bpy) and 1,10-phenanthroline (phen) homoleptic complexes with Ru(II).

The vertical transitions that lead to the observed UV-Vis absorption spectrum are represented in Figure 7. They have been organized in four groups, depending on the MOs involved in the excitation. Due to the nature of these complexes, where the ligands are assumed to weakly interact with the metal centre, the excitation process is considered as a charge transfer that creates a temporary intramolecular charge separation. Although the energy distribution of the MOs is dependent on the metal and ligand nature, the general

assumption is that the most energetic vertical transitions are those involving the ligands. They can either be *ligand-centred* transitions (LC), or *intra-ligand transitions* (IL), "**1**" in Figure 7. These transitions are intense sharp absorption bands, and appear in the UV region of the absorption spectrum. Supporting the fact that these transitions are ligand-related, that is, that MOs are indeed localized orbitals, is the observation that the absorption bands of both the free and complexed ligand overlap. This means that the binding of the metal centre does not significantly alter the energy of the ligand-centred orbitals.

Another type of electronic transition is depicted in Figure 7 as "**2**", where the excitation occurs from a ligand-centred orbital towards a metal-centred orbital. These *ligand-to-metal charge transfers* (LMCT) are also highly energetic, and usually fall in the same spectral region of the absorption spectrum as the LLCT. A third type of electronic transitions is *metal-to-ligand charge transfers* (MLCT, **3** Figure 7), responsible for the broad structured absorption band at around 450 nm, typical of Ru(II)-related complexes. Finally there are also *metal-centred* (MC) transitions (**4** Figure 7), where only orbitals belonging to the metal participate. These transitions display low molar absorption coefficients, a signature of symmetry-forbidden transitions.

The MOT is successful in giving a general picture of the electronic nature behind the absorption spectrum of ruthenium(II) complexes. It should be mentioned however that it does not include neither the phenomena responsible for the broadening of absorption bands, nor excitation to higher excited states, vibrational modes, vibronic coupling or the heavy-atom effect that produce a manifold of possible transitions.

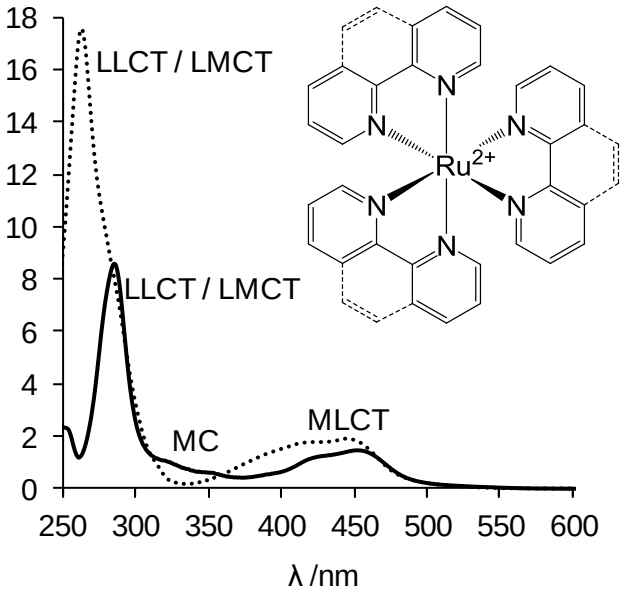

Figure 8. Absorption spectra of the parent complexes $Ru(bpy)_3Cl_2$ (in water, solid line) and $Ru(phen)_3Cl_2$ (in methanol, dotted line). The band assignment is a qualitative exercise based on the MOT and literature reports.[51] See text for details.

1.9.3. Electronic excited states

Once a photon is absorbed and a vertical transition occurs, the electronically excited molecule has several deactivation pathways towards the ground state. The latter involves either *radiative* (emission of a photon) or *non-radiative* processes. As a starting point it is useful to introduce a modified *Jablonski* diagram, where the molecular orbitals and their energy shown in Figure 7 are converted into the relevant electronic states involved in the photophysics of ruthenium complexes.

Figure 9 shows the ground state (S_0), the excited states of *singlet* multiplicity S_1 and S_2 together with the thermally-activated metal-centred state (^{1}MC), and the excited state with spin inversion (T_1). Naturally, the triplet excited state is the lowest energy one due to diminished electron repulsion (parallel spin in separate orbitals). The manifold of electron energies at the ground state leads to a manifold of vertical excitations which are responsible for the broad bands in the absorption spectrum. These excitations may populate *singlet* excited states of higher energy such as S_2 which undergo fast internal conversion (IC) towards the lowest lying S_1 excited state as predicted by the *Kasha*'s rule. After rapid vibrational relaxation (Vr), the excited molecule can go back to the ground state via a non-radiative pathway[1] (for example, collision with solvent). Another possibility is intersystem crossing (ISC) towards the more stable triplet excited state (T_1). In fact, the presence of the ruthenium (heavy) atom is responsible for this process to occur with a high efficiency ($\Phi_{ISC} = 1$ for many Ru(II) complexes, but not for all of them),[52] so that no radiative emission has ever been observed from the S_1 excited state. This T_1 state is the source of the characteristic broad orange-red (peaking around 600 nm) emission band of Ru(II) polypyridyl complexes displaying a long luminescence lifetime (0.1 – 10 μs).[53] In addition to this phosphorescence, the triplet excited state can also return to the ground state by non-radiative pathways. One important deactivation pathway of the triplet excited state of Ru(II) polypyridyls is the thermally-activated population of a (luminescence-silent) metal-centred excited state (^{3}MC), which deactivates undergoing a non-radiative *d-d* transition to the ground state.[54] This cross-over process is evidenced by a decrease in the luminescence lifetime as temperature increases. One drawback from populating this ^{3}MC excited state is related to *photobleaching*, because of its σ* nature that leads to ligand photolabilisation by weakening of the Ru-N σ-bond.[54]

The photophysical description above is based on the assumption that the energy of the ligand orbitals is such that the emission comes from a MLCT state. One of the many

[1] In Photochemistry, the use of the term "non-radiative pathway" refers to a process that does not involve the emission of a UV or visible photon. Nevertheless, this process is actually "radiative" as it leads to the ground state of the molecule by heat emission (infrared radiation).

advantages of this type of compounds is that the photophysical pathways can be modified to yield different results. For example, if the ligand of Figure 7 had a π orbital with lower energy than the *d* orbitals of the metal, then the resulting HOMO orbital (see section 1.4) would have ligand character. The emissive state of such compound would probably be of LLCT type.

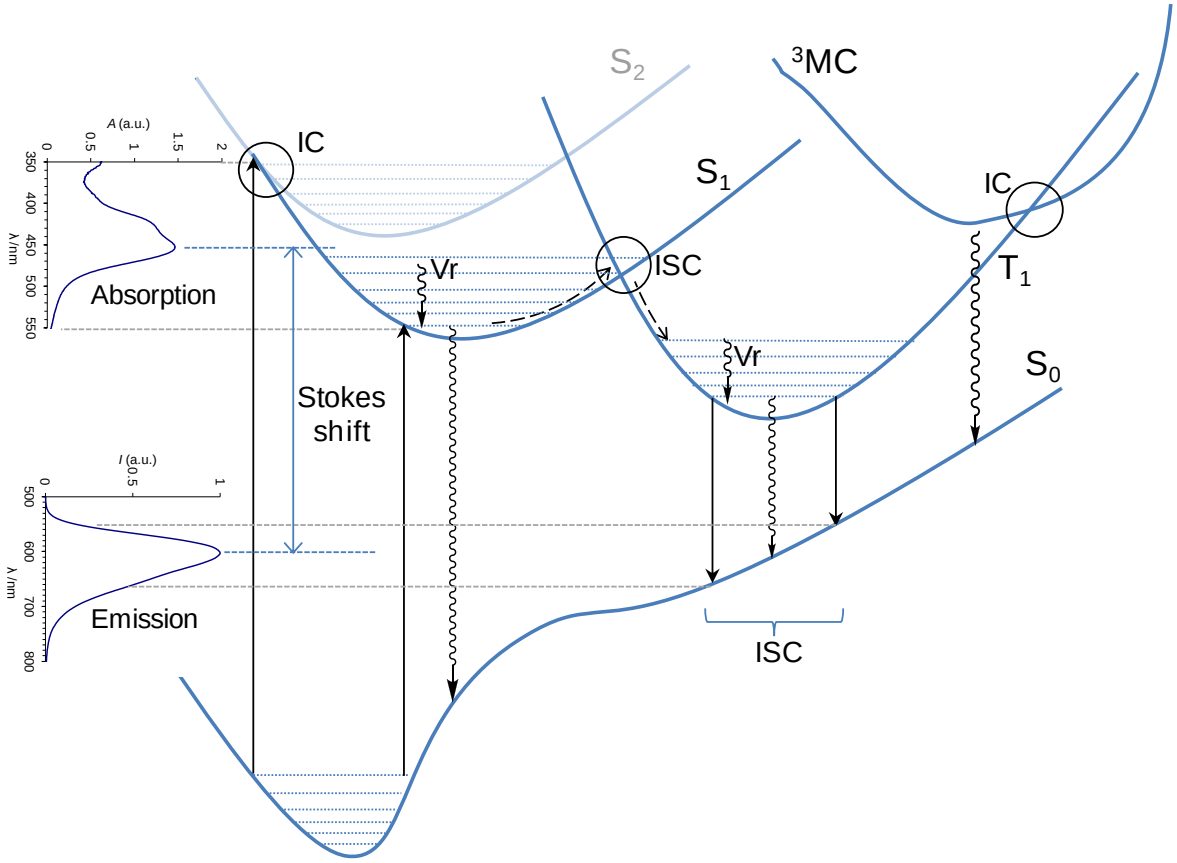

Figure 9. Energy diagram of a hypothetical ruthenium(II) polypyridyl complex. The represented electronic levels are the ground state (S_0), the first and second *singlet* excited states S_1 and S_2 respectively, the *triplet* excited state T_1 and the thermally-activated metal-centred excited state (^{3}MC). IC stands for internal conversion, Vr for vibrational relaxation and ISC for intersystem crossing. See text for details.

Considering the photophysical properties of ruthenium(II) complexes discussed so far, it is of no surprise that this versatile, class of compounds has found applications across different areas such as synthetic catalysts,[55] supramolecular devices,[52a] photodynamic therapy of cancer,[56] dye-sensitized solar cells,[57] artificial photosynthesis,[58] and fuel cells,[59] to name a few.

Ru(II) polypyridyls are also excellent candidates for **luminescent sensing**,[20-21, 60] with some specific examples given in section 1.6. Among the advantageous characteristics that render polypyridyl complexes of ruthenium(II) most suitable for sensor applications are: i) their large Stokes shifts (> 150 nm) as a result of charge-transfer excited states, that

simplifies the sensor optical requirements by reducing interferences; ii) long luminescence lifetimes (up to 10 μs) arising from triplet excited states, which allow for affordable electronics for emission lifetime-based robust sensor systems; iii) significant photostability compared to purely organic indicator dyes, and iv) tunability of their photochemical and physical properties by a judicious selection of the coordinating polyazaheterocyclic ligands (up to three different ligands can be used to form the Ru(II) coordination sphere). The latter is responsible for the application of such indicator dyes to the detection of a wide variety of analytes. By modifying the chemical structure of the ligands, a specific analyte probe/receptor may be devised, the solubility properties of the overall complex can be modified, and/or tethering the indicator dye to a polymer support by electrostatic, covalent or affinity binding may be achieved. Ligand selection may also alter the photophysics of the ruthenium complex by changing the nature of the emissive excited state.[53-54, 60b]

1.10. Solvent and temperature effects

Several external factors influence the observed spectroscopic features of a Ru(II) dye and other luminophores. Among them, PET (section 1.4), probe-probe interactions (aggregates), solvent polarity and temperature (via ^{3}MC population, section 1.9.3) can have dramatic effects on the luminescence of a Ru(II) complex.

1.10.1. Solvent polarity

A simple way of rationalizing solvent polarity effects on the spectroscopic properties of luminescent compounds can be explained according to the Lippert-Mataga model.[61] Its approach is in fact quite similar to the polarizable continuum model (PCM) used in quantum calculations, described in section 1.8.3.

Eq. 32 below describes their model,

$$\bar{\nu}_{abs} - \bar{\nu}_{em} = \frac{2}{hc} \times \Delta f \times \frac{\left(\mu_{exc} - \mu_{gr}\right)^2}{a^3} + b$$

$$\Delta f = \left(\frac{\varepsilon - 1}{2\varepsilon + 1} - \frac{n^2 - 1}{2n^2 + 1}\right) \qquad \text{Eq. 32}$$

where $\bar{\nu}_{abs}$ and $\bar{\nu}_{em}$ stand for the energy of the absorption and emission maxima (in cm^{-1}), h is the Plank constant, c is the speed of light in vacuum, μ_{exc} and μ_{gr} are the luminophore dipole moments in the excited state and ground state, respectively. The term a represents the radius of the fluorophore and b is a constant. In this model, the luminophore is regarded as a dipole surrounded by a homogeneous field (the bulk solvent) of a given dielectric constant, ε and refractive index, n. The term Δf (orientation polarizability) is responsible for the measurable spectral shifts, so that the Lippert-Mataga plot represents $\bar{\nu}_{abs} - \bar{\nu}_{em}$ as a function of Δf. The model takes into account the electron movement inside the solvent molecules that allows stabilization of the fluorophore dipoles (refractive index, n) as well as the solvent relaxation that allows the nuclei movement (dielectric constant, ε) and hence the orientation polarizability term.[17] Similarly to the PCM approach, this model does not account for specific luminophore-solvent interactions such as hydrogen bonding, induced dipole moments, or delayed solvent relaxation.[17]

Due to its localized electrostatic charges, a cationic ruthenium complex is expected to be stabilised in a polar medium compared to a non-polar one. The solvent-driven stabilization of the ground state lowers the HOMO orbital leading to an increase in the absorption energy and a blue shift occurs. Upon photon absorption, the long lifetime of the ^{3}MLCT state allows the assumption that the solvent relaxation is complete prior to emission.

Under this scenario, the charge-transfer excited state of the ruthenium complex leads to a net increase in its dipole moment. For this reason, the solvent stabilization effects are more evident for the emission band, compared to the absorption bands. The polar solvent-stabilised excited state is now lower in energy hence a red-shift in the emission occurs.[23]

1.10.2. Dependence of the luminescence lifetime on temperature

The average time that a molecule in its excited state takes to return to the ground state (either via radiative or non-radiative pathways) is described by its luminescence lifetime τ, which can be rationalized according to eq 33,

$$\frac{1}{\tau} = k_{\mathrm{r}} + k_{\mathrm{nr}} \qquad \text{Eq. 33}$$

where k_{r} and k_{nr} are the radiative and non-radiative deactivation rate constants. On the other hand, k_{nr} comprises all pathways that "silently" deactivate the excited state such as vibrational relaxation, internal conversion and excited state deactivation processes. Since the latter is temperature-dependant, Eq. 33 can be reformulated separating the temperature-dependant term (Eq. 33),

$$\frac{1}{\tau}(\mathrm{T}) = k_0 + k_{\mathrm{T}}(\mathrm{T}) \qquad \text{Eq. 34}$$

where k_0 comprises both the radiative and non-radiative temperature-independent rate constants and k_{T} is the temperature-dependant term assigned to the thermally activated ^{3}MC population.[62] The latter is described by an Arrhenius-type equation (Eq. 35),[63]

$$k_{\mathrm{T}} = A \times e^{-\frac{\mathrm{B}}{\mathrm{RT}}} \qquad \text{Eq. 35}$$

By developing the temperature dependant term of Eq. 35 in Eq. 33 one gets,

$$\frac{1}{\tau}(\mathrm{T}) = k_0 + \left(A \times e^{-\frac{B}{RT}}\right) \qquad \text{Eq. 36}$$

The assignment of the A and B parameters of Eq. 35 can be made by studying the kinetic scheme for the ^{3}MC population,

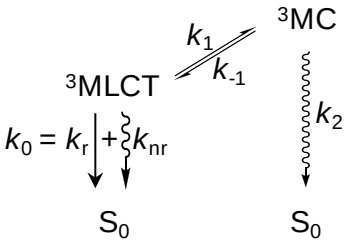

The approach lies in considering two possible limit situations: a) the deactivation rate of the ^{3}MC state dominates, namely $k_2 >> k_{-1}$, so that the thermal activation of the metal-centred state becomes irreversible, or b) $k_2 << k_{-1}$ which means that both states are in equilibrium. In the first situation, the parameter A represents the pre-exponential term of the ^{3}MLCT-^{3}MC surface crossing, and B is the activation energy of the cross-over process.[64] In the second case where equilibrium exists, the parameter A represents the rate constant k_2 while B is the Gibbs energy difference between both triplet states.[63] Qualitative values to distinguish both situations have been reported,[63-64] where for the irreversible picture A ≈ 10^{12}–10^{14} s^{-1} and B ≈ 3000–4000 cm^{-1}, in contrast to the equilibrium situation where A ≈ 10^9–10^{10} s^{-1} and B ≈ 2000 cm^{-1}, but the most precise way to distinguish both situations is to find out the effect of a nucleophile (e.g. Cl^-) in a relative non-polar solvent on the emission lifetime variation with temperature (an irreversible cross-over should not be influenced by the reaction of a nucleophile with the ^{3}MC state).[65]

A third possibility exists, which does not involve cross-over to the ^{3}MC state but rather to a fourth ^{3}MLCT state (the first ^{3}MLCT is in fact a mixture of three thermally-equilibrated close-lying ^{3}MLCT as demonstrated for $Ru(bpy)_3^{2+}$ by Crosby et al.[66]). Under this scenario, the fourth triplet metal-centred state is accessible by thermal activation and the parameter B (now the energy difference between both ^{3}MLCT states) is estimated to be lower than 2000 cm^{-1}.[63]

Therefore, the data from plotting the reciprocal of the luminescence lifetime τ as a function of the reciprocal of temperature can be fitted to Eq. 36 to calculate the parameters k_0, A and B providing a complete picture of the photophysics of the investigated ruthenium complex.

The population of the higher-lying triplet state (either the MC or the fourth MLCT) can also be described by the luminescence quantum yield according to Eq. 37.

$$\Phi_T = \frac{k_T}{(k_0 + k_T)} \qquad \text{Eq. 37}$$

Both the A and B parameters show dependencies on the temperature range of the experiment so that it has been shown that for the sake of comparison and discussion purposes it is better to use the Φ_T value.[63]

1.11. Scope of this Thesis

The work described in this Thesis was presented in a pyramidal manner, reducing the number of compounds under study as the chapter number increased. It was separated into three different chapters, each containing a section dedicated to each compound.

The main objective of this Thesis has been to develop novel luminescent polypyridyl ruthenium(II) complexes for aqueous sensing applications. These compounds are widely used as oxygen, pH or temperature sensors, in robust, commercially available devices which are based on phase-sensitive luminescence shifts. Nonetheless, the application of polypyridyl Ru(II) complexes as sensors for heavy metals in aqueous media is still under development and this is where the presented work gains relevance. Both copper(II) and mercury(II) ions were chosen as target analytes not only because they are found everywhere in aqueous environments but especially due to their toxicity. Taking advantage of the existing technology behind O_2 sensors, expanding the use of luminescent polypyridyl ruthenium(II) complexes to Cu(II) and Hg(II) ions should lead to cheap sensor schemes. This aim was to be achieved by a judicious molecular design which led to the synthesis of polypyridyl ligands with specific receptor moieties and, eventually, to their ruthenium(II) heteroleptic complexes. In order to increase sensitivity and selectivity (a key factor in heavy metal sensing), the receptor moieties were sought in order to display high affinities towards the analytes. Naturally, high affinities lead to strong binding which impedes the sensor of being reusable, rendering it a dosimeter. For this reason, a regeneration step is mandatory to achieve *online*, continuous operating modes.

Since interferences from by-products are a major drawback in luminescent indicator dyes, a special care was devoted to purification procedures. In order to evaluate their potential use as molecular probes, a photochemical characterisation was performed in the absence and in the presence of the target analyte. A computational chemistry study was also carried out to rationalize better the observed spectroscopic properties and to guide the molecular design of future indicator dyes of this family. Moreover, two luminescent ruthenium(II) polypyridyl complexes functionalized with polyalkyl chains were also synthesised. Their spectroscopic properties were studied under the scope of solvent-sensitive dyes for waterborne hydrocarbons sensing.

In this way, the work carried out and described in this Thesis has tackled four major areas: organic synthesis, analytical chemistry, photochemistry and computational chemistry.

References

[1] J.-M. Lehn in *Design of organic complexing agents. Strategies towards properties*, Alkali Metal Complexes with Organic Ligands, *Vol. 16,* Springer Berlin / Heidelberg, **1973**, pp. 1-69.
[2] a) N. K. Srivastava and C. B. Majumder, *J. Hazard. Mater.* **2008**, *151*, 1-8; b) L. Järup, *Brit. Med. Bull.* **2003**, *68*, 167-182.
[3] G. Orellana, C. Cano-Raya, J. López-Gejo and A. R. Santos in *Online Monitoring Sensors*, (P. Wilderer), Treatise on Water Science, *Vol. 3,* Elsevier, Oxford: Academic Press, **2011**, pp. 221–262.
[4] F. Fu and Q. Wang, *J. Environ. Manage.* **2011**, *92*, 407-418.
[5] in *National Primary Drinking Water Regulations*, Environmental Protection Agency, **2009**.
[6] in *Drinking Water Directive*, European Commission, **1998**.
[7] O. S. Wolfbeis, *Fresen. J. Anal. Chem.* **1990**, *337*, 522-527.
[8] A. Hulanicki, S. Glab and F. Ingman, *Pure Appl. Chem.* **1991**, *63*, 1247-1250.
[9] a) C. McDonagh, C. S. Burke and B. D. MacCraith, *Chem. Rev.* **2008**, *108*, 400-422; b) G. G. Cammann, E. A. Guilbault, H. Hal, R. Kellner and O. S. Wolfbeis in *Proceedings of the Cambridge Workshop on Chemical Sensors and Biosensors*, The Cambridge Definition of Chemical Sensors, *Vol. 1,* Cambridge University Press, New York, **1996**.
[10] X.-D. Wang and O. S. Wolfbeis, *Anal. Chem.* **2012**, *85*, 487-508.
[11] T. Mayr in *Optical sensors for the determination of heavy metal ions*, *Ph.D. Thesis*, Regensburg, Regensburg, **2002**, p. 140.
[12] J. M. Lehn, *Struct. Bonding* **1973**, *16*, 1-69.
[13] J. M. Lehn, *Supramolecular Chemistry: Concepts and Perspectives*, Ed., **1995**, p.
[14] a) S. Joo and R. B. Brown, *Chem. Rev.* **2008**, *108*, 638-651; b) G. Orellana in *Fluorescence-based sensors*, (F. Baldini, A. N. Chester, J. Homola and S. Martellucci), Optical Chemical Sensors, *Vol. 224,* Springer Netherlands, **2006**, pp. 99-116.
[15] G. Orellana and D. Haigh, *Curr. Anal. Chem.* **2008**, *4*, 273-295.
[16] R. A. Bissell, A. P. de Silva, H. Q. N. Gunaratne, P. L. M. Lynch, G. E. M. Maguire and K. R. A. S. Sandanayake, *Chem. Soc. Rev.* **1992**, *21*, 187.
[17] J. R. Lakowicz, *Principles of fluorescence spectroscopy*, 3rd Ed., Springer, New York, **2006**, p. 954.
[18] a) G. A. Crosby and J. N. Demas, *J. Am. Chem. Soc.* **1970**, *92*, 7262-7270; b) V. Balzani, S. Campagna, F. Puntoriero, F. Nastasi and G. Bergamini in *Photochemistry and Photophysics of Coordination Compounds: Ruthenium*, Photochemistry and Photophysics of Coordination Compounds I, *Vol. 280,* Springer Berlin / Heidelberg, **2007**, pp. 117-214.
[19] B. Valeur and I. Leray, *Coord. Chem. Rev.* **2000**, *205*, 3-40.
[20] J. López-Gejo, D. Haigh and G. Orellana, *Langmuir* **2009**, *26*, 2144-2150.
[21] L. Tormo, N. Bustamante, G. Colmenarejo and G. Orellana, *Anal. Chem.* **2010**, *82*, 5195-5204.
[22] a) W. Rettig and R. Lapouyade in *Fluorescence probes based on twisted intramolecular charge transfer (TICT) states and other adiabatic photoreactions*, (J. R. Lakowicz), Topics in fluorescence spectroscopy, *Vol. 4,* Plenum Press, New York, **1994**, pp. 109-149; b) N. Ghoneim, *Spectrochim. Acta, Part A* **2000**, *56*, 1003-1010.
[23] A. M. Castro, J. Delgado and G. Orellana, *J. Mater. Chem.* **2005**, *15*, 2952-2958.
[24] S. E. Braslavsky, A. U. Acuna, W. Adam, F. Amat, D. Armesto, T. D. Z. Atvars, A. Bard, E. Bill, L. O. Bjoern, C. Bohne, J. Bolton, R. Bonneau, H. Bouas-Laurent, A. M. Braun, R. Dale, K. Dill, D. Doepp, H. Duerr, M. A. Fox, T. Gandolfi, Z. R. Grabowski, A. Griesbeck, A. Kutateladze, M. Litter, J. Lorimer, J. Mattay, J. Michl, R. J. D. Miller, L. Moggi, S. Monti, S. Nonell, P. Ogilby, G. Olbrich, E. Oliveros, M. Olivucci, G. Orellana, V. Prokorenko, K. R. Naqvi, W. Rettig, A. Rizzi, R. A. Rossi, R. E. San, F. Scandola, S. Schneider, E. W. Thulstrup, B. Valeur, J. Verhoeven, J. Warman, R. Weiss, J. Wirz and K. Zachariasse, *Pure Appl. Chem.* **2007**, *79*, 293-465.

[25] W. D. Bare, N. H. Mack, W. Xu, J. N. Demas and B. A. DeGraff, *Anal. Chem.* **2002**, *74*, 2198-2209.
[26] G. Orellana, M. C. Moreno-Bondi, D. Garcia-Fresnadillo and M. D. Marazuela, *Springer Ser. Chem. Sens. Biosens.* **2005**, *3*, 189-225.
[27] T. Mayr, I. Klimant, O. S. Wolfbeis and T. Werner, *Anal. Chim. Acta* **2002**, *462*, 1-10.
[28] in *Technical Notes on Drinking Water Methods*, Environmental Protection Agency, **1994**, p. 112.
[29] a) http://www.astisensor.com; b) http://www.nexsens.com; c) https://www.ysi.com; d) http://www.hach.com; e) http://www.swan.ch; f) http://www.nico2000.net; g) http://www.in-situ.com; h) http://www.s-can.at; i) http://www.horiba.com; j) http://www.hannainst.com; k) http://www.environnement-sa.com
[30] H. Smyth and D. Cozzolino, *Chem. Rev.* **2013**, *113*, 1429-1440.
[31] A. P. de Silva and S. A. de Silva, *J. Chem. Soc., Chem. Commun.* **1986**, 1709-1710.
[32] K. Hiratani, M. Nomoto, H. Sugihara and T. Okada, *Analyst* **1992**, *117*, 1491-1495.
[33] A. P. de Silva, H. Q. N. Gunaratne, T. Gunnlaugsson, A. J. M. Huxley, C. P. McCoy, J. T. Rademacher and T. E. Rice, *Chem. Rev.* **1997**, *97*, 1515-1566.
[34] a) E. M. Nolan and S. J. Lippard, *Chem. Rev.* **2008**, *108*, 3443-3480; b) L. N. Neupane, J.-Y. Park, J. H. Park and K.-H. Lee, *Org. Lett.* **2013**, *15*, 254-257; c) K. H. El, P. Estevez, S. Ibeas, F. C. Garcia, F. Serna, F. B. Benabdelouahab and J. M. Garcia, *Dyes Pigments* **2013**, *96*, 414-423; d) K. H. El, P. Estevez, F. C. Garcia, F. Serna and J. M. Garcia, *Anal. Methods* **2013**, *5*, 54-58; e) S. H. Lee, A. Parthasarathy and K. S. Schanze, *Macromol. Rapid Commun.* Ahead of Print; f) Y. Cao, L. Ding, W. Hu, L. Wang and Y. Fang, *Appl. Surf. Sci.* Ahead of Print.
[35] a) E. Coronado, J. R. Galan-Mascaros, C. Marti-Gastaldo, E. Palomares, J. R. Durrant, R. Vilar, M. Gratzel and M. K. Nazeeruddin, *J. Am. Chem. Soc.* **2005**, *127*, 12351-12356; b) X. Li, Y. Chen, J. Meng, K. Lü, A. Zhang and B. Zhang, *Chinese J. Chem.* **2011**, *29*, 1947-1950; c) P. Comba, R. Kramer, A. Mokhir, K. Naing and E. Schatz, *Eur. J. Inorg. Chem.* **2006**, 4442-4448; d) A. M. Josceanu, P. Moore, S. C. Rawle, P. Sheldon and S. M. Smith, *Inorg. Chim. Acta* **1995**, *240*, 159-168.
[36] K. A. Connors, *Binding Constants: The Measurement of Molecular Complex Stability*, 1st Ed., Wiley, **1987**, p. 432.
[37] a) G. D. Johnson and R. E. Bowen, *J. Am. Chem. Soc.* **1965**, *87*, 1655-1660; b) K. A. Connors and J. A. Mollica, *J. Pharm. Sci.* **1966**, *55*, 772-780.
[38] A. Job, *Annales de Chimie* **1928**, *9*, 113-203.
[39] a) R. Sang and L. Xu, *Acta Crystallogr. E* **2005**, *E61*, m793-m795; b) A. Bencini and F. Mani, *Inorg. Chim. Acta* **1988**, *154*, 215-219.
[40] K. K. Kamar, L. R. Falvello, P. E. Fanwick, J. Kim and S. Goswami, *Dalton Trans.* **2004**, 1827-1831.
[41] a) J. B. Foresman and A. Frisch, *Exploring Chemistry with Electronic Structure Methods*, 2nd Ed., Gaussian, Inc., Pittsburgh, **1996**, p. 302; b) A. Hinchliffe, *Molecular Modelling for Beginners*, 2nd Ed., John Wiley & Sons Ltd, **2008**, p. 428; c) I. N. Levine, *Quantum Chemistry*, 5th Ed., Prentice-Hall, New Jersey, **2000**, p. 739.
[42] M. J. Frisch, G. W. Trucks, H. B. Schlegel, G. E. Scuseria, M. A. Robb, J. R. Cheeseman, G. Scalmani, V. Barone, B. Mennucci, G. A. Petersson, H. Nakatsuji, M. Caricato, X. Li, H. P. Hratchian, A. F. Izmaylov, J. Bloino, G. Zheng, J. L. Sonnenberg, M. Hada, M. Ehara, K. Toyota, R. Fukuda, J. Hasegawa, M. Ishida, T. Nakajima, Y. Honda, O. Kitao, H. Nakai, T. Vreven, J. A. Montgomery, J. E. Peralta, F. Ogliaro, M. Bearpark, J. J. Heyd, E. Brothers, K. N. Kudin, V. N. Staroverov, R. Kobayashi, J. Normand, K. Raghavachari, A. Rendell, J. C. Burant, S. S. Iyengar, J. Tomasi, M. Cossi, N. Rega, J. M. Millam, M. Klene, J. E. Knox, J. B. Cross, V. Bakken, C. Adamo, J. Jaramillo, R. Gomperts, R. E. Stratmann, O. Yazyev, A. J. Austin, R. Cammi, C. Pomelli, J. W. Ochterski, R. L. Martin, K. Morokuma, V. G. Zakrzewski, G. A. Voth, P. Salvador, J. J. Dannenberg, S. Dapprich, A. D. Daniels, Farkas, J. B. Foresman, J. V. Ortiz, J. Cioslowski and D. J. Fox in *Gaussian 09, Revision A.02*, *Vol.* Wallingford CT, **2009**.
[43] J. C. Slater, *Phys. Rev.* **1930**, *36*, 57-64.
[44] S. F. Boys, *Proc. R. Soc. London, Ser. A* **1950**, *200*, 542-554.

[45] W. J. Hehre, R. F. Stewart and J. A. Pople, *J. Chem. Phys.* **1969**, *51*, 2657-2664.
[46] R. Ditchfield, W. J. Hehre and J. A. Pople, *J. Chem. Phys.* **1971**, *54*, 724-728.
[47] a) P. Hohenberg and W. Kohn, *Phys. Rev.* **1964**, *136*, B864-B871; b) W. Kohn and L. J. Sham, *Phys. Rev.* **1965**, *140*, A1133-A1138.
[48] A. D. Becke, *J. Chem. Phys.* **1993**, *98*, 1372-1377.
[49] D. Escudero in *Spectroscopy and photochemistry of transition metal complexes: a quantum chemical study*, *Ph.D. Thesis*, Friedrich-Schiller, Jena, **2011**, p. 209.
[50] a) V. Balzani, A. Juris, M. Venturi, S. Campagna and S. Serroni, *Chem. Rev.* **1996**, *96*, 759-834; b) M. Montalti, A. Credi, L. Prodi and M. T. Gandolfi, *Handbook of Photochemistry*, 3rd Ed., CRC Press, **2006**, p. 650.
[51] A. Juris, V. Balzani, F. Barigelletti, S. Campagna, P. Belser and A. Vonzelewsky, *Coord. Chem. Rev.* **1988**, *84*, 85-277.
[52] a) V. Balzani, G. Bergamini, F. Marchioni and P. Ceroni, *Coord. Chem. Rev.* **2006**, *250*, 1254-1266; b) G. Orellana and A. M. Braun, *J. Photochem. Photobiol. A* **1989**, *48*, 277-289.
[53] D. Garcia-Fresnadillo and G. Orellana, *Helv. Chim. Acta* **2001**, *84*, 2708-2730.
[54] S. Campagna, F. Puntoriero, F. Nastasi, G. Bergamini and V. Balzani in *Photochemistry and photophysics of coordination compounds: Ruthenium*, (S. Campagna and V. Balzani), Photochemistry and Photophysics of Coordination Compounds I, *Vol. 280,* Springer-Verlag Berlin, Berlin, **2007**, pp. 117-214.
[55] J. M. R. Narayanam and C. R. J. Stephenson, *Chem. Soc. Rev.* **2011**, *40*, 102-113.
[56] F. Schmitt, P. Govindaswamy, G. Süss-Fink, W. H. Ang, P. J. Dyson, L. Juillerat-Jeanneret and B. Therrien, *J. Med. Chem.* **2008**, *51*, 1811-1816.
[57] a) C. Sahin, C. Tozlu, K. Ocakoglu, C. Zafer, C. Varlikli and S. Icli, *Inorg. Chim. Acta* **2008**, *361*, 671-676; b) M. K. Nazeeruddin, S. M. Zakeeruddin, J. J. Lagref, P. Liska, P. Comte, C. Barolo, G. Viscardi, K. Schenk and M. Graetzel, *Coord. Chem. Rev.* **2004**, *248*, 1317-1328; c) C. Klein, M. K. Nazeeruddin, D. Di Censo, P. Liska and M. Graetzel, *Inorg. Chem.* **2004**, *43*, 4216-4226.
[58] a) L. Sun, L. Hammarstrom, B. Akermark and S. Styring, *Chem. Soc. Rev.* **2001**, *30*, 36-49; b) R. Konduri, H. Ye, F. M. MacDonnell, S. Serroni, S. Campagna and K. Rajeshwar, *Angew. Chem. Int. Ed.* **2002**, *41*, 3185-3187.
[59] M. Nielsen, E. Alberico, W. Baumann, H.-J. Drexler, H. Junge, S. Gladiali and M. Beller, *Nature* **2013**, *495*, 85-89.
[60] a) M. Bedoya, M. T. Diez, M. C. Moreno-Bondi and G. Orellana, *Sens. Actuators, B* **2006**, *B113*, 573-581; b) E. N. Dixon, M. Z. Snow, J. L. Bon, A. M. Whitehurst, B. A. DeGraff, C. Trindle and J. N. Demas, *Inorg. Chem.* **2012**, *51*, 3355-3365; c) H. M. Rowe, W. Xu, J. N. Demas and B. A. DeGraff, *Appl. Spectrosc.* **2002**, *56*, 167-173; d) G. Orellana and D. Garcia-Fresnadillo in *Environmental and industrial optosensing with tailored luminescent Ru(II) polypyridyl complexes*, (O. S. Wolfbeis), Springer Series on Chemical Sensors and Biosensors, *Vol. 1,* **2004**, pp. 309-357.
[61] a) V. E. Lippert, *Z. Elektrochem.* **1957**, *61*, 962–975; b) N. Mataga, Y. Kaifu and M. Koizumi, *Bull. Chem. Soc. Jpn.* **1956**, *29*, 465–470.
[62] J. V. Caspar and T. J. Meyer, *J. Am. Chem. Soc.* **1983**, *105*, 5583-5590.
[63] L. Jacquet and A. K.-D. Mesmaeker, *J. Chem. Soc., Faraday Trans.* **1992**, *88*, 2471-2480.
[64] J. V. Caspar and T. J. Meyer, *J. Am. Chem. Soc.* **1983**, *105*, 5583-5590.
[65] a) A. Masschelein, L. Jacquet, M. A. Kirsch-De and J. Nasielski, *Inorg. Chem.* **1990**, *29*, 855-860; b) J.-P. Lecomte, A. Kirsch-De Mesmaeker and G. Orellana, *J. Phys. Chem.* **1994**, *98*, 5382-5388.
[66] G. D. Hager and G. A. Crosby, *J. Am. Chem. Soc.* **1975**, *97*, 7031-7037.

Chapter II

Synthesis

Having introduced most of the relevant concepts in the Introduction to this Thesis, chapter II will describe in detail the synthetic procedures carried out and the suggested reaction mechanisms. At the same time, relevant discussions of the results are also included at each synthetic procedure. From ligand design to purification techniques, *solubility* has played a major role in demanding the use of less conventional methods. Reactions in boiling ethylene glycol or purifications by cotton chromatography are some of these rather unusual methods. Undoubtedly, the most time-consuming step of the work developed in this Thesis is related to the purification of the target molecules. Polypyridyl ligands can be extremely insoluble (see section 2.2), and some of them were ditopic (i.e. two-binding sites are available). Furthermore, ruthenium(II) ions can yield bis- or tris-chelate complexes (the latter homo or heteroleptic), a feature that added to the ditopic nature of the ligands led to many by-products.

2.1. Materials and instrumentation

Type I water was from a Millipore Direct-Q purification system. Organic solvents were of HPLC grade and used without further purification.

Synthesis setup. Reactions were carried out inside ventilating fume hoods equipped with 99.995% argon (Praxair) and high vacuum (Edwards 8 dual stage pump) lines. For refrigeration purposes, Huber Polystat CC1 circulators were used. The reaction mixture heating (< 310 °C) and stirring (< 1500 rpm) were carried out with IKA hotplates with magnetic stirrer (RCT BASIC), fitted with flask heat-on blocks/inserts (Radleys) and electronic contact thermometer (IKA, ETS-D5). When possible, the course of the reactions was followed by thin layer chromatography (TLC) analysis on both alumina and silica gel (aluminium oxide 60 neutral F_{254} and silica gel 60 F_{254}, Merck) and UV examination (254 and 365 nm).

Evaporation. Rotary evaporators from BÜCHI (R-215) and Heidolph (Hei-VAP Precision) were connected to a double-Schlenk line with 4 double oblique stopcocks each connected to a different vacuum pump for versatility. The first one, a BÜCHI V-700 vacuum pump equipped with a BÜCHI V-850 vacuum controller allowed evaporation of solvents up to 10 mbar. The second one, a Telstar 2F-3 pump provided a higher vacuum for difficult cases of solvent evaporation such as dimethyl sulfoxide (DMSO) and was protected by a nitrogen trap.

Both pumps were also connected through the double-vacuum line to a vacuum oven (Lab-line, Squaroid) which allowed final drying of the products.

Preparation and cleaning. All reaction protocols were devised after careful study of Chemical Abstracts Service (CAS) literature searches through its SciFinder engine tool. Two scales were used for weighting, namely a Denver Instruments TP-303 unit and a Mettler AT-260 (0.01 mg) one for more precise measurements. Filtrations were performed through sintered glass plate funnels no. 4 and 5 (pore size range 1-15 μm). The filters were cleaned by oxidation with piranha solution (a freshly prepared mixture of concentrated H_2SO_4 and 30% H_2O_2 in a 3:1 v/v ratio), thorough washing with tap water and Type I water, and final rinsing with acetone (twice) followed by oven dry (50 °C). Stubborn stains on glassware were also removed by piranha solution, whereas regularly stained glassware was cleaned by overnight immersion in a KOH-saturated solution in isopropyl alcohol, thoroughly rinsed with water, subsequently washed with phosphate-free liquid lab detergent (PCC-Pfree Thermo Scientific), rinsed with Type I water and oven dried. Samples for nuclear magnetic resonance (NMR) spectroscopy were prepared by weighting ca. 10 mg of the product, adding ca. 0.7 mL of the desiccator-stored deuteriated solvent (98.5 to >99% D-atom) and promoting dissolution in a sonicator bath (Fungilab). The resulting solution was filtered with a glass/PTFE syringe (SGL) equipped with a 0.22 μm nylon filter (GE Osmonics).

Product purification. Preparative thin-layer chromatography (PTLC) 1 mm-thick silica or alumina glass-backed plates were from Merck. Flash column chromatography was performed using silica or alumina (Merck). Semi-preparative high performance liquid chromatography (HPLC) was carried out in an Agilent 1100 series chromatograph with a 1100 quaternary pump, automatic injector and fraction collector, fitted with a C_{18} Agilent ZORBAX Eclipse XDB column (5 μm, 9.4 x 250 mm).

Product characterisation. Melting points were measured with a Stuart Scientific SMP3 melting point apparatus. Fourier transform infrared (FT-IR) absorption spectra (KBr disk) were recorded in a Bruker Tensor 27 spectrophotometer. ^{1}H NMR and ^{13}C NMR spectra were recorded on a Bruker AVANCE DPX at 300 MHz (UCM NMR Central Instrumentation Facilities, CIF) in DMSO-d_6, MeOD-d_4 and CD_3CN-d_3 (>99% D). All spectra were processed by the software package Bruker TOPSPIN (v2.1) and calibrated to meet the solvent shifts as reported by Gottlieb et al.[1] The chemical shifts were assigned taking into consideration literature reports,[2] careful study of 2D heteronuclear multiple-quantum correlation (HMQC) ^{1}H-^{13}C NMR spectra, or with the aid of the prediction software ChemBioDraw Ultra (v11.0.1). ESI-MS spectra were obtained on a LTQ XL linear ion trap mass spectrometer fitted with an electrospray ionization (ESI) sample inlet (UCM MS-CIF). Elemental analyses were performed on a LECO CHNS-932 (UCM Microanalytical CIF).

2.2. Synthesis of polypyridyl ligands

The polyazaheteroaromatic ligands prepared in this work are derivatives of commercially available 1,10-phenanthroline (phen) or 2,2'-bipyridine (bpy) (Figure 10). Being pyridine-related compounds, their reactivity lies on i) the electron-donor properties of the nitrogen atom which may undergo N-oxidation, protonation, alkylation or acylation, and ii) the electron deficiency at *para* and *ortho* positions. For this reason, these heterocyclic compounds show poor reactivity in electrophilic substitutions (S_E). As with pyridines, the nitrogen atom is responsible for the electron-deficient character of the heteroaromatic system. Moreover, the first pK_a value of the conjugated base is 4.95[3] for phen and 4.35[4] for bpy, similar to its parent pyridine compound (pK_a = 5.25). Both ligands are planar and relatively hydrophobic (the solubility in water at 25 °C is 2.7 g L^{-1} for phen[5] and 5.9 g L^{-1} for bpy[6]). Bpy ligands can twist around the 2-2' bond, while phen ligands are rigid with a pre-organized tweezers-like structure. Their σ-donor capability is reinforced by π-symmetry accepting orbitals, thus increasing its affinity towards transition metal cations.[3] Such low energy π* orbitals are responsible for the characteristic MLCT absorption and emission bands of bpy and phen complexes.

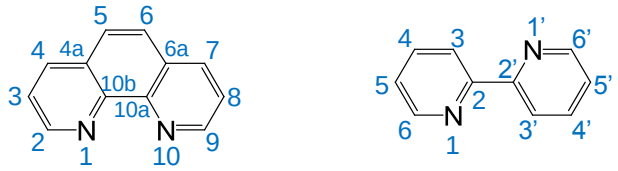

1,10-Phenanthroline (phen) 2,2'-bipyridine (bpy)

Figure 10. Structure of the precursor ligands. Their nomenclature and numbering follows IUPAC rules.[7]

2.2.1. 1,10-phenanthroline-5,6-dione (pdo)

The synthetic route to the pdo ligand is shown in Scheme 1. It follows the work of Yamada et al. which is probably the most frequently used procedure for obtaining this ligand.[8] In this reaction, 1,10-phenanthroline is oxidized by a H_2SO_4/HNO_3 mixture in the presence of solid KBr. The presence of the bromide anion has been shown to significantly accelerate the reaction rate,[9] possibly by in-situ formation of the oxidizing bromine molecule. Several publications since then have introduced small modifications to further optimize the yield.[10] Comparing the initial protocol of Yamada et al. with the suggested improvements of other authors, it is clear that the mixture of acids has to be cooled below 0 °C and that the neutralization step must be performed with due care to avoid degradation of

the product. If 1,10-phenanthroline is kept under basic conditions, it can undergo loss of carbon monoxide to yield 4,5-diazafluoren-9-one.[11] In terms of purification, the best results were obtained by recrystallization from boiling ethanol (> 99.8%) as indicated by Paw et al.[10b] Some authors refer to the same procedure but using methanol as solvent,[10d] and others go further to purification with column chromatography on neutral alumina using dichloromethane as eluent.[12] Unfortunately, the latter method led to complete degradation of the pdo ligand.

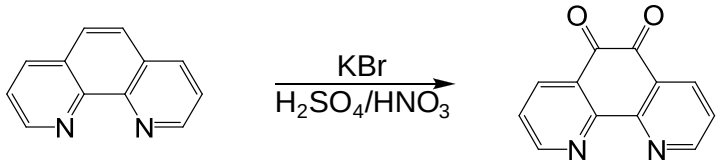

phen **pdo**

Reagent	Supplier	Mass/g	Mol	Volume/mL	Purity
phen	Acros	1.000	5.3×10^{-3}	---	99%
KBr	Panreac	1.200	10.1×10^{-3}	---	99%
H_2SO_4	Scharlau	---	---	10	98%
HNO_3	Fluka	---	---	5	>90%

Scheme 1. Synthesis of 1,10-phenanthroline-5,6-dione (pdo) following the procedure by Yamada et al.[8]

The experimental procedure that provided better results (yield and purity) was as follows, using the amounts shown in Scheme 1. A mixture of potassium bromide and 1,10-phenanthroline (phen) was placed into a two-necked round bottom flask equipped with a condenser and pressure-compensated dropping funnel. The flask containing the solid mixture was dipped into an acetone-ice bath (T ~ -10 °C). Then a freezer-cooled H_2SO_4/HNO_3 mixture (T ~ -20 °C) was added dropwise as to make each drop touch the cooled flask walls prior to contacting with the solid reagents. The resulting red solution was stirred for 10 min at -10 °C and then it was warmed up to room temperature with evolution of Br_2. After 4 h of stirring, the reaction was quenched by pouring it into a beaker containing 50 g of ice-water. The pH was risen to 6 by adding concentrated NaOH and then by adding $NaHCO_3$. The desired product precipitated in the process and was extracted with ca. 400 mL of chloroform, which was eliminated by rotary evaporation. Yellow needles were obtained after recrystallization from boiling ethanol (> 99.8%). A second crop affords more of the desired compound (1.010 g, 4.8 mmol, 90% yield overall). Characterisation by ^{1}H-NMR and IR confirmed the product structure (Figure A1, section 6.1.1). ^{1}H-NMR (DMSO-d_6): δ/ppm 9.02 (2H-2, *dd*, ^3J = 4.6 Hz, ^4J = 1.8 Hz); 8.43 (2H-4, *dd*, ^3J = 7.8 Hz, ^4J = 1.8 Hz); 7.70 (2H-3, *dd*, ^3J = 4.6 Hz, ^3J = 7.8 Hz). IR (KBr): $\nu_{C=O}$ 1685 cm^{-1}.

2.2.2. 2-(1*H*-imidazol-2-yl)-1*H*-imidazo[4,5-*f*]-1,10-phenanthroline (iip)

This procedure was adapted from the original work of Steck and Day.[13] They noticed that 9,10-phenanthrenequinone reacted with aldehydes and ammonium acetate in glacial acetic acid to yield phenanthrene imidazoles. Apparently, the reaction of the quinone with ammonium acetate leads to an isolatable diimine triacetate intermediate which undergoes an aldol-type condensation with protonated aldehydes. Several reports adapted this method to the condensation of other di-ketones such as 1,10-phenanthroline-5,6-dione with aldehydes.[14] During our work on the iip ligand, one Chinese patent has been filed claiming the synthesis of this ligand, but no synthetic details or proof of it are given.[15] Scheme **2** shows the reaction mechanism suggested by Steck and Day adapted to the current synthesis.

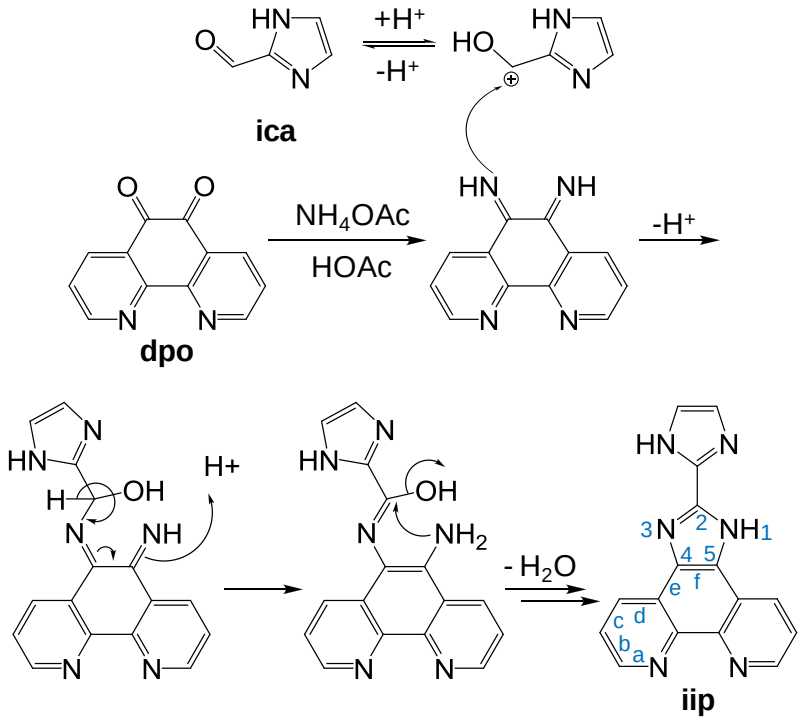

Reagent	Supplier	Mass/g	Mol	Volume/mL	Purity
pdo	---	0.555	2.6×10^{-3}	---	---
ica	Aldrich	0.250	2.6×10^{-3}	---	97%
NH_4OAc	Aldrich	10	130×10^{-3}	---	≥ 98%
Acetic acid	Panreac	---	---	20	99%

Scheme 2. Synthesis of the ditopic ligand 2-(1*H*-imidazol-2-yl)-1*H*-imidazo[4,5-*f*]-1,10-phenanthroline (iip). Adapted from the work by Steck and Day.[13] The blue numbers and letters on the iip ligand follow the IUPAC nomenclature.[7]

A mixture of 2-imidazolecarboxaldehyde (ica), 1,10-phenanthroline-5,6-dione (pdo), ammonium acetate and glacial acetic acid was refluxed for 15 h, then poured onto 50 g of ice. Careful neutralization by dropwise addition of concentrated aqueous ammonia until pH 7.5

gave a green suspension, which was left to cool in the refrigerator. After 1 h, the precipitate was collected and washed thoroughly with water. The resulting solid was found to be extremely difficult to dissolve, even using a large amount of boiling solvent. Therefore, the solid was vigorously stirred in 900 mL of boiling methanol in presence of a small amount of activated charcoal and filtered while hot. The filtrate volume was reduced until turbidity appeared (≈ 200 mL), cooled to room temperature and left for 2 h in the refrigerator. Vacuum filtration of the pale green solid suspension and drying in a vacuum desiccator gave the product in 47% yield. It decomposes above 350 °C without melting. The NMR (^{1}H, ^{13}C and ^{13}C dept, HMQC), IR and ESI-MS spectra are depicted in section 6.1.2. ^{1}H-NMR (MeOD-d_4): δ/ppm 9.05 (2H-2, *dd*, ^{3}J = 4.4 Hz, ^{4}J = 1.7 Hz); 8.92 (2H-4, *dd*, ^{3}J = 8.2 Hz, ^{4}J = 1.7 Hz); 7.83 (2H-3, *dd*, ^{3}J = 8.2 Hz, ^{3}J = 4.4 Hz); 7.33 (2H-5'', *s*). ^{13}C-NMR (DMSO-d_6): δ/ppm 148 (2C-2); 144 (4C-10b+5, *q*); 139 (2C-4a, *q*); 135 (1C-biim, *q*); 134 (1C-biim, *q*); 130 (2C-4); 124 (2C-3); 122 (1C-biim, *q*); 117 (1C-biim, *q*). IR (KBr): $\nu_{N\text{-}H}$ 3417, 1500, 735 cm^{-1}. MS (ESI, positive ion detection) *m/z*: 1255 [4(iip−H$^+$)+5(Na$^+$)]$^+$; 592 [2(iip)+(Na$^+$)]$^+$; 331 [(iip−H$^+$)+2(Na$^+$)]$^+$; 309 [(iip)+(Na$^+$)]$^+$.

2.2.3. 2-(1*H*-imidazo[4,5-*f*]-1,10-phenanthrolin-2-yl)-4-methoxyphenol (hmip)

The synthesis of the hmip ligand was similar to that described above for the iip analogue.[13] In the course of our study, this ligand has been described by others.[16] Nonetheless, in their publication it is described as a "brown solid". This result is often synonym of impurities, as imidazo[4,5-*f*]-1,10-phenanthrolines are colourless or light coloured.[13-14, 14c, 17] In contrast to what is reported, our preparation procedure leads to a white solid.

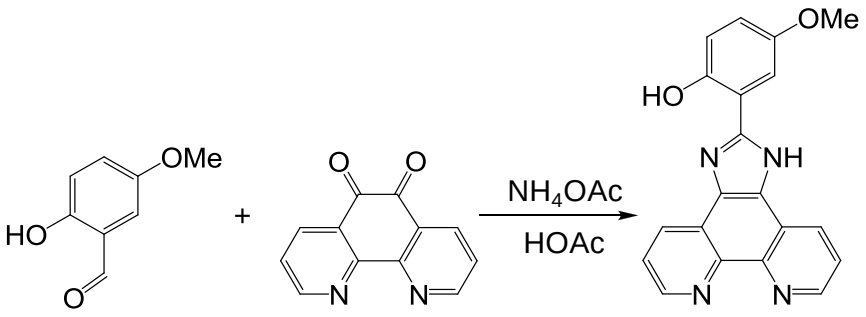

Reagent	Supplier	Mass/g	Mol	Volume/mL	Purity
pdo	---	0.200	1.0×10^{-3}	---	---
hmba	Aldrich	0.200	1.3×10^{-3}	0.164	98%
NH_4OAc	Aldrich	1.467	19×10^{-3}	---	≥ 98%
Acetic acid	Panreac	---	---	10	99%

Scheme 3. Synthesis of the ditopic ligand 2-(1*H*-imidazo[4,5-*f*]-1,10-phenanthrolin-2-yl)-4-methoxyphenol (hmip). Adapted from the procedure by Steck and Day.[13]

A mixture of 1,10-phenanthroline-5,6-dione (pdo), ammonium acetate and glacial acetic acid was kept at 80 °C for 1 h, after which 2-hydroxy-5-methoxybenzaldehyde (hmba) was added. The brown mixture was refluxed for 4 h, then poured onto 40 g of ice. A precipitate was obtained after careful neutralization by dropwise addition of concentrated aqueous ammonia and was left to cool in the refrigerator. After 1 h, the precipitate was collected and washed thoroughly with water. The resulting solid was recrystallized from hot methanol, acetone and water (80/15/5 v/v/v). Vacuum filtration and drying in a vacuum desiccator provided the white product (flakes) in 30% yield. It decomposes without melting above 280 °C. The NMR (^{1}H, ^{13}C and ^{13}C dept) and IR spectra are collected in section 6.1.3. ^{1}H-NMR (DMSO-d_6): δ/ppm 12.30 (1H-NH, br); 9.06 (2H-2, dd, ^{3}J = 4.3 Hz, ^{4}J = 1.6 Hz); 8.92 (2H-4, d, ^{3}J = 7.9 Hz); 7.86 (2H-3, dd, ^{3}J = 7.8 Hz, ^{3}J = 4.2 Hz); 7.76 (1H-6', *s*); 7.03 (1H-3' and 1H-4', *s*); 3.85 (3H-CH_3, *s*). ^{13}C-NMR (DMSO-d_6): δ/ppm 152 (1C-5'', *q*); 151 (1C-2', *q*); 150 (1C-5+2'', *q*); 148 (2C-2); 144 (4C-10b+4a, *q*); 129 (2C-4); 124 (2C-3); 118 (2C-3''+4''); 112 (1C-1'', *q*); 110 (1C-6''). IR (KBr): $\nu_{N\text{-}H}$ 3417, 1500, 735 cm^{-1}. IR (KBr): $\nu_{N\text{-}H}$ 3442, 1493, 737 ; $\nu_{O\text{-}H}$ 3442 cm^{-1}.

2.2.4. 5-Acetyl-2-hydroxybenzaldehyde (ahb)

This reagent has been synthesized as a precursor for the desired ditopic 1-(4-hydroxy-3-(1*H*-imidazo[4,5-*f*]-1,10-phenanthrolin-2-yl)phenyl)ethanone (haip) ligand. Its preparation has been described.[18]

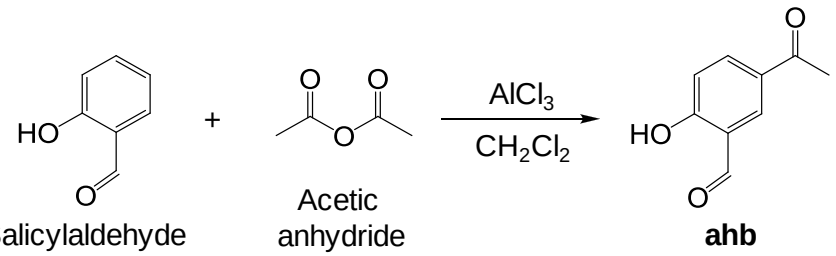

Reagent	Supplier	Mass/g	Mol	Volume/mL	Purity
Salicylaldehyde	Acros	1.550	12.7×10^{-3}	1.336	99%
Acetic anhydride	Prolabo	1.700	16.7×10^{-3}	1.574	98%
$AlCl_3$	Aldrich	5.380	40.3×10^{-3}	---	99%

Scheme 4. Synthesis of the precursor reagent 5-acetyl-2-hydroxybenzaldehyde (ahb). The method of preparation has been adapted from Kahnberg et al.[18c]

A mixture of salicylaldehyde, acetic anhydride and aluminium chloride in 20 mL of dichloromethane (HPLC grade) were refluxed under argon atmosphere for 24 h in a two-necked round bottom flask equipped with a condenser. The resulting yellow raw mixture was carefully quenched with cold HCl (50 mL in 60 g of ice). After that, dichloromethane (4 × 40

mL) was used to extract it, the combined extracts were dried with anhydrous $MgSO_4$ and evaporated under reduced pressure. A yellow oil was obtained thereof which required further purification because it showed several spots on TLC (silica, hexane-ethyl acetate 6:1) and was obtained in a 107% yield. Its purification was performed by column chromatography on silica gel using an initial mixture of hexane-ethyl acetate 6:1 and ending with 100% ethyl acetate. The product was obtained in 50% yield (after vacuum drying) as the third fraction of the column. The light yellow oil readily solidifies at 25 °C into a white product. The ^{1}H and ^{13}C NMR spectra of the ahb aldehyde are represented in section 6.1.4. ^{1}H-NMR (MeOD-d_4): δ/ppm 10.12 (1H-CHO, *s*); 8.38 (1H-6, *d*, $^{4}J = 2.3$ Hz); 8.14 (1H-4, *dd*, $^{3}J = 8.8$ Hz, $^{4}J = 2.3$ Hz); 7.03 (1H-3, *d*, $^{3}J = 8.7$ Hz); 4.85 (1H-OH, br); 2.58 (3H-CH_3, *s*). ^{13}C-NMR (MeOD-d_4): δ/ppm 198 (1C-CO, *q*); 196 (1C-CHO); 166 (1C-COH, *q*); 137 (1C-4); 135 (1C-6); 131 (1C-5, *q*); 122 (1C-1, *q*); 119 (1C-3); 26 (1C-CH_3).

2.2.5. 1-(4-Hydroxy-3-(1*H*-imidazo[4,5-*f*]-1,10-phenanthrolin-2-yl)phenyl)ethanone (haip)

To the best of our knowledge, this is the first description of 1-(4-hydroxy-3-(1*H*-imidazo[4,5-*f*]-1,10-phenanthrolin-2-yl)phenyl)ethanone (haip). The synthetic procedure is similar to the one followed for the iip and hmip ligands.[13]

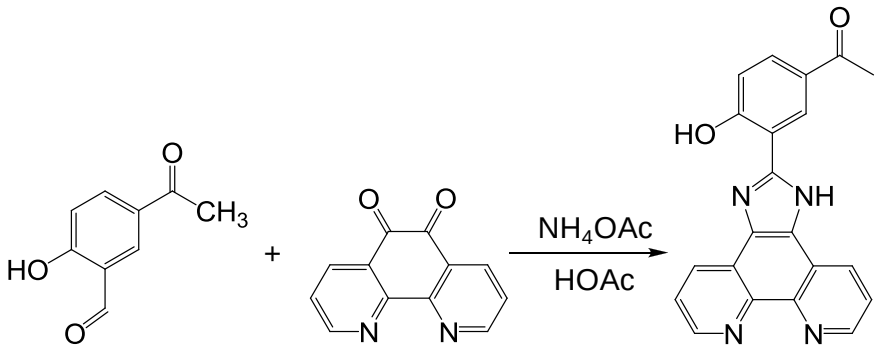

Reagent	Supplier	Mass/g	Mol	Volume/mL	Purity
pdo	---	0.400	1.9×10^{-3}	---	---
ahb	---	0.310	1.9×10^{-3}	---	---
NH_4OAc	Aldrich	5	65×10^{-3}	---	≥ 98%
Acetic acid	Panreac	---	---	30	99%

Scheme 5. Synthesis of the ditopic ligand 1-(4-hydroxy-3-(1*H*-imidazo[4,5-*f*]-1,10-phenanthrolin-2-yl)phenyl)ethanone (haip). Adapted from the work of Steck and Day.[13]

A mixture of 1,10-phenanthroline-5,6-dione (pdo), ammonium acetate and glacial acetic acid were heated at 80 °C for 1 h in a two-necked round bottom flask equipped with a condenser. To the resulting yellow solution, 5-acetyl-2-hydroxybenzaldehyde was added and

the dark red solution was refluxed for 5 h until TLC showed full consumption of the aldehyde (silica layer, 1:1 hexane-ethyl acetate with 1% methanol). The reaction was poured onto 50 g of ice and neutralized by careful addition of concentrated aqueous ammonia with precipitation of a yellow compound. The collected solid was washed thoroughly with water, acetone and dichloromethane and dried under vacuum (65% yield). The raw product was further purified by treating a boiling DMSO solution for 10 min with activated charcoal. The filtrate was placed in the refrigerator for 1 h and the resulting solid was isolated to yield the pure product in 36% yield. Its ^{1}H and IR spectra are depicted in section 6.1.5. ^{1}H-NMR (DMSO-d_6): δ/ppm 13.79 (1H-NH, br); 8.99 (2H-2, dd, $^{3}J = 4.4$ Hz, $^{4}J = 1.6$ Hz); 8.82 (2H-4, dd, $^{3}J = 8.1$ Hz, $^{4}J = 1.7$ Hz); 8.74 (1H-6', *d*, $^{4}J = 1.9$ Hz); 7.93 (1H-4', *dd*, $^{3}J = 8.6$ Hz, $^{4}J = 2.0$ Hz); 7.75 (2H-3, dd, $^{3}J = 8.2$ Hz, $^{3}J = 4.4$ Hz); 7.06 (1H-3', *d*, $^{3}J = 8.6$ Hz); 3.00 (1H-OH, broad); 2.54 (3H-CH_3, *s*). IR (KBr): ν_{N-H} 3406, 1501, 740; ν_{O-H} 3406; $\nu_{C=O}$ 1668; $\nu_{C=N}$ 1620; ν_{C-N} 1266 cm^{-1}.

2.2.6. 2,2'-Bipyridine-4,4'-diamine (dab)

The synthesis of this precursor ligand was reported for the first time by Maerker and Case,[19] to which Kavanagh and Leech have introduced modifications that led to a 4-fold increase in the overall yield.[20] The first step is nitration at the 4,4' positions of 2,2'-bipyridine-*N*,*N*'-dioxide (dob) which, after reduction, yields the desired product. Scheme 6 shows the two-step reaction.

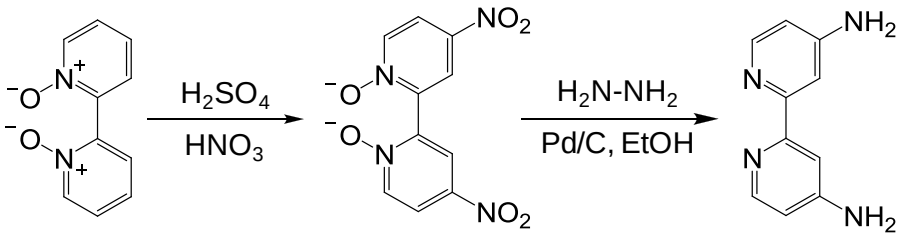

dob **dnob** **dab**

Reagent	Supplier	Mass/g	Mol	Volume/mL	Purity
dob	Acros	1.500	8.0×10^{-3}	---	98%
H_2SO_4	Scharlau	---	---	7.2	98%
HNO_3	Fluka	---	---	2.5	>90%
dnob	---	0.945	3.4×10^{-3}	---	---
Hydrazine hydrate	Fluka	7.972	159×10^{-3}	7.74	99%
Pd/C	Aldrich	0.850	---	---	10%

Scheme 6. Synthesis of the precursor ligand 2,2'-bipyridine-4,4'-diamine (dab) following the procedure described by Kavanagh and Leech.[20]

A 25 mL round bottom flask equipped with a condenser containing a mixture of 2,2'-bipyridine-*N,N*-dioxide (dob) and sulphuric acid was placed into an ice-water bath for 20 min. To the pre-cooled mixture, nitric acid was added dropwise and then the temperature was risen to 95 °C. After 20h, the reaction mixture was quenched with 40 g of ice and then placed into an acetone/dry ice bath at -40 °C to promote precipitation. The resulting yellow precipitate was vacuum filtered and thoroughly washed with water. The vacuum dried solid (43% yield) was used without further purification as reagent in the following step.

A 250 mL two-necked round bottom flask equipped with a pressure-compensated dropping funnel (with rubber septum) and a condenser, containing 4,4'-dinitro-2,2'-bipyridine-*N,N*-dioxide (dnob) and Pd/C was purged with argon for 10 min. Then, 100 mL of ethanol (> 99.8%) were added dropwise via the dropping funnel while maintaining a mild argon flux. The temperature was risen to reflux and the hydrazine hydrate (dissolved in 27 mL of ethanol (> 99.8%)) was introduced in the dropping funnel and added dropwise to the reaction mixture for 1 h. After 18 h of reflux, the hot solution was filtered through Celite to remove the catalyst-loaded charcoal. The Celite layer was washed with 10 mL of boiling ethanol. The solvent was eliminated in a rotavapor and the raw solid sonicated with 80 mL of water for 5 min. The suspension was left in the refrigerator overnight, and then vacuum filtered and dried to yield the white 2,2'-bipyridine-4,4'-diamine (dab) ligand in 73% yield (31% overall yield). Its ^{1}H NMR, ^{13}C NMR and IR spectra are plotted in section 6.1.6. ^{1}H-NMR (DMSO-d_6): δ/ppm 8.02 (2H-6, *d*, $^{3}J = 5.5$ Hz); 7.54 (2H-3, d, $^{4}J = 2.3$ Hz); 6.45 (2H-5, dd, $^{3}J = 5.5$ Hz, $^{4}J = 2.3$ Hz); 6.03 (4H-NH_2, *s*). ^{13}C-NMR (DMSO-d_6): δ/ppm 156 (1C-2, *q*); 155 (1C-4, *q*); 149 (1C-6); 109 (1C-3); 106 (1C-5). IR (KBr): ν_{NH2} 3451, 3414;ν_{N-H} 3300, 3149, 1641, 1597 cm^{-1}.

2.2.7. 2-(Thymin-1-yl)-1-(1*H*-imidazol-1-yl)ethanone (tymim)

This thymine-based precursor has been prepared following the method of Inaki and Hiratsuka.[21] It is based on the activation of thymine acetic acid with 1,1'-carbonyldiimidazole (cdi). As shown in Scheme 7, the process leads to formation of CO_2 thus shifting the reaction pathway towards the product.

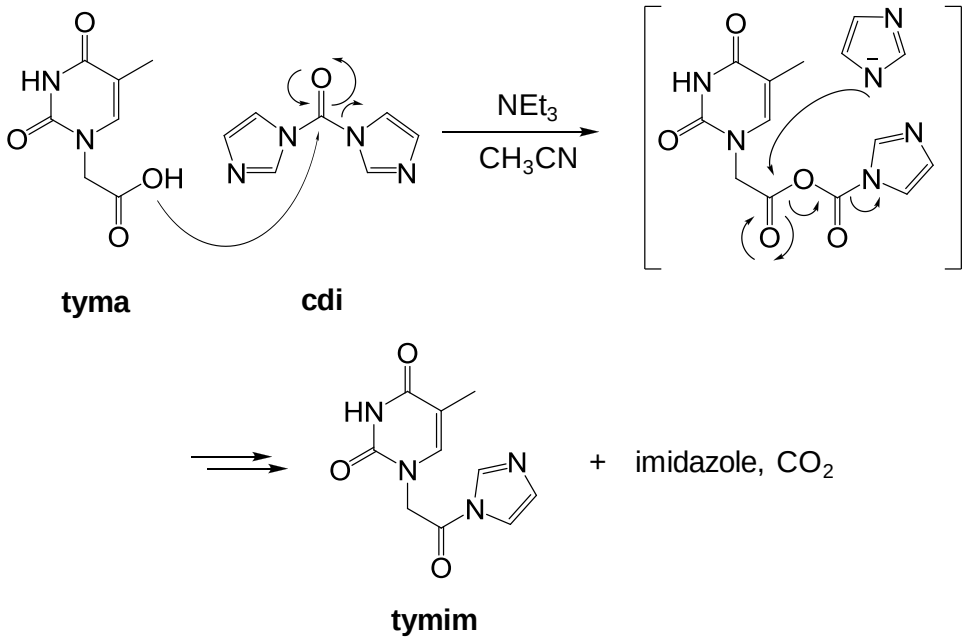

Reagent	Supplier	Mass/g	Mol	Volume/mL	Purity
tyma	Aldrich	0.500	2.7×10^{-3}	---	98%
cdi	Aldrich	0.530	3.3×10^{-3}	---	98%
NEt_3	Aldrich	0.436	4.3×10^{-3}	0.6	99%

Scheme 7. Reaction mechanism for the acid group activation by 1,1'-carbonyldiimidazole (cdi).[22]

The synthesis was carried out as follows. A 5 mL test tube equipped with a magnetic stirrer, a septum and a balloon was filled with thymine-1-acetic acid (tyma), 1,1'-carbonyldiimidazole (cdi), triethylamine and 3 mL of acetonitrile. Within 30 min, CO_2 was released and a precipitate appeared. The reaction was stirred at room temperature for 12 h after which 3 mL of acetonitrile were added to facilitate filtering of the thick suspension. The collected precipitate was washed with acetonitrile and vacuum dried, leading to the white solid product (57% yield). The ^{1}H NMR spectrum of tymim is shown in section 6.1.7. ^{1}H-NMR (DMSO-d_6): δ/ppm 11.35 (1H-NH, *s*); 7.76 (1H-2', s); 7.51 (1H-6'', s); 7.08 (2H-4'+5', s); 4.36 (2H-2, s); 1.77 (3H-CH_3, *s*).

2.2.8. *N,N'*-(2,2'-bipyridine-4,4'-diyl)bis(2-(thymin-1-yl)acetamide) (bpytym)

This ditopic ligand was successfully synthesized by amide formation between the diamine derivative dab and the thymine derivative tymim. To the best of our knowledge, this is the first description of the ligand.

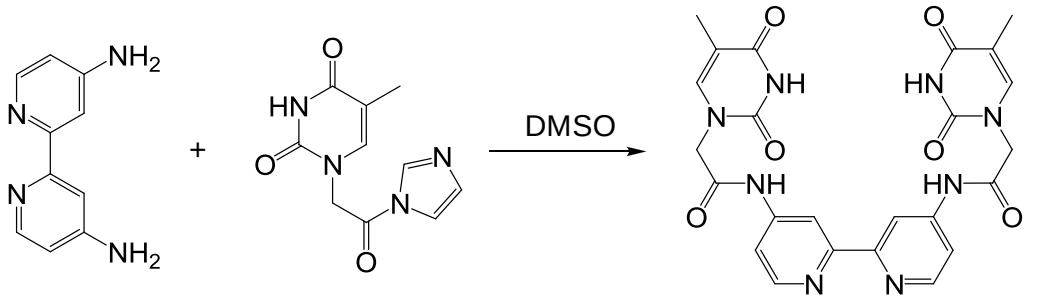

dab **tymim** **bpytym**

Reagent	Supplier	Mass/g	Mol	Volume/mL	Purity
dab	---	0.040	0.21×10^{-3}	---	---
tymim	---	0.110	0.47×10^{-3}	---	---

Scheme 8. Synthesis of the ditopic ligand *N,N'*-(2,2'-bipyridine-4,4'-diyl)bis(2-(thymin-1-yl)acetamide) (bpytym).

In a 5 ml round bottom flask equipped with a condenser, 2,2'-bipyridine-4,4'-diamine (dab) and 2-(thymin-1-yl)-1-(1H-imidazol-1-yl)ethanone (tymim) were placed together with 3 mL of anhydrous DMSO (dried over molecular sieves). Under an argon atmosphere, the mixture was heated at 130 °C and stirred for 12 h. Then the solvent was removed in a rotary evaporator and the resulting raw solid was sonicated in 20 mL of chloroform for 5 min. The suspension was filtered and the beige solid product further washed with 10 mL of chloroform and 10 mL of methanol to selectively remove unreacted tymim (55% yield). The ^{1}H NMR, ^{13}C NMR and ESI-MS spectra are plotted in section 6.1.8. ^{1}H-NMR (DMSO-d_6): δ/ppm 11.39 (2H-$NH_{thymine}$, *s*); 10.82 (2H-NH_{amide}, *s*); 8.61 (2H-3', d, $^{4}J = 1.9$ Hz); 8.55 (2H-6', d, $^{3}J = 5.4$ Hz); 7.65 (2H-5', dd, $^{3}J = 5.5$ Hz, $^{4}J = 2.2$ Hz); 7.53 (2H-6'', d, $^{4}J = 1.1$ Hz); 4.57 (4H-2, s); 1.78 (6H-CH_3, *s*). ^{13}C-NMR (DMSO-d_6): δ/ppm 167 (2C-1, *q*); 164 (2C-4, *q*); 156 (2C-2'); 151 (2C-4', *q*); 150 (2C-2'', *q*); 146 (2C-6''); 142 (2C-6'); 113 (2C-5'', *q*); 110 (2C-3'); 108 (2C-5'); 50 (2C-2); 12 (2C-CH_3). MS (ESI, positive ion detection) *m/z*: 519 $[(\text{bpytym})+H^+]^+$; 353 $[(\text{bpytym})-(\text{thymine-1-acetyl})^+ + 2(H^+)]^+$; 157 $[(\text{1-methyl-thymine})+(H_2O)-(H^-)]^+$.

The electrospray ionization mass spectrometry (ESI-MS) of the bpytym ligand showed three major mass peaks, one corresponding to the protonated ligand and the other two corresponding to smaller molecules (Figure A23 of section 6.1.8). As ESI is considered a mild technique of ionization, it is assumed that ionization-induced fragmentations are less common. Still, the two lighter fragments seem to result from a fragmentation of the parent compound, as indicated by the mechanism depicted in Figure 11. Aromatic amides are known to fragment by losing a ketene which produce the peak of the corresponding aniline.[23] In this case, the ketene group is a substituted thymine, bearing an urea group. The predominant

fragmentation is α-cleavage at the amide group, with a resulting charge on the amide ion, which is stabilized by the aromatic thymine heterocycle.[23]

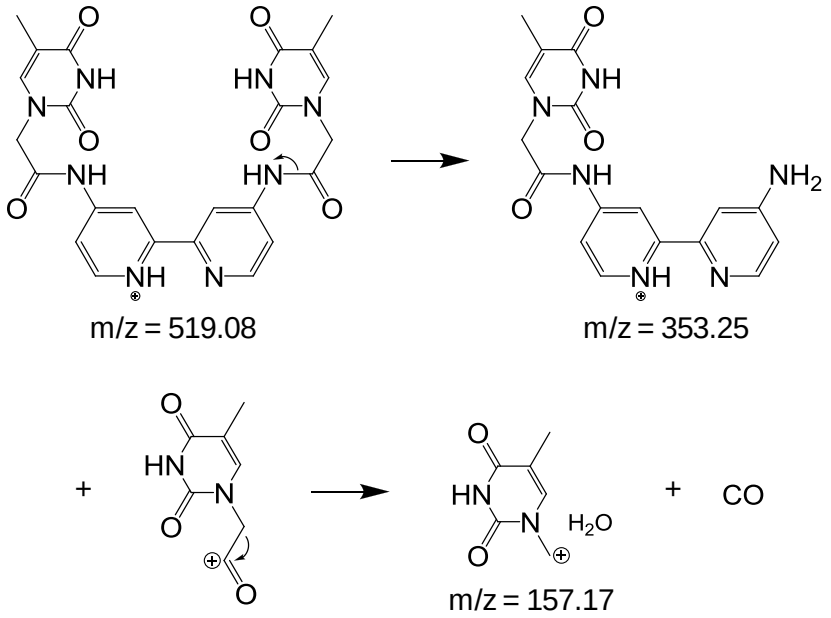

Figure 11. Possible fragmentation pathway of the bpytym molecular ion.[23]

2.2.9. *N,N'*-dioctadecyl-2,2'-bipyridine-4,4'-dicarboxamide (nody)

The synthesis of this 2,2'-bipyridine carboxamide ligand was realized in two steps in a one-pot synthesis due to the reactivity of the acyl chloride intermediate. A report on this ligand has been published, but the authors do not provide any information on its NMR characterisation.[24] Moreover, their preparation procedure was not followed. The ligand was obtained by a modification to the work of Cappuccio et al.[25] Firstly, the activation of the 2,2'-bipyridine-4,4'-dicarboxylic acid (dcab) via transformation of the carboxylic acid into the corresponding acyl chloride was achieved by thionyl chloride with dimethylformamide (DMF) as catalyst. The second step was the amide formation by nucleofilic attack of the octadecylamine. The *N,N*-diisopropylethylamine (DIEA) accelerates the reaction by acting as proton quencher.

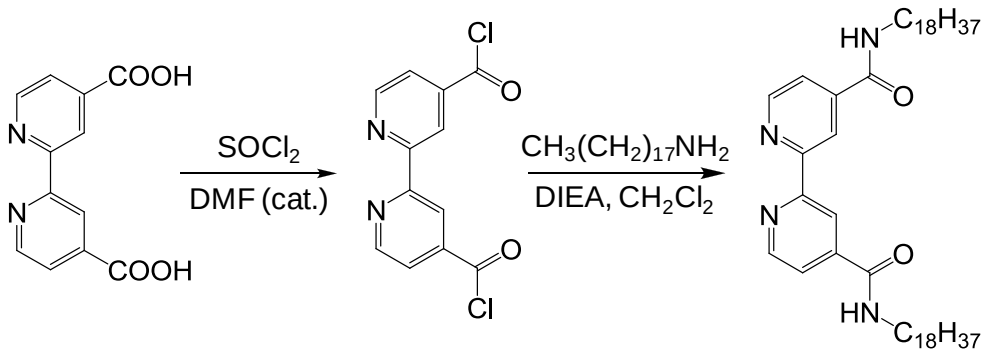

dcab **nody**

Reagent	Supplier	Mass/g	Mol	Volume/mL	Purity
dcab	Aldrich	0.280	1.1×10^{-3}	---	98%
Octadecylamine	Aldrich	0.680	2.5×10^{-3}	---	97%
DIEA	Aldrich	0.385	3.0×10^{-3}	0.492	99.5%
$SOCl_2$	Fluka	---	---	20	99%

Scheme 9. Synthesis of the ligand *N,N*-dioctadecyl-2,2'-bipyridine-4,4'-dicarboxamide (nody). Adapted from the work of Cappuccio et al.[25].

2,2'-Bipyridine-4,4'-dicarboxylic acid (dcab), 5 drops of DMF (anhydrous) and thionyl chloride were placed inside a 50 mL two-necked round bottom flask equipped with a condenser and a $CaCl_2$ drying tube. This white suspension was refluxed for 2 h to yield a red solution. The thionyl chloride was removed by vacuum distillation and the remaining raw product was further dried under vacuum ($P < 1$ mbar) for 1 h. The second step of the reaction started by the addition of 20 mL of dichloromethane, octadecylamine and *N,N*-diisopropylethylamine (DIEA). Stirring at room temperature for 12 h yielded an orange solution. Vacuum evaporation of the solvent and unreacted DIEA, followed by washing with methanol, led to a white solid in 66% yield. This solid was further purified by recrystallization from boiling DMF being the final yield 61%. Melting point: 203 °C. The ^{1}H and IR spectra are depicted in section 6.1.9. ^{1}H-NMR (DMSO-d_6 at 100 °C): δ/ppm 8.81 (2H-6, *d*, $^3J = 5.2$ Hz); 8.74 (2H-3, *s*); 8.49 (2H-NH, br); 7.79 (2H-5, dd, $^3J = 5.1$ Hz, $^4J = 1.6$ Hz); 3.33 (4H-1', *q*); 1.61 (4H-2', *q*); 1.26 (60H-CH_2, *s*); 1.08 (6H-CH_3, *s*). IR (KBr): ν_{N-H} 3406, 1501, 740; ν_{O-H} 3406; $\nu_{C=O}$ 1668; $\nu_{C=N}$ 1620; ν_{C-N} 1266 cm^{-1}.

2.2.10. 1,10-phenanthrolin-5-amine (ap)

This ligand was prepared by catalysed reduction of the commercially available 5-nitro-1,10-phenanthroline precursor with hydrazine and Pd/C, following the successful procedure described by our group.[26] It is similar to the reduction described for the synthesis of 2,2'-bipyridine-4,4'-diamine (dab) seen in section 2.2.6.

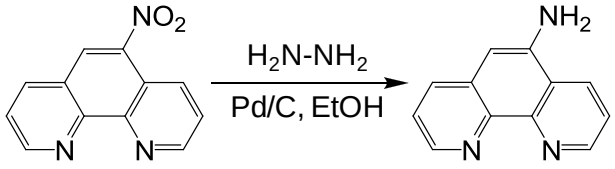

nop **ap**

Reagent	Supplier	Mass/g	Mol	Volume/mL	Purity
nop	Aldrich	2.060	9.1×10^{-3}	---	97%
Hydrazine monohydrate	Fluka	2.060	41×10^{-3}	2	99%
Pd/C	Aldrich	0.270	---	---	10%

Scheme 10. Synthesis of the 1,10-phenanthrolin-5-amine (ap) ligand.[26]

5-Nitro-1,10-phenanthroline (nop) and Pd/C were placed into a 250 mL two-necked round bottom flask equipped with a condenser and a pressure-compensated addition funnel. Under argon atmosphere, 90 mL of ethanol (> 99.8%) were added dropwise. The hydrazine hydrate was dissolved in 10 mL of ethanol (> 99.8%) and introduced in the addition funnel. The temperature was risen to reflux and the hydrazine added dropwise for 30 min. After further 3 h of reflux, the solution was filtered by suction through a sintered glass filter containing a Celite layer and the solvent evaporated. Then, 25 mL of ethanol (> 99.8%) were added, and after sonication for 5 min the flask was kept overnight at 4 °C. The precipitated 1,10-phenanthrolin-5-amine (ap) was collected by filtration, washed with ethyl ether and dried under vacuum (74% yield). A second batch of the same purity was obtained after evaporation of the ethanol (> 99.8%) + ethyl ether mixture and running a second precipitation (final yield 86% vs. the reported 77%). The ^{1}H NMR of this second batch is plotted in section 6.1.10. ^{1}H-NMR (DMSO-d_6): δ/ppm 9.05 (1H-2, *dd*, ^{3}J = 4.3 Hz, ^{4}J = 1.7 Hz); 8.68(4) (1H-4, *dd*, ^{3}J = 8.3 Hz, ^{4}J = 1.7 Hz); 8.68(0) (1H-9, *dd*, ^{3}J = 4.3 Hz, ^{4}J = 1.7 Hz); 8.04 (1H-7, *dd*, ^{3}J = 8.2 Hz, ^{4}J = 1.7 Hz); 7.73 (1H-3, *dd*, ^{3}J = 4.3 Hz, ^{3}J = 8.4 Hz); 7.50 (1H-8, *dd*, ^{3}J = 4.3 Hz, ^{4}J = 8.1 Hz); 6.86 (1H-6, *s*); 6.17 (2H-NH_2, *s*).

2.3. Synthesis of polyazaheterocyclic ruthenium(II) complexes

The synthesis of the tris-chelated ruthenium(II) complexes has followed a similar procedure for all cases. For heteroleptic complexes of the $[Ru(L_1)_2L_2]$ type, the synthesis was performed in two steps, firstly preparing and isolating the bis-substituted precursor *cis*-$[Ru(L_1)_2Cl_2]$ and then incorporating the third ligand (L_2). The ancillary ligands L_1 were either commercially available 1,10-phenanthroline (phen) or 4,4′-dinonyl-2,2′-dipyridyl (nbpy). However, the functional ligands L_2 were tailored to the specific applications and their synthesis has been described in the previous section 2.2. Unlike the latter section, the names of the tris-chelated ruthenium(II) complexes do not follow the IUPAC's recommendations. All the syntheses of the Ru(II) complexes were carried out under argon atmosphere and in the dark. Attempts to synthesize the ruthenium complexes by more recent methods have either failed or gave low yields,[27] so the adopted procedure was the one reported in 1978 by Sullivan et al.[28] In the case of $[Ru(phen)_2Cl_2]$, modifications to its preparation procedure have been introduced, especially with regard to its thorough purification required.

2.3.1. $[Ru(phen)_2Cl_2]$

The synthesis of this ruthenium complex has been adapted from the described procedure for $[Ru(bpy)_2Cl_2]$;[28] nevertheless its purification has been improved. It was found that the major subproduct of this reaction, the luminescent $[Ru(phen)_3]Cl_2$, does not elute in a column chromatography using cotton as stationary phase and dichloromethane (DCM) as eluent. Since $[Ru(phen)_2Cl_2]$ requires hot DCM to achieve solubilisation, the separation was performed using a Soxhlet extractor equipped with a cotton plug (stationary phase) and a 1:1 (v/v) mixture of dry toluene (to avoid drying of the solvent by evaporation) and DCM (mobile phase). Selective evaporation of the dichloromethane at reduced pressure allows filtration of the precipitated $[Ru(phen)_2Cl_2]$ from the toluene. This novel method of purification affords the *cis*-dichloro(bischelate) complex with +99% purity (single spot in neutral aluminium oxide TLC, $CHCl_3$-MeOH 95:5 v/v). A single peak in mass spectrometry also supports the high purity of the precursor compound (see Figure A27 in section 6.1.11). MS (ESI, positive ion detection) *m*/*z*: 497 $[Ru(phen)_2Cl]^+$.

2.3.2. $[Ru(nbpy)_2Cl_2]$

This bis-chelate complex has been synthesized using commercially available reagents and according to the procedure described for $[Ru(bpy)_2Cl_2]$.[28] It has been obtained in 50% yield after purification by filtration of a chloroform solution through a sintered glass filter with a silica gel layer. TLC on alumina (ethyl acetate-methanol 9:1) showed a single spot. The compound was used as precursor without further purification.

2.3.3. $[Ru(phen)_2(pdo)](PF_6)_2$

The synthesis of [bis(1,10-phenanthroline)(1,10-phenanthroline-5,6-dione)]ruthenium(II) bis(hexafluorophosphate $[Ru(phen)_2(pdo)](PF_6)_2$ was carried out by adapting a procedure described for ruthenium(II) dichloride complexes.[28]

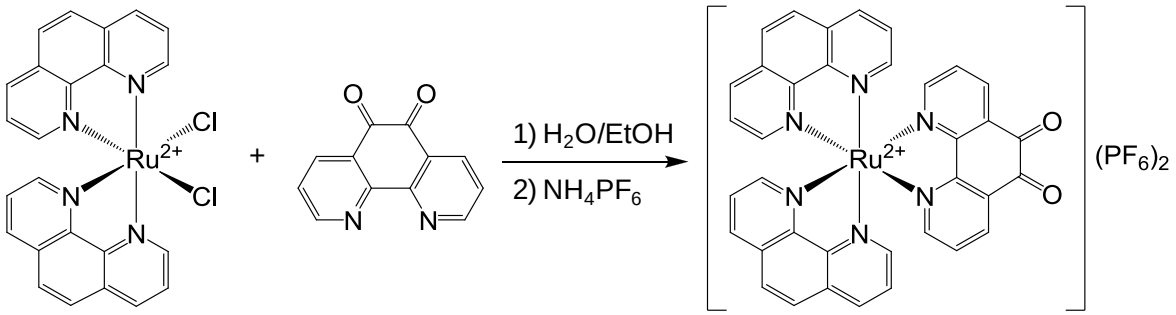

$Ru(phen)_2Cl_2$ **pdo** **$[Ru(phen)_2(pdo)](PF_6)_2$**

Reagent	Supplier	Mass/g	Mol	Purity
$[Ru(phen)_2Cl_2]$	---	0.300	5.6×10^{-4}	---
pdo	---	0.130	6.2×10^{-4}	---

Scheme 11. Synthesis of the ruthenium complex $[Ru(phen)_2(pdo)](PF_6)_2$.

A round bottom flask containing 300 mg of $Ru(phen)_2Cl_2$ (section 2.3.1) and 130 mg of pdo (section 2.2.1) dissolved in 15 mL of 1:1 water-methanol was heated to reflux and stirred overnight. TLC on alumina (MeOH-aq. NH_3 30:1 by volume as eluent) showed complete consumption of both starting materials. After evaporating the methanol, the crude was vacuum filtered. Addition of NH_4PF_6 led to precipitation of the product, which was collected by vacuum filtration through a 0.1-μm Nylon filter (GE Osmonics). The solid was dried at 50 °C and 1 mbar for 48 h yielding the pure orange product in 89% yield. The NMR (^1H, ^{13}C and ^{13}C dept) and IR spectra are shown in section 6.1.12. ^1H-NMR (CD_3CN-d_3) δ/ppm: 8.68 (2H-4_{phen}, *d*, ^3J = 8.2 Hz); 8.58 (2H-7_{phen}, *d*, ^3J = 8.2 Hz); 8.46 (2H-4_{pdo} + 2H-2_{pdo}, *br*, overlapped); 8.25 (4H-5_{phen}, *d*); 7.90 (2H-2_{phen}, *d*, ^3J = 5.1 Hz); 7.81 (2H-9_{phen} + 2H-8_{phen}, *br*, overlapped); 7.56 (2H-3_{phen}, *dd*, ^3J = 8.4 Hz, ^3J = 5.3 Hz); 7.43 (2H-3_{pdo}, *dd*, ^3J = 8.1 Hz, ^3J = 5.5 Hz). ^{13}C-NMR (CD_3CN-d_3) δ/ppm: 174 (2C-5_{pdo}, *q*); 156, 155 and 154 (2C-2_{pdo} and 4C-2_{phen}); 149 (4C-$10b_{phen}$, *q*); 145 (2C-$10b_{pdo}$, *q*); 138 (4C-4_{phen}); 136 (2C-4_{pdo}); 134 (2C-$4a_{pdo}$, *q*); 132 (4C-$4a_{phen}$, *q*); 129 (4C-5_{phen}); 127 (6C-$3_{pdo+phen}$). IR (KBr): $\nu_{C=O}$ 1698 cm^{-1}; ν_{PF6} 837 cm^{-1}.

2.3.4. $[Ru(phen)_2(iip)](PF_6)_2$

This synthetic procedure was similar to the one described for $[Ru(phen)_2(pdo)](PF_6)_2$, but in a different solvent. The dichloride raw product required additional purification by HPLC prior to its precipitation as the water-insoluble

bis(hexafluorophosphate) salt. Preparation of this compound has been reported within an international patent (WO2011009981) submitted by our group.[29]

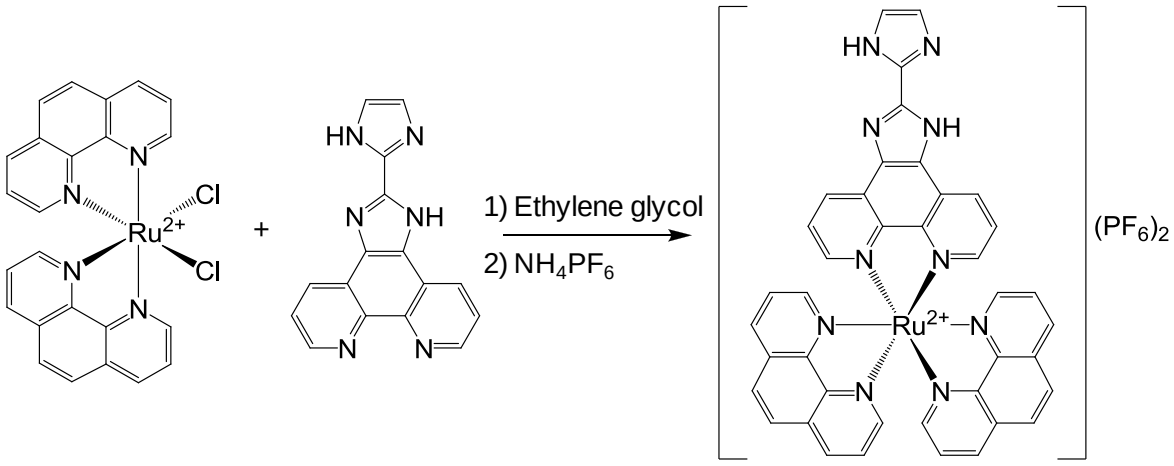

$Ru(phen)_2Cl_2$ **iip** **$[Ru(phen)_2(iip)](PF_6)_2$**

Reagent	Supplier	Mass/g	Mol	Purity
$[Ru(phen)_2Cl_2]$	---	0.060	1.1×10^{-4}	---
iip	---	0.035	1.2×10^{-4}	---

Scheme 12. Synthesis of the indicator dye $[Ru(phen)_2(iip)](PF_6)_2$.

A round bottom flask containing 60 mg of $Ru(phen)_2Cl_2$ (section 2.3.1) and 35 mg of iip (section 2.2.2) dissolved in 20 mL of ethylene glycol was heated to 150 °C and stirred for 20 h until TLC (alumina, CH_3CN-H_2O-satd. KNO_3 89:10:1 by volume as eluent) showed consumption of the starting materials. After cooling to room temperature, the solution was vacuum filtered and the solvent removed with a rotary evaporator. The resulting solid was washed with hot DCM over a cotton plug to remove unreacted $Ru(phen)_2Cl_2$. Increasing the polarity to $CHCl_3$ allowed desorption of the target ruthenium(II) complex from the cotton. The target product was purified by semi-preparative HPLC chromatography (Agilent 1100 series with quaternary pump, automatic injector and fraction collector) using a C18 Agilent ZORBAX Eclipse XDB column (5 μm, 9.4 x 250 mm). The elution pattern (CH_3CN-H_2O (with TFA 1%), 2 mL min^{-1}) consisted of 10 min isocratic 30:70 ratio followed by a 3 min ramp to 33:67 ratio. After neutralizing the fraction collected at 15 min retention time with $NaHCO_3$ and evaporating the solvent, the product was extracted with acetone. The extract was filtered to remove unwanted salts, and evaporated once more. Addition of NH_4PF_6 to a concentrated aqueous solution of the resulting solid, led to precipitation of the desired $[Ru(phen)_2(iip)](PF_6)_2$ complex. The solid was dried at 50 °C and 1 mbar for 48 h yielding 35 mg of orange solid (30%). The NMR (^1H, ^{13}C and ^{13}C dept, HMQC), MS and IR spectra are represented in section 6.1.13. ^1H-NMR (CD_3CN-d_3) δ/ppm: 8.93 (2H-4_{iip}, *d*, ^3J = 7.9 Hz); 8.59 (4H-4_{phen}, *d*, ^3J = 8.3 Hz); 8.25 (4H-5_{phen}, *s*); 8.08 (2H-2_{phen}, *d*, ^3J = 5.3 Hz); 8.02 (2H-2_{iip}, *dd*, ^3J

= 5.3 Hz, ^4J = 1.2 Hz); 7.97 (2H-9_{phen}, *d*, ^3J = 5.3 Hz); 7.66 (2H-3_{iip} overlapped); 7.63 (4H-3_{phen}, *dd*, ^3J = 8.3 Hz, ^3J = 5.3 Hz); 7.32 (2H-5'', *s*). ^{13}C-NMR (CD_3CN-d_3) δ/ppm: 154 (2C-2_{iip} and 2C-2_{phen}); 152 (2C-9_{phen}); 149 (6C-$10b_{iip+phen}$, *q*); 148 (2C-5_{iip}, *q*); 138 (4C-4_{phen}); 132 (4C-$4a_{phen}$, *q*); 132 (2C-4_{iip}); 129 (4C-5_{phen}); 127 (6C-$3_{iip+phen}$). IR (KBr, cm^{-1}): ν_{N-H} 3441; $\nu_{C=N}$ 1608; ν_{PF6} 835. MS (alpha-cyano-4-hydroxycinnamic acid (CHCA) MALDI-TOF, positive ion detection) *m/z*: 893 $[M-(PF_6)^-]^+$; 747 $[M-H^+-2(PF_6)^-]^+$; 568 $[M-(phen)-2(PF_6)^-]^+$; 378 $[M+CHCA-(phen)-2(PF_6)^-]^{2+}$; 334 $[M-(iip)-2(PF_6)^-]^{2+}$. Microanalysis (calculated/found) for $C_{40}H_{26}F_{12}N_{10}P_2Ru\cdot 8H_2O\cdot 0.5NH_4PF_6\cdot 0.6NaCF_3CO_2$: C 36.79/36.72; H 3.30/3.25; N 10.94/10.94.

2.3.5. $[Ru(phen)_2(hmip)](PF_6)_2$

This ruthenium(II) complex has been synthesized in the same way as the heteroleptic complexes described above. To the best of our knowledge, this is the first description of the $[Ru(phen)_2(hmip)](PF_6)_2$ luminescent dye.

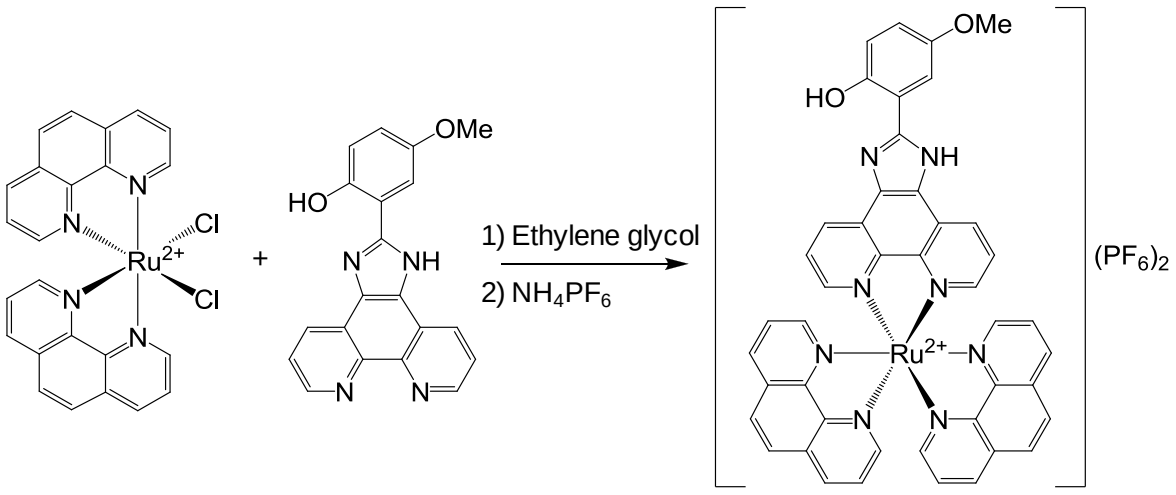

$Ru(phen)_2Cl_2$ **hmip** **$[Ru(phen)_2(hmip)](PF_6)_2$**

Reagent	Supplier	Mass/g	Mol	Purity
$[Ru(phen)_2Cl_2]$	---	0.015	2.8×10^{-5}	---
hmip	---	0.010	2.8×10^{-5}	---

Scheme 13. Synthesis of the ruthenium complex $[Ru(phen)_2(hmip)](PF_6)_2$.

A round bottom flask containing 15 mg of $[Ru(phen)_2Cl_2]$ (section 2.3.1) and 10 mg of hmip (section 2.2.3) dissolved in 8 mL of ethylene glycol was heated to 150 °C and stirred for 2 h until TLC (alumina; MeOH) showed complete consumption of both starting materials. After cooling to room temperature, the solution was filtered under vacuum and the filter washed with 40 mL of Type I water that was then added to the filtrate. The addition of solid ammonium hexafluorophosphate led to precipitation of the desired product, which was collected by vacuum filtration through a 0.1-μm Nylon filter (GE Osmonics). The resulting

orange solid was dried at 50 °C and 1 mbar for 48 h to yield 29 mg (93%). The ^{1}H NMR, IR and ESI-MS spectra are displayed in section 6.1.14. ^{1}H-NMR (CD_3CN-d_3) δ/ppm: 8.82 (2H-4_{hmip}, *d*, ^{3}J = 7.9 Hz); 8.53 (4H-4_{phen}, *t*, ^{3}J = 7.8 Hz); 8.21 (4H-5_{phen}, *s*); 8.10 (2H-2_{phen}, *d*, ^{3}J = 5.1 Hz); 8.03 (2H-2_{hmip}, *dd*, ^{3}J = 5.2 Hz, ^{4}J = 1.3 Hz); 7.79 (2H-9_{phen}, *d*, ^{3}J = 5.1 Hz); 7.75 (1H-OH, overlapped); 7.58 (4H-3_{phen} and 1H-6''$_{hmip}$ overlapped); 7.44 (2H-3_{hmip}, br); 6.76 (1H-4'' and 1H-3'', ^{3}J = 8.5 Hz); 3.68 (3H-CH_3, s). IR (KBr): $\nu_{O\text{-}H}$ 3424 cm^{-1}; ν_{CH3} 2926 cm^{-1}; ν_{PF6} 839 cm^{-1}. MS (ESI, positive ion detection) *m/z*: 948 $[M-(PF_6)^-]^+$; 803 $[M-H^+-2(PF_6)^-]^+$; 402 $[M-2(PF_6)^-]^{2+}$.

2.3.6. $[Ru(phen)_2(haip)](PF_6)_2$

This ruthenium(II) complex has been synthesized in the same way as the heteroleptic complexes described above. To the best of our knowledge, this is the first description so far of the $[Ru(phen)_2(haip)](PF_6)_2$ luminescent dye.

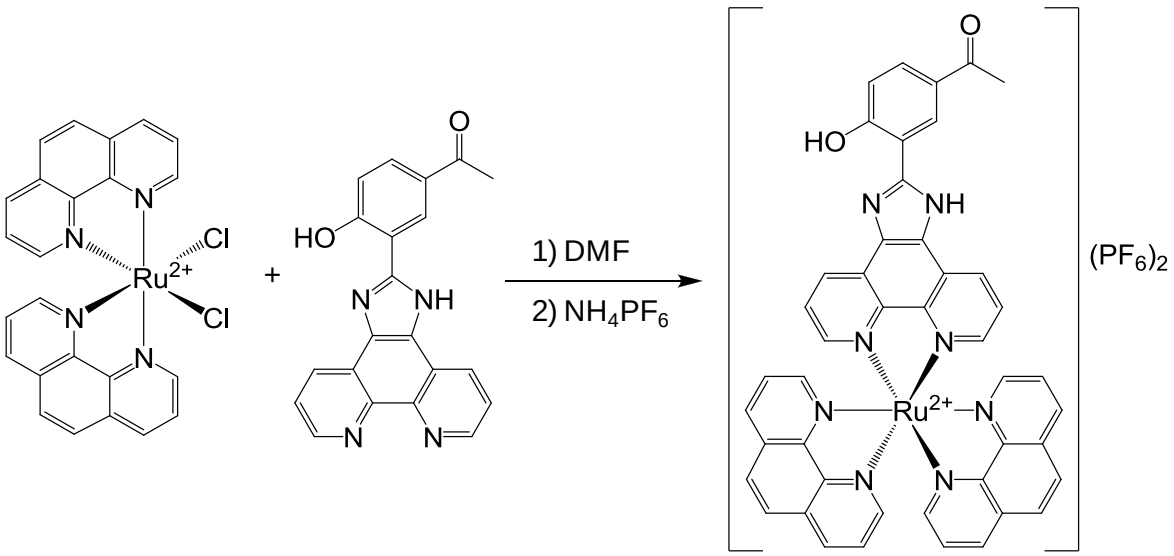

$Ru(phen)_2Cl_2$ **haip** **$[Ru(phen)_2(haip)](PF_6)_2$**

Reagent	Supplier	Mass/g	Mol	Purity
$[Ru(phen)_2Cl_2]$	---	0.088	1.7×10^{-4}	---
haip	---	0.058	1.7×10^{-4}	---

Scheme 14. Synthesis of the indicator dye $[Ru(phen)_2(haip)](PF_6)_2$.

A round bottom flask equipped with a condenser containing 88 mg of $[Ru(phen)_2Cl_2]$ (section 2.3.1) and 58 mg of haip (section 2.2.5) dissolved in 10 mL of dry DMF was refluxed under argon atmosphere for 2.5 h. A TLC on silica (acetonitrile-satd. aq KNO_3-water 89:1:10 v/v/v) showed complete consumption of $[Ru(phen)_2Cl_2]$. The reaction mixture was cooled to room temperature, 50 mL of water were added and then was filtered under vacuum. The raw product was precipitated by addition of a small amount of solid ammonium

hexafluorophosphate and cooling to 4 °C for 10 min. The precipitate was filtered through sintered glass *without* applying any vacuum, washed with water and allowed to dry under vacuum overnight. An orange solid was obtained in 77% yield. The ^{1}H NMR, IR and ESI-MS spectra are depicted in section 6.1.15. ^{1}H-NMR (CD_3CN-d_3) δ/ppm: 12.9 (1H-NH, *s*); 8.94 (2H-4_{haip}, br); 8.75 (1H-6'', *s*); 8.60 (4H-4_{phen}, *d*, ^{3}J = 8.2 Hz); 8.26 (4H-5_{phen}, *s*); 8.14 (2H-2_{phen}, *d*, ^{3}J = 5.2 Hz); 8.03 (2H-2_{haip}, *dd*, ^{3}J = 5.2 Hz, ^{4}J = 1.2 Hz); 8.00 (2H-9_{phen}, *dd*, ^{3}J = 5.2 Hz, ^{4}J = 1.2 Hz); 7.93 (1H-4'', *s*); 7.64 (2H-3_{haip} and 4H-3_{phen}, *dd*, ^{3}J = 8.3 Hz, ^{3}J = 5.1 Hz); 7.24 (1H-3'', *d*, ^{3}J = 8.6 Hz); 2.2 (3H-CH_3, s). IR (KBr): $\nu_{O\text{-}H}$ 3441 cm^{-1}; ν_{CH3} 2924 cm^{-1}; $\nu_{C=O}$ 1724 cm^{-1}; ν_{PF6} 841 cm^{-1}. MS (ESI, positive ion detection) *m/z*: 961.1 $[M-(PF_6)^-]^+$; 887.3 $[M-H^+-2(PF_6)^-+DMF]^+$; 815.3 $[M-H^+-2(PF_6)^-]^+$.

2.3.7. $[Ru(phen)_2(bpytym)](PF_6)_2$

This ruthenium(II) complex has been synthesized in the same way as the heteroleptic complexes described above. To the best of our knowledge, this is the first description of the $[Ru(phen)_2(bpytym)](PF_6)_2$ dye reported so far.

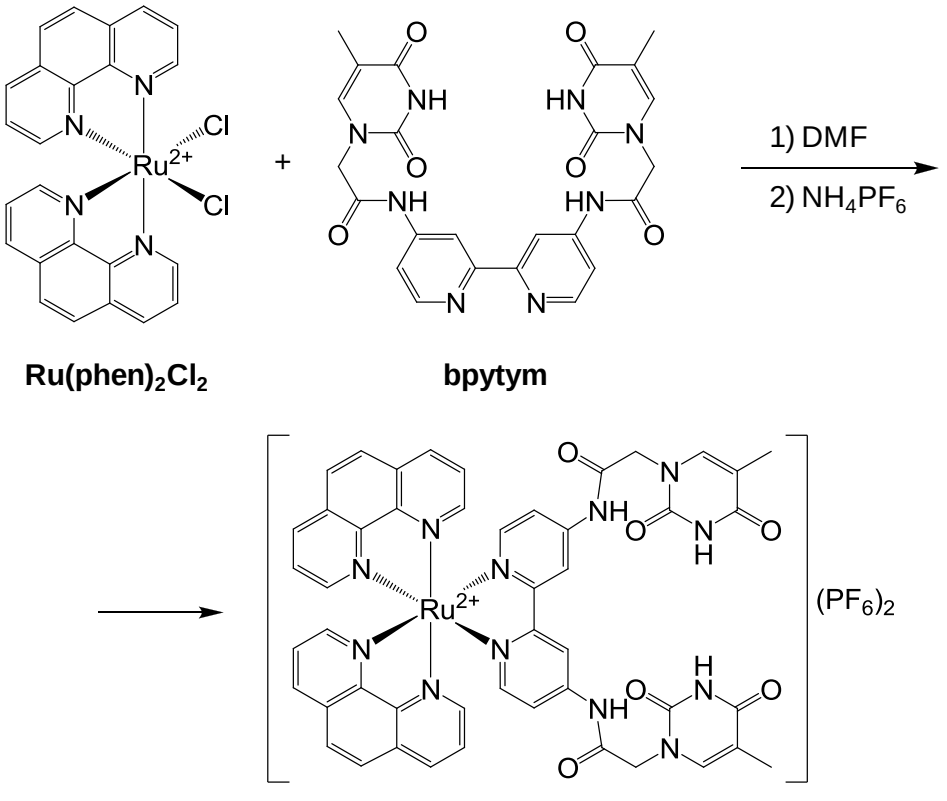

$Ru(phen)_2Cl_2$ **bpytym**

$[Ru(phen)_2(bpytym)](PF_6)_2$

Reagent	Supplier	Mass/g	Mol	Purity
$[Ru(phen)_2Cl_2]$	---	0.04580	8.6×10^{-5}	---
bpytym	---	0.04500	8.7×10^{-5}	---

Scheme 15. Synthesis of the indicator dye $[Ru(phen)_2(bpytym)](PF_6)_2$.

A 25 mL round bottom flask equipped with a condenser was loaded with 45.8 mg of $[Ru(phen)_2Cl_2]$ (section 2.3.1) and 45 mg of the bpytym ligand (section 2.2.8). The mixture was dissolved with 4 mL of dry DMF and the reaction was allowed to proceed at reflux for 26 h under argon atmosphere, until TLC (silica, methanol) showed complete consumption of the $[Ru(phen)_2Cl_2]$ Reagent. After cooling to room temperature, the reaction mixture was diluted with 20 mL of water and passed through a 0.2 µm Nylon syringe filter to remove unreacted bpytym ligand. Addition of NH_4PF_6 led to precipitation of the product, which was collected by filtration through a sintered glass filter without applying any vacuum. The resulting solid was dried under vacuum (64% yield). Two molecules of DMF co-crystallise with the metal complex as shown by NMR. The MS, IR and ^1H, ^{13}C and ^{13}C DEPT NMR are shown in section 6.1.16. ^1H-NMR (CD_3CN-d_3) δ/ppm: 9.7 (2H-NH, *s*); 9.3 (2H-NH, *s*); 8.83 (2H-3', *d*, ^4J = 1.9 Hz); 8.64 (2H-4_{phen}, *dd*, ^3J = 8.3 Hz, ^4J = 1.2 Hz); 8.53 (2H-7_{phen}, *dd*, ^3J = 8.3 Hz, ^4J = 1.2 Hz); 8.28 (2H-2_{phen}, *dd*, ^3J = 5.2 Hz, ^4J = 1.2 Hz); 8.22 (4H-5_{phen}, *d*, overlapped); 7.88 (2H-9_{phen}, *dd*, ^3J = 5.2 Hz, ^4J = 1.2 Hz); 7.79 (2H-3_{phen}, *dd*, ^3J = 5.3 Hz, ^3J = 8.2 Hz); 7.54 (2H-8_{phen}, *dd*, ^3J = 5.3 Hz, ^3J = 8.2 Hz); 7.44 (2H-6', *d*, ^3J = 6.3 Hz); 7.30 (2H-5', *dd*, ^3J = 6.5 Hz, ^4J = 2.2 Hz); 7.17 (2H-6'', *s*); 4.5 (4H-CH_2, *s*); 1.9 (6H-CH_3, *s*). ^{13}C-NMR (CD_3CN-d_3) δ/ppm: 169 (2C-1_{bpytym}, *q*); 165 (2C-4''$_{bpytym}$, *q*); 159 (2C-2'$_{bpytym}$, *q*); 154 (2C-6'$_{bpytym}$ and 2C-2_{phen} and 2C-9_{phen}); 152 (4C-$10b_{phen}$, *q*); 149 (2C-4'$_{bpytym}$ and 2C-2''$_{bpytym}$, *q*); 142 (4C-4_{phen}); 138 (2C-6''$_{bpytym}$); 132 (4C-$4a_{phen}$, *q*); 129 (4C-5_{phen}); 127 (4C-3_{phen}); 118 (2C-3'$_{bpytym}$); 114 (2C-5'$_{bpytym}$); 111 (2C-5''$_{bpytym}$, *q*); 52 (2C-$CH2_{bpytym}$); 12 (2C-$CH3_{bpytym}$). IR (KBr): ν_{NH} 3343 cm^{-1}; ν_{CH} 3084 cm^{-1}; $\nu_{C=O}$ 1683 cm^{-1}; δ_{NH} 1599 cm^{-1}; ν_{PF6} 838 cm^{-1}. MS (MALDI-TOF, positive ion detection) *m/z*: 1125.2 $[M-(PF_6)^-]^+$; 979.2 $[M-H^+-2(PF_6)^-]^+$; 813.1 $[M-(\text{thymine-1-acetyl})^+-2(PF_6)^-]^+$; 647.0 $[M-(\text{thymine-1-acetaldehyde})-(\text{thymine-1-acetyl})^+-2(PF_6)^-]^+$.

2.3.8. $[Ru(nody)_3]Cl_2$

This ruthenium(II) complex was synthesized in the same way as the homoleptic complexes described in the literature.[30] However, due to its inherent hydrophobicity, it was not isolated as hexafluorophosphate but rather as its dichloride salt. To the best of our knowledge, this is the first description of the $[Ru(nody)_3]Cl_2$ indicator dye.

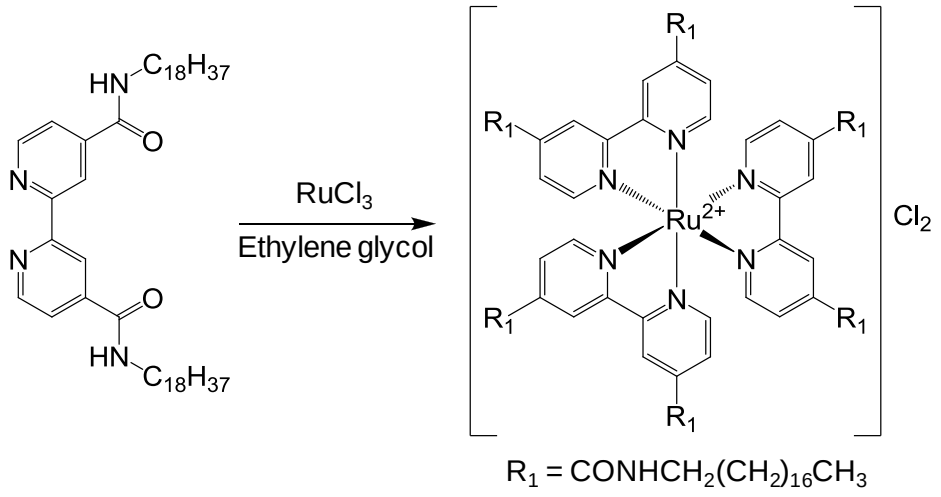

nody		**[Ru(nody)$_3$](Cl)$_2$**		
Reagent	Supplier	Mass/g	Mol	Purity
$RuCl_3$	Alfa Aesar	0.00410	2.0×10^{-5}	99%
nody	---	0.04540	6.1×10^{-5}	---

Scheme 16. Synthesis of the ruthenium indicator dye $[Ru(nody)_3]Cl_2$.

A round bottom flask equipped with a condenser containing a mixture of 4.1 mg of $RuCl_3$ (Alfa Aesar) and 45.4 mg of nody ligand (section 2.2.9) were refluxed under argon atmosphere in ethylene glycol for 4 h. The reaction was cooled to room temperature and addition of water led to precipitation of the product. The latter was vacuum filtered and the filter washed with dichloromethane to selectively dissolve the product but not the nody ligand. Evaporation under reduced pressure led to the pure product in 94% yield. The MS, IR and ^{1}H-NMR spectra are displayed in section 6.1.17. ^{1}H-NMR ($CDCl_3$-d_3) δ/ppm: 10.05 (2H-NH, *s*); 8.91 (2H-3, *s*); 8.02 (2H-6, s); 7.67 (2H-5, s); 3.42 (4H-1', s); 1.68 (4H-2', s); 1.24 (60H-$C_{15}H_{30}$, br); 0.87 (6H-CH_3, s). IR (KBr): ν_{NH} 3259 cm^{-1}; ν_{CH3} 2923 cm^{-1}; ν_{CH2} 2853 cm^{-1}; $\nu_{C=O}$ 1662 cm^{-1}; δ_{NH} 1546 cm^{-1}. MS (MALDI-TOF, positive ion detection) *m/z*: 2341.7 $[M-2Cl^-]^+$; 1632.1$[M+H^+-(nody)-Cl^-]^+$; 747.5 $[nody+H^+]$.

2.3.9. [Ru(nbpy)$_2$(nody)](PF$_6$)$_2$

This ruthenium(II) complex was obtained by the same procedures as those described in the previous sections. Since several spots on TLC were observed, it required further purification by preparative thin layer chromatography (PTLC). To the best of our knowledge, this is the first description of the $[Ru(nbpy)_2(nody)](PF_6)_2$ dye.

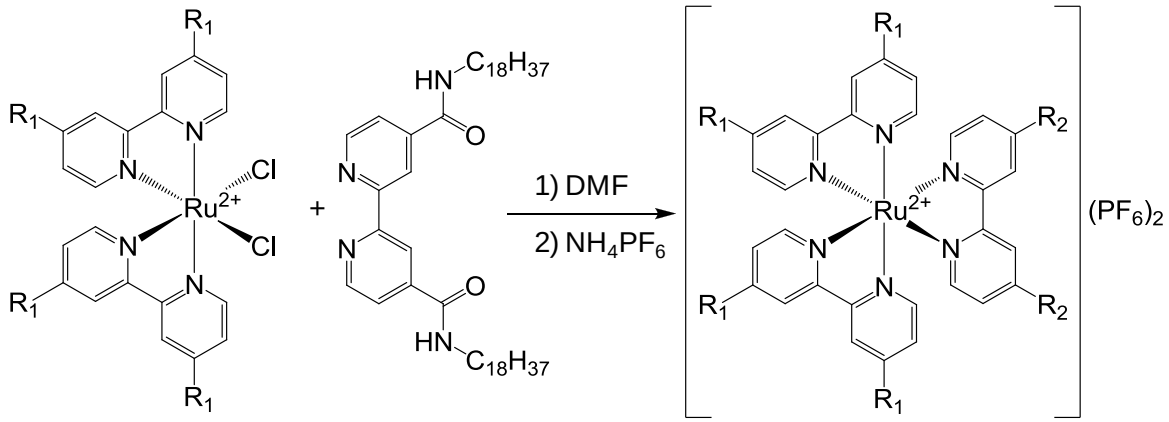

$Ru(nbpy)_2Cl_2$ **nody** **$[Ru(nbpy)_2(nody)](PF_6)_2$**

Reagent	Supplier	Mass/g	Mol	Purity
$[Ru(nbpy)_2Cl_2]$	---	0.050	5.1×10^{-5}	---
nody	---	0.058	6.1×10^{-5}	---

Scheme 17. Synthesis of the ruthenium indicator dye $[Ru(nbpy)_2(nody)](PF_6)_2$.

A round bottom flask equipped with a condenser containing 50 mg of $Ru(nbpy)_2Cl_2$ (section 2.3.2) and 58 mg of nody (section 2.2.9) was loaded with 10 mL of dry DMF. The reaction was carried out under argon atmosphere and reflux temperature for 12 h. After cooling to room temperature, the dark orange crude was filtered under vacuum to remove excess of nody ligand. The filtrate was diluted with 50 mL of water and addition of NH_4PF_6 led to precipitation of the product which, after ca. 1 h at 4 °C, was collected by vacuum filtration through a 0.1-μm Nylon filter (GE Osmonics). Analysis by mass spectrometry evidenced impurities of $[Ru(nbpy)(nody)_2]^{2+}$ and $[Ru(nbpy)_3]^{2+}$. Therefore, the raw product was purified by PTLC (silica gel, 2 mm) using a mixture of toluene-acetonitrile-ethanol (> 99.8%) 4:5:1 volume ratio as eluent. The luminescent spot of highest R_f was extracted with methanol containing 2% of acetic acid and the silica filtered out through paper. The resulting solution was evaporated under reduced pressure. Water was added to the product (still containing a small amount of silica gel) and the product was extracted with chloroform which, upon drying with $MgSO_4$ and evaporation, led to the sought $[Ru(nbpy)_2(nody)](PF_6)_2$ in 50% yield. The ^{1}H-NMR, IR and ESI-MS spectra are shown in section 6.1.18. ^{1}H-NMR ($CDCl_3$-d_3) δ/ppm: 9.29 (2H-NH, *s*); 8.14 (4H-3_{nbpy} and 2H-3_{nody}, *s*); 8.07, 7.85, 7.71 and 7.55 (2H-6_{nody}, 2H-5_{nody}, 4H-6_{nbpy} and 4H-5_{nbpy}, s); 3.48 (4H-$1'_{nody}$, s); 2.80 (8H-$1'_{nbpy}$, s); 1.69 (4H-$2'_{nody}$ and 8H-$2'_{nbpy}$, s); 1.25 (48H-$C_6H_{12\ nbpy}$ and 60H-$C_{15}H_{30\ nody}$, br); 0.87 (12H-$CH_{3\ nbpy}$ and 6H-$CH_{3\ nody}$, s). IR (KBr): ν_{CH3} 2924 cm^{-1}; ν_{CH2} 2854 cm^{-1}; $\nu_{C=O}$ 1666 cm^{-1}; δ_{NH} 1544 cm^{-1}; ν_{PF6} 837 cm^{-1}. MS (ESI, positive ion detection) *m/z*: 1956.9 $[M+H^+]^+$; 1810.6 $[M-(PF_6)^-]^+$; 1664.5 $[M-H^+-2(PF_6)^-]^+$.

2.4. NMR chemical shifts assignment

Given the structural similarities of the ligands and their corresponding ruthenium complexes, the NMR chemical shifts were assigned using literature reports on phen and its Ru(II) complexes as starting point.[2a] Another tool for proton and carbon chemical shift assignment was the prediction tool included in the software package ChemBioDraw Ultra (v11.0.1). Finally, the experimental data were also used for the most reliable method of assigning the chemical shifts by careful analysis of the coupling constants, by the 2D heteronuclear multiple-quantum correlation (HMQC) ^{1}H-^{13}C NMR spectra, and by comparison between the various compounds synthesised in this work (see Table 1 and Table 2). The assignment of the NMR chemical shifts was achievable for most compounds. Still, the iip ligand did show some unexpected features. Figure 12 depicts the ^{1}H-NMR (in MeOD-d_4) of the iip ligand and of the same sample in the presence of increasing concentrations of deuterated DMSO. The same compound exhibits a dramatic dependence on the solvent nature. For instance, in DMSO the peaks appear broadened and split into signals of different intensity. At first glance, the ^{1}H-NMR spectrum in this solvent would lead to think that the sample is impure or that the ligand is an asymmetric molecule. In contrast to this observation, as shown in Figure A3, the same sample in 100% protic deuterated methanol shows a clean spectrum, the peaks being sharp and well defined.

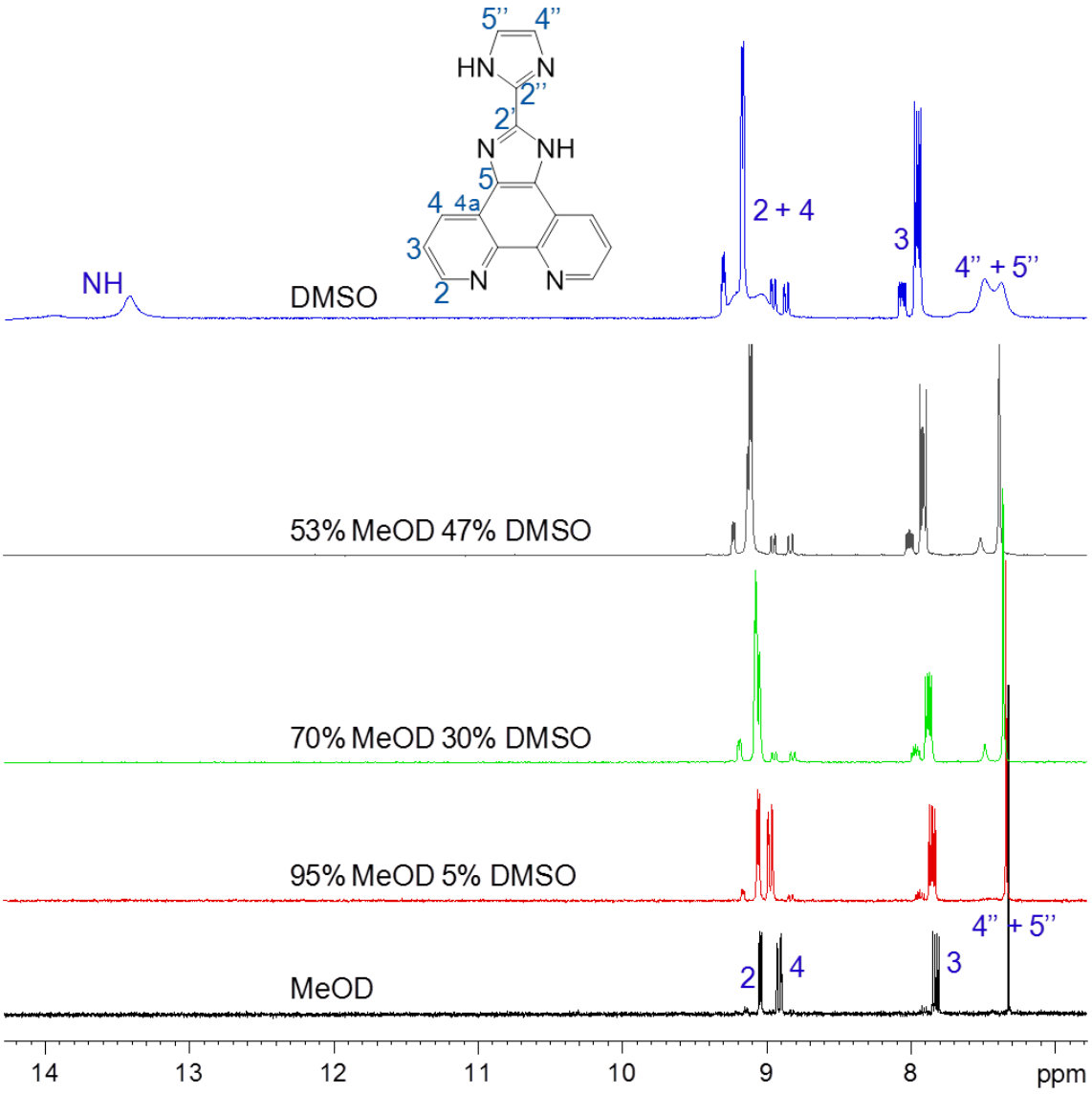

Figure 12. Aromatic region of ^{1}H-NMR spectra of the iip ligand dissolved in methanol with increasing concentrations of DMSO. The spectra were calibrated for the TMS reference signal.

The explanation for such spectral differences lies in the formation of *aggregates* in the aprotic DMSO. The iip ligand is extremely insoluble, requiring temperature and vigorous stirring to obtain a clear solution. By dissolving it in boiling methanol, it is observed that upon complete dissolution of the solid, there is no precipitation upon cooling indicating that an excess of solvent is required. This is in agreement with the breaking of intermolecular interactions that cause aggregates, by the hydrogen-bonding methanol. For this reason DMSO was the solvent of choice for the 2D NMR characterization, due to its high boiling point. Figure 13 shows a proposed structure for the iip aggregation, where two iip ligands are facing opposite to each other and interact by hydrogen-bonding.[31] In this manner, self-assembly macrostructures may occur, which due to anisotropic effects produce an effective asymmetry

of the iip ligand from the point of view of NMR spectroscopy. The structure implies that the interaction between the NH groups has an influence on the nearby H4, H4'' and H5'' protons. To a lower extent the H3 proton is also affected by the vicinal distal imidazole ring of another iip ligand. This is in agreement with the ^{1}H-NMR (DMSO-d_6) spectrum, where the above mentioned protons display increasing splitting with higher DMSO concentration. The H2 proton is also affected by the aggregation phenomena but to a much lower extent, as the relative intensity of the signal at 9.1 ppm remains practically unaltered. The results of electrospray ionization mass spectrometry shown in Figure A8 (section 6.1.2) support this hypothesis, by showing mass peaks corresponding to iip_n aggregates.

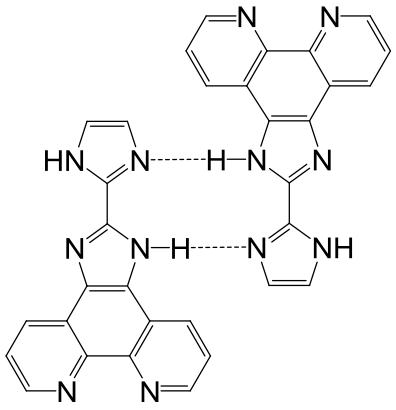

Figure 13. Proposed structure for the iip supramolecular aggregation by hydrogen bonding between the imidazole moieties.

Table 1 summarizes the ^{1}H-NMR chemical shifts of the different functional ligands in DMSO-d_6. It can be observed that the three 1,10-phenanthroline-based ligands show similar chemical shifts and coupling constants for their H2, H3 and H4 pyridine protons. The same trend is found for the pyridine protons of the 2,2'-bipyridine-based ligands bpytym and nody.

Also, an unexpected feature was observed in the ^{13}C-NMR DEPT of both iip ligand and ruthenium complex. The C4'' and C5'' sp^2 atoms of the distal imidazole ring do not display a signal in the ^{13}C-NMR DEPT spectrum. The same feature has an effect on the 2D HMQC ^{1}H-^{13}C NMR spectra of the iip ligand (DMSO-d_6) and the $[Ru(phen)_2(iip)]^{2+}$ complex (CD_3CN-d_3). This probably arises from a coalescence phenomenon (due to the slow proton exchange at the imidazole ring) which leads to a broadening of the signal and its disappearance into the baseline. This would justify why there are no peaks related to the C4''-H4'' or C5''-H5'' coupling on the 2D HMQC ^{1}H-^{13}C NMR spectrum.

The complexation induced shift (CIS) observed for the α proton (H2 for the phen derivatives, H6 for nody and H6'' for bpytym, see Figure 82) in the ruthenium complex, lead

to a ca. 1 ppm upfield shift. This shielding effect is justified by the anisotropic effects, where the electronic current of one of the other two aromatic ligands lies beneath the α proton.[2b] The ^{1}H-NMR chemical shifts of the ruthenium complexes in CD_3CN are summarized in Table 2.

Table 1. ^{1}H-NMR aromatic region chemical shifts in DMSO-d_6 for the synthesised functional ligands.[a]

Ligand	Proton chemical shift /ppm and Coupling constant /Hz						
	NH	Hα[b]	Hβ[c]	H4	H3(bpy)/3'/3''	H4''/5''	H6'/6''
iip	13.3	9.08 $^3J_{2\text{-}3} = 4.3$ $^4J_{2\text{-}4} = 1.7$	7.87 $^3J_{3\text{-}4} = 8.2$ $^3J_{3\text{-}2} = 4.4$	8.82[d] $^3J_{4\text{-}3} = 8.1$ $^4J_{4\text{-}2} = 1.8$	---	7.34[e]	---
hmip	12.3	9.06 $^3J_{2\text{-}3} = 4.3$ $^4J_{2\text{-}4} = 1.6$	7.86 $^3J_{3\text{-}4} = 7.8$ $^3J_{3\text{-}2} = 4.2$	8.92 $^3J_{4\text{-}3} = 7.9$	7.03	7.03	7.76
haip	13.8	8.99 $^3J_{2\text{-}3} = 4.4$ $^4J_{2\text{-}4} = 1.6$	7.75 $^3J_{3\text{-}4} = 8.2$ $^3J_{3\text{-}2} = 4.4$	8.82 $^3J_{4\text{-}3} = 8.1$ $^4J_{4\text{-}2} = 1.7$	7.06 $^3J_{3''\text{-}4''} = 8.6$	7.93 $^3J_{4''\text{-}3''} = 8.6$ $^4J_{4''\text{-}6''} = 2.0$	8.74 $^4J_{6'\text{-}4'} = 1.9$
bpytym	11.4 10.8	8.55 $^3J_{6'\text{-}5'} = 5.4$	7.65 $^3J_{5'\text{-}6'} = 5.5$ $^4J_{5'\text{-}3'} = 2.2$	---	8.61 $^4J_{3'\text{-}5'} = 1.9$	---	7.53
nody	8.5	8.81 $^3J_{6\text{-}5} = 5.2$	7.79 $^3J_{5\text{-}6} = 5.1$ $^4J_{5\text{-}3} = 1.6$	---	8.74	---	---

[a] At 300 MHz. Values referenced for the DMSO-d_6 solvent peak at 2.54 ppm. Ligands shown in Figure 82. Spectra shown in sections 6.1.2 to 6.1.8.

[b] Hα = H2, H6' or H6

[c] Hβ = H3(phen), H5(bpy) or H5'(bpy)

[d] The chemical shift of H_4 in the iip ligand is the average value between two split proton signals at 8.86 and 8.78 ppm

[e] The chemical shift of H4''/5'' in the iip ligand is the average value between two broad singlets at 7.40 and 7.28 ppm

Table 2. ^{1}H-NMR aromatic region chemical shifts in CD_3CN-d_3 for the synthesised ruthenium(II) complexes.[a]

Ru(II) complex	Proton chemical shift /ppm and Coupling constant /Hz										
	Functional ligand						Ancillary ligand				
	Hα[b]	Hβ[c]	H4	H3(bpy)/3'/3''	H4''/5''	H6'/6''	H2/6	H3/8	H4/7	H5	H9
Ru(phen)$_2$(iip)	8.02 $^3J_{2\text{-}3} = 5.3$ $^4J_{2\text{-}4} = 1.2$	7.66	8.93 $^3J_{4\text{-}3} = 7.9$	---	7.32	---	8.08 $^3J_{2\text{-}3} = 5.3$	7.63 $^3J_{3\text{-}4} = 8.3$ $^3J_{3\text{-}2} = 5.3$	8.59 $^3J_{4\text{-}3} = 8.3$	8.25	7.97 $^3J_{2\text{-}3} = 5.3$
Ru(phen)$_2$(hmip)	8.03 $^3J_{2\text{-}3} = 5.2$ $^4J_{2\text{-}4} = 1.3$	7.44	8.82 $^3J_{4\text{-}3} = 7.9$	6.76 $^3J_{3''\text{-}4''} = 8.5$	6.76 $^3J_{4''\text{-}3''} = 8.5$	7.58 overlapped	8.10 $^3J_{2\text{-}3} = 5.1$	7.58 overlapped	8.53 $^3J_{4\text{-}3} = 7.8$	8.21	7.79 $^3J_{2\text{-}3} = 5.1$
Ru(phen)$_2$(haip)	8.03 $^3J_{2\text{-}3} = 5.2$ $^4J_{2\text{-}4} = 1.2$	7.64 $^3J_{3\text{-}4} = 8.3$ $^3J_{3\text{-}2} = 5.1$	8.94	7.24 $^3J_{3''\text{-}4''} = 8.6$	7.93	8.75	8.14 $^3J_{2\text{-}3} = 5.2$	7.64 $^3J_{3\text{-}4} = 8.3$ $^3J_{3\text{-}2} = 5.1$	8.60 $^3J_{4\text{-}3} = 8.2$	8.26	8.00 $^3J_{9\text{-}8} = 5.2$ $^4J_{9\text{-}7} = 1.2$
Ru(phen)$_2$(bpytym)	7.44 $^3J_{6'\text{-}5'} = 6.3$	7.30 $^3J_{5'\text{-}6'} = 6.5$ $^4J_{5'\text{-}3'} = 2.2$	---	8.83 $^4J_{3'\text{-}5'} = 1.9$	---	7.17	8.08 $^3J_{2\text{-}3} = 5.2$ $^4J_{2\text{-}4} = 1.2$	7.79/7.54[d] $^3J_{3\text{-}4} = 8.2$ $^3J_{3\text{-}2} = 5.3$	8.64/8.53[d] $^3J_{4\text{-}3} = 8.3$ $^4J_{4\text{-}2} = 1.2$	8.22	7.88 $^3J_{9\text{-}8} = 5.2$ $^4J_{9\text{-}7} = 1.2$
Ru(nbpy)$_2$(nody)	8.07	7.85	---	8.14	---	---	7.71	8.14	---	7.55	---
Ru(nody)$_3$	8.02	7.67	---	8.91	---	---	---	---	---	---	---

[a] At 300 MHz. The chemical shifts for NH or OH were omitted. Values referenced for the CD_3CN-d_3 solvent peak at 1.94 ppm. Ligands shown in Figure 82. Spectra shown in sections 6.1.13 to 6.1.16.

[b] Hα = H2, H6' or H6

[c] Hβ = H3(phen), H5(bpy) or H5'(bpy)

[d] The two chemical shifts refer to the protons 3 and 8 or 4 and 7 of the phen ancilary ligands.

References

[1] H. E. Gottlieb, V. Kotlyar and A. Nudelman, *J. Org. Chem.* **1997**, *62*, 7512-7515.
[2] a) A. Marker, A. Canty and R. Brownlee, *Aust. J. Chem.* **1978**, *31*, 1255-1263; b) G. Orellana, C. Alvarez Ibarra and J. Santoro, *Inorg. Chem.* **1988**, *27*, 1025-1030.
[3] A. Bencini and V. Lippolis, *Coord. Chem. Rev.* **2010**, *254*, 2096-2180.
[4] L. A. Summers in *The Bipyridines*, *Vol. 35* (Ed. R. K. Alan), Academic Press, **1984**, pp. 281-374.
[5] J. Burgess and R. I. Haines, *J. Chem. Eng. Data* **1978**, *23*, 196-197.
[6] Samuel H. Yalkowsky, Y. He and P. Jain, *Handbook of Aqueous Solubility Data*, 2nd Ed., CRC press, **2010**, p. 1620.
[7] G. P. Moss, *Pure Appl. Chem.* **1998**, *70*, 143-216.
[8] M. Yamada, Y. Tanaka, Y. Yoshimoto, S. Kuroda and I. Shimao, *Bull. Chem. Soc. Jpn.* **1992**, *65*, 1006-1011.
[9] R. D. Gillard, R. E. E. Hill and R. Maskill, *J. Chem. Soc. A* **1970**, *0*, 1447-1451.
[10] a) R. D. Gillard and R. E. E. Hill, *J. Chem. Soc., Dalton Trans.* **1974**, 1217-1236; b) W. Paw and R. Eisenberg, *Inorg. Chem.* **1997**, *36*, 2287-2293; c) G. A. Shabir and N. J. Forrow, *J. Chromatogr. Sci.* **2005**, *43*, 207-212; d) L. Calucci, G. Pampaloni, C. Pinzino and A. Prescimone, *Inorg. Chim. Acta* **2006**, *359*, 3911-3920; e) C. Hiort, P. Lincoln and B. Norden, *J. Am. Chem. Soc.* **1993**, *115*, 3448-3454.
[11] G. E. Inglett and G. F. Smith, *J. Am. Chem. Soc.* **1950**, *72*, 842-844.
[12] C. V. Sastri in *DNA Binding and Photocleavage Studies on New Metallointercalators Incorporating Electroactive or Photoactive Ligands*, *Ph.D. Thesis*, Hyderabad, **2003**.
[13] E. A. Steck and A. R. Day, *J. Am. Chem. Soc.* **1943**, *65*, 452-456.
[14] a) J.-G. Liu, B.-H. Ye, H. Li, Q.-X. Zhen, L.-N. Ji and Y.-H. Fu, *J. Inorg. Biochem.* **1999**, *76*, 265-271; b) F. Zapata, A. Caballero, A. Espinosa, A. Tal rraga and P. Molina, *J. Org. Chem.* **2008**, *73*, 4034-4044; c) Y. Pellegrin, R. J. Forster and T. E. Keyes, *Inorg. Chim. Acta* **2009**, *362*, 1715-1722; d) P. Lenaerts, A. Storms, J. Mullens, J. D'Haen, C. Görller-Walrand, K. Binnemans and K. Driesen, *Chem. Mater.* **2005**, *17*, 5194-5201.
[15] W. Mei and D. Sun, *Preparation of imidazole[4,5-f][1,10]phenanthroline derivatives and application as antitumor agents*, Guangdong Pharmaceutical University, Peop. Rep. China . **2010**, p. 12.
[16] A. O. Eseola, O. Adepitan, H. Goerls and W. Plass, *New J. Chem.* **2012**, *36*, 891-902.
[17] a) V. K. Gupta, R. N. Goyal and R. A. Sharma, *Electrochim. Acta* **2009**, *54*, 4216-4222; b) Z. Zheng, Q. Zhang, Z. Yu, M. Yang, H. Zhou, J. Wu and Y. Tian, *J. Mater. Chem. C* **2013**, *1*, 822-830.
[18] a) N. U. Hofsløkken and L. Skattebøl, *Acta Chem. Scand.* **1999**, *53*, 258-262; b) A. Tromelin, P. Demerseman and R. Royer, *Synthesis* **1985**, *1985*, 1074-1076; c) P. Kahnberg, C. W. Lee, R. H. Grubbs and O. Sterner, *Tetrahedron* **2002**, *58*, 5203-5208.
[19] G. Maerker and F. H. Case, *J. Am. Chem. Soc.* **1958**, *80*, 2745-2748.
[20] P. Kavanagh and D. Leech, *Tetrahedron Lett.* **2004**, *45*, 121-123.
[21] Y. Inaki and H. Hiratsuka, *J. Photopolym. Sci. Technol.* **2000**, *13*, 739-744.
[22] H. A. Staab, *Angew. Chem. Int. Ed.* **1962**, *1*, 351-367.
[23] T. A. Lee, *A Beginner's Guide to Mass Spectral Interpretation*, 1st Ed., John Wiley & Sons Ltd., Chichester, **1998**, p. 186.
[24] D. Pucci, G. Barberio, A. Bellusci, A. Crispini, M. Ghedini and E. I. Szerb, *Mol. Cryst. Liq. Cryst.* **2005**, *441*, 251-260.
[25] F. E. Cappuccio, J. T. Suri, D. B. Cordes, R. A. Wessling and B. Singaram, *J. Fluoresc.* **2004**, *14*, 521-533.
[26] D. Garcia-Fresnadillo and G. Orellana, *Helv. Chim. Acta* **2001**, *84*, 2708-2730.
[27] a) M. K. Nazeeruddin, S. M. Zakeeruddin, J. J. Lagref, P. Liska, P. Comte, C. Barolo, G. Viscardi, K. Schenk and M. Graetzel, *Coord. Chem. Rev.* **2004**, *248*, 1317-1328; b) P. Valerga, M. C. Puerta and D. S. Pandey, *J. Organomet. Chem.* **2002**, *648*, 27-32; c) C. Viala and C.

Coudret, *Inorg. Chim. Acta* **2006**, *359*, 984-989; d) C. Klein, M. K. Nazeeruddin, D. Di Censo, P. Liska and M. Graetzel, *Inorg. Chem.* **2004**, *43*, 4216-4226.
[28] B. P. Sullivan, D. J. Salmon and T. J. Meyer, *Inorg. Chem.* **1978**, *17*, 3334-3341.
[29] M. G. Orellana, R. J. L. Urraca and A. Ribeiro dos Santos, *Method for preparing thin films for chemical optical sensors*, Universidad Complutense de Madrid, Spain, **2011**, p. 19.
[30] a) G. Orellana and D. Garcia-Fresnadillo in *Environmental and industrial optosensing with tailored luminescent Ru(II) polypyridyl complexes*, (O. S. Wolfbeis), Springer Series on Chemical Sensors and Biosensors, *Vol. 1,* **2004**, pp. 309-357; b) D. P. Rillema, G. Allen, T. J. Meyer and D. Conrad, *Inorg. Chem.* **1983**, *22*, 1617-1622.
[31] A. Morsali, *J. Coord. Chem.* **2006**, *59*, 1015-1024.

Chapter III

Photochemical study

This chapter will deal with the photochemical characterization of the ruthenium(II) complexes described in section 2.3. The presented data derives from spectroscopic studies of UV-Vis absorption together with steady-state and time-resolved luminescence spectra. The photophysics of these compounds stem from the interplay of the ruthenium(II) atom and the three ligands. Upon formation of the metal complex, a new electronic structure appears but there are some electronic transitions remaining that can be readily assigned to the *free* ligand, namely those based on LLCT or IL charge-transfers (see Figure 8 in section 1.9.2). For this reason, a short account of the photophysical properties of the *free* ligands follows.

A dichloromethane solution of the *1,10-phenanthroline* (phen) ligand displays two UV absorption bands at 231 and 264 nm.[1] The chelating ligand shows two UV absorption bands in diluted aqueous solution at 265 nm and 229 nm.[2] It has been shown that there are little changes in the absorption profile when changing the medium.[1-3] The *2,2'-bipyridine* (bpy) ligand is also rather insensitive to the medium (variations in the absorption maxima smaller than 2 nm), showing two UV absorption bands at 233 nm and 281 nm.[2] In contrast to the absence of solvatochromic effects, protonation on the nitrogen atom of either phen or bpy leads to significant changes in both the absorption and emission energies.[2] This dependence on the solution acidity is not expected to occur for ruthenium complexes with those ligands as their nitrogen atoms of the α-diimine moiety are involved in the Ru(II) chelation. Falling in the same spectral region is the absorption maximum of the 2,2'-biimidazole (bim) ligand in methanol, with a measured absorption maximum (λ_{max}^{abs}) of 270 nm. The fusion of this ligand with the phen scaffold leads to the iip ligand (see section 2.2.2) which displays one absorption band at 275 nm in methanol (Figure 14). Upon addition of methoxide, a second absorption band appears at 310 nm due to deprotonation at the 2,2'-biimidazole moiety.

3.1. Materials and methods

UV-Vis absorption and emission spectra were recorded at 25 °C in the 4-mm optical pathlength of 10 x 4 mm Suprasil QS-117.104F matched fluorescence cells (Hellma) by using a Varian Cary-3Bio spectrophotometer or a Horiba Fluoromax-4 spectrofluorometer, respectively.

The luminescence quantum yields (Φ_{em}) were measured in deoxygenated conditions after purging the solution for 20 min with solvent-saturated 99.995% pure argon (Praxair) at

25.0 ± 0.2 °C. A deoxygenated aqueous solution of $[Ru(bpy)_3](PF_6)_2$ was used as standard ($\Phi_{em} = 0.042 \pm 0.002$),[4] and a correction for the solvent refractive index was applied according to Eq. 38.[5] In this equation, Ru represents the ruthenium complex being measured, and the term referred as "slope" is obtained from the linear regression of a plot of the area under the corrected emission spectrum vs. the sample absorbance at the excitation wavelength for different concentrations ($A_{exc} < 0.15$).

$$\Phi_{em}^{Ru} = \Phi_{em}^{Ru(bpy)_3} \left(\frac{Slope_{Ru}}{Slope_{Ru(bpy)_3}} \right) \left(\frac{\eta_{solv.}^2}{\eta_{H_2O}^2} \right) \qquad \text{Eq. 38}$$

Emission lifetimes were determined by single photon timing (SPT) using a Horiba Fluoromax-4TCSPC spectrofluorometer equipped with a Horiba NanoLED 07N 405-nm pulsed laser diode head, an Ortec 416A delay generator and a Hamamatsu R928 red-sensitive photomultiplier. The emitted light was monitored through a monochromator plus a 495-nm cut-off filter (coloured glass, CVI Technical Optics). Spectrometer and multichannel analyser control and data collection (1024 channels, minimum 10^4 counts at the peak channel), were extracted from the decay profiles by fitting, without deconvolution for the instrument response, to a sum of the minimum number of exponential functions and a baseline term using the grid-search algorithm contained in the Horiba original decay analysis software package (v6.4.4). The reduced χ_r^2 (<1.1), weighted residuals and autocorrelation functions were employed to judge the goodness of the fits. Both steady-state and time-resolved emission measurements were carried out at the controlled temperature provided by Huber Polystat CC1 circulators. For the stability constants determination, Microsoft Excel (2007) and HypSpec (v1.1.50, Protonic Software, www.hyperquad.co.uk) were used.

3.2. $[Ru(phen)_2(iip)](PF_6)_2$

The synthesis of this complex is detailed in section 2.3.4. The luminescent coordination compound displays the characteristic spectroscopic features of the polypyridyl ruthenium(II) family, both in the ground and in the excited state (compare Figure 8 in section 1.9.2 with Figure 14).[6]

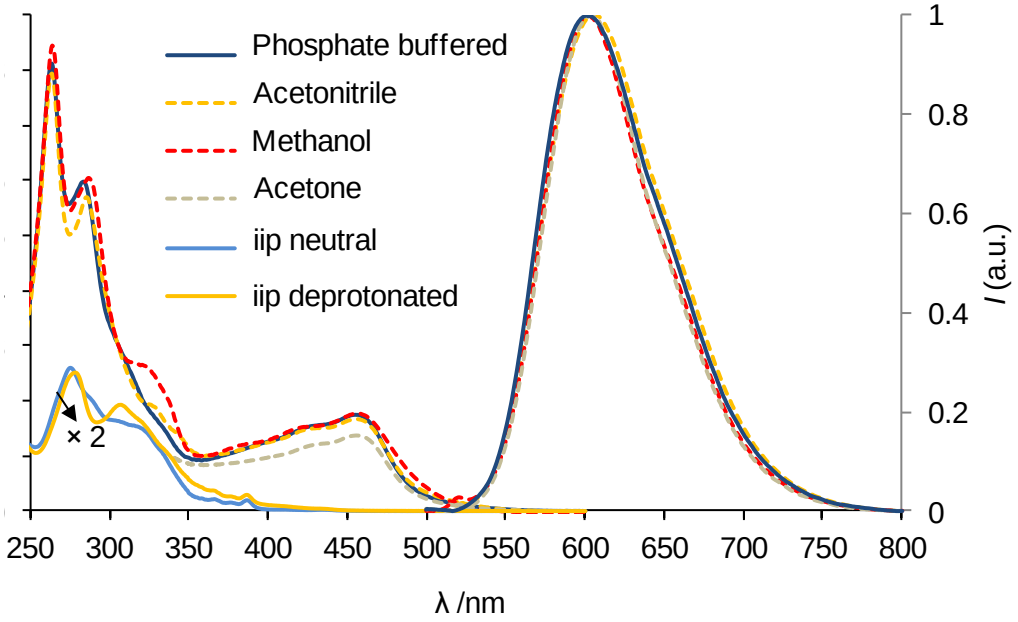

Figure 14. Absorption (left axis) and normalized emission (right axis, corrected for the instrument response) spectra of 10 μM $[Ru(phen)_2(iip)]^{2+}$ in polar organic solvents and in 50-mM PBS at pH 7.5 (1% methanol). The absorption spectrum in acetone was recorded down to 340 nm due to solvent cut-off. The absorption spectra (2X) of the *free* iip ligand (51 μM) in methanol and in the presence of sodium methoxide are also depicted.

Table 3 summarizes the relevant photophysical data of $[Ru(phen)_2(iip)]^{2+}$ in polar organic solvents and in 50-mM pH-7.5 phosphate buffer solution containing 1% methanol (by volume) to allow dissolution of the PF_6 salt of the dye. Its absorption spectrum contains the intra-ligand transitions already observed in the free iip ligand (a maximum at 275 nm and a shoulder at 310 nm in methanol, Figure 14). The maximum at 263 nm corresponds to the strong π-π* transition of the phen moieties (the tris-phen complex shows absorption at 263 nm, Figure 8), together with the π-π* transition of bim feature taking into account that the free bim ligand also absorbs at 270 nm in methanol.[7] The band at 285 nm and the shoulder at 330 nm can be assigned to n-π* transitions of the imidazole moiety because of their sensitivity to the pH changes (see Figure 14), as well as to the addition of copper(II) (see Figure 27). The absorption spectra of the Ru(II) complex in both polar protic and polar

aprotic solvents (Table 3, Figure 14) show a significant variation of the intensity of the shoulder at 330 nm, the band being negligible in aqueous medium. This result indicates that such a band corresponds to the n-π* transition of the imidazole moiety, sensitive to hydrogen bonding to solvent or other type of interactions such as self-aggregation or metal coordination, as reported for other biimidazole derivatives.[8] The broad visible metal-to-ligand charge transfer (MLCT) band at 456 nm displays different transitions that cannot be resolved, due to both the typical vibronic structure of this band in the Ru(II) polypyridyl complexes and the heteroleptic character of the investigated $[Ru(phen)_2(iip)]^{2+}$ that allows MLCT transitions to the different ligands in the coordination sphere (the homoleptic $[Ru(phen)_3]^{2+}$ complex absorbs at 445 in methanol, Figure 8).[6a] The red-orange emission maximum of $[Ru(phen)_2(iip)]^{2+}$ (Table 3) is also similar to that of the tris-phenanthroline complex (λ^{max}(corr.) = 595 nm in methanol). The spectroscopic features of the former are similar to those of related imidazo[4,5-*f*]phenanthroline complexes.[9]

Table 3. Electronic absorption and emission band maxima, molar absorption coefficients, luminescence quantum yields (Φ_{em}) and ^{3}MLCT excited state lifetimes for $[Ru(phen)_2(iip)](PF_6)_2$ (10 μM) in polar solvents and 50-mM phosphate buffer (PBS) at pH 7.5.[a]

Solvent	λ_{abs}^{max} /nm (ε/M^{-1} cm^{-1})	λ_{em}^{max} /nm[b]	Φ_{em} (Ar) Ru-iip[c]	Ru-phen[c]	τ/ns Air	Argon
Acetone[d]	456 (13100)	605	0.062	0.026	155	1230
Acetonitrile	264 (79700), 285 (60000), 330 (18200, s), 456 (17600)	605	0.034	0.028[e]	110	1030
Methanol	264 (81900), 286 (60700), 325 (26000, s), 456 (18400)	601	0.035	0.020	147	167(65), 1082(35)[f]
PBS	263 (80400), 283 (61100), 455 (17100)	602	0.107	0.056[e]	514	1200

[a] Estimated uncertainties: λ ± 1 nm; ε ± 4%; $\Phi_{em} \leq 10\%$; τ ± 1% (1-exp.), ± 2% (2-exp.); s: shoulder.
[b] Corrected for the instrument response.
[c] The abbreviations Ru-iip and Ru-phen stand for $[Ru(phen)_2(iip)]^{2+}$ and $[Ru(phen)_3]^{2+}$, respectively.
[d] Solvent cut-off 350 nm.
[e] From reported data in Juris et al.[10]
[f] The values given in parentheses represent the relative amplitude (*%*) of the individual components: $\%_i = B_i\tau_i/\Sigma B_i\tau_i$, being B_i the pre-exponential factors in the bi-exponential fit.

As shown in Figure 14, the luminescence spectrum of the Ru(II) complex remains almost unchanged in acetone, acetonitrile, methanol or aqueous media (summarized in Table 3), reflecting the small sensitivity of the ^{3}MLCT transition energy to hydrogen bonding. Orbital calculations on similar heteroleptic imidazo-phenanthroline Ru(II) complexes show

that the emissive (triplet) excited state is localized in the phenanthroline moiety of the functional ligand and not on the π electron-rich biimidazole moiety.[9d] The computational study in chapter IV reveals similar results. In this way, interactions of the solvent molecules with the polar imidazole ring will not perturb the excited state energy.

The emission quantum yields (Φ_{em}) of the $[Ru(phen)_2(iip)]^{2+}$ ion were measured in acetone, acetonitrile, methanol and in a phosphate buffered solution at pH 7.5. This parameter can be defined as the ratio between the number of emitted photons (defined by a *radiative* rate, k_r) and the number of absorbed photons (defined by an *absorption* rate, k_{abs}). Assuming the unity value of the quantum yield of ^{3}MLCT formation per absorbed photon, Φ_{em} is equal to the fraction of excited molecules that decay to the ground state with emission of a photon (Eq. 39),[11] where k_{nr} represents the sum of all non-radiative decay pathways.

$$\Phi_{em} = \frac{k_r}{k_r + k_{nr}} \qquad \text{Eq. 39}$$

This equation can be rewritten by noticing that the excited state lifetime, τ is given by,

$$\tau = \frac{1}{k_r + k_{nr}} \qquad \text{Eq. 40}$$

Hence k_r can be determined by Eq. 41.

$$\Phi_{em} = k_r \times \tau \quad \text{or} \quad k_r = \frac{\Phi_{em}}{\tau} \qquad \text{Eq. 41}$$

The results are summarized in Table 3 which, for the sake of comparison, also contains the Φ_{em} of the homoleptic compound $[Ru(phen)_3]^{2+}$. The emission quantum yields of the iip complex are always higher than those of its parent homoleptic complex in the four solvents studied. However, while the homoleptic compound displays a similar Φ_{em} in all the investigated solvents (ranging from 0.020 for methanol to 0.028 for acetonitrile), the $[Ru(phen)_2(iip)]^{2+}$ dye is strongly affected by the solvent, as it displays a higher emission quantum yield in the less polar acetone (0.062), than in acetonitrile or methanol (0.034 and 0.035 respectively). These interactions with the solvent are behind the 3-fold increase of the luminescence quantum yield of the dye in aqueous solution (0.107) compared to that measured in methanol, taking into account that the Φ_{em} of the homoleptic tris(1,10-phenanthroline)ruthenium(II) complex under the same conditions is reported to be 0.056.[10] Such differences are somewhat larger than those also reported for tris(2,2'-bipyridine)ruthenium(II),[12] and might be attributed to the same solvent effects that control

the *radiative* excited state deactivation constant (Eq. 41) in the Ru-dipyrido[3,2-a:2',3'-c]phenazine (dppz) complexes but to a lower extent.[13]

Table 3 also gathers the emission lifetimes of $[Ru(phen)_2(iip)]^{2+}$ in air-equilibrated and deaerated organic solvents and phosphate buffer. The small difference among the excited state lifetimes in air-equilibrated organic solvents is probably due to the strong quenching by dissolved molecular oxygen rather than an effect of the solvent polarity, according to the Lippert-Mataga dielectric continuous medium model.[14] The striking difference between the emission lifetime values in aqueous solution (514 ns) and those in organic solvents (slightly higher than 100 ns) is mostly due to the 10-fold difference in the solubility of molecular oxygen, taking into account the similarity of the measured O_2 quenching constants (3×10^9 and 4×10^9 in PBS and methanol, respectively).

The excited state lifetimes in argon-saturated acetone (ACT) and acetonitrile (ACN) solutions follow the observed quantum yield ordering (0.062 and 0.034, respectively), as a result of the combination of a larger *radiative* excited state deactivation constant ($k_r^{ACT} = 5.0 \times 10^4$ s^{-1}, $k_r^{ACN} = 3.3 \times 10^4$ s^{-1}) and a smaller *non-radiative* excited state deactivation constant ($k_{nr}^{ACT} = 7.6 \times 10^5$ s^{-1}, $k_{nr}^{ACN} = 9.4 \times 10^5$ s^{-1}). Nevertheless, the emission lifetime of $[Ru(phen)_2(iip)]^{2+}$ in methanol requires a bi-exponential fit, indicative of the presence of at least two luminescent species, with a component ($\tau = 167$ ns) that is significantly shorter than the expected value for the excited state decay in this solvent (Table 3). The fast decaying species might arise from *aggregates* formed in this solvent, as pointed out above and further discussed in section 2.4, undergoing self-quenching.[8, 15] Such phenomenon does not seem to occur in the case of (aqueous) PBS, where the $[Ru(phen)_2(iip)]^{2+}$ dye displays a single exponential decay, with an excited state lifetime similar to the one observed for the aprotic and less polar acetone (1230 ns). Since the dye has a similar k_{nr} in both solvents ($k_{nr}^{ACT} = 7.6 \times 10^5$ s^{-1}, $k_{nr}^{PBS} = 7.4 \times 10^5$ s^{-1}) but an emission quantum yield in aqueous solution that is more than 1.7-fold the one measured in acetone, then the difference must lie on the *radiative* excited state deactivation constant, calculated to be 8.9×10^4 s^{-1} in PBS (1.7-fold that observed in acetone). Luminescence lifetime studies of $[Ru(phen)_2(dppz)]^{2+}$ and derivatives in polyol solvents have confirmed the influence of hydrogen bonding with the solvent in the quenching rate constant.[13] Hence, since the $[Ru(phen)_2(iip)]^{2+}$ dye in PBS undergoes hydrogen bonding with water molecules, its radiative rate constant is also expected to increase with respect to acetone.

3.2.1. Effect of the solution pH

Due to the acid/base properties of the biimidazole ring, a study of the pH influence on the spectroscopic properties of the ruthenium(II) dye was performed by measuring the

absorption and emission spectra (Figure 15), as well as the excited state lifetimes (Figure 16), of a $[Ru(phen)_2(iip)]^{2+}$ solution in PBS.

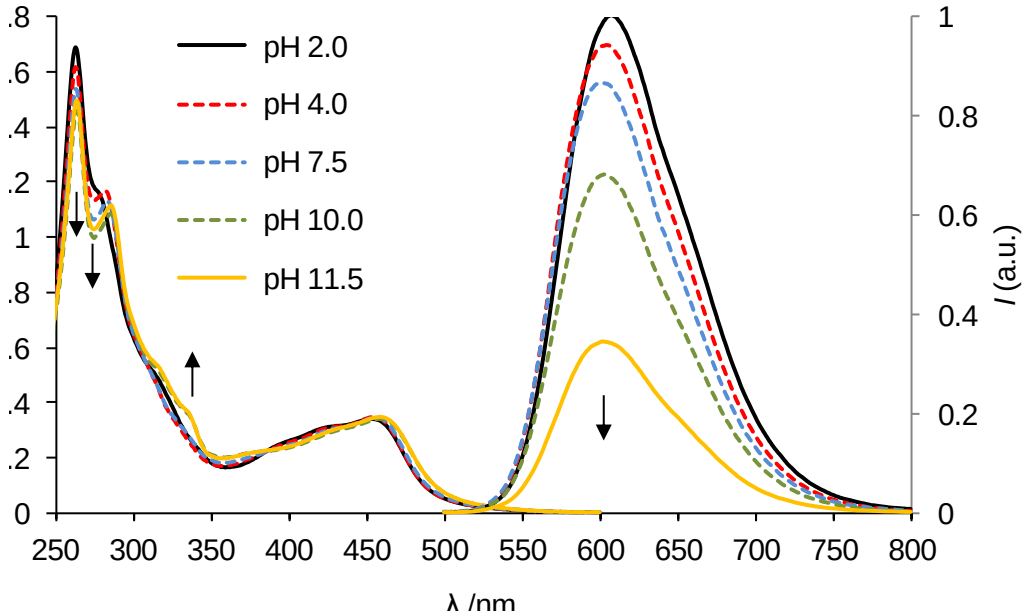

Figure 15. Absorption (left axis) and normalized emission spectra (right axis, corrected for the instrument response and for the absorption changes at the excitation wavelength, A_{450}) of 20 µM $[Ru(phen)_2(iip)]^{2+}$ in 50 mM PBS solution as a function of the pH.

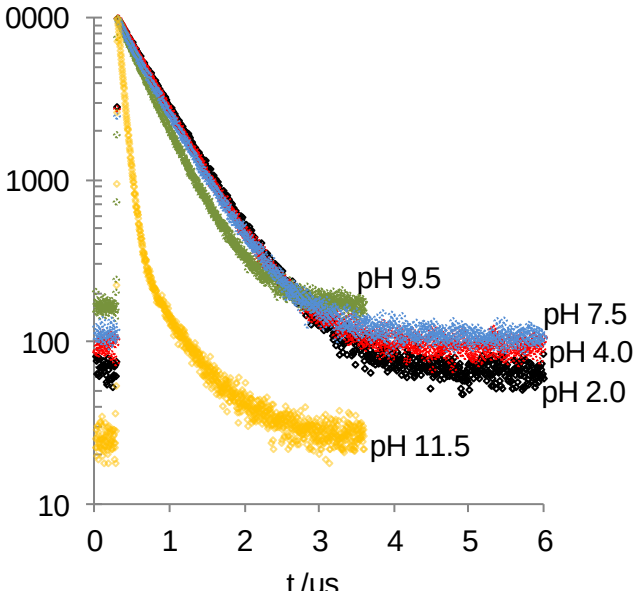

Figure 16. Emission decay profile of 20 µM $[Ru(phen)_2(iip)]^{2+}$ in 50 mmol L^{-1} PBS solution at different pH values. The excited state lifetimes calculated from the exponential fit to the experimental decays are summarized in Table 4.

A global analysis of the absorption data in the 263-430 nm region using the commercially available HypSpec software (39 pH data points) yields four different pK_a values in the investigated range (2 < pH < 11.5). The global fit yielded pK_a values of 3.35 ± 0.01, 5.02 ± 0.01, 8.35 ± 0.02, and 12.10 ± 0.05. An acid-base study of the free bim ligand in the pH range of 3.24 to 6.76 reveals a similar protonation constant of 5.15.[16] Table 4 summarizes the data obtained. All the optical changes are fully reversible.

Figure 17a depicts the absorbance values measured at 263 and 283 nm as a function of the solution pH and the pK_a values calculated with the help of HypSpec. Similar plots using the d-π* (metal-to-phen ligand, see above) absorption at 455 nm do not show the same spectral variation with the solution pH. These results demonstrate that the iip ligand does not significantly participate in the 455 nm transitions but is heavily involved in the 263-430 nm absorption bands as the electronic absorption spectra already pointed out (see above).

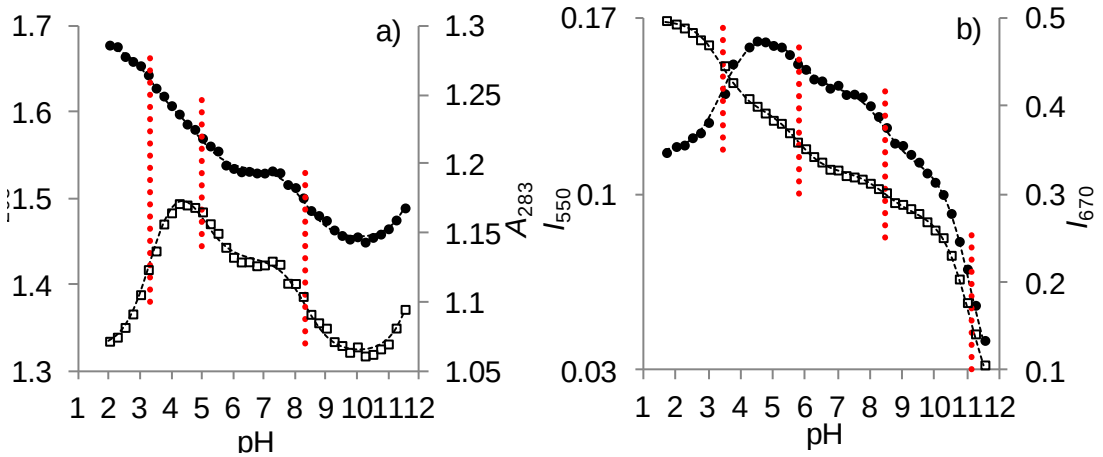

Figure 17. Selected wavelengths showing the changes in (a) absorption (A_{263}, ● and A_{283}, □) and (b) emission intensity (I_{550}, ● and I_{670}, □) of a 20 µM aqueous solution of $[Ru(phen)_2(iip)]^{2+}$ (1% methanol) as a function of the solution pH (50 mM phosphate buffer of constant ionic strength). The black dashed lines (r^2 = 0.998, r^2 = 0.993, r^2 = 0.998 and r^2 = 1.000 for A_{263}, A_{283}, I_{550} and I_{670}, respectively) are the absorbance and emission intensity values calculated by the HypSpec software. The vertical red lines indicate the pK_a (a) and pK_{ap} (b) values obtained from the best fit of the spectral data.

In order to assign the experimental acidity constants to the individual acid-base equilibriums of the multifunctional iip chelating ligand, the expected pK_a values of the $iipH_2^{2+}$ ligand were computed using ChemAxon MarvinSketch (v5.2.5) molecular properties calculator software (www.chemaxon.com). Calculations performed using the diprotonated phen moiety of iip try to model the effect of the coordination of the ligand to the Ru(II) metal atom. In this way, protonation of the biimidazole nitrogen atoms is predicted to occur at pK_a values of 2.7 (phen-fused imidazole) and 4.9 (distal imidazole), while its deprotonation might

be found around pK_a 9.6 (phen-fused imidazole) and 11.9 (distal imidazole). Therefore, the first nitrogen atom to be protonated would be the one at the distal imidazole ring of the biimidazole moiety (pK_a found at 5.02), while the second would be the one at the phen-fused imidazole (pK_a found at 3.35, see above). The deprotonation of the pyrrolic-nitrogen of the phen-fused imidazole occurs at a pK_a value of 8.35 and, finally, the pyrrolic-nitrogen of the distal imidazole ring deprotonates at a pK_a value of 12.10. It is worth highlighting the similarity between the measured pK_a values and those predicted by MarvinSketch. The small deviation between the predicted and calculated pK_a values of the fused imidazole ring of iip can be explained by the different electron withdrawing effect of the two protonated N phen atoms in the model vs. the actual metal-coordinated phen moiety. These results are in excellent agreement with the data shown in the computational chemistry chapter 4, which predicts the same protonation/deprotonation pattern (see Figure 62 in page 152).

A similar study has been carried out using luminescence measurements. Figure 15 also depicts the variation of the emission spectra in the 2.0-11.5 pH range upon excitation of waterborne $[Ru(phen)_2(iip)]^{2+}$ in its MLCT absorption maximum (450 nm). The changes in the emission profile become notorious at pH $>$ 7.5, with a significant decrease of the luminescence intensity at high pH values. This result suggests that a change in the photophysical picture of the dye occurs upon deprotonation of the biimidazole moiety.

As performed for the absorption data, a global analysis of the luminescence plot in the 540-740 nm range using the HypSpec software (38 pH values) reveals four apparent pK values (pK_{ap}) for $[Ru(phen)_2(iip)]^{2+}$ in the investigated pH range. The calculation yielded pK_{ap} values of 3.45 $\pm$ 0.01, 5.80 $\pm$ 0.01, 8.46 $\pm$ 0.01 and 11.13 $\pm$ 0.01 (see Figure 17b). The pK_{ap} values are summarized in Table 4.

Table 4. Acidity constants of $[Ru(phen)_2(iip)]^{2+}$ extracted from absorption (pK_a) and steady-state emission (pK_{ap}) experiments. The pK_a* values were calculated from Eq. 42, see text. The excited state lifetimes were extracted from an exponential fit of Eq. 2 to the decays shown in Figure 16.

Equilibrium	pK_a [a] (predicted)[b]	pK_{ap} [c]	pK_a*[d]	τ /ns[e]	
$RP_2(iip)^{2+} \rightleftharpoons RP_2(iip)^{+}$	3.35 ± 0.01 (2.7)	3.45 ± 0.01	3.45	552	pH 2
				530	pH 4.5
$RP_2(iip)^{+} \rightleftharpoons RP_2(iip)$	5.02 ± 0.01 (4.9)	5.80 ± 0.01	5.80	525	pH 6.5
				514	pH 7.5
$RP_2(iip) \rightleftharpoons RP_2(iip)^{-}$	8.35 ± 0.02 (9.6)	8.46 ± 0.01	8.46	509	pH 8.5
				$\tau_M = 499$[f]	pH 9.5
$RP_2(iip)^{-} \rightleftharpoons RP_2(iip)^{2-}$	12.10 ± 0.05 (11.9)	11.13 ± 0.01	11.84	$\tau_M = 418$[f]	pH 10.5
				$\tau_M = 97$[f]	pH 11.5

[a] From the HypSpec software global fit (263-430 nm range) using 39 pH data points.
[b] Values predicted using ChemAxon MarvinSketch (v5.2.5).
[c] From the HypSpec software global fit (540-740 nm range) using 38 pH data points.
[d] Calculated from Eq. 42.
[e] In air-equilibrated solution.
[f] $\tau_M = \Sigma B_i \tau_i / \Sigma B_i$. At pH 9.5, $\tau_1 = 257$ (4%) and $\tau_2 = 510$ (96%); at pH 10.5, $\tau_1 = 204$ (5%) and $\tau_2 = 430$ (95%); at pH 11.5, $\tau_1 = 79$ (96%) and $\tau_2 = 515$ (4%).

Figure 18 shows both the luminescence intensity and excited state lifetimes of the Ru(II) complex (Figure 15, Figure 16 and Table 4) as a function of the pH. While the former gradually decreases with increasing pH, the emission lifetime (499 ns) does not change significantly up to pH 9.5 but a pronounced decrease (down to 97 ns) is observed for a higher alkalinity. Moreover, the emission profile of $[Ru(phen)_2(iip)]^{2+}$ clearly becomes double-exponential at and above this value. The observation of a single emission lifetime for species that undergo acid-base processes in their excited state may indicate that a fast equilibrium is established between them (i.e. the return to the ground state is much slower than equilibration for the acidic and basic excited species).[17] However, the constancy of the excited state lifetime in the pH 2 to 9 region might also be explained if the protonation/deprotonation equilibria barely affect the lowest-lying π*(ligand) level responsible for the π*→d emission typical of Ru(II) polypyridyls (e.g. if the emission is centred on the phen ligands of $[Ru(phen)_2(iip)]^{2+}$ while the acid/base equilibriums occur in the iip ligands). TD-DFT calculations in chapter IV indicate that the lowest-lying π* of the dye involves the phenanthroline moiety of the iip ligand at pH < 7. At higher pH values, there is a change in the photophysical picture with the emissive state now depending on the pH-sensitive biimidazole moiety. On the other hand, the origin of the double-exponential decay of the Ru(II) indicator dye above pH 9.5 might be related to the fact that the complex becomes

electrically neutral at high pH values (see above). Such electroneutrality would favour aggregation of the metal complex and the change of the corresponding excited state lifetime.

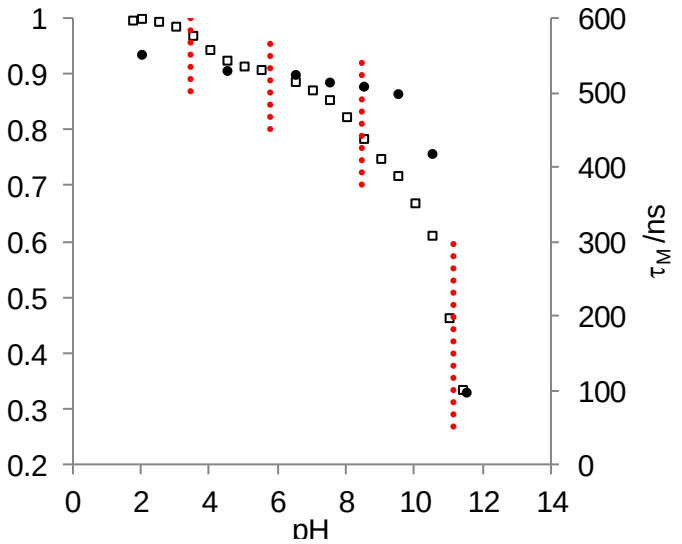

Figure 18. Emission intensity (I, □) upon excitation at 450 nm, corrected for the A_{450}, and pre-exponentially weighted excited state lifetime (τ_M, ●) of $[Ru(phen)_2(iip)]^{2+}$ in 50 M PBS solution as a function of the pH. The excited state lifetimes at pH ≥ 9.5 are extracted from a double-exponential fit of the luminescence decay profiles to Eq. 2; $\tau_M = \Sigma B_i \tau_i / \Sigma B_i$. The vertical red lines indicate each measured pK_{ap} value calculated by using the software HypSpec.

Furthermore, if we assume that the electronically excited species are indeed equilibrated among them, then the pK_a* values are related to the corresponding apparent pK_{ap} values by Eq. 42:[18]

$$pK_a^* = pK_{ap} + \log\frac{\tau_A}{\tau_B} \qquad \text{Eq. 42}$$

Where τ_A and τ_B are the excited state lifetimes of the protonated and deprotonated species, respectively. From Eq. 42 pK_a* = pK_{ap} for the first three protonation constants since $\tau_A \approx \tau_B$. The last pK_a* value is calculated to be 11.84 ± 0.01, although this value is probably underestimated, since at pH 11.5 the equilibrium is not completely shifted towards the basic *Ru-iip^{2-} form. The pKa and pK_a* values are the same for the first and third protonation constants (within the experimental uncertainty). These equilibriums are related to the fused-ring imidazole moiety (see above). On the other hand, if the proton transfer involves the distal imidazole moiety (second and fourth protonation constants) the pKa and pK_a* values are no longer identical. A reason for different protonation constants at the distal imidazole moiety but not at the fused-ring imidazole could be related to the formation of aggregates

already pointed out above. The less hindered distal imidazole ring is more capable of interacting with the other Ru(II) molecules and thus have higher effect on the acid/base equilibrium of such moiety.

Figure 19 shows the species distribution diagram of the excited state acid/base species obtained from the calculated pK_a* values (see above). A superposition of the pre-exponentially weighted excited state lifetime (τ_M) on the excited state speciation diagram clearly shows a dependency on the mole fraction of the species. Around pH 9.5, the dominant species is *Ru-iip$^-$ with $\tau_M = 499$ ns. Increasing the pH value to 10.5 leads to an excited state equilibrium with a relative concentration of ca. 5% for the double-deprotonated *Ru-iip^{2-} species. If this species has a notably lower luminescence lifetime (as stated above) then the resulting τ_M value should decrease accordingly. This is in agreement with the experimentally observed luminescence lifetime, $\tau_M = 418$ ns. Finally, increasing another pH unit to 11.5 should shift the excited state equilibrium towards ca. 30% of the rapid decaying *Ru-iip^{2-} species, accounting for the observed luminescence lifetime of 97 ns. This is in agreement with the computational study shown in chapter IV, where the emissive state of Ru(phen)$_2$(iip) evolves from ^{3}MLCT to ^{3}LLCT at high pH values. Lower radiative decay rates are expected for the ^{3}LLCT-based and ^{3}IL-based emission, as it has been observed before.[6b]

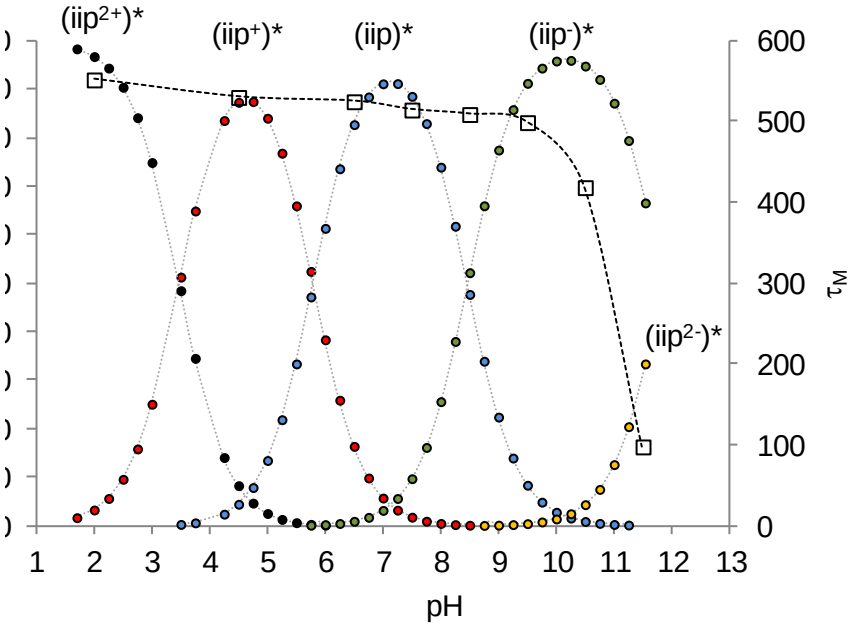

Figure 19. Species distribution diagram as a function of pH using the measured pK_a* values for [Ru(phen)$_2$(iip)]$^{2+}$. The pre-exponentially weighted excited state lifetimes (τ_M, □) are also included.

3.2.2. Response of the indicator dye to metal ions

The selectivity of the metal-organic dye towards several metal ions was evaluated by studying the changes in the absorption and emission properties of $[Ru(phen)_2(iip)]^{2+}$ in 50-mM PBS (pH 7.5, 1% methanol) upon addition of 5 mol per mole of indicator dye of a selected divalent ion. Figure 20 shows the efficiency of the emission quenching (in percentage) upon addition of the metal ion. As expected, the biimidazole moiety displays the highest sensitivity to copper(II) ions, which quench its emission by 92%. Four other metals produce luminescence quenching namely Ni(II), Hg(II), Co(II) and Pb(II), reducing the luminescence of the indicator dye by 35%, 31%, 10% and 8%, respectively. There is no change on the luminescence intensity of $[Ru(phen)_2(iip)]^{2+}$ upon addition of Cd(II), Ca(II), Mg(II), Fe(II) or Zn(II).

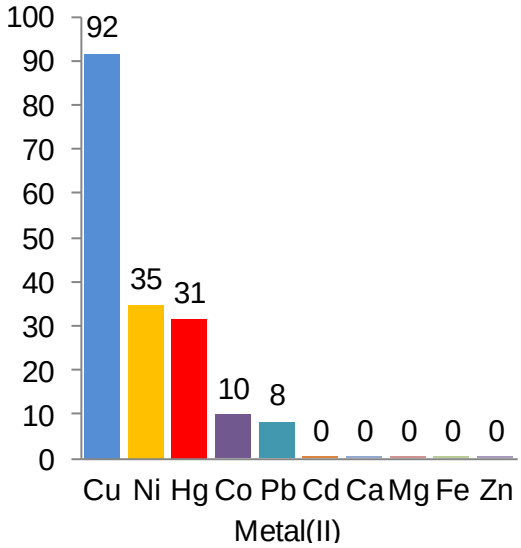

Figure 20. Luminescence quenching efficiency (%) of $[Ru(phen)_2(iip)]^{2+}$ in 50-mM PBS at pH 7.5 with 1% methanol, upon addition of 5 equivalents of several divalent metal ions.

Restricting our analysis to those metals that quench more than 30% of the emission of the indicator dye, we found that only Hg(II) provokes changes on the absorption spectrum (Figure 21). It seems that neither Cu(II) nor Ni(II) affect the ground state electronic structure of the ruthenium complex, in contrast to what is observed in the presence of Hg(II). This result indicates that an interaction in the ground state occurs within the Ru(II)-Hg(II) dyad but not in either the Ru(II)-Cu(II) or Ru(II)-Ni(II) dyads. To better understand the mechanism of such interaction that leads to the luminescence quenching, measurements of the indicator excited state decay at different metal(II) concentrations were conducted.

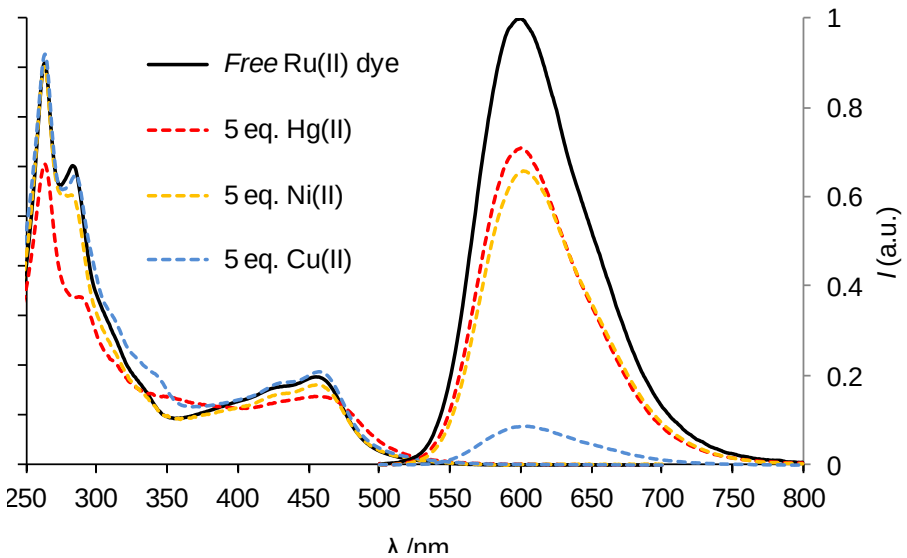

Figure 21. Absorption (left axis) and normalized emission spectra (right axis, corrected for the instrument response and for the A_{475} at the excitation wavelength) of $[Ru(phen)_2(iip)]^{2+}$ in 50 mM PBS solution upon addition of 5 mol of Hg(II), Ni(II) and Cu(II) per mole of Ru(II) indicator dye. The concentration of $[Ru(phen)_2(iip)]^{2+}$ is 10 μM throughout the experiment.

Quenching Mechanism. To investigate the type of quenching that these three metals produce on the emission of $[Ru(phen)_2(iip)]^{2+}$, the excited state lifetime of the latter was measured in presence of increasing metal concentrations up to 10 equivalents. Figure 22 shows the ratio of both the excited state lifetime (τ_0/τ,) and emission intensity (I_0/I) of the iip complex in the absence and in the presence of the quencher (Figure 22a, 19b and 19c, respectively). The emission quenching values obtained after addition of 10 equivalents of each metal ion were omitted in the plots since they are identical to those observed for the last two data points (at 5 equivalents).

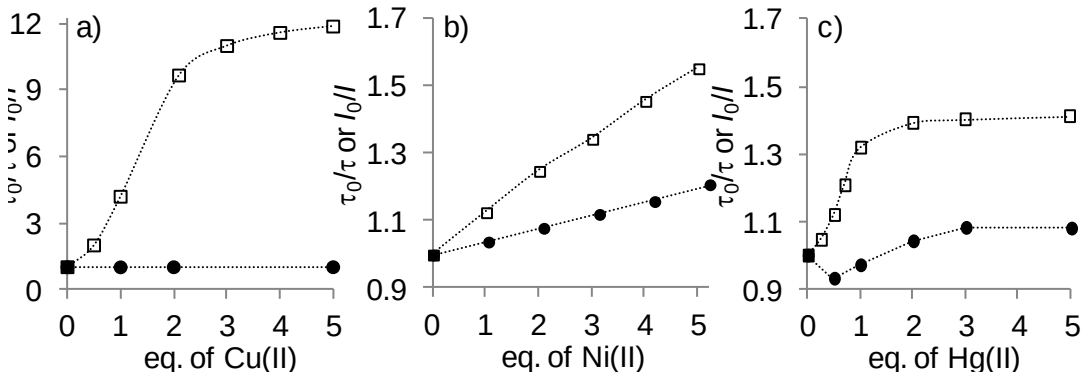

Figure 22. Excited state lifetimes (τ_0/τ, ●) and emission intensity (I_0/I, □) ratios in the absence and in the presence of quencher for $[Ru(phen)_2(iip)]^{2+}$ in pH 7.5 PBS (50 mM) at increasing Cu(II) (a), Ni(II) (b) and Hg(II) (c) concentrations. The concentration of $[Ru(phen)_2(iip)]^{2+}$ is 10 μM throughout the experiment. The τ_0/τ plot for Ni(II) yields a linear regression with $r^2 = 0.999$.

It is was observed that even in the presence of 10 eq of copper(II) there is no change in the measured excited state lifetime of the dye (514 ns) in contrast to its emission intensity, suggesting a purely *static quenching* mechanism. This result is in agreement with X-ray diffraction data studies, which show that biimidazole forms ground state quadrangular plane Cu(II) complexes in 2:1, 1:1 and 1:2 biimidazole-to-copper ratios (Figure 23).[8a, b, 19]

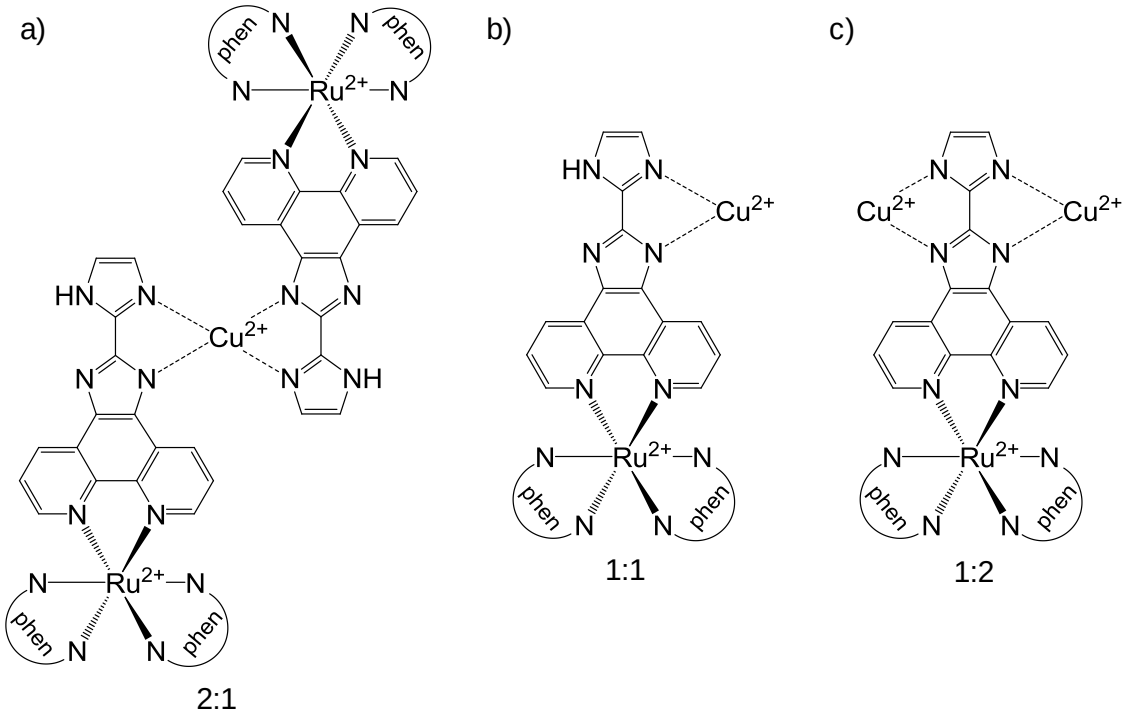

Figure 23. Supramolecular arrangements for $[Ru(phen)_2(iip)]^{2+}$-Cu(II) based on crystal structures of biimidazole complexes of Cu(II) in a) 2:1, b) 1:1 and c) 1:2 Ru-to-Cu ratios.

In the case of Hg(II), the luminescence decay profiles are bi-exponential upon addition of the metal (see Table 5), with one long lived component (ca. 650 ns) and one short lived component (ca. 200 ns). Therefore, the weighted average emission lifetime, τ_M, was represented in Figure 22c. It is seen that there is actually a slight increase of the excited state lifetime of the indicator dye, reaching its maximum at a 2:1 ruthenium-to-mercury mole ratio; after this value, the excited state lifetime decreases, reaching a plateau at 3 equivalents of Hg(II), after which no further changes occur. Although there is a variation of the emission lifetime, the Ru(II) quenching mechanism by Hg(II) is considered as static quenching (see explanation below).

Table 5. ^{3}MLCT excited state lifetimes of $[Ru(phen)_2(iip)](PF_6)_2$ (10 μM) in pH 7.5 PBS (50 mM) at increasing Hg(II) concentration.[a]

Hg(II) /equivalents	τ_i/ns [b]	τ_M/ns
0	563 (100)	---
0.5	303(13), 648(87)	604
1	236(17), 649(83)	580
2	206(22), 633(78)	540
3	200(26), 632(74)	521
5	204(30), 655(70)	521
10	172(29), 650(71)	509

[a] Estimated uncertainty: τ ± 2%

[b] The values given in parentheses represent the relative amplitude (*%*) of the individual components: $\%_i = B_i\tau_i/\Sigma B_i\tau_i$, being B_i the pre-exponential factors in the multi-exponential fit.

The graphical representation of the individual components and corresponding amplitudes of Table 5 is shown in Figure 24. While the longer lifetime (τ_2) is independent of Hg(II) concentration, the shorter lifetime (τ_1) seems to decrease up to 2 equivalents of quencher, after which no more significant changes occur (Figure 24a). The amplitude of τ_2 gradually decreases up to 5 equivalents of Hg(II) and the amplitude of τ_1 increases similarly. After 5 equivalents there are no changes in both lifetimes and amplitudes, evidence of a static quenching mechanism.

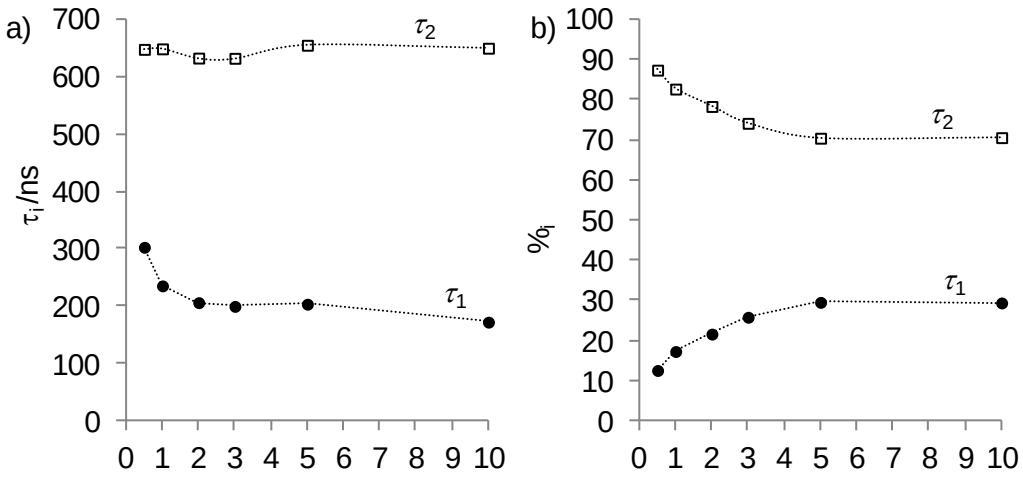

Figure 24. Excited state lifetimes components and corresponding relative amplitudes (τ_1, ● and τ_2, □) for $[Ru(phen)_2(iip)]^{2+}$ in pH 7.5 PBS (50 mM) at increasing Hg(II) concentration.

Aggregation of the luminophore in solution provides an important deactivation mechanism to the excited state of Ru(II) polypyridyls.[14] The fact that the weighted average emission lifetime up to a 1:1 ruthenium-to-mercury ratio (Figure 22c) is higher than that measured for the free dye, might be due to Hg(II)-induced detachment of aggregates between molecules of $[Ru(phen)_2(iip)]^{2+}$, as imidazoles are known to undergo extensive self-aggregation in most solvents (including water) through hydrogen bond interactions (see Figure 25a).[19-20] Mercury is known to form 2:1 complexes with imidazole in linear fashion or 1:1 with biimidazole in a distorted tetrahedral environment.[21] Figure 25 depicts possible supramolecular species responsible for the measured lifetimes, based on literature reports for imidazole complexes of Hg(II).[19-22]

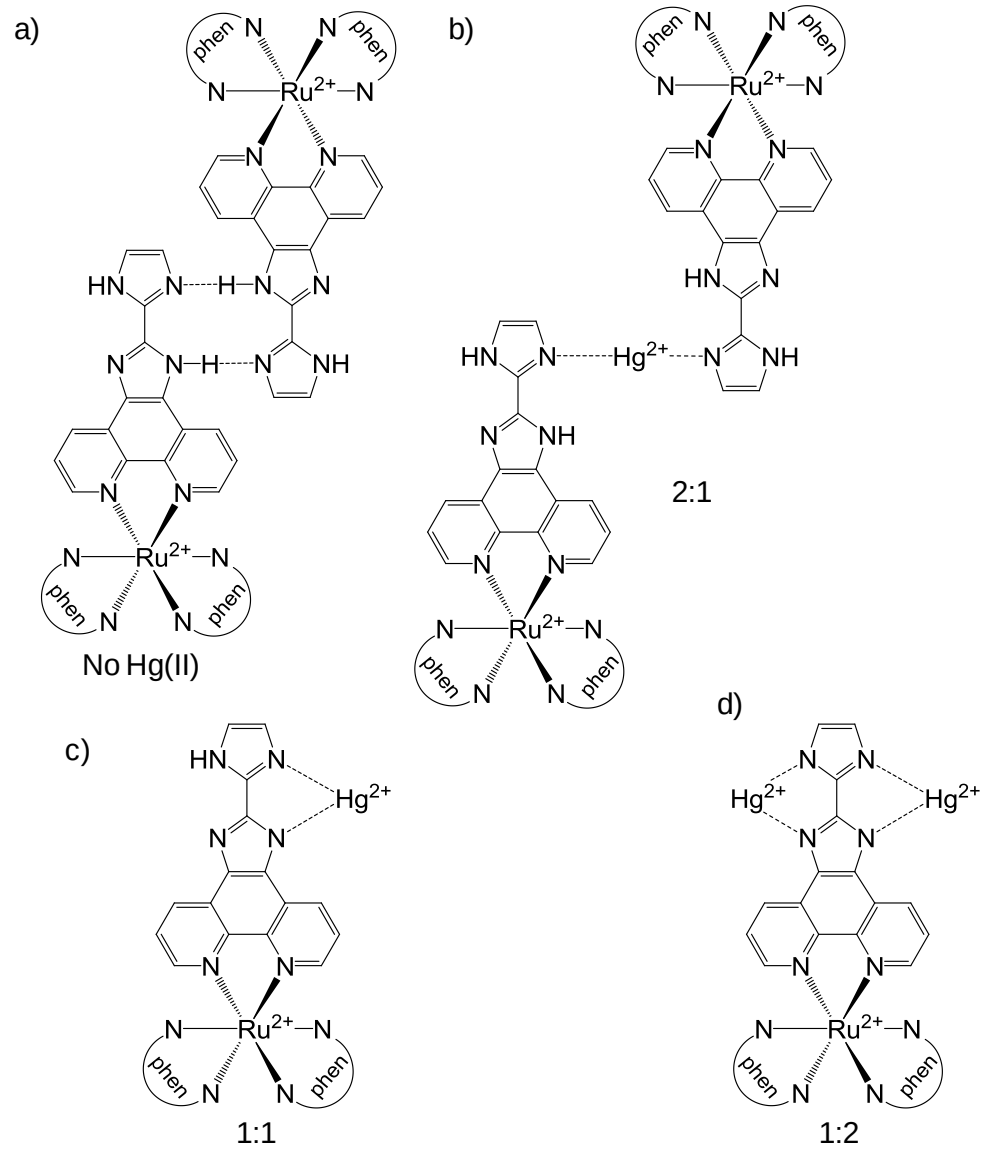

Figure 25. Supramolecular arrangements for $[Ru(phen)_2(iip)]^{2+}$-Hg(II) based on reported structures of imidazole and biimidazole complexes of Hg(II) in b) 2:1, c) 1:1 and d) 1:2 ruthenium-to-mercury ratios.

The decrease in the relative contribution of the longer lived species with increasing Hg(II) concentration is consistent with a 2:1 ruthenium-to-mercury mole ratio arrangement (Figure 25b). At higher quencher concentrations, the formation of 1:1 mole ratio arrangements becomes accessible for which it seems reasonable to associate such species with the shorter lived lifetime, τ_1. The fact that τ_1 decreases with increasing mercury concentration can be explained if this quencher induces the formation of more than one short lived emissive species (for instance a 2:3 ruthenium-to-mercury mole ratio structure resulting from the mixture of Figure 25b and c), whose individual lifetimes are not resolved by the bi-exponential fit to the decay profile. At quencher concentrations higher than 3 equivalents, the excited state lifetime τ_M changes very little, again pointing towards a static quenching mechanism.

These results show that for copper(II) and mercury(II), the emission deactivation mechanism is not based on random collisions between the dye and the metal ions but they are consistent with the binding of the guest metal ion to the biimidazole moiety of the host dye.

Unlike Cu(II) and Hg(II), nickel(II) produces a steady linear decrease in the excited state lifetime of $[Ru(phen)_2(iip)]^{2+}$, with a slope of the Stern-Volmer smaller than the slope measured for the almost-linear decrease in the emission intensity of the probe. This situation points out to a mixed static-dynamic quenching mechanism, in which some of the host dye molecules do form stable supramolecular complexes with nickel(II), and others are quenched by random collisions with this metal ion.[11] The linearity of the τ_0/τ vs. the Ni(II) concentration plot ($r^2 = 0.999$) allows the determination of the quenching rate constant of the photoexcited $[Ru(phen)_2(iip)]^{2+}$ by that metal ion ($k_q = 7.1 \times 10^9$ M^{-1} s^{-1}). This value is close to the diffusion–limit for the rate constant in aqueous solution of a reaction between a polypyridyl Ru(II) dication and a 2+ ion at 298 K in water at the constant salinity given by the buffer used (ca. $0.8\text{-}1 \times 10^{10}$ M^{-1} s^{-1}).[11, 23]

Analysis of Figure 22(c) and Figure 24 confirm that a specific interaction occurs in the ground state of the Ru(II)-Hg(II) dyad, as suggested by its absorption spectrum (see Figure 21 above).[24] It also shows the pure static quenching mechanism induced by Cu(II), as expected to occur due to the copper binding properties of the biimidazole moiety. In all those cases, the quenching mechanism is probably a photoinduced electron transfer from the photoexcited Ru(II) polypyridyl to the (solvated) metal(II) ion, as described for the quenching of the ^{3}MLCT excited state of tris(2,2'-bipyridine)ruthenium(II) by transition metal ions.[25]

Influence of the pH on the sensitivity of $[Ru(phen)_2(iip)]^{2+}$ to Cu(II) and Hg(II). Having noticed that only copper(II) and mercury(II) interact strongly with $[Ru(phen)_2(iip)]^{2+}$ in the ground state, an analysis on the pH effect over their quenching efficiency was performed. Figure 26a shows the influence of the pH on the binding capabilities of the dye towards Cu(II) or Hg(II) by comparing the emission intensity of the free dye (▲) in 50-mM PBS against its emission in the presence of 5 equivalents of Cu(II) (●) or Hg(II) (□) in the 2.5-10.5 pH range. The ratio between the emission intensity of the dye in presence (I_M) and absence (I_{Ru}) of the metal quencher is shown in Figure 26b.

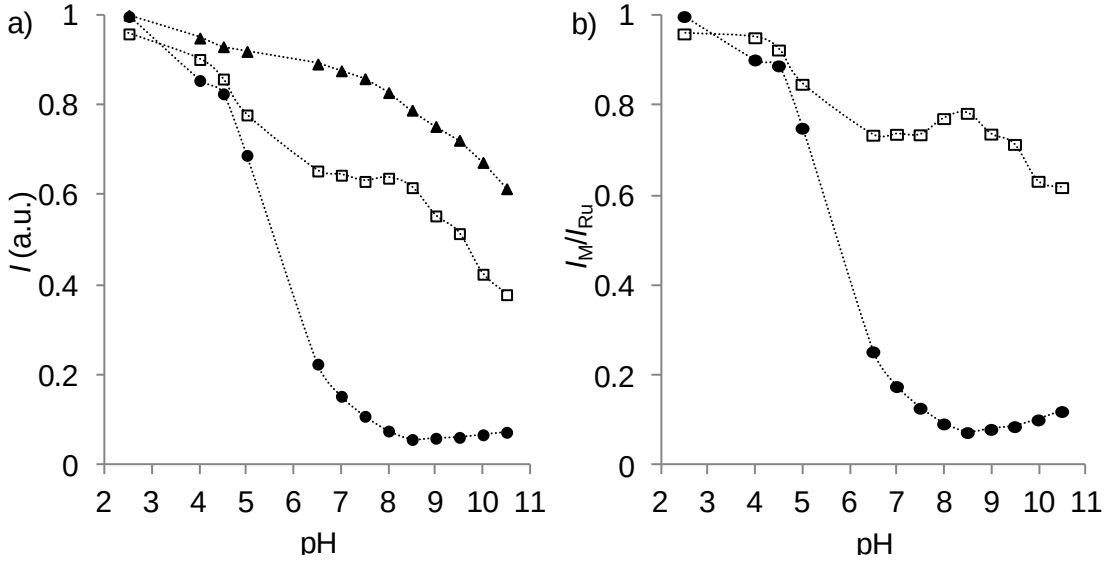

Figure 26. a) Emission intensity of the free $[Ru(phen)_2(iip)]^{2+}$ (▲) in PBS (50 mmol L^{-1}) and in the presence of 5 equivalents of Cu(II) (●) or Hg(II) (□) as a function of the pH. b) Emission intensities corrected for the emission of the free dye at each pH value (I_M/I_{Ru}) under the same conditions.

At pH values below 4.5 the luminescence of the dye ($pK_a = 3.45$, see above) remains practically unaltered (<10%), possibly due to the high proton concentration which competes with the metal ions for the biimidazole binding site. After this value, the quenching efficiency starts to increase, the Cu(II) producing a decrease in the luminescence of the probe higher than 90% at pH values above 7.5, being the maximum quenching at pH 8.5 (97%). In contrast to other reports,[26] there is no significant decrease in the quenching efficiency at pH values higher than 8 where hydroxides compete with other ligands by precipitating copper(II) as $Cu(OH)_2$. Such precipitates seem however to influence the luminescence quenching when increasing further the pH up to 10.5, close to pH 12 where significant precipitation is known to occur.[27]

In the case of the Hg(II) ions, there is a working range between pH 6.5 and pH 7.5 in which the quenching efficiency remains roughly the same (≈30%). Between pH 8 and pH 8.5 the luminescence slightly increases, possibly due to precipitation of mercury(II) as $Hg(OH)_2$ thus reducing its *free* concentration. For pH values above 8.5, there is a further increase in the quenching efficiency of Hg(II) until pH 10.5 possibly due to the deprotonation of the phen-fused imidazole pyrrolic-nitrogen (calculated pK_a value of 8.35, see above) which determines a higher affinity towards the Hg(II) ions.

Considering the results obtained, a pH value of 7.5 was selected for the metal binding studies as it yields good sensitivity of the $[Ru(phen)_2(iip)]^{2+}$ dye for both copper(II) and mercury(II) without interferences such as precipitation of the metals or protonation of the dye.

3.2.3. Binding constants of $[Ru(phen)_2(iip)]^{2+}$ to Cu(II) and Hg(II)

The effect of the addition of Cu(II) or Hg(II) on the spectroscopic properties of $[Ru(phen)_2(iip)]^{2+}$ in 50 mM PBS at pH 7.5 was measured by absorption, emission and excited state lifetime measurements. Figure 27 and Figure 28 show the absorption spectrum of the Ru(II) complex in the presence of increasing amounts of Cu(II) or Hg(II), respectively. In spite of displaying only small changes in the molar absorption coefficient up to a 2:1 Cu-to-Ru mole ratio, those are specifically found at 285 nm and at 330 nm which correspond to intra-ligand transitions of the iip ligand (see above). By producing changes in the (ground state) iip conformation and its electronic features, the Cu(II) ions are expected to interact solely with the bi-dentate biimidazole ligand upon complexation with this moiety, not involved in the coordination with the Ru(II) core. In contrast to it, Figure 28 shows that the addition of Hg(II) ions produces significant changes in the molar absorption coefficients of $[Ru(phen)_2(iip)]^{2+}$, both in the ligand-centred and the MLCT bands. Similarly to the addition of Cu(II), these changes are more important in the iip ligand absorption maximum (284 nm) and occur up to a 2:1 Hg-to-Ru mole ratio.

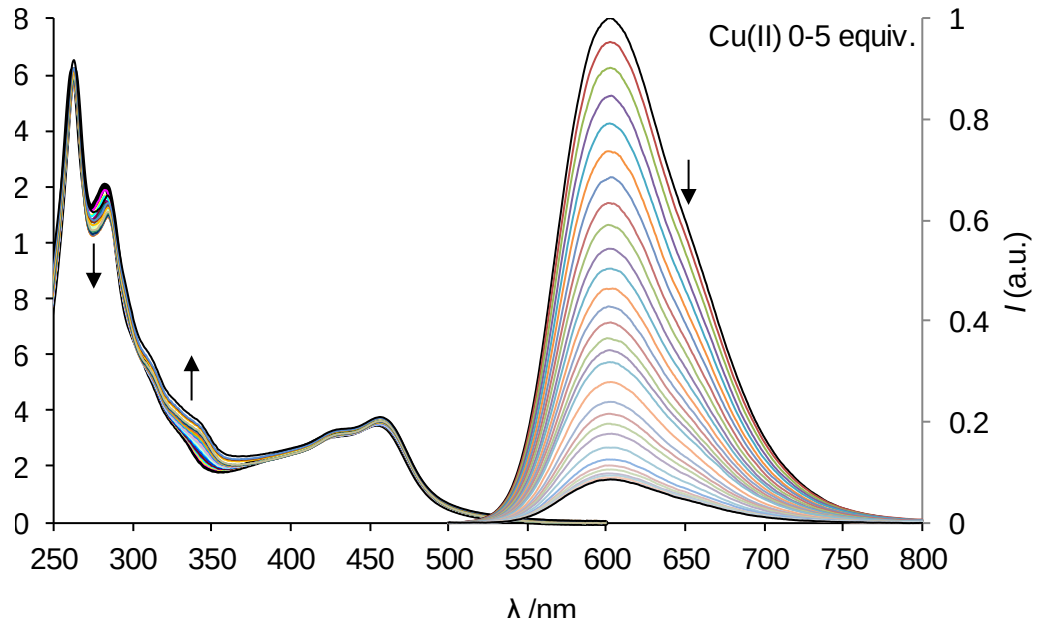

Figure 27. Absorption (left axis) and emission (right axis, corrected for the absorption at λ_{exc} = 475 nm) spectra of 20 μM $[Ru(phen)_2(iip)]^{2+}$ in 50-mM PBS at pH 7.5, in the absence and in the presence of increasing amounts (up to 100 μM) of Cu(II).

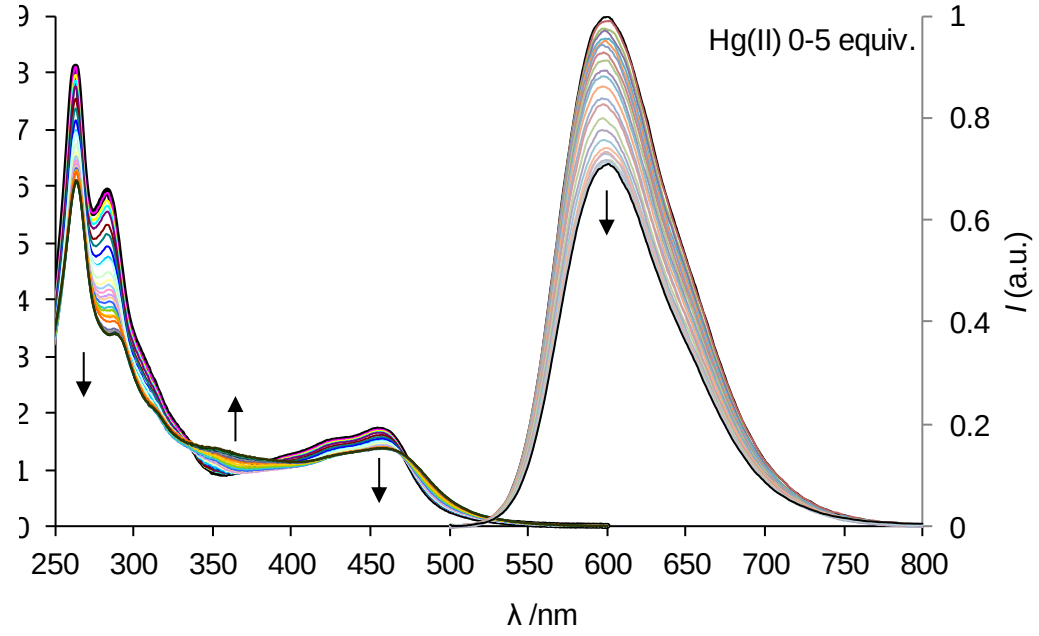

Figure 28. Absorption (left axis) and emission (right axis, corrected for the absorption at λ_{exc} = 475 nm) spectra of 10 μM $[Ru(phen)_2(iip)]^{2+}$ in 50-mM PBS at pH 7.5, in the absence and in the presence of increasing amounts (up to 50 μM) of Hg(II).

The variations in the emission of the Ru(II) indicator dye in the presence of copper or mercury are also shown in Figure 27 and Figure 28, respectively. Changes occur up to a 2:1 metal-to-dye mole ratio (the same range observed for the absorption changes). At this ratio,

the luminescence intensity of the iip complex is approximately 92% quenched by Cu(II) while Hg(II) only produces a luminescence variation of 30%. These changes do not seem to affect either the energy of the LUMO or the t_{2g} orbitals of the Cu(II)-ruthenium dye supramolecular complex, as no shift of the emission maximum is observed. This would suggest again that the binding of Cu(II) takes place specifically at the biimidazole moiety, where the conformational and electronic changes produced upon binding of the metal do not affect the energy of the $[Ru(phen)_2(iip)]^{2+}$ LUMO (see above). Unlike the Cu(II) complexation, the addition of Hg(II) ions do alter slightly the indicator emission band shape, as evidenced by the different changes of the emission curves at two selected wavelengths (see Figure 30, below). Such differences might indicate that the mode of Hg(II) binding by the iip complex is not similar to that of Cu(II). These conclusions are supported by the results obtained in the excited state lifetime measurements up to 10 equivalents of the metal ion (Figure 22a and 22c), where while both metals produce static quenching, several binding modes between Hg(II) and biimidazole are possible (Figure 25).

The stoichiometry of the metal-ligand complex is normally determined by absorption spectroscopy using the Job's plot method, which involves measuring the absorbance of a series of solutions of constant molarity, but of varying metal-to-ligand ratio.[28] This measurement must be corrected for both the *free* ligand and metal ion concentrations, precluding the application of the Job's method to the work presented here as there is no region of the spectrum specifically attributable to the free $[Ru(phen)_2(iip)]^{2+}$, Cu(II) or Hg(II) species (Figure 27 and Figure 28). Still, it is possible to track the changes in any of those spectra vs. the Cu(II) or Hg(II) concentration by means of a binding isotherm that describes the equilibrium of the system. This method allows the determination of stability constants of the complexes, together with ligand/metal stoichiometry, by finding the best fit of the experimental points to the appropriate binding model. The process has been explained in page 14 of the Introduction section 1.7.

The absorption and emission changes observed upon addition of Cu(II) or Hg(II) to an aqueous solution (PBS, pH 7.5) of $[Ru(phen)_2(iip)]^{2+}$ (Figure 27 and Figure 28) were successfully fitted to the corresponding 2:1 binding isotherms (Eq. 22 and Eq. 24, respectively), obtained by means of simple mathematical transformations as described in section 1.7.2,

$$\frac{\Delta A}{[L_T]} = \frac{\Delta\varepsilon_{11}K_1[G] + \Delta\varepsilon_{21}K_1K_2[G][L]}{1+K_1[G] + 2K_1K_2[G][L]} \qquad \text{Eq. 22}$$

where, ΔA is the difference between the absorbance in the absence and in the presence of G (copper or mercury ion), $[L]_T$ is the *total* concentration of $[Ru(phen)_2(iip)]^{2+}$, [L] is the

concentration of *free* $[Ru(phen)_2(iip)]^{2+}$, [G] is the concentration of *free* metal(II), $\Delta\varepsilon_{11}$ is the difference between the molar absorption coefficients of the 1:1 supramolecular complex and the $[Ru(phen)_2(iip)]^{2+}$ species and $\Delta\varepsilon_{21}$ is the difference between the molar absorption coefficient of the 2:1 supramolecular complex and twice the molar absorption coefficient of the $[Ru(phen)_2(iip)]^{2+}$ species.

Similarly,

$$\frac{I_F}{I_0} = \frac{1 + \alpha K_1[G] + \gamma K_1 K_2[L][G]}{1 + K_1[G] + 2K_1 K_2[L][G]} \qquad \text{Eq. 24}$$

where I_0 is the luminescence intensity of the Ru complex in absence of copper or mercury, the term α is given by the $(\varepsilon\Phi_f)^{RuG}/(\varepsilon\Phi_f)^{G}$ ratio and γ by the $(\varepsilon\Phi_f)^{Ru2M}/(\varepsilon\Phi_f)^{M}$ ratio. Φ_f and ε are the luminescence quantum yield and molar absorption coefficient of each emitting species, respectively.

The powerful HypSpec software was used to fit globally the full absorption data of copper(II) addition (26 data points) in the range where larger changes occur (270–480 nm). By introducing the parameters calculated thereof in Eq. 22 and plotting the absorption variation at a single wavelength vs. copper equivalents, the plot of Figure 29a has been produced. The same method has been applied to model the emission changes in the range 540–700 nm (31 data points) upon Cu(II) addition by using Eq. 24 (Figure 29b). Similar procedures were conducted to rationalize the results in the presence of Hg(II) (Figure 30) for absorption (263–510 nm range, 27 data points) and emission (540–700 nm range, 26 data points).

Table 6 summarizes the $[Ru(phen)_2(iip)]^{2+}$-metal ion binding constants obtained for Cu(II) and Hg(II) in pH-7.5 50-mM PBS solution.

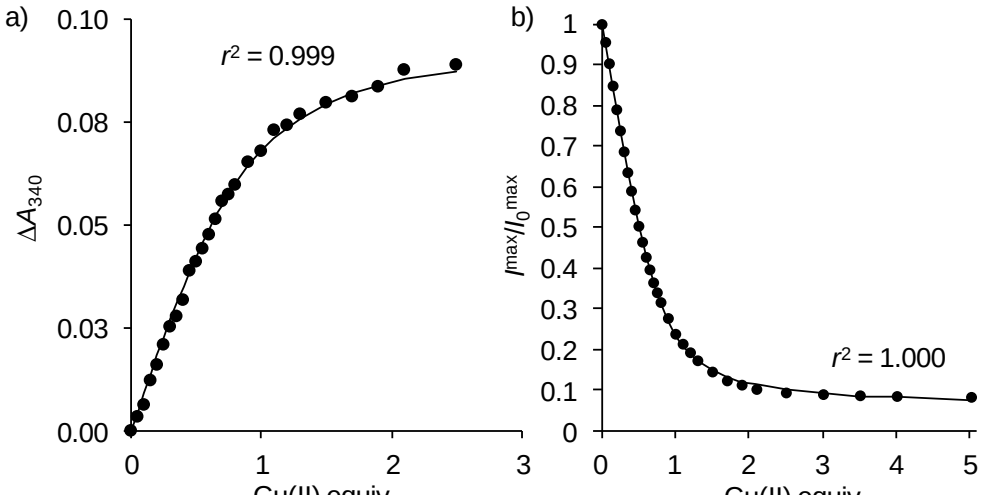

Figure 29. Variation of the absorbance excursion at 340 nm (ΔA_{340}) (a), and relative luminescence intensity (b) ($I^{max}/I_0{}^{max}$) as a function of the amount of Cu(II) added to the $[Ru(phen)_2(iip)]^{2+}$ solution. The solid lines represent the best fit of the experimental points to Eq. 22 (a) or Eq. 24 (b) using the binding constants calculated by the software HypSpec (see text).

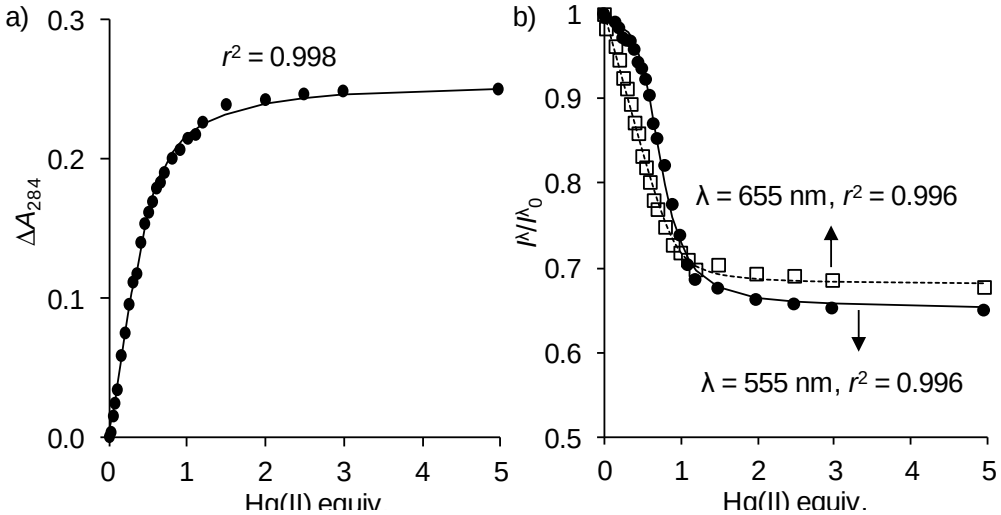

Figure 30. Variation of the absorbance excursion at 284 nm (ΔA_{284}) (a) (●), and relative luminescence intensity (b) ($I^{555}/I_0{}^{555}$ ●, $I^{655}/I_0{}^{655}$ □) as a function of the amount of Hg(II) added to the $[Ru(phen)_2(iip)]^{2+}$ solution. The solid and dashed lines are the best fit of the experimental points to Eq. 22 (a) or Eq. 24 (b) using the binding constants calculated by the software HypSpec (see text).

As showed above, the presence of Cu(II) in an aqueous solution of $[Ru(phen)_2(iip)]^{2+}$ provokes small changes in the absorption spectrum of the latter in contrast to the dramatic quenching of its emission (Figure 27). Therefore, it is not surprising to obtain somewhat different log K_i values from the absorption and emission variations (Table 6). In fact, the

stability constants obtained by fitting the absorbance data upon the Cu(II) addition should not be taken into consideration due to the experimental uncertainty determined by such little variation. On the other hand, Hg(II) addition produces significant changes in absorption and emission which explains the good agreement between the stability constants obtained when using either method. For the sake of comparison only stability constants obtained using the emission data will be discussed.

Table 6. Stability constants of the 1:1 and 2:1 $[Ru(phen)_2(iip)]^{2+}$-Cu(II) and -Hg(II) complexes in pH-7.5 50-mM phosphate-buffered solution.

Method	Cu(II)		Hg(II)	
	log (K_1 /M^{-1})	log (K_2 /M^{-1})	log (K_1 /M^{-1})	log (K_2 /M^{-1})
Absorption	5.446 ± 0.007[a]	3.87 ± 0.05[a]	6.73 ± 0.01[a]	5.97 ± 0.01[a]
Emission[b]	6.196 ± 0.005[a]	5.028 ± 0.008[a]	7.81 ± 0.03[a]	6.19 ± 0.04[a]

[a] Standard deviation of the Hyperquad global fit

[b] The emission data (I_{obs}) were corrected at each point for the absorbance of the solution at the excitation wavelength (A_{475}) according to $I = I_{obs}(1\text{-}10^{-A_{475}})^{-1}$

The host-guest stoichiometry found is in agreement with literature reports for copper(II) and mercury(II) biimidazole-derivative complexes, where two bidentate ligands bind to one metal ion.[21b, 22] When comparing emission data, it seems that $[Ru(phen)_2(iip)]^{2+}$ has higher affinity towards Hg(II) ($\log \beta_{21} = 14$) than Cu(II) ($\log \beta_{21} = 11.2$). The same behaviour but to a lower extent is described for Hg(II) and Cu(II) complexes of imidazole, which show global equilibrium constant values up to $10^{16.7}$ and 10^{14} respectively.[21b, 22b, 24, 29] The observed enhanced affinity towards mercury can be explained by taking into consideration the geometry of the 2:1 $[Ru(phen)_2(iip)]^{2+}$-metal supramolecular complex. Crystal structure studies show that two biimidazole moieties can coordinate Cu(II) ions in a coplanar fashion, and that the coordination uses four nitrogen atoms (Figure 23a – above).[22a] Such coordination geometry lowers the stability of the 2:1 $[Ru(phen)_2(iip)]^{2+}$-Cu^{2+} complex due to steric hindrance between the two bulky ruthenium complexes. In the case of Hg(II), the metal ion is either coordinated by one bidentate biimidazole moiety[21a] (Figure 25c above) or by two nitrogen atoms of two biimidazole ligands in a linear geometry (Figure 25b – above).[30] This arrangement allows coordination of Hg(II) to the *distal* imidazole moieties of the two ruthenium-iip complexes, leading to less proximity of both dyes and, therefore, smaller steric hindrance between them.

Needless to say, a more stable complex formed between mercury(II) and $Ru(phen)_2(iip)$ does not necessarily involve larger changes in the spectroscopic features of the luminophore (higher sensitivity). The formation of the supramolecular ground state complex yields a new fluorophore, with its own electronic properties and excited state energy levels that can be similar to the ones of the free dye (less sensitivity).

3.3. $[Ru(phen)_2(hmip)](PF_6)_2$

The synthesis of this complex is detailed in section 2.3.5. The ion-recognition site of $[Ru(phen)_2(hmip)]^{2+}$ differs from the iip complex (see above) in that it has an imidazo-phenol instead of a biimidazole moiety. Moreover, the phenol ring has an electron donating methoxy group at the *para* position. This group is expected to increase the electron density at the oxygen atom of the hydroxyl group. As seen for $[Ru(phen)_2(iip)]^{2+}$ in the previous section, the luminescent $[Ru(phen)_2(hmip)]^{2+}$ compound also displays the typical spectroscopic features of polypyridyl ruthenium(II) complexes,[6] both in the ground and in the excited state (Figure 31).

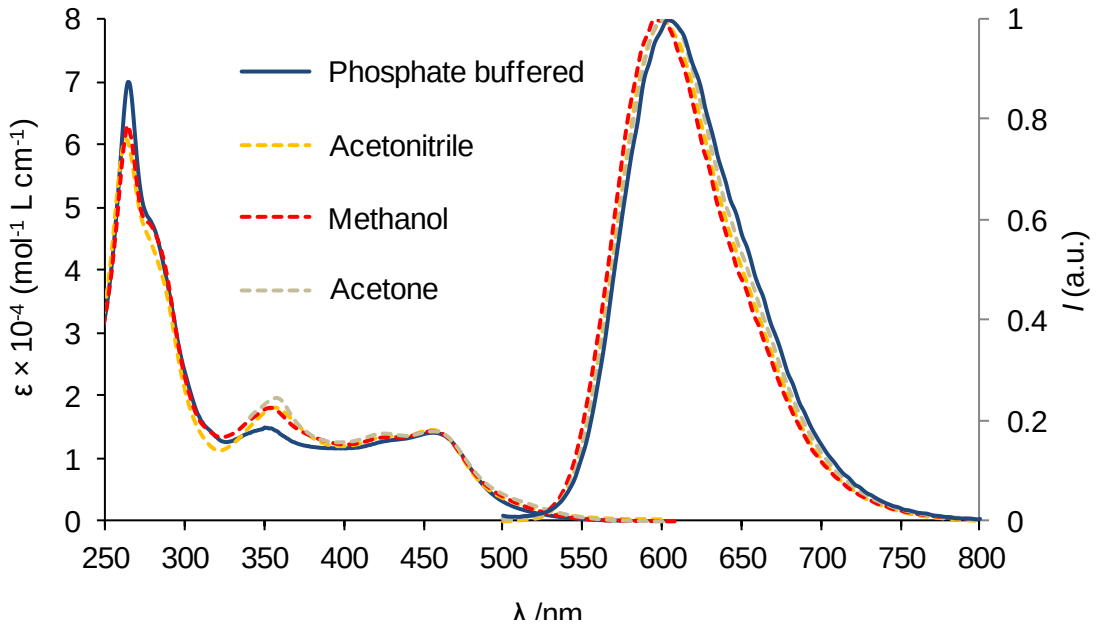

Figure 31. Absorption (left axis) and normalized emission (right axis, corrected for the instrument response) spectra of 10 μM $[Ru(phen)_2(hmip)]^{2+}$ in polar solvents and in 50-mM PBS at pH 7.5 (1% methanol). The absorption spectrum in acetone was only recorded down to 340 nm due to the solvent cut-off wavelength.

Table 7 summarizes the relevant photophysical data of $[Ru(phen)_2(hmip)]^{2+}$ in polar solvents and in 50-mM pH-7.5 phosphate buffer solution containing 1% methanol (by volume) to allow solubilization of the dye. Its absorption spectrum contains similar intraligand transitions to those already observed for $[Ru(phen)_2(iip)]^{2+}$. Following the same reasoning, the maximum at 263 nm corresponds to the intense π-π* absorption of the phen moieties (the tris-phen complex shows absorption at 263 nm, Figure 8). The shoulder at 280 nm (stronger in methanol) and the band centred at 350 nm are related to the hmip functional ligand as they are not observed in the homoleptic tris-phen compound either. Moreover, this

is the spectral region that displays the largest changes upon a pH increase (see Figure 32), supporting again its correlation with the hmip pH sensitive ligand. The fact that the shoulder at 280 nm (π-π* absorption of the hmip ligand) is not observed in the hydrogen-bonding aqueous medium suggests that the functional ligand renders the ruthenium complex solvent-dependent. The broad visible metal-to-ligand charge transfer (MLCT) band at 456 nm is located at the very same energy than that of its related imidazo[4,5-*f*]phenanthroline $[Ru(phen)_2(iip)]^{2+}$ complex. This band shows different transitions that cannot be resolved, due to both the typical vibronic structure of this band in the Ru(II) polypyridyl complexes and the heteroleptic character of the investigated $[Ru(phen)_2(hmip)]^{2+}$. The latter allows MLCT transitions to the different ligands in the coordination sphere (the homoleptic $[Ru(phen)_3]^{2+}$ complex absorbs at 445 in methanol, Figure 8).[6a] The red-orange emission maxima of $[Ru(phen)_2(hmip)]^{2+}$ (Table 7) in different solvents are also similar to those of $[Ru(phen)_2(iip)]^{2+}$ and tris(phenanthroline) complex (λ^{max}(corr.) = 601 nm and 595 nm in methanol, respectively). The spectroscopic features of the former are equivalent to those of related imidazo[4,5-*f*]phenanthroline complexes.[9]

Table 7. Electronic absorption and emission band maximums, molar absorption coefficient, luminescence quantum yield (Φ_{em}) and ^{3}MLCT excited state lifetime of $[Ru(phen)_2(hmip)](PF_6)_2$ (10 μM) in polar organic solvents and in 50-mM phosphate buffer (PBS) at pH 7.5.[a]

Solvent	λ_{abs}^{max} /nm (ε/M^{-1} cm^{-1})	λ_{em}^{max} /nm[b]	Φ_{em} (Ar)	τ/ns (Ar)
Acetone[c]	358 (19430), 426 (13830), 456 (14170)	602	n.d.	n.d.
Acetonitrile	264 (60880), 357 (17920), 456 (14320)	600	n.d.	n.d.
Methanol	264 (63140), 280 (46200, s), 353 (18100), 456 (14350)	596	0.020	n.d.
PBS	263 (70500), 350 (14300), 456 (14000)	604	0.016	87 (87), 673 (13) τ_M = 163[d]

[a] Estimated uncertainties: λ ± 1 nm; ε ± 4%; $\Phi_{em} \leq 10\%$; τ ± 1% (1-exp.), ± 2% (2-exp.); s: shoulder.
[b] Corrected for the instrument response; λ_{exc} = 475 nm.
[c] Solvent cut-off 350 nm.
[d] The values given in parentheses represent the relative amplitude (*%*) of the individual components ($\%_i = B_i\tau_i/\Sigma B_i\tau_i$), being B_i the pre-exponential factors in the multi-exponential fit.

As shown in Figure 31, the luminescence spectrum of the Ru(II) complex has a similar profile in the different polar solvents and aqueous media. However, its maximum is somewhat red-shifted when comparing aqueous media with methanol (605 nm vs 596 nm, respectively) showing that $[Ru(phen)_2(hmip)]^{2+}$ possesses some sensitivity of its ^{3}MLCT *transition energy* to hydrogen bonding. The computational study (see chapter IV) supports this observation by showing that the emissive (triplet) excited state is distributed over the hmip functional ligand. In this way, interactions between solvent molecules and the imidazo-phenol moiety of the hmip ligand may alter the energy of the emissive triplet state hence changing the emission maximum.

The emission quantum yield (Φ_{em}) of the $[Ru(phen)_2(hmip)]^{2+}$ ion was measured in methanol and 50 mM PBS pH-7.5 following the procedure in section 3.1. Table 7 shows that this indicator dye displays the same value of Φ_{em} as its parent homoleptic tris-phen compound (0.020 in argon purged methanol, see Table 3). In contrast, it presents half the value of Φ_{em} of the homoleptic compound in aqueous medium (0.056, see Table 3). This result provides further evidence of a solvent-specific interaction with the hmip complex. Table 8 gathers the emission lifetimes of $[Ru(phen)_2(hmip)]^{2+}$ in air-equilibrated organic solvents and phosphate buffer. Unlike the iip complex (Table 3), this compound presents comparable emission lifetimes in organic solvents and water (in the 100-300 ns range). Since the oxygen concentration in water is approximately 10-fold its value in organic solvents, this finding indicates that the net emission of $[Ru(phen)_2(hmip)]^{2+}$ is rather insensitive to oxygen quenching. In fact, the emission lifetime of the dye in argon-purged aqueous solution (Table 7) is similar to the value obtained in air-equilibrated solution (Table 8). Compounds bearing similar structures to the 2-(imidazol-2-yl)phenol moiety of the hmip ligand are known to undergo excited state intramolecular proton transfer (ESIPT), a photochemical process that is sensitive to the solvent polarity.[31] However, a Lippert-Mataga dielectric continuous medium model does not yield a linear plot of emission lifetimes vs. the probe orientation polarizability term (Lippert equation).[14] This could simply be due to the absence of solvent-solute terms, one of many simplifications required in this model.[11]

Table 8. ^{3}MLCT excited state lifetimes of $[Ru(phen)_2(hmip)](PF_6)_2$ (10.5 μM) in several air-equilibrated organic solvents and 50-mM phosphate buffer (PBS) at pH 7.5.[a]

Solvent	Δf[b]	τ_i/ns [c]	τ_M/ns
Chloroform	0.15	126(87), 370(13)	159
DMSO	0.26	80(20), 440(80)	292
DMF	0.28	168(75), 512(25)	244
Ethanol	0.29	150(72), 459(28)	233
Methanol	0.31	87(93), 258(7)	99
Acetonitrile	0.31	131(85), 715(15)	217
PBS	0.32	71(87), 374(13)	110

[a] Estimated uncertainty: $\tau \pm 2\%$

[b] Orientation polarizability term of the Lippert-Mataga Eq. 32 (section 1.10.1)

[c] The values given in parentheses represent the relative amplitude (*%*) of the individual components: $\%_i = B_i\tau_i / \Sigma B_i\tau_i$, being B_i the pre-exponential factors in the multi-exponential fit.

The luminescence decay of the hmip complex requires a bi-exponential fit for all the solvents studied. This observation indicates that at least two luminescent species are present, a result that is compatible with the aggregates hypothesis already suggested for the iip complex. Comparing the two emission lifetimes measured in aqueous medium under argon-flushed and air-equilibrated conditions, it can be observed that the relative amplitude (*%*) of the individual components does not change. Nonetheless, while the shorter lifetime is rather constant (71 ns in air-equilibrated and 87 ns in oxygen-free solution), the value for the longer lifetime does show a dependence on the presence of oxygen, changing from 374 ns under air to 673 ns in deoxygenated solution. Therefore, the *free* non-aggregated dye is affected by the oxygen quenching, in contrast to the oxygen-protected aggregated dye that shows a shorter lifetime due to self-quenching independent of the quenching gas concentration.

3.3.1. Effect of the solution pH

Due to the acid/base properties of the 2-(imidazol-2-yl)phenol moiety, a study of the pH effect on the spectroscopic properties of the hmip complex was performed by measuring the absorption and emission features of a 10 μM $[Ru(phen)_2(hmip)]^{2+}$ solution in 50-mM PBS (Figure 32).

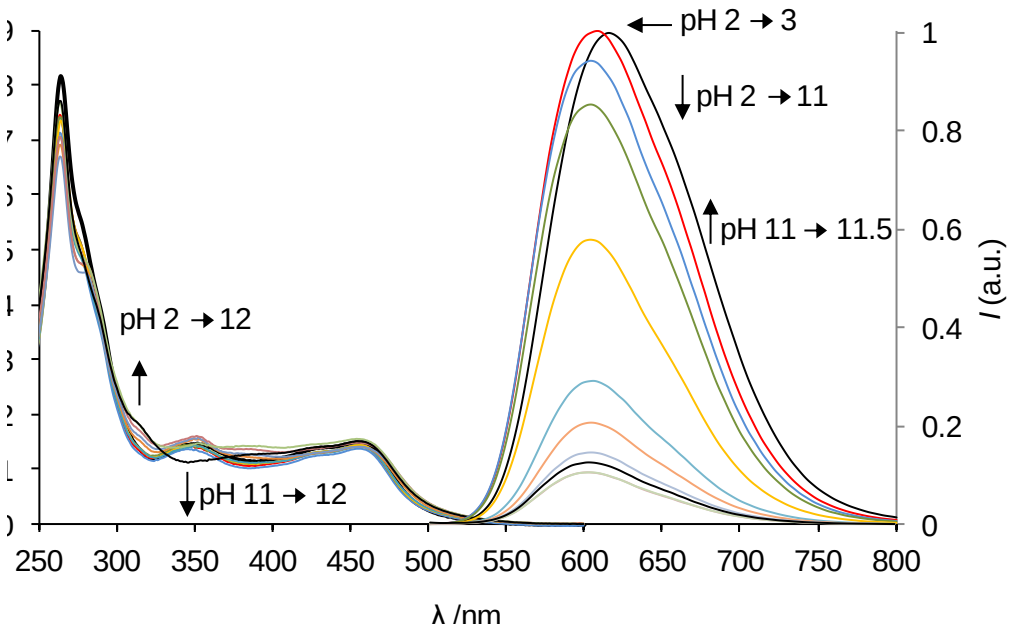

Figure 32. Absorption (left axis) and normalized emission (right axis, corrected for the instrument response and for the absorbance at the excitation wavelength, A_{475}) spectra of 10 μM $[Ru(phen)_2(hmip)]^{2+}$ in 50 mmol L^{-1} PBS solution as a function of the pH.

A global analysis of the absorbance data in the 250-490 nm range using the HypSpec software (11 pH data points) yields three different pK_a values in the investigated range ($2 <$ pH < 12). The refinement yielded pK_a values of 2.03 ± 0.06, 7.92 ± 0.03 and 10.36 ± 0.02. The acidity constants are calculated from the inflexion points of the sigmoidal curve (A vs. pH). However, the pK_a value of 2.03 lies at the acidic edge of the investigated pH range, where the curve does not reach a plateau. By using the global analysis method, the HypSpec software is capable of identifying pK_a values that would be otherwise missed. Table 9 summarizes the data obtained. All the optical changes are fully reversible by adding acid or base.

Figure 33a depicts the molar absorption coefficient measured at 263 nm and at 314 nm as a function of the solution pH and the values calculated by the HypSpec program. Similar plots using the d-π* (metal-to-phen ligand CT absorption band, see above) transition at 455 nm do not show the pK_a values. This is a similar observation to that found for the iip complex. These results demonstrate that the hmip ligand does not significantly participate in the 455 nm transitions but is heavily involved in the 263-430 nm absorption bands as the electronic absorption spectra already pointed out (see above).

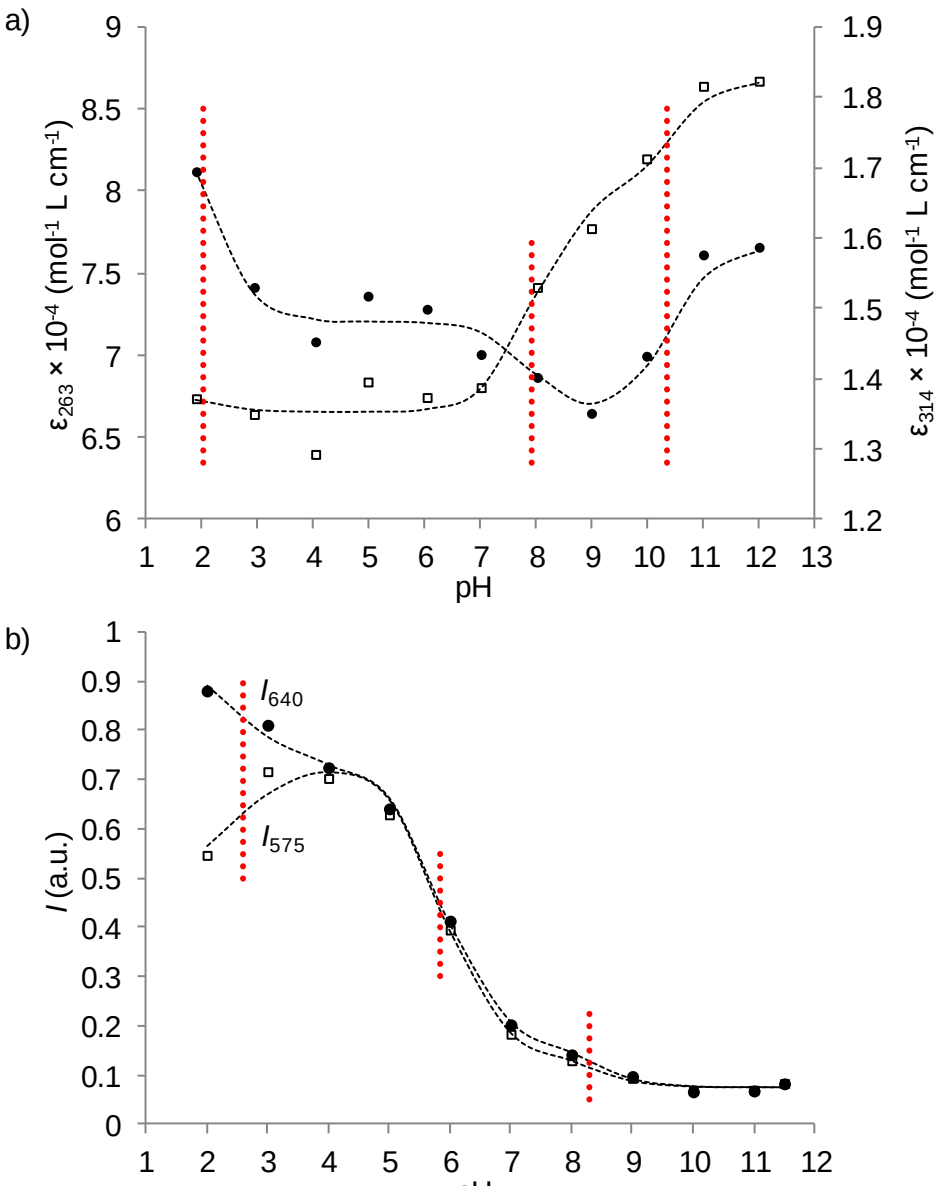

Figure 33. Selected wavelengths showing the changes in (a) the absorption (ε_{263}, ● and ε_{314}, □) and (b) the emission intensity (I_{640}, ● and I_{575}, □) of a 10 μM aqueous $[Ru(phen)_2(hmip)]^{2+}$ solution (1% methanol) as a function of the solution pH (50 mM phosphate buffer). The thin black dashed lines (r^2 = 0.946, r^2 = 0.982, r^2 = 0.999 and r^2 = 0.995 for ε_{263}, ε_{314}, I_{640} and I_{575}, respectively) are the absorbance and emission intensity curve fits calculated by the HypSpec software. The vertical red lines indicate the pK_a (a) and pK_{ap} (b) values obtained thereof.

In order to assign the experimental acidity constants to the individual acid-base equilibriums of the multifunctional hmip chelating ligand bound to the Ru core, the expected pK_a values of the $hmipH_2^{2+}$ ligand were computed using ChemAxon MarvinSketch (v5.2.5) molecular properties calculator software (www.chemaxon.com). Calculation using the diprotonated phen moiety of hmip tries to emulate the effect of coordination of the Ru(II)

atom. In this way, protonation of the pyridine-type nitrogen atom of the imidazole moiety is predicted at pK_a value of 4.4 (pK_a^{exp} = 2.03), deprotonation of the pyrrolic nitrogen at pK_a 11.0 (pK_a^{exp} = 10.36) and deprotonation of the phenol moiety might be found around pK_a 9.1 (pK_a^{exp} = 7.92) (Table 9). Unlike what it was found for the pK_a values of the complexed iip ligand, the predicted pK_a values of the hmip complex differ from the experimentally determined ones. The major difference lies in the protonation of the pyridine-type nitrogen atom (> 2 pK_a units), which can be explained if we consider the stabilization that derives from the intramolecular hydrogen bonding interaction between the pyridine-like nitrogen atom and the hydrogen atom of the phenol group (see below).

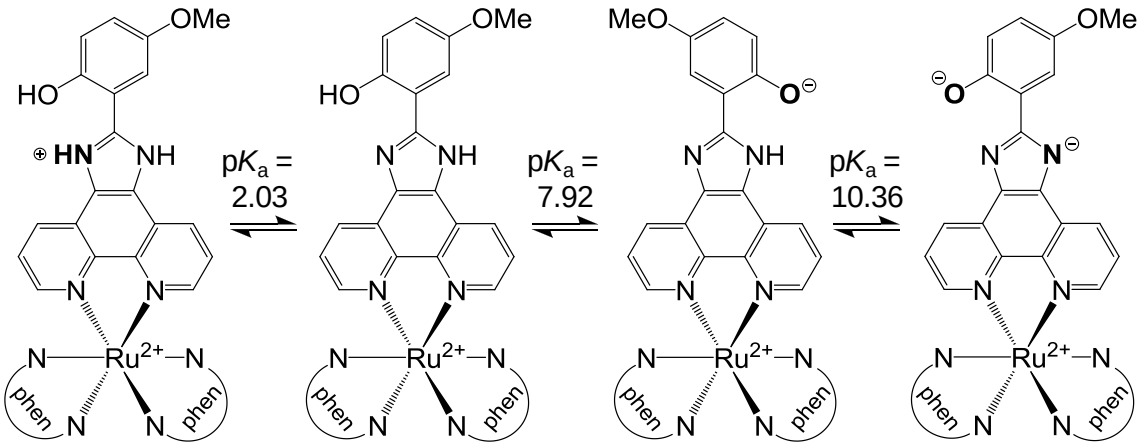

Figure 34. Acid-base species of [Ru(phen)$_2$(hmip)]$^{2+}$. The pK_a values were obtained by absorption spectroscopy.

A similar study has been carried out using luminescence measurements. Figure 32b depicts the variation of the emission spectrum of [Ru(phen)$_2$(hmip)]$^{2+}$ in the 2-11.5 pH range upon excitation of the indicator dye in its MLCT absorption maximum (475 nm). The intensity of its emission band decreases from 100% to 10% in going from pH 2 to pH 11 after which it increases slightly up to pH 11.5. The pH rise also leads to a 12 nm hypsochromic shift of the emission when going from pH 2 to pH 3. Such shifts in the emission are possibly due to ESIPT stabilization effects, as mentioned above. The fact that the shift is observed at low pH values, where protonation of the pyridine-type nitrogen atom is expected to occur, is consistent with the excited state proton transfer from the phenol moiety to the nitrogen atom. An increase of the pH would deprotonate the pyridine nitrogen atom which is now available for ESIPT.[31b]

As performed for the absorption data, a global analysis of the luminescence plot in the range 535-770 nm using the HypSpec software (11 pH values) gives three different excited state apparent pK_{ap} values for the photoexcited [Ru(phen)$_2$(hmip)]$^{2+}$ in the investigated pH

range. The calculation yielded pK_{ap} values of 2.60 ± 0.01, 5.85 ± 0.01 and 8.29 ± 0.02 (see Figure 33b). These values should not be confused with the actual acid-base equilibrium constants as they are not corrected by the excited state luminescence lifetime of the species involved. If one of the acid-base species has shorter lifetime, it is deactivating to the ground state faster and being depleted faster. This tilts the equillibrium as the longer lived excited state species is constantly being converted to the shorter lived species as to maintain the equilibrium conditions. The latter will then have a greater emission than that expected from the equilibrium concentrations.[18a]The obtained pK_{ap} values are summarized in Table 9.

Table 9. Acidity constants of $[Ru(phen)_2(hmip)]^{2+}$ extracted from the absorption (pK_a) and steady-state emission (pK_{ap}) experiments.

Step	pK_a [a] (predicted)[b]	pK_{ap} [c]
$RP_2(hmip)^+ \rightleftharpoons RP_2(hmip)$	2.03 ± 0.06 (4.4)	2.60 ± 0.01
$RP_2(hmip) \rightleftharpoons RP_2(hmip)^-$ (OH)	7.92 ± 0.03 (9.1)	5.85 ± 0.01
$RP_2(hmip)^- \rightleftharpoons RP_2(hmip)^{2-}$	10.36 ± 0.02 (11.0)	8.29 ± 0.02

[a] From the HypSpec software global fit (250-490 nm range) using 11 pH data points
[b] In brackets are the predicted values using ChemAxon MarvinSketch (v5.2.5)
[c] From the HypSpec software global fit (535-770 nm range) using 11 pH data points

3.3.2. Response of the $[Ru(phen)_2(hmip)]^{2+}$ indicator dye towards metal ions

The selectivity of the dye towards complexation with different metal ions was evaluated by studying the changes in the absorption and emission properties of $[Ru(phen)_2(hmip)]^{2+}$ in 50-mM PBS (pH 7.5 with 1% methanol) upon addition of 5 equivalents of each selected divalent ion. Figure 35 shows the quenching efficiency (in percentage) of the emission upon addition of the metal ion. It is observed that copper(II) ions yield the highest quenching of the indicator dye emission, up to 45%. Three other metal ion, namely Pb(II), Cd(II) and Zn(II), reduce the emission of the indicator dye by 26%, 15%, and 12%, respectively. Five metal ions yield a luminescence quenching between 10% and 4%: Fe(II), Co(II), Ni(II), Hg(II) and Ca(II). Within the tested metal ions, the only that does not affect the luminescence properties of $[Ru(phen)_2(hmip)]^{2+}$ is Mg(II).

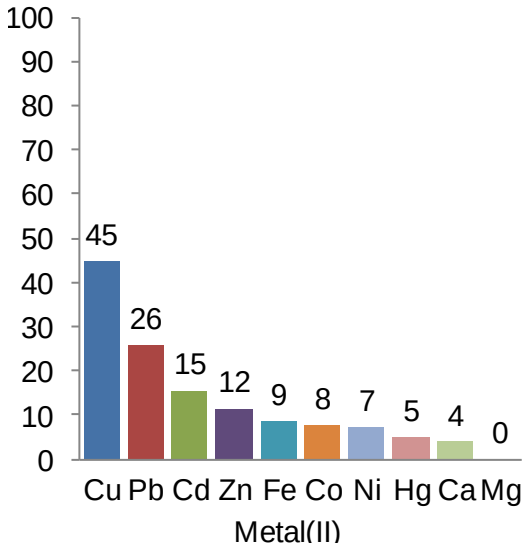

Figure 35. Quenching efficiency (%) of $[Ru(phen)_2(hmip)]^{2+}$ in 50-mM PBS at pH 7.5 with 1% methanol after addition of 5 equivalents of several divalent metal ions.

Restricting the analysis to those metals that quench more than 10% of the indicator emission (copper, lead, cadmium and zinc), only Cu(II) and Pb(II) provoke changes on the absorption spectrum (Figure 36). The presence of Pb(II) leads to a precipitate observable with the naked eye, which do not appear in the absence of the ruthenium dye. Therefore, the changes in both absorption and emission spectroscopy upon addition of Pb(II) are probably caused by (partial) precipitation of the dye. In contrast, the absorption profile of $[Ru(phen)_2(hmip)]^{2+}$ changes in the presence of copper ions with a 20 nm bathochromic shift of the 350 nm band. Since this band is attributed to electronic transitions that involve the hmip functional ligand, it seems that the interaction between the dye and copper(II) ions occurs in the ground state. The remaining Cd(II) and Zn(II) ions do not alter the absorption spectrum, demonstrating either an absence of ground state interaction (dynamic quenching) or the absence of an absorption change upon ion binding (in the ground state). Regarding the excited state, it is seen that the presence of the metal ions does not alter the emission maximum of the indicator dye, as previously observed for the iip complex.

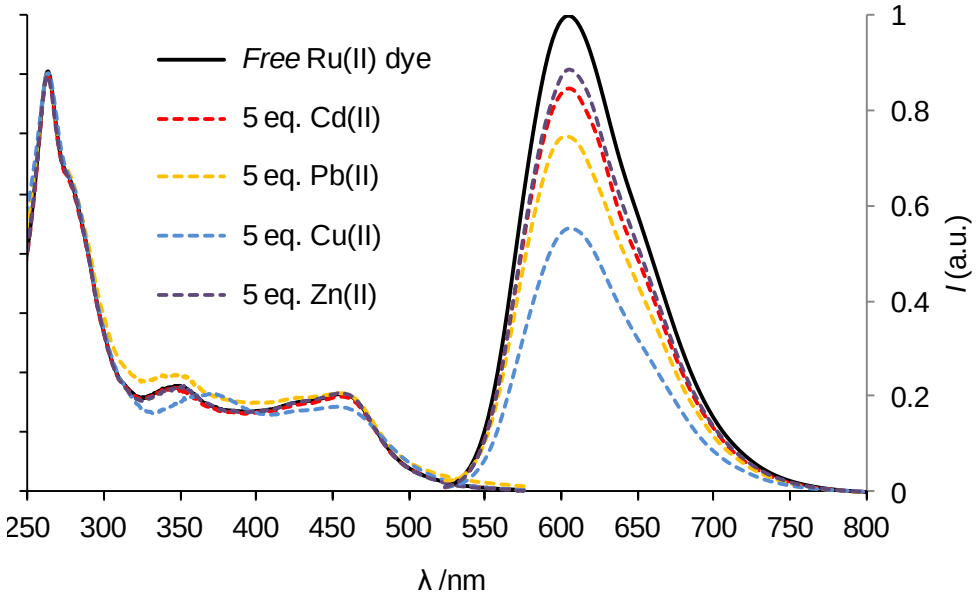

Figure 36. Absorption (left axis) and normalized emission (right axis, corrected for the instrument response and for the absorption at the excitation wavelength, A_{475}) spectra of $[Ru(phen)_2(hmip)]^{2+}$ in 50 mM PBS solution at pH 7.5 upon addition of 5 equivalents of metal ion.

Effect of pH on the sensitivity of $[Ru(phen)_2(hmip)]^{2+}$ to Cu(II). Having noticed that only copper(II) interacts with $[Ru(phen)_2(hmip)]^{2+}$ in the ground state, an analysis on the pH effect on its quenching efficiency was performed. Figure 37 shows the influence of pH on the Cu(II) binding capability of the dye measured by comparing the emission intensity of the free luminophore (▲) in 50-mM PBS against its emission in the presence of 5 equivalents of Cu(II) (●) in the 1.6-11.5 pH range.

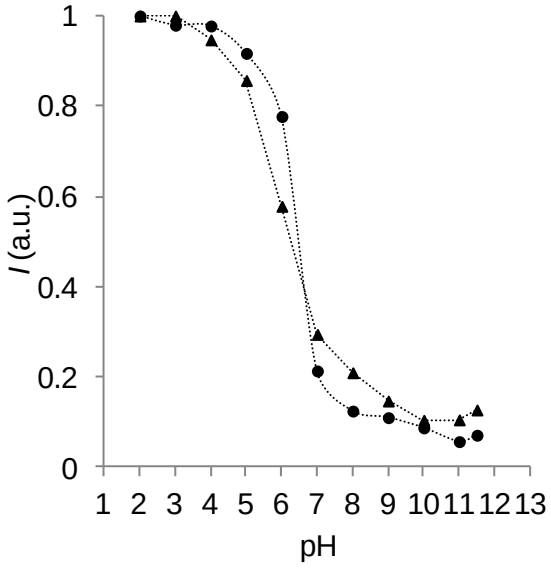

Figure 37. a) Emission intensity of the free $[Ru(phen)_2(hmip)]^{2+}$ (▲) in PBS (50 mM) and in the presence of 5 equivalents of Cu(II) (●) as a function of the pH.

At pH values below 4, the luminescence of the dye ($pKa = 2.03$, see above) is not affected by the Cu(II) ions. As seen for the iip complex, a high concentration of protons competes with the binding site of the hmip functional ligand thus limiting the interaction between Cu(II) and the dye. At pH values between 4 and 6, there is a mild turn-on fluorescence of the ruthenium dye upon the Cu(II) addition (up to 134% at pH 6). However, this effect is reversed at higher pH values where the luminescence of the dye is now quenched, reaching 45% of luminescence quenching at pH 7.5 as previously shown in Figure 35.

Unlike the iip complex, the $[Ru(phen)_2(hmip)]^{2+}$ dye shows only a mild decrease in its luminescence intensity upon copper(II) quenching. Although several organic ligands containing similar moieties to hmip are known to bind ions selectively,[32] the hmip complex has shown response to the presence of practically all tested metals. This difference must be a consequence of the steric hindrance to metal complexation provided by the bis(phenanthroline)ruthenium(II) moiety. The lack of a strong specific metal ion response in either absorbance or emission spectroscopy led us to stop further characterization of this indicator dye, for which no more spectroscopic experiments were conducted.

3.4. $[Ru(phen)_2(haip)](PF_6)_2$

The synthesis of this indicator dye is detailed in section 2.3.6. The ion-recognition site of $[Ru(phen)_2(haip)]^{2+}$ is very similar to the previous hmip complex, which also consists of an imidazo-phenol moiety. However, in this case, the substituent at *para* position is an electron withdrawing acetyl group instead of an electron donating methoxy group. As a consequence, this complex is expected to have less electron density at the oxygen atom of the phenol ring. As described for both $[Ru(phen)_2(iip)]^{2+}$ and $[Ru(phen)_2(hmip)]^{2+}$ in the previous sections, the luminescent $[Ru(phen)_2(haip)]^{2+}$ compound also presents the typical spectroscopic features of polypyridyl ruthenium(II) complexes,[6] both in the ground and in the excited state (Figure 38).

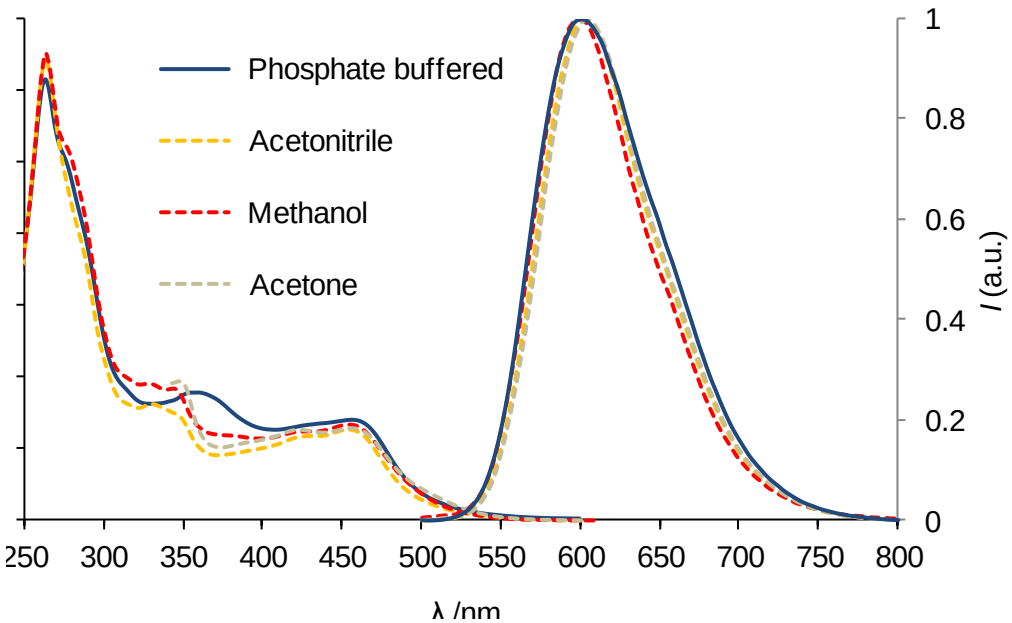

Figure 38. Absorption (left axis) and normalized emission (right axis, corrected for the instrument response) spectra of 10 □M $[Ru(phen)_2(haip)]^{2+}$ in polar solvents and 50-mM PBS at pH 7.5 (1% methanol). The absorption spectrum in acetone was recorded down to 340 nm due to solvent cut-off wavelength. The excitation wavelength for the emission spectrum was 475 nm.

Table 10 summarizes the relevant photophysical data of $[Ru(phen)_2(haip)]^{2+}$ in polar solvents and in 50-mM pH-7.5 phosphate buffer solution containing 1% methanol (by volume) to allow solubilization of the dye. Its absorption spectrum contains similar intra-ligand transitions to those already observed for the ruthenium(II) complexes described in the previous sections. Following the same reasoning applied to the hmip complex, the maximum at 264 nm corresponds to the intense π-π* transition of the phen moieties (the tris-phen complex shows absorption at 263 nm, Figure 8). The shoulder at 280 nm (more pronounced

in methanol) and the band centred at 330 nm in acetonitrile and methanol or at 360 nm in PBS are related to the haip functional ligand as they are not observed in the homoleptic tris-phen compound. This band seems to be dependent on the medium, as there is a 30-nm bathochromic shift when changing from acetonitrile (or methanol) to aqueous solution. In addition, this is the spectral region that changes the most upon a pH increase (see Figure 39), again supporting its correlation with the pH-sensitive haip ligand. The fact that the band at 330-360 nm strongly changes with the solvent indicates that the haip ligand yields a ruthenium complex sensitive to the medium. The broad visible metal-to-ligand charge transfer (MLCT) band at ca. 455 nm is located at the very same energy than its related imidazo[4,5-*f*]phenanthroline $[Ru(phen)_2(iip)]^{2+}$ and $[Ru(phen)_2(hmip)]^{2+}$ complexes. It shows different transitions that cannot be resolved, due to both the typical vibronic structure of this band observed in the Ru(II) polypyridyl complexes and the heteroleptic character of the investigated $[Ru(phen)_2(haip)]^{2+}$ that allows MLCT transitions to the different ligands in the coordination sphere (the homoleptic $[Ru(phen)_3]^{2+}$ complex absorbs at 445 in methanol, Figure 8).[6a] The red-orange emission maximum of $[Ru(phen)_2(haip)]^{2+}$ (Table 10) is also similar to those of the ruthenium(II) complexes described in the previous sections and the tris(phenanthroline) complex (λ^{max}(corr.) = 601 nm and 595 nm in methanol, respectively). The spectroscopic features of the heteroleptic haip-Ru(II) complex are equivalent to those of related imidazo[4,5-*f*]phenanthroline complexes.[9]

Table 10. Electronic absorption and emission band maximums, molar absorption coefficient, luminescence quantum yield (Φ_{em}) and ^{3}MLCT excited state lifetime of $[Ru(phen)_2(haip)](PF_6)_2$ (10 ?M) in polar organic solvents and in 50-mM phosphate buffer (PBS) at pH 7.5.[a]

Solvent	λ_{abs}^{max} /nm (ε/M^{-1} cm^{-1})	λ_{em}^{max} /nm[b]	Φ_{em} (Ar)	τ/ns
Acetone[c]	423 (12600), 457 (12800)	605	n.d.	n.d.
Acetonitrile	264 (64000), 330 (16200), 454 (12640)	603	n.d.	n.d.
Methanol	264 (65100), 328 (19000), 455 (13360)	598	n.d.	n.d.
PBS	264, (61400), 360 (17650), 456 (13850)	600	0.053	455 (950)[d]

[a] Estimated uncertainties: $\lambda \pm 1$ nm; $\varepsilon \pm 4\%$; $\Phi_{em} \leq 10\%$; $\tau \pm 1\%$ (1-exp.).

[b] Corrected for the instrument response; $\lambda_{exc} = 475$ nm

[c] Solvent cut-off wavelength: 350 nm.

[d] The value given in paranthesis is the lifetime of the dye in argon atmosphere.

As shown in Figure 38, the luminescence spectrum of $[Ru(phen)_2(haip)]^{2+}$ remains almost unchanged in acetone, acetonitrile, methanol or aqueous media (summarized in Table 10) showing the small sensitivity of the ^{3}MLCT transition energy to hydrogen bonding. The computational study (see chapter IV) shows that the emissive (triplet) excited state involves mainly the phenanthroline moiety of the haip functional ligand. In this way, interactions of the solvent molecules with the polar imidazo-phenol moiety of the haip ligand would not perturb the lowest excited state energy.

The emission quantum yield (Φ_{em}) and luminescence lifetime of the $[Ru(phen)_2(haip)]^{2+}$ ion were measured in a phosphate buffered solution at pH 7.5 (containing 1% methanol) following the procedure described in section 3.1. It displays a similar Φ_{em} than the homoleptic phen-ruthenium(II) complex (0.056, see Table 3). An approximately two-fold increase in the luminescence lifetime of the dye is observed upon removing the oxygen from solution, which is consistent with the ^{3}MLCT dynamic quenching caused by dissolved oxygen.

3.4.1. Effect of the solution pH

Due to the acid-base properties of the 2-(imidazol-2-yl)phenol moiety, a study of the pH influence on the spectroscopic properties of the haip complex was performed by measuring the absorption and emission (Figure 39) of $[Ru(phen)_2(haip)]^{2+}$ in 50-mM PBS.

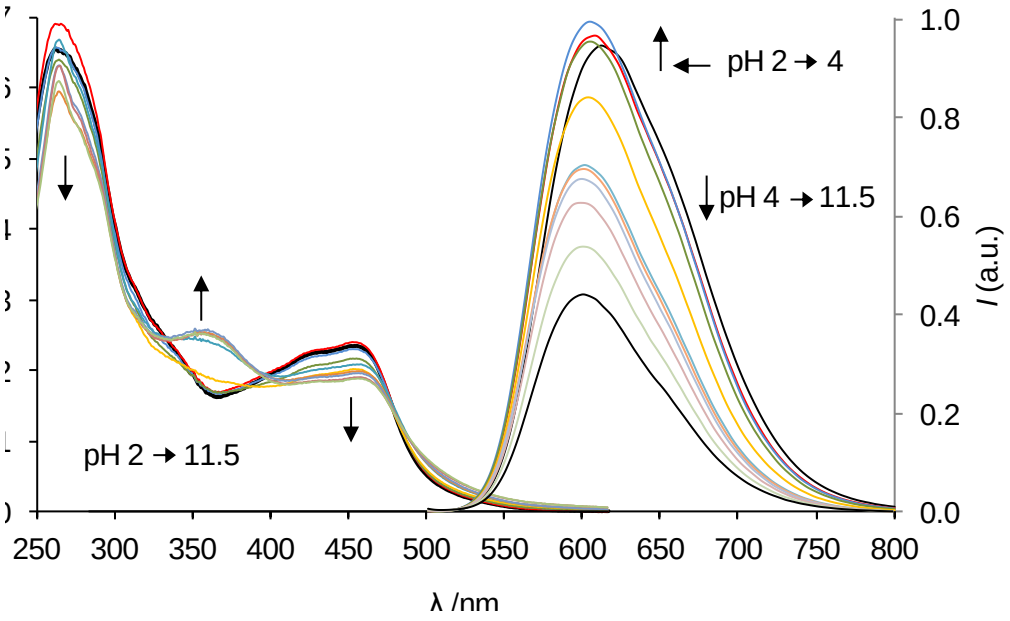

Figure 39. Absorption (left axis) and normalized emission (right axis, corrected for the instrument response and for the absorbance at the excitation wavelength, A_{475}) spectra of 10 µM $[Ru(phen)_2(haip)]^{2+}$ in 50 mM PBS solution as a function of the pH.

A global analysis of the absorption data in the 250-525 nm range using the HypSpec software (39 pH data points) gives three different pK_a values in the investigated range ($2 <$ pH < 11.5). The data refinement yielded pK_a values of 4.29 ± 0.01, 6.56 ± 0.01 and 9.26 ± 0.03. Table 11 summarizes the data obtained. All the optical changes are fully reversible by adding acid or base to the starting solution.

Figure 40a depicts the experimental absorbance values measured at 366 nm and at 450 nm as a function of the solution pH and the values calculated by HypSpec. Similar plots using the π-π* (ligand-to-ligand or intra-ligand, see above) region at 260 nm do not show the pK_a sigmoidal curves. These results demonstrate that, unlike the case of both the iip and hmip complexes, the haip ligand does not significantly participate in the 260 nm transitions but is heavily involved in the lowest energy 360-450 nm absorption band as the electronic absorption spectra show (see above).

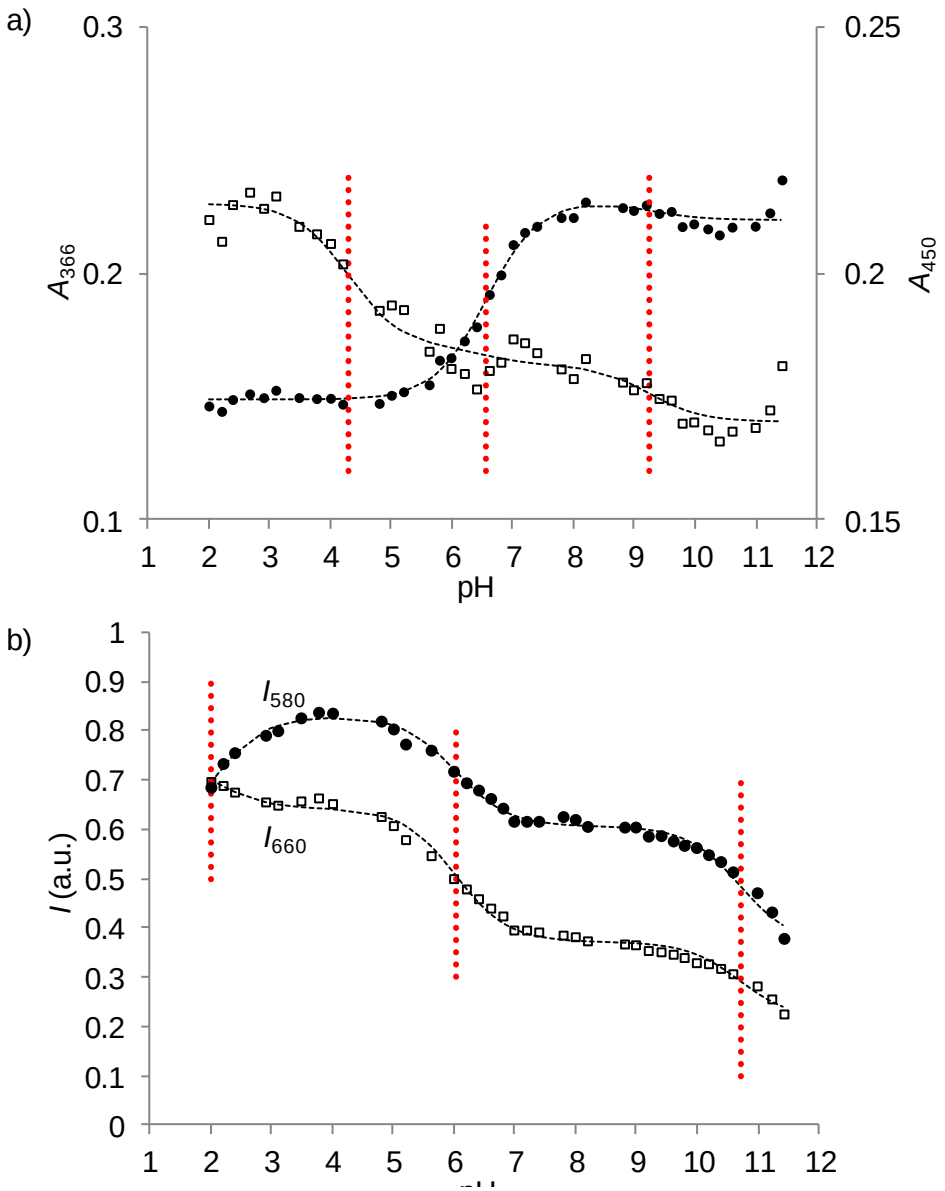

Figure 40. Selected wavelengths showing the changes in (a) the absorption (ε_{366}, ● and ε_{455}, □) and (b) the emission intensity (I_{580}, ● and I_{660}, □) of a 10 μM aqueous $[Ru(phen)_2(haip)]^{2+}$ (1% methanol) solution as a function of the pH (50 mM phosphate buffer). The thin black dashed lines ($r^2 = 0.988$, $r^2 = 0.947$, $r^2 = 0.991$ and $r^2 = 0.994$ for ε_{366}, ε_{455}, I_{580} and I_{660}, respectively) represent the absorbance and emission intensity values calculated by the HypSpec software. The vertical red lines indicate the pK_a (a) and pK_{ap} (b) values obtained thereof.

In order to assign the experimental acidity constants to the individual acid-base equilibriums of the multifunctional haip chelating ligand, the expected pK_a values of the $haipH_2^{2+}$ ligand were computed using ChemAxon MarvinSketch (v5.2.5) molecular properties calculator software (www.chemaxon.com). Calculations performed on the diprotonated phen moiety of haip tries to emulate the effect of coordination of the Ru(II) atom. In this way,

protonation of the pyridine-type nitrogen atom is predicted at a pK_a of 4.4 (pK_a^{exp} = 4.29), deprotonation of the pyrrole-type nitrogen at pK_a 11.0 (pK_a^{exp} = 9.26) and deprotonation of the phenol moiety might be found around pK_a 7.0 (pK_a^{exp} = 6.56) (Table 11). The predicted pK_a values are identical to those predicted for the nitrogen atoms of the hmip complex, but different to that predicted for the hydroxyl group of hmip, being lower by more than 2 pK_a units for the haip ligand. This calculation is in agreement with the expected electron withdrawing effect of the acetyl substituent of the haip ligand compared to the electron releasing nature of the methoxy group in the hmip ligand. Moreover, the experimental values also agree with this hypothesis as the phenol group of the hmip complex displays a pK_a^{exp} of 7.92, almost 1.5 pK_a units higher than the value found for the haip complex.

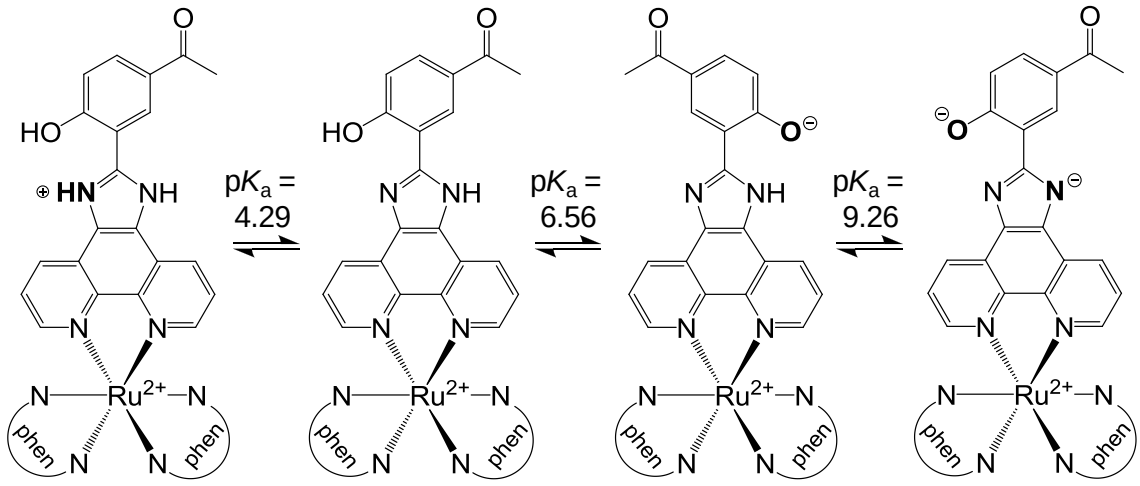

Figure 41. Acid-base species of [Ru(phen)$_2$(haip)]$^{2+}$. The pK_a values were obtained by absorption spectroscopy.

A similar study has been carried out using luminescence measurements. Figure 39b depicts the variation of the emission spectra in the 2-11.5 pH range upon excitation of [Ru(phen)$_2$(haip)]$^{2+}$ in its MLCT absorption band (475 nm). The intensity of the emission band decreases to 44% from pH 2 to pH 11.5. Similarly to the hmip complex, the pH change also leads to a 10 nm hypsochromic shift of the emission maximum when going from pH 2 to pH 11.5. As performed for the absorption data, a global analysis of the luminescence plot in the range 540-720 nm using the HypSpec software (36 pH values) gives three different apparent pK_{ap} values of [Ru(phen)$_2$(haip)]$^{2+}$ in the investigated pH range: 2.00 ± 0.02, 6.03 ± 0.01 and 11.71 ± 0.01 (see Figure 40b). As mentioned before (see section 3.3.1), these values should not be confused with the actual acid-base equilibrium constants.[18a] The pK_{ap} values are summarized in Table 11.

Table 11. Acidity constants of $[Ru(phen)_2(haip)]^{2+}$ extracted from the absorption (pK_a) and steady-state emission (pK_{ap}) experiments.

Step	pK_a [a] (predicted)[b]	pK_{ap} [c]
$RP_2(haip)^+ \rightleftharpoons RP_2(haip)$	4.29 ± 0.01 (4.4)	2.00 ± 0.02
$RP_2(haip) \rightleftharpoons RP_2(haip)^-$ (OH)	6.56 ± 0.01 (7.0)	6.03 ± 0.01
$RP_2(haip)^- \rightleftharpoons RP_2(haip)^{2-}$	9.26 ± 0.03 (11.0)	11.71 ± 0.01

[a] From the HypSpec software global fit (250-525 nm range) using 39 pH data points
[b] In brackets are the predicted values using ChemAxon MarvinSketch (v5.2.5)
[c] From the HypSpec software global fit (540-720 nm range) using 36 pH data points

3.4.2. Response of the indicator dye to selected metal ions

The selectivity of the dye towards metal ions was evaluated by studying the changes in the absorption and emission properties of $[Ru(phen)_2(haip)]^{2+}$ in 50-mM PBS solution (pH 7.5 with 1% methanol) upon addition of 5 equivalents of each chosen divalent ion. Figure 42 shows the quenching efficiency (in percentage) of the initial emission upon addition of the metal ion. Unlike the hmip complex, the imidazo-phenol moiety of Ru(II)-complexed haip displays significant selectivity towards copper(II) ions, which quench its emission by 83%. Of the remaining metal ions tested, only lead(II) and mercury(II) produce a luminescence quenching higher than 10% (25% and 14%, respectively) while the other metal ions produce little or no changes in the luminescence of $[Ru(phen)_2(haip)]^{2+}$.

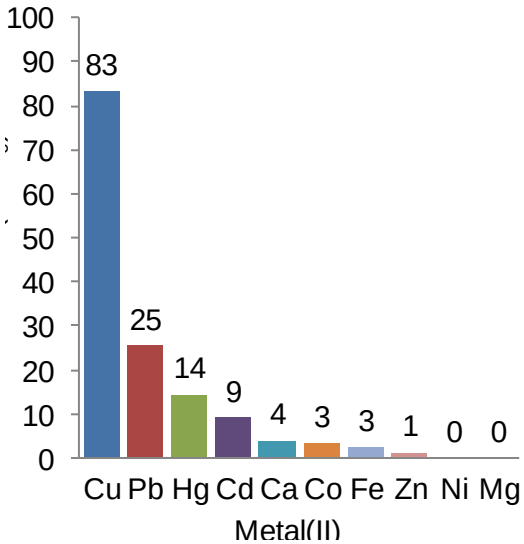

Figure 42. Efficiency of quenching (%) of the luminescence of $[Ru(phen)_2(haip)]^{2+}$ in 50-mM PBS at pH 7.5 with 1% methanol, upon addition of 5 equivalents of several divalent metal ions.

Narrowing down the analysis to those metals that quench more than 10% of the indicator dye emission (copper, lead and mercury), only Cu(II) induces significant changes on its absorption profile (Figure 43). The presence of copper produces a decrease in the molar absorption coefficient of the 360 nm band of $[Ru(phen)_2(haip)]^{2+}$. Since this band is attributed to electronic transitions involving the haip functional ligand, it seems that the interaction between the dye and copper(II) ions occurs in the ground state. The remaining Pb(II) and Hg(II) ions do not alter the absorption spectrum profile, but rather the molar absorption coefficient on the whole spectral range. As for the indicator dye emission spectra, while no spectral shift is observed, a significant luminescence quenching (up to 83%) of the emission occurs in the presence of 5 equivalents of Cu(II), as shown in Figure 42. Unlike the similar $[Ru(phen)_2(hmip)]^{2+}$ complex, which exhibits practically no distinction between the tested metals, the haip complex displays a very high selectivity towards copper(II) ions.

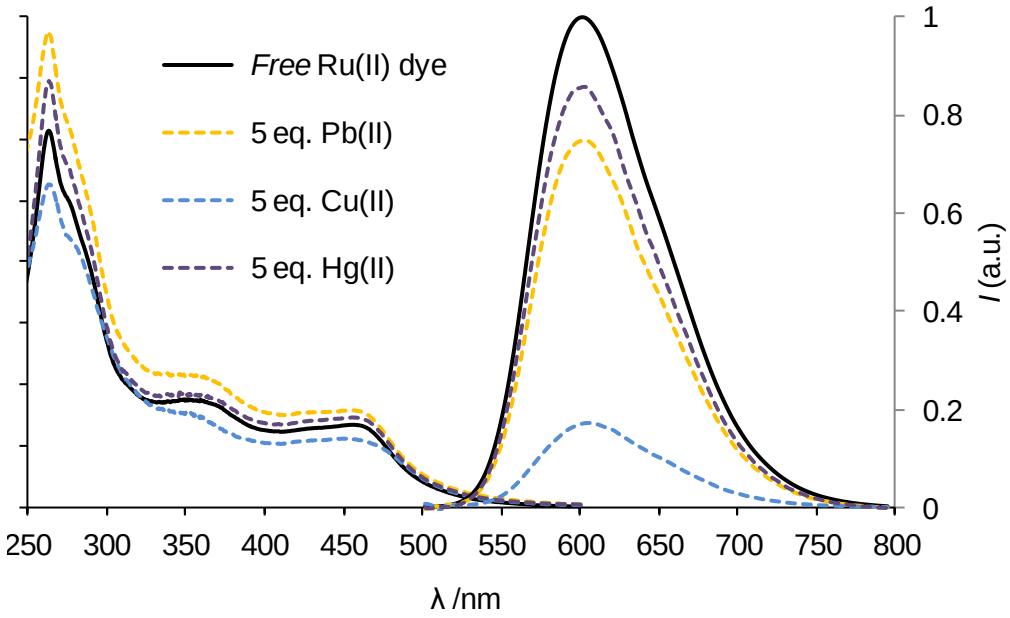

Figure 43. Absorption (left axis) and normalized emission (right axis, corrected for the instrument response and for the absorption at the excitation wavelength, A_{475}) spectra of $[Ru(phen)_2(haip)]^{2+}$ in 50 mM PBS solution at pH 7.5 upon addition of 5 equivalents of metal ions.

To investigate the type of quenching that copper(II) ions produce on the emission of $[Ru(phen)_2(haip)]^{2+}$, its excited state lifetime was measured in presence of 5 equivalents of Cu(II). It was observed that even in the presence of 5 equivalents of copper(II) there is no change in the excited state lifetime of the dye (455 ± 5 ns vs. 459 ± 5 ns in the absence and in the presence of Cu(II), respectively). As the emission intensity is quenched by copper ions, this result indicates that a purely static quenching mechanism occurs. This result is in

agreement with the predicted pre-established ground state interaction of the imidazo-phenol moiety of $[Ru(phen)_2(haip)]^{2+}$ with the Cu(II) ions.[32] Taking into account the redox potential of the Cu(II)/Cu(I) pair (0.16 V vs NHE),[33] the most probable quenching mechanism is single-electron transfer from the photoexcited dye to the (solvated) metal ion.

Influence of the pH on the sensitivity of $[Ru(phen)_2(haip)]^{2+}$ indicator dye. Having noticed that only copper(II) interacts with $[Ru(phen)_2(haip)]^{2+}$ in the ground state, an analysis on the pH effect over its quenching efficiency was performed. Figure 44a shows the influence of the pH on the binding capabilities of the luminescent indicator dye towards Cu(II) by comparing the emission intensity of the free dye (▲) in 50-mM PBS and its emission in the presence of 5 equivalents of Cu(II) (●) in the 2-11 pH range. The ratio between the emission intensity of the dye in presence (I_{Cu}) and absence (I_{Ru}) of the metal ion quencher is shown in Figure 44b.

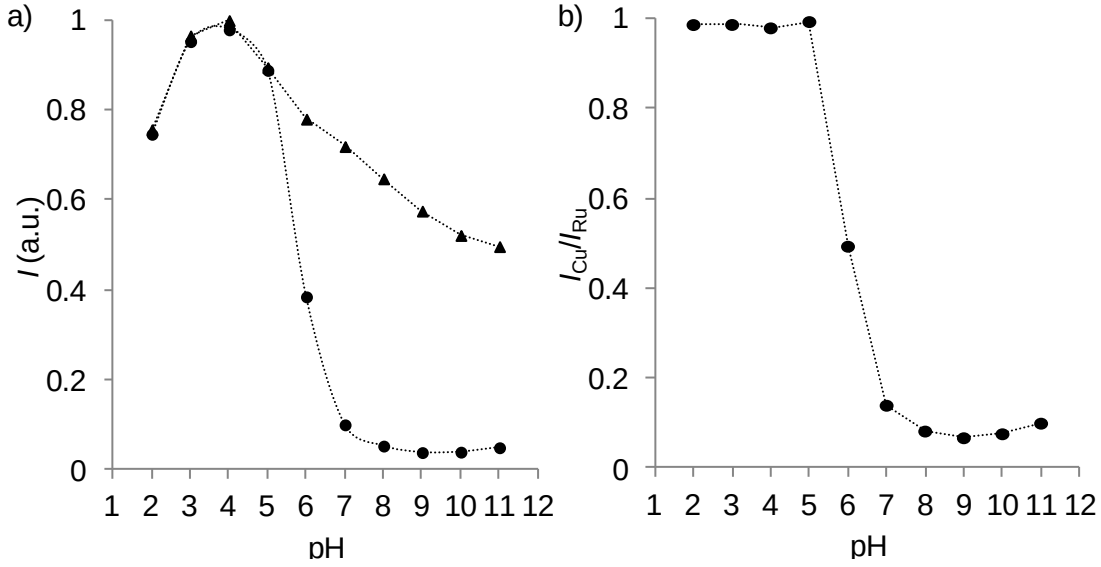

Figure 44. a) Emission intensity of the free $[Ru(phen)_2(haip)]^{2+}$ indicator dye (▲) in PBS (50 mM) and in the presence of 5 equivalents of Cu(II) (●) as a function of the solution pH. b) Emission intensity of the $[Ru(phen)_2(haip)]^{2+}$-Cu(II) complex corrected for the emission of the free dye at each pH value (I_{Cu}/I_{Ru}) under the same conditions.

At pH values below 5 the luminescence of the dye (pKa 4.29, see above) remains practically unaltered, possibly due to the high proton concentration which competes with the copper(II) ion for the binding site. The quenching efficiency then starts to increase in sigmoidal fashion, the inflexion point of which is located at ca. pH 6 (pK_a 6.56, see above). The Cu(II) ions produce a >90% decrease in the luminescence of the indicator dye at pH values above 8, being the maximum quenching at pH 9 (93%). In contrast to other reports,[26] there is no further decrease in the quenching efficiency at pH values higher than 8 where

hydroxides compete with other ligands by precipitating copper(II) as $Cu(OH)_2$. Such precipitates seem however to influence the luminescence quenching when increasing further the pH up to 11, close to pH 12 where important precipitation is known to occur.[27] Considering the results obtained, a pH value of 7.5 was selected for the binding studies as it yields good sensitivity (83% quenching) of the $[Ru(phen)_2(haip)]^{2+}$ dye for copper(II) without interferences such as precipitation of the metal or protonation of the dye.

3.4.3. Binding constants of $[Ru(phen)_2(haip)]^{2+}$ to Cu(II)

The effect of the addition of Cu(II) on the spectroscopic properties of $[Ru(phen)_2(haip)]^{2+}$ in 50 mM PBS at pH 7.5 was measured by the absorption and emission changes. Figure 45 shows the absorption spectrum of the Ru(II) complex in the presence of Cu(II). It is seen that only slight changes occur up to a 2:1 copper-to-ruthenium mole ratio, pointing out that this interaction does not significantly affect the ground state electronic structure of $[Ru(phen)_2(haip)]^{2+}$.

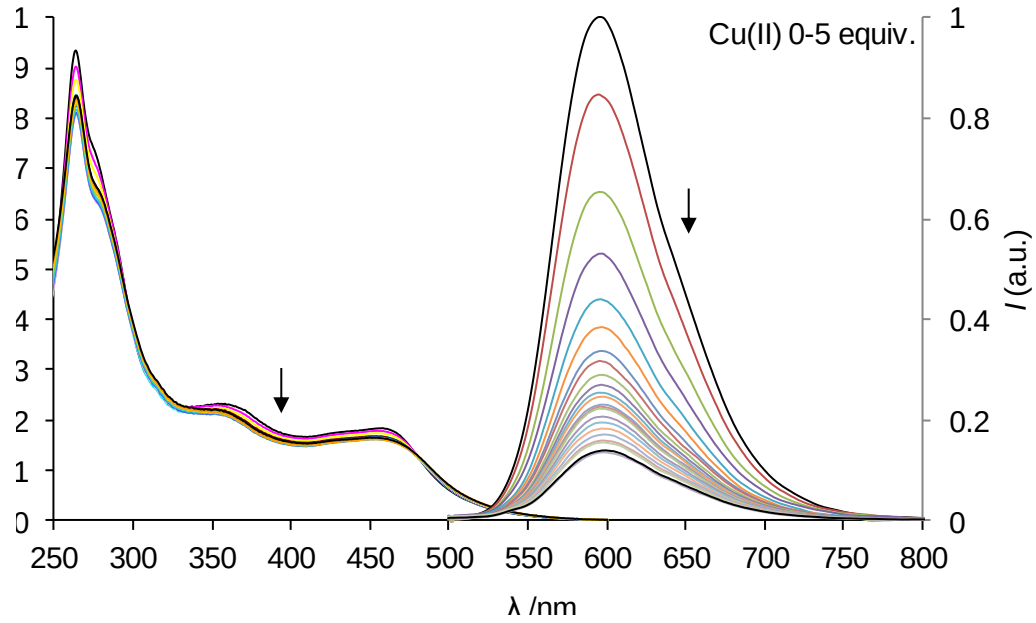

Figure 45. Absorption (left axis) and emission (right axis, corrected for the absorption at λ_{exc} = 450 nm) spectra of 15 μM $[Ru(phen)_2(haip)]^{2+}$ in 50-mM PBS at pH 7.5, in the absence and in the presence of increasing amounts of Cu(II).

The emission changes of the Ru(II) complex in the presence of copper(II) are also shown in Figure 45. Changes occur up to a 2:1 metal-to-ruthenium mole ratio (the same than that observed for the absorption measurements) where the luminescence intensity of the haip complex is 83% quenched by Cu(II). These changes do not seem to affect the energy of

the ^{3}MLCT state, since there is no shift in the emission maximum. This observation would again suggest that the copper(II) binding takes place specifically at the imidazo-phenol moiety, where the conformational changes upon binding do not interfere with the lowest ^{3}MLCT state of the haip complex (located at the phen ligands, see above).

As explained in section 3.2.3 for $[Ru(phen)_2(iip)]^{2+}$, the stoichiometry of the metal-ligand complex was not determined by the Job's plot method but rather by means of a binding isotherm describing the equilibrium between copper(II) and the ruthenium indicator dye. The process has been explained in the Introduction section 1.7.2, page 18. Nevertheless, and in contrast with the binding constants determination for the iip complex, the $[Ru(phen)_2(haip)]^{2+}$-Cu(II) dyad only allowed the study to be performed for emission spectroscopy. This is consequence of the little absorption variations upon the copper(II) addition (Figure 45), precluding successfully fitting any binding isotherm to the experimental data.

However, the emission changes observed upon addition of Cu(II) to an aqueous solution (PBS, pH 7.5) of $[Ru(phen)_2(haip)]^{2+}$ (Figure 45) were successfully fitted to the corresponding 2:1 binding isotherm (Eq. 24), obtained by means of simple mathematical transformations as described in section 1.7 and applied in section 3.2.3 for the $[Ru(phen)_2(iip)]^{2+}$ complex. The powerful HypSpec software was used to fit globally the full emission data of copper(II) addition (23 data points) in the 540–710 nm range. By introducing the parameters calculated thereof in Eq. 24 and plotting the emission intensity variation vs. copper equivalents, the curve on Figure 46 has been produced.

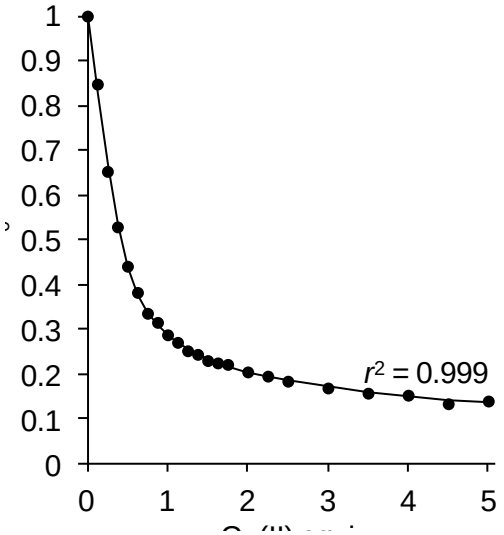

Figure 46. Variation of the relative luminescence intensity (I^{max}/I_0^{max}) as a function of Cu(II) equivalents. The solid line is the best fit of the experimental points to Eq. 24 using the binding constants calculated by the HypSpec software (see text).

As already observed for the case of the $[Ru(phen)_2(iip)]^{2+}$-Cu^{2+} dyad (Figure 27), the presence of copper(II) in an aqueous solution of $[Ru(phen)_2(haip)]^{2+}$ yields little changes in the absorption spectrum of the latter, in contrast to the significant quenching of its emission (Figure 45). While in the iip complex the binding constants to Cu(II) were still determined by absorption, they were different from the results obtained by emission spectroscopy. In the case of the latter, the changes in absorption were even weaker so that no binding constants could be determined using this method. Table 12 summarizes the $[Ru(phen)_2(haip)]^{2+}$-Cu^{2+} binding constants obtained by emission spectroscopy of a pH-7.5 50-mM PBS solution. These binding constants ($\log \beta = 12.2$) are several orders of magnitude higher than a reported imidazo-phenol ligand ($\log K_1 = 4.6$).[34]

Table 12. Stability constants of the 2:1 $[Ru(phen)_2(haip)]^{2+}$-Cu(II) complex in pH-7.5 50-mM phosphate-buffered solution determined by luminescence spectroscopy (see text).

Method	Cu(II)	
	$\log (K_1/M^{-1})$	$\log (K_2/M^{-1})$
Emission[a]	5.991 ± 0.006[b]	6.216 ± 0.005[b]

[a] The emission data (I_{obs}) were corrected at each point by the absorbance of the solution at the excitation wavelength (A_{475}) according to $I = I_{obs}(1\text{-}10^{-A475})^{-1}$

[b] Standard deviation of the Hyperquad global fit

3.5. $[Ru(phen)_2(bpytym)](PF_6)_2$

The synthesis of this complex is detailed in section 2.3.7. This designed ruthenium(II) complex bears a functional ligand that is not related to those of the imidazo[4,5-*f*]-1,10-phenanthroline family (see above). It consists of a 4,4'-bipyridine derivative containing two thymine moieties, which are known to efficiently bind Hg(II) ions.[35] Despite the structural differences of the functional ligand, the assembly of Ru(II) with three polypyridyl ligands yields the typical spectroscopic features of this family both in the ground and in the excited state,[6] as shown in Figure 47.

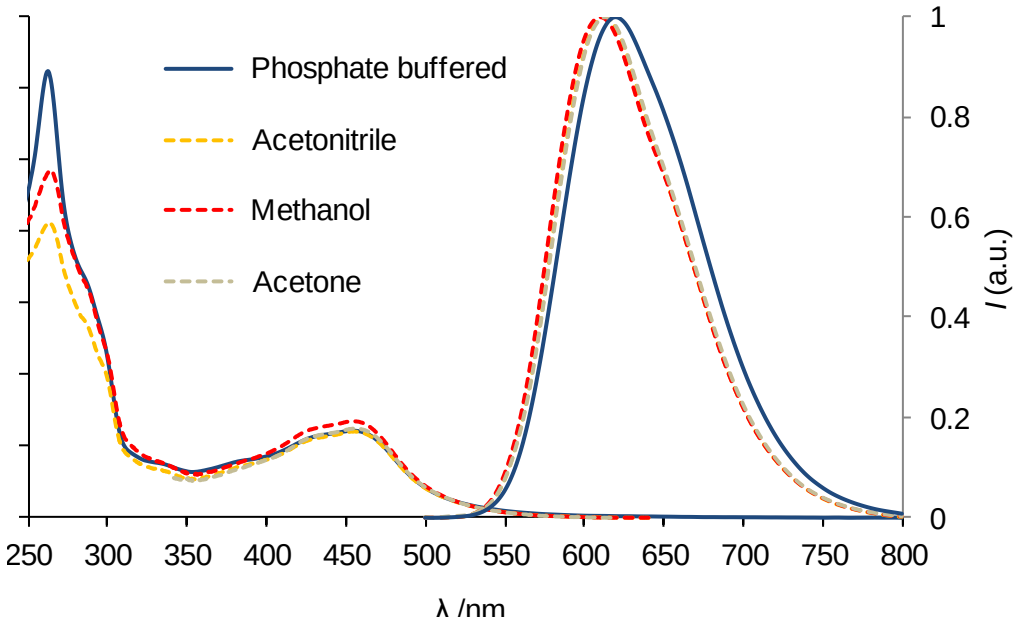

Figure 47. Absorption (left axis) and normalized emission (right axis, corrected for the instrument response) spectra of 10 μM $[Ru(phen)_2(bpytym)]^{2+}$ in polar organic solvents and in 50-mM PBS at pH 7.5 (1% methanol).

Table 13 summarizes the relevant photophysical data of $[Ru(phen)_2(bpytym)]^{2+}$ in polar organic solvents and in 50-mM pH-7.5 phosphate buffer solution containing 1% methanol (by volume) to allow solubilization of the dye. Its absorption spectrum contains similar but less intense intra-ligand transitions to those already observed for the ruthenium(II) complexes described in the previous sections. Following the same reasoning applied above, the maximum at 263 nm corresponds to the intense π-π* transition of the phen moieties (the tris-phen complex shows absorption at 263 nm, Figure 8). In this case and unlike the previous complexes, there is no distinct shoulder at 280 nm although the band at 263 is broadened in this region, possibly due to lower intensity bpytym ligand transitions. The weak band at 320 nm is also related to the bpytym functional ligand as they are not

observed in the homoleptic tris-phen compound. In addition, this is the spectral region that displays the most pronounced changes at high pH values (see Figure 48), again supporting its assignment to the bpytym ligand. The broad visible metal-to-ligand charge transfer (MLCT) band at ca. 455 nm is located at the very same energies than those of the other heteroleptic ruthenium complexes containing iip, hmip or haip. Similarly, it shows different transitions that cannot be resolved, due to both the typical vibronic structure of this band in the Ru(II) polypyridyl complexes and the heteroleptic character of the investigated $[Ru(phen)_2(bpytym)]^{2+}$ dye that allows MLCT transitions to the different ligands in the coordination sphere (the homoleptic $[Ru(phen)_3]^{2+}$ complex absorbs at 445 in methanol, Figure 8).[6a] In contrast to the imidazophen functional ligands present in the previous ruthenium(II) complexes, the $[Ru(phen)_2(bpytym)]^{2+}$ dye displays much lower molar absorption coefficients, as detailed in Table 13. This feature indicates that the electronic structure of the bpytym complex is more similar to the homoleptic tris-bpy ruthenium complex rather than that of the tris-phen dye (see Figure 8).

The red-orange emission maximum of $[Ru(phen)_2(bpytym)]^{2+}$ (Table 13) is somewhat red-shifted when compared to those of the ruthenium(II) complexes described in the previous sections and the tris(phenanthroline) Ru(II) complex (λ^{max}(corr.) = 601 nm and 595 nm in methanol, respectively). It also shows a 7 nm red-shift when changing from acetone to aqueous medium, possibly due to hydrogen-bond stabilization of the thymine moieties.

Table 13. Electronic absorption and emission band maximums, molar absorption coefficient, luminescence quantum yield (Φ_{em}) and ^{3}MLCT excited state lifetime for $[Ru(phen)_2(bpytym)](PF_6)_2$ (10 ⍰M) in polar organic solvents and 50-mM phosphate buffer (PBS) at pH 7.5.[a]

Solvent	λ_{abs}^{max} /nm (ε/M^{-1} cm^{-1})	λ_{em}^{max} /nm[b]	Φ_{em} (Ar)	τ/ns
Acetone[c]	455 (12500)	613	n.d.	n.d.
Acetonitrile	263 (41360),455 (12000)	612	n.d.	n.d.
Methanol	264 (48400), 454 (13430)	610	n.d.	n.d.
PBS	263 (62200), 455 (12100)	620	0.034	369 (538)[d]

[a] Estimated uncertainties: $\lambda \pm 1$ nm; $\varepsilon \pm 4\%$; $\Phi_{em} \leq 10\%$; $\tau \pm 1\%$ (1-exp.).

[b] Corrected for the instrument response; $\lambda_{exc} = 475$ nm

[c] Solvent cut-off wavelength: 350 nm.

[d] The value given in paranthesis is the lifetime of the dye in deoxygenated solution.

As shown in Figure 47, the luminescence spectrum of $[Ru(phen)_2(bpytym)]^{2+}$ remains almost unchanged in acetone, acetonitrile or methanol (see also Table 13) showing the small sensitivity of the ^{3}MLCT transition energy to these solvents. The computational study (chapter IV) shows that the emissive (triplet) excited state is distributed over the electron-rich phen ancillary ligands. In this way, interactions of the solvent molecules with the bpytym ligand would not perturb the excited state energy.

The emission quantum yield (Φ_{em}) and luminescence lifetime of $[Ru(phen)_2(bpytym)]^{2+}$ were measured in a phosphate buffered solution at pH 7.5 (containing 1% methanol) following the procedure described in section 3.1. It displays a smaller Φ_{em} in O_2-free solution at room temperature than the homoleptic tris-phen ruthenium complex (0.056, see Table 3) and also smaller than the homoleptic tris-bpy complex (0.042). As observed also for the iip and haip complexes, there is a significant increase in the luminescence lifetime of the dye upon removing the oxygen from solution, which is consistent with the ^{3}MLCT dynamic quenching caused by dissolved oxygen.

3.5.1. Effect of the solution pH

Due to the acidic properties of the imide moiety of the thymine ring, a study of the pH influence on the spectroscopic properties of the bpytym complex was performed by measuring the absorption and emission of a 10 µM $[Ru(phen)_2(bpytym)]^{2+}$ solution in 50-mM PBS (Figure 48).

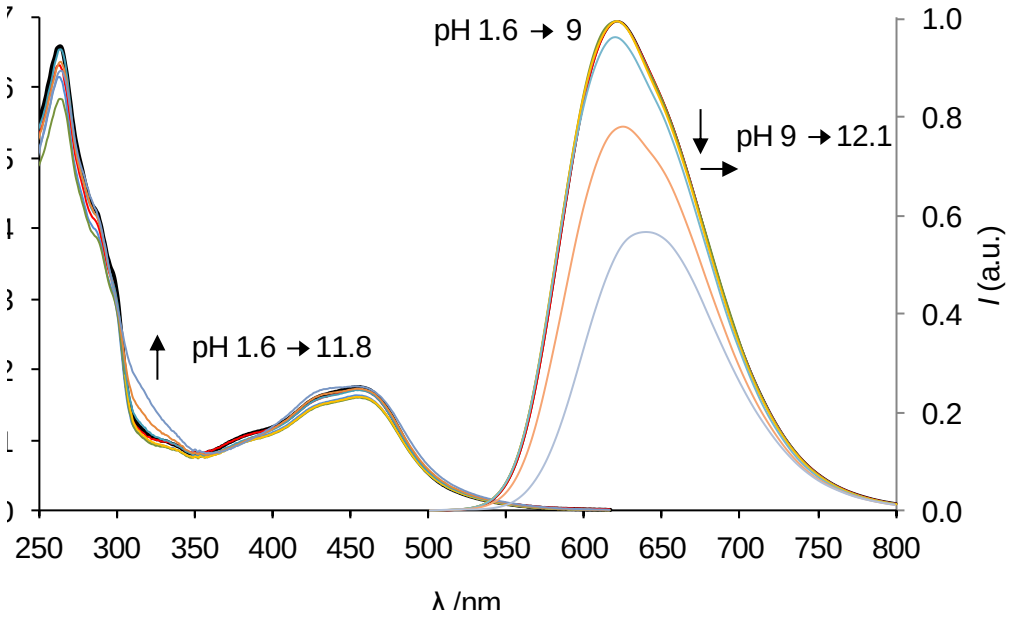

Figure 48. Absorption (left axis) and normalized emission (right axis, corrected for the instrument response and for the absorption at the excitation wavelength, A_{475}) spectra of 10 µM $[Ru(phen)_2(bpytym)]^{2+}$ in 50 mM PBS solution as a function of the pH.

A global analysis of the absorbance data in the 300-510 nm range using the HypSpec software (14 pH data points) reveals not just one but two pK_a values in the investigated range ($7.5 < \text{pH} < 11.8$). The global fit yielded pK_a values of 9.42 ± 0.01 and 11.92 ± 0.01. The first acidity constant is similar to the one found for thymine ($\text{p}K_a = 9.5$)[36] so it should be associated with the imide moieties of the two thymine heterocycles. The second acidity constant is probably due to the acid-base equilibrium at one (or two) amide group adjacent to the bpy heterocycle.

Similarly to what was obtained when calculating the pK_a values of $[Ru(phen)_2(hmip)]^{2+}$ in section 3.3.1, the acidity constant of 11.92 is at the edge of the investigated pH range, where the curve does not reach a plateau. By using the global analysis method, the HypSpec software is capable of identifying pK_a values that would be otherwise missed. Table 14 summarizes the data obtained. All the optical changes are fully reversible by changing the acidity/basicity of the solution.

Figure 49a depicts the molar absorption coefficient measured at 320 nm and at 405 nm as a function of the solution pH and the values calculated by HypSpec. Similar plots using the π-π* (ligand-to-ligand or intra-ligand, see above) region at 260 nm do not show the sigmoidal absorption changes. These results are similar to those obtained for the haip complex and, unlike either the iip or the hmip complexes, the bpytym ligand does not significantly participate in the 260 nm transitions but is heavily involved in the lower energy 320-450 nm absorption bands as the electronic absorption spectra already pointed out (see above).

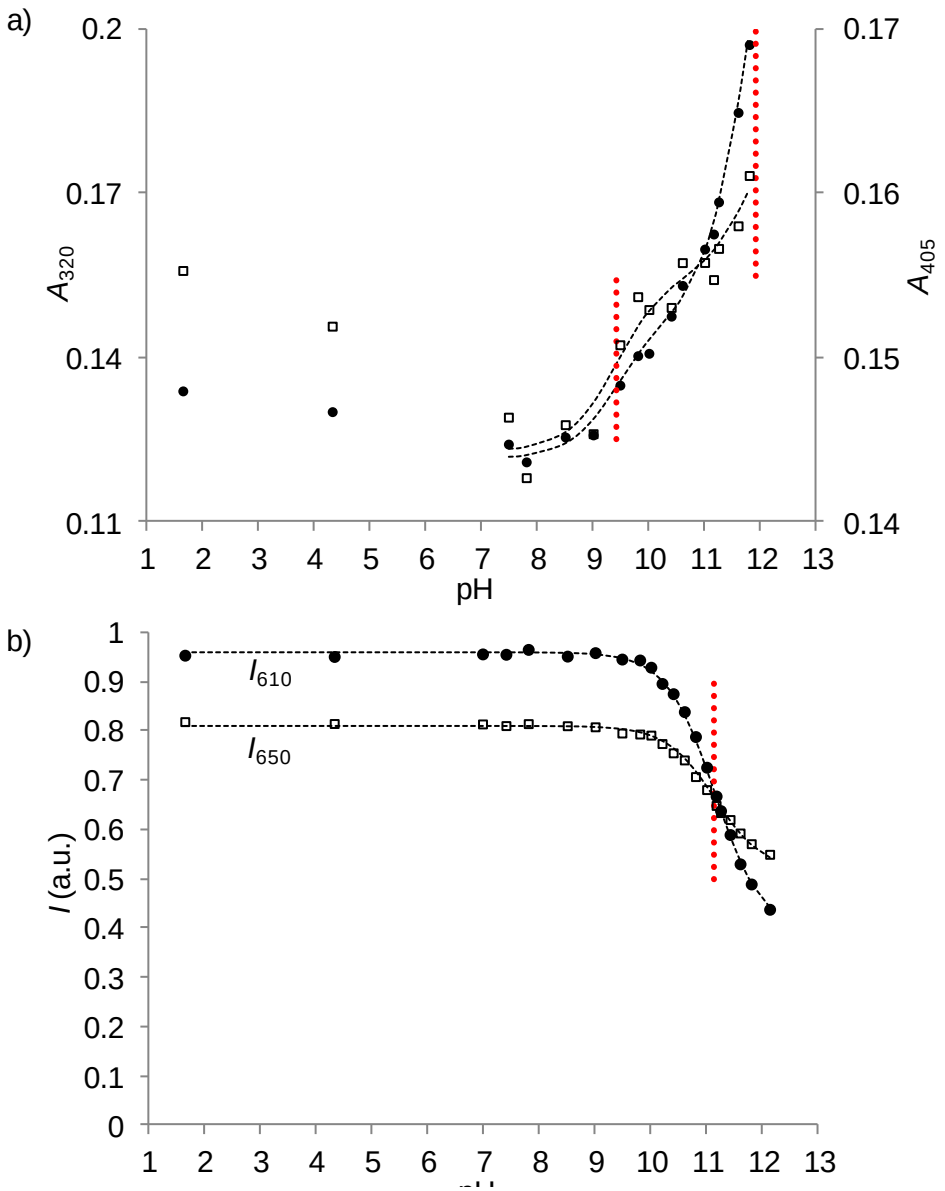

Figure 49. Selected wavelengths showing the changes in (a) the absorption (ε_{320}, ● and ε_{405}, □) and (b) the emission intensity (I_{610}, ● and I_{650}, □) of a 10 μM aqueous $[Ru(phen)_2(bpytym)]^{2+}$ solution (1% methanol) as a function of the pH (50 mM phosphate buffer). The thin black dashed lines (r^2 = 0.996, r^2 = 0.942, r^2 = 0.999 and r^2 = 0.996 for ε_{320}, ε_{405}, I_{610} and I_{650}, respectively) are the absorbance and emission intensity values calculated by the HypSpec software. The vertical red lines indicate each pK_a (a) and pK_{ap} (b) value obtained thereof.

In order to assign the experimental acidity constants to the individual acid-base equilibriums of the imide functional groups in the bpytym chelating ligand, the expected pK_a values of the $bpytymH_2^{2+}$ ligand were computed using ChemAxon MarvinSketch (v6.2.0) molecular properties calculator software (www.chemaxon.com). Calculation on the diprotonated bpy moiety of bpytym tries to emulate the effect of coordination of the Ru(II)

atom. In this way and under the investigated pH range, deprotonation of the imide nitrogen atoms is predicted at pK_a value of 9.7 and 10.0 (pK_a^{exp} = 9.42) while the deprotonation of the amide group would occur at pK_a 12.4 (pK_a^{exp} = 11.92) (Table 14). A third pK_a value at 11.98 is predicted which accounts for the acid-base equillibrium of the alpha hydrogen in the CH_2 group. The experimental data does not allow us to identify which is the moiety associated to pK_a^{exp} = 11.92. Nonetheless, literature reports of bpy derivatives identify such acid-base equilibria to the amide group, which would also justify the 20 nm bathochromic shift in the emission (see below).[37] Both predicted pK_a values are practically identical to the experimental values.

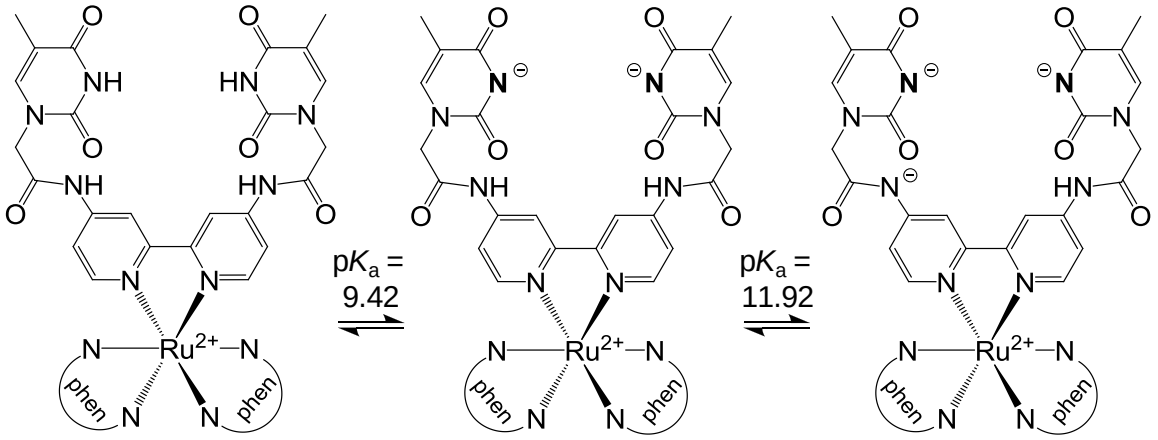

Figure 50. Acid-base species of $[Ru(phen)_2(bpytym)]^{2+}$. The p$K_a$ values were obtained by absorption spectroscopy.

A similar study has been carried out using luminescence measurements. Figure 48 also depicts the variation of the emission spectra in the 1.6-12.1 pH range upon excitation of $[Ru(phen)_2(bpytym)]^{2+}$ in its MLCT absorption band (475 nm). The intensity and profile of the emission band remain unchanged below pH 9. At higher pH values, there is a marked decrease in the intensity and also in the emission energy. A 20 nm bathochromic shift is observed when comparing the emission maximums at pH 1.6 with pH 12.1. As performed for the absorption data, a global analysis of the luminescence plots in the 540-730 nm range using the HypSpec software (21 pH values) reveals one apparent pK_{ap} value of 11.14 ± 0.01 in the investigated pH range (see Figure 49b and Table 14).

Table 14. Acidity constants of $[Ru(phen)_2(bpytym)]^{2+}$ extracted from the absorption (pK_a) and steady-state emission (pK_{ap}) experiments.

Step	pK_a [a] (predicted)[b]	pK_{ap} [c]
$RP_2(bpytym) \rightleftharpoons RP_2(bpytym)^-$	9.42 ± 0.01 (9.7)	11.14 ± 0.01
$RP_2(bpytym)^- \rightleftharpoons RP_2(bpytym)^{2-}$	11.92 ± 0.01 (12.4)	---

[a] From the HypSpec software global fit (300-510 nm range) using 14 pH data points
[b] In brackets are the predicted values using ChemAxon MarvinSketch (v6.2.0)
[c] From the HypSpec software global fit (540-730 nm range) using 21 pH data points

3.5.2. Response of the indicator dye towards metal ions

The selectivity of the dye towards several metal ions was evaluated by studying the changes in the absorption and emission properties of $[Ru(phen)_2(bpytym)]^{2+}$ in 50-mM PBS (pH 7.5 with 1% methanol) upon addition of 5 equivalents of each selected divalent ion. Figure 51 shows the quenching efficiency (in percentage) of the emission upon addition of the metal ion. Unfortunately, and unlike the ruthenium dyes described above, this Hg(II)-targeted thymine-derivative dye is practically insensitive to any of the tested metals at pH 7.5. Even the addition of mercury results in no change of the luminescence of the dye. The metal ions that produce some (slight) changes are lead(II) and iron(II), the former quenching the emission of the bpytym complex by 5% and the latter producing an increase of 8% in the initial luminescence. The remaining metals produce negligible changes of the emission intensity of the dye under the experimental conditions tested (less than 3%).

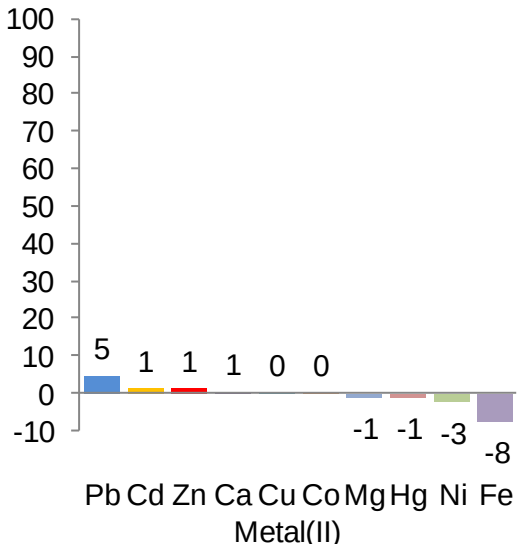

Figure 51. Quenching efficiency (%) of $[Ru(phen)_2(bpytym)]^{2+}$ in 50-mM PBS at pH 7.5 with 1% methanol, upon addition of 5 equivalents of several divalent metal ions.

Despite the small changes in the luminescence of $[Ru(phen)_2(bpytym)]^{2+}$ upon addition of the metal ions, the dye reveals different results in the ground state absorption spectrum. Narrowing down the analysis to mercury and those metals that change more than 5% the emission intensity of the dye (lead and iron), only Hg(II) provokes significant changes on its absorption profile (Figure 52). The presence of mercury(II) leads to a general decrease in the molar absorption coefficient of $[Ru(phen)_2(bpytym)]^{2+}$, with a higher decrease in the 260 nm region. Both Pb(II) and Fe(II) produce a slight increase in the molar absorption coefficient of the dye, although in the case of Pb(II) some precipitation was observed. The formation of precipitates can be responsible for the absorption changes observed in the case of the Pb(II) addition.

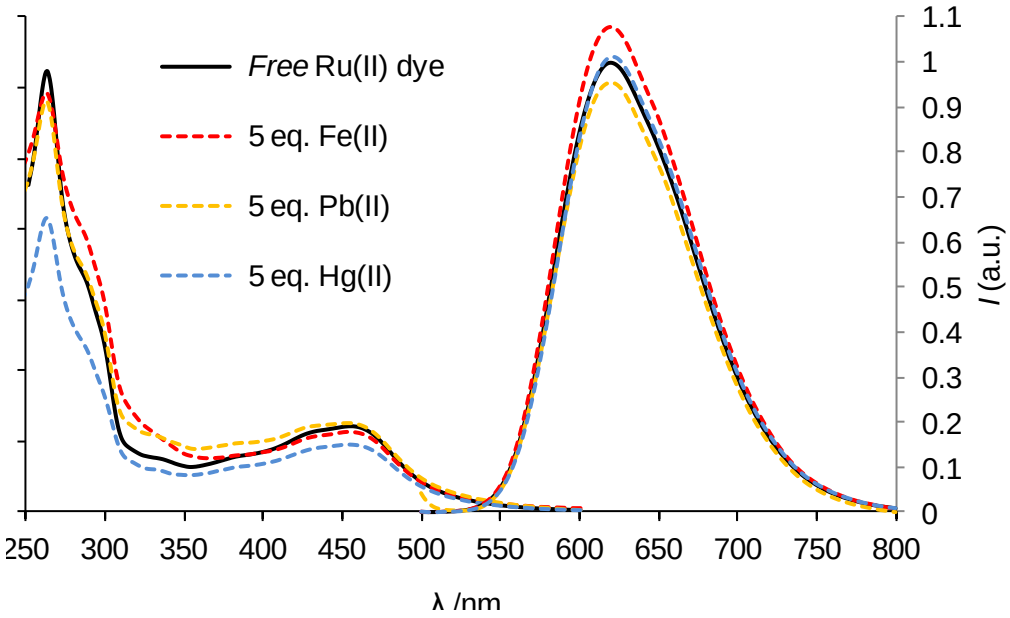

Figure 52. Absorption (left axis) and normalized emission (right axis, corrected for the instrument response and for the absorption at the excitation wavelength, A_{475}) spectra of $[Ru(phen)_2(bpytym)]^{2+}$ in 50 mM PBS at pH 7.5 upon addition of 5 equivalents of metal ions.

The fact that the luminescent properties of $[Ru(phen)_2(bpytym)]^{2+}$ are practically insensitive to the presence of metal ions might be explained if the emissive ^{3}MLCT state of the dye lies far away from the binding site. In fact, computational studies in chapter IV support this hypothesis, showing that the excited state of the bpytym dye lies preferably in the phen ancillary ligands, even after the binding of mercury(II) ions. Since the goal of this work was to study dyes that upon addition of metal ions reveal excited state changes, no more work was carried out using the $[Ru(phen)_2(bpytym)]^{2+}$ luminescent complex.

3.6. $[Ru(nody)_3]Cl_2$

The synthesis of this complex is detailed in section 2.3.8. It is the homoleptic complex of the nody ligand (described in section 2.2.9), a luminescent Ru(II) complex lacking a permanent dipole moment due to its symmetry, and synthesized to serve as a comparison for the heteroleptic $[Ru(nbpy)_2(nody)](PF_6)_2$ indicator dye (section 3.7). Introduction of hydrophobic (long) alkyl chains increases the solvation of the cationic complex by less polar solvents. Its absorption and emission spectra were measured in several solvents of different polarities (Figure 53). The absorption profile of this compound shows similar transitions to the ones previously discussed for the other ruthenium(II) dyes as well as for the reference compounds $Ru(phen)_3$ and $Ru(bpy)_3$ (see section 1.9.2). Nevertheless, the absorption wavelengths at which the IL or LLCT occur are shifted towards lower energies (ca. 30 nm) now being found at ca. 300 nm. Another distinct aspect related to the absorption profile of $[Ru(nody)_3]^{2+}$ lies in the observed broadening of the absorption bands, being more evident for the MLCT band (ca. 470 nm), which shows a tail that extends up to 700 nm in some solvents. The hydrophobic C_{18} alkyl chains of the nody ligand allow the formation of aggregates (overcoming electrostatic repulsion),[38] which can explain the increased manifold of the absorption transitions.

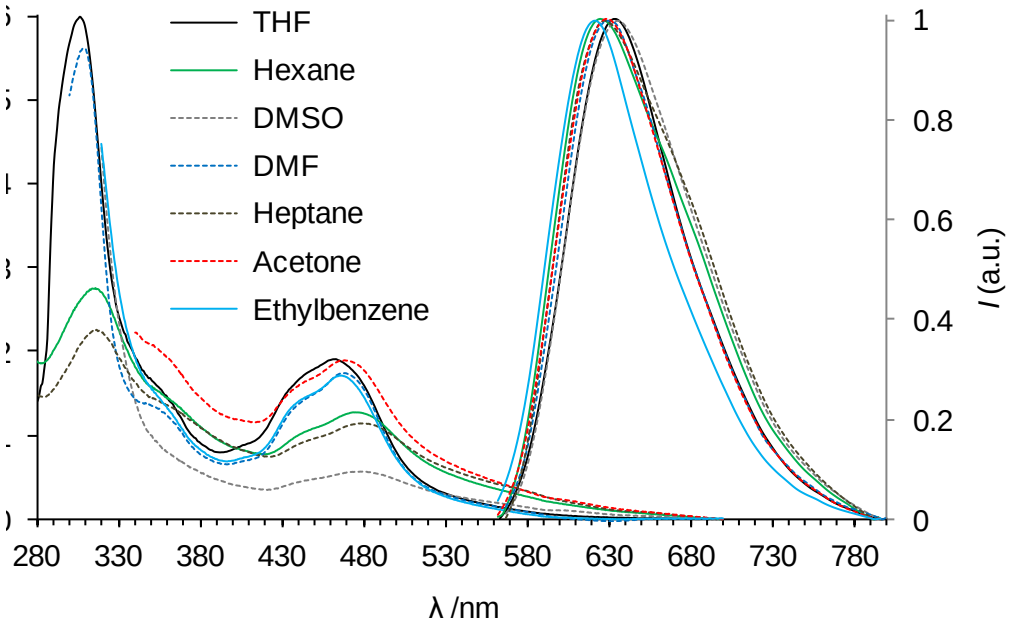

Figure 53. Absorption (left axis) and normalized emission (right axis, corrected for the instrument response) spectra of 10 ?M $[Ru(nody)_3]^{2+}$ in tetrahydrofuran (THF), hexane, dimethyl sulfoxide (DMSO), *N*,*N*-dimethylformamide (DMF), heptane, acetone and ethylbenzene. The investigated absorption range of the dye in DMSO (>320 nm), DMF (>300 nm), acetone (>340 nm) and ethylbenzene (>320 nm) is limited at high energies due to the solvent cut-off wavelength.

Unlike the other ruthenium complexes described in this Thesis, the absorption profile of the homoleptic $[Ru(nody)_3]^{2+}$ does change noticeably with the solvent. The MLCT absorption maximum shifts to the blue when increasing the solvent polarity. Similarly, solvent sensitivity is also observed in the emission spectrum, where increasing solvent polarity leads to a bathochromic shift of the emission maximum. Hence, both ground and excited states of $[Ru(nody)_3]^{2+}$ are stabilized in polar solvents. This is in agreement with the solvent stabilization effects explained in the introductory section 1.10 and with literature reports for other homoleptic complexes bearing hydrophobic alkyl chains in their periphery.[14, 39]

The emission band of $[Ru(nody)_3]^{2+}$ shows the typical features of the ruthenium complexes described above, but it lies at lower energies by approximately 30 nm ($Ru(phen)_2(iip)$ emits at 605 nm in acetone, Table 3). This is due to the electron-withdrawing effect of the 4,4'-dicarboxamide groups, that stabilize the π* orbitals of the chelating ligands, The main spectroscopic features of the novel complex are summarized in Table 15.

Table 15. Electronic absorption and emission band maximums, molar absorption coefficients and ^{3}MLCT excited state lifetimes for $[Ru(nody)_3]Cl_2$ (10 μM) at 25 °C in solvents of increasing polarity.[a]

Solvent	λ_{abs}^{max} /nm (ε/M^{-1} cm^{-1})	λ_{em}^{max} /nm[b]	τ_M /ns	Solvent properties[c]		
				ε	n_D	$[O_2]$ /mM
Heptane	316 (22600), 476 (11400)	629	220	1.9	1.38	2.8
Hexane	315 (27500), 473 (12700)	625	201	1.9	1.37	3.1
Ethylbenzene[d]	469 (17100)	620	618	2.4	1.49	2.1
THF	306 (60000), 463 (19100)	635	557	7.6	1.40	2.1
DMSO[d]	478 (5600)	635	259	47.2	1.48	0.46
DMF	309 (56200), 467 (17400)	630	483	38.3	1.43	2.1
Acetone[d]	467 (18800)	630	333	20.7	1.36	2.4

[a] Estimated uncertainties: λ ± 2 nm; ε ± 4%; τ ± 2% (2-exp.).
[b] Corrected for the instrument response; λ_{exc} = 475 nm.
[c] Values at 20 °C. Oxygen concentrations for 0.213 bar partial pressure.[40]
[d] Solvent cut-off at 320 nm for ethylbenzene and dimethyl sulfoxide (DMSO) and 340 nm for acetone.

3.6.1. Solvent effects

As already explained in section 1.10, the Lippert model is often used to describe the interaction between the solvent and a fluorophore. However, it does not take into consideration specific molecule-molecule interactions either solvent- (hydrogen bonding) or fluorophore-related (aggregates or self-quenching). Figure 54 shows a plot of the difference between the absorption and emission energies ($\bar{\nu}_{abs} - \bar{\nu}_{em}$, in cm^{-1}) as a function of the solvent-specific *orientation polarizability* term (Δf, from the Lippert-Mataga Eq. 32).

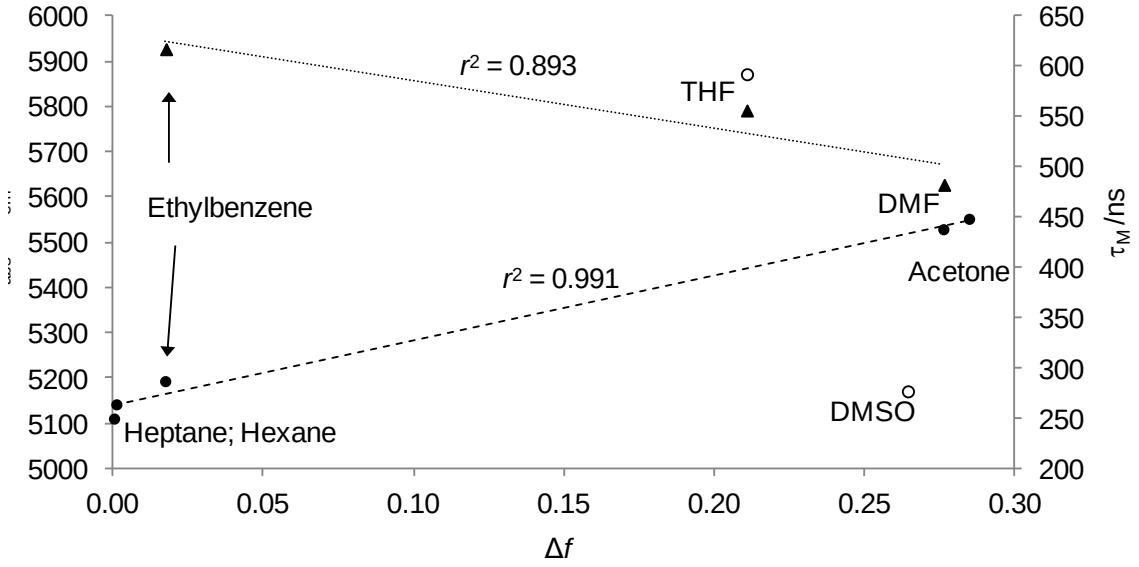

Figure 54. Energy difference between the energies of the absorption and emission maximums (ν_{abs}-ν_{abs}, ●) and luminescence lifetime (τ_M, ▲) for $[Ru(nody)_3]Cl_2$ as a function of the orientation polarizability term, Δf of the Lippert-Mataga equation (section 1.10). The dashed line (b[0] = 5139 cm^{-1}; b[1] = 1434 cm^{-1}) results from a linear regression of the data points (●). The Lippert-Mataga equation does not predict the behaviour in either THF or DMSO (○). The dotted line is a linear regression of the τ_M data points.

The fact that the energy differences between the absorption and emission maximums in THF and DMSO are outliers with respect to the other solvent data points demonstrates that the model is somewhat insufficient to describe the whole range of possible dye-solvent interactions. Nonetheless, a linear regression of the remaining five data points ($r^2 = 0.991$) clearly shows that the dye follows the expected trend for this type of plots. As the polarity of the medium increases (higher Δf), the energy difference between absorption and emission maxima also increases. This is reflected in the hypsochromic and bathochromic shifts observed for the absorption and emission bands, respectively. As mentioned in the introductory section 1.10, when the absorption band is shifted to higher energies, it is due to a stabilization of the ground state of the Ru(II) dye, from where the absorption transition

takes place. In contrast, a shift to lower energies in the emission band arises from the LUMO stabilization of the excited state Ru(II) complex, from where the emission takes place. Therefore, the cationic dye is more stabilized in polar media.

Table 15 also includes the excited state lifetime of the ruthenium complex in solvents of different polarity. The emission lifetime of the dye was studied under air-equilibrated conditions in order to evaluate the O_2 effect vs. the solvent polarity on the deactivation of the excited state of $[Ru(nody)_3]Cl_2$. As already seen for similar polyalkyl derivative ruthenium complexes,[14] the luminescence decay profiles were multi-exponential. This is an indication of the presence of aggregates due to the low solubility of the indicator dye in non-polar solvents. Therefore, the weighted average emission lifetime, τ_M, was used to compare the experimental kinetics data. Figure 55 shows the luminescence lifetime of the dye as a function of the concentration of oxygen in different air-equilibrated solvents. It is clear that, except for DMSO, the oxygen quenching dominates the deactivation pathway of the excited state of the dye rather than the nature of the solvent. As for the DMSO solvent, there must be specific solvent-solute interactions other than those predicted by the Lippert-Mataga equation or oxygen quenching that determines the absence of correlation. In any case, to observe a linear correlation between the lifetime and the oxygen concentration, several requirements must be met. The bi-molecular oxygen quenching constants must be solvent independent and the solvent must not have a significant effect on the luminescent lifetime of the dye. The latter does have an influence on the observed emission maximums, as the emission of the dye changes from 620 nm in ethylbenzene to 635 nm in THF. Such stabilization of the LUMO will have an effect over the emission lifetime of the dye, as predicted by the energy-gap rule.[12, 41]

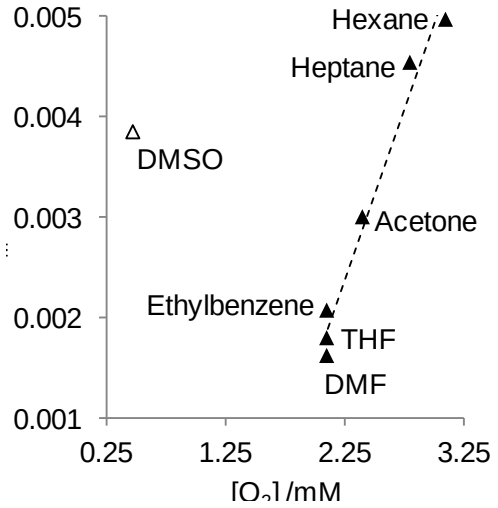

Figure 55. Reciprocal of the (pre-exponentially weighted) luminescence lifetime of $[Ru(nody)_3]^{2+}$, τ_M, as a function of the oxygen concentration in different air-equilibrated solvents. The dashed line is the linear regression ($r^2 = 0.972$) of the data points, ▲.

Figure 54 also shows the weighted average emission lifetime, τ_M, of $[Ru(nody)_3]Cl_2$ as a function of Δf in three solvents (ethylbenzene, THF and DMF) of similar oxygen solubility (2.1 mM). Assuming that the rate of oxygen quenching is identical in all three solvents (see above), it is seen that the lifetime tends to decrease with increasing polarity of the medium. The poor correlation might be due to solubility issues, leading different degrees of aggregation of dye molecules depending on the solvent. Still, the stabilization and lowering of the excited state energy (bathochromic shift of the emission maximum) with increasing polarity is perfectly compatible with a faster decay rate as predicted by the energy-gap rule.[12, 41] A competitive deactivation process that leads to the ground state lies in the population of the non radiative metal centred excited state. To evaluate if the ^{3}MC excited state of the dye is accessible at room temperature, the excited state lifetime of $[Ru(nody)_3]Cl_2$ in argon saturated solution was measured as a function of the temperature.[42]

3.6.2. Temperature effects

By now it is useful to recall Eq. 36 (section 1.10.2) which describe the luminescence lifetime of Ru(II) complexes as a function of temperature.

$$\frac{1}{\tau}(T) = k_0 + \left(A \times e^{-\frac{B}{RT}}\right) \qquad \text{Eq. 36}$$

Figure 56 shows the double reciprocal plot of τ_M vs. temperature × R (8.314 J mol^{-1} K^{-1}) in the apolar ethylbenzene and in polar butyronitrile. In the latter, two regions were observed. In the low temperature range (270-300 K), the lifetime increases with increasing temperature while at higher temperatures (300-365 K) it decreases. The fact that the lifetime increases from 270 K to 300 K might be due to an increase in the solubility of the dye, reducing the number of aggregates hence less self-quenching.

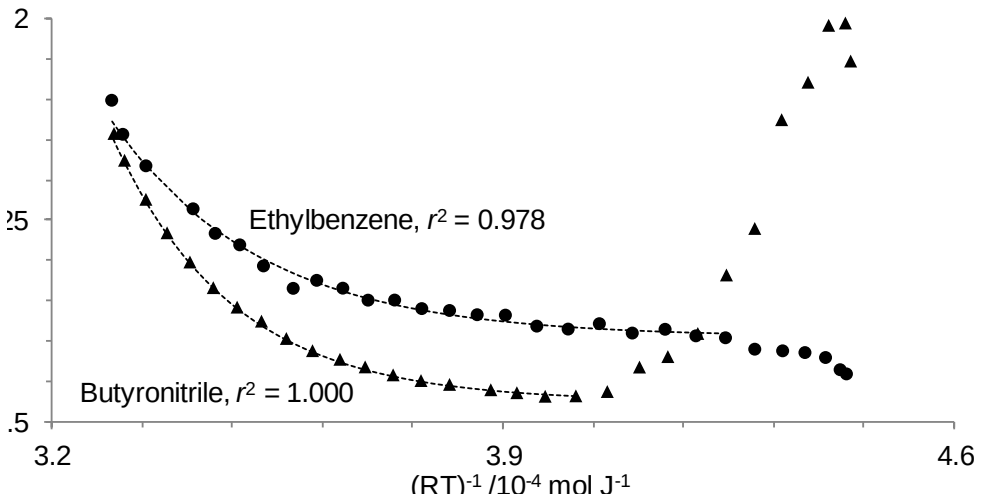

Figure 56. Double-reciprocal plot of $[Ru(nody)_3]^{2+}$ luminescence lifetime τ_M (deaerated solution) as a function of temperature × R in butyronitrile (▲) and ethylbenzene (●). The dashed lines are the calculated values using Eq. 36.

Eq. 36 was used to successfully fit the experimental data points in Figure 56 in the region where the lifetime decreases with the temperature, and the values extracted thereof are summarized in Table 16.

Table 16. Parameters calculated from Eq. 36 for the τ_M dependence of $Ru(nody)_3Cl_2$ with temperature in two solvents (under Ar) of different polarity.

Solvent	k_0 /s^{-1}	A /s^{-1}	B /cm^{-1}	Φ_T [a]
Ethylbenzene	8×10^5	1.3×10^{12}	3623	0.04
Butyronitrile	6×10^5	5.2×10^{13}	4505	0.03

[a] Values calculated from Eq. 37 at 298 K; Estimated uncertainties: $\tau \pm 2\%$ (2-exp.).

In the two investigated solvents and according to section 1.10.2, the order of magnitude for the values of both A (10^{12}–10^{14} s^{-1}) and B (3000–4000 cm^{-1}) seem to indicate that the excited ^{3}MLCT and ^{3}MC states of $Ru(nody)_3Cl_2$ *are not* in equilibrium.[42-43]

In this case, A represents the pre-exponential term for the ^{3}MLCT-^{3}MC surface crossing and B is the activation energy of the metal-centred state. The value for ^{3}MC population quantum yield at room temperature is 0.04 and 0.03 for ethylbenzene and butyronitrile, respectively. This result supports the hypothesis (see above) that the non-radiative ^{3}MC state of the ruthenium complex is practically not accessible at room temperature.

3.7. $[Ru(nbpy)_2(nody)](PF_6)_2$

The synthesis of this complex is detailed in section 2.3.9. It consists of two bpy ligands containing two alkyl C_9 chains and one bpy ligand functionalized with two alkyl C_{18} chains via an amide group. It is similar to the ruthenium complex described in the previous section which contained three polyalkyl amide-derivative nody ligands. As with its homoleptic analogue, the introduction of the hydrophobic alkyl chains increases the solubility of the cationic complex in less polar solvents. By having different ligands, this compound is expected to show higher dipole moment than the homoleptic $[Ru(nody)_3]^{2+}$ and hence higher solvent-dependent luminescence properties. Also, by having less amide groups, this compound is expected to show less interaction with solvents via hydrogen-bonding and for this reason to show better agreement with the Lippert-Mataga plot (see above). Its absorption and emission spectra were measured in several solvents of different polarities (Figure 57). Unlike what was observed for the homoleptic $[Ru(nody)_3]^{2+}$, the absorption profile of $[Ru(nbpy)_2(nody)]^{2+}$ shows narrower transitions, at energies similar to those found for the polypyridyl ruthenium(II) family (Figure 8, section 1.9.2).[6] This is in agreement with the hypothesis that the homoleptic complex is more involved in self-aggregates due to its six C_{18} alkyl chains (see above). On the other hand, the emission band of $[Ru(nbpy)_2(nody)]^{2+}$ lies at lower energies similarly to its homoleptic compound due to the higher energy difference between the π^* orbitals of the nody and nbpy ligands.

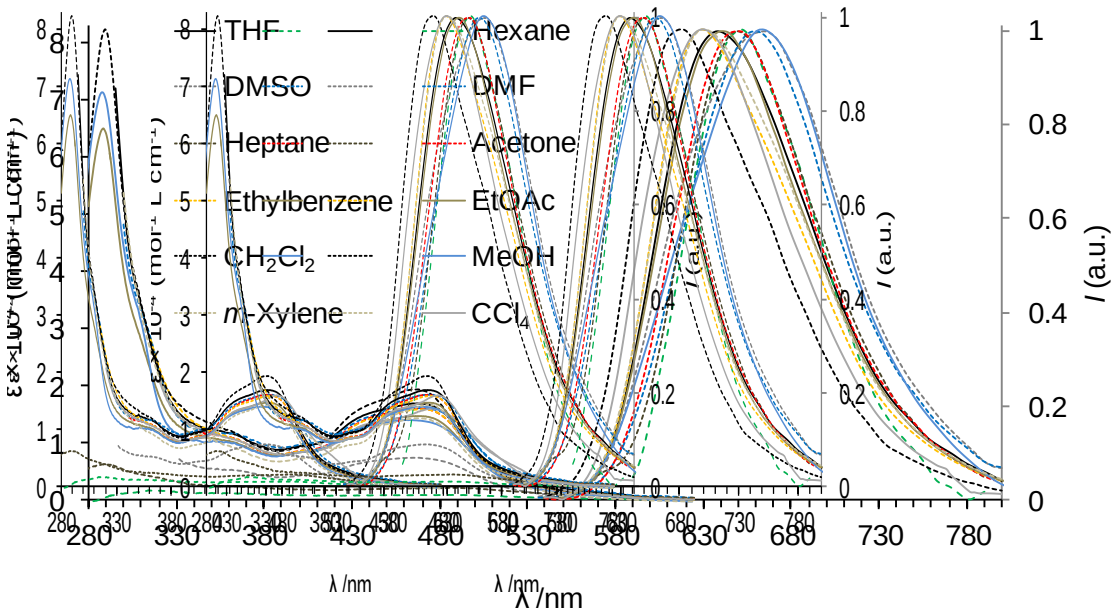

Figure 57. Absorption (left axis) and normalized emission (right axis, corrected for the instrument response) spectra of 10 μM $[Ru(nbpy)_2(nody)](PF_6)_2$ in tetrahydrofuran (THF), hexane, dimethyl sulfoxide (DMSO), *N*,*N*-dimethylformamide (DMF), heptane, acetone, ethylbenzene, ethyl acetate (EtOAc), dichloromethane (CH_2Cl_2), methanol (MeOH), *m*-xylene and carbon tetrachloride (CCl_4). The absorption range of the dye in acetone (<340 nm), DMSO (<330 nm), ethylbenzene and CCl_4 (<320 nm), DMF, THF and *m*-xylene (<300 nm) is limited at high energies due to the solvent cut-off wavelength.

This ruthenium complex also shows sensitivity to the solvent, where the MLCT absorption maximum is blue-shifted and λ_{ems} is red-shifted when increasing solvent polarity. In this way and similarly to the related homoleptic compound, both the ground and excited states of $[Ru(nbpy)_2(nody)]^{2+}$ are stabilized in polar solvents. This is in agreement with the solvent stabilization effects explained in the introductory section 1.10. The main spectroscopic features of the novel polarity probe are summarized in Table 17.

Table 17. Electronic absorption and emission band maximums, molar absorption coefficient and ^{3}MLCT excited state lifetimes for $[Ru(nbpy)_2(nody)](PF_6)_2$ (10 ⍰M) at 25 °C in solvents of increasing polarity.[a]

Solvent[b]	λ_{abs}^{max} /nm (ε/M^{-1} cm^{-1})	λ_{em}^{max} /nm[c]	τ_M /ns[d]	Solvent Properties[e]	
				ε	n_D
Heptane (1)	290 (6200), 487 (2100)	651	n.d.	1.9	1.38
Hexane (2)	483 (<1000)	653	n.d.	1.9	1.37
CCl_4[f] (3)	474 (15900)	631	1327	2.2	1.46
m-Xylene[f] (4)	468 (14400)	631	n.d.	2.4	1.50
Ethylbenzene[f] (5)	469 (15800)	629	884	2.4	1.49
EtOAc (6)	288 (65000), 464 (14650)	641	1230	6.0	1.37
THF[f] (7)	466 (17000)	639	n.d.	7.6	1.40
CH_2Cl_2	280 (82000), 468 (19350)	617	n.d.	9.1	1.42
DMSO[f] (8)	467 (7400)	665	731	47.2	1.48
DMF[f] (9)	467 (16000)	660	n.d.	38.3	1.43
Acetone[f] (10)	466 (16000)	651	n.d.	20.7	1.36
MeOH (11)	287 (71000), 463 (14000)	664	577	32.6	1.33

[a] Estimated uncertainty: $\lambda \pm 2$ nm; $\varepsilon \pm 4\%$; $\tau \pm 2\%$ (2-exp.).
[b] The numbers in parenthesis are labels for Figure 58.
[c] Corrected for the instrument response; $\lambda_{exc} = 475$ nm.
[d] Under argon atmosphere at 25 °C.
[e] Values at 20 °C.[40]
[f] Solvent cut-off limit, see Figure 57.

3.7.1. Solvent effects

Figure 58 shows a plot of the difference between the absorption and emission maxima ($\bar{\nu}_{abs}$ - $\bar{\nu}_{em}$, in cm^{-1}) as a function of the solvent-specific *orientation polarizability* term (Δf, from the Lippert-Mataga Eq. 32).

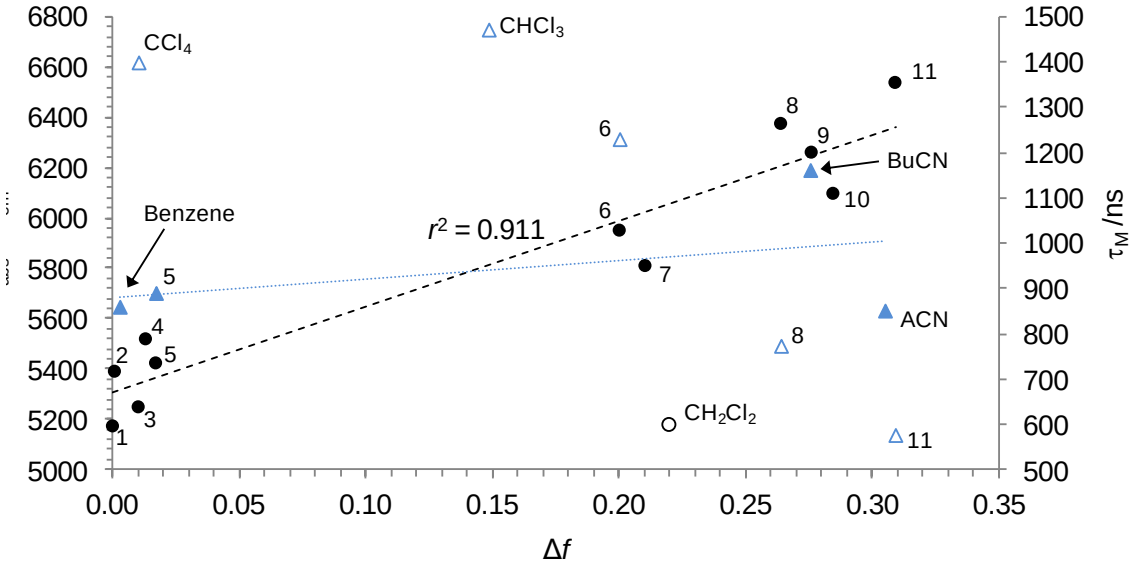

Figure 58. Energy difference between the energies of the absorption and emission maximums (ν_{abs}-ν_{abs}, ● and ○) and luminescence lifetimes (τ_M, ▲ and ∠) for $[Ru(nbpy)_2(nody)](PF_6)_2$ as a function of the orientation polarizability term, Δf, of the Lippert-Mataga equation (section 1.10). The reference numbers of solvents (1-11) are assigned in Table 17. The dashed black (b[0] = 5310 cm^{-1}; b[1] = 3410 cm^{-1}) and dotted blue lines result from a linear regression of the data points (●) and (▲), respectively. The Lippert-Mataga equation does not predict the behaviour in dichloromethane (○).

The spectroscopic properties of the ruthenium dye show a dependency on the solvent nature, as predicted by the Lippert-Mataga equation. However, the behaviour in dichloromethane seems to be off the chart possibly due to some solvent-specific effect not tackled by the Lippert model. The energy difference between both absorption and emission maxima increase with solvent polarity, to which a linear regression (r^2 = 0.991) of 11 data points is successfully fitted. This effect shows up in the hypsochromic and bathochromic shifts observed for absorption and emission, respectively. Therefore, the cationic dye is more stabilized in polar media.

Table 17 also includes the excited state lifetime of the ruthenium complex in solvents of different polarity. As already seen for $[Ru(nody)_3]Cl_2$ and similar polyalkyl derivative ruthenium complexes,[14] the luminescence decay profiles were of multi-exponential character. This is indication of low solubility or aggregates, for which the use of the weighted

average emission lifetime, τ_M was used. Figure 58 shows the measured τ_M as a function of Δf for the solvents gathered in Table 17 as well as for butyronitrile (BuCN), acetonitrile (ACN), chloroform and benzene. Unlike the results obtained for steady-state measurements ($\bar{\nu}_{abs}$ - $\bar{\nu}_{em}$), the plot of the luminescence lifetime does not follow a defined trend with increasing solvent polarity. The wavelengths of absorption or luminescence maxima are not affected by those phenomena responsible for quenching of the luminescence lifetime. A lower solubility which might lead to aggregates or oxygen-containing solvents that can dynamically interact with the amide group of the ruthenium(II) complex play an important role in the deactivation of the excited state. This might be the reason that the luminescence lifetime does not show a linear dependency with the solvent orientation polarizability term. In fact, anomalous luminescence results for solvatochromic dyes in halogenated solvents have been described by others as a possible effect of the contribution of exciplexes.[44] Nonetheless, by excluding those solvents containing oxygen (hydrogen-bonds) or chlorinated atoms, the plot seems to adopt a more linear tendency, which shows an increase in the excited lifetime with the polarity of the solvent (see dotted blue line in Figure 58. Under this scenario, namely, in the absence of specific solvent interactions, and opposite to what was observed for the homoleptic complex (see above) the stabilization and lowering of the excited state energy (bathochromic shift of the emission maximum) with increasing polarity leads to longer excited state lifetimes. The deactivation of the ^{3}MLCT excited state is a fine balance between the population of a thermally activated state, ^{3}T (either ^{3}MC or ^{3}MLCT$_{fourth}$, section 1.10.2) and by the energy-gap rule.[12, 41, 45] This balance depends on the energy difference between the ^{3}MLCT and ^{3}T, and the energy difference between the ^{3}MLCT and the ^{1}GS.[14] The fact that the lifetime of $[Ru(nbpy)_2(nody)](PF_6)_2$ increases with solvent polarity as well as its emission maximum seems to indicate that the lowering of the ^{3}MLCT energy increases the ^{3}MLCT-^{3}T energy difference. This would suggest that for the solvents under study, the population of a thermally activated ^{3}MC or ^{3}MLCT$_{fourth}$ plays an important role in the deactivation pathways of this complex.

To confirm this hypothesis and evaluate how accessible the thermally activated state is, the excited state lifetime of $[Ru(nbpy)_2(nody)]^{2+}$ in argon saturated solution was measured as a function of the temperature.[42]

3.7.2. Temperature effects

Using the same methodology as the one explained for the homoleptic complex in section 3.6.2, a plot compatible with Eq. 36 (section 1.10.2) was generated for solvents of different nature and polarities (protic, aprotic, polar, apolar, halogenated). Figure 59 shows the double reciprocal plot of τ_M vs. temperature × R (8.314 J mol^{-1} K^{-1}) in the apolar ethylbenzene and halogenated CCl_4, in the medium polarity halogenated chloroform and in the polar aprotic solvents DMSO, BuCN and ACN and in the polar protic MeOH.

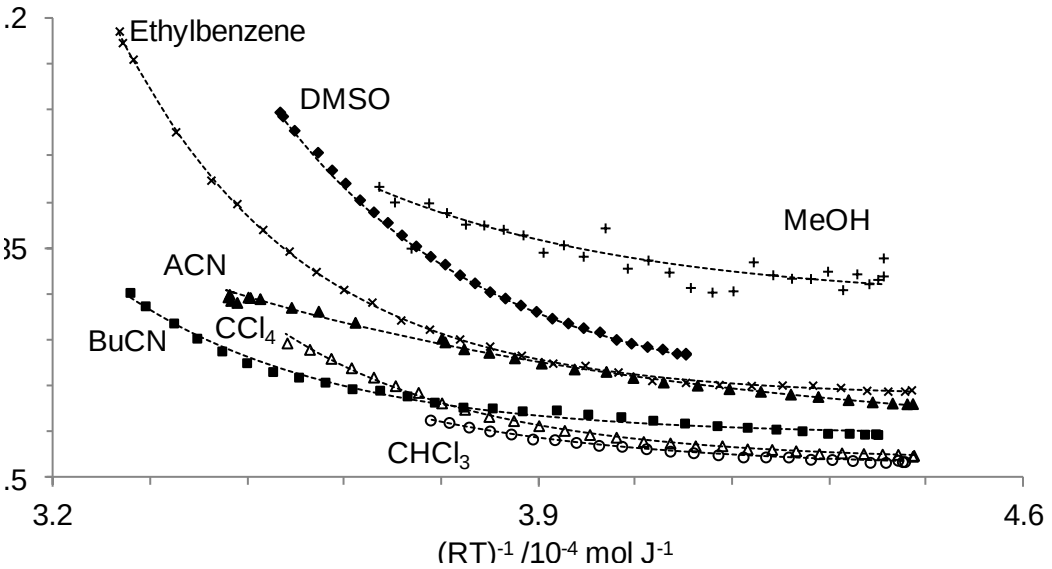

Figure 59. Double-reciprocal plot of $[Ru(nbpy)_2(nody)]^{2+}$ luminescence lifetime τ_M (deaerated solution) as a function of temperature × R in a variety of solvents. The dashed lines are the calculated values using Eq. 36 ($r^2 = 0.766$, $r^2 = 0.987$, $r^2 > 0.997$ for MeOH, BuCN and the remaining solvents, respectively).

Eq. 36 was used to successfully fit the experimental data points of Figure 59 in the 270-360 K range, and the values extracted thereof are summarized in Table 18. By analysing the order of magnitude for the calculated values of both A and B parameters it seems that they fall under a defined range throughout the variety of solvents, that is, A ≈ 10^{10}-10^{11} s^{-1} and B ≈ 2000-3000 cm^{-1}. Recalling section 1.10.2, the obtained values for A and B indicate that $[Ru(nbpy)_2(nody)]^{2+}$ displays a behaviour which is exactly between the two extreme situations of i) equilibrium and ii) non-equilibrium between the ^{3}MLCT and ^{3}MC excited states. A similar behaviour was observed for Ru(II) complexes bearing bpy and hat (hat = 1,4,5,8,9,12-hexaazatriphenyIene) ligands. In that case, both ^{3}MC and $^3MLCT_{fourth}$ were suggested as participants in the deactivation processes.[42] However in our case, since the B

parameter is higher than 2600 cm^{-1} in all cases, it seems safe to assume that the population of the $^3MLCT_{fourth}$ is not relevant (typical values below 2000 cm^{-1}).

Table 18. Parameters calculated from fitting Eq. 36 to the luminescence lifetime, τ_M of $[Ru(nbpy)_2(nody)](PF_6)_2$ vs. temperature (Figure 59) in several deoxygenated solvents of increasing polarity.

Solvent	k_0 /s^{-1}	A /s^{-1}	B /cm^{-1}	Φ_T [a]
CCl_4	6.9×10^5	3.5×10^{11}	3069	0.17
Ethylbenzene	9.8×10^5	5.2×10^{11}	3145	0.13
$CHCl_3$	5.7×10^5	1.4×10^{11}	2934	0.15
DMSO	9.7×10^5	1.4×10^{11}	2687	0.26
Butyronitrile	7.5×10^5	4.6×10^{10}	2750	0.10
Acetonitrile	9.1×10^5	6.0×10^{10}	2663	0.14
Methanol	1.6×10^6	8.3×10^{10}	2687	0.11

[a] Values calculated from Eq. 37 at 298 K; Estimated uncertainties: $\tau \pm 2\%$ (2-exp.).

The values for ^3MC population quantum yield at room temperature are higher than 10% again suggesting that this state is also involved in the deactivation of the complex. These results are in contrast with the homoleptic compound, in which the ^3MC state did not participate in the deactivation of the excited state. The calculated value of Φ_T in DMSO is the double of the average. If the ^3MC of $[Ru(nbpy)_2(nody)]^{2+}$ in DMSO is in fact more accessible, then the luminescent lifetime should show higher temperature dependence than in butyronitrile, a solvent of similar polarity. In fact, Figure 59 shows that not only the τ_M dependence with temperature is higher in DMSO than in BuCN but it is also comparable to the apolar ethylbenzene (closer ^3MLCT-^3MC gap). This analysis again supports the mixed-states hypothesis that the excited state luminescence lifetime of the dye depends on the decay of both ^3MC and ^3MLCT, as previously suggested by the A and B parameters.

References

[1] N. Armaroli, L. De Cola, V. Balzani, J.-P. Sauvage, C. O. Dietrich-Buchecker and J.-M. Kern, *J. Chem. Soc., Faraday Trans.* **1992**, *88*, 553-556.
[2] M. S. Henry and M. Z. Hoffman, *J. Phys. Chem.* **1979**, *83*, 618-625.
[3] A. Bencini and V. Lippolis, *Coord. Chem. Rev.* **2010**, *254*, 2096-2180.
[4] J. Van Houten and R. J. Watts, *J. Am. Chem. Soc.* **1976**, *98*, 4853-4858.
[5] a) G. A. Crosby and J. N. Demas, *J. Am. Chem. Soc.* **1970**, *92*, 7262-7270; b) U. Resch-Genger in *Standardization and Quality Assurance in Fluorescence Measurements I*, (U. Resch-Genger), Springer Series on Fluorescence, *Vol. 5,* **2008**, p. 493.
[6] a) A. Juris, V. Balzani, F. Barigelletti, S. Campagna, P. Belser and A. Vonzelewsky, *Coord. Chem. Rev.* **1988**, *84*, 85-277; b) S. Campagna, F. Puntoriero, F. Nastasi, G. Bergamini and V. Balzani in *Photochemistry and photophysics of coordination compounds: Ruthenium*, (S. Campagna and V. Balzani), Photochemistry and Photophysics of Coordination Compounds I, *Vol. 280,* Springer-Verlag Berlin, Berlin, **2007**, pp. 117-214.
[7] G. Orellana in *Síntesis y caracterización espectrocóspica, electroquímica y fotoquímica de nuevos sensibilizadores tris (alfa-diimina) rutenio(II) que contienen heterociclos de cinco miembros*, *Ph.D. Thesis*, Universidad Complutense, Madrid, **1988**, p. 342.
[8] a) X. L. Gao, Y. B. Wei, Y. P. Li and P. Yang, *Acta Crystallogr. C* **2005**, *C61*, m10-m12; b) R. Sang and L. Xu, *Acta Crystallogr. E* **2005**, *E61*, m793-m795; c) L. Öhrström, K. Larsson, S. Borg and S. T. Norberg, *Chem. Eur. J.* **2001**, *7*, 4805-4810; d) M. Tadokoro and K. Nakasuji, *Coord. Chem. Rev.* **2000**, *198*, 205-218.
[9] a) J.-G. Liu, B.-H. Ye, H. Li, Q.-X. Zhen, L.-N. Ji and Y.-H. Fu, *J. Inorg. Biochem.* **1999**, *76*, 265-271; b) A. Quaranta, F. Lachaud, C. Herrero, R. Guillot, M.-F. Charlot, W. Leibl and A. Aukauloo, *Chem. Eur. J.* **2007**, *13*, 8201-8211; c) F. Gao, X. Chen, F. Zhou, L.-P. Weng, L.-T. Guo, M. Chen, H. Chao and L.-N. Ji, *Inorg. Chim. Acta* **2009**, *362*, 4960-4966; d) J.-F. Yin, D. Bhattacharya, P. Thanasekaran, C.-P. Hsu, T.-W. Tseng and K.-L. Lu, *Inorg. Chim. Acta* **2009**, *362*, 5064-5072.
[10] A. Juris, V. Balzani, F. Barigelletti, S. Campagna, P. Belser and A. von Zelewsky, *Coord. Chem. Rev.* **1988**, *84*, 85-277.
[11] J. R. Lakowicz, *Principles of fluorescence spectroscopy*, 3rd Ed., Springer, New York, **2006**, p. 954.
[12] J. V. Caspar and T. J. Meyer, *J. Am. Chem. Soc.* **1983**, *105*, 5583-5590.
[13] J. Olofsson, L. M. Wilhelmsson and P. Lincoln, *J. Am. Chem. Soc.* **2004**, *126*, 15458-15465.
[14] A. M. Castro, J. Delgado and G. Orellana, *J. Mater. Chem.* **2005**, *15*, 2952-2958.
[15] J. López-Gejo, D. Haigh and G. Orellana, *Langmuir* **2009**, *26*, 2144-2150.
[16] D. Buist, N. J. Williams, J. H. Reibenspies and R. D. Hancock, *Inorg. Chem.* **2010**, *49*, 5033-5039.
[17] J. N. Demas, *Excited state lifetime measurements*, 1st Ed., Academic Press, **1983**, p. 273.
[18] a) J. F. Ireland and P. A. H. Wyatt in *Acid-Base Properties of Electronically Excited States of Organic Molecules*, (V. Gold), Adv. Phys. Org. Chem., *Vol. 12,* Academic Press, **1976**, pp. 131-221; b) G. Orellana, M. C. Moreno-Bondi, E. Segovia and M. D. Marazuela, *Anal. Chem.* **1992**, *64*, 2210-2215.
[19] R. Atencio, K. Ramirez, J. A. Reyes, T. Gonzalez and P. Silva, *Inorg. Chim. Acta* **2005**, *358*, 520-526.
[20] a) R.-L. Sang and L. Xu, *Polyhedron* **2006**, *25*, 2167-2174; b) A. K. Ghosh, D. Ghoshal, E. Zangrando and N. R. Chaudhuri, *Polyhedron* **2007**, *26*, 4195-4200; c) J. Carranza, C. Brennan, J. Sletten, B. Vangdal, P. Rillema, F. Lloret and M. Julve, *New J. Chem.* **2003**, *27*, 1775-1783; d) M. Tadokoro, J. Toyoda, K. Isobe, T. Itoh, A. Miyazaki, T. Enoki and K. Nakasuji, *Chem. Lett.* **1995**, 613-614.
[21] a) A. Morsali, *J. Coord. Chem.* **2006**, *59*, 1015-1024; b) P. Brooks and N. Davidson, *J. Am. Chem. Soc.* **1960**, *82*, 2118-2123.

[22] a) A. Bencini and F. Mani, *Inorg. Chim. Acta* **1988**, *154*, 215-219; b) M. Tanaka and M. Tabata, *Bull. Chem. Soc. Jpn.* **2009**, *82*, 1258-1265; c) I. Török, P. Surdy, A. Rockenbauer, L. Korecz Jr, G. J. Anthony A. Koolhaas and T. Gajda, *J. Inorg. Biochem.* **1998**, *71*, 7-14.
[23] S. A. Rice in *Diffusion-Limited Reactions*, (C. H. Bamford, C. F. H. Tipper and R. G. Compton), Comprehensive Chemical Kinetics *Vol. 25,* Elsevier, Amsterdam, **1985**, pp. 66-67.
[24] S. Sjoberg, *Pure Appl. Chem.* **1997**, *69*, 1549-1570.
[25] M. Z. Hoffman, F. Bolletta, L. Moggi and G. L. Hug, *J. Phys. Chem. Ref. Data* **1989**, *18*, 219-543.
[26] a) X.-B. Zhang, J. Peng, C.-L. He, G.-L. Shen and R.-Q. Yu, *Anal. Chim. Acta* **2006**, *567*, 189-195; b) C.-L. He, F.-L. Ren, X.-B. Zhang, Y.-Y. Dong and Y. Zhao, *Anal. Sci.* **2006**, *22*, 1547-1551; c) M. Koneswaran and R. Narayanaswamy, *Sens. Actuators, B* **2009**, *139*, 104-109.
[27] J. G. Martins, P. Gameiro, M. T. Barros and H. M. V. M. Soares, *J. Chem. Eng. Data* **2010**, *55*, 3410-3417.
[28] P. MacCarthy, *Anal. Chem.* **1978**, *50*, 2165-2165.
[29] N. C. Li, J. M. White and E. Doody, *J. Am. Chem. Soc.* **1954**, *76*, 6219-6223.
[30] A. R. Norris, E. Buncel and S. E. Taylor, *J. Inorg. Biochem.* **1982**, *16*, 279-295.
[31] a) F. S. Rodembusch, F. P. Leusin, L. F. da Costa Medina, A. Brandelli and V. Stefani, *Photochem. Photobiol. Sci.* **2005**, *4*, 254-259; b) S. R. Vazquez, M. C. R. Rodriguez, M. Mosquera and F. Rodriguez-Prieto, *J. Phys. Chem. A* **2008**, *112*, 376-387.
[32] a) V. Luxami and S. Kumar, *RSC Adv.* **2012**, *2*, 8734-8740; b) Z. Fang, S. Wang, L. Zhao, B. Dong, Z. Xu, J. Ren and Q. Yang, *Mater. Lett.* **2008**, *62*, 1514-1517.
[33] P. Patnaik, *Dean's Analytical Chemistry Handbook*, 2nd Ed., McGraw-Hill Handbooks, New York, **2004**, p. 1280.
[34] H.-h. Liu and Y. Chen, *Eur. J. Org. Chem.* **2009**, *2009*, 5261-5265.
[35] a) X. Liu, C. Qi, T. Bing, X. Cheng and D. Shangguan, *Anal. Chem.* **2009**, *81*, 3699-3704; b) Z. Wang, J. Heon Lee and Y. Lu, *Chem. Commun.* **2008**, 6005-6007; c) J. Lv, C. Ouyang, X. Yin, H. Zheng, Z. Zuo, J. Xu, H. Liu and Y. Li, *Macromol. Rapid Commun.* **2008**, *29*, 1588-1592; d) Y. Tang, F. He, M. Yu, F. Feng, L. An, H. Sun, S. Wang, Y. Li and D. Zhu, *Macromol. Rapid Commun.* **2006**, *27*, 389-392.
[36] A. P. M. Camargo, H. Baumgartel and C. Donner, *Phys. Chem. Chem. Phys.* **2003**, *5*, 1657-1664.
[37] L. Tormo, N. Bustamante, G. Colmenarejo and G. Orellana, *Anal. Chem.* **2010**, *82*, 5195-5204.
[38] S. W. Snyder, S. L. Buell, J. N. Demas and B. A. DeGraff, *J. Phys. Chem.* **1989**, *93*, 5265-5271.
[39] a) M. K. Brennaman, T. J. Meyer and J. M. Papanikolas, *J. Phys. Chem. A* **2004**, *108*, 9938-9944; b) S. Finn in *Ruthenium polypyridyl complexes with long aliphatic chains; photophysics, interfacial assembly and cell imaging*, *Ph.D. Thesis*, Dublin City University, Dublin, **2011**, p. 277.
[40] M. Montalti, A. Credi, L. Prodi and M. T. Gandolfi, *Handbook of Photochemistry*, 3rd Ed., CRC Press, **2006**, p. 650.
[41] D. P. Rillema, G. Allen, T. J. Meyer and D. Conrad, *Inorg. Chem.* **1983**, *22*, 1617-1622.
[42] L. Jacquet and A. K.-D. Mesmaeker, *J. Chem. Soc., Faraday Trans.* **1992**, *88*, 2471-2480.
[43] J. V. Caspar and T. J. Meyer, *J. Am. Chem. Soc.* **1983**, *105*, 5583-5590.
[44] a) N. Ghoneim and P. Suppan, *J. Lumin.* **1989**, *44*, 83-86; b) N. Ghoneim, *Spectrochim. Acta, Part A* **2000**, *56*, 1003-1010.
[45] J.-P. Lecomte, A. Kirsch-De Mesmaeker and G. Orellana, *J. Phys. Chem.* **1994**, *98*, 5382-5388.

Chapter IV

Computational chemistry

Computational methods are powerful tools to characterize the underlying photophysical processes, both of radiative or non-radiative nature, as it has been reported for other ruthenium(II) complexes.[1] Nevertheless, at the moment of this writing, there have been only few detailed computational investigations where the cation-binding quenching photoluminescence mechanisms on ruthenium(II) dyes[2] have been explored.[3]

The photophysical features of some of the ruthenium(II) complexes characterized in the previous chapter have also been studied on the grounds of the quantum chemistry theoretical models described in the introductory section 1.8. Using them, only the electronic structure of the ion-sensitive dyes has been computed. Being large cationic dyes (> 75 atoms) some simplifications have been applied for the sake of computational time: for example, no hexafluorophosphate counter-ions have been included and specific interactions between the dye and the cationic quencher were restricted to the copper(II) ion.

4.1. Computational methods employed

Geometry optimizations were performed for the molecules in the gas-phase using the hybrid functional B3LYP[4] in combination with the polarized valence triple-ξ basis set (6-31G*) for all atoms. The heavy atoms Cu(II) and Ru(II) were treated including relativistic effects by means of the Stuttgart/Dresden ECP-MDF10[5] and ECP-MWB28[6] pseudopotentials, respectively. The nature of the stationary points was confirmed by computing the Hessian at the same level of theory. The UV-Vis spectra were successfully reproduced by calculating the lowest-lying 75, and when necessary 130 or 200 vertical singlet electronic excitation energies using the time-dependent DFT (TD-DFT) at the S_0 optimized geometry. The phosphorescence maxima were simulated on the basis of ΔSCF-DFT and TD-DFT calculations. These calculations yield the energy difference between the lowest triplet excited state at its optimized geometry (T_1) and the closed-shell ground state at the same geometry (i.e. adiabatic electronic emission, AEE). The latter approach is a simple but reliable way to determine the emission maxima.[1a] The TD-DFT, ΔSCF-DFT and single point calculations were performed in solution using water and methanol as solvents with the polarization continuum model (PCM).[7] All calculations were carried out using the Gaussian09 software package.[8] The graphical analysis and plotting of the results were done with the Gabedit (v.2.3.0) software.[9]

4.2. $[Ru(phen)_2(iip)]^{2+}$

The spectroscopic features of this ruthenium complex are detailed in section 3.2. It has been shown that the luminescence intensity of the dye is significantly reduced at high pH values or in the presence of copper(II) ions. In contrast, neither copper nor high pH values lead to significant changes in the ground state absorption spectrum of the dye.

In order to get an insight into the photophysical properties of the dye, DFT and TD-DFT calculations have been performed (Computational methods section 4.1). To this aim, the PCM-TD-DFT UV-Vis spectrum of $[Ru(phen)_2(iip)]^{2+}$ using two different exchange–correlation functionals, namely B3LYP[4] and CAM-B3LYP,[10] were computed. The main PCM-TD-DFT vertical excitations are collected in section 6.2.1 (Table S1 and Table S2, respectively). Figure 60 shows the experimental absorption spectrum of the dye in methanol, superimposed to the computed PCM-TD-DFT vertical excitation energies. Using the latter, a Gaussian-convoluted spectrum was generated, which is also shown for the sake of completeness. Similarly to other ruthenium(II) complexes,[11] the UV-Vis absorption spectrum contains an intense absorption band peaking at ca. 260 nm which is mainly due to intra-ligand (IL) transitions (see Table S1), with a shoulder at ca. 285 nm, originated mainly from ligand-to-ligand charge transfer (LLCT) excitations. The low-energy region of the absorption spectrum is characterized by a broad band centred at ca. 460 nm, bearing a tail which extends up to 550 nm. The excitations responsible of this band are of metal-to-ligand charge transfer (MLCT) character. These results are in agreement with the experimental assignment of the absorption spectrum bands performed in section 3.2.

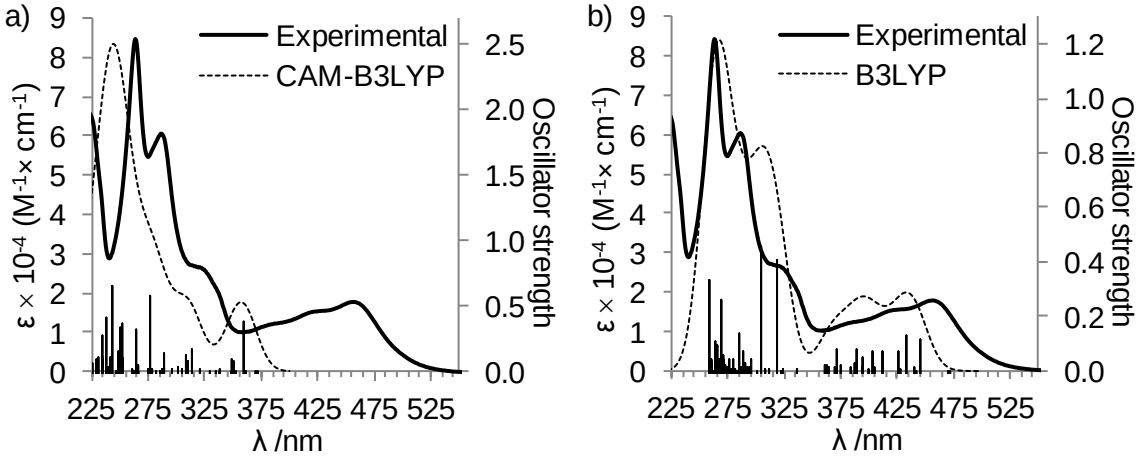

Figure 60. Absorption spectrum of $[Ru(phen)_2(iip)]^{2+}$ in methanol (solid line) and computed PCM-TD-DFT vertical excitation energies in methanol using the functional CAM-B3LYP (a) and B3LYP (b). The dashed line represents a Gaussian convolution of the vertical excitation energies.

A comparison of the computed UV-Vis spectra with the experimental one clearly indicates that the B3LYP functional outperforms the CAM-B3LYP functional. This result is in agreement to other computational studies describing the spectroscopic properties of Ru(II) polypyridyl complexes.[12] It is generally observed that the CAM-B3LYP functional overestimates the MLCT excitation energies. The IL band peaking experimentally at ca. 260 is also better reproduced with the B3LYP functional, as it is observed in Figure 60. In view of these evidences, the B3LYP functional was chosen for the rest of calculations. Additionally, various basis sets for the TD-DFT calculations of the different acid/base species of $[Ru(phen)_2(iip)]^{2+}$ in aqueous media were evaluated, namely the 6-31G* and 6-31+G*. The PCM-TD-DFT UV-Vis spectra of the five acid/base species in water for the different basis sets are depicted in section 6.2.1 (Figure A56 to Figure A60). Since no significant differences between both basis sets was found, the less time-consuming 6-31G* basis set was considered for the remaining calculations.

In order to get an insight into the main photochemical deactivation pathways and on the quenching mechanisms, DFT (B3LYP/6-31G*) calculations were performed. These calculations provide a continuous adiabatic description of the relevant stationary points along the photodeactivation channels. Time-resolved ultrafast experiments demonstrate that, after population of the lowest-lying singlet excited states (S_n), very fast and efficient intersystem crossing (ISC) to the triplet manifold takes place in Ru(II) polypyridyl complexes.[13] Hence, the photochemical deactivation processes are dominated by the decay of the triplet excited states. Typically a fast decay to the lowest triplet excited state is observed and, once its well is populated, photoluminescence takes place. Radiative processes compete with non-radiative deactivation pathways. Thus, non-emissive ^{3}MC states are involved in thermally-activated deactivation pathways leading to the ground state (S_0) without emission of light,[11] as it has been demonstrated by locating minimum energy crossing points (MECP) between the ^{3}MC and the S_0 potential energy surfaces (PES).[14] Additionally, temperature-independent non-radiative pathways are also operative for electronically excited Ru(II) complexes, which are associated with the Franck-Condon overlap of the S_0 and T_1 vibrational wavefunctions and obeys the energy gap law.[15] In order to characterize these mechanisms, the geometries of the relevant stationary points along the photodeactivation pathway of $[Ru(phen)_2(iip)]^{2+}$, namely S_0, ^{3}MLCT and ^{3}MC minima, were fully optimized. The main geometrical parameters are included in section 6.2.1, Figure A61. The geometry of the singlet ground state (S_0) resembles other Ru(II) complexes as far as bond lengths and bond-angles is concerned.[2d, 16] The ground state HOMO and LUMO Kohn-Sham orbitals for the $[Ru(phen)_2(iip)]^{2+}$ dye are represented in Figure 61. While the HOMO has a mixed Ru-d and π_{iip} character, the LUMO is mainly of π^*_{phen} character. The lowest triplet

excited state is of ^{3}MLCT character, as demonstrated by analysing the spin density distributions, which show an unpaired electron at the Ru atom and the second unpaired electron at the iip ligand (see Figure 61). The optimized ^{3}MLCT geometry displays a small distortion of the octahedral coordination sphere, specifically in the angle formed by the equatorial N_{phen}-Ru-N_{iip} angle. This angle changes from 173.2° to 172.1° when going from the S_0 to the ^{3}MLCT geometry. As seen in Figure A61, the Ru-N_2(iip) bond distance is shortened at the ^{3}MLCT whilst the trans Ru-N_5(phen) bond distance increases. These effects have their grounds on the increased electrostatic interaction between the Ru core and the iip ligand as the ^{3}MLCT is characterized by a formally oxidized Ru(III) metal atom and a coordinated negatively-charged iip ligand.

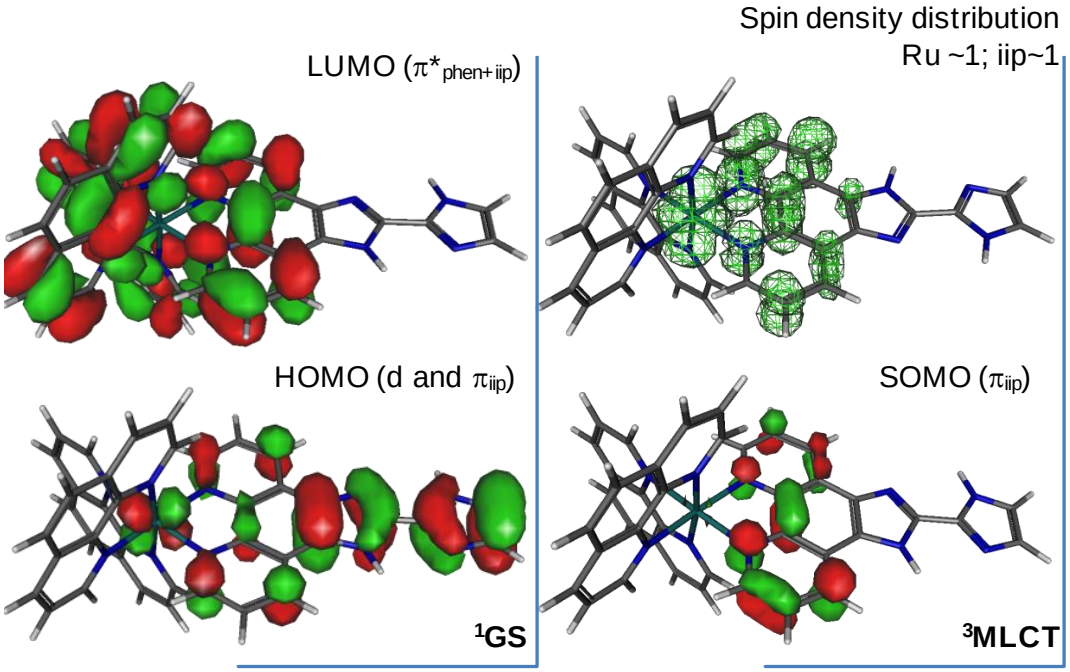

Figure 61. Ground state (^{1}GS) and excited state (^{3}MLCT) Kohn-Sham orbitals of $[Ru(phen)_2(iip)]^{2+}$. Upper right: Spin density plot for the lowest T_1 state.

The theoretical emission spectrum was simulated by two different approaches: i) the lowest vertical triplet PCM-TD-DFT excitation at the optimized ^{3}MLCT geometry and ii) by the ΔSCF-DFT method (see Computational methods). The former yields a value of 607 nm while the latter provides a value of 595 nm. As shown in Table 3, the experimental value is 602 nm, demonstrating that both results are in excellent agreement with the experimental data. As stated above, non-radiative pathways compete with photoluminescence. Aiming at characterizing these pathways, the lowest non-emissive ^{3}MC state was optimized. Its optimized geometry bears longer axial Ru-$N_{3,6}$ bond lengths (see Figure A61), as results from

the promotion of an electron into the $d_{z^2}\sigma^*$ orbital (with some antibonding character along the Ru-N bond). The computed spin density at the Ru atom is 1.88, consistent with its metal-centred nature. The ^{3}MC minimum lies adiabatically 6 kcal mol^{-1} (0.26 eV) below the ^{3}MLCT, a trend that is observed in other Ru(II) polypyridyl complexes.[1a] For all those complexes, it is usually observed an energy barrier to populate the ^{3}MC minimum from the ^{3}MLCT, as it has been shown for the parent $[Ru(bpy)_3]^{2+}$ complex.[17] This energy barrier determines the kinetics of the thermal non-radiative deactivation mechanisms. Hence, if enough vibrational energy is available, the system will be able to overcome the barrier and readily decay to the ground state surface through the MECP, recovering in this way the geometry of the ground state.

4.2.1. Acid/base quenching of the photoluminescence

The experimental titration study of $[Ru(phen)_2(iip)]^{2+}$ in section 3.2.1 (Table 4) showed a pK_a value of 5.0 for the first protonation and a pK_a value of 8.4 for the first deprotonation. However, these experimental results lack the information about which one of the N atoms of iip (distal or fused-ring imidazole) is actually involved in the protonation/deprotonation step. To shed some light into the acid/base behaviour of the iip complex, the geometries of the mono- and totally-deprotonated as well as the mono- and totally-protonated complexes with different protonation patterns were optimized. The main geometrical parameters of the most stable tautomers are included in Figure A62 and Figure A63. As depicted in Figure 62 (below), the calculations indicate that the most stable tautomers are those in which protonation occurs at the distal imidazole and deprotonation occurs at the fused-ring imidazole.

The computed PCM-TD-DFT UV-Vis spectra of the most stable tautomers of the five acid/base species show in general a good agreement with the experimental ones, as shown in section 6.2.1, Figure A56 to Figure A60. The main PCM-TD-DFT vertical excitations as well as the corresponding Kohn-Sham orbitals assignment are also summarized in section 6.2.1 (Table S3 to Table S7). The experimentally recorded absorption spectra of the Ru(II) dye with varying pH values has been detailed above (see section 3.2.1). The comparison of the UV-Vis spectra between the different species reveals that the main changes occur at lower wavelengths (< 340 nm), mostly assigned as IL and LLCT transitions. This behavior has also been reported for a related imidazole-bearing Ru(II) complex.[16] For the totally deprotonated forms of $[Ru(phen)_2(iip)]^{2+}$, the PCM-TD-DFT calculations show that the two most intense bands are centred at ca. 375 and 280 nm and they involve the deprotonated biimidazole moiety. This result supports that *the iip ligand is responsible for the major spectral changes*

upon deprotonation, although the band theoretically predicted at ca. 375 nm is slightly overestimated.

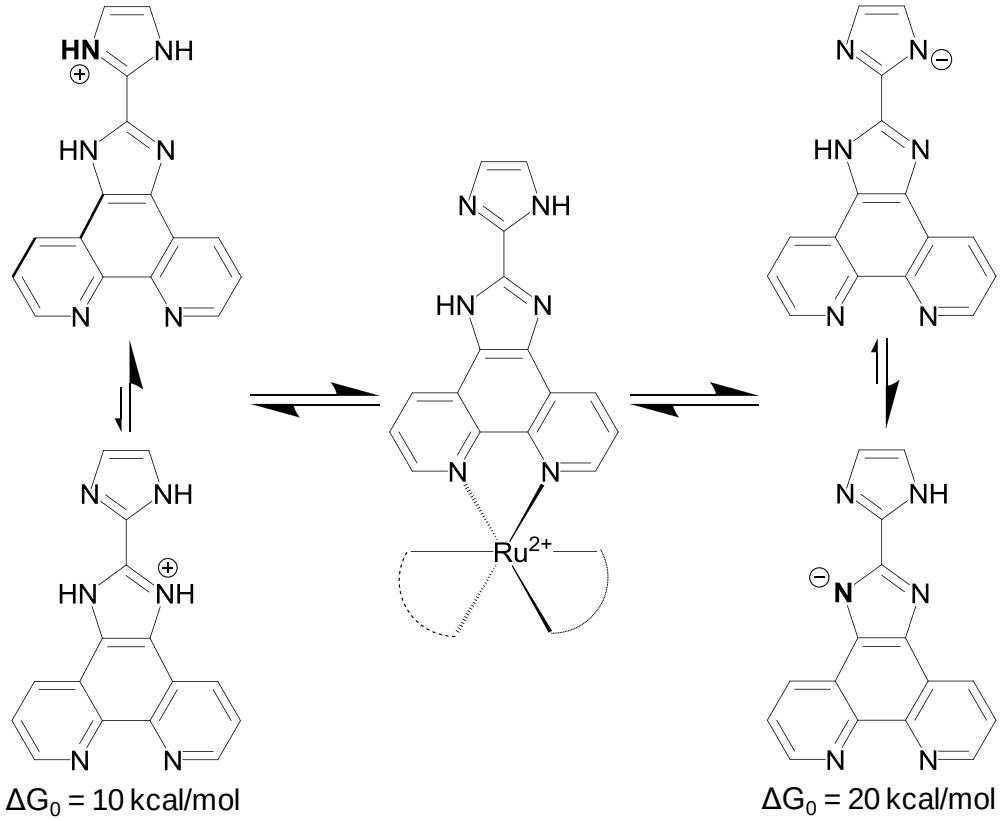

Figure 62. Possible structures upon protonation (left) or deprotonation (right) of $[Ru(phen)_2(iip)]^{2+}$. A B3LYP/6-31G* geometry optimization indicates that the most stable structures are those in which protonation occurs at the distal imidazole moiety and deprotonation occurs at the fused-ring imidazole.

In Figure 18 (section 3.2.1) the luminescence (both steady-state and time-resolved) of $[Ru(phen)_2(iip)]^{2+}$ as a function of the solution pH is plotted. A dramatic decrease in both the luminescence intensity (77% quenching) and lifetime (from 550 ns to 100 ns) of the dye when increasing the pH value is observed. Similarly to the neutral form of the complex, and aiming at rationalizing the quenching of photoluminescence at higher pH values, the relevant stationary points along the photochemical deactivation channels for the mono- and totally-deprotonated species were optimized. As expected, the protonation state of the iip ligand has little structural effect on the coordination to the Ru(II) atom, as shown in related complexes.[16] The main structural changes are observed in the bond lengths of the deprotonated biimidazole moiety, shown in detail in Figure A63. The lowest triplet excited state of the mono- and totally-deprotonated species is of ^{3}IL and ^{3}LLCT character,

respectively, as reflected by the analysis of the spin density distribution at their optimized geometries (Figure 63). Hence, the singly deprotonated species displays both unpaired electrons on the iip ligand, while the totally deprotonated species has one unpaired electron located at the phen ligands and the other unpaired electron at the iip ligand.

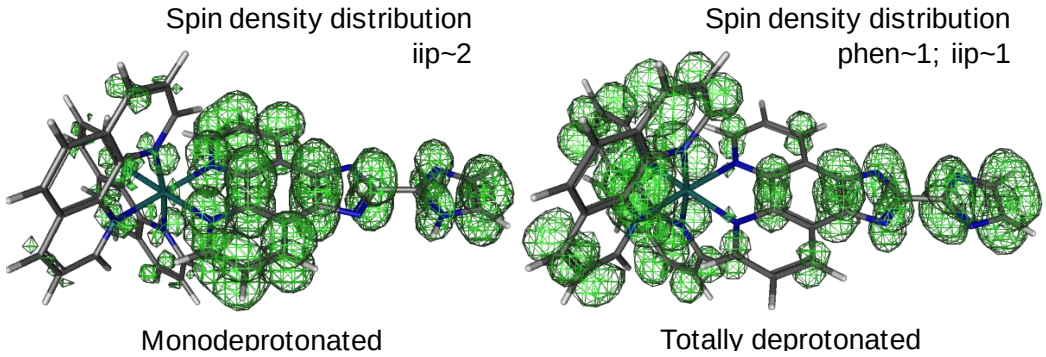

Figure 63. Spin density plots for the lowest T_1 state of the mono- and totally deprotonated species of $[Ru(phen)_2(iip)]^{2+}$.

These results show that there is a radical change on the photophysical picture of the $Ru(phen)_2(iip)$ dye upon the pH changes. Therefore, *the nature of the lowest triplet changes from a ^{3}MLCT state at neutral pH to a ^{3}IL state at high pH values*. The theoretical emission maximum of the monodeprotonated species was found to be 670 and 663 nm with the PCM-TD-DFT and ΔSCF-DFT approaches, respectively. Experimentally, emission is observed at 602 nm at pH 7.5, preliminary pointing out to a red-shift of ca. 0.2 eV of the theoretical values if we assume a ^{3}IL-based emission. As shown in Figure 15, the emission maximum of $[Ru(phen)_2(iip)]^{2+}$ is experimentally observed at the same wavelength, independently of the solution pH. This result clearly demonstrates that within the entire pH range the ^{3}MLCT state of the complex is always responsible for the observed emission. However, at higher pH values and depending on the acid-base equilibrium, a lower concentration of the (emissive) neutral species is expected. Therefore, the lower concentration of the latter at higher pH values explains the observed quenching of photoluminescence. The question which arises now is why the lowest ^{3}IL and ^{3}LLCT states of the singly and completely deprotonated species are not luminescent. Similarly, for the fully deprotonated species, and assuming a ^{3}LLCT-based emission, the theoretical emission maximum is predicted at 977 and 1055 nm with the PCM-TD-DFT and ΔSCF-DFT approaches, respectively. Similarly to singly deprotonated species, the apparent discrepancy between theory and experiment point out to a ^{3}MLCT-based emission of the residual concentration of the neutral complex in equilibrium with the fully deprotonated metal complex. Based on these results, the lack of luminescence from the

deprotonated species can be ascribed partly to the energy-gap rule.[18] Hence, the considerable red-shift of the lowest triplet excited states leads to an increase of the temperature-independent non-radiative decay rate, which compromises the luminescence quantum yield and shortens the lifetime of the lowest-lying excited state. Another factor that might be behind the observed quenching is the change of character of the luminescence state when going from pH 7.5 to pH 11 (from ^{3}MLCT to ^{3}LLCT), since slower radiative decay rates are expected for the ^{3}LLCT-based and ^{3}IL-based emission, because of smaller spin-orbit coupling effects.[11] Summarizing, the quenching of the observed emission band at 602 nm might originate simply from the decrease in the concentration of the neutral species. Nonetheless, luminescence lifetime measurements indicate a dynamic quenching mechanism which can be easily explained if a photoinduced proton transfer between the dye and the phosphate anionic species occurs.

4.2.2. Addition of copper and quenching of the photoluminescence

The influence of copper(II) on the optical properties of the Ru(II) indicator dye has been described by means of absorption, fluorescence and time-resolved spectroscopy in section 3.2.3. The stoichiometry of the resulting supramolecular complexes upon addition of Cu(II) to an aqueous $[Ru(phen)_2(iip)]^{2+}$ solution was determined to be 1:1 + 2:1 ruthenium-to-copper ratio. Under an excess concentration of Cu(II), where the equilibrium is shifted towards the 1:1 complex, the luminescence intensity is reduced by 92% with no spectral shift. Despite the observed quenching, the absorption profile of the dye remains practically unaltered, the main change being a general lower absorption coefficient in the presence of the quencher. Moreover, by means of time-resolved spectroscopy, the luminescence quenching was shown to occur *via* a static mechanism.

In order to get an insight into the quenching mechanisms upon the addition of Cu(II), calculations on the model $[Ru(phen)_2(iip)]^{2+}$-$CuCl_2$ dinuclear coordination complex, which holds a 1:1 ruthenium-to-copper ratio, were performed. For computational ease, the 2:1 complex was not considered for the calculations. In the supramolecular complex, the Cu(II) atom is coordinated to two chloride anions and two pyridine-like nitrogen atoms of the biimidazole moiety in a planar fashion (see Figure 64b). This coordination mode has been previously observed in other Cu(II)-imidazole complexes.[19] The optimized geometry (doublet ground state, D_0) is depicted in section 6.2.1, Figure A64. The main structural difference with respect to the *free* complex is observed in the "bite" angle of the imidazole moieties, which undergoes a 15° closure upon binding to Cu(II). For steric reasons, the copper atom is closer to the distal imidazole ring than to the fused-ring imidazole, being the

calculated Cu-N distances 2.04 and 2.41, respectively. Biimidazole complexes of Ru(II) show Ru-N distances of 2.2 and 2.1 Å.[20]

The main PCM-TD-DFT vertical excitations and their orbital assignment are collected in Table S8 (section 6.2.1). The computed UV-Vis spectrum is shown in Figure 64. As pointed out above, there are very few changes in the absorption spectra of the complex observed after addition of Cu(II). The first nine computed PCM-TD-DFT vertical transitions (see Table S8) are charge transfer (CT) excitations towards the $CuCl_2$ moiety, starting either from the Ru(II) atom, the iip ligand or the $CuCl_2$ moiety itself. They are found at the very low-energy region (between 536 and 1240 nm) and display almost negligible oscillator strengths. This is in agreement with a previously reported Ru(II)-Cu(II) supramolecular dyad containing an aza crown ether bridging ligand.[21] Experimentally, these absorption bands were not observed, mostly due to the wavelength range of the spectrophotometer (up to 900 nm) but also because of their weakness.

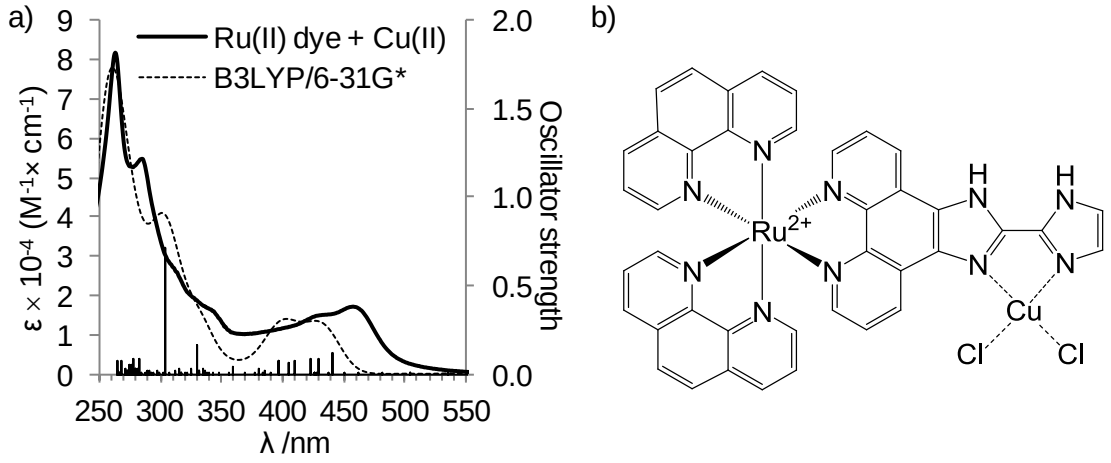

Figure 64. a) Experimental UV-Vis absorption spectrum of $[Ru(phen)_2(iip)]^{2+}$ in pH 7.5 phosphate buffer solution in presence of 5 equivalents of Cu(II) (solid line) and computed water PCM-TD-B3LYP/6-31G*//B3LYP/6-31G* vertical excitation energies. The dashed line represents a Gaussian convolution of the TD-DFT transitions. b) Structure of the $[Ru(phen)_2(iip)]^{2+}$-$CuCl_2$ complex (D_0).

Similarly to the calculations for the *monometallic* Ru(II) complex, the relevant stationary points along the photochemical deactivation channels of $[Ru(phen)_2(iip)]^{2+}$-$CuCl_2$ were optimized. The ground state is a doublet (D_0), bearing the unpaired electron mainly at the Cu(II) atom according to the spin density distribution (Figure 65). As pointed out above, the lowest-lying doublet excited states correspond to CT excitations to the Cu(II) moiety. These states open up new deactivation channels that are not present in the copper-free Ru(II) complex. An optimization job was also run for the geometry of the lowest lying quartet state, which in a similar way to the *uncomplexed* Ru(II) dye, and due to strong SOCs can be

populated after ISC from the doublet manifold of states. The lowest quartet state is of metal-metal-to-ligand CT (^{4}MMLCT), as reflected by the spin densities of ca. 1, 1 and 1 at the Ru, Cu and iip moieties, respectively (Figure 65).

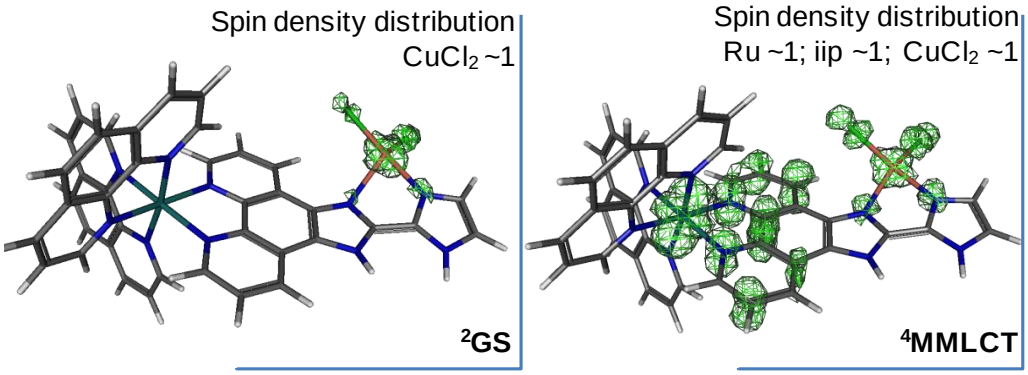

Figure 65. Ground state (^{2}GS) and excited state (^{4}MMLCT) spin density plots of $[Ru(phen)_2(iip)]^{2+}$-$CuCl_2$.

Formally, the latter state can be considered a MLCT transition from the Ru to the iip ligand but using as a reference the doublet ground state. Its optimized geometry is characterized by a strengthening of the coordination between iip and Ru(II), with a concomitant weakening of the Ru(II)-phen bond distance (Figure A64). These structural changes on the coordination sphere are consistent with a MLCT Ru-to-iip transition and are similar to what is observed for the ^{3}MLCT of the *Cu-free* dye. Another significant geometrical rearrangement upon excitation predicts the twist between the imidazole moieties, as the dihedral angle is smaller in the ^{4}MMLCT than in the ground state by ca. 5°. Moreover, the distance between the fused-ring imidazole and the copper atom is shortened by 0.22 Å, while both Cl-Cu bonds increase their length. This changes support the augmented electron density in the iip ligand upon photoexcitation. In order to reproduce the emission features, the main TD-DFT transitions at the ^{4}MMLCT geometry were computed and the results are summarized in Table S9. The first seven PCM-TD-DFT transitions were found to be of doublet-doublet character and involved ruthenium-to-copper CTs or copper-centred excitations in the 673-936 nm range (1.3–1.8 eV). Since these MC transitions are known to be non-radiative, we can assume that the theoretical emission maximum should be given by the 8th transition, which is a doublet-quadruplet Ru-to-iip MLCT at 640 nm (1.94 eV). The latter value is in agreement with the theoretical emission maximum of 650 nm (1.91 eV) provided by the ΔSCF-DFT approach at the same geometry. Hence, the presence of the low-lying states centred on the $CuCl_2$ moiety opens up new photodeactivation channels that account for the luminescence

quenching of the metal probe without any spectral shift upon the addition of Cu(II). A likely explanation follows. In Figure 66 the main photochemical deactivation channels for the dinuclear $[Ru(phen)_2(iip)]^{2+}$-$CuCl_2$ complex and the corresponding states involved are schematically depicted. In order to characterize the deactivation channels as already carried out for $[Ru(phen)_2(iip)]^{2+}$, the optimization of the lowest non-emissive metal-metal-centred (^{4}MMC) state (which is formally a MC excitation at the Ru atom, using the doublet ground state as reference) was performed. Indeed, the main geometrical features of the ^{3}MC and the ^{4}MMC geometries are quite similar. Thus, stretched axial Ru-N bonds are also observed at the ^{4}MMC optimized geometry (see Figure A64). As shown in Figure 66, and in comparison to the ^{3}MC state of the Cu-free dye, the ^{4}MMC state is located ca. 3 kcal mol^{-1} (0.14 eV) at higher energies than the ^{4}MMLCT state. Therefore, this state will be most likely unreachable at room temperature, so that it is not expected to be involved in the main non-radiative deactivation pathways.

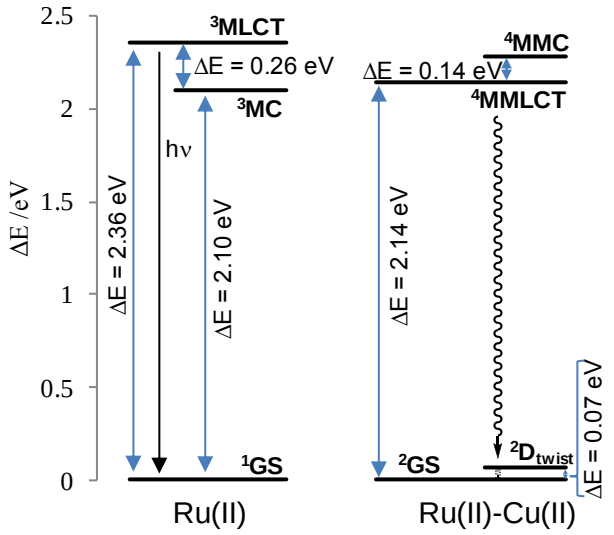

Figure 66. Computed energy diagram (water PCM-B3LYP/6-31G*) for the relevant electronic states of $Ru(phen)_2(iip)$ and $Ru(phen)_2(iip)$-$CuCl_2$. Values normalized to the energy of the corresponding optimized ground states.

This is not surprising taking into account, as discussed above, that the incorporation of Cu(II) leads to a complete different photochemical picture. New photochemical pathways involving the lowest-lying CT doublet excited states to the Cu(II) moiety arise. Consequently, competitively to crossover to the ^{4}MMLCT, those states can also be populated in the course of photodeactivation. Since these states involve population of virtual 3d Cu(II) orbitals (see Table S9), partial detachment of Cu-bonded ligands will take place. In order to prove this hypothesis, another doublet structure with such an electronic character (herein denoted as

$^2D_{twist}$, see its main geometrical features in Figure A64) has been optimized. As it was expected, such Cu-centred excited state shows partial detachment of the fused-ring imidazole pyridine-like nitrogen atom. There is also a proton migration to the *free* nitrogen atom, which now adopts pyrrole-like character to stabilize the chlorine atom by H-bonding (hence the twist notation). As seen in Figure 66, this doublet state is located at much lower energies (only 0.07 eV above the D_0 minimum). In such a scenario, the lowest-lying doublet CT excited states involving the Cu(II) will be populated through efficient ISC to the ^{4}MMLCT state. From these states, relaxation to the $^2D_{twist}$ minimum will take place. Due to the smaller energy gap with the doublet ground state (D_0), it is reasonable to speculate that the non-radiative deactivation pathways finally leading to the ground state geometry will be enhanced on the bimetallic Ru(II)-Cu(II) species. Therefore, this enhancement of the non-radiative pathways is ultimately responsible of the luminescence quenching taking place upon incorporation of Cu(II) to the Ru(II) entity. Therefore, with this photophysical picture in mind, it is reasonable to propose a PET quenching mechanism from the $Ru(phen)_2(iip)$ dye (^{4}MMLCT state) towards the Cu(II) ion ($^2D_{twist}$). This electron-transfer quenching mechanism with Cu(II) has been reported for a series of ruthenium(II) polypyridyl complexes in solution.[22]

4.3. $[Ru(phen)_2(hmip)]^{2+}$

The spectroscopic features of this ruthenium complex are detailed in section 3.3. It has been shown that the luminescence intensity of the dye is significantly lower at high pH values, with little changes in the absorption profile. In contrast to the ruthenium-iip complex, the addition of a series of metal cations did not produce any noticeable quenching of the luminescence intensity, demonstrating that the hmip complex is insensitive to these species. In order to get an insight into the main photochemical deactivation pathways, DFT and TD-DFT (B3LYP/6-31G*) calculations were also performed on this metal complex (see Computational methods).

The geometry of the Ru-hmip complex in its ground state S_0 was fully optimized starting from four different geometries, yielding three rotamer structures (Figure 67) where the phenol ring is coplanar with the hmip ligand. Gas-phase energy differences of 8.5 and 1.8 kcal mol^{-1} were found between the two local minima and the global minimum structure. The latter is stabilized by sharing the NH hydrogen atom with the oxygen atom of the phenol moiety. One of the local minima is characterised by a hydrogen bonding between the OH group and the pyridine-like nitrogen atom of the imidazole moiety. The ΔE (1.8 kcal/mol) between one of the local minima and global minimum indicates that both structures are likely to exist at room temperature, especially when taking into account that this result is modelled in vacuum where no solvent-specific stabilization occurs. To support that both structures are possible in solution, a PCM (water) optimization of the two isomers was performed. Not only we have found an inversion where the local minimum is now the global minimum, but also the energy difference between them is lowered to 0.3 kcal mol^{-1}. Hence, the structure containing a N-HO stabilization is presumed to be the global minimum **GM,** while the isomer NH-O is a local minimum **LM** (Figure 67).

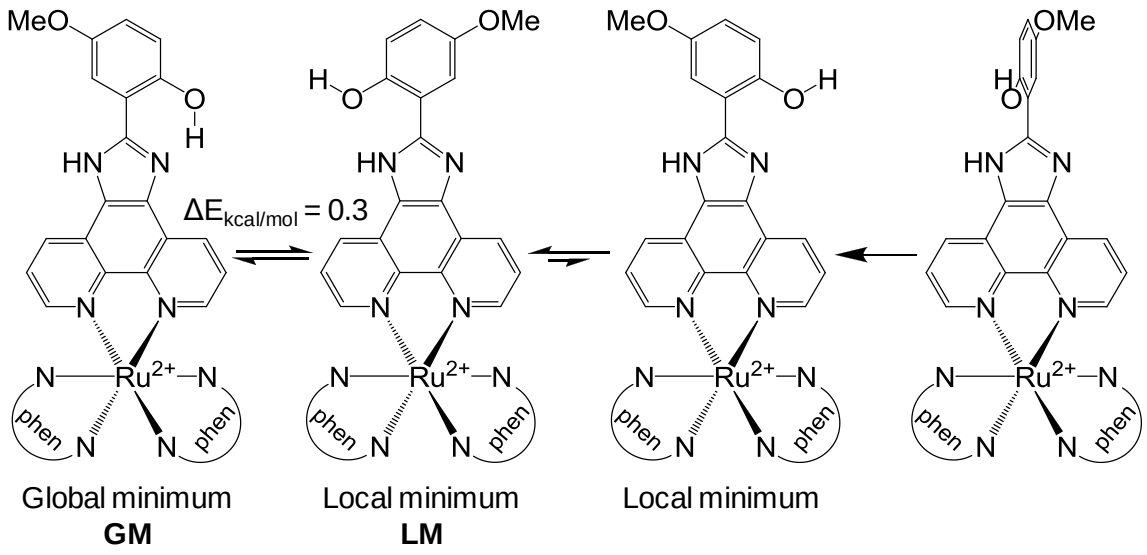

Figure 67. Structures used as inputs for the gas-phase geometry optimization (DFT B3LYP/6-31G*) of ground state $Ru(phen)_2(hmip)^{2+}$. The energy difference was calculated from the optimized structures in water.

The PCM-TD-DFT UV-Vis spectrum of $[Ru(phen)_2(hmip)]^{2+}$ was computed. The main PCM-TD-DFT vertical excitations of both GM and LM are collected in section 6.2.2 (Table S10 and Table S11). Figure 68 shows the experimental absorption spectrum of the dye in PBS solution at pH 7.5, superimposed to the computed PCM-TD-DFT vertical excitation energies for both rotamers. With these PCM-TD-DFT vertical excitations, a Gaussian-convoluted spectrum was generated, which is also shown for the sake of completeness.

Similarly to other ruthenium(II) complexes,[11] the UV-Vis absorption spectrum comprises an intense absorption band peaking at ca. 260 nm that is mainly due to ligand-to-ligand charge transfer (LLCT) excitations (see Table S10 and Table S11). A weak band is observable at ca. 350 nm, originated mainly by intra-ligand (IL) excitations centred at the hmip functional ligand. The low-energy region of the spectrum is characterized by a broad band centred at ca. 460 nm, bearing a tail that extends up to 520 nm. The excitations responsible for this band are of metal-to-ligand charge transfer (MLCT) character, although their energies are somewhat over-estimated. These results are in agreement with the experimental assignment of the absorption spectrum bands performed in section 3.3.

Not surprisingly, the TD-DFT results show that both isomers produce similar UV-Vis spectra with excitations at similar energies. For this reason, the photophysical study of $[Ru(phen)_2(hmip)]^{2+}$ was only performed for the **GM** rotamer.

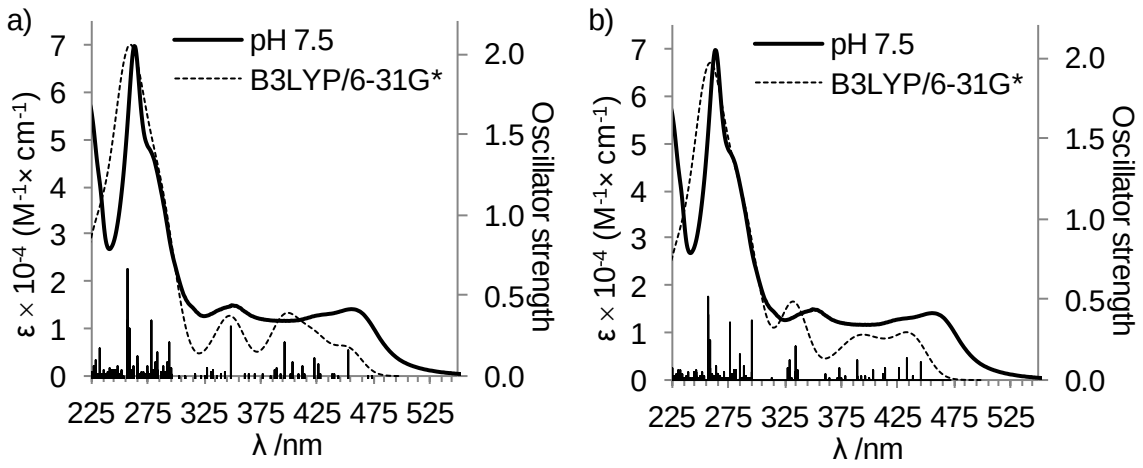

Figure 68. Absorption spectrum of $[Ru(phen)_2(hmip)]^{2+}$ in PBS 50-mM pH 7.5 (solid line) and computed (water) PCM-TD-DFT (B3LYP/6-31G*) vertical excitation energies for a) the energy global minimum **GM** isomer, and b) the local minimum **LM** isomer. The dashed line represents a Gaussian convolution of the vertical excitation energies.

In order to get a deeper insight into the photophysical picture of $[Ru(phen)_2(hmip)]^{2+}$, DFT (B3LYP/6-31G*) calculations were performed, where the geometries of the S_0 and T_1 minima of $[Ru(phen)_2(hmip)]^{2+}$ were fully optimized. The main geometrical parameters obtained thereof are included in section 6.2.2, Figure A65. The geometry of the singlet ground state (S_0) is similar to that obtained for the iip complex and resembles other Ru(II) complexes with regard to bond lengths and bond-angles.[2d, 16] The ground state HOMO and LUMO Kohn-Sham orbitals for the $[Ru(phen)_2(hmip)]^{2+}$ dye are represented in Figure 69. While the HOMO is mainly of π_{hmip} character, the LUMO has a mixed π_{hmip}* and π^*_{phen} character. The lowest triplet excited state is of ^{3}IL character, as clearly reflected by the analysis of the spin density distributions, which show two unpaired electrons at the hmip ligand (see Figure 69). The optimized ^{3}IL geometry is very similar to the ground state counterpart, where a small distortion of the octahedral coordination sphere occurs, specifically in the equatorial N_{phen}-Ru-N_{hmip} angle. This angle varies from 173.3° to 172.3° in going from the S_0 to the ^{3}IL geometry. As seen in Figure A65, the Ru-N bond distances are barely altered upon excitation. *Unlike the ^{3}MLCT character of the lowest-lying excited state of the iip complex, the hmip dye shows an equivalent one of ^{3}IL nature.* The latter is characterized by smaller charge separation (intra-ligand) than the former (metal-to-ligand) so that, upon excitation, there are less changes on the electrostatic interaction between the hmip ligand and the Ru atom.

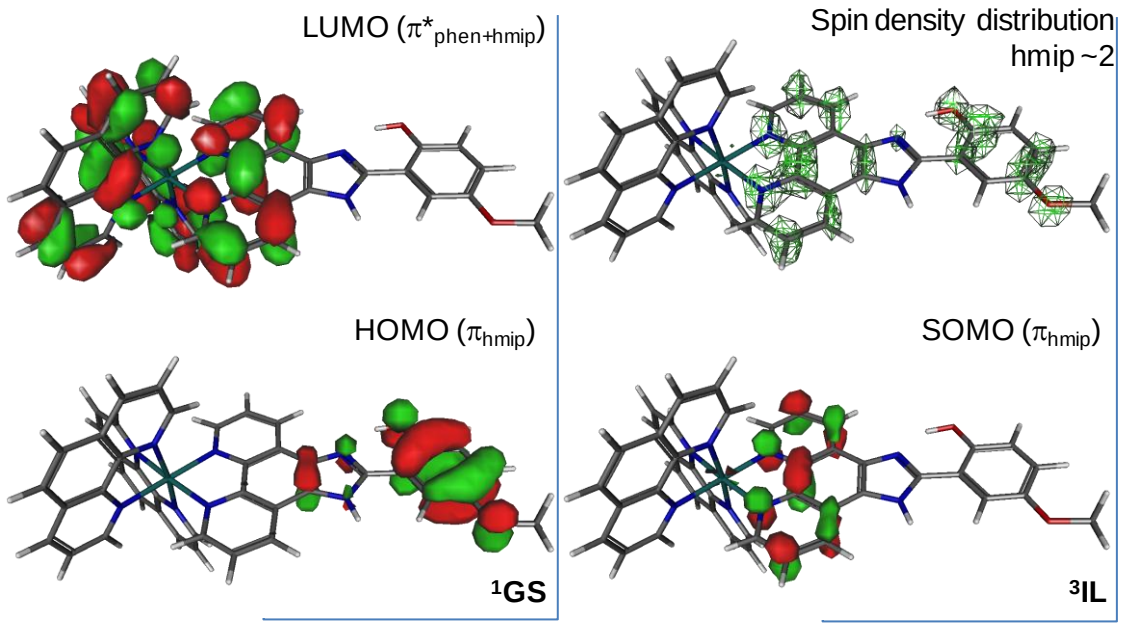

Figure 69. Ground state (^{1}GS) and lowest-lying excited state (^{3}IL) Kohn-Sham orbitals of $[Ru(phen)_2(hmip)]^{2+}$. Upper right: Spin density plot for the lowest T_1 state.

Similarly to the Ru-iip complex, the theoretical emission spectrum was simulated by two different approaches: i) the lowest vertical triplet PCM-TD-DFT excitation at the optimized ^{3}IL geometry, and ii) the ΔSCF-DFT method (see Computational methods). The former yields a value of 601 nm and the latter a value of 591 nm for the luminescence maximum. As seen in Table 7, the experimental value is 604 nm, demonstrating that both results are in excellent agreement with the experimental data.

4.3.1. Acid/base quenching of the photoluminescence

The experimental titration study of $[Ru(phen)_2(hmip)]^{2+}$ described in section 3.3.1 (Table 9) showed three pK_a values of 2.0, 7.9 and 10.3. As mentioned above, the luminescence intensity of the dye is significantly reduced at high pH values despite the small changes observed in the absorption profile. To shed some light onto the behaviour of the deprotonated hmip complex, the geometry of the fully-deprotonated complex was optimized. The main geometrical parameters are included in Figure A66.

The computed PCM-TD-DFT UV-Vis spectrum of the basic species shows in general a good agreement with the experimental one, as evidenced in Figure 70. The main PCM-TD-DFT vertical excitations, as well as the corresponding assignment of the Kohn-Sham orbitals, are also summarized in section 6.2.2 (Table S12). The recorded absorption spectra of the Ru(II) dye with varying pH values has shown that, at high pH values, the 350 nm band no longer exists (see section 3.3.1). The analysis of the PCM-TD-DFT vertical excitations of the

neutral compound attributed this band to hmip-centred IL transitions (see above). For the deprotonated compound, the same intra-ligand transition appears at higher energies (ca. 330 nm). This band is now overlapped with the intense UV region of phen-related IL and LLCT transitions thus disappearing from the experimental spectrum. This result supports that *the hmip ligand is responsible for the major spectral changes observed upon deprotonation*.

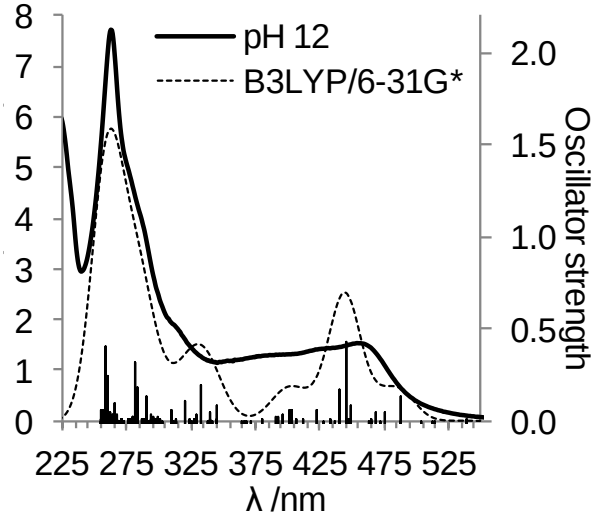

Figure 70. Absorption spectrum of $[Ru(phen)_2(hmip)]^{2+}$ in 50-mM pH 12 PBS (solid line) and computed (in water) PCM-TD-DFT (B3LYP/6-31G*) vertical excitation energies for the fully deprotonated optimized geometry. The dashed line represents a Gaussian convolution of the vertical excitation energies.

Figure 33b (section 3.3.1) depicts the variation of the luminescence of $[Ru(phen)_2(hmip)]^{2+}$ with the solution pH. A dramatic decrease of the luminescence intensity of the dye when increasing the pH value is observed. Similarly to the neutral form of the complex and aiming at rationalizing the quenching of photoluminescence at higher pH values, the relevant stationary points along the photochemical deactivation channels for the deprotonated species were optimized. As it was expected, the protonation state of the hmip ligand has little structural effect on the coordination to the Ru(II) atom, as already shown for the iip complex and in related complexes.[16] The main structural changes are observed in the bond lengths of the deprotonated imidazo-phenol moiety, shown in detail in Figure A66. The lowest triplet excited state of the deprotonated species is of ^{3}LLCT character, as shown by the analysis of the spin density distribution at the optimized geometry (Figure 71). Therefore, as demonstrated for the excited state of the deprotonated iip complex, the fully deprotonated form of $[Ru(phen)_2(hmip)]^{2+}$ has one unpaired electron located at the phen ligands whilst the other unpaired electron is located at the hmip ligand.

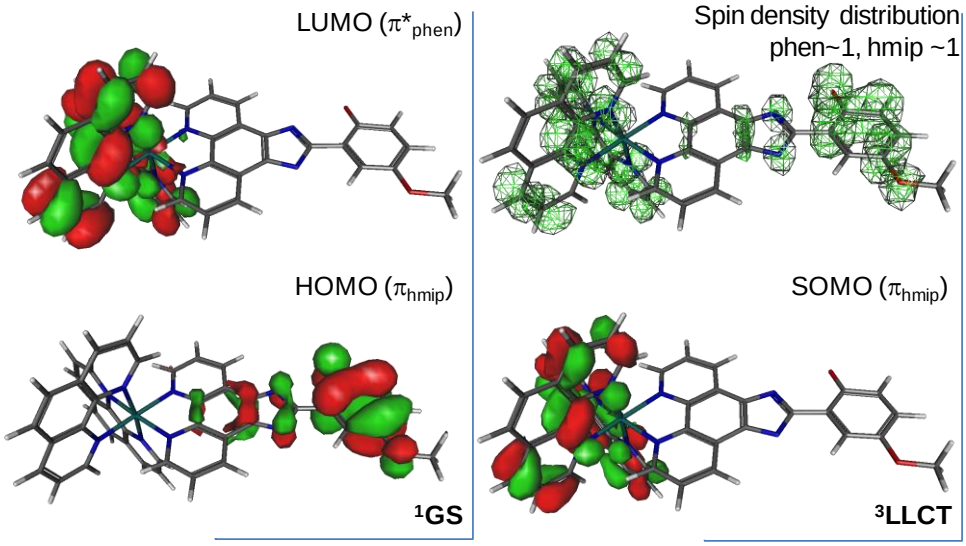

Figure 71. Ground state (^{1}GS) and excited state (^{3}LLCT) Kohn-Sham orbitals of the deprotonated form of $[Ru(phen)_2(hmip)]^{2+}$. Upper right: Spin density plot for the lowest T_1 state.

These results show that there is a drastic change on the photophysical picture of the $Ru(phen)_2(hmip)$ dye upon changes on the pH. Thus, *the nature of the lowest triplet changes from a ^{3}IL state at neutral pH to a ^{3}LLCT state at high pH values*. The theoretical emission maximums of the deprotonated species were found at 1225 and 1423 nm with the PCM-TD-DFT and ΔSCF-DFT approaches, respectively. Both calculations indicate that the luminescence is expected at low energies, with concomitant increase in the k_{nr} rate constant due to the energy-gap rule .[18]

As shown in Figure 32, the emission maximum of $[Ru(phen)_2(hmip)]^{2+}$ is experimentally observed at the same wavelength in all the 3-12 pH range. This piece of evidence demonstrates that at pH values higher than 3 the ^{3}IL state of the complex is responsible for the emissive behaviour. At higher pH values and depending on the pH equilibrium, a reduced concentration of the neutral species is expected. Therefore, the lower concentration of the emissive complex at higher pH values explains the observed photoluminescence quenching . The discrepancy between the λ_{em}^{max} obtained by theoretical calculations and the experimental one points out to a ^{3}IL-based emission due to the residual concentration of the neutral complex.

As it was mentioned above, the remarkable red-shift of the lowest triplet excited state leads to an increase of the temperature-independent non-radiative decay rate, compromising in this way the luminescence quantum yield. Another factor that might promote quenching is the change of the luminescence state type when going from pH 7 to pH 12 (namely, from ^{3}IL to ^{3}LLCT), since lower radiative decay rates are expected for the ^{3}LLCT-based, as it has been observed before.[11] Summarizing, quenching of the *non-shifted* emission band at 604 nm might originate simply from the decrease of the concentration of the neutral dye.

4.4. $[Ru(phen)_2(haip)]^{2+}$

The spectroscopic features of the haip complex are detailed in section 3.4. They were found to be similar to those of the iip complex: the luminescence intensity of the dye decreases at high pH values with little changes in the absorption profile, while the addition of copper(II) produces a significant quenching of the luminescence intensity. In order to get an insight into the main photochemical deactivation pathways, DFT and TD-DFT (B3LYP/6-31G*) calculations were performed (see Computational methods).

The approach for optimizing the geometry of $[Ru(phen)_2(haip)]^{2+}$ was the same than for the hmip complex. Hence, the geometry of the haip complex S_0 minimum was optimized starting from four geometries to yield three rotamer structures (Figure 72) where the phenol ring is coplanar with the haip ligand. Gas-phase energy differences of 8.7 and 2.0 kcal mol^{-1} were found between the two local minima and the global minimum structure. The latter is stabilized by hydrogen bonding between the N-H atom and the oxygen of the phenol moiety. One of the local minima is characterised by a hydrogen bond between the OH atom and the pyridine-like nitrogen atom of the imidazole moiety. The ΔE (2.0 kcal mol^{-1}) between the two minima indicates that both structures are likely to exist at room temperature, especially when taking into account that this result is obtained from gas-phase calculations where no solvent-specific stabilization occurs. To support the fact that both structures are possible in solution, the PCM (water) optimization of the two isomers was performed. Not only there is an inversion where the local minimum is now the global minimum, but also the energy difference between them decreases to 0.4 kcal mol^{-1}. Hence, the structure with a N-HO hydrogen bond is found to be the global minimum **GM** while the isomer NH-O is the local minimum **LM** (Figure 72).

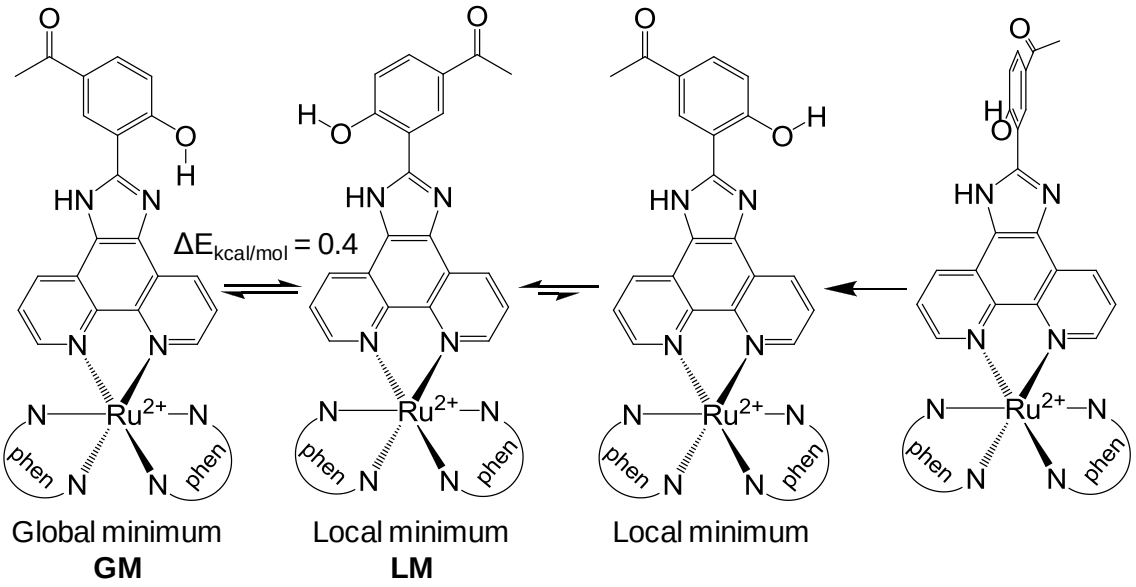

Figure 72. Structures used as inputs for the gas-phase geometry optimization (DFT B3LYP/6-31G*) of the ground state of $Ru(phen)_2(haip)^{2+}$. The energy difference was calculated from the optimized structures in water.

The PCM-TD-DFT UV-Vis spectrum of $[Ru(phen)_2(haip)]^{2+}$ was computed. The main PCM-TD-DFT vertical excitations of both **GM** and **LM** isomers are collected in section 6.2.3 (Table S13 and Table S14). Figure 73 shows the experimental absorption spectrum of the dye in PBS solution at pH 7.5, superimposed to the computed PCM-TD-DFT vertical excitation energies for both rotamers. With these PCM-TD-DFT vertical excitations, a Gaussian-convoluted spectrum was generated, and also shown in Figure 73. It can be observed that for both isomers the computed vertical excitation energies are overestimated, falling at higher energies than those found in the experimental spectrum.

In a similar way to other ruthenium(II) complexes,[11] the UV-Vis absorption spectrum comprises an intense absorption band peaking at ca. 260 nm, which is mainly due to ligand-to-ligand charge transfer (LLCT) and intra-ligand (IL) excitations (Table S13 and Table S14). A pH-sensitive band is observable at ca. 360 nm, originated mainly by metal-to-ligand charge transfer (MLCT) excitations towards the haip functional ligand, yet somewhat overestimated in energy. As in the hmip complex, the low-energy region of $[Ru(phen)_2(haip)]^{2+}$ is characterized by a broad absorption band centred at ca. 460 nm, bearing a tail which extends up to 520 nm. The excitations responsible for this band are of metal-to-ligand charge transfer (MLCT) character, although their energies are also overestimated. These results are in agreement with the experimental assignment of the absorption spectrum bands described in section 3.4. on page 112.

Following the same pattern than for the hmip complex, the TD-DFT results show that both isomers of the haip complex produce similar UV-Vis spectra with excitations at similar energies. For this reason, the photophysical study of $[Ru(phen)_2(haip)]^{2+}$ was only performed for the **GM** rotamer.

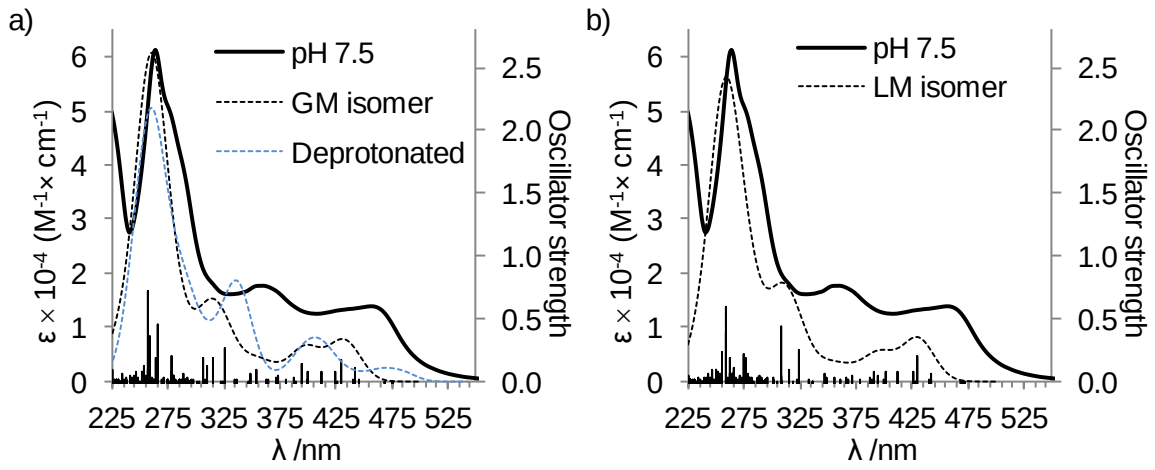

Figure 73. Absorption spectrum of $[Ru(phen)_2(haip)]^{2+}$ in 50-mM pH 7 PBS (solid black line) and computed (water) PCM-TD-DFT (B3LYP/6-31G*) vertical excitation energies for a) the global minimum **GM** isomer and b) the local minimum **LM** isomer. The dashed and blue lines represent a Gaussian convolution of the vertical excitation energies for both isomers and the mono-deprotonated species, respectively.

The pH titration study on section 3.4.1 showed a pK_a value for the protonation of the phenol moiety of 6.56. This result shows that the absorption spectrum of the haip complex at pH 7.5 must be a mixture of both acid/base species. For this reason, the PCM-TD-DFT UV-Vis spectrum of the monodeprotonated haip complex was also computed. Its main PCM-TD-DFT vertical excitations are collected in section 6.2.3 (Table S15). Figure 73a also shows a Gaussian convolution of the computed PCM-TD-DFT vertical excitation energies obtained for the monodeprotonated species. It can be observed that not only the band at 360 nm but also the tail at 475 nm are more similar to the experimental spectrum, supporting in this way the co-existence of the acid/base forms as responsible for the final absorption spectrum.

The geometries of the S_0 and T_1 minima of $[Ru(phen)_2(haip)]^{2+}$ were fully optimized. Also, the S_0 minimum geometry of $[Ru(phen)_2(haip)]^{2+}$ in its mono-deprotonated form was optimized. The computed main geometrical parameters are included in section 6.2.3, Figure A67. The geometry of the singlet ground state (S_0) for both structures is similar to that obtained for the iip complex and resembles that of other Ru(II) complexes with regard to bond lengths and bond angles.[2d, 16] In the singly-deprotonated form, a proton is shared between the oxygen and nitrogen atoms of the phenol and imidazole rings, respectively. The

ground state HOMO and LUMO Kohn-Sham orbitals for the neutral form of $[Ru(phen)_2(haip)]^{2+}$ dye are represented in Figure 74. Our results show that the HOMO is mainly of d_{z2} character while the LUMO is mainly of π* character and located throughout the phen and haip ligands. The lowest triplet excited state is of ^{3}MLCT character, as clearly reflected by the analysis of the spin density distributions, which show one unpaired electron at the Ru(d orbitals) and one at the haip ligand (see Figure 74). Similarly to the luminescent Ru(II) complexes described in the previous sections, the optimized ^{3}MLCT geometry is quite similar to that of the ground state, the main differences being found in the coordination of the ruthenium atom. A small distortion of the octahedral coordination sphere occurs, specifically in the angle formed by the equatorial N_{phen}-Ru-N_{haip} angle. This angle varies from 173.3° to 171.9° in going from the S_0 to the ^{3}MLCT geometry. As seen in Figure A67, and unlike the structurally similar hmip complex, the Ru-N bond distances do change upon excitation. The Ru-N_{haip} bond is shortened while the opposite N_{phen}-Ru bond is lengthened. This increase in electrostatic attraction between the haip ligand and the Ru(II) atom is in agreement with the charge-separated ^{3}MLCT excited state.

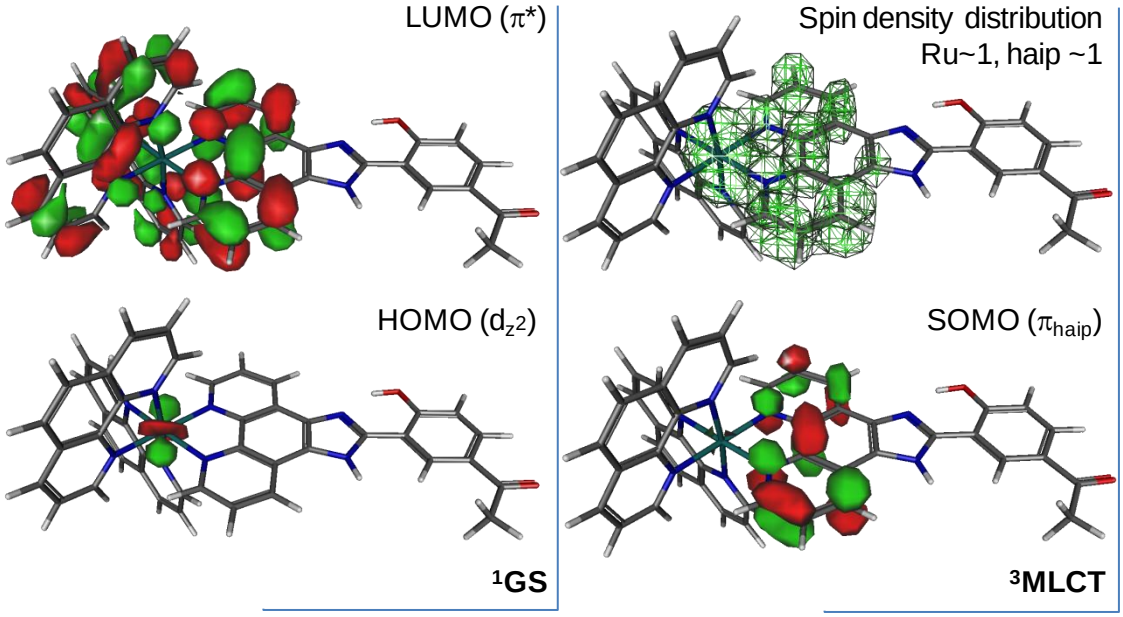

Figure 74. Ground state (^{1}GS) and excited state (^{3}MLCT) Kohn-Sham orbitals of $[Ru(phen)_2(haip)]^{2+}$. Upper right: spin density plot for the lowest T_1 state.

As observed for the iip and hmip complexes, the theoretical emission spectrum was simulated by two different approaches: i) lowest vertical triplet PCM-TD-DFT excitation at the optimized ^{3}MLCT geometry, and ii) the ΔSCF-DFT method (see Computational methods). The former yields a value of 602 nm for the luminescence maximum while a value of 599 nm

is computed for the latter. The experimental value (600 nm) is collected in Table 10, showing that both results are in excellent agreement with the experimental data.

4.4.1. Acid/base quenching of the photoluminescence

The experimental titration study of $[Ru(phen)_2(haip)]^{2+}$ described in section 3.4.1 (Table 11) revealed three pK_a values of 4.29, 6.56 and 9.26. As it was mentioned above, the luminescence intensity of the dye decreases at high pH values in spite of the small changes with the solution pH found in the absorption profile. To shed some light onto the behavior of the deprotonated haip complex, the geometry of the fully deprotonated complex was optimized. The main geometrical parameters are depicted in Figure A68.

The computed PCM-TD-DFT UV-Vis spectrum of the basic form shows a good general agreement with the experimental one, as evidenced in Figure 75. The main PCM-TD-DFT vertical excitations and the corresponding Kohn-Sham orbitals assignment are also summarized in section 6.2.3 (Table S16). The recorded absorption spectra of the Ru(II) dye in different pH values shows that, at pH > 6, the 360 nm band increases in intensity (section 3.4.1). The analysis of the PCM-TD-DFT vertical excitations of the neutral compound attributes this band to a MLCT transition towards the haip ligand (see above). For the deprotonated form, the same spectral region is now mainly composed of IL (hmip) transitions. Since IL transitions are usually more intense than the MLCT ones, this result explains the increase of the 360 nm band intensity at higher alkalinity. Moreover, this result confirms that the haip ligand is responsible for the major spectral changes upon deprotonation.

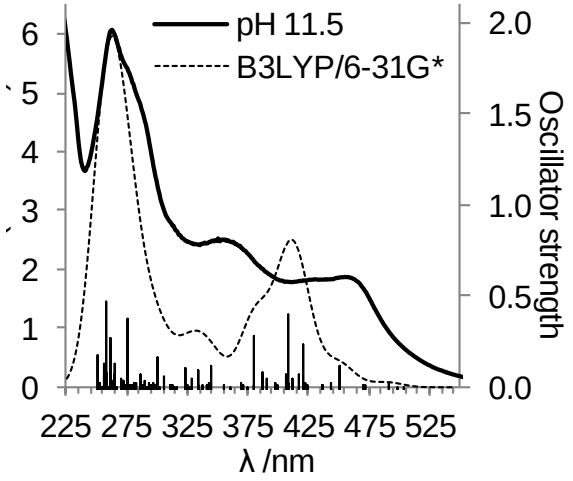

Figure 75. Absorption spectrum of $[Ru(phen)_2(haip)]^{2+}$ in 50-mM pH 11.5 PBS (solid line) and computed (water) PCM-TD-DFT (B3LYP/6-31G*) vertical excitation energies for the fully deprotonated optimized geometry. The dashed line represents a Gaussian convolution of the vertical excitation energies.

Figure 39b (section 3.4.1) depicts the variation of the luminescence of $[Ru(phen)_2(haip)]^{2+}$ with the solution pH. Following the same trends than the Ru-iip and Ru-hmip complexes, a significant decrease of the luminescence intensity of the dye is observed upon increasing pH. Similarly to the neutral form of the complex and aiming at rationalizing the photoluminescence quenching at high pH values, the relevant stationary points along the photochemical deactivation channels for the deprotonated species were optimized. As it was expected, the protonation state of the haip ligand has a small structural effect on its coordination to the Ru(II) atom, as already shown for the iip and hmip complexes and also in related complexes.[16] The main structural changes are observed in the bond lengths of the deprotonated imidazo-phenol moiety, shown in detail in Figure A68. The lowest triplet excited state of the deprotonated species is of ^{3}LLCT character, as deduced from the analysis of the spin density distribution at the optimized geometry (Figure 76). Hence, and as seen for the excited state of the deprotonated iip and haip complexes, the fully deprotonated form of $[Ru(phen)_2(haip)]^{2+}$ has one unpaired electron located at the phen ligands whilst the other unpaired electron is located at the haip functional ligand.

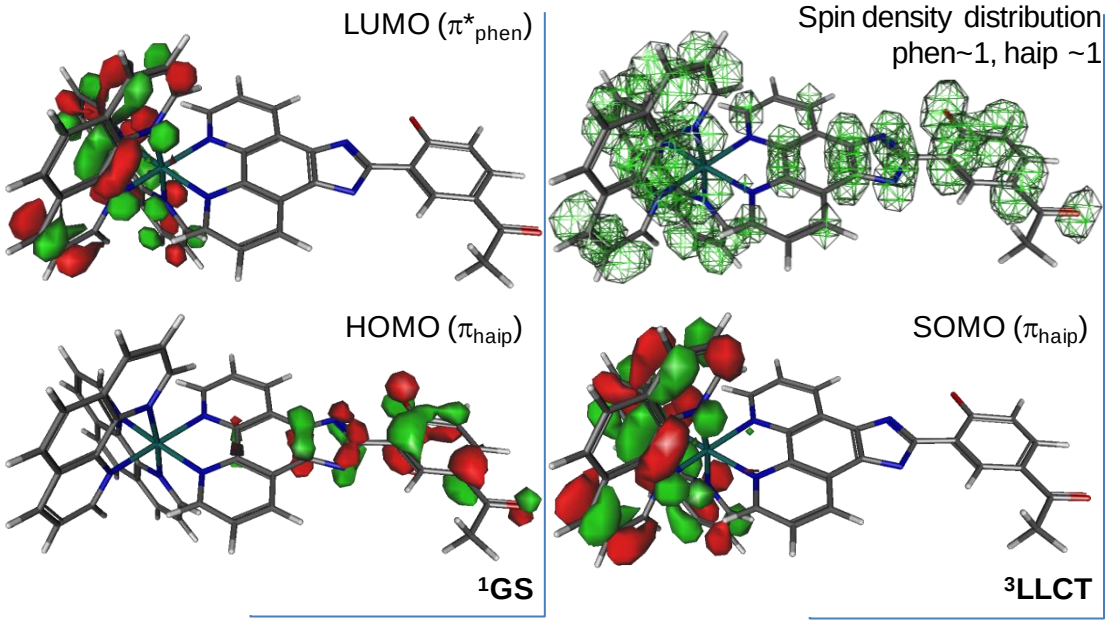

Figure 76. Ground state (^{1}GS) and excited state (^{3}LLCT) Kohn-Sham orbitals of the deprotonated form of $[Ru(phen)_2(haip)]^{2+}$. Upper right: spin density plot for the lowest T_1 state.

These results show that there is a drastic change on the photophysical picture of the $Ru(phen)_2(haip)$ dye upon changes on the solution pH. This same result was observed for the iip and hmip imidazo[4,5-*f*]-1,10-phenanthroline derivative complexes. Thus, the nature of the lowest triplet changes from a ^{3}MLCT state at neutral pH to a ^{3}LLCT state at high pH values.

The theoretical emission maximum of the deprotonated species was found to be 808 nm and 870 nm with the PCM-TD-DFT and ΔSCF-DFT approaches, respectively. Both approaches indicate that the luminescence of the complex is expected at low energies, which due to the energy-gap rule leads to a larger k_{nr} rate constant.[18]

As shown in Figure 39, the emission maximum of $[Ru(phen)_2(haip)]^{2+}$ is experimentally observed at a constant wavelength in the 4.0-11.5 pH range. This result evidences that at pH values higher than 4 the ^{3}MLCT state of the complex is responsible for the emissive behaviour. At higher pH values, and depending on the pH equilibrium, a lower concentration of the neutral species is expected. Therefore, the lower concentration of the emissive complex at higher pH values explains the observed photoluminescence quenching . The discrepancy between the λ_{em}^{max} obtained by computation and the experimental result point out to a ^{3}MLCT -based emission due to the residual concentration of the neutral complex.

As it was mentioned above, the significant red-shift of the lowest triplet excited state leads to an increase of the temperature-independent non-radiative decay rate which compromises the luminescence quantum yield. Another factor that could promote the quenching is the change of character (from ^{3}MLCT to ^{3}LLCT) of the luminescence state when going from pH 7 to pH 11.5, since lower radiative decay rates are expected for the ^{3}LLCT-based state.[11] Summarizing, *the quenching of the original emission band at 600 nm might arise just from the decrease of the concentration of the neutral species*.

4.5. $[Ru(phen)_2(bpytym)]^{2+}$

The spectroscopic features of this ruthenium complex are detailed in section 3.5. It has been shown that both the absorption and the luminescence intensity of the dye are rather insensitive to pH variation and to the presence of metal(II) ions, specifically Hg(II) ions. In order to get an insight into the photophysical properties of the dye and, more specifically, to explain the lack of luminescence quenching, DFT and TD-DFT calculations have been performed (see details in Computational methods). To this aim, the PCM-TD-DFT UV-Vis spectrum of $[Ru(phen)_2(bpytym)]^{2+}$ was computed. The main PCM-TD-DFT vertical excitations are collected in section 6.2.4 (Table S17). Figure 77 shows the experimental absorption spectrum of the dye in 50-mM pH 7.5 PBS, superimposed to the computed PCM-TD-DFT vertical excitation energies. With these PCM-TD-DFT vertical transitions, a Gaussian-convoluted spectrum was generated, which is also shown in the Figure. Similarly to other ruthenium(II) complexes,[11] the UV-Vis absorption spectrum contains an intense absorption band peaking at ca. 260 nm, comprising ligand-to-metal charge transfer (LMCT), intra-ligand (IL) and ligand-to-ligand charge transfer (LLCT) excitations (see Table S17). The shoulder at 290 nm is attributable to specific bpytym-phen ligand-to-ligand charge transfer (LLCT) excitations. The low-energy region is characterized by a broad absorption band centred at ca. 460 nm, bearing a tail which extends up to 525 nm. The excitations responsible for this band are of metal-to-ligand charge transfer (MLCT) character, despite their energy being slightly overestimated. These results are in agreement with the experimental assignment of the absorption spectrum bands performed in section 3.5.

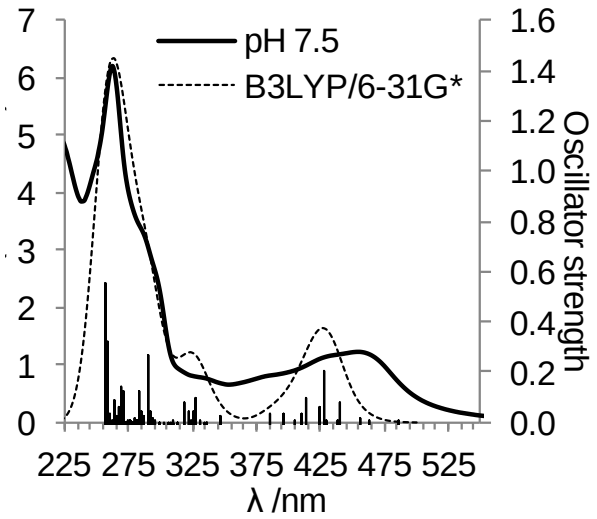

Figure 77. Absorption spectrum of $[Ru(phen)_2(bpytym)]^{2+}$ in 50-mM pH 7.5 PBS (solid black line) and computed (water) PCM-TD-DFT (B3LYP/6-31G*) vertical excitation energies. The dashed line represents a Gaussian convolution of the vertical excitation energies.

In order to get an insight into the main photochemical deactivation pathways and the luminescence quenching mechanisms, DFT (B3LYP/6-31G*) calculations were performed, which provide a continuous adiabatic description of the relevant stationary points along the photodeactivation channels. In order to characterize these mechanisms, the geometries of both S_0 and ^{3}MLCT minima of $[Ru(phen)_2(bpytym)]^{2+}$ were optimized. The resulting main geometrical parameters are included in section 6.2.4, Figure A69. The geometry of the singlet ground state (S_0) of this complex is similar to that obtained for the other ruthenium complexes of this Thesis, and resembles them with regard to bond lengths and bond angles.[2d, 16] The ground state HOMO and LUMO Kohn-Sham orbitals for the $[Ru(phen)_2(bpytym)]^{2+}$ dye are represented in Figure 78. The HOMO is of Ru-d character while the LUMO is mainly of π^*_{phen} character. The lowest triplet excited state of the complex is of ^{3}MLCT character, as clearly deduced from the analysis of the spin density distributions, which show an unpaired electron at the Ru atom and the second unpaired electron at the phen ligands (Figure 78). *Unlike the other ruthenium indicator dyes* described in this work where the lowest triplet excited state involves the functionalized ligand*, the ^{3}MLCT excited state* of $[Ru(phen)_2(bpytym)]^{2+}$ *involves the ancillary phen ligands*.

The optimized ^{3}MLCT geometry displays small changes of the octahedral coordination sphere, with an increase of the three angles formed by each N_{Li}-Ru-N_{Lii} triad. The bite angle of both phen ligands is also increased, changing from 78.8° to 79.6° in going from the S_0 to the ^{3}MLCT geometry. As observed in Figure A69, the four Ru-N_i(phen) bond distances are shortened in the ^{3}MLCT state whilst both Ru-N_i(bpytym) bond distances increases. These effects lie on the increased electrostatic interaction between Ru and the two phen ligands since the ^{3}MLCT is characterized by a formally oxidized Ru(III) and the equally (negatively) charged phen ligands.

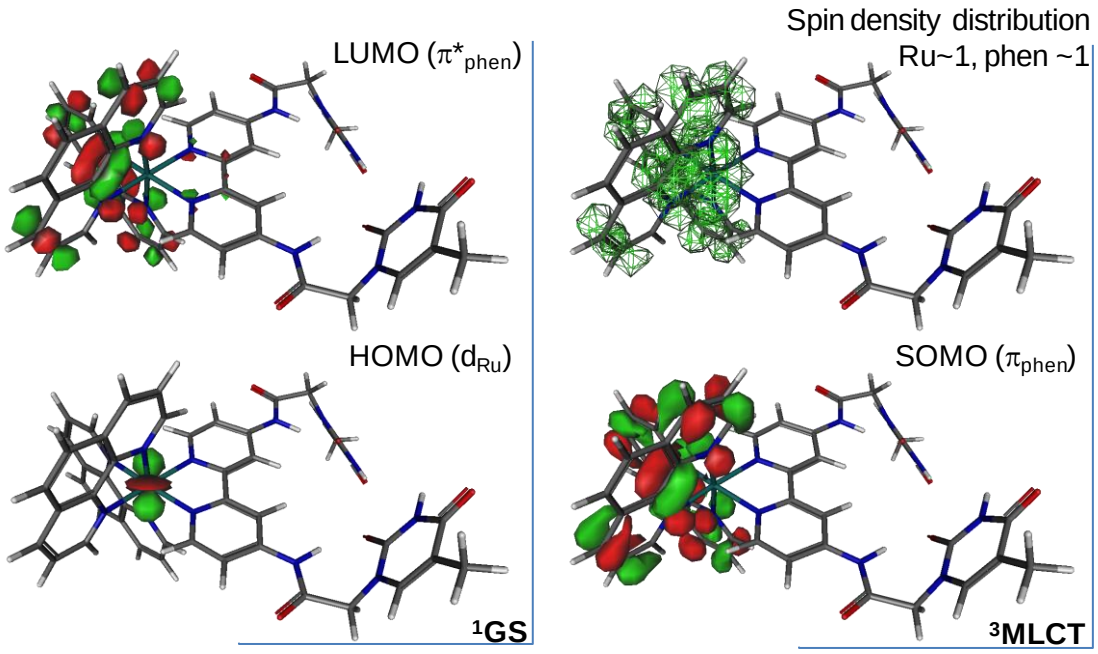

Figure 78. Ground state (^{1}GS) and excited state (^{3}MLCT) Kohn-Sham orbitals of $[Ru(phen)_2(bpytym)]^{2+}$. Upper right: spin density plot for the lowest T_1 state.

The theoretical emission spectrum was simulated by two different approaches: i) the lowest vertical triplet PCM-TD-DFT excitation at the optimized ^{3}MLCT geometry and ii) the ΔSCF-DFT method (see Computational methods). The former yields a value of 576 nm for the luminescence maximum while the latter furnishes a value of 602 nm. As collected in Table 13, the experimental value is 620 nm, showing that the ΔSCF-DFT method yields better results in the prediction (2% error /eV).

4.5.1. Addition of mercury

The effect of the addition of 5 equivalents of mercury(II) on the optical properties of the Ru(II) dye has been monitored by means of the absorption and fluorescence (section 3.5.2). Other than a general decrease of the molar absorption coefficient, no significant changes in the luminescence have been observed even at high pH values. This result indicates that either there is no binding event between $[Ru(phen)_2(bpytym)]^{2+}$ and Hg(II) or the photophysical picture of the supramolecular complex is identical to the Hg-free one. The former is unlikely as thymine is known to be one of the most specific ligands for Hg(II).[23]

In order to get an insight into the photophysical picture upon mercury(II) addition, calculations on the model $[Ru(phen)_2(bpytym)]^{2+}$-Hg entity, which bears a 1:1 ruthenium-to-mercury ratio, were performed. This is expected to be the dominant species under an excess

of Hg(II). In the supramolecular complex, the Hg(II) atom is coordinated to the two pyrrole-like nitrogen atoms of the thymine moiety in a linear fashion (see Figure 79b). This coordination mode has been previously observed in other Hg(II)-thymine complexes.[23c, d, 24] The optimized geometry (singlet ground state, S_0) is detailed in section 6.2.4, Figure A70. The main structural difference with regard to the Hg-*free* complex is observed in *the rotation of both thymine moieties*, which go from *perpendicular* to *parallel* conformations upon binding to Hg(II).

The main PCM-TD-DFT vertical excitations and their orbital assignment are collected in Table S18 (section 6.2.4). In Figure 79a, the computed UV-Vis spectra is also depicted. As pointed out before, there are very few changes observed in the absorption profile of the complex upon addition of Hg(II): only the molar absorption coefficient decreases slightly.

The computed PCM-TD-DFT vertical transitions for both the Hg-*free* dye and the supramolecular complex are indeed very similar, but in the latter some of the transitions have lower probability. This result supports the observed lack of spectral shifts and also the lower molar absorption coefficient upon Hg(II) complexation.

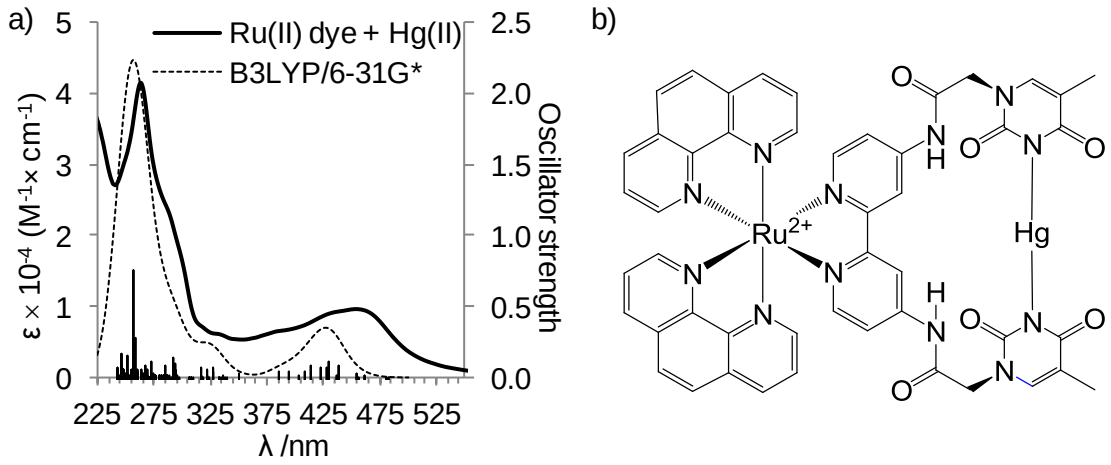

Figure 79. a) UV-Vis absorption spectrum of $[Ru(phen)_2(bpytym)]^{2+}$ in pH 7.5 phosphate buffer solution in presence of 5 equivalents of Hg(II) (solid line) and computed (water) PCM-TD-B3LYP/6-31G*//B3LYP/6-31G* vertical excitation energies. The dashed line represents a Gaussian convolution of the TD-DFT transitions. b) Structure of the supramolecular $[Ru(phen)_2(bpytym)]^{2+}$-Hg(II) complex ($S_0$).

Similarly to the Hg-*free* complex, the geometry of the lowest triplet excited state of $[Ru(phen)_2(bpytym)]^{2+}$-Hg(II) was optimized. The main geometrical parameters calculated are included in section 6.2.4, Figure A70. The ground state HOMO and LUMO Kohn-Sham orbitals for the $[Ru(phen)_2(bpytym)]^{2+}$-Hg dye are represented in Figure 80. Exactly like in the Hg-*free* dye, the HOMO is of Ru-d character while the LUMO is mainly of π^*_{phen} character.

The lowest triplet excited state is also of ^{3}MLCT character, as deduced by analysing the spin density distributions, which show an unpaired electron at the Ru atom and the second unpaired electron at the phen ligands (see Figure 80). Unlike what it was observed for the Ru-iip-Cu(II) supramolecular complex, the lowest excited state of $[Ru(phen)_2(bpytym)]^{2+}$-Hg(II) *does not involve the functional ligand*, indicating that the moiety responsible for the binding has little influence on the photophysics of the complex. Its optimized geometry is characterized by a strengthening of the coordination between phen and Ru(II) with a concomitant weakening of the Ru(II)-bpytym bond distance (Figure A70). These structural changes on the coordination sphere are consistent with a MLCT Ru-to-phen transition and are similar to what is observed for the ^{3}MLCT of the *free* dye.

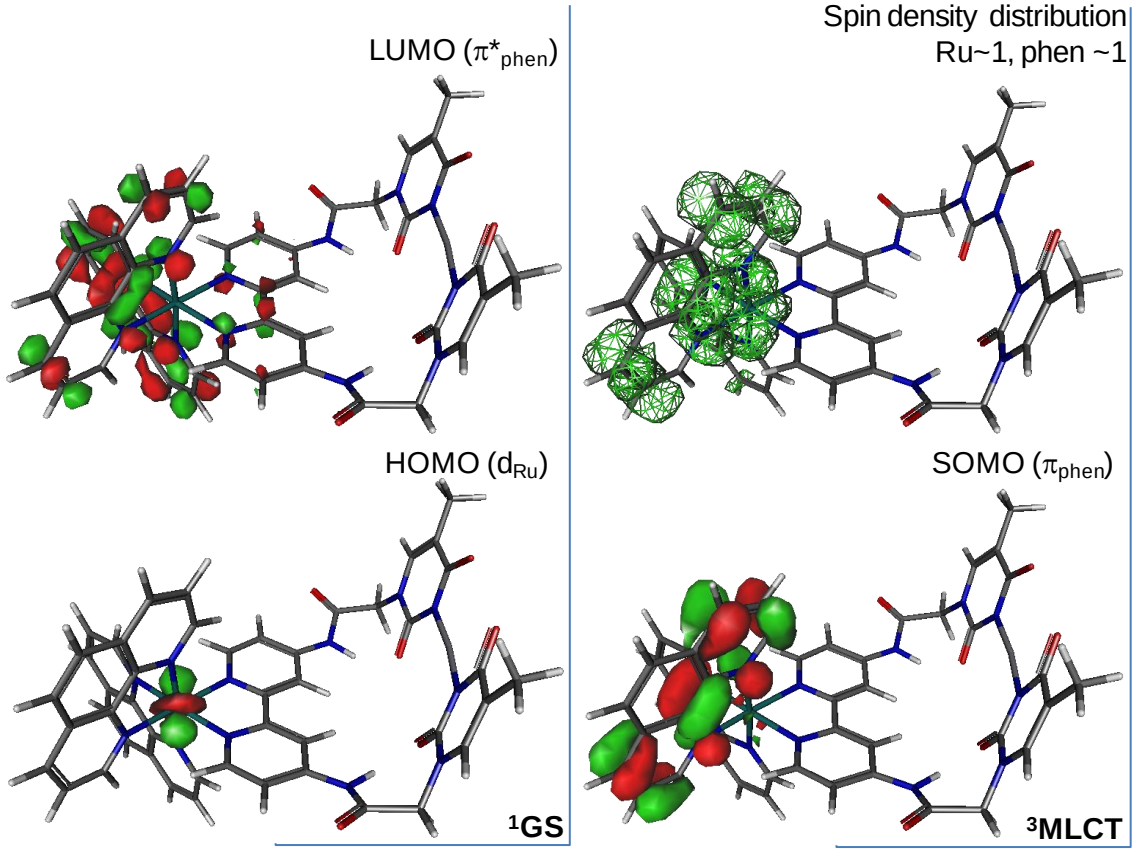

Figure 80. Ground state (^{1}GS) and excited state (^{3}MLCT) Kohn-Sham orbitals of $[Ru(phen)_2(bpytym)]^{2+}$-Hg(II). Upper right: spin density plot for the lowest T_1 state.

In section 4.2.2, it was pointed out that the first seven lowest-energy TD-DFT transitions in the excited state of $[Ru(phen)_2(iip)]^{2+}$-$CuCl_2$ involved metal-centred transitions to or from the copper moiety, which are known to be non-emissive. Similarly, in order to reproduce the emission features of the supramolecular $[Ru(phen)_2(bpytym)]^{2+}$-Hg(II)

edifice, the first five TD-DFT transitions at the ^{3}MLCT geometry were computed and the results summarized in Table S19. The first transition yields a value of 587 nm. This value is in agreement with the theoretical emission maximum of 591 nm given by the ΔSCF-DFT approach at the same geometry. As shown in Figure 52, there is no shift in the emission maximum upon addition of Hg(II), and the experimental value is 620 nm, demonstrating that both approaches yield good results.

In contrast to what was it was observed for the Ru-iip complex, the first TD-DFT transition occurs at similar energies than the experimental value and there are no Hg-centred transitions at higher energies. In fact, the closest valence Hg-centred orbitals are found at 0.05 eV (LUMO+7) and 0.09 eV (HOMO-18) above and below the LUMO and HOMO, respectively. This result shows that the Hg-centred transitions lie at much higher energies than the ^{3}MLCT state. This result seems to support that the addition of Hg(II) to an aqueous solution of $[Ru(phen)_2(bpytym)]^{2+}$ leads indeed to a binding event, but *without any changes in the photophysical properties of dye*, explaining in this way the absence of luminescence quenching upon addition of the analyte.

References

[1] a) B. Schulze, D. Escudero, C. Friebe, R. Siebert, H. Görls, S. Sinn, M. Thomas, S. Mai, J. Popp, B. Dietzek, L. González and U. S. Schubert, *Chem. Eur. J.* **2012**, *18*, 4010-4025; b) D. Escudero, B. Happ, A. Winter, M. D. Hager, U. S. Schubert and L. González, *Chem. Asian J.* **2012**, *7*, 667-671; c) B. Schulze, D. Escudero, C. Friebe, R. Siebert, H. Görls, U. Köhn, E. Altuntas, A. Baumgaertel, M. D. Hager, A. Winter, B. Dietzek, J. Popp, L. González and U. S. Schubert, *Chem. Eur. J.* **2011**, *17*, 5494-5498; d) A. Vlček Jr and S. Záliš, *Coord. Chem. Rev.* **2007**, *251*, 258-287.
[2] a) A. L. Kaledin, Z. Huang, Y. V. Geletii, T. Lian, C. L. Hill and D. G. Musaev, *J. Phys. Chem. A* **2009**, *114*, 73-80; b) S. J. Dickson, M. J. Paterson, C. E. Willans, K. M. Anderson and J. W. Steed, *Chem. Eur. J.* **2008**, *14*, 7296-7305; c) F. Zapata, A. Caballero, A. Espinosa, A. Tárraga and P. Molina, *J. Org. Chem.* **2008**, *73*, 4034-4044; d) D. A. Jose, P. Kar, D. Koley, B. Ganguly, W. Thiel, H. N. Ghosh and A. Das, *Inorg. Chem.* **2007**, *46*, 5576-5584.
[3] Z.-B. Zheng, Z.-M. Duan, Y.-Y. Ma and K.-Z. Wang, *Inorg. Chem.* **2013**, *52*, 2306-2316.
[4] a) A. D. Becke, *J. Chem. Phys.* **1993**, *98*, 1372-1377; b) C. Lee, W. Yang and R. G. Parr, *Phys. Rev. B* **1988**, *37*, 785-789.
[5] D. Figgen, G. Rauhut, M. Dolg and H. Stoll, *Chem. Phys.* **2005**, *311*, 227-244.
[6] D. Andrae, U. Häusermann, M. Dolg, H. Stoll and H. Preuss, *Theor. Chim. Acta* **1990**, *77*, 123-141.
[7] a) M. Cossi, V. Barone, B. Mennucci and J. Tomasi, *J. Chem. Phys. Lett.* **1998**, *286*, 253-260; b) B. Mennucci and J. Tomasi, *J. Chem. Phys.* **1997**, *106*, 5151-5158.
[8] M. J. Frisch, G. W. Trucks, H. B. Schlegel, G. E. Scuseria, M. A. Robb, J. R. Cheeseman, G. Scalmani, V. Barone, B. Mennucci, G. A. Petersson, H. Nakatsuji, M. Caricato, X. Li, H. P. Hratchian, A. F. Izmaylov, J. Bloino, G. Zheng, J. L. Sonnenberg, M. Hada, M. Ehara, K. Toyota, R. Fukuda, J. Hasegawa, M. Ishida, T. Nakajima, Y. Honda, O. Kitao, H. Nakai, T. Vreven, J. A. Montgomery, J. E. Peralta, F. Ogliaro, M. Bearpark, J. J. Heyd, E. Brothers, K. N. Kudin, V. N. Staroverov, R. Kobayashi, J. Normand, K. Raghavachari, A. Rendell, J. C. Burant, S. S. Iyengar, J. Tomasi, M. Cossi, N. Rega, J. M. Millam, M. Klene, J. E. Knox, J. B. Cross, V. Bakken, C. Adamo, J. Jaramillo, R. Gomperts, R. E. Stratmann, O. Yazyev, A. J. Austin, R. Cammi, C. Pomelli, J. W. Ochterski, R. L. Martin, K. Morokuma, V. G. Zakrzewski, G. A. Voth, P. Salvador, J. J. Dannenberg, S. Dapprich, A. D. Daniels, Farkas, J. B. Foresman, J. V. Ortiz, J. Cioslowski and D. J. Fox in *Gaussian 09, Revision A.02*, *Vol.* Wallingford CT, **2009**.
[9] A.-R. Allouche, *J. Comput. Chem.* **2011**, *32*, 174-182.
[10] T. Yanai, D. P. Tew and N. C. Handy, *Chem. Phys. Lett.* **2004**, *393*, 51-57.
[11] S. Campagna, F. Puntoriero, F. Nastasi, G. Bergamini and V. Balzani in *Photochemistry and photophysics of coordination compounds: Ruthenium*, (S. Campagna and V. Balzani), Photochemistry and Photophysics of Coordination Compounds I, *Vol. 280,* Springer-Verlag Berlin, Berlin, **2007**, pp. 117-214.
[12] D. Escudero and L. González, *J. Chem. Theory Comput.* **2012**, *8*, 203-213.
[13] A. Cannizzo, F. van Mourik, W. Gawelda, G. Zgrablic, C. Bressler and M. Chergui, *Angew. Chem. Int. Ed.* **2006**, *45*, 3174-3176.
[14] J.-L. Heully, F. Alary and M. Boggio-Pasqua, *J. Chem. Phys.* **2009**, *131*, 184308.
[15] J. S. Wilson, N. Chawdhury, M. R. A. Al-Mandhary, M. Younus, M. S. Khan, P. R. Raithby, A. Köhler and R. H. Friend, *J. Am. Chem. Soc.* **2001**, *123*, 9412-9417.
[16] A. Quaranta, F. Lachaud, C. Herrero, R. Guillot, M.-F. Charlot, W. Leibl and A. Aukauloo, *Chem. Eur. J.* **2007**, *13*, 8201-8211.
[17] F. Alary, M. Boggio-Pasqua, J.-L. Heully, C. J. Marsden and P. Vicendo, *Inorg. Chem.* **2008**, *47*, 5259-5266.
[18] a) J. V. Caspar and T. J. Meyer, *J. Am. Chem. Soc.* **1983**, *105*, 5583-5590; b) D. P. Rillema, G. Allen, T. J. Meyer and D. Conrad, *Inorg. Chem.* **1983**, *22*, 1617-1622.
[19] A. Bencini and F. Mani, *Inorg. Chim. Acta* **1988**, *154*, 215-219.

[20] M. P. Garcia, A. M. Lopez, M. A. Esteruelas, F. J. Lahoz and L. A. Oro, *J. Chem. Soc., Dalton Trans.* **1990**, 3465-3472.
[21] M. Schmittel and H.-W. Lin, *Angew. Chem. Int. Ed.* **2007**, *46*, 893-896.
[22] M. A. Hoselton, C. T. Lin, H. A. Schwarz and N. Sutin, *J. Am. Chem. Soc.* **1978**, *100*, 2383-2388.
[23] a) X. Liu, C. Qi, T. Bing, X. Cheng and D. Shangguan, *Anal. Chem.* **2009**, *81*, 3699-3704; b) Y. Che, X. Yang and L. Zang, *Chem. Commun.* **2008**, 1413-1415; c) Y. Miyake, H. Togashi, M. Tashiro, H. Yamaguchi, S. Oda, M. Kudo, Y. Tanaka, Y. Kondo, R. Sawa, T. Fujimoto, T. Machinami and A. Ono, *J. Am. Chem. Soc.* **2006**, *128*, 2172-2173; d) Y. Tanaka, S. Oda, H. Yamaguchi, Y. Kondo, C. Kojima and A. Ono, *J. Am. Chem. Soc.* **2007**, *129*, 244-245; e) H. Sugiyama, N. Adachi, S. Kawauchi, T. Kozasa, T. Katayama, H. Torigoe, A. Ono and Y. Tamura, *Nucleic Acids Symp. Ser.* **2005**, 215-216.
[24] Z. Wang, J. Heon Lee and Y. Lu, *Chem. Commun.* **2008**, 6005-6007.

Chapter V

Conclusions and outlook

The data gathered in the previous chapters for each polypyridyl ruthenium(II) complex is now used to allow a comparison between the indicator dyes. Some remarks on their synthesis are also discussed, namely the ^{1}H- and ^{13}C-NMR shift assignments and purification challenges.

In section 2.2, seven functional ligands were described, namely pdo, iip, hmip, haip, bpytym, nody and ap. The latter ligand, 1,10-phenanthroline-5-amine, was synthesised as a precursor for a crown ether-based ligand. Unfortunately, several attempts to its preparation (Figure 81) failed to yield the target molecule, probably due to the low reactivity of the precursor together with steric hindrance on the carboxylic acid.

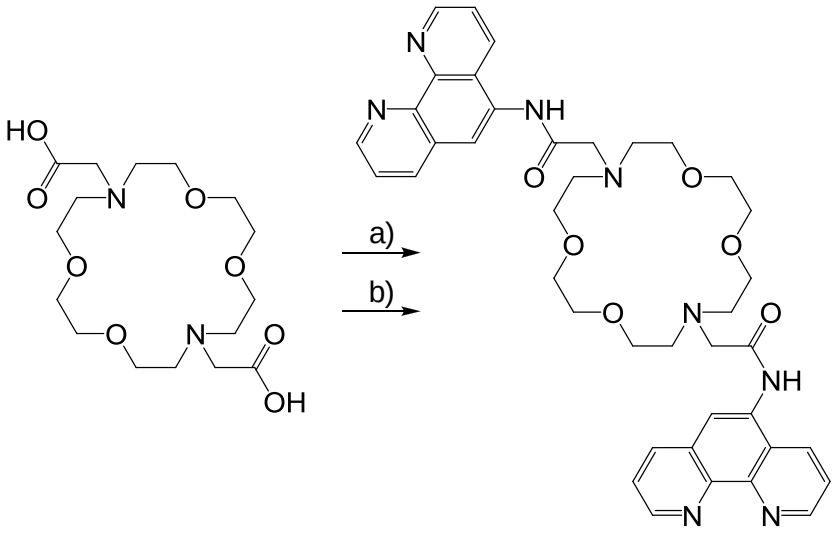

Figure 81. Attempts to prepare a phen ligand containing a crown ether moiety from 1,10-phenanthroline-5-amine (ap). a) $SOCl_2$, DMF (cat.), diisopropylethylamine, CH_2Cl_2; b) 1,1'-carbonyldiimidazole, NEt_3, CH_3CN, DMSO.

The first six ligands led to the synthesis of seven ruthenium(II) complexes, as detailed in section 2.3. These included five heteroleptic $[Ru(phen)_2L]^{2+}$ complexes, the heteroleptic $[Ru(nbpy)_2(nody)]^{2+}$ complex and the homoleptic $[Ru(nody)_3]^{2+}$ complex. The $[Ru(phen)_2(pdo)]^{2+}$ complex was synthesised to be used as precursor for preparation of any or all of the three imidazo-[4,5-*f*]-1,10-phenanthroline (iip, hmip or haip) ruthenium(II) complexes, but attempts to obtain the target compounds led to complex crude products. Figure 82 shows the five functional ligands used as precursors for the successful synthesis of the sought luminescent ruthenium dyes.

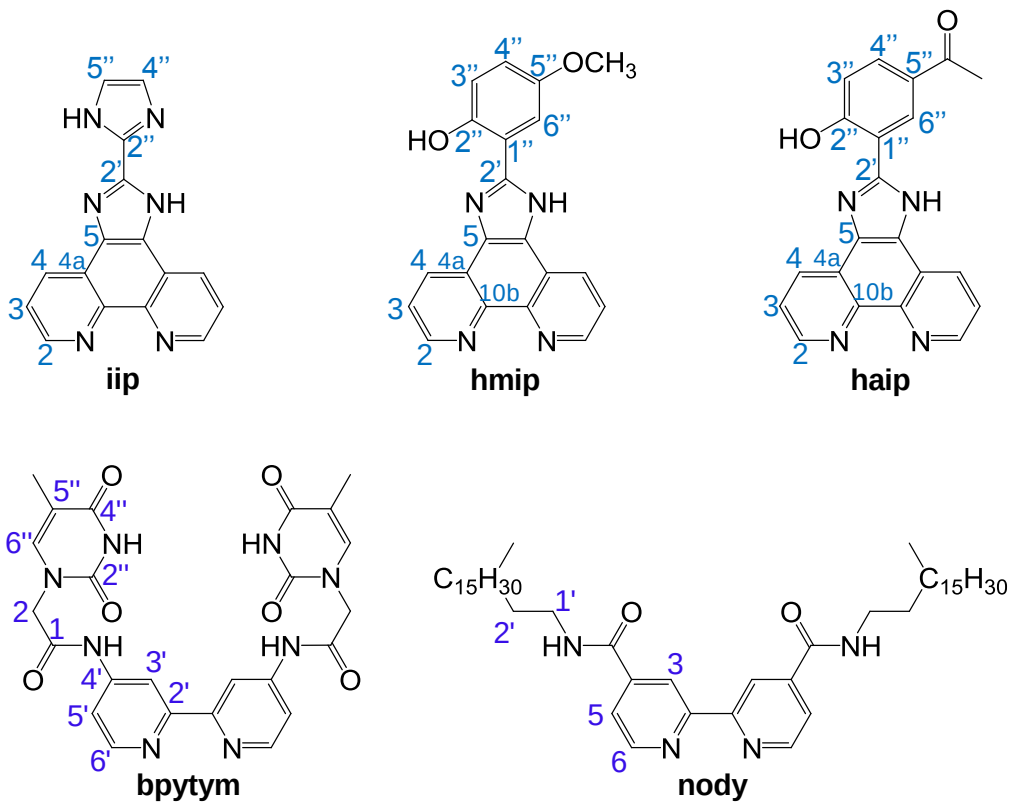

Figure 82. Structure of the five functional ligands used to synthesise the six luminescent indicator dyes. The atom numbers follow IUPAC recommendations.[1]

Obtaining spectroscopically pure ruthenium(II) dyes was a somewhat challenging and time demanding task. Although both of their precursors were previously purified (recrystallization of the ligand and purification of $Ru(phen)_2Cl_2$) a complex mixture of products was still obtained. This was partially due to the ditopic character of the functional ligand which leads to the formation of a ligand-bridged di-ruthenium complex and to similar affinities towards Ru(II) which led to the competition between both functional and ancillary ligands for the substitution. An example of the complexity of the obtained crude products is shown in Figure A38 (chapter VI), where 5 different Ru(II) species were identified by ESI-MS. The secondary products were also luminescent, and displayed similar properties than the target molecule (e.g. solubility and affinity to stationary phases). This fact precluded purification via faster methods such as precipitation or column chromatography. For this reason, the crude products were purified by means of PLC chromatography or HPCL chromatography (experimental details in section 2.1).

5.1. Ion-sensitive dyes

The four ion-sensitive heteroleptic ruthenium based dyes prepared in this work contained two 1,10-phenanthroline ancillary ligands. The latter yields higher thermal and photostability to the Ru(II) complex due to its higher affinity constants than 2,2'-bipyridine, and also shows a higher molar absorption coefficient due to the larger delocalized π system of the phen. The reason for using two identical ancillary ligands and a third functional ligand lies on the photophysical properties of the dye. The excited state of the Ru(II) dyes is usually of ^{3}MLCT character and it must be centred on the functional ligand to behave as a luminescent indicator dye. In this way any changes in the environment should lead to a response of the functional ligand and therefore a change in the excited state of the dye.

Among the synthesised functional ligands, four were tailored to the aim of ion-binding capabilities. The final design of each functional ligand was a consequence of an attempt to mimic mechanisms already found in Nature.

The biimidazole-containing iip ligand was synthesised with the purpose of showing metal ion sensitivity. The coordination between imidazole-containing ligands and Cu(II) has been widely studied.[2] Such interaction is often found in Biology, with various Cu(II)-binding imidazole-containing histidine residues present in hemocyanines, superoxide dismutase and plastocyanin.[2a, 2d] Imidazole is also known for binding other metal ions, of which imidazole complexes of Hg(II) are also reported.[3]

The high affinity of imidazole towards Cu(II) is predicted in the Pearson's classification of Hard and Soft Acids and Bases (HSAB), since this metal ion is an "intermediate" acid and the pyridine-type nitrogen of imidazole is an "intermediate" base.[4] Other features can also explain such affinity. The basicity of imidazole ($pK_a = 7.02$), makes it a worse proton acceptor than saturated amines which have higher ionization constants ($pK_a = 9.5$-10.5). This means that at a biological pH of 7.5 the imidazole moiety is still largely unprotonated whereas, in the case of primary amines, the Cu(II) ions would have to compete with protons. The same holds true for the affinity of the metal ion for the hydroxyl ion, OH^-. The pK value for the first hydrolysis step of Cu(II) and Hg(II) is 7.9 and 3.5, respectively.[5] This means that at pH 7.5, half of the copper ions are still in the *free* Cu(II) form whereas the majority of Hg(II) ions are already bound to the hydroxyl ion. Another important characteristic of imidazole is that its unsaturated pyridine-like nitrogen atom is sp^2 hybridized. This fact leads to a higher s (σ-donor) character in the orbitals used for bonding to the metal ion, which results in more stable covalent ligand-metal bonds than those involving aliphatic amines.[2a] Not surprisingly, affinity constants of Cu(II) for imidazole-containing ligands as high as 10^{14} M^{-1} have been reported.[2b, c, 2f-h, 2j, 6] Particularly efficient is the interaction with the 2,2'-biimidazole moiety due to addition of the "chelate" effect.[2e, 2i]

The two hmip and haip ligands have similar binding sites, comprised by the pyridine-like nitrogen atom of an imidazole ring and the hydroxyl group of a phenol ring. They were prepared to investigate the influence of the methoxy and acetyl substituent group at the 5'' position (*para*) of the phenol ring on the metal ion binding properties. The results obtained in the photochemical sections 3.3.2 and 3.4.2 revealed that there is indeed a dramatic change in their properties since the hmip complex is only mildly sensitive to the tested metal ions, whereas the haip complex shows a distinct selectivity towards the copper(II) ion. It was shown that the phenol group at pH 7.5 was already partly deprotonated for the haip ligand (pK_a 6.6) in contrast to the hmip ligand which has a phenol group pK_a value of 7.9. This is direct consequence of the electron releasing properties of the methoxy group in the hmip ligand vs. the electron withdrawing properties of the acetyl group in the haip ligand. The fact that at pH 7.5 the binding site of the hmip ligand is mostly of the imidazo-phenol type may account for the less sensitivity of this ligand towards metal ions. The affinity of a metal ion towards negatively charged oxygen donors like the phenoxide group is related to the acidity of the metal.[4] At higher pH values, the hmip phenol group can deprotonate and, therefore, display a higher affinity towards metal ions. However, such increased affinity is balanced by the increased stability of hydroxide complexes of those metal ions, preventing in this way complexation of the hmip ligand throughout the whole pH range.

The last ion-sensitive ruthenium complex we prepared contains the functional ligand bpytym (Figure 82), a thymine-based ligand specifically designed for Hg(II) ion sensing. Mismatched thymine-thymine base pairs in DNA are known to bind mercury ions in a linear fashion.[7] Section 3.5.2 contains the photophysical study of the bpytym complex with metal ions. Despite its specific tailored structure, not only did the luminescent ruthenium dye fail to show sensitivity towards Hg(II), but it also lacked any response to the tested metal ions. The rationalization for these findings is found in the computational chemistry section 4.5.1, where it was shown that the bound Hg(II) has no effect on the photophysical features of the ruthenium dye, so that no response is observed. Unlike the other ion-sensitive dyes, the excited state of the bpytym complex was found to be of ^{3}MLCT Ru(d-orbital)–phen(π^*) character. This result also suggests that if the ancillary ligands were to be substituted by the higher-lying LUMO of the 2,2'-bipyridine ligands, then the excited state would probably be found at the functional bpytym ligand and therefore activate the Hg(II) response.

5.1.1. Photochemical study

Table 19 summarizes the main features of the ion-sensitive ruthenium complexes in 50 mM pH 7.5 PBS buffer. As mentioned throughout the characterization of each complex in chapter 3, the four ion-sensitive dyes present similar spectroscopic properties both in their ground and excited states. The one that displays a slightly different emission energy from the others is the bpytym complex, probably due to its bpy-derivative ligand, resulting in a 20 nm bathochromic shift. The iip complex presents a much higher luminescent quantum yield (Φ_{em}) than all others (more than 6-fold the Φ_{em} measured for hmip complex). With the data from Φ_{em} and the luminescent lifetimes, it turns out that according to Eq. 41 in section 3.2, the non-radiative constant of the hmip complex is 8-fold higher than that for the iip complex ($k_{nr}^{hmip} = 6.0 \times 10^6$ s^{-1}, $k_{nr}^{iip} = 7.4 \times 10^5$ s^{-1}). This difference indicates that the low quantum yield of $[Ru(phen)_2(hmip)]^{2+}$ lies in the faster non-radiative pathways responsible for the deactivation of the excited state. Such highighly probable non-radiative pathways may also justify why the luminescence lifetime of the hmip complex changes so little after removing oxygen from solution ($\tau^{air} = 110$ ns).

The apparently small structural difference between the hmip and haip complexes, centred on the *para* substituent at the phenol group (methoxy vs. acetyl) have important consequences in the properties of the resulting molecule. As shown above, not only did the acetyl group render the hmip dye more sensitive and selective to copper, but its photophysical properties are also somewhat different: Bboth the luminescent quantum yield and excited state lifetime of $[Ru(phen)_2(haip)]^{2+}$ are significantly higher than those measured for the $[Ru(phen)_2(hmip)]^{2+}$ dye.

The measured binding constants for Cu(II) and Hg(II) are also reported in Table 19. Comparing the measured affinity for Cu(II) of the iip and haip complexes, it seems that both display 1:1 binding constants of similar magnitude, but the latter shows slightly higher 2:1 (ruthenium-to-copper) binding constants (by one order of magnitude). Nevertheless, and as already shown for the comparison between the iip-Cu and iip-Hg complexes (section 3.2.3), a higher affinity constant does not always provide a better sensitivity. Copper ions produce larger changes in both the absorption and emission spectra of $[Ru(phen)_2(iip)]^{2+}$ (Figure 27) than they do in the case of $[Ru(phen)_2(haip)]^{2+}$ (Figure 45) leading to slightly higher sensitivity of the iip dye for this metal ions. Nevertheless, we should highlight the remarkable selectivity of the haip luminescent indicator dye for copper.

Table 19. Selected spectroscopic features of the synthesised ion-sensitive ruthenium complexes in 50-mM phosphate buffer (PBS) at pH 7.5, together with their acidity constants (pK_a) and affinity for metal(II) ions (log K_i).[a]

Complex[b]	λ_{abs}^{max}/nm (ε/M^{-1} cm^{-1})	λ_{em}^{max}/nm[c]	Φ_{em}	τ/ns (Ar)	pK_a[d]	log (K_i/M^{-1})[e]	
iip	263 (80400), 283 (61100), 455 (17100)	602	0.107	1200	3.3 5.0 8.3 12.1	Cu(II) $K_1 = 6.2$ $K_2 = 5.0$	Hg(II) $K_1 = 7.8$ $K_2 = 6.2$
hmip	263 (70500), 350 (14300), 456 (14000)	604	0.016	163	2.0 7.9 10.4	n.d.	
haip	264, (61400), 360 (17650), 456 (13850)	600	0.053	950	4.3 6.6 9.3	$K_1 = 6.0$ $K_2 = 6.2$	
bpytym	263 (62200), 455 (12100)	620	0.034	538	9.4 11.9	n.d.	

[a] Estimated uncertainties: $\lambda \pm 1$ nm; $\varepsilon \pm 4\%$; $\Phi_{em} \leq 10\%$; $\tau \pm 1\%$ (1-exp.), $\pm 2\%$ (2-exp.).

[b] The names of the Ru(II) complexes have been abbreviated: iip stands for $[Ru(phen)_2(iip)]^{2+}$, hmip for $[Ru(phen)_2(hmip)]^{2+}$, haip for $[Ru(phen)_2(haip)]^{2+}$ and bpytym for $[Ru(phen)_2(bpytym)]^{2+}$.

[c] Corrected for the instrument response.

[d] pK_a values calculated from absorption spectroscopy, truncated for the sake of space.

[e] log K_i values calculated from emission spectroscopy, truncated for the sake of space. The affinity constants, K_1 and K_2, were calculated from Eq. 24.

Figure 83 shows the quenching efficiency of the four ion-sensitive ruthenium indicator dyes prepared in this work, namely, iip, hmip, haip and bpytym complexes. The response of the dyes to the metal ions (sensitivity and selectivity) is different for each dye. Nevertheless, it is clear that copper(II) is the metal ion that produces stronger luminescence quenching for the iip, hmip and haip complexes. Further spectroscopic studies on these compounds (sections 3.2.2, 3.3.2 and 3.4.2) also indicated that this metal ion produces a *static quenching* of the luminescence, unlike other metals such as lead or nickel. In contrast, the Ca(II) and Mg(II) ions have almost no effect on the luminescence of any of the ruthenium dyes. The luminescence response of $[Ru(phen)_2(bpytym)]^{2+}$ to the metallic cations differs from the other Ru(II) dyes. Not only this complex shows little to nil cation sensitivity, but it also shows an increase of the luminescence in some cases, Fe(II) being the most noticeable one (8%).

As a future perspective, and as a continuation to the goals of this Thesis, immobilization of the ruthenium dyes into suitable polymer films would allow testing their on-line response to real complex samples. Successful chemometric multivariate calibration

schemes have been reported in systems where interferences and similar responses lead to seemingly complex data matrices.[8] A consequence of all four dyes being of the polyazaheterocyclic ruthenium(II) complex family is that they all display similar spectroscopic properties. This similarity, together with different response towards the studied metal ions, means that the four indicator dyes might eventually be used together in one sensing scheme that would allow a spectroscopic-based simultaneous determination of metal ions by way of chemometrical methods. Still, there are other factors responsible for an increase in the complexity of the acquired data when it comes to real sample analysis at on-line responses. Among them, we often find that most samples are not clear but rather turbid matrices and might even absorb at the same wavelength as the luminophore. Continuous use of the opto-electronics can also lead to drifts in the signal.[9] A powerful method that can overcome the mentioned drawbacks is called Dual Lifetime Referencing (DLR). This method, introduced by I. Klimant et al.,[10] converts the changes in *intensity* of the fluorophore upon analyte addition into *lifetime*-based measurements using phase-sensitive detection. It uses two luminophores of different lifetime but similar absorption and emission spectral regions. The phase-shifted luminophore of longer lifetime is inert to the sample (e.g. a Ru(II) complex immobilized in a polymer matrix) while the shorter lifetime luminophore is the sensing dye. The resulting time-dependent signal depends on the relative luminescence intensity of both luminophores and is affected by the changes in the emission intensity of the sensing dye.[11] This method is especially useful for the Ru(II) complexes described in this Thesis, where the presence of Cu(II) or Hg(II) changes their luminescence intensity but not their excited state lifetime.

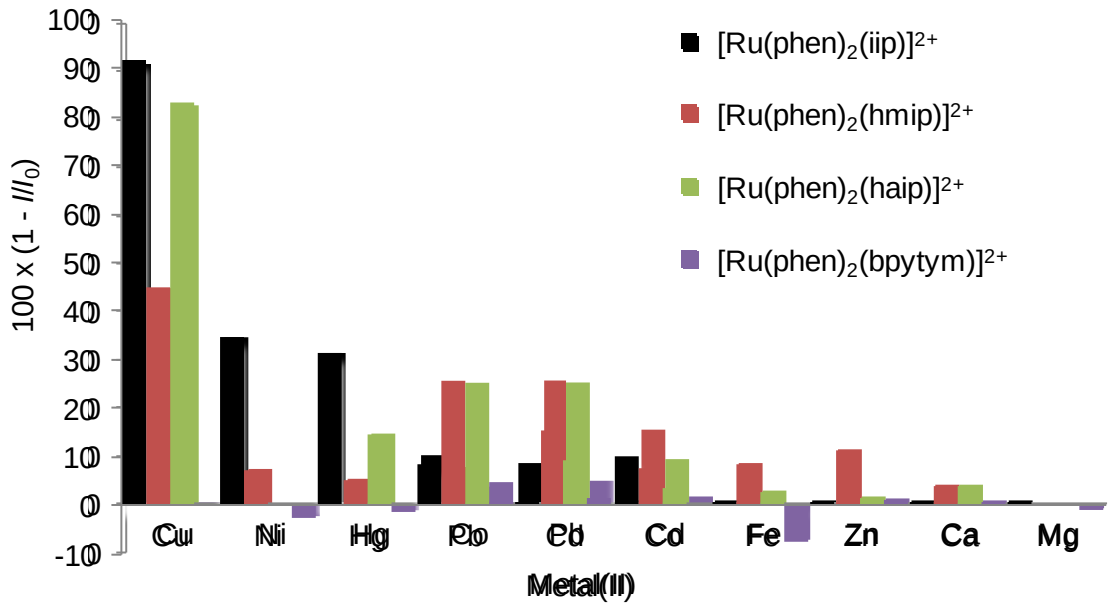

Figure 83. Quenching efficiency (%) of the four ion-sensitive Ru(II) dyes in 50-mM pH-7.5 PBS with 1% methanol, upon addition of 5 equivalents of several divalent metal ions. Negative values indicate an increase of the luminescence.

5.1.2. Computational methods

The advanced DFT and TD-DFT computational methods used in this work have allowed rationalization of the observed photophysical properties of the ion-sensitive dyes, their acid/base species and the supramolecular dyad $Ru(phen)_2(iip)$-$CuCl_2$ aimed to engineer novel Ru(II) indicator dyes. In addition, the photochemical mechanisms of deactivation of the $Ru(phen)_2(iip)$ indicator dye upon Cu(II) binding were also unveiled.

The UV-Vis spectra of the metal polypyridyls have been successfully reproduced under solvent influence (PCM) by the B3LYP hybrid functional, which outperformed the CAM-B3LYP. The theoretical emission maximums were accurately predicted by the PCM-TD-DFT and ΔSCF-DFT approaches. Table 20 summarizes the data and includes the error (in percentage) of each theoretical maximum comparing with the experimental one (in eV). Both methods yield an excellent agreement for the three $[Ru(phen)_2(iip)]^{2+}$, $[Ru(phen)_2(hmip)]^{2+}$ and $[Ru(phen)_2(haip)]^{2+}$ complexes with an error below 1% and 2% for the PCM-TD-DFT and ΔSCF-DFT approaches, respectively. The values obtained for the $[Ru(phen)_2(bpytym)]^{2+}$ complex demonstrate computed emission maximums somewhat overestimated, yielding 7% and 3% errors for the PCM-TD-DFT and ΔSCF-DFT approaches, respectively. In this case, it seems that the ΔSCF-DFT approach leads to somewhat better agreement with the experimental values for the computed complex.

The lowest triplet excited state of the ruthenium complexes was identified to be of variable character, depending on the functional ligand (see Table 20). The iip and haip complexes are of ^{3}MLCT (metal-to-*functional* ligand charge transfer) character, the hmip complex is of ^{3}IL (intra-ligand functional ligand transitions) character and the bpytym complex is of ^{3}MLCT (metal-to-*ancillary* ligand charge transfer) character. Nonetheless, a clear change in their photophysical picture occurs when increasing the pH, as their lowest-lying excited state evolves to ^{3}LLCT, justifying the lower photoluminescence quantum yield of the Ru(II) dyes at high pH values (not calculated for the bpytym complex). The structurally similar $[Ru(phen)_2(hmip)]^{2+}$ and $[Ru(phen)_2(haip)]^{2+}$ complexes differ only in the acidity of the *p*-substituted phenol ring, a methoxy (ERG) or an acetyl group (EWG), respectively. However, the computational study demonstrates that they display different excited state character (see above). Even though the theoretical investigation of the Cu(II) binding was not performed for these complexes, the DFT calculations indicate that the excited state of the dyes is indeed quite different.

Upon binding of copper(II) to $[Ru(phen)_2(iip)]^{2+}$, the lowest triplet excited state is similar to the Cu-free dye in both energy and electronic nature. However, a new copper-centred non-radiative photodeactivation pathway has been found to be responsible for the population drainage of the emissive state. Our results indicate that the luminescence quenching of the Ru(II) polypyridyl by Cu(II) ions occurs via a *photoinduced electron transfer mechanism*. In the case of mercury(II) and $[Ru(phen)_2(bpytym)]^{2+}$, the lowest triplet excited state of the latter remains the same as that of the Hg-*free* dye because the orbitals involving the Hg(II) moiety were found at low energies, deep into the core of the molecule. This result explain why the mercury ion does not participate in the photodeactivation processes of the ruthenium dye, and therefore justifies the lack of luminescence quenching.

Table 20. Calculated luminescence maximums of the novel ion-sensitive Ru(II) luminescent dyes according to the PCM-TD-DFT and ΔSCF-DFT approaches, together with the experimental values in 50 mM PBS solution.[a] Identified lowest-lying excited states according to their corresponding spin density distribution.

Ru(II) complex	λ_{em}^{max} /nm (eV; error)[b]			Excited state
	TD-DFT	ΔSCF-DFT	Exp.	
iip	607 (2.04; 1%)	595 (2.08; 1%)	602 (2.06)	^{3}MLCT (Ru to iip)
iip-2H$^+$	977	1055	602	^{3}LLCT (phen and iip)
iip+Cu^{2+}	640 (1.94; 6%)	650 (1.91; 8%)	602 (2.06)	^{4}MMLCT (Ru to iip)
hmip	601 (2.06; 0%)	591 (2.10; 2%)	604 (2.05)	^{3}IL (hmip)
hmip-2H$^+$	1225	1423	604	^{3}LLCT (phen and hmip)
haip	602 (2.06; 0%)	599 (2.07; 0%)	600 (2.07)	^{3}MLCT (Ru to haip)
haip-2H$^+$	808	870	600	^{3}LLCT (phen and haip)
bpytym	576 (2.15; 7%)	602 (2.06; 3%)	620 (2.00)	^{3}MLCT (Ru to phen)
bpytym+Hg^{2+}	587 (2.11; 5%)	591 (2.10; 5%)	620 (2.00)	^{3}MLCT (Ru to phen)

[a] Estimated uncertainty: $\lambda \pm 1$ nm.

[b] The uncertainties (in percentage) are given by the ratio of the theoretical and experimental maximums.

5.2. Polarity-sensitive dyes

Two luminescent bipyridine derivative ruthenium(II) complexes containing long alkyl chains in their chelating ligands were synthesised for the first time. The nbpy ligand consisted in a 2,2'-bipyridine functionalized with a C_9 alkyl chain at its 4,4' positions, whereas the nody ligand bears a C_{18} alkyl chain on its amide function at the 4,4' positions of a bipyridine (Figure 82, see above). The contrast between the cationic character of the Ru(II) atom and the apolar polyalkyl chains was the key in designing both homoleptic $[Ru(nody)_3]^{2+}$ and heteroleptic $[Ru(nbpy)_2(nody)]^{2+}$ dyes as polarity-sensitive indicator dyes. The heteroleptic symmetrical dye was expected to present larger changes of its dipole moment upon population of the ^{3}MLCT excited state. This would lead to higher spectroscopic changes when changing the solvent polarity.

Figure 84 shows a plot of the difference between the absorption and emission maxima ($\bar{\nu}_{abs} - \bar{\nu}_{em}$, in cm^{-1}) as a function of the solvent-specific *orientation polarizability* term (Δf, from the Lippert-Mataga Eq. 32) for both ruthenium dyes. An increase of the energy difference between the absorption and emission maxima with the increase of the solvent polarity indicates that the electronic excited state of both dyes is stabilized in polar media. The Lippert-Mataga model was insufficient to describe the behaviour of either dye in all tested solvents and, for that reason, some data points were omitted. This might be due to the presence of the amide group in the nody ligand, responsible for *specific* solvent-probe interactions which are not taken into account by the Lippert-Mataga model. Nonetheless,

even if the data points are more dispersed in the case of the heteroleptic complex, it shows a higher dependency with the solvent polarity than its homoleptic analogue (the linear regression yields slopes of 3410 cm^{-1} and 1434 cm^{-1}, respectively). This result indicates that the stabilization of the heteroleptic compound by polar solvents is higher, pointing out to a higher dipole moment of its excited state compared to the homoleptic one. A previously reported study of the $[Ru(nbpy)_3]^{2+}$ complex showed a slope of 2061 cm^{-1} in a series of solvents of different polarity.[12] Despite having zero dipole moment in its ground state, it shows a significant dependency on the solvent polarity due to the metal-to-ligand nature of its excited state. In light of the obtained results, it seems that the heteroleptic $[Ru(nbpy)_2(nody)]^{2+}$ indicator dye should perform even better as solvent polarity probe.

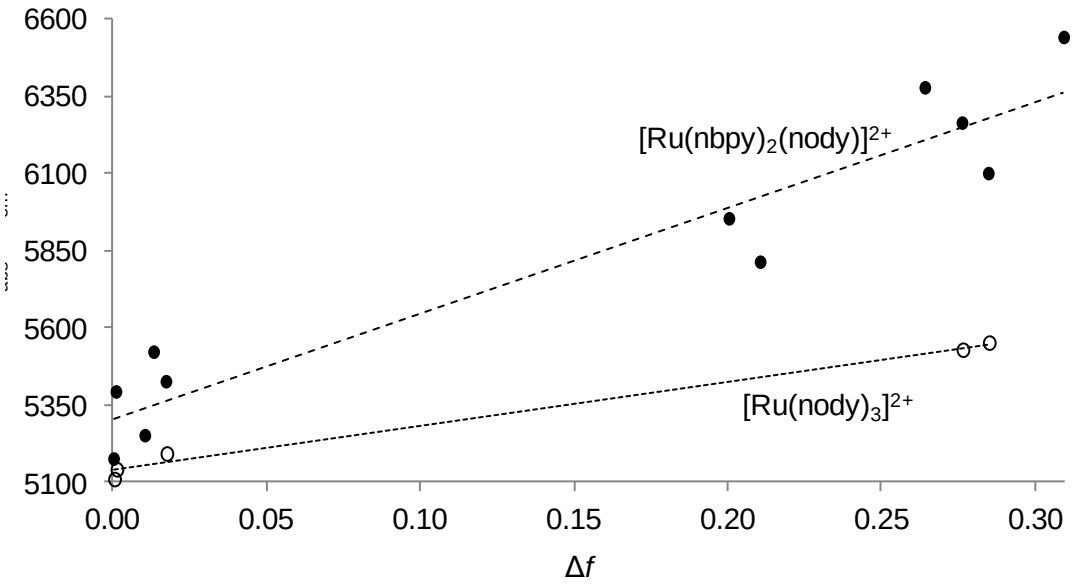

Figure 84. Energy difference between λ_{abs} and λ_{em} (ν_{abs}-ν_{abs}) for $[Ru(nbpy)_2(nody)]^{2+}$ (●) and $[Ru(nody)_3]^{2+}$ (○) as a function of the orientation polarizability term, Δf of the Lippert-Mataga equation (section 1.10). The dashed and dotted lines (b[0] = 5139 cm^{-1}; b[1] = 1434 cm^{-1} and b[0] = 5310 cm^{-1}; b[1] = 3410 cm^{-1}, respectively) have been calculated from a linear regression of the data points (● and ○, respectively).

The accessibility of the ^{3}MC non-emissive excited state of the dyes was also investigated. It was shown that while the homoleptic nody complex shows low ^{3}MC population quantum yields (0.04 and 0.03 in ethylbenzene and butyronitrile, respectively, at room temperature), the heteroleptic dye shows slightly higher values in the same solvents (0.13 and 0.10, respectively). Our study reveales that while the homoleptic complex does not readily deactivate via a dark ^{3}MC state, the heteroleptic dye undergoes some ^{3}MC deactivation by this pathway. These results are in agreement with the measured excited state

lifetimes of the dyes in media of increasing polarity. The homoleptic dye displays lower lifetimes by having a more stable ^{3}MLCT excited state than the heteroleptic analogue. The same stabilization effects lead to higher energy separation between the ^{3}MC and ^{3}MLCT excited states of the heteroleptic complex, justifying its higher emission lifetime.

5.3. Highlights

- The **fundamental contributions** of this Thesis are in the fields of:
  i) *Organic* and *Coordination Chemistry*, in the synthesis and careful structural characterization of novel heterocyclic ligands (ditopic or hydrophobic) as well as their corresponding luminescent Ru(II) complexes, useful for transition metal probes or solvent polarity probes;
  ii) *Photochemistry* and *Computational Chemistry*, where significant progress has been made in the prediction and rationalization of the excited state deactivation pathways of α-diimine Ru(II) complexes induced by either pH variations or the presence of an external transition metal coordinated by the ditopic ligand, or the temperature*;*
  iii) *Analytical Chemistry*, underlined by the contribution with an international patent (WO2011009981),[13] for the future development of opto-electronic sensing devices, capable of in-situ and online monitoring Cu(II) ion or waterborne hydrocarbons concentrations, thanks to the development of specific ionophores of which luminescent characteristics allow using the commercial technology already developed for dissolved oxygen monitoring in water;
  iv) *Environmental Chemistry*, in which this work represents a genuine possibility of having sensors capable of Cu(II) monitoring in both ground and surface waters, as well as waterborne hydrocarbons produced by accidental spillages.
- The main objective of this Thesis, –to develop novel luminescent polypyridyl Ru(II) complexes for aqueous sensing applications–, was successfully achieved with two of the four ionophores (iip and haip complexes) showing selectivity towards Cu(II). The remaining hmip and bpytym complexes do not show selectivity to any of the tested metals.
- Five new heterocyclic ligands were synthesised and thoroughly characterized. Two were bpy derivatives, nody and bpytym. The latter, together with the three imidazo[4,5-*f*]-1,10-phenanthroline derivatives iip, hmip and haip were of ditopic nature, capable of binding simultaneously to two transition metals.
- Six new tris-substituted Ru(II) complexes were synthesised and characterized. Four of them were designed for being heavy-metal sensitive dyes: $[Ru(phen)_2(iip)](PF_6)_2$;

$[Ru(phen)_2(hmip)](PF_6)_2$; $[Ru(phen)_2(haip)](PF_6)_2$ and $[Ru(phen)_2(bpytym)](PF_6)_2$. The other two were designed as solvent polarity-sensitive dyes: $[Ru(nbpy)_2(nody)](PF_6)_2$ and $[Ru(nody)_3]Cl_2$.

- A new method for purification of the bis-substituted $[Ru(phen)_2]Cl_2$ has been developed.
- The pK_a values for the heavy metal sensing dyes were determined by means of absorption and emission spectroscopy. The *electron releasing* vs *electron withdrawing* nature of the *para*-substituent in the phenol ring of hmip and haip complexes has a dramatic effect on the acidity constants of the dyes.
- The binding constant values, K_i, were determined by means of absorption and emission for $[Ru(phen)_2(iip)](PF_6)_2$ in the presence of Cu(II) and Hg(II) ions. They were also determined for the $[Ru(phen)_2(haip)](PF_6)_2$ in the presence of Cu(II). In all cases the determined stoichiometry was 2:1 ruthenium-to-metal mole ratio. The iip complex shows global binding constant (log β_{21}) values of 11.2 for Cu(II) and 14 for Hg(II). The haip complex shows a log β_{21} value of 12.2 for Cu(II).
- The two luminescent solvent sensing Ru(II) complexes (homoleptic and heteroleptic nody dyes) display opposite behaviours with increasing polarity: the emission lifetime of the homoleptic complex decreases while that of the heteroleptic complex increases. Luminescence lifetime measurements vs temperature show that the heteroleptic complex can undergo non radiative deactivation via the ^{3}MC state.
- The Lippert-Mataga model is not suited for predicting the behaviour of the both nody dyes, as some data points were scattered throughout the plot. Still, it was shown that the heteroleptic complex displays higher response to solvent polarity than its peer homoleptic compound and also higher than another homoleptic Ru(II) nbpy based luminescent probe.[12]
- The computational study (B3LYP/6-31G* DFT and TD-DFT) successfully predicted the spectroscopic properties of the heavy metal sensing dyes. The B3LYP hybrid functional produces more accurate results than the CAM-B3LYP functional. The luminescence emission maximum was predicted by two approaches, TD-DFT and Δ-SCF, the latter yielding slightly better results.
- The excited state of the iip, haip and bpytym dyes is of ^{3}MLCT nature while that of the hmip dye is of ^{3}IL nature. The $[Ru(phen)_2(iip)]^{2+}$-Cu(II) dyad was also computed, revealing an excited state Cu(II) centred state responsible for the emission quenching of the iip dye. Contrary to $[Ru(phen)_2(iip)]^{2+}$, calculations on the $[Ru(phen)_2(bpytym)]^{2+}$-Hg(II) dyad show that no change in the photophysics of the dye occurs upon binding.

References

[1] G. P. Moss, *Pure Appl. Chem.* **1998**, *70*, 143-216.
[2] a) A. E. Martell and R. D. Hancock in *Metal Complexes in Aqueous Solutions*, Modern Inorganic Chemistry, *Vol.* **1996**, p. 253; b) Q. Zeng, P. Cai, Z. Li, J. Qin and B. Z. Tang, *Chem. Commun.* **2008**, 1094-1096; c) A. Salinas-Castillo, M. Camprubi-Robles and R. Mallavia, *Chem. Commun.* **2010**, *46*, 1263-1265; d) M. Haga, *Comprehensive Coordination Chemistry II* **2004**, *1*, 125-134; e) A. Bencini and F. Mani, *Inorg. Chim. Acta* **1988**, *154*, 215-219; f) H. Fu, Y.-H. Zhou, W.-L. Chen, Z.-G. Deqing, M.-L. Tong, L.-N. Ji and Z.-W. Mao, *J. Am. Chem. Soc.* **2006**, *128*, 4924-4925; g) T. Kowalik-Jankowska, M. Ruta-Dolejsz, K. Wisniewska and L. Lankiewicz, *J. Inorg. Biochem.* **2001**, *86*, 535-545; h) J. G. Martins, P. Gameiro, M. T. Barros and H. M. V. M. Soares, *J. Chem. Eng. Data* **2010**, *55*, 3410-3417; i) F. Holmes, K. M. Jones and E. G. Torrible, *J. Chem. Soc.* **1961**, 4790-4794; j) A. Matera, J. Brasun, M. Cebrat and J. Swiatek-Kozlowska, *Polyhedron* **2008**, *27*, 1539-1555.
[3] a) A. Morsali, *J. Coord. Chem.* **2006**, *59*, 1015-1024; b) A. R. Norris, E. Buncel and S. E. Taylor, *J. Inorg. Biochem.* **1982**, *16*, 279-295.
[4] R. D. Hancock and A. E. Martell, *Chem. Rev.* **1989**, *89*, 1875-1914.
[5] D. D. Perrin, *Pure Appl. Chem.* **1969**, *20*, 133–236.
[6] N. C. Li, J. M. White and E. Doody, *J. Am. Chem. Soc.* **1954**, *76*, 6219-6223.
[7] a) A. Ono and H. Togashi, *Angew. Chem. Int. Ed.* **2004**, *43*, 4300-4302; b) A. Okamoto, Y. Ochi and I. Saito, *Bioorg. Med. Chem. Lett.* **2005**, *15*, 4279–4281; c) Y. Miyake, H. Togashi, M. Tashiro, H. Yamaguchi, S. Oda, M. Kudo, Y. Tanaka, Y. Kondo, R. Sawa, T. Fujimoto, T. Machinami and A. Ono, *J. Am. Chem. Soc.* **2006**, *128*, 2172-2173.
[8] a) K. Zarei, M. Atabati and Z. Malekshabani, *Anal. Chim. Acta* **2006**, *556*, 247-254; b) L. Gao and S. Ren, *Spectrochim. Acta, Part A* **2010**, *76*, 363-368; c) S. Lopes Pinheiro, A. Descalzo, I. Raimundo, Jr., G. Orellana and M. Moreno-Bondi, *Anal. Bioanal. Chem.* **2012**, *402*, 3253-3260.
[9] T. Mayr, I. Klimant, O. S. Wolfbeis and T. Werner, *Anal. Chim. Acta* **2002**, *462*, 1-10.
[10] I. Klimant, C. Huber, G. Liebsch, G. Neurauter, A. Stangelmayer and O. S. Wolfbeis in *Dual Lifetime Referencing (DLR) — a New Scheme for Converting Fluorescence Intensity into a Frequency-Domain or Time-Domain Information*, (B. Valeur and J.-C. Brochon), New Trends in Fluorescence Spectroscopy, *Vol. 1,* Springer Berlin Heidelberg, **2001**, pp. 257-274.
[11] G. Orellana in *Fluorescence-based sensors*, (F. Baldini, A. N. Chester, J. Homola and S. Martellucci), Optical Chemical Sensors, *Vol. 224,* Springer Netherlands, **2006**, pp. 99-116.
[12] A. M. Castro, J. Delgado and G. Orellana, *J. Mater. Chem.* **2005**, *15*, 2952-2958.

Chapter VI

Appendices

6.1. Spectra

6.1.1. 1,10-phenanthroline-5,6-dione (pdo)

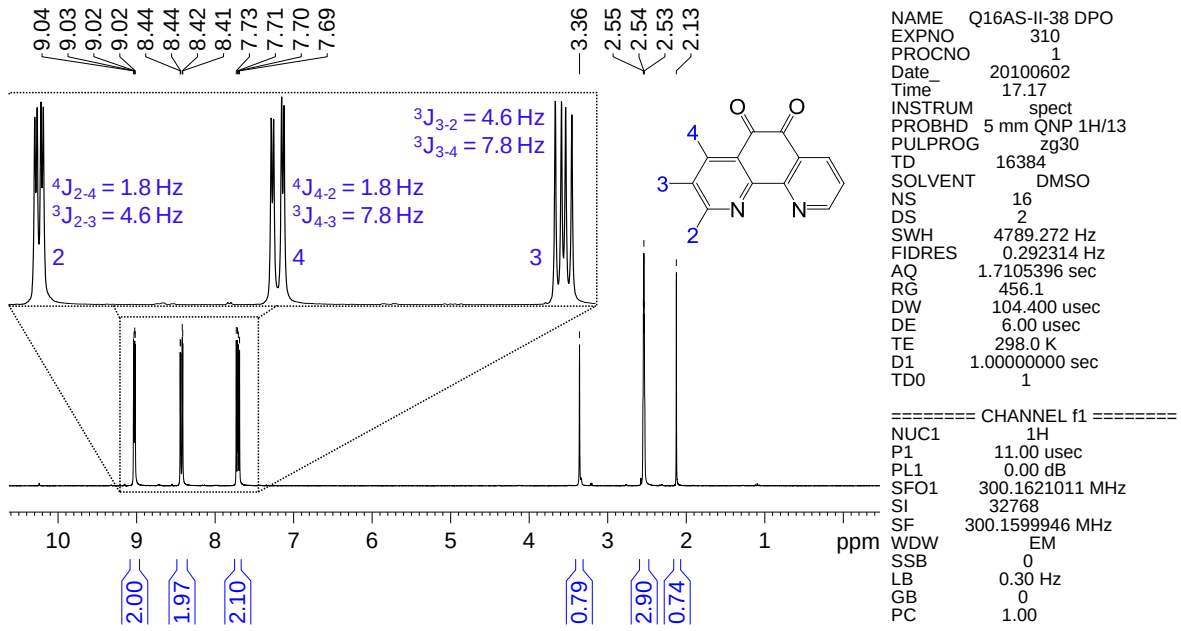

Figure A1. ^{1}H-NMR (DMSO-d_6) spectrum of 1,10-phenanthroline-5,6-dione (pdo). Preparation procedure described in section 2.2.1.

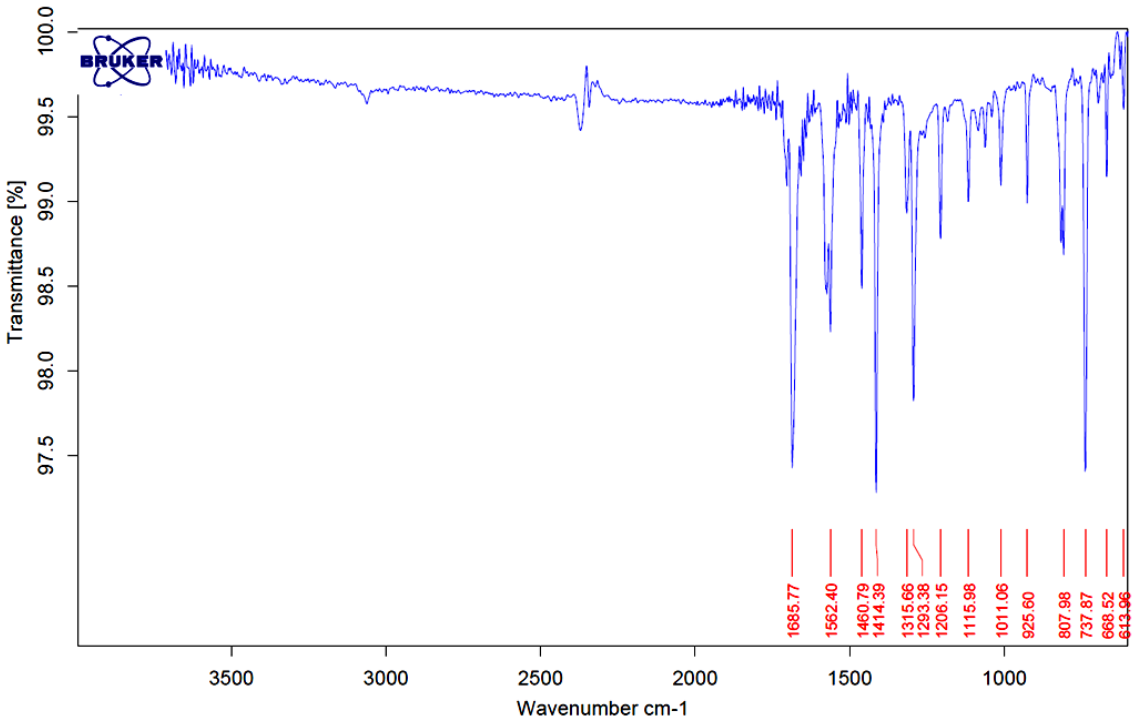

Figure A2. FT-IR (KBr disc) spectrum of 1,10-phenanthroline-5,6-dione (pdo). Preparation procedure described in section 2.2.1.

6.1.2. 2-(1H-imidazol-2-yl)-1H-imidazo[4,5-*f*]-1,10-phenanthroline (iip)

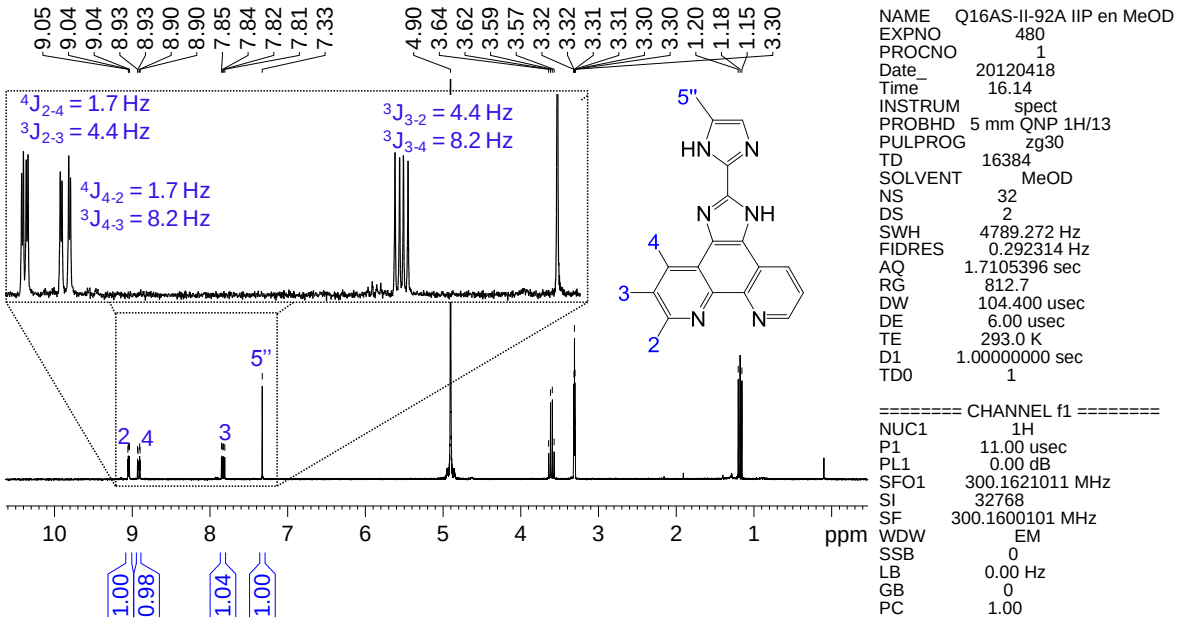

Figure A3. ^{1}H-NMR (MeOD-d_4) spectrum of 2-(1H-imidazol-2-yl)-1H-imidazo[4,5-*f*]-1,10-phenanthroline (iip). Preparation procedure described in section 2.2.2.

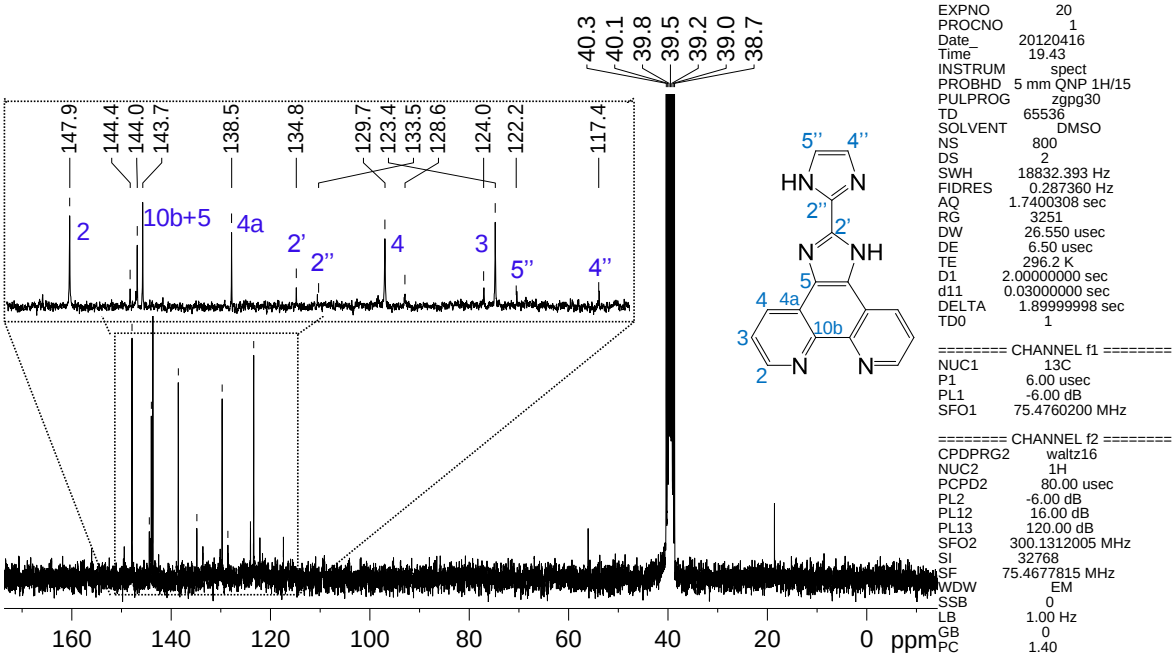

Figure A4. ^{13}C-NMR (DMSO-d_6) spectrum of 2-(1H-imidazol-2-yl)-1H-imidazo[4,5-*f*]-1,10-phenanthroline (iip). Preparation procedure described in section 2.2.2.

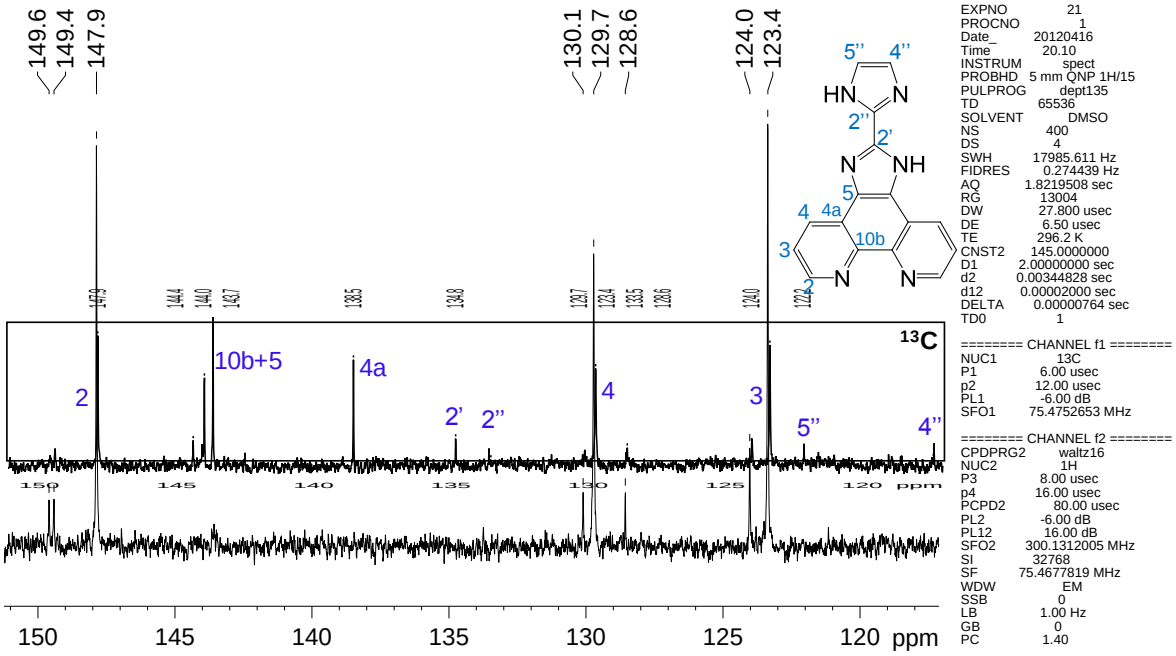

Figure A5. ^{13}C-NMR DEPT 135 (DMSO-d_6) spectrum of 2-(1H-imidazol-2-yl)-1H-imidazo[4,5-*f*]-1,10-phenanthroline (iip). The ^{13}C-NMR spectrum is inserted for comparison. Preparation procedure described in section 2.2.2.

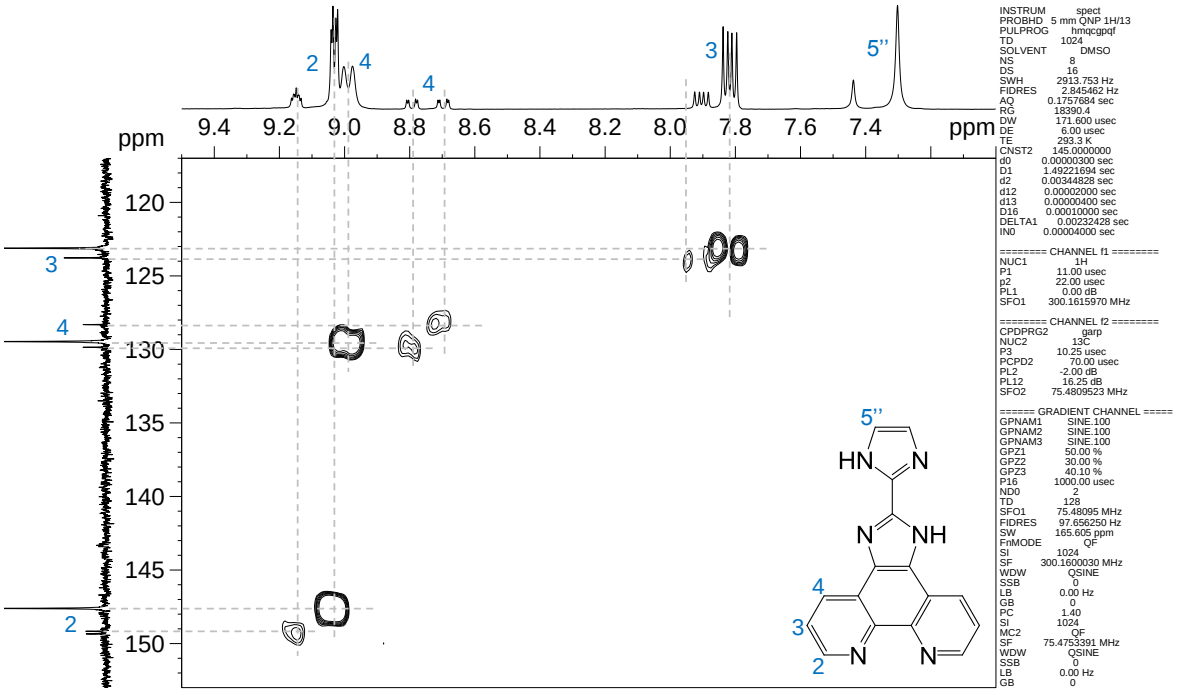

Figure A6. ^{1}H-^{13}C HMQC NMR (DMSO-d_6) spectrum of 2-(1H-imidazol-2-yl)-1H-imidazo[4,5-*f*]-1,10-phenanthroline (iip). For the sake of clarity, the spectrum on the left axis is the ^{13}C-NMR DEPT 135. Preparation procedure described in section 2.2.2. Chemical shifts assignment discussed on section 2.4.

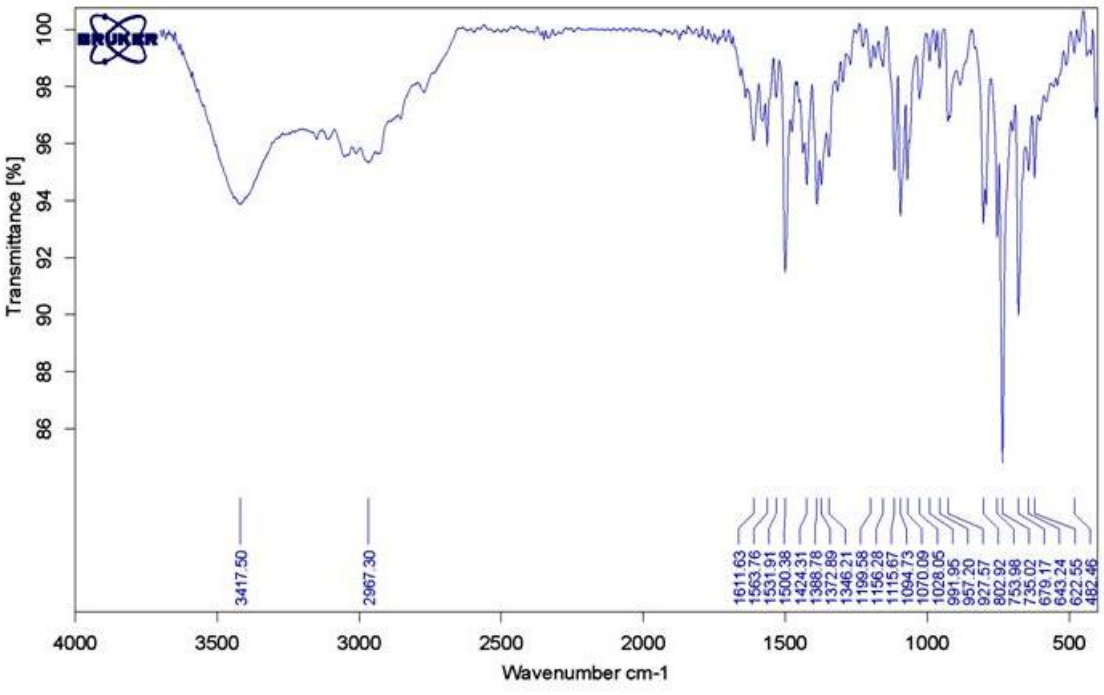

Figure A7. FT-IR (KBr disc) spectrum of 2-(1H-imidazol-2-yl)-1H-imidazo[4,5-*f*]-1,10-phenanthroline (iip). Preparation procedure described in section 2.2.2.

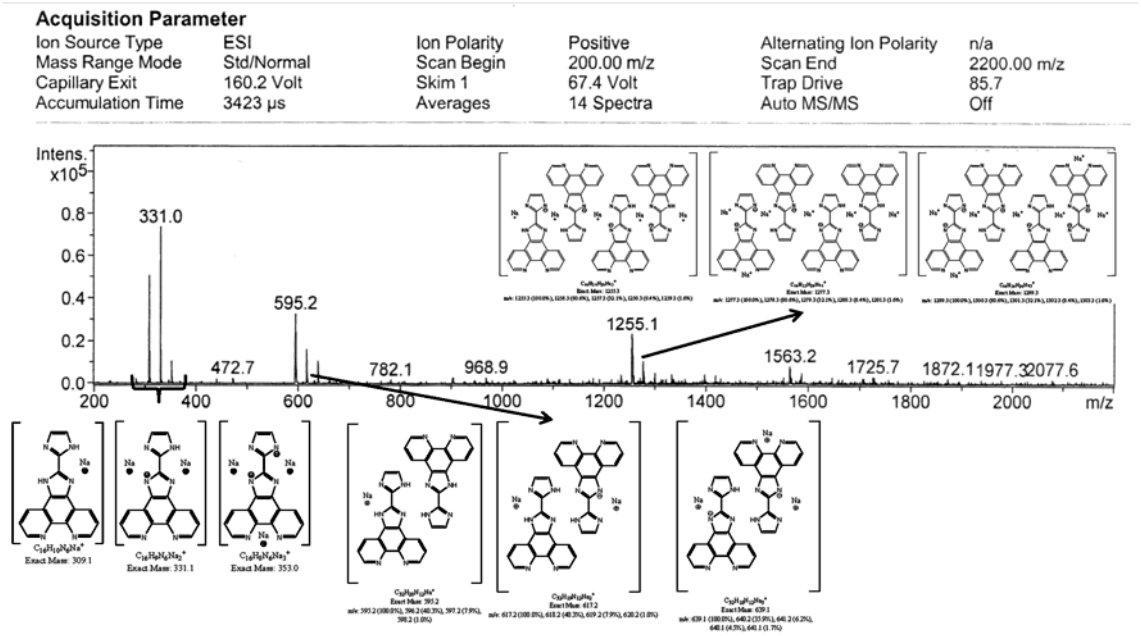

Figure A8. ESI-MS (positive) spectrum of the ditopic ligand 2-(1H-imidazol-2-yl)-1H-imidazo[4,5-*f*]-1,10-phenanthroline (iip). Preparation procedure described in section 2.2.2.

6.1.3. 2-(1H-imidazo[4,5-*f*][1,10]phenanthrolin-2-yl)-4-methoxyphenol (hmip)

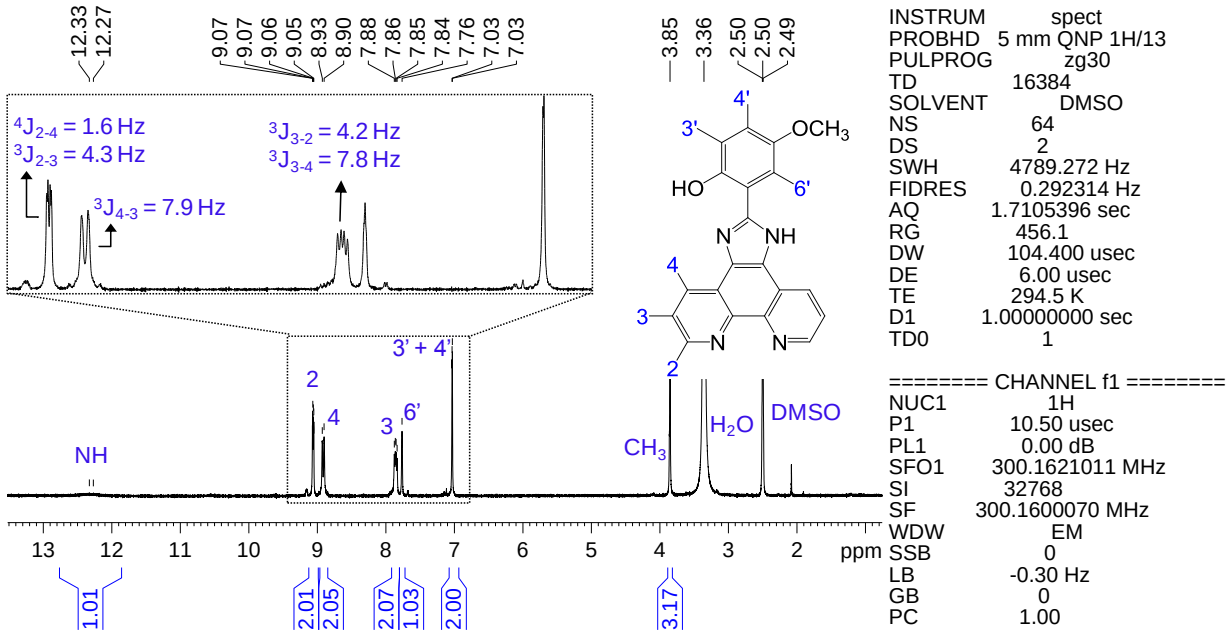

Figure A9. ^{1}H-NMR (DMSO-d_6) spectrum of 2-(1H-imidazo[4,5-*f*]-1,10-phenanthrolin-2-yl)-4-methoxyphenol (hmip). Preparation procedure described in section 2.2.3.

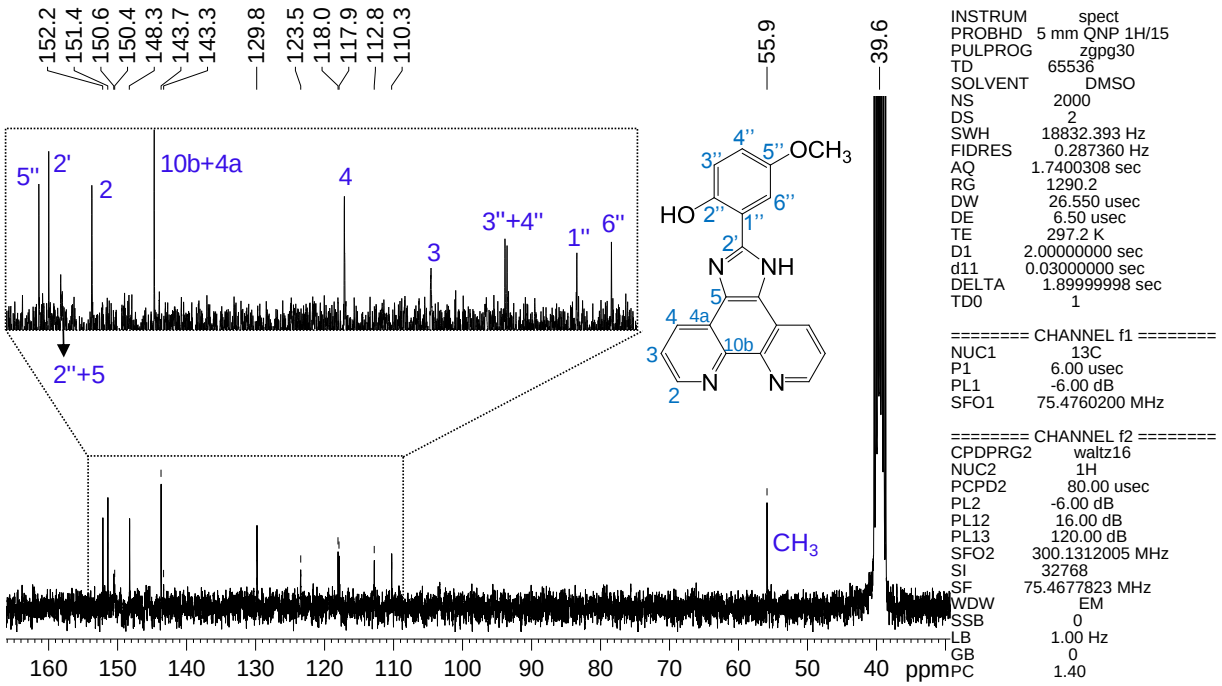

Figure A10. ^{13}C-NMR (DMSO-d_6) spectrum of 2-(1H-imidazo[4,5-*f*]-1,10-phenanthrolin-2-yl)-4-methoxyphenol (hmip). Preparation procedure described in section 2.2.3.

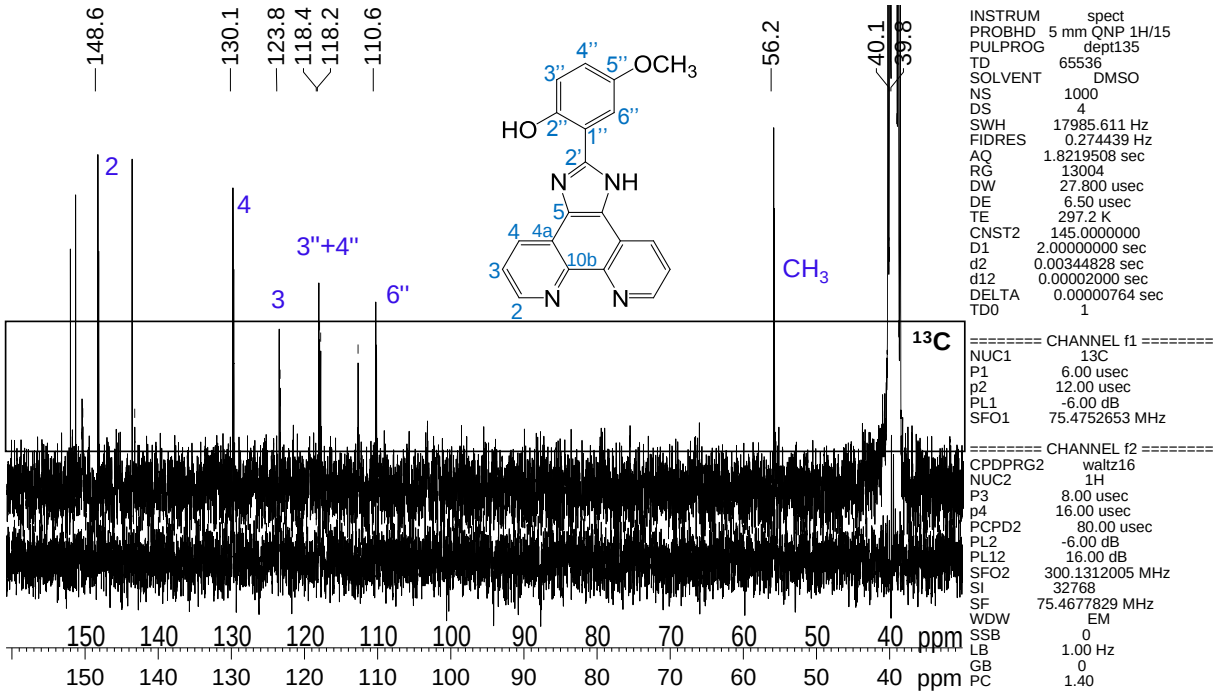

Figure A11. ^{13}C-NMR dept 135 (DMSO-d_6) spectrum of 2-(1H-imidazo[4,5-*f*]-1,10-phenanthrolin-2-yl)-4-methoxyphenol (hmip). Preparation procedure described in section 2.2.3.

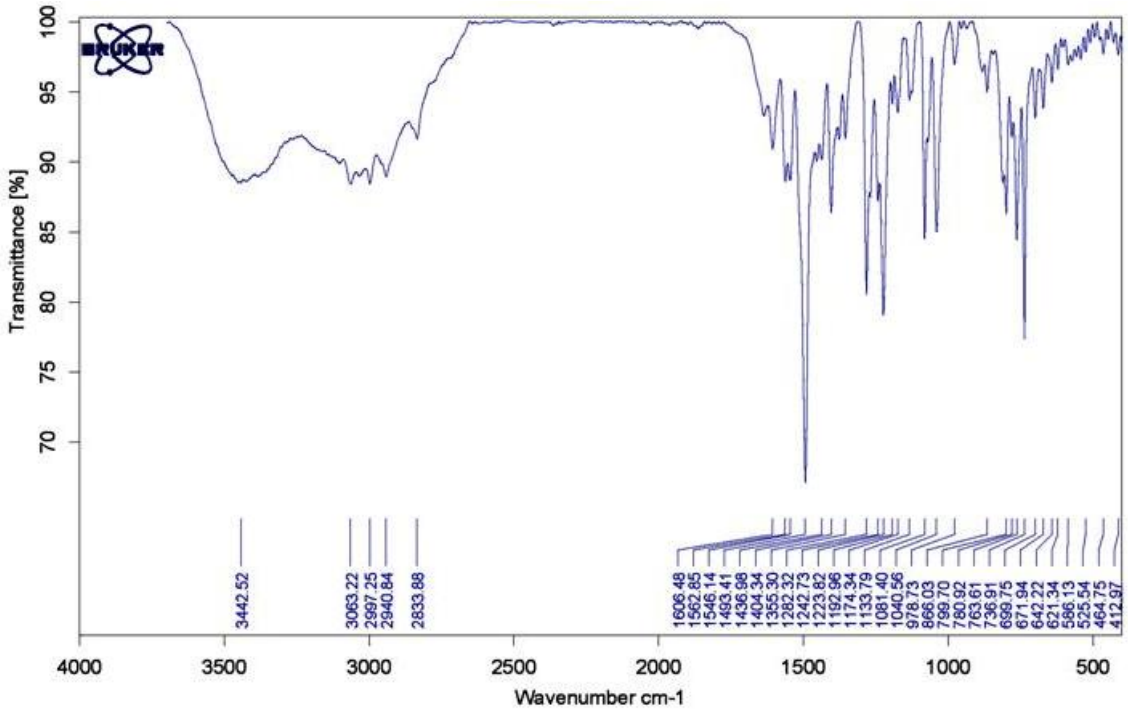

Figure A12. FT-IR (KBr disc) spectrum of 2-(1H-imidazo[4,5-*f*]-1,10-phenanthrolin-2-yl)-4-methoxyphenol (hmip). Preparation procedure described in section 2.2.3.

6.1.4. 5-Acetyl-2-hydroxybenzaldehyde (ahb)

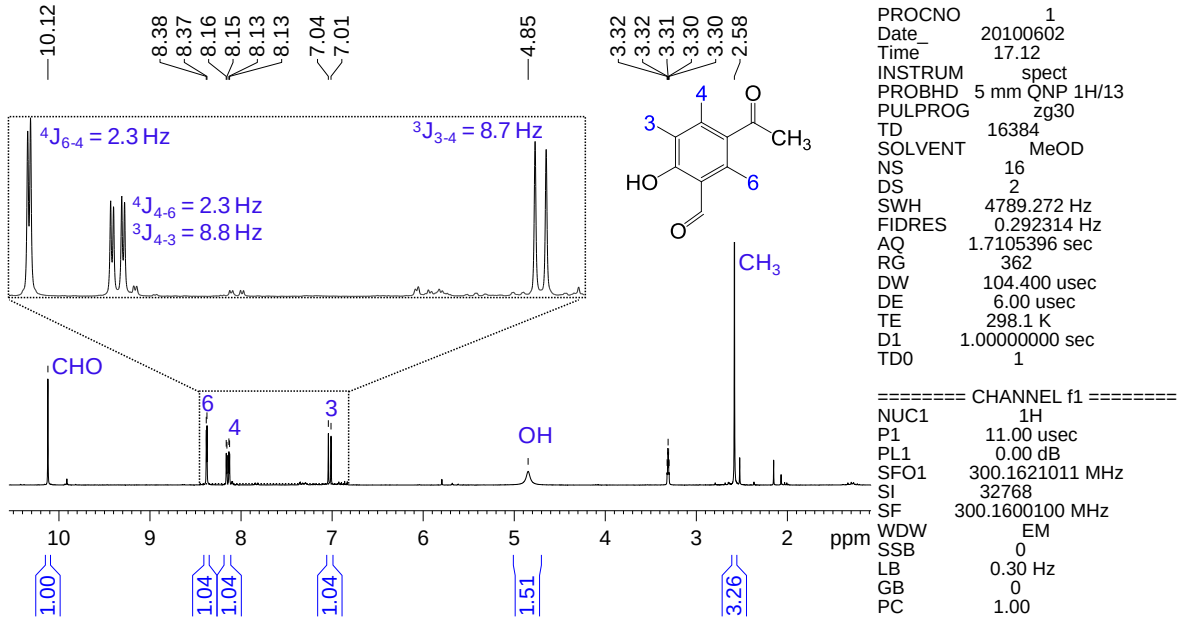

Figure A13. ^{1}H-NMR (MeOD-d_4) spectrum of 5-acetyl-2-hydroxybenzaldehyde (ahb). Preparation procedure described in section 2.2.4.

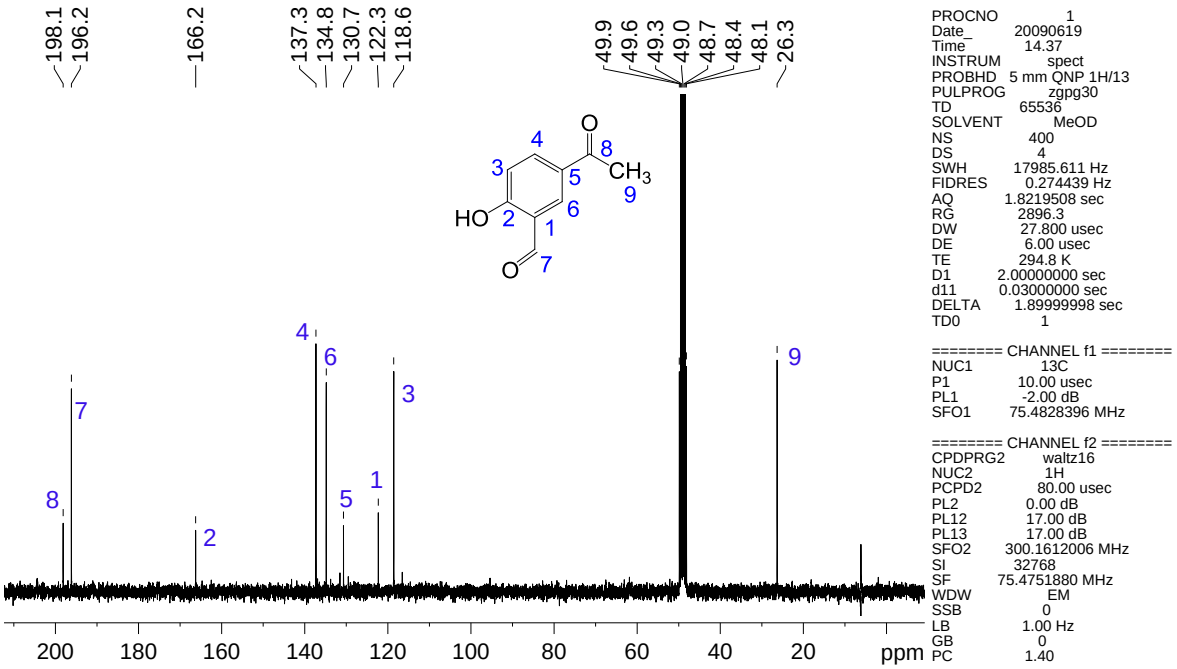

Figure A14. ^{13}C-NMR (MeOD-d_4) spectrum of 5-acetyl-2-hydroxybenzaldehyde (ahb). Preparation procedure described in section 2.2.4.

6.1.5. 1-(4-Hydroxy-3-(1H-imidazo[4,5-*f*]-1,10-phenanthrolin-2-yl)phenyl)ethanone (haip)

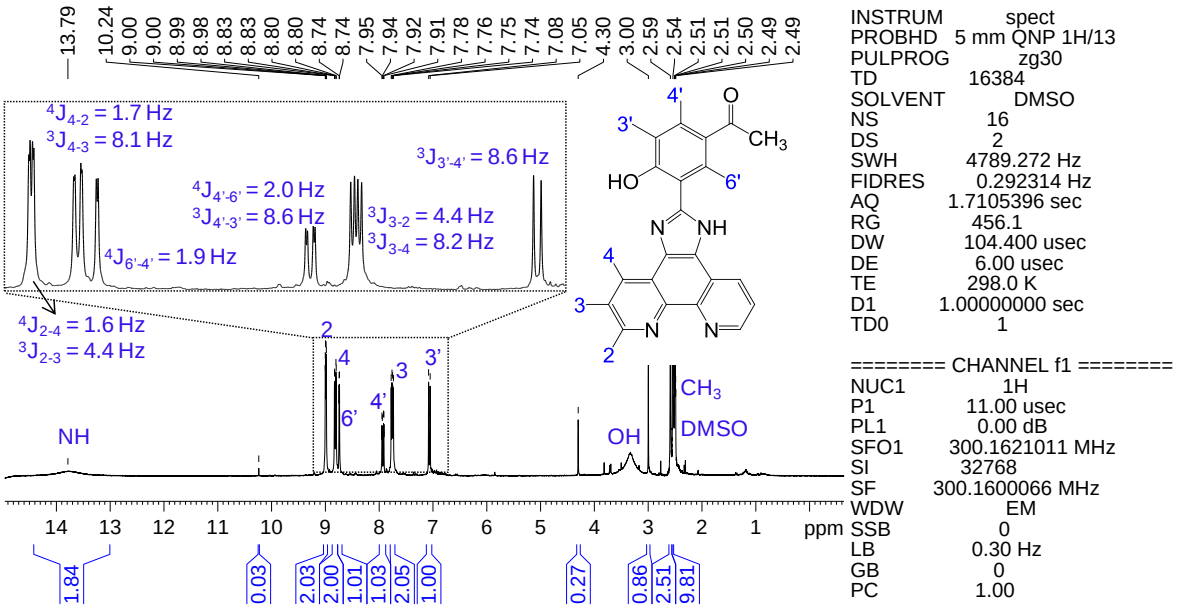

Figure A15. ^{1}H-NMR (DMSO-d_6) spectrum of 1-(4-Hydroxy-3-(1H-imidazo[4,5-*f*]-1,10-phenanthrolin-2-yl)phenyl)ethanone (haip). Preparation procedure described in section 2.2.5.

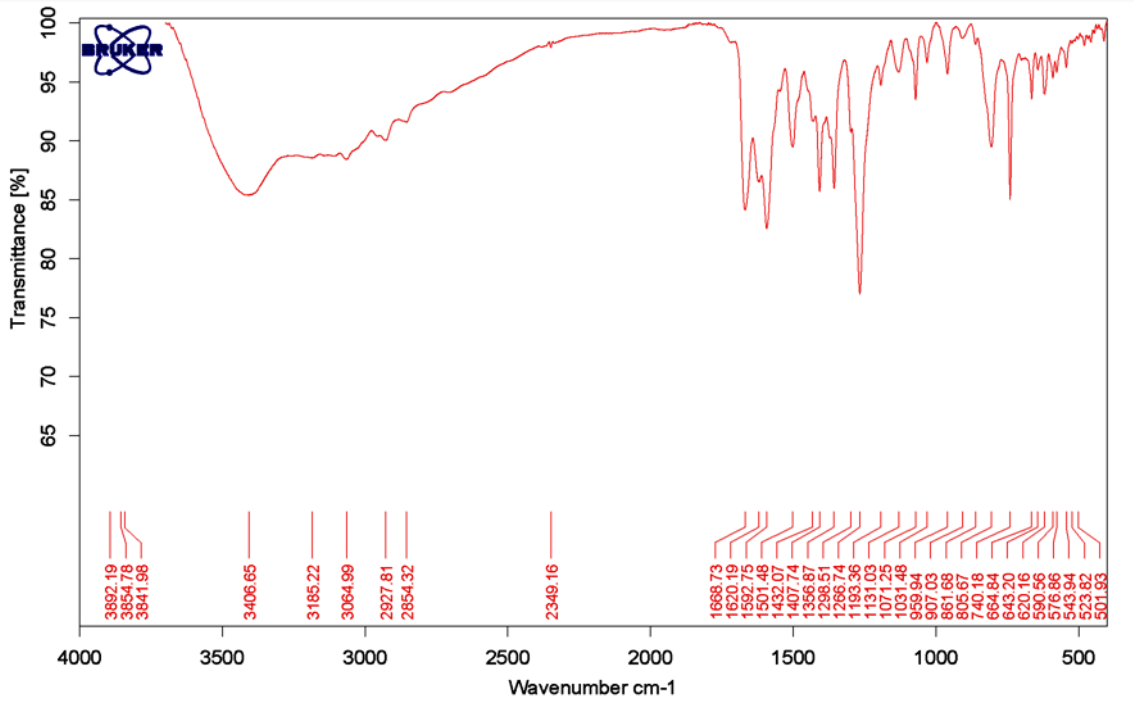

Figure A16. FT-IR (KBr disc) spectrum of 1-(4-Hydroxy-3-(1H-imidazo[4,5-*f*]-1,10-phenanthrolin-2-yl)phenyl)ethanone (haip). Preparation procedure described in section 2.2.5.

6.1.6. 2,2'-Bipyridine-4,4'-diamine (dab)

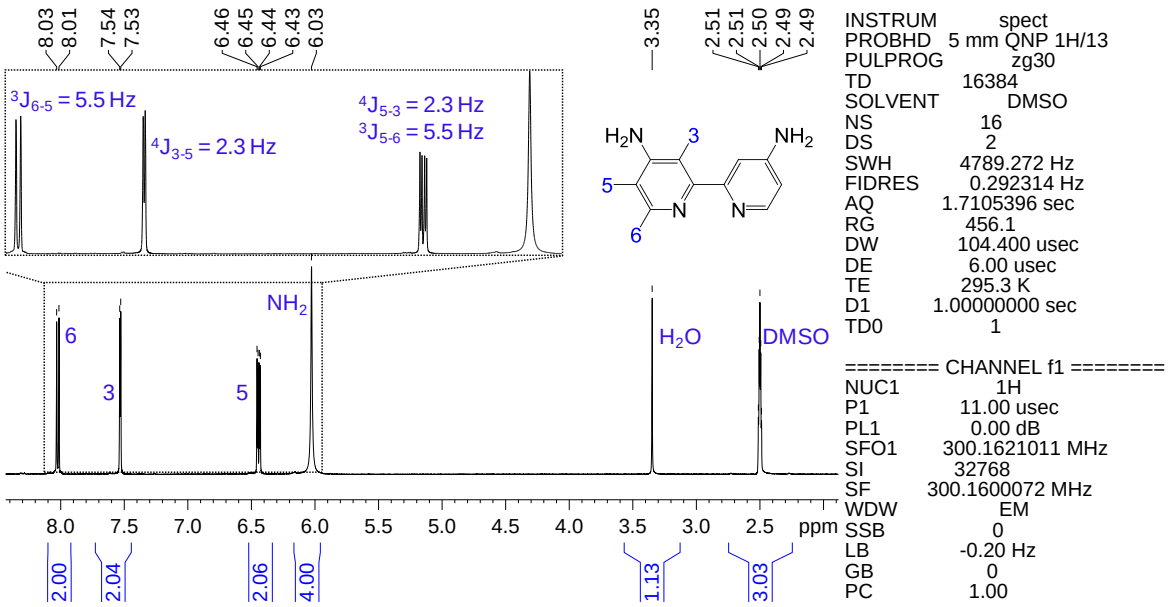

Figure A17. ^{1}H-NMR (DMSO-d_6) spectrum of 2,2'-Bipyridine-4,4'-diamine (dab). Preparation procedure described in section 2.2.6.

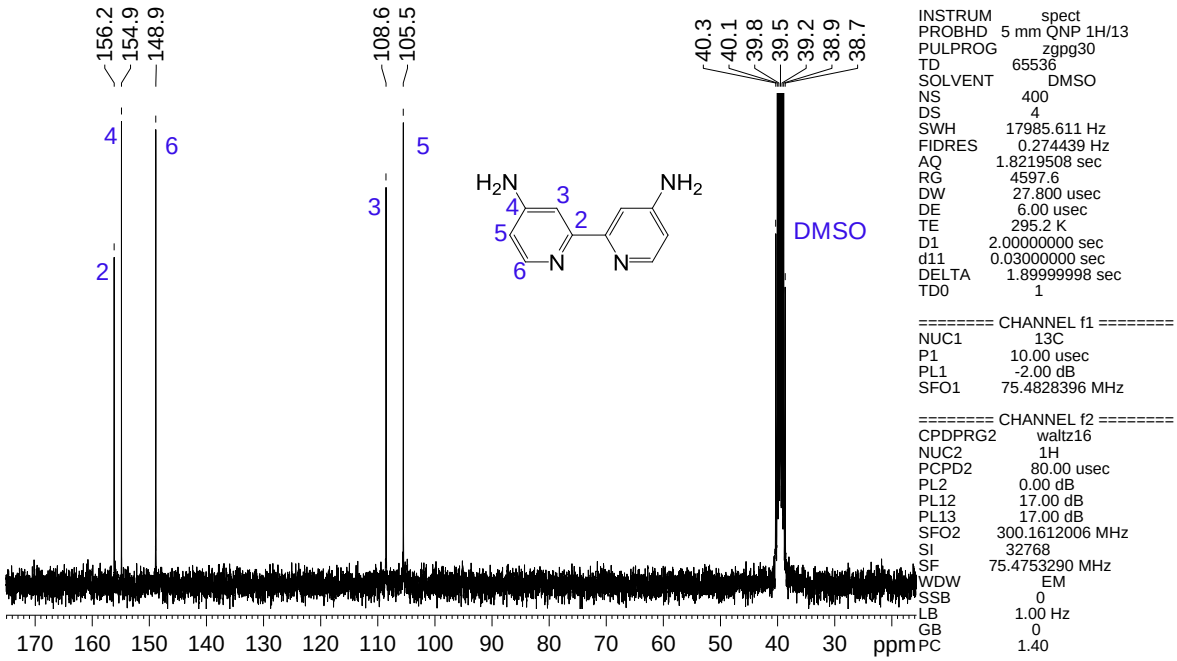

Figure A18. ^{13}C-NMR (DMSO-d_6) spectrum of 2,2'-Bipyridine-4,4'-diamine (dab). Preparation procedure described in section 2.2.6.

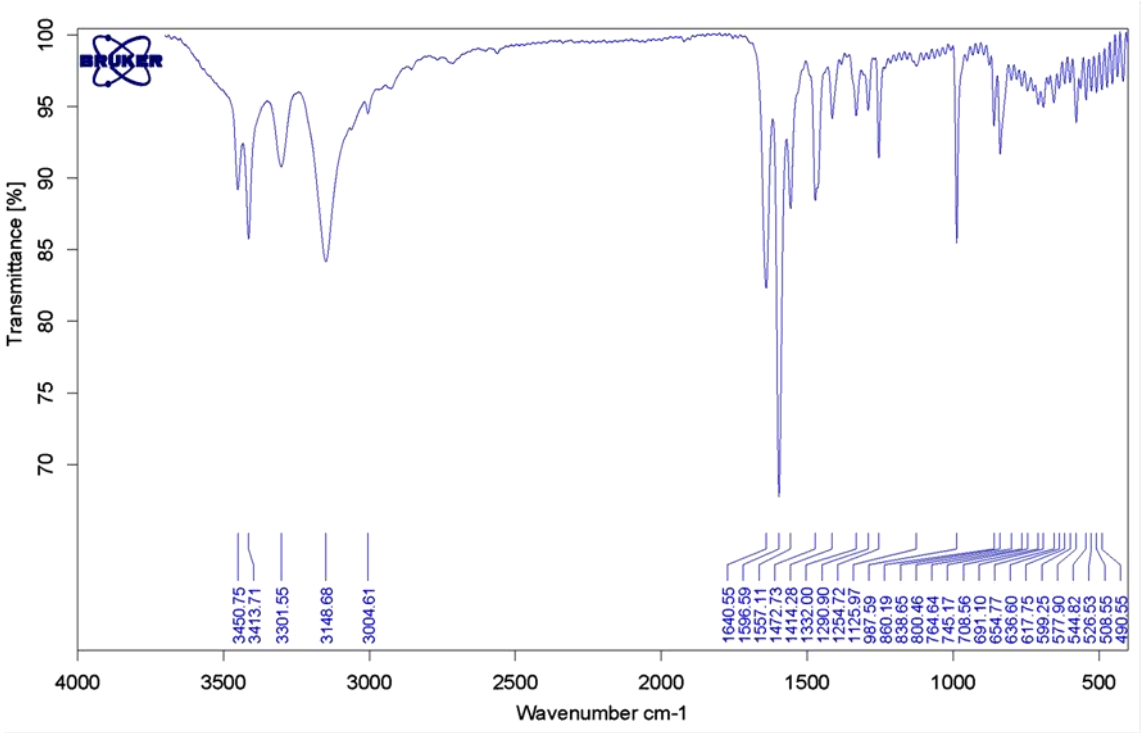

Figure A19. FT-IR (KBr disc) spectrum of 2,2'-Bipyridine-4,4'-diamine (dab). Preparation procedure described in section 2.2.6.

6.1.7. 2-(Thymin-1-yl)-1-(1H-imidazol-1-yl)ethanone (tymim)

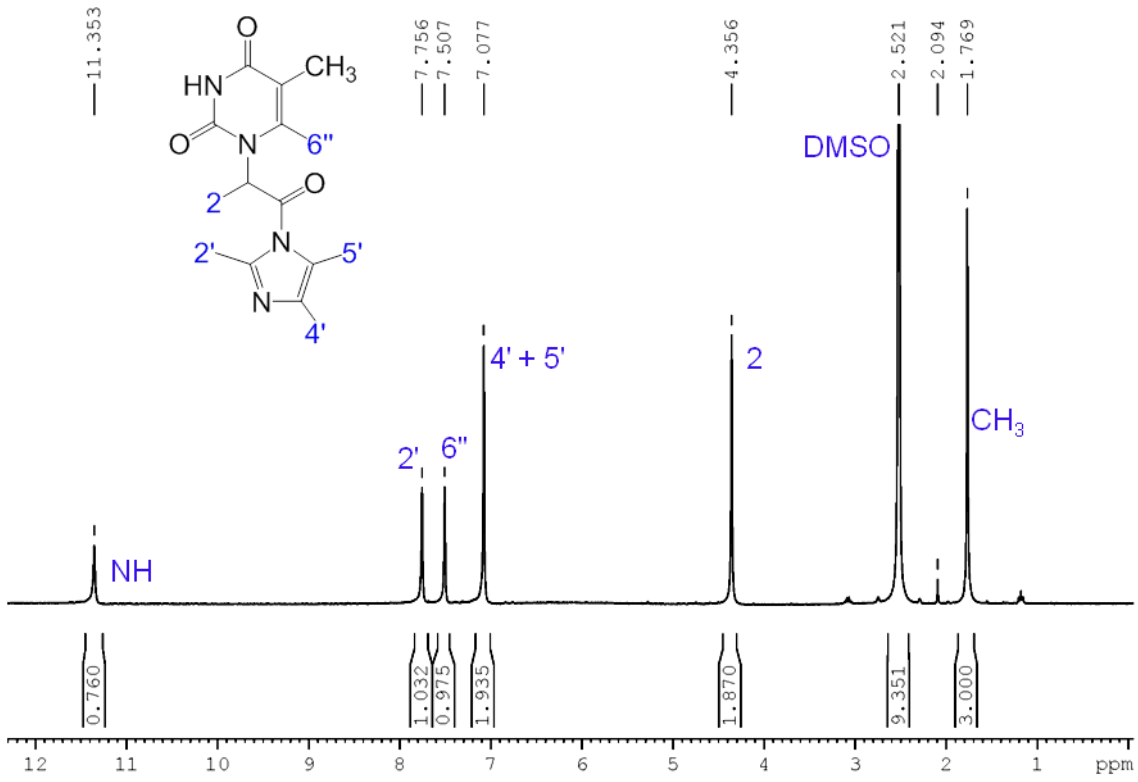

Figure A20. ^{1}H-NMR (DMSO-d_6) spectrum of the thymine-based precursor 2-(thymin-1-yl)-1-(1H-imidazol-1-yl)ethanone (tymim). Preparation procedure described in section 2.2.7.

6.1.8. *N,N'*-(2,2'-bipyridine-4,4'-diyl)bis(2-(thymin-1-yl)acetamide) (bpytym)

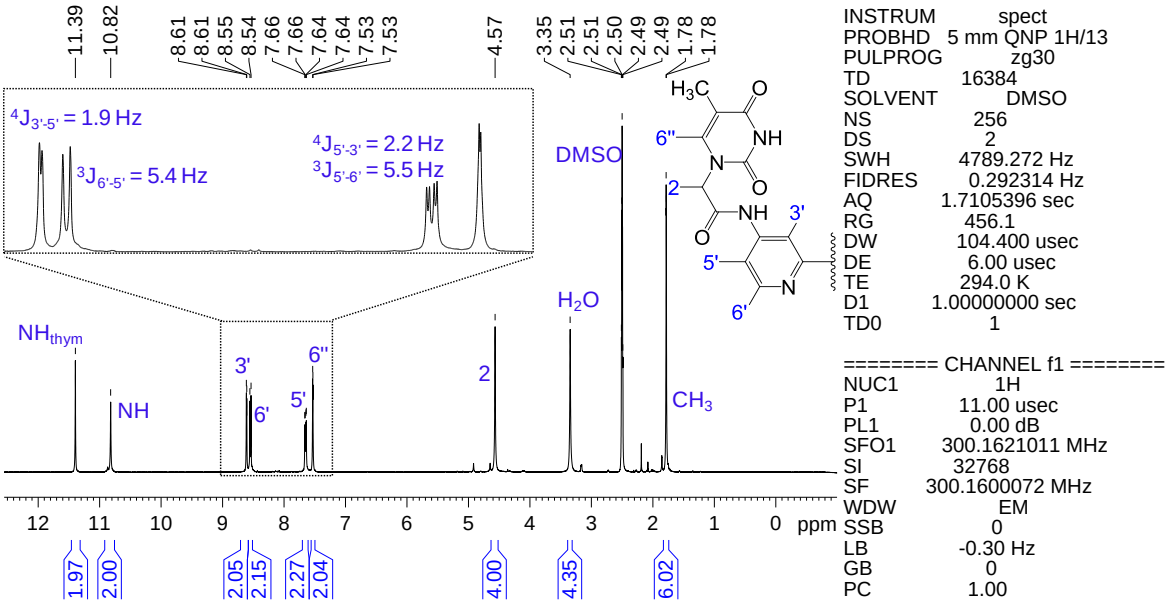

Figure A21. ^{1}H-NMR (DMSO-d_6) spectrum of the ditopic ligand *N,N'*-(2,2'-bipyridine-4,4'-diyl)bis(2-(thymin-1-yl)acetamide) (bpytym). In the inserted structure, the symmetric ligand has been cut in two for the sake of simplicity. Preparation procedure described in section 2.2.8.

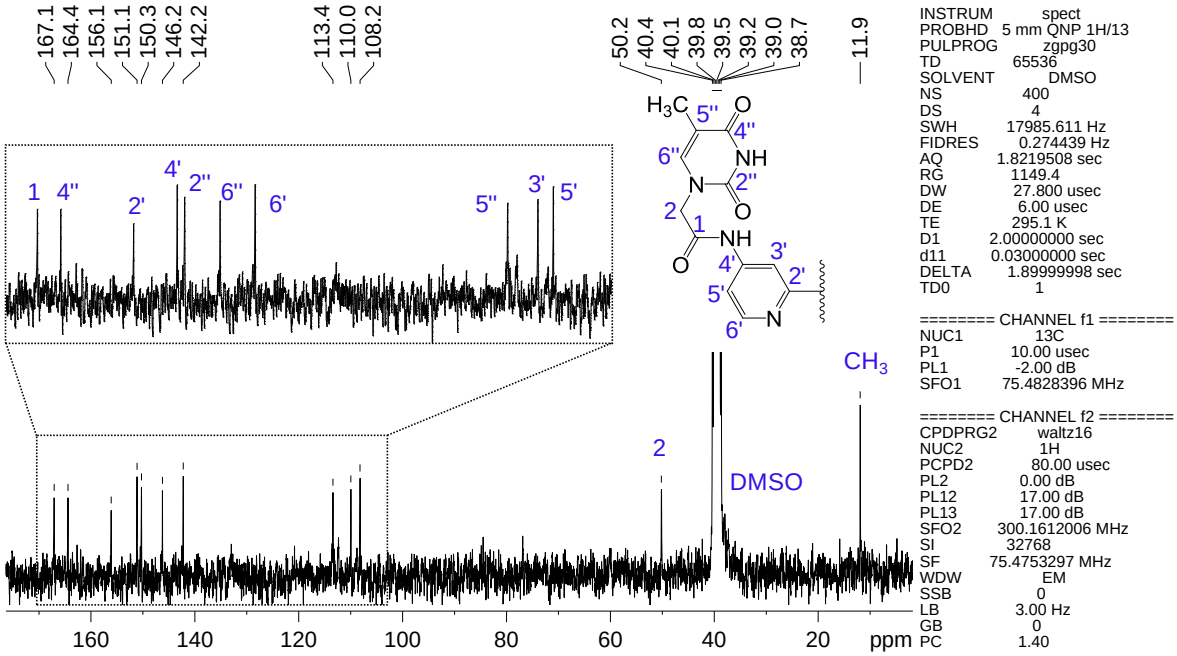

Figure A22. ^{13}C-NMR (DMSO-d_6) spectrum of the ditopic ligand *N,N'*-(2,2'-bipyridine-4,4'-diyl)bis(2-(thymin-1-yl)acetamide) (bpytym). In the inserted structure, the symmetric ligand has been cut in two for the sake of simplicity. Preparation procedure described in section 2.2.8.

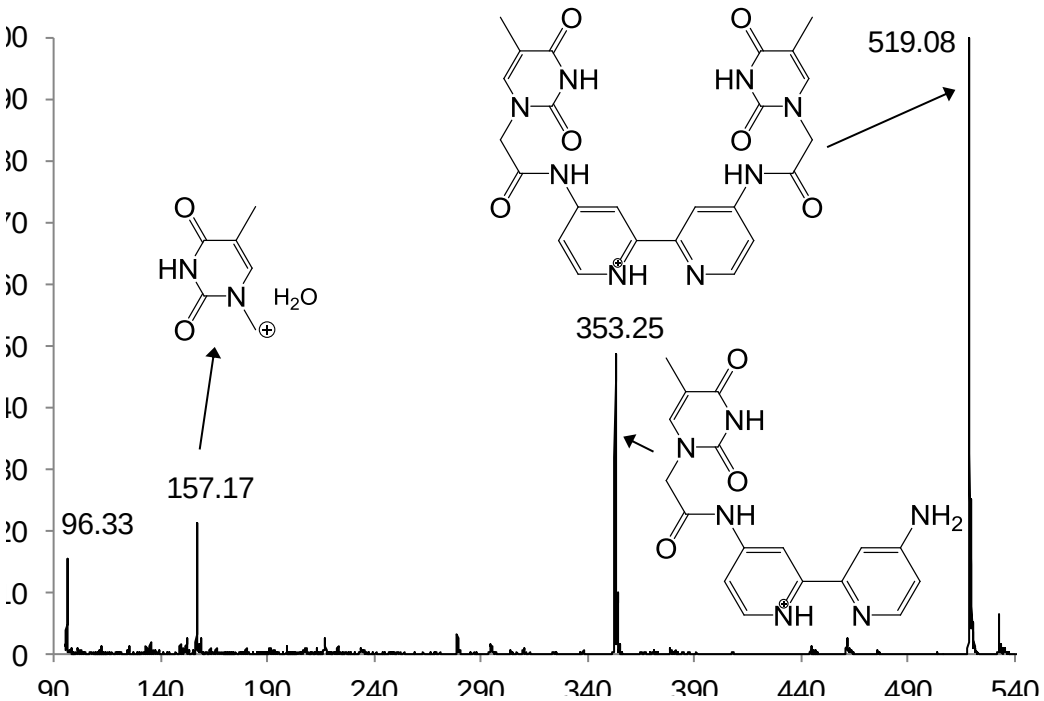

Figure A23. ESI-MS (positive ion detection) spectrum of the ditopic ligand *N*,*N*'-(2,2'-bipyridine-4,4'-diyl)bis(2-(thymin-1-yl)acetamide) (bpytym). Preparation procedure described in section 2.2.8.

6.1.9. *N*⁴,*N*⁴'-dioctadecyl-2,2'-bipyridine-4,4'-dicarboxamide (nody)

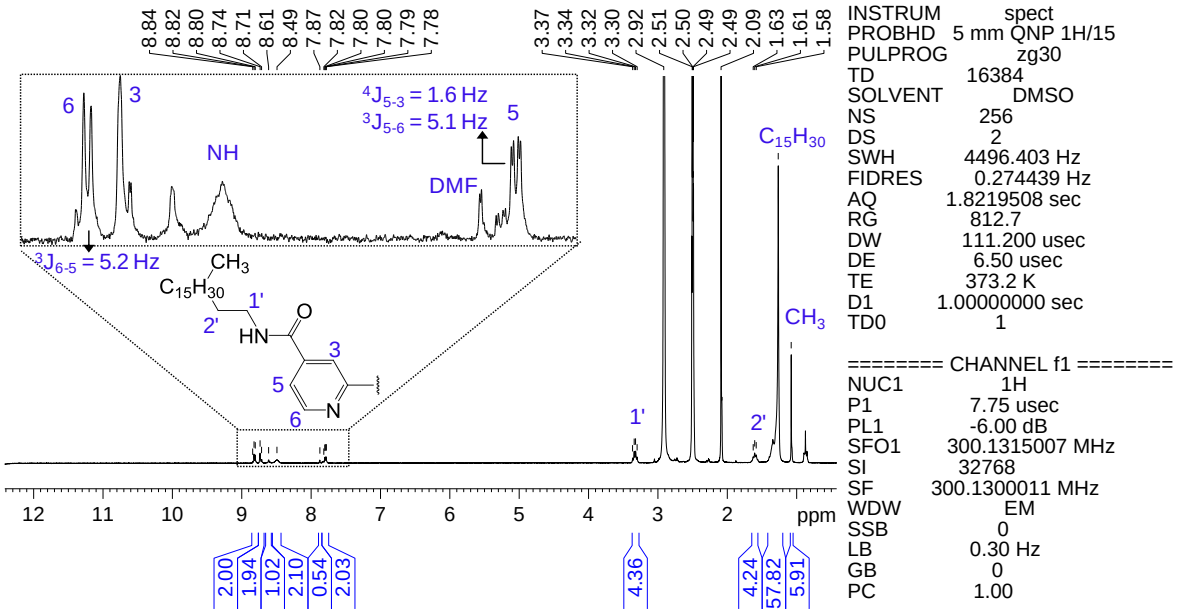

Figure A24. ^{1}H-NMR (DMSO-d_6 at 100 °C) spectrum of *N*⁴,*N*⁴'-dioctadecyl-2,2'-bipyridine-4,4'-dicarboxamide (nody). Preparation procedure described in section 2.2.9.

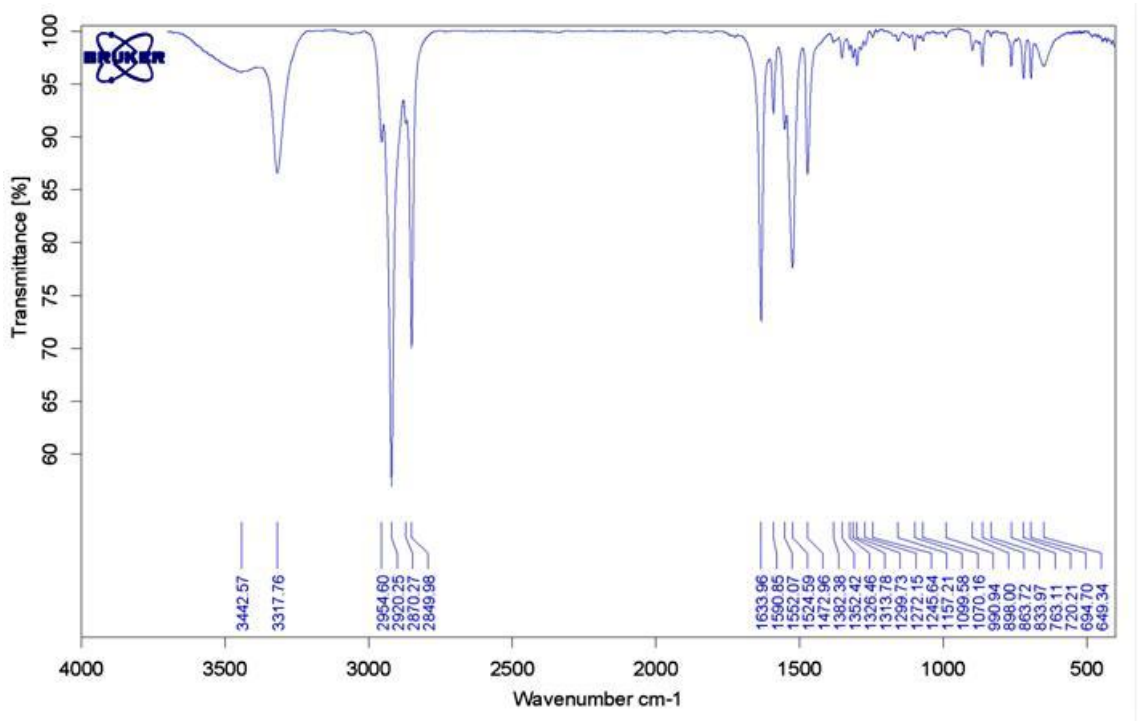

Figure A25. FT-IR (KBr disc) spectrum of *N*⁴,*N*⁴'-dioctadecyl-2,2'-bipyridine-4,4'-dicarboxamide (nody). Preparation procedure described in section 2.2.9.

6.1.10. 1,10-phenanthrolin-5-amino (ap)

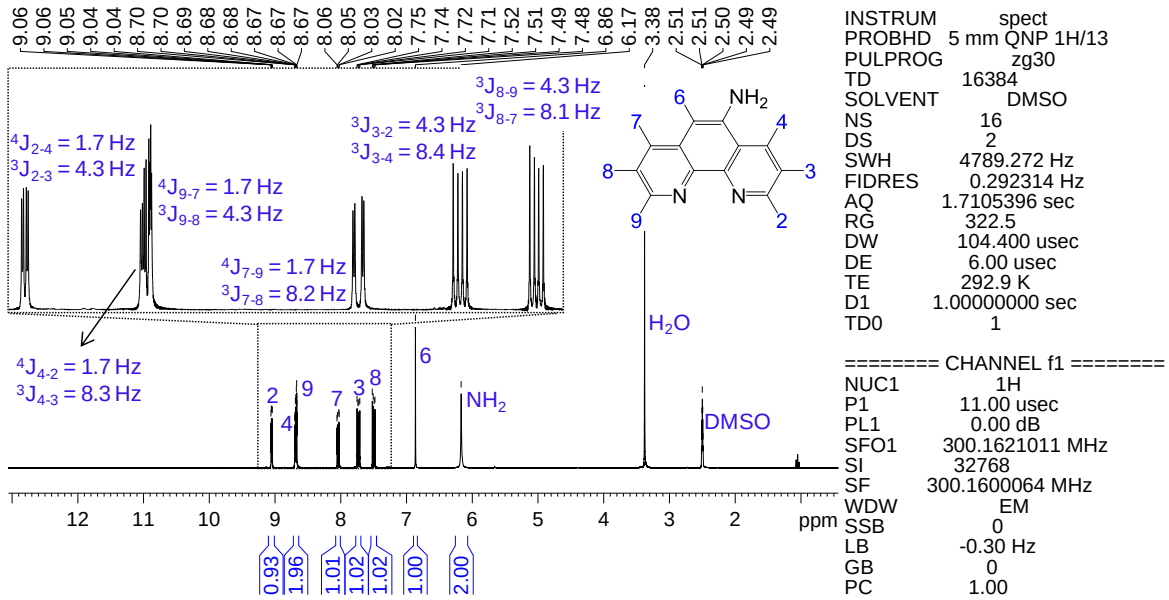

Figure A26. ^{1}H-NMR (DMSO-d_6) spectrum of 1,10-phenanthrolin-5-amino (ap). Preparation procedure described in section 2.2.10.

6.1.11. $Ru(phen)_2Cl_2$

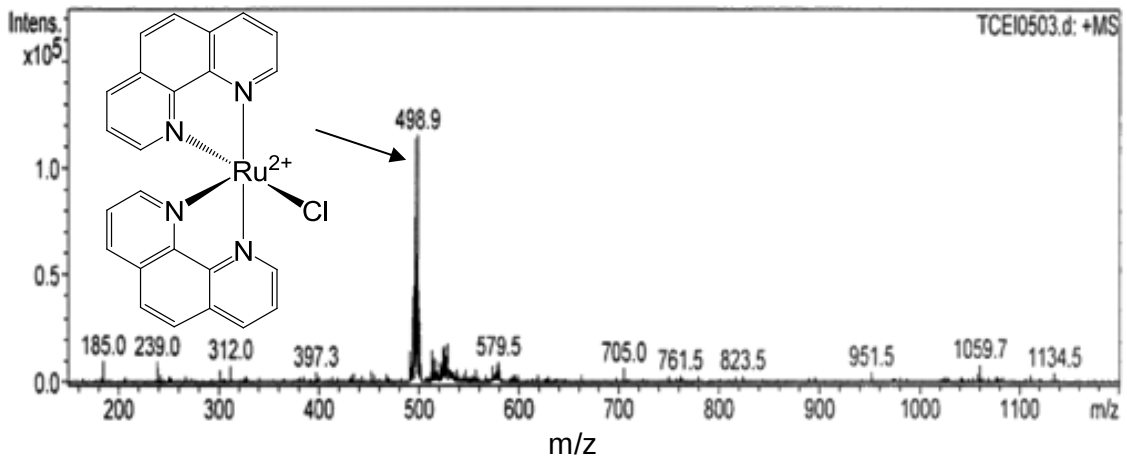

Figure A27. ESI-MS (positive ion detection) spectrum of $Ru(phen)_2Cl_2$. Preparation procedure described in section 2.3.1.

6.1.12. $[Ru(phen)_2(pdo)](PF_6)_2$

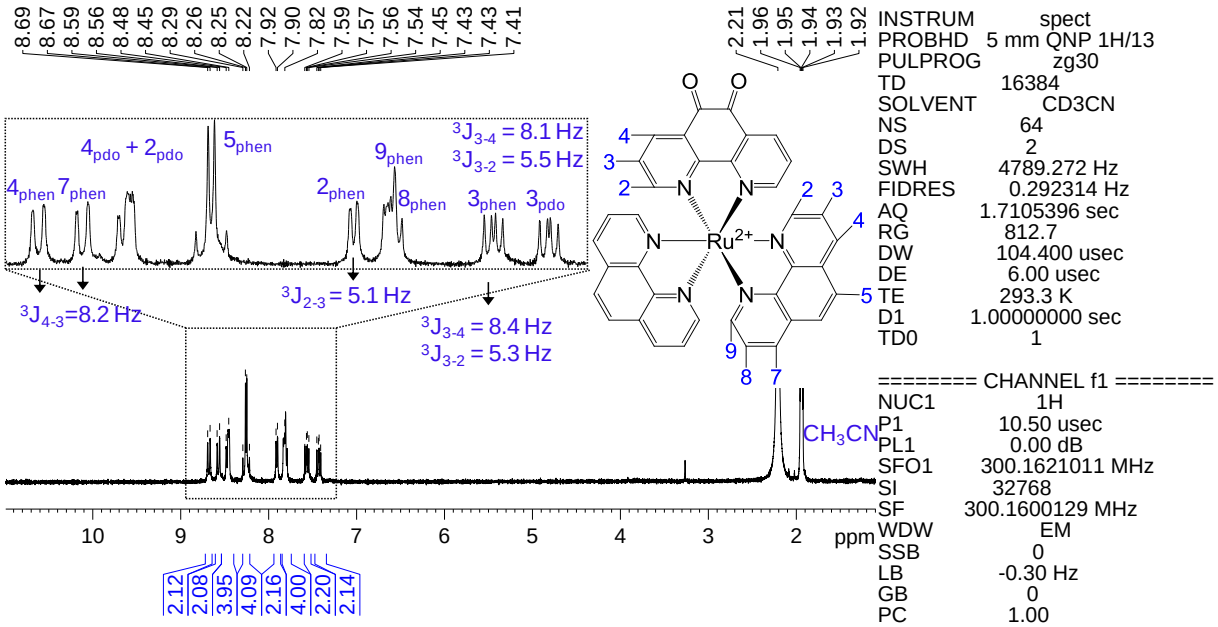

Figure A28. ^{1}H-NMR (CD_3CN-d_3) spectrum of $[Ru(phen)_2(pdo)](PF_6)_2$. Preparation procedure described in section 2.3.3.

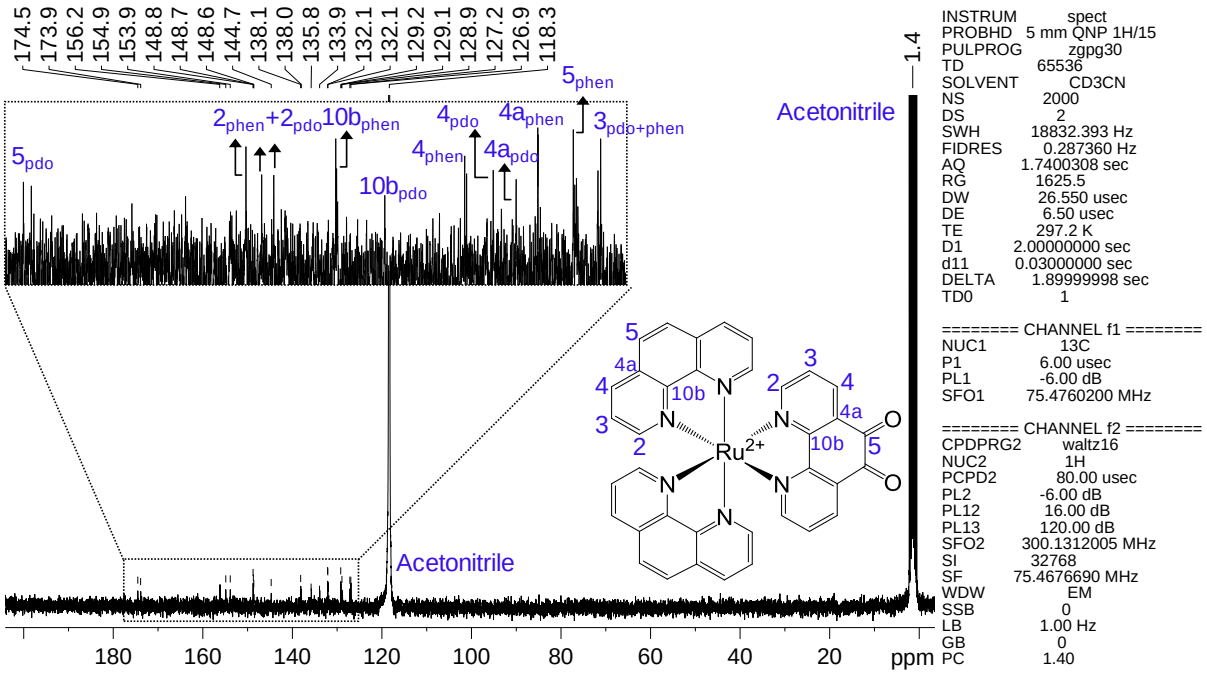

Figure A29. ^{13}C-NMR (CD_3CN-d_3) spectrum of $[Ru(phen)_2(pdo)](PF_6)_2$. Preparation procedure described in section 2.3.3.

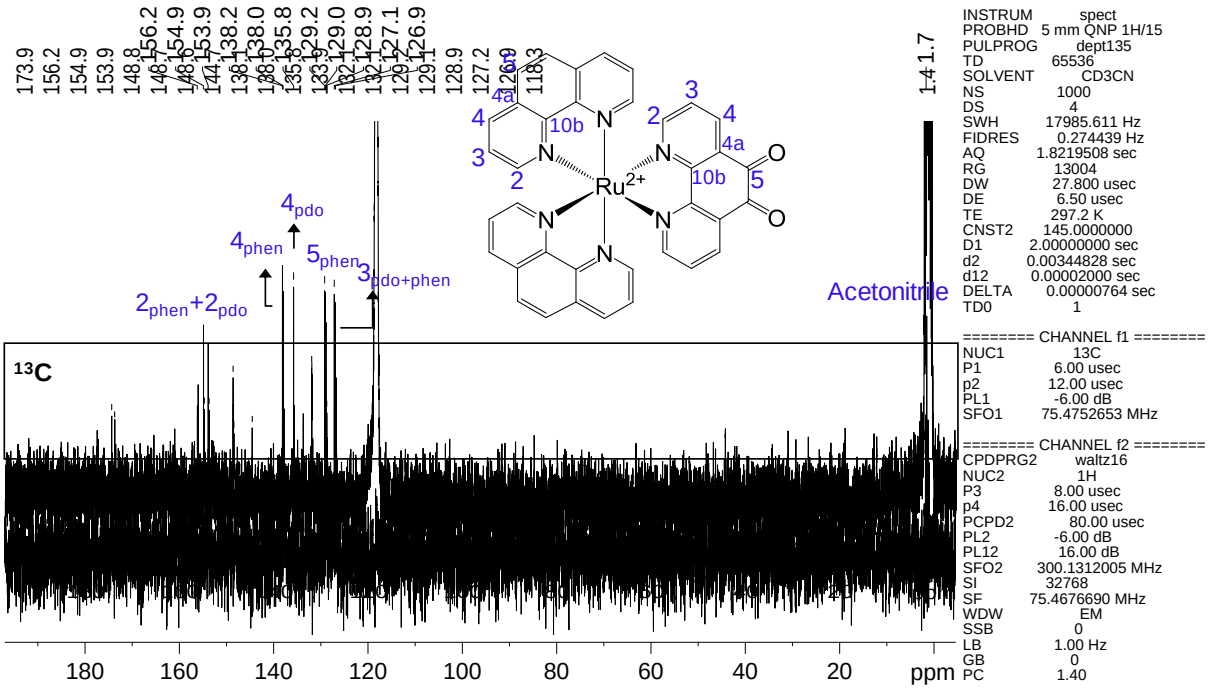

Figure A30. ^{13}C-NMR dept 135 (CD_3CN-d_3) spectrum of $[Ru(phen)_2(pdo)](PF_6)_2$. Preparation procedure described in section 2.3.3.

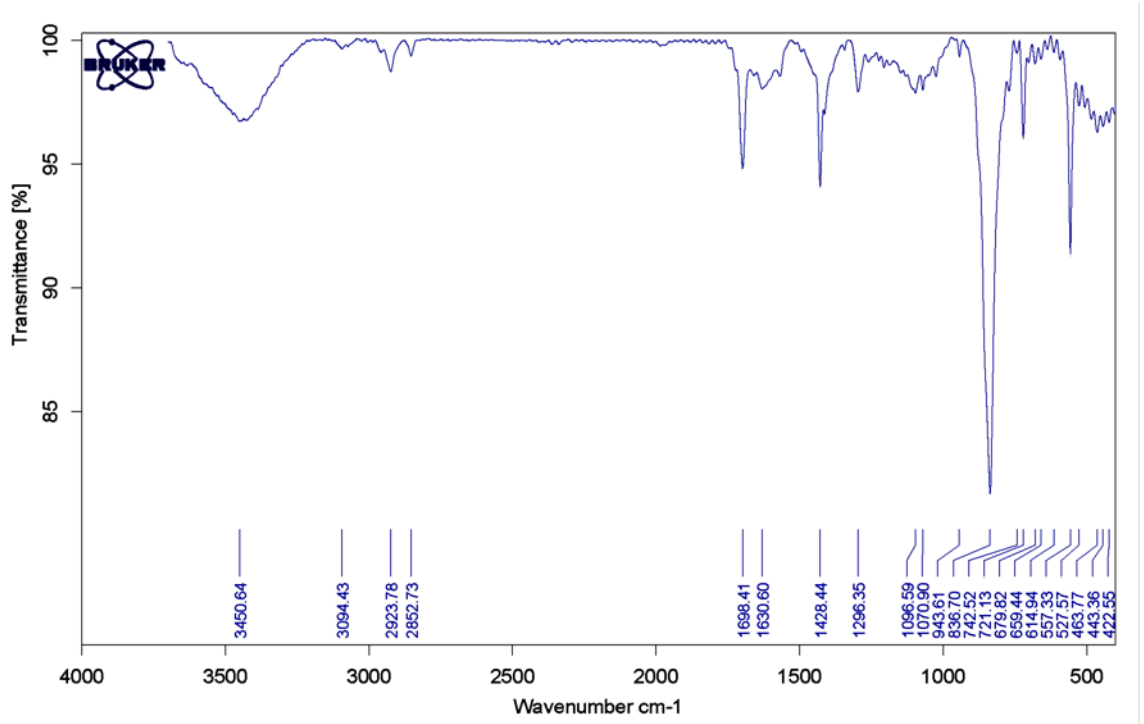

Figure A31. FT-IR (KBr disc) spectrum of $[Ru(phen)_2(pdo)](PF_6)_2$. Preparation procedure described in section 2.3.3.

6.1.13. $[Ru(phen)_2(iip)](PF_6)_2$

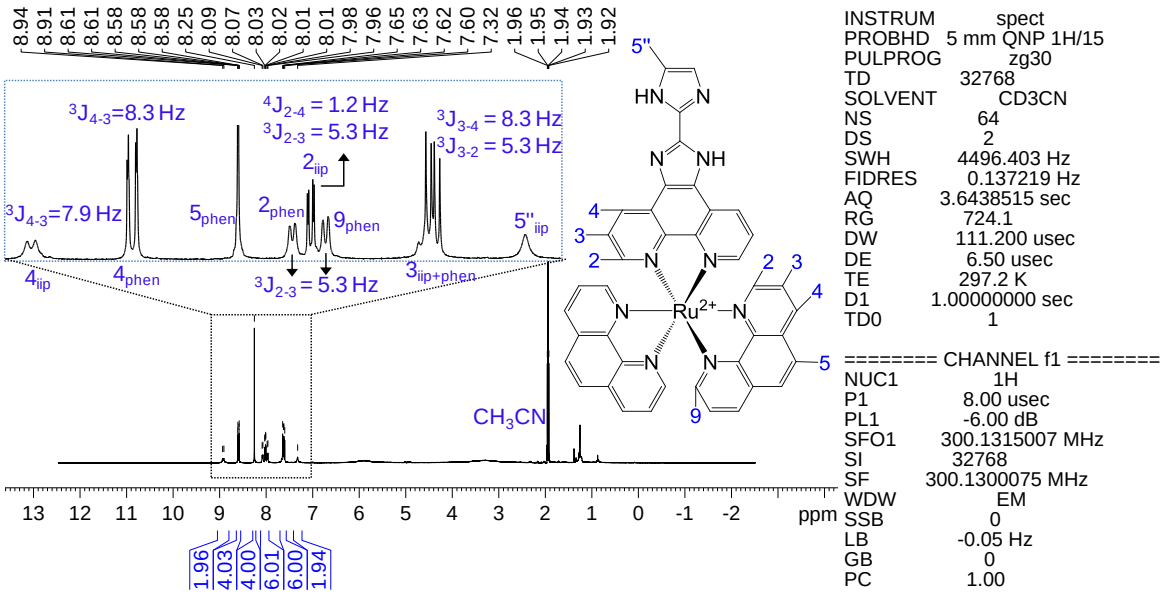

Figure A32. ^{1}H-NMR (CD_3CN-d_3) spectrum of $[Ru(phen)_2(iip)](PF_6)_2$. Preparation procedure described in section 2.3.4.

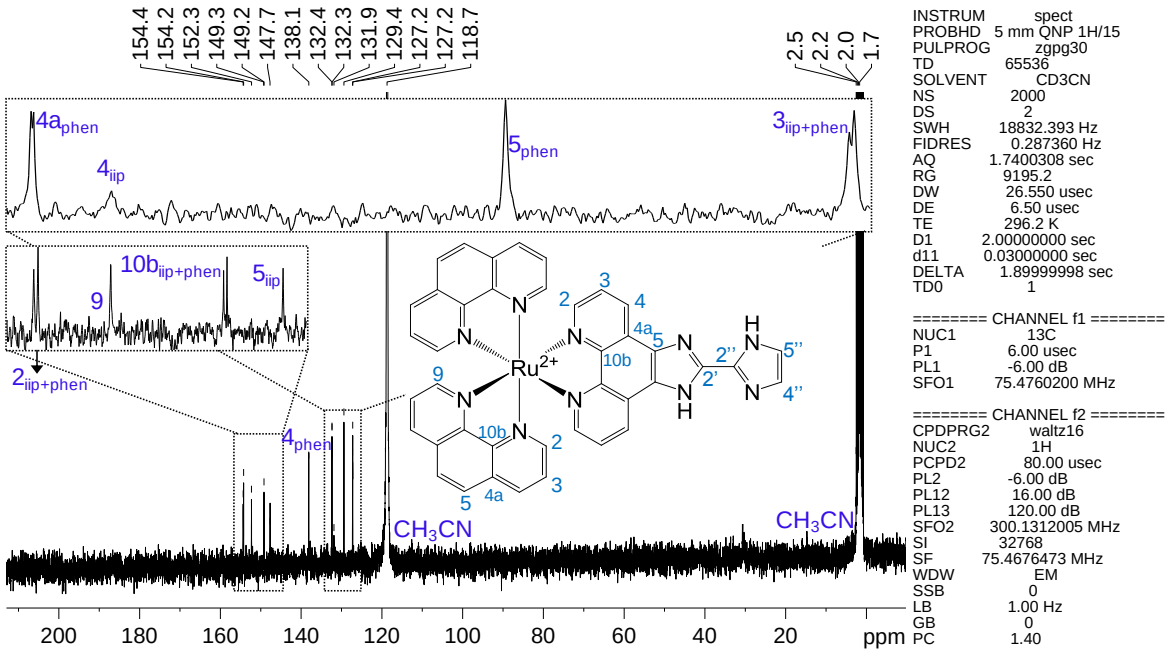

Figure A33. ^{13}C-NMR (CD_3CN-d_3) spectrum of $[Ru(phen)_2(iip)](PF_6)_2$. Preparation procedure described in section 2.3.4.

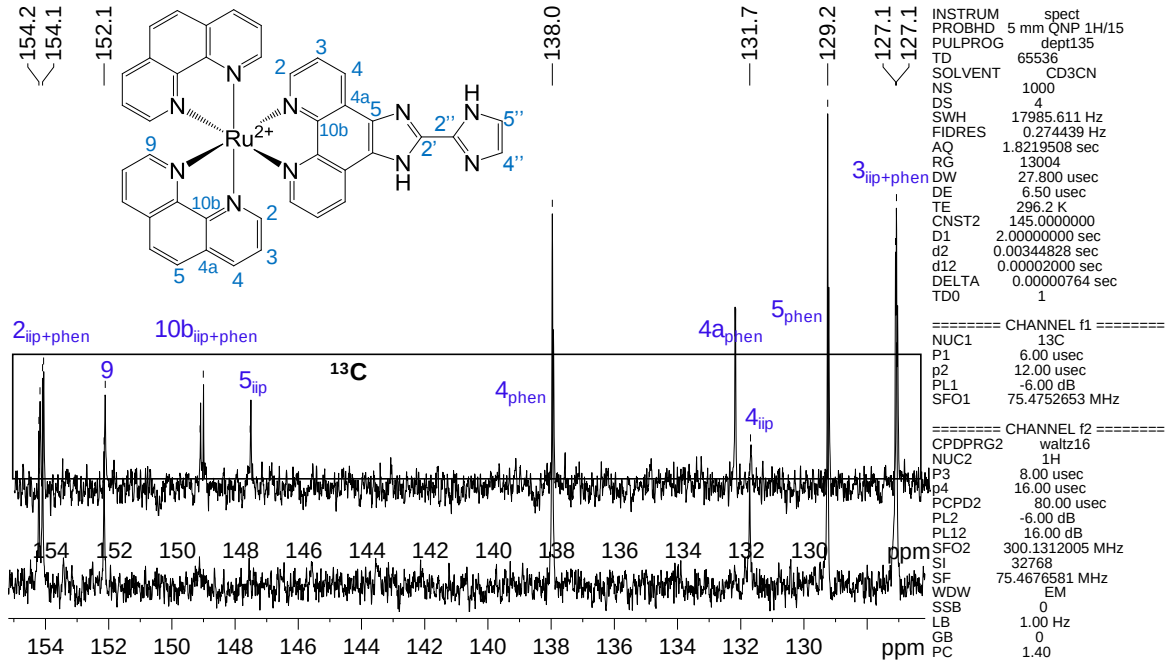

Figure A34. ^{13}C-NMR DEPT 135 (CD_3CN-d_3) spectrum of $[Ru(phen)_2(iip)](PF_6)_2$. The ^{13}C-NMR spectrum is inserted for comparison. Preparation procedure described in section 2.3.4.

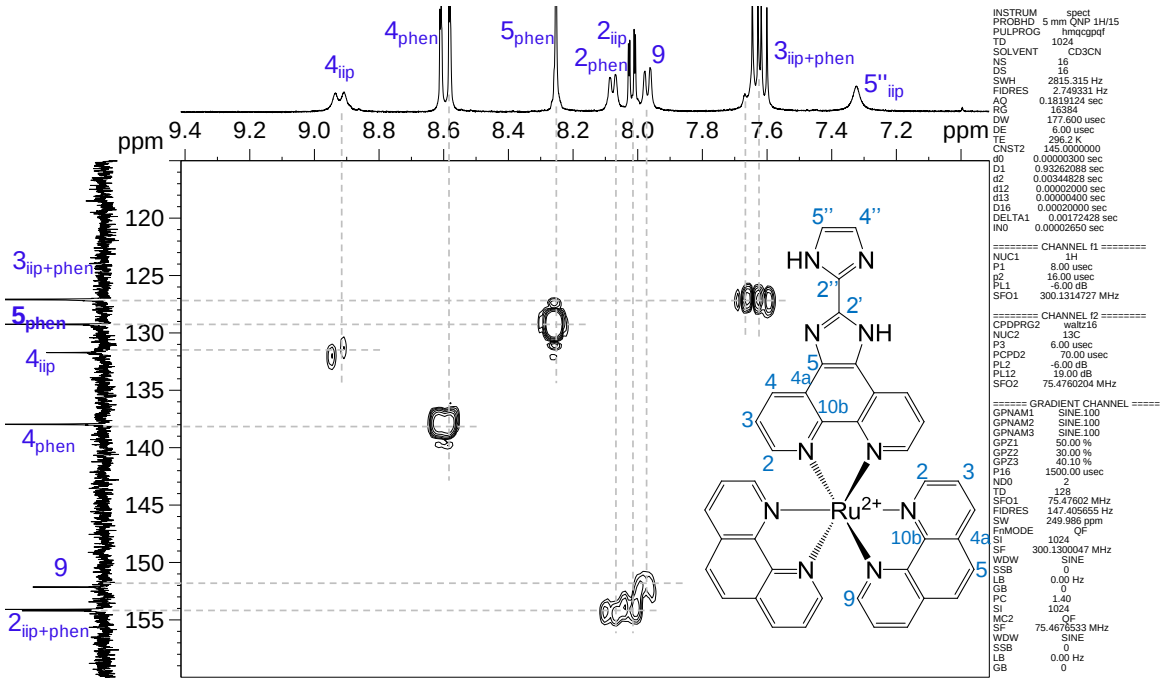

Figure A35. ^{1}H-^{13}C HMQC NMR (CD_3CN-d_3) spectrum of $[Ru(phen)_2(iip)](PF_6)_2$. For the sake of clarity, the spectrum on the left axis is the ^{13}C-NMR DEPT 135. Preparation procedure described in section 2.3.4. Chemical shifts assignment discussed on section 2.4.

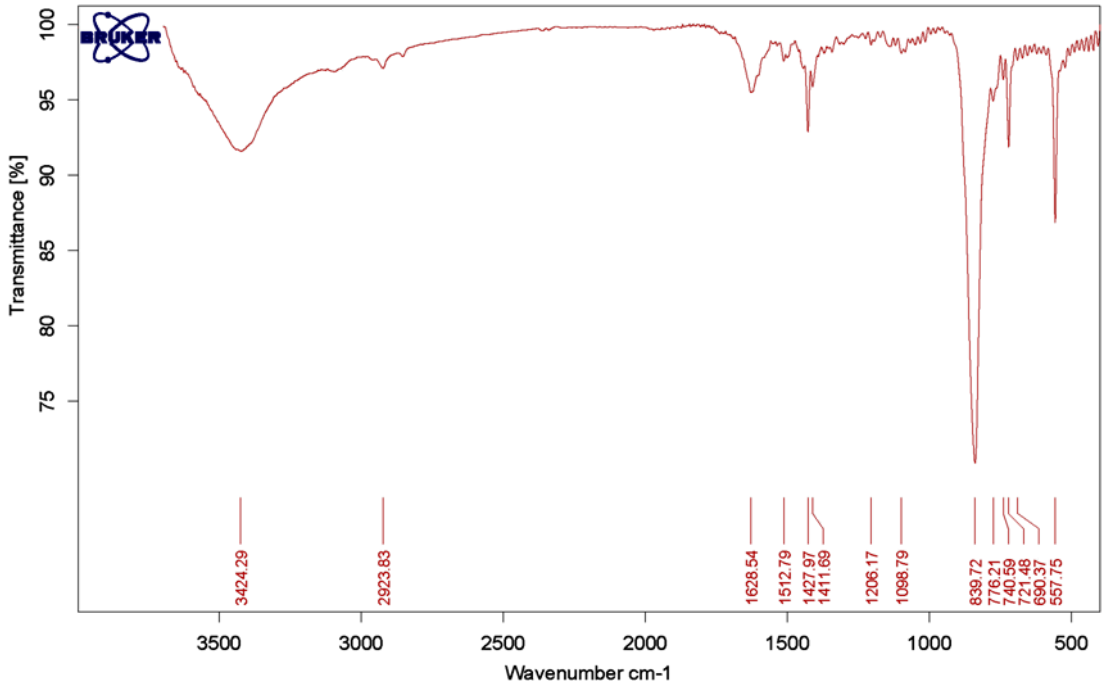

Figure A36. FT-IR (KBr disc) spectrum of $[Ru(phen)_2(iip)](PF_6)_2$. Preparation procedure described in section 2.3.4.

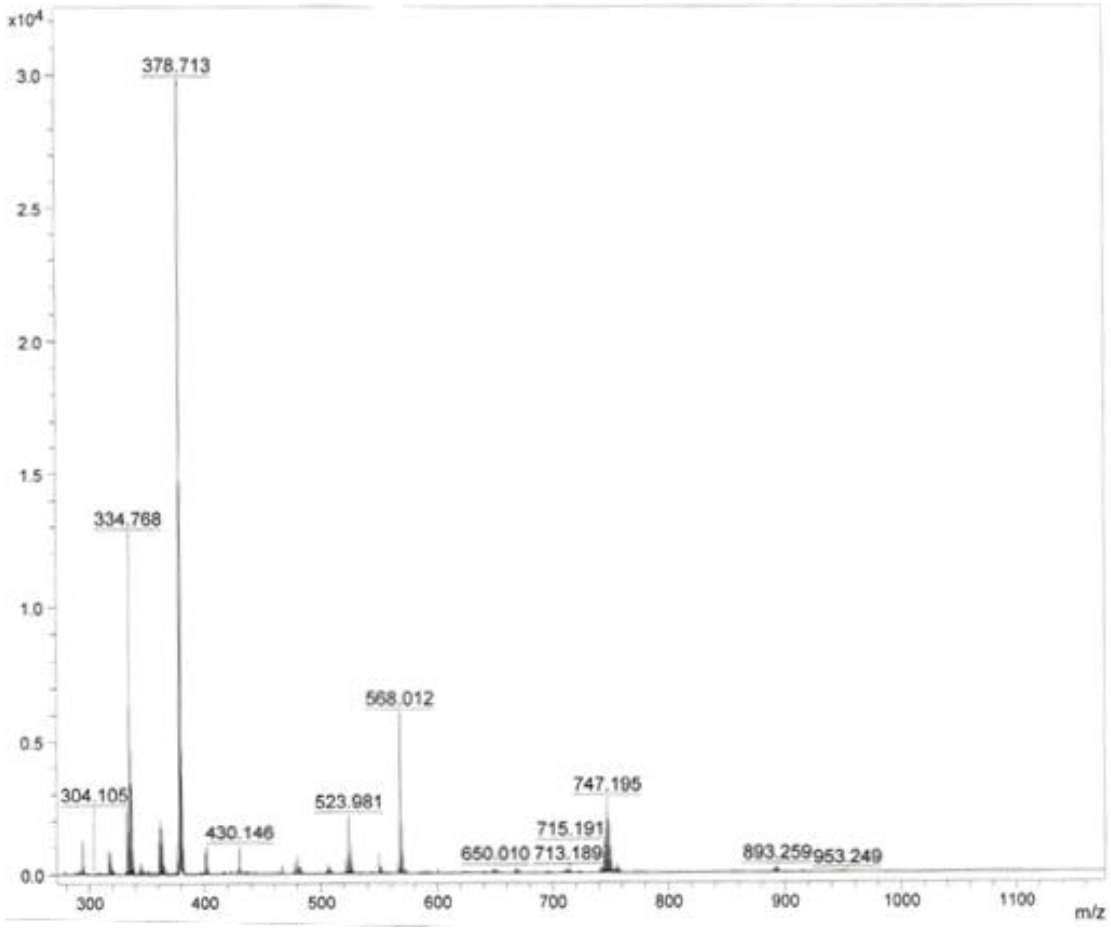

Figure A37. MS (MALDI-TOF, positive ion detection) spectrum of $[Ru(phen)_2(iip)](PF_6)_2$. Preparation procedure described in section 2.3.4.

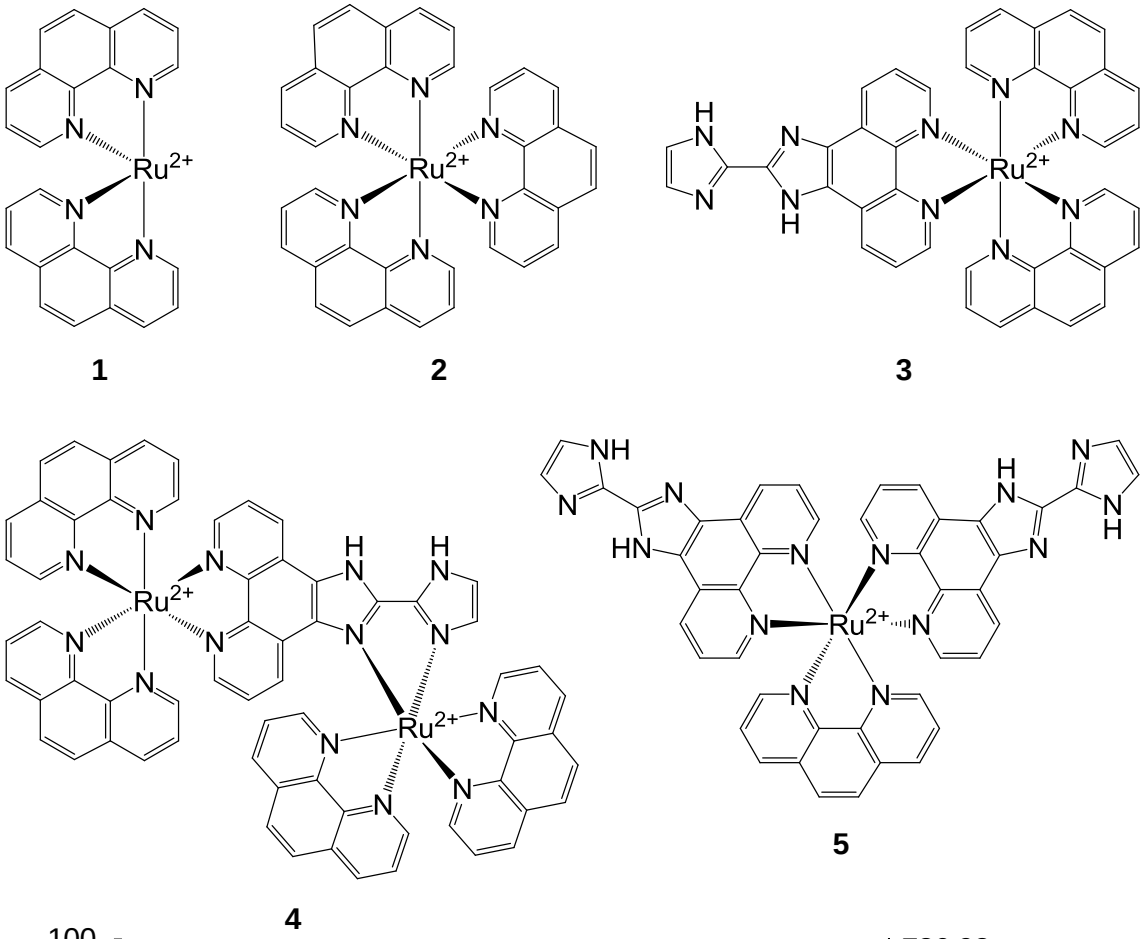

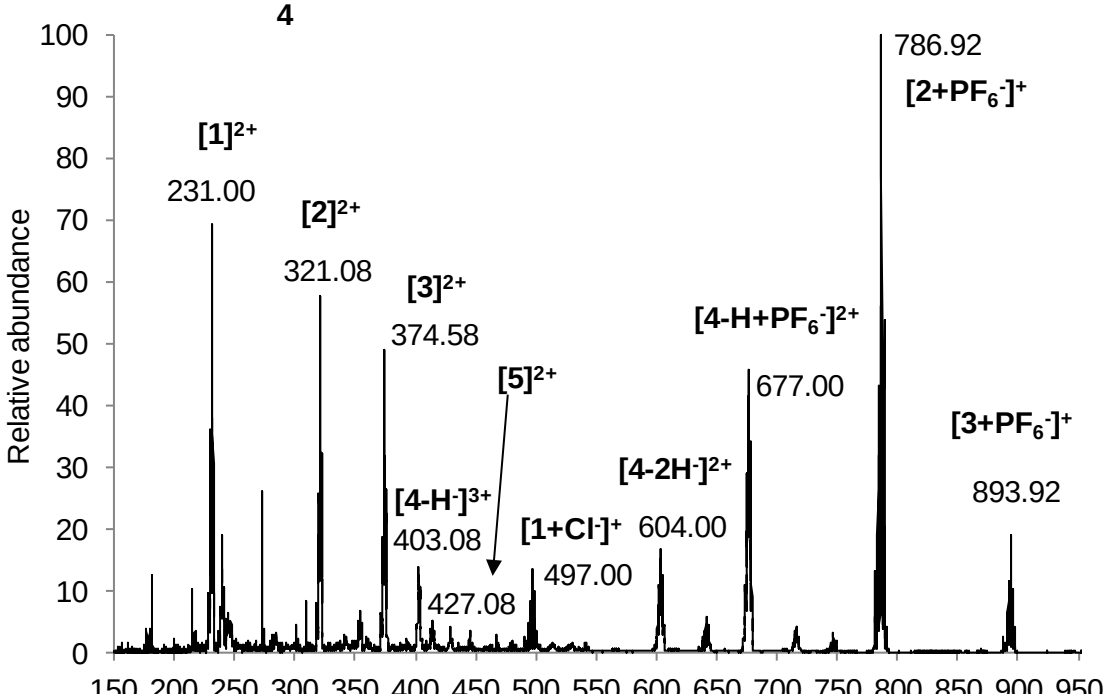

Figure A38. ESI-MS (positive) spectrum of $[Ru(phen)_2(iip)](PF_6)_2$ prior to purification by HPLC chromatography. Preparation procedure described in section 2.3.4.

6.1.14. $[Ru(phen)_2(hmip)](PF_6)_2$

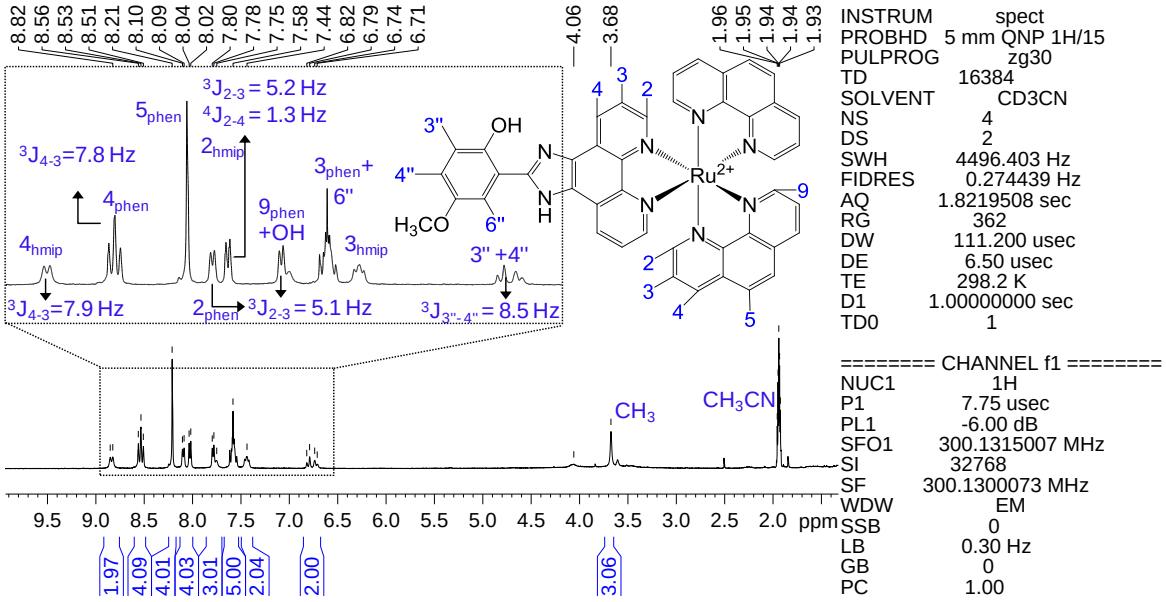

Figure A39. ^{1}H-NMR (CD_3CN-d_3) spectrum of $[Ru(phen)_2(hmip)](PF_6)_2$. Preparation procedure described in section 2.3.5.

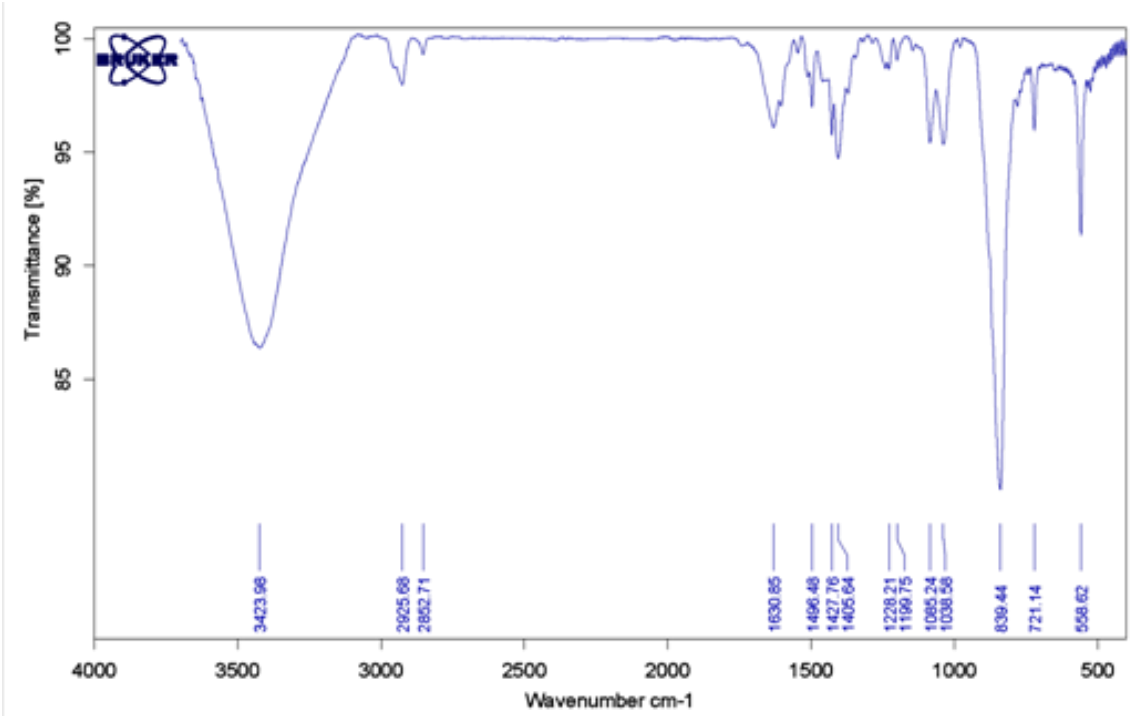

Figure A40. FT-IR (KBr disc) spectrum of $[Ru(phen)_2(hmip)](PF_6)_2$. Preparation procedure described in section 2.3.5.

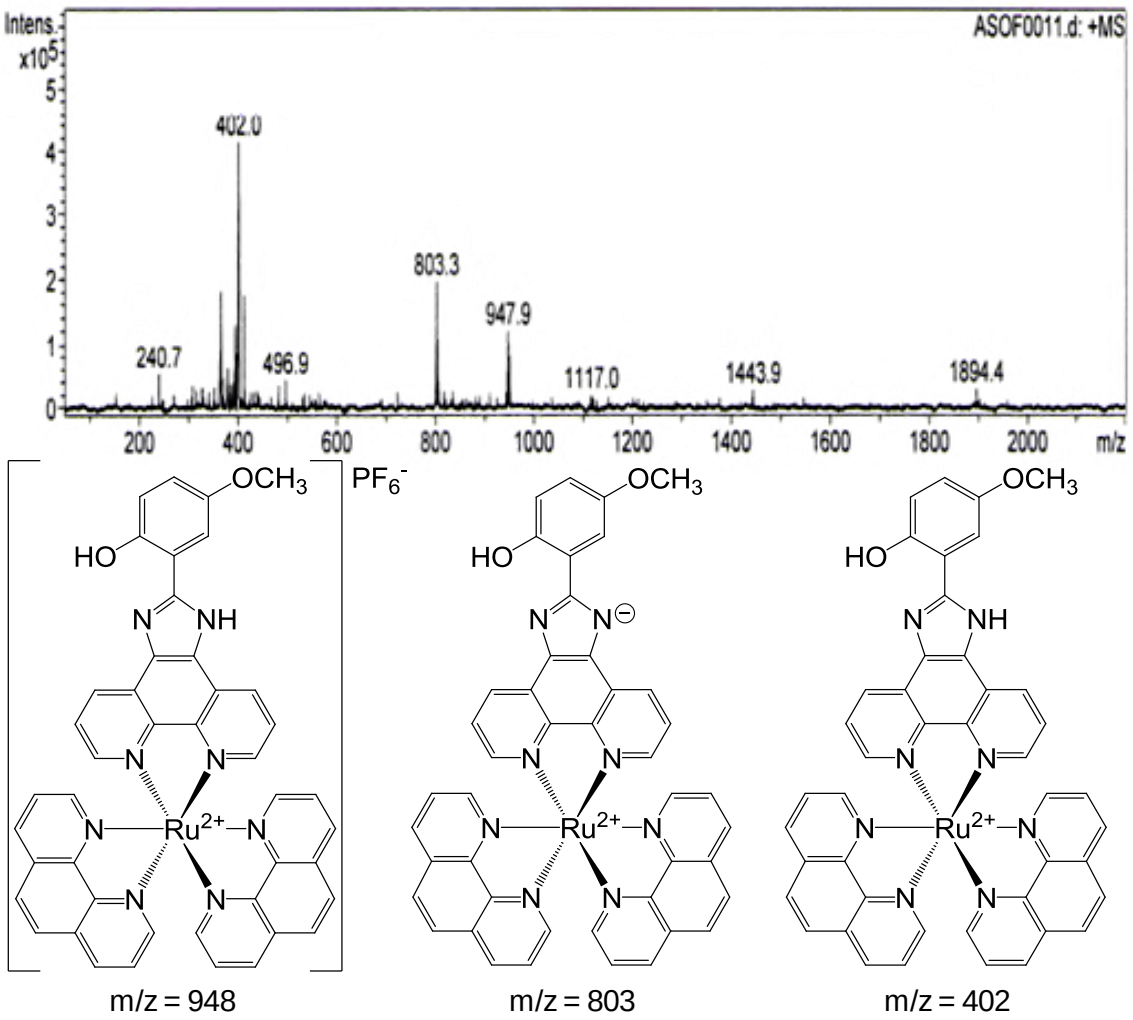

Figure A41. ESI-MS (positive) spectrum of $[Ru(phen)_2(hmip)](PF_6)_2$. Preparation procedure described in section 2.3.5.

6.1.15. $[Ru(phen)_2(haip)](PF_6)_2$

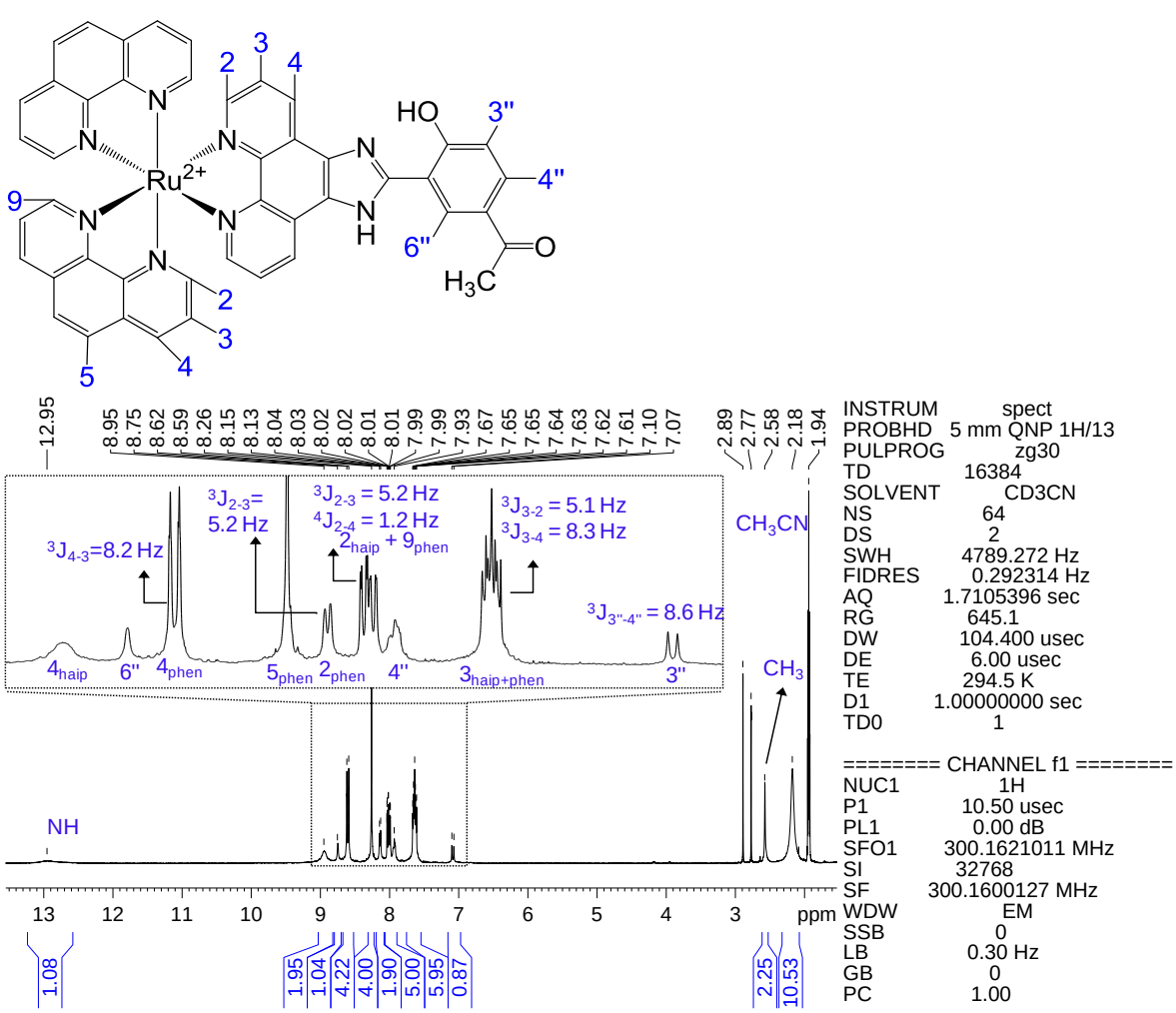

Figure A42. ^{1}H-NMR (CD_3CN-d_3) spectrum of $[Ru(phen)_2(haip)](PF_6)_2$. Preparation procedure described in section 2.3.6.

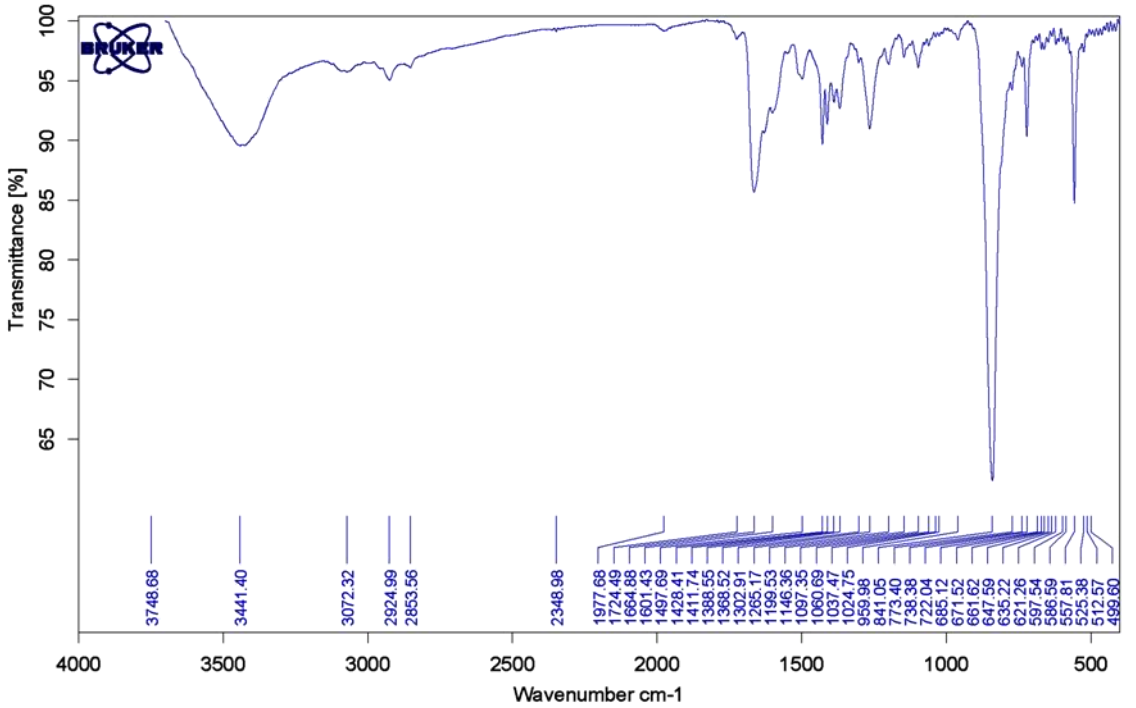

Figure A43. FT-IR (KBr disc) spectrum of $[Ru(phen)_2(haip)](PF_6)_2$. Preparation procedure described in section 2.3.6.

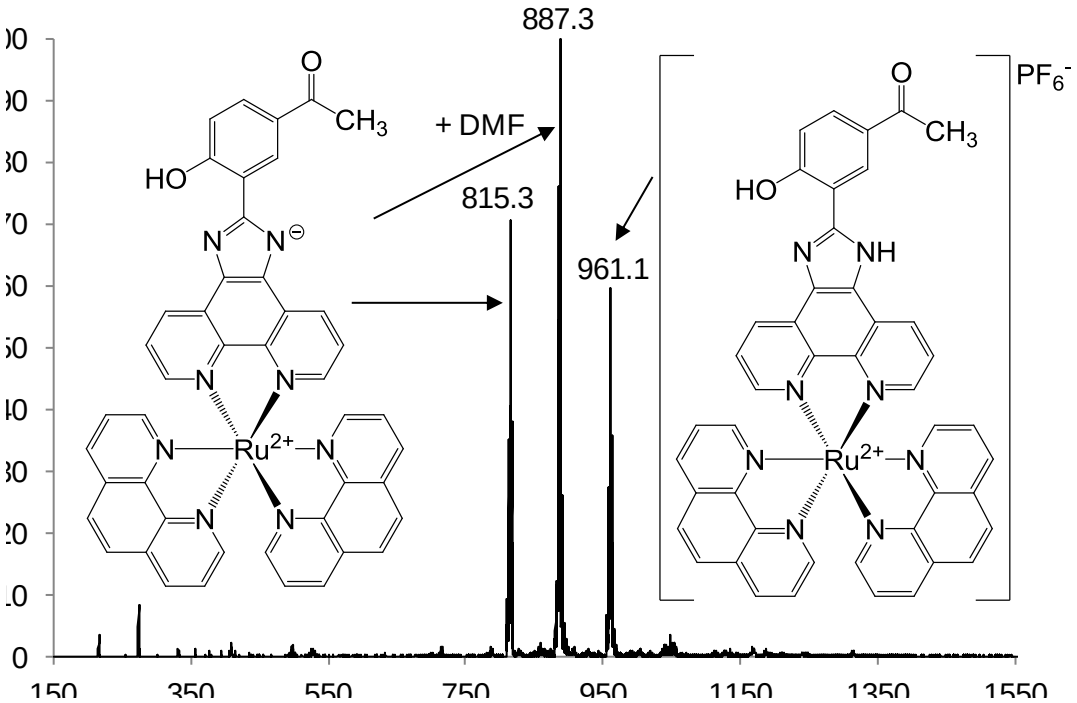

Figure A44. ESI-MS (positive ion detection) spectrum of $[Ru(phen)_2(haip)](PF_6)_2$. Preparation procedure described in section 2.3.6.

6.1.16. [Ru(phen)$_2$(bpytym)](PF$_6$)$_2$

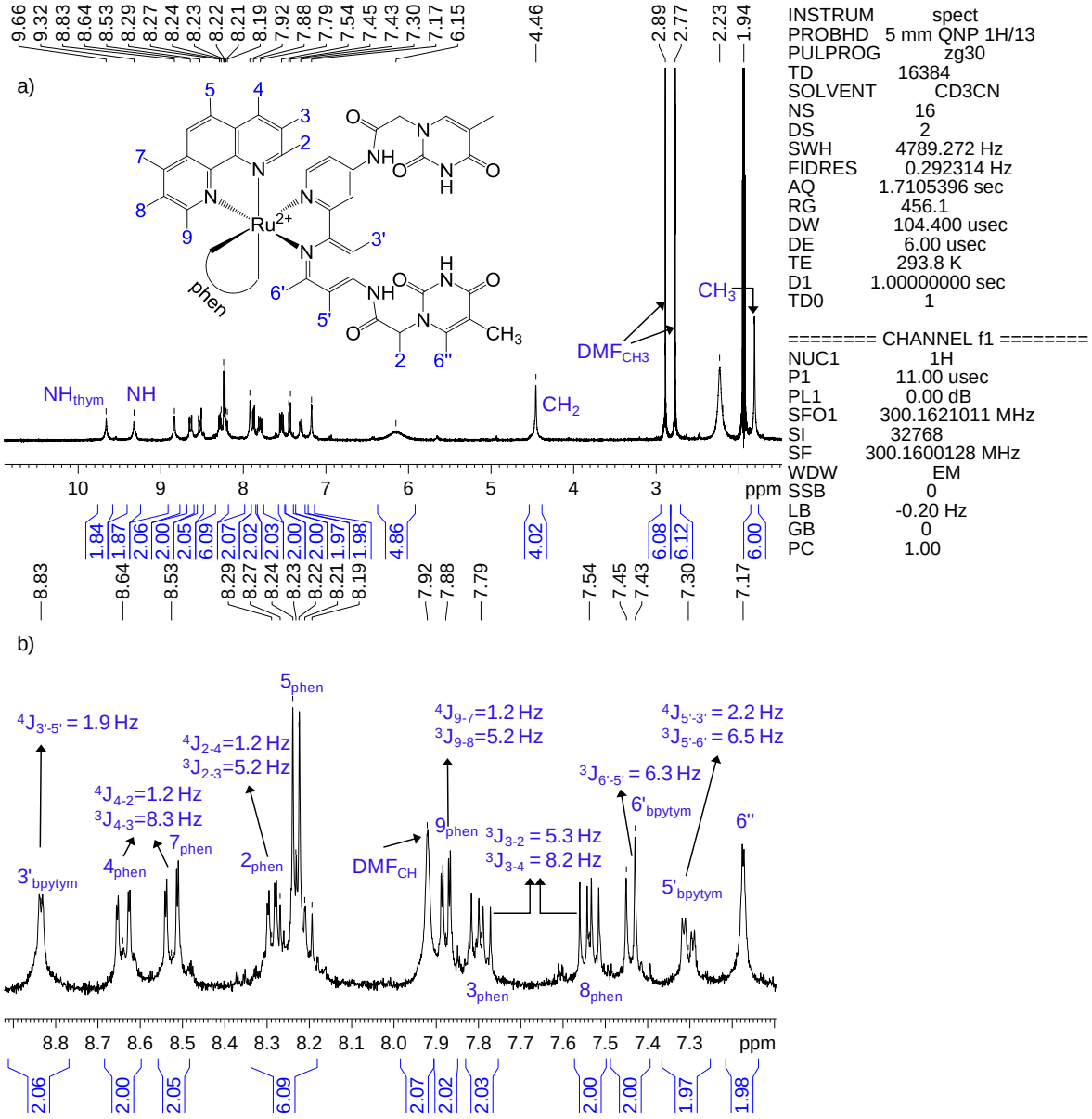

Figure A45. ^{1}H-NMR (CD$_3$CN-d_3) spectrum of [Ru(phen)$_2$(bpytym)](PF$_6$)$_2$ (a) and detailed aromatic region (7.1 to 8.9 ppm range) (b). Preparation procedure described in section 2.3.7.

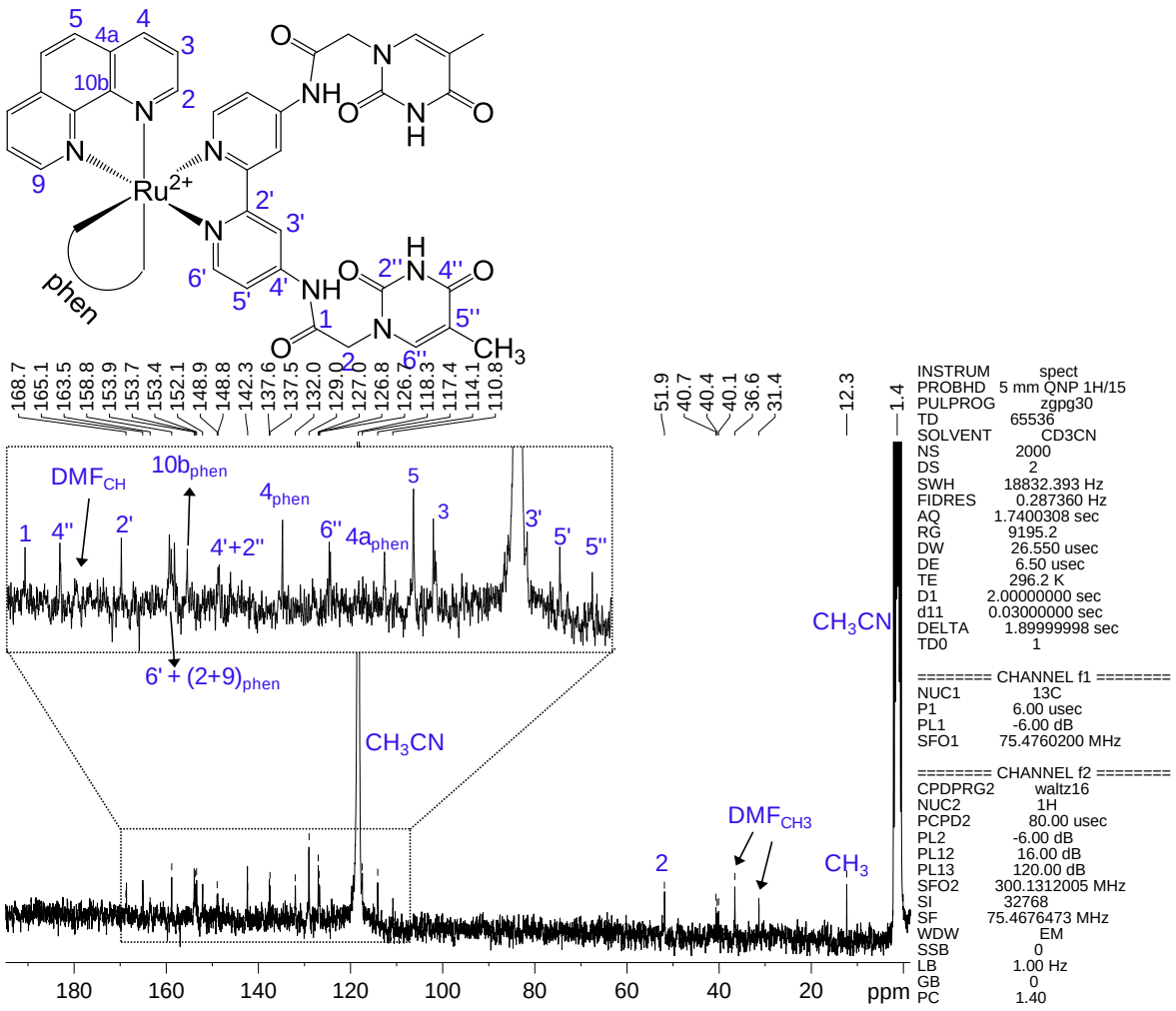

Figure A46. ^{13}C-NMR (CD_3CN-d_3) spectrum of $[Ru(phen)_2(bpytym)](PF_6)_2$. Preparation procedure described in section 2.3.7.

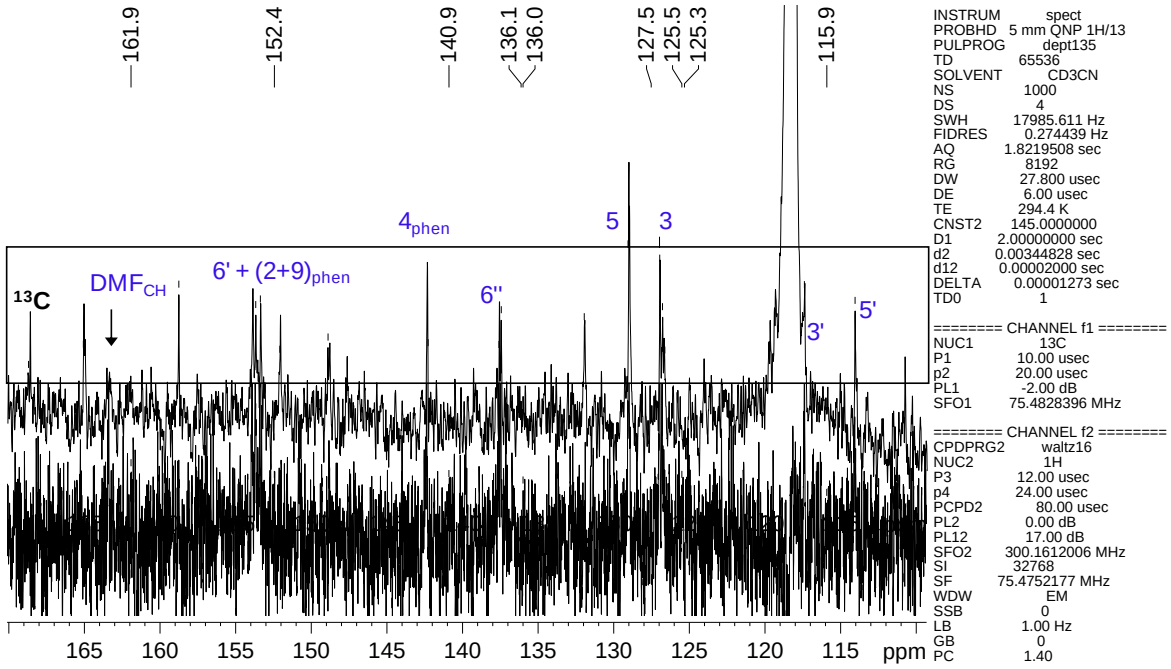

Figure A47. ^{13}C-NMR DEPT 135 (CD_3CN-d_3) spectrum of $[Ru(phen)_2(bpytym)](PF_6)_2$. The ^{13}C-NMR spectrum is inserted for comparison. Preparation procedure described in section 2.3.7.

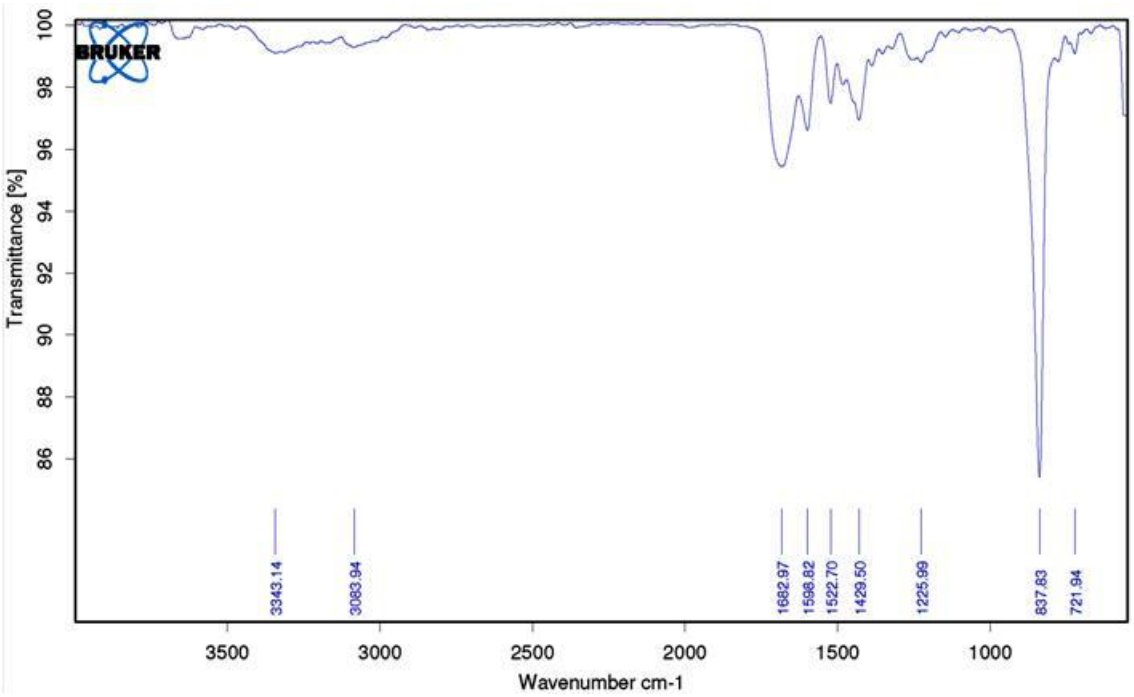

Figure A48. FT-IR (KBr disc) spectrum of $[Ru(phen)_2(bpytym)](PF_6)_2$. Preparation procedure described in section 2.3.7.

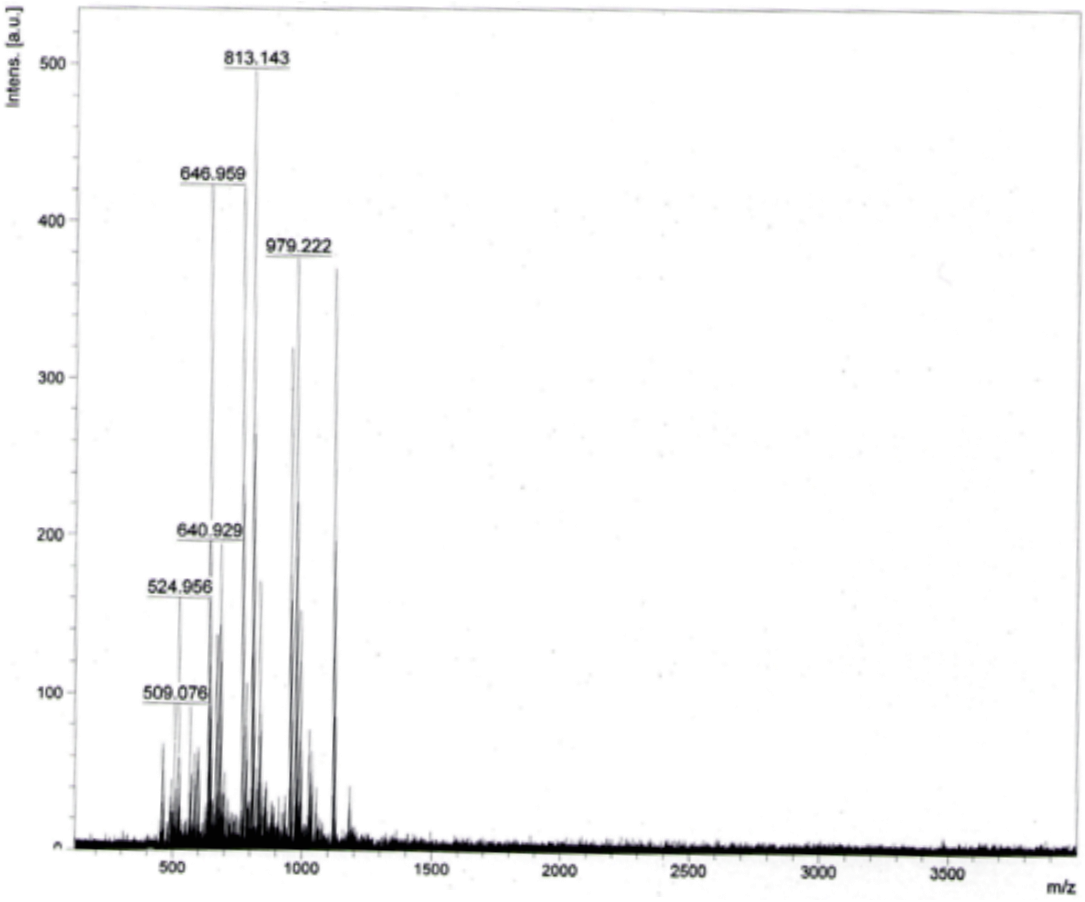

Figure A49. MALDI-TOF MS (positive ion detection) spectrum of $[Ru(phen)_2(bpytym)](PF_6)_2$. Preparation procedure described in section 2.3.7.

6.1.17. $[Ru(nody)_3]Cl_2$

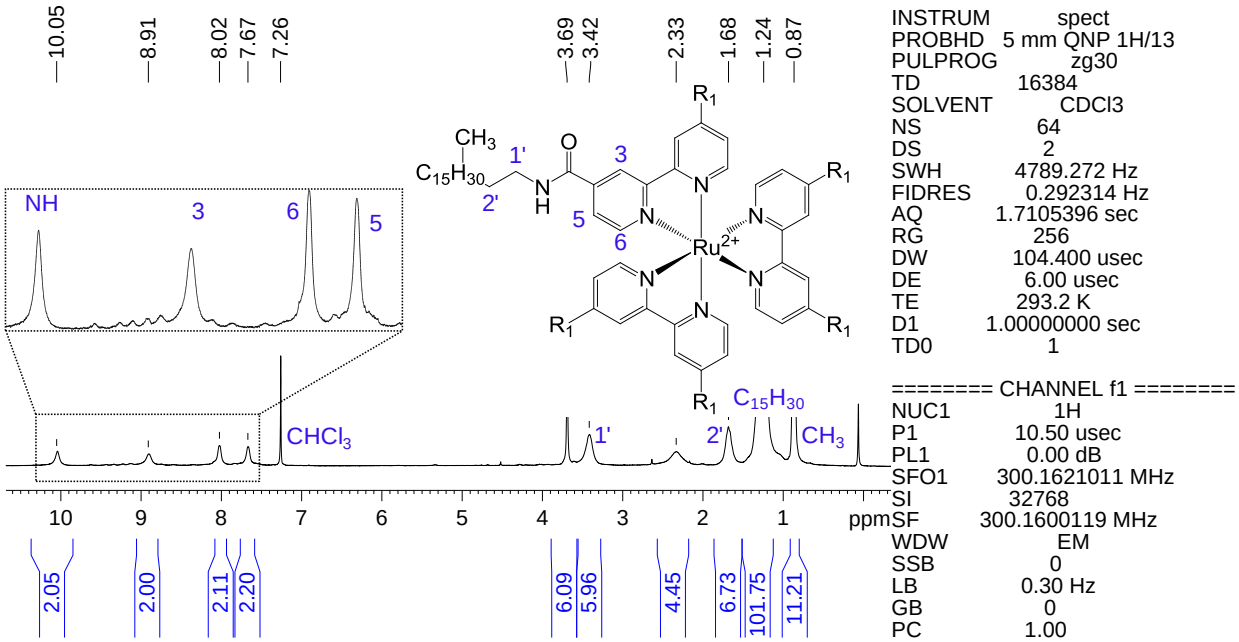

Figure A50. ^{1}H-NMR ($CDCl_3$-d_1) spectrum of $[Ru(nody)_3]Cl_2$. Preparation procedure described in section 2.3.8.

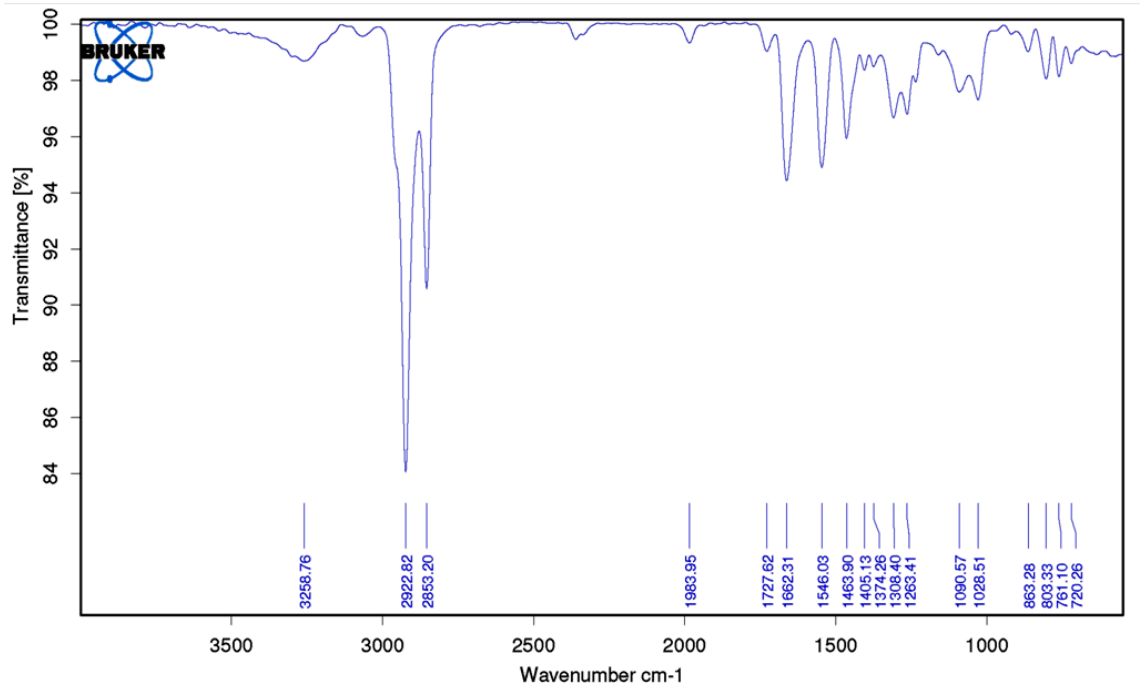

Figure A51. FT-IR (KBr disc) spectrum of $[Ru(nody)_3]Cl_2$. Preparation procedure described in section 2.3.8.

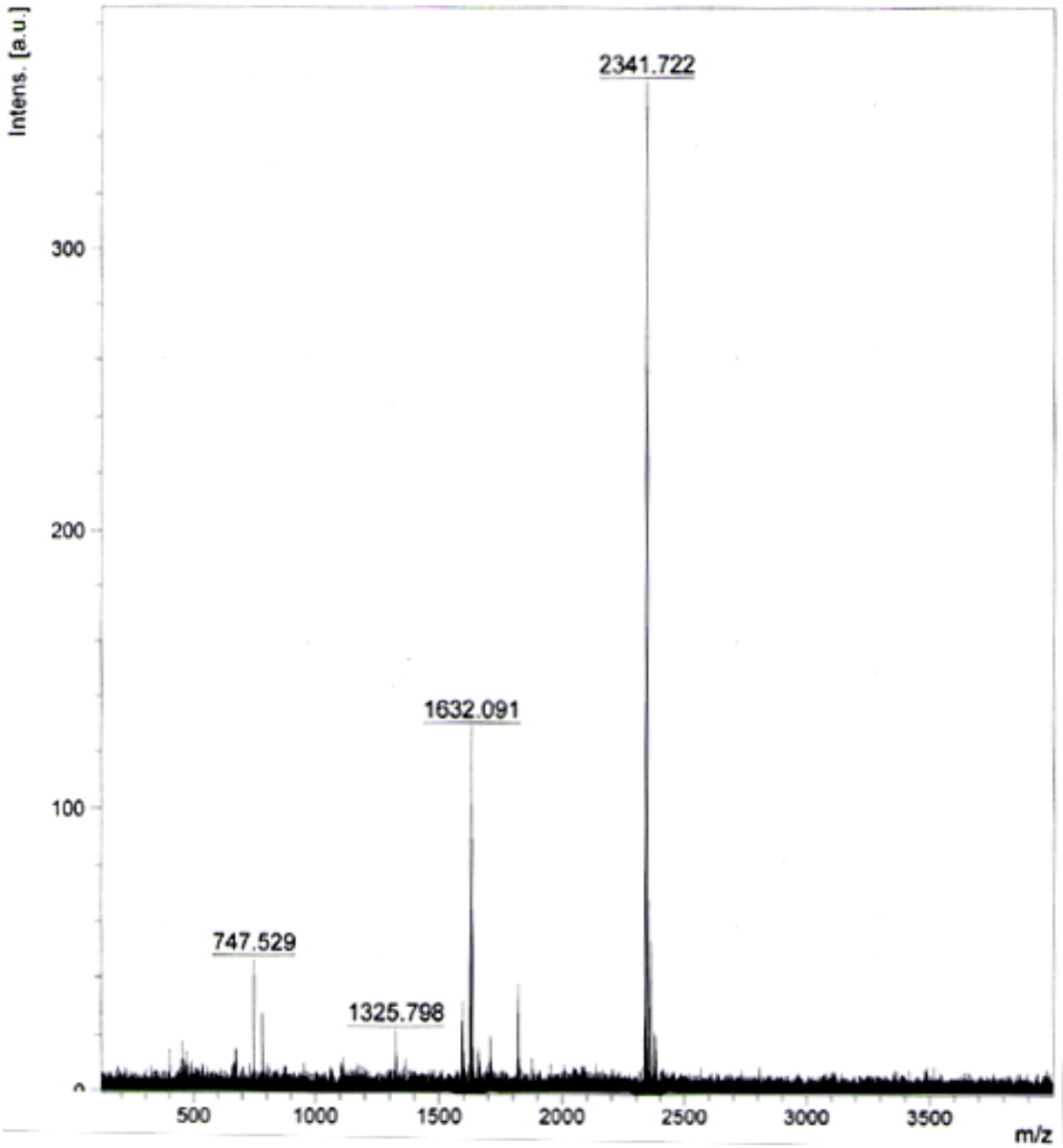

Figure A52. MALDI-TOF MS (positive ion detection) spectrum of $[Ru(nody)_3]Cl_2$. Preparation procedure described in section 2.3.8.

6.1.18. $[Ru(nbpy)_2(nody)](PF_6)_2$

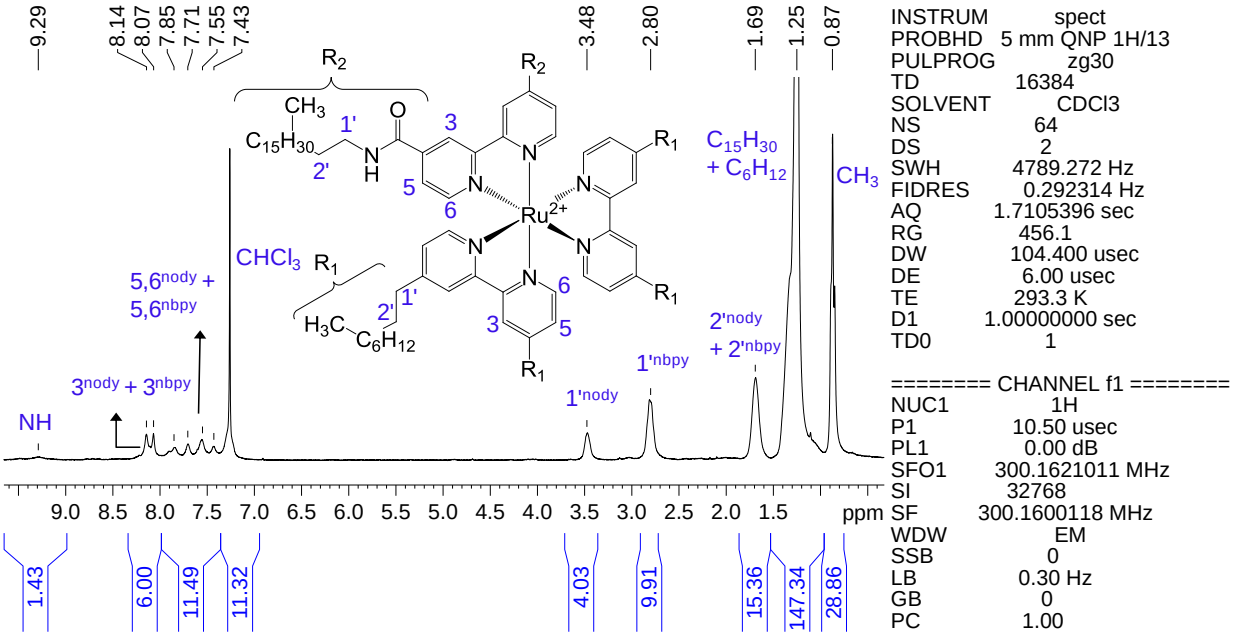

Figure A53. ^{1}H-NMR ($CDCl_3$-d_1) spectrum of $[Ru(nbpy)_2(nody)](PF_6)_2$. Preparation procedure described in section 2.3.9.

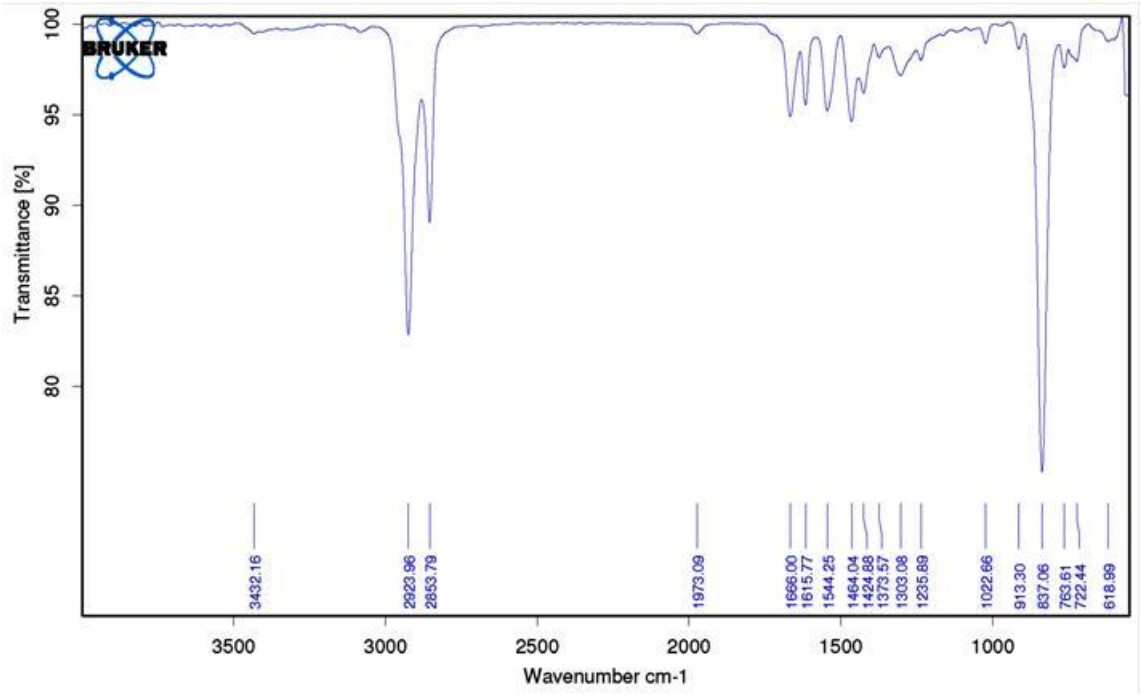

Figure A54. FT-IR (KBr disc) spectrum of $[Ru(nbpy)_2(nody)](PF_6)_2$. Preparation procedure described in section 2.3.9.

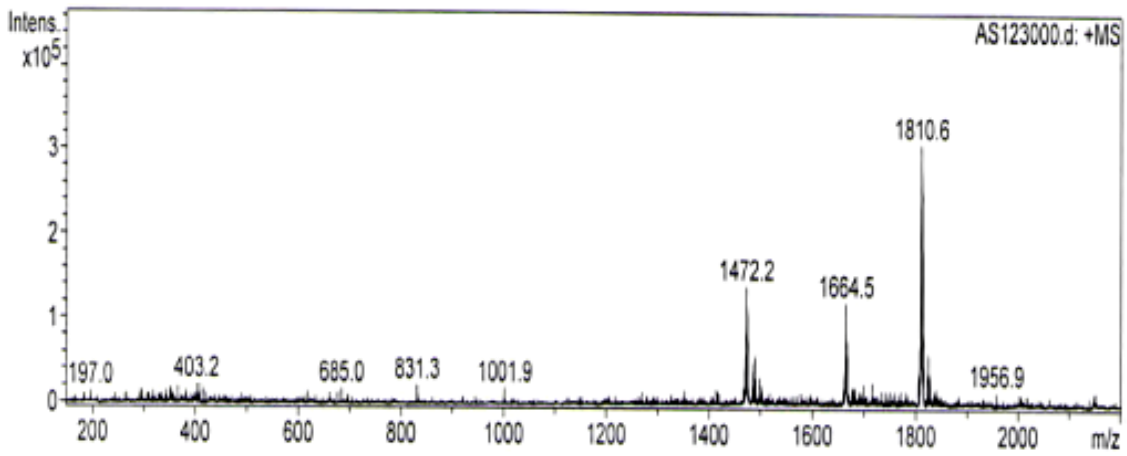

Figure A55. ESI-MS (positive ion detection) spectrum of $[Ru(nbpy)_2(nody)](PF_6)_2$. Preparation procedure described in section 2.3.9.

6.2. Computational chemistry

6.2.1. $[Ru(phen)_2(iip)]^{2+}$

Table S1. Major computed PCM-TD-DFT vertical excitation energies ΔE at B3LYP/6-31G*//B3LYP/6-31G* level for $[Ru(phen)_2(iip)]^{2+}$ in methanol. Plot shown in Figure 60a, section 4.2.

Excited state	ΔE /eV (nm)	f[a] /(a.u.)	Orbitals	Coeff.	Assignment[b]
4	2.79 (445)	24	HOMO→LUMO HOMO-3→LUMO	0.55 0.40	$\pi_{iip} \rightarrow \pi_p^*$ (LLCT)[c] $d_{xy}, d_{xz} \rightarrow \pi_p^*$ (MLCT)[d]
7	2.86 (433)	28	HOMO→LUMO+1 HOMO-2→LUMO+2 HOMO-3→LUMO+1	0.50 -0.31 0.29	$\pi_{iip} \rightarrow \pi_p^*$ (LLCT) $d_{x^2-y^2}, d_{yz} \rightarrow \pi_{Phen}^*$ (MLCT) $d_{xy}, d_{xz} \rightarrow \pi_p^*$ (MLCT)
16	3.18 (390)	17	HOMO-1→LUMO+5	0.53	$d_{z^2} \rightarrow \pi_{iip(phen)}^*$ (MLCT)
20	3.34 (371)	17	HOMO→LUMO+5	0.60	$\pi_{iip} \rightarrow \pi_{iip(phen)}^*$ (IL)[e]
29	3.89 (319)	89	HOMO→LUMO+6	0.67	$\pi_{iip} \rightarrow \pi_{iip}^*$ (IL)
33	4.08 (304)	100	HOMO-3→LUMO+6	0.65	$d_{xy}, d_{xz} \rightarrow \pi_{iip}^*$ (MLCT)
48	4.35 (285)	30	HOMO-7→LUMO HOMO-7→LUMO+1	0.36 0.33	$\pi_{iip} \rightarrow \pi_p^*$ (LLCT) $\pi_{iip} \rightarrow \pi_p^*$ (LLCT)
64	4.62 (269)	56	HOMO-5→LUMO+5	0.41	$\pi_p^* \rightarrow \pi_{iip\ (phen)}^*$ (LLCT)
67	4.67 (265)	21	HOMO-6→LUMO+5 HOMO-5→LUMO+5	0.52 0.37	$\pi \rightarrow \pi_{iip\ (phen)}^*$ (LLCT) $\pi_p^* \rightarrow \pi_{iip\ (phen)}^*$ (LLCT)
69	4.71 (263)	23	HOMO-8→LUMO+3 HOMO-7→LUMO+3	0.45 0.38	$\pi_{Phen} \rightarrow \pi_{Phen}^*$ (IL) $\pi_{iip} \rightarrow \pi_{Phen}^*$ (LLCT)
75	4.79 (259)	72	HOMO-9→LUMO+2	0.45	$\pi_{Phen} \rightarrow \pi_{Phen}^*$ (IL)

[a] Oscillator strength intensities are shown in percentage

[b] π_p – orbitals centred at the phenanthroline moiety of the three ligands
π_{iip} – orbital centred at the iip ligand
π_{Phen} – orbitals centred at the phenanthroline ligands
$\pi_{iip(phen)}$ – orbital centred at the phenanthroline moiety of the iip ligand

[c] Ligand-to-ligand charge transfer

[d] Metal-to-ligand charge transfer

[e] Intra-ligand charge transfer

Table S2. Major computed PCM-TD-DFT vertical excitation energies ΔE at B3LYP-CAM/6-31G*//B3LYP/6-31G* level for $[Ru(phen)_2(iip)]^{2+}$ in methanol. Plot shown in Figure 60b, section 4.2.

Excited state	ΔE /eV (nm)	f[a] /(a.u.)	Orbitals	Coeff.	Assignment[b]
4	3.44 (360)	57	HOMO → LUMO HOMO → LUMO+1 HOMO-3 → LUMO	0.43 0.30 0.30	d_{xy} → π_{iip}^* (MLCT)[c] d_{xy} → π_{iip}^* (MLCT) d_{xy}; d_{xz} → π_{iip}^* (MLCT)
14	3.96 (313)	26	HOMO → LUMO+5 HOMO-3 → LUMO+3 HOMO → LUMO+3	0.51 -0.25 -0.25	d_{xy} → π_{iip}^* (MLCT) d_{xy}; d_{xz} → d_{z^2} (MC)[d] d_{xy} → d_{z^2} (MC)
28	4.47 (277)	88	HOMO → LUMO+6	0.56	d_{xy} → π_{iip}^* (MLCT)
32	4.69 (264)	49	HOMO-4 → LUMO HOMO-5 → LUMO HOMO-4 → LUMO+1	0.27 0.22 0.22	π_{Phen} → π_{iip}^* (LLCT)[e] d_{xy}; π_{Phen} → π_{iip}^* (MLLCT)[f] π_{Phen} → π_{iip}^* (LLCT)
35	4.93 (251)	55	HOMO-4 → LUMO+5 HOMO-5 → LUMO+5 HOMO-6 → LUMO+5	0.34 0.29 -0.25	π_{Phen} → π_{iip}^* (LLCT) d_{xy}; π_{Phen} → π_{iip}^* (MLLCT) $d_{x^2-y^2}$; d_{yz}; π_{Phen} → π_{iip}^* (MLLCT)
37	4.96 (250)	50	HOMO-9 → LUMO+2 HOMO-6 → LUMO+3	0.26 -0.22	$d_{x^2-y^2}$; π_{Phen} → π_{Phen}^* (MLLCT) $d_{x^2-y^2}$; d_{yz}; π_{Phen} → d_{z^2} (MC, LMCT)[g]
38	4.98 (249)	23	HOMO → LUMO+3 HOMO-1 → LUMO+6	0.38 0.29	d_{xy} → d_{z^2} (MC) d_{z^2} → π_{iip}^* (MLCT)
40	5.10 (243)	100	HOMO-1 → LUMO+6 HOMO-2 → LUMO+6	0.41 0.23	d_{z^2} → π_{iip}^* (MLCT) $d_{x^2-y^2}$; d_{yz} → π_{iip}^* (MLCT)
43	5.23 (237)	63	HOMO-2 → LUMO+6 HOMO-9 → LUMO+4 HOMO-7 → LUMO+3	0.27 -0.27 0.25	$d_{x^2-y^2}$; d_{yz} → π_{iip}^* (MLCT) $d_{x^2-y^2}$; π_{Phen} → π_{Phen}^* (MLLCT) π_{iip} → d_{z^2} (LMCT)
45	5.3 (234)	41	HOMO-1 → LUMO+7	0.59	d_{z^2} → π_{Phen}^* (MLCT)

[a] Oscillator strength intensities are shown in percentage

[b] π_{iip} – orbital centred at the iip ligand

π_{Phen} – orbitals centred at the phenanthroline ligands

[c] Metal-to-ligand charge transfer

[d] Metal-centred

[e] Ligand-to-ligand charge transfer

[f] Metal/Ligand-to-ligand charge transfer

[g] Ligand-to-metal charge transfer

Table S3. Major computed PCM-TD-DFT vertical excitation energies ΔE at B3LYP/6-31G*//B3LYP/6-31G* level for the totally protonated species of $[Ru(phen)_2(iip)]^{2+}$ in water. Plot shown in Figure A56.

Excited state	ΔE /eV (nm)	f[a] /(a.u.)	Orbitals	Coeff.	Assignment[b]
3	2.67 (464)	26	HOMO-2 → LUMO	0.56	d_{xy}; d_{xz} → π_{iip}* (MLCT)[c]
			HOMO-2 → LUMO+1	0.32	d_{xy}; d_{xz} → π_{iip}* (MLCT)
13	2.99 (414)	19	HOMO-2 → LUMO+4	0.50	d_{xy}; d_{xz} → $d_{x^2-y^2}$; d_{yz} (MC)[d]
			HOMO-1 → LUMO+3	0.44	$d_{x^2-y^2}$; d_{yz} → d_{xy} (MC)
15	3.04 (408)	25	HOMO → LUMO+5	0.49	d_{z^2} → π_{Phen}* (MLCT)
			HOMO-2 → LUMO+1	-0.34	d_{xy}; d_{xz} → π_{iip}* (MLCT)
16	3.12 (398)	13	HOMO → LUMO+6	0.66	d_{z^2} → π_{Phen}* (MLCT)
27	3.96 (313)	100	HOMO-5 → LUMO	0.60	π_{iip} → π_{iip}* (IL)[e]
33	4.11 (301)	96	HOMO-5 → LUMO+1	0.45	π_{iip} → π_{iip}* (IL)
			HOMO-2 → LUMO+7	0.36	d_{xy}; d_{xz} → π_{iip}* (MLCT)
66	4.66 (266)	74	HOMO-8 → LUMO+2	0.55	π_{iip} → π_{iip}* (IL)
67	4.67 (265)	77	HOMO-8 → LUMO+1	0.44	π_{iip} → π_{iip}* (IL)
72	4.77 (260)	58	HOMO-7 → LUMO+4	0.43	π_{Phen} → $d_{x^2-y^2}$; d_{yz} (LMCT)[f]
			HOMO-3 → LUMO+6	-0.28	π_{Phen} → π_{Phen}* (IL)
73	4.78 (259)	13	HOMO-8 → LUMO+3	0.63	π_{iip} → d_{xy} (LMCT)

[a] Oscillator strength intensities are shown in percentage

[b] π_{iip} – orbital centred at the iip ligand

π_{Phen} – orbitals centred at the phenanthroline ligands

[c] Metal-to-ligand charge transfer

[d] Metal centred

[e] Intra-ligand

[f] Ligand-to-metal charge transfer

Table S4. Major computed PCM-TD-DFT vertical excitation energies ΔE at B3LYP/6-31G*//B3LYP/6-31G* level for the monoprotonated species of $[Ru(phen)_2(iip)]^{2+}$ in water. Plot shown in Figure A57.

Excited state	ΔE /eV (nm)	f[a] /(a.u.)	Orbitals	Coeff.	Assignment[b]
5	2.82 (440)	36	HOMO-1 → LUMO	0.59	d_{xy}; d_{xz} → π_{iip}* (MLCT)[c]
13	3.13 (396)	21	HOMO-1 → LUMO+4	0.41	d_{xy}; d_{xz} → π_{Phen}* (MLCT)
			HOMO-2 → LUMO+4	-0.36	$d_{x^2-y^2}$; d_{yz} → π_{Phen}* (MLCT)
			HOMO-2 → LUMO+3	0.32	$d_{x^2-y^2}$; d_{yz} → π_{iip}* (MLCT)
25	3.78 (328)	100	HOMO-3 → LUMO+1	0.62	d_{xy}; π_{iip} → π_{Phen}* (MLLCT)[d]
27	3.81 (325)	28	HOMO-3 → LUMO+3	0.54	d_{xy}; π_{iip} → π_{iip}* (MLLCT)
			HOMO-3 → LUMO+1	-0.31	d_{xy}; π_{iip} → π_{Phen}* (MLLCT)
29	3.97 (312)	27	HOMO-3 → LUMO+4	0.62	d_{xy}; π_{iip} → π_{Phen}* (MLLCT)
31	4.01 (309)	41	HOMO-3 → LUMO+6	0.42	d_{xy}; π_{iip} → π_{iip}* (MLLCT)
			HOMO-4 → LUMO+1	0.30	π_{Phen} → π_{Phen}* (IL)[e]
54	4.46 (278)	20	HOMO-8 → LUMO	0.47	π_{Phen} → π_{iip}* (LLCT)[f]
			HOMO-6 → LUMO+3	0.30	π_{iip} → π_{iip}* (IL)
61	4.57 (271)	36	HOMO → LUMO+9	0.53	d_{z^2} → π_{iip}* (MLCT)
			HOMO-6 → LUMO	-0.24	π_{iip} → π_{iip}* (IL)
63	4.65 (266)	25	HOMO-7 → LUMO+4	0.37	π_{Phen} → π_{Phen}* (IL)
			HOMO-7 → LUMO+3	-0.35	π_{Phen} → π_{iip}* (LLCT)
			HOMO-2 → LUMO+9	-0.21	$d_{x^2-y^2}$; d_{yz} → π_{iip}* (MLCT)
74	4.78 (259)	83	HOMO-8 → LUMO+2	0.43	π_{Phen} → $d_{x^2-y^2}$; d_{yz} (LMCT)[g]
			HOMO-4 → LUMO+5	-0.26	π_{Phen} → π_{Phen}* (IL)

[a] Oscillator strength intensities are shown in percentage

[b] π_{iip} – orbital centred at the iip ligand

π_{Phen} – orbitals centred at the phenanthroline ligands

[c] Metal-to-ligand charge transfer

[d] Metal/Ligand-to-ligand charge transfer

[e] Intra-ligand

[f] Ligand-to-ligand charge transfer

[g] Ligand-to-metal charge transfer

Table S5. Major computed PCM-TD-DFT vertical excitation energies ΔE at B3LYP/6-31G*//B3LYP/6-31G* level for the neutral species of $[Ru(phen)_2(iip)]^{2+}$ in water. Plot shown in Figure A58.

Excited state	ΔE /eV (nm)	f[a] /(a.u.)	Assignment	Coeff.	Character[b]
4	2.79 (445)	22	HOMO → LUMO	0.56	d_{xy}; d_{xz}; π_{iip} → π^* (MLCT; LLCT)[c]
			HOMO-3 → LUMO	0.40	d_{xy} → π^* (MLCT)
7	2.86 (433)	28	HOMO → LUMO+1	0.50	d_{xy}; d_{xz}; π_{iip} → d_{xy}; d_{xz}; π_{iip}^* (MLCT; MC; IL)[d]
			HOMO-2 → LUMO+2	-0.31	$d_{x^2-y^2}$ → π_{Phen}^* (MLCT)
			HOMO-3 → LUMO+1	0.29	d_{xy} → d_{xy}; d_{xz}; π_{iip}^* (MLCT; MC)
29	3.89 (319)	77	HOMO → LUMO+6	0.67	d_{xy}; d_{xz}; π_{iip} → π_{iip}^* (MLCT; IL)
33	4.07 (304)	100	HOMO-3 → LUMO+6	0.65	d_{xy} → π_{iip}^* (MLCT)
48	4.36 (284)	29	HOMO-7 → LUMO	0.37	π_{iip} → π^* (LLCT)
			HOMO-7 → LUMO+1	0.33	π_{iip} → d_{xy}; d_{xz}; π_{iip}^* (IL; LMCT)[e]
64	4.62 (268)	48	HOMO-5 → LUMO+5	0.44	π → π_{iip}^* (LLCT)
			HOMO-7 → LUMO+1	-0.32	π → π_{iip}^* (LLCT)
75	4.79 (259)	51	HOMO-9 → LUMO+2	0.33	π → π_{Phen}^* (LLCT)
			HOMO-7 → LUMO+4	-0.29	π → π_{Phen}^* (LLCT)
			HOMO-7 → LUMO+5	0.25	π → π_{iip}^* (LLCT)

[a] Oscillator strength intensities are shown in percentage

[b] π_{iip} – orbital centred at the iip ligand
π_{Phen} – orbitals centred at the phenanthroline ligands
π – orbital centred at the three ligands

[c] Metal-to-ligand charge transfer and Ligand-to-ligand charge transfer

[d] Metal centred and Intra-ligand

[e] Ligand-to-metal charge transfer

Table S6. Major computed PCM-TD-DFT vertical excitation energies ΔE at B3LYP/6-31G*//B3LYP/6-31G* level for the monodeprotonated species of $[Ru(phen)_2(iip)]^{2+}$ in water. Plot shown in Figure A59.

Excited state	ΔE /eV (nm)	f[a] /(a.u.)	Orbitals			Coeff.	Assignment[b]			
13	2.94 (422)	27	HOMO-1	→	LUMO+3	0.47	d_{z^2}	→	π_{Phen}^*	(MLCT)[c]
			HOMO-2	→	LUMO	0.32	d_{yz}	→	π_{Phen}^*	(MLCT)
16	3.08 (403)	29	HOMO-2	→	LUMO+2	0.60	d_{yz}	→	π_{Phen}^*	(MLCT)
27	3.70 (336)	100	HOMO	→	LUMO+6	0.68	π_{iip}	→	π_{iip}^*	(IL)[d]
31	3.82 (325)	34	HOMO-4	→	LUMO+3	0.46	π_{iip}	→	π_{Phen}^*	(IL)
			HOMO-4	→	LUMO+4	-0.34	π_{iip}	→	π_{iip}^*	(IL)
34	3.91 (317)	54	HOMO	→	LUMO+7	0.66	π_{iip}	→	π_{iip}^*	(IL)
42	4.17 (297)	32	HOMO-5	→	LUMO+4	0.39	π_{iip}	→	π_{iip}^*	(IL)
			HOMO-3	→	LUMO+6	-0.38	d_{xy}; d_{xz}	→	π_{iip}^*	(MLCT)
52	4.35 (285)	89	HOMO-4	→	LUMO+5	0.32	π_{iip}	→	π_{iip}^*	(IL)
			HOMO-2	→	LUMO+8	0.31	d_{yz}	→	π_{Phen}^*	(MLCT)
54	4.38 (283)	92	HOMO-4	→	LUMO+5	0.47	π_{iip}	→	π_{iip}^*	(IL)
			HOMO-3	→	LUMO+12	-0.23	d_{xy}; d_{xz}	→	d_{xz}; d_{xy}	(MC)[e]
73	4.69 (265)	34	HOMO-9	→	LUMO+2	0.56	π_{Phen}	→	π_{Phen}^*	(IL)
			HOMO-10	→	LUMO+3	0.23	π_{Phen}	→	π_{Phen}^*	(IL)
82	4.80 (258)	76	HOMO-10	→	LUMO+1	0.39	π_{Phen}	→	$d_{x^2-y^2}$; π_{Phen}^*	(LMCT, IL)[f]
			HOMO-9	→	LUMO+4	-0.39	π_{Phen}	→	π_{iip}^*	(LLCT)
85	4.83 (257)	64	HOMO	→	LUMO+14	0.32	π_{iip}	→	π_{iip}^*	(IL)
			HOMO-4	→	LUMO+6	-0.29	π_{iip}	→	π_{iip}^*	(IL)
			HOMO	→	LUMO+13	-0.24	π_{iip}	→	$d_{x^2-y^2}$; d_{yz}	(LMCT)
87	4.87 (255)	68	HOMO	→	LUMO+13	0.42	π_{iip}	→	$d_{x^2-y^2}$; d_{yz}	(LMCT)
			HOMO-1	→	LUMO+10	0.34	d_{z^2}	→	π_{Phen}^*	(MLCT)
			HOMO-11	→	LUMO	0.28	π_{iip}	→	π_{Phen}^*	(LLCT)
105	5.11 (243)	87	HOMO-11	→	LUMO+4	0.51	π_{iip}	→	π_{iip}^*	(IL)
			HOMO-3	→	LUMO+10	-0.24	d_{xy}; d_{xz}	→	π_{Phen}^*	(MLCT)
			HOMO	→	LUMO+14	-0.23	π_{iip}	→	π_{iip}^*	(IL)

[a] Oscillator strength intensities are shown in percentage

[b] π_{iip} – orbital centred at the iip ligand

π_{Phen} – orbitals centred at the phenanthroline ligands

[c] Metal-to-ligand charge transfer

[d] Intra-ligand

[e] Metal-centred

[f] Intra-ligand

Table S7. Major computed PCM-TD-DFT vertical excitation energies ΔE at B3LYP/6-31G*//B3LYP/6-31G* level for the totally deprotonated species of $[Ru(phen)_2(iip)]^{2+}$ in water. Plot shown in Figure A60.

Excited state	ΔE /eV (nm)	f[a] /(a.u.)	Orbitals			Coeff.	Assignment[b]			
16	2.96 (419)	30	HOMO-1	→	LUMO+2	0.36	d_{z^2}	→	d_{z^2}; π_{Phen}*	(MC; MLCT)[c]
			HOMO-3	→	LUMO+1	-0.35	d_{yz}; $d_{x^2-y^2}$	→	$d_{x^2-y^2}$; π_{Phen}*	(MC; MLCT)
19	3.05 (406)	27	HOMO-3	→	LUMO+2	0.63	d_{yz}; $d_{x^2-y^2}$	→	d_{z^2}; π_{Phen}*	(MC; MLCT)
23	3.27 (379)	35	HOMO-4	→	LUMO	0.41	d_{xz}; d_{xy}; π_{iip}	→	π_{Phen}*	(MLCT; LLCT)[d]
			HOMO	→	LUMO+8	0.34	π_{iip}	→	π_{iip}*	(IL)[e]
25	3.30 (376)	71	HOMO	→	LUMO+8	0.58	π_{iip}	→	π_{iip}*	(IL)
66	4.25 (291)	100	HOMO-5	→	LUMO+5	0.60	π_{iip}	→	π_{iip}*	(IL)
96	4.66 (266)	31	HOMO	→	LUMO+19	0.36	π_{iip}	→	π_{iip}*	(IL)
97	4.67 (265)	24	HOMO-12	→	LUMO+2	0.51	π_{Phen}	→	d_{z^2}; π_{Phen}*	(IL; LMCT)[f]
105	4.75 (261)	23	HOMO-13	→	LUMO+3	0.54	π_{Phen}	→	π_{Phen}*	(IL)
106	4.79 (259)	91	HOMO-12	→	LUMO+1	0.30	π_{Phen}	→	$d_{x^2-y^2}$; π_{Phen}*	(IL; LMCT)
			HOMO-13	→	LUMO+3	-0.28	π_{Phen}	→	π_{Phen}*	(IL)
			HOMO-13	→	LUMO	0.23	π_{Phen}	→	π_{Phen}*	(IL)
124	4.98 (249)	22	HOMO-4	→	LUMO+7	0.51	d_{xz}; d_{xy}; π_{iip}	→	π_{Phen}*	(MLCT; LLCT)
127	5.04 (246)	48	HOMO-14	→	LUMO+4	0.44	d_{z^2}; π_{iip}	→	d_{xz}; d_{xy}; π_{iip}*	(MC; LMCT; IL)
			HOMO-5	→	LUMO+8	-0.43	π_{iip}	→	π_{iip}*	(IL)

[a] Oscillator strength intensities are shown in percentage

[b] π_{iip} – orbital centred at the iip ligand; π_{Phen} – orbitals centred at the phenanthroline ligands

[c] Metal-centred and Metal-to-ligand charge transfer

[d] Ligand-to-ligand charge transfer

[e] Intra-ligand

[f] Ligand-to-metal charge transfer

Table S8. Major computed PCM-TD-DFT vertical excitation energies ΔE at B3LYP/6-31G*//B3LYP/6-31G* level for the supramolecular complex 1:1 $[Ru(phen)_2(iip)]^{2+}$-$CuCl_2$ in water. Plot shown in Figure 64.

Excited state	ΔE /eV (nm)	f[a] /(a.u.)	Orbitals	Coeff.	Assignment[b]
1	1.00 (1240)	0	HOMO-9β → LUMOβ	0.54	p_{Cl} → Cu d_{xz} (LMCT)[c]
2	1.17 (1062)	0	HOMO-1β → LUMOβ	0.51	d_{xz}; d_{yz} → Cu d_{xz} (MMCT)[d]
3	1.25 (988)	0	HOMOβ → LUMOβ	0.58	d_{z^2} → Cu d_{xz} (MMCT)
4	1.28 (966)	0	HOMOβ → LUMOβ	0.73	d_{z^2} → Cu d_{xz} (MMCT)
5	1.34 (923)	0	HOMO-1β → LUMOβ	0.59	d_{xz}; d_{yz} → Cu d_{xz} (MMCT)
6	1.41 (876)	0	HOMO-2β → LUMOβ	0.98	$d_{x^2-y^2}$ → Cu d_{xz} (MMCT)
7	1.50 (829)	0	HOMO-3β → LUMOβ	0.62	d_{xz}; d_{xy}; π_{iip} → Cu d_{xz} (MMCT; LMCT)
			HOMO-1β → LUMOβ	0.54	d_{xz}; d_{yz} → Cu d_{xz} (MMCT)
8	1.64 (758)	0	HOMO-3β → LUMOβ	0.54	d_{xz}; d_{xy}; π_{iip} → Cu d_{xz} (MMCT; LMCT)
9	2.31 (536)	0	HOMO-13β → LUMOβ	0.49	p_{Cl} → Cu d_{xz} (LMCT)
28	2.82 (440)	17	HOMO-1β → LUMO+1β	0.62	d_{xz}; d_{yz} → π_{iip}* (MLCT)[e]
			HOMO-1α → LUMOα	0.61	d_{xz}; d_{xy} → π_{iip}* (MLCT)
35	2.89 (429)	13	HOMO-1β → LUMO+2β	0.50	d_{xz}; d_{yz} → d_{xz}; d_{xy} (MC)[f]
			HOMO-1α → LUMO+1α	-0.50	d_{xz}; d_{xy} → d_{xz}; d_{xy} (MC)
39	2.93 (423)	11	HOMO-1β → LUMO+3β	0.42	d_{xz}; d_{yz} → $d_{x^2-y^2}$ (MC)
			HOMO-1α → LUMO+2α	0.42	d_{xz}; d_{xy} → $d_{x^2-y^2}$ (MC)
			HOMO-2β → LUMO+2 β	0.42	$d_{x^2-y^2}$ → d_{xz}; d_{xy} (MC)
			HOMO-2α → LUMO+1α	-0.41	$d_{x^2-y^2}$ → d_{xz}; d_{xy} (MC)
43	3.03 (410)	10	HOMOβ → LUMO+5β	0.62	d_{z^2} → π_{Phen}* (MLCT)
			HOMOα → LUMO+4α	0.62	d_{z^2} → π_{Phen}* (MLCT)
44	3.07 (404)	9	HOMOβ → LUMO+6β	0.64	d_{z^2} → π_{iip}* (MLCT)
			HOMOα → LUMO+5α	0.62	d_{z^2} → π_{iip}* (MLCT)
49	3.12 (397)	11	HOMO-1β → LUMO+4β	0.59	d_{xz}; d_{yz} → π_{Phen}* (MLCT)
			HOMO-1α → LUMO+3α	0.59	d_{xz}; d_{xy} → π_{Phen}* (MLCT)
50	3.13 (397)	11	HOMO-2α → LUMO+3α	0.58	$d_{x^2-y^2}$ → π_{Phen}* (MLCT)
			HOMO-2β → LUMO+4β	0.57	$d_{x^2-y^2}$ → π_{Phen}* (MLCT)
85	3.75 (331)	24	HOMO-3β → LUMO+6 β	0.41	d_{xz}; d_{xy}; π_{iip} → π_{iip}* (MLLCT)[g]
			HOMO-3α → LUMO+5α	0.41	d_{xz}; d_{xy}; π_{iip} → π_{iip}* (MLLCT)
			HOMO-3α → LUMO+2α	0.38	d_{xz}; d_{xy}; π_{iip} → $d_{x^2-y^2}$ (MC; LMCT)
100	4.08 (304)	100	HOMO-3α → LUMO+6α	0.55	d_{xz}; d_{xy}; π_{iip} → π_{iip}* (MLLCT)
			HOMO-3β → LUMO+7β	0.55	d_{xz}; d_{xy}; π_{iip} → π_{iip}* (MLLCT)
128	4.37 (284)	12	HOMO-6α → LUMOα	0.56	π_{iip} → π_{iip}* (IL)[h]
			HOMO-6β → LUMO+1β	0.55	π_{iip} → π_{iip}* (IL)

142	4.47 (278)	12	HOMO-6β	→	LUMO+2β	0.36	π_{iip}	→	d_{xz}; d_{xy} (LMCT)
			HOMO-5α	→	LUMO+5α	0.32	$d_{x^2-y^2}$; π_{Phen}	→	π_{iip}* (MLLCT)
			HOMO-6α	→	LUMO+1α	-0.32	π_{iip}	→	d_{xz}; d_{xy} (LMCT)
			HOMO-4α	→	LUMO+5α	-0.32	π_{Phen}	→	π_{iip}* (LLCT)[i]
			HOMO-5β	→	LUMO+6β	0.32	$d_{x^2-y^2}$; π_{Phen}	→	π_{iip}* (MLLCT)
145	4.48 (277)	8	HOMO-8α	→	LUMOα	0.35	d_{z^2}; d_{xz}; d_{yz}	→	π_{iip}* (MLCT)
			HOMO-1α	→	LUMO+8α	-0.27	d_{xz}; d_{xy}	→	π_{Phen}* (MLCT)
152	4.51 (275)	7	HOMO-6β	→	LUMO+3β	0.51	π_{iip}	→	$d_{x^2-y^2}$ (LMCT)
			HOMO-6α	→	LUMO+2α	0.35	π_{iip}	→	$d_{x^2-y^2}$ (LMCT)
			HOMO-4β	→	LUMO+6β	-0.34	π_{Phen}	→	π_{iip}* (LLCT)

[a] Oscillator strength intensities are shown in percentage

[b] π_{Phen} – orbitals centred at the phenanthroline ligands; π_{iip} – orbital centred at the iip ligand

[c] Ligand-to-metal charge transfer

[d] Metal-to-metal charge transfer

[e] Metal-to-ligand charge transfer

[f] Metal-centred

[g] Metal/Ligand-to-ligand charge transfer

[h] Intra-ligand

[i] Ligand-to-ligand charge transfer

Table S9. First 10 computed PCM-TD-DFT vertical excitation energies (ΔE) at B3LYP/6-31G*//B3LYP/6-31G* level and corresponding assignment for the optimized quadruplet of the supramolecular complex 1:1 $[Ru(phen)_2(iip)]^{2+}$-$CuCl_2$ in water.

Excited state	ΔE /eV (nm)	f[a] × 10^4	Coeff.	Assignment[b]			
D_1	1.32 (936)	8	0.60	Cu d_{xy}; Cu $d_{x^2-y^2}$; p_{Cl}	→	Cu d_{xz}	(MC; LMCT)[c]
D_2	1.45 (856)	15	0.65	Ru d_{xz}; Ru d_{z^2}	→	Cu d_{xz}	(MMCT)[d]
D_3	1.56 (795)	12	0.49	p_{Cl}	→	Cu d_{xz}	(LMCT)
D_4	1.59 (781)	8	0.48	Ru d_{xz}; Ru d_{z^2}	→	Cu d_{xz}	(MMCT)
D_5	1.68 (737)	2	0.63	Ru d_{z^2}	→	Cu d_{xz}	(MMCT)
D_6	1.82 (681)	2	0.66	Ru d_{z^2}	→	Cu d_{xz}	(MMCT))
D_7	1.84 (673)	0	0.96	Ru $d_{x^2-y^2}$	→	Cu d_{xz}	(MMCT)
Q_1	1.93 (641)	0	0.65	Ru d_{xz}; Ru d_{z^2}	→	π_{Phen}*	(MLCT)[e]
D_8	1.98 (624)	7	0.80	Ru d_{xz}	→	Cu d_{xz}	(MMCT)
Q_2	2.20 (564)	0	0.63	Ru d_{z^2}	→	π_{Phen}*	(MLCT)

[a] Oscillator strength intensities in arbitrary units

[b] p_{Cl} – orbital centred at the chlorine atoms; π_{Phen} – orbitals centred at the phen. ligands

[c] Metal-centred and Ligand-to-metal charge transfer

[d] Metal-to-metal charge transfer

[e] Metal-to-ligand charge transfer

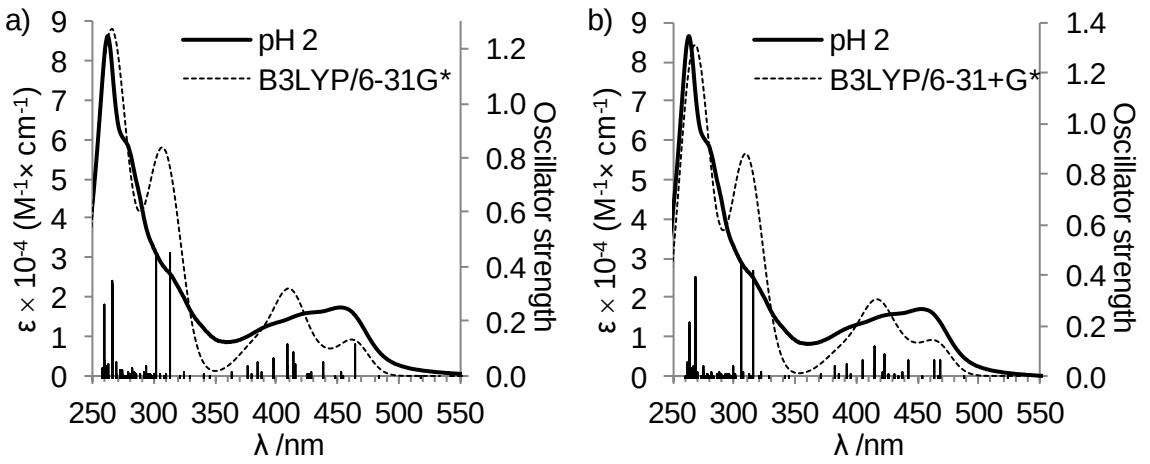

Figure A56. Absorption spectrum of $[Ru(phen)_2(iip)]^{2+}$ in pH 2 phosphate buffer solution (solid line) and computed PCM-TD-DFT vertical excitation energies (Nstates = 75) using the basis set 6-31G* (a) and 6-31+G* (b). The dashed line represents a Gaussian convolution of the vertical excitation energies.

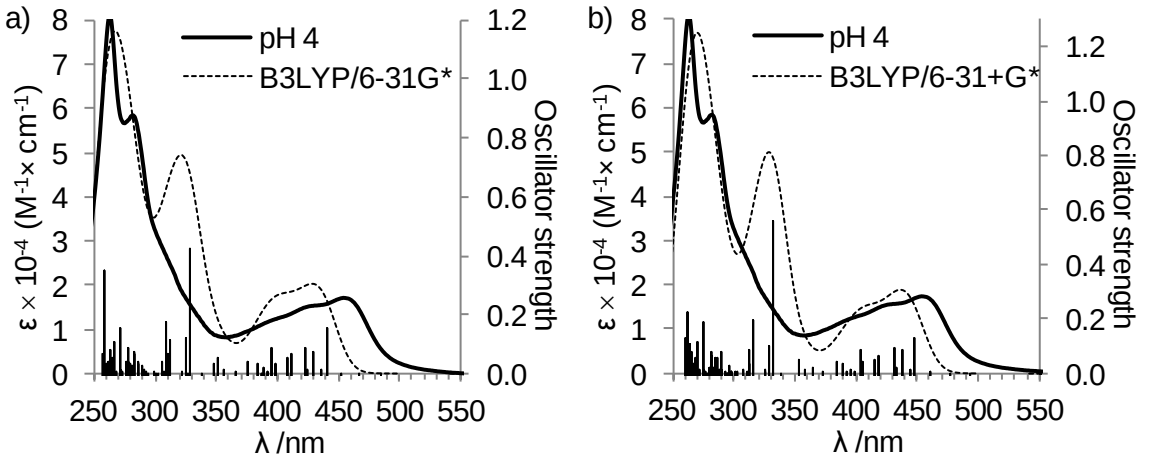

Figure A57. Absorption spectrum of $[Ru(phen)_2(iip)]^{2+}$ in pH 4 phosphate buffer solution (solid line) and computed PCM-TD-DFT vertical excitation energies (Nstates = 75) using the basis set 6-31G* (a) and 6-31+G* (b). The dashed line represents a Gaussian convolution of the vertical excitation energies.

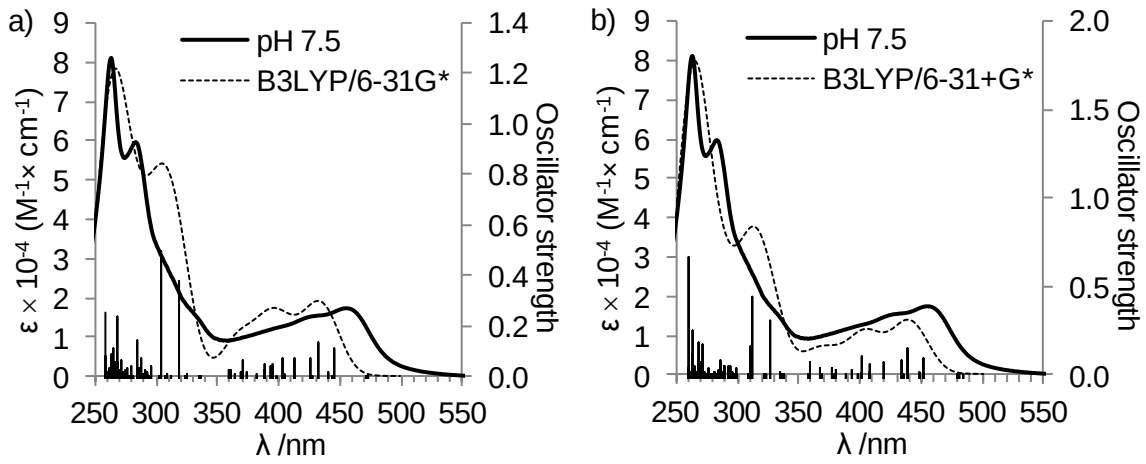

Figure A58. Absorption spectrum of $[Ru(phen)_2(iip)]^{2+}$ in pH 7.5 phosphate buffer solution (solid line) and computed PCM-TD-DFT vertical excitation energies (Nstates = 75) using the basis set 6-31G* (a) and 6-31+G* (b). The dashed line represents a Gaussian convolution of the vertical excitation energies.

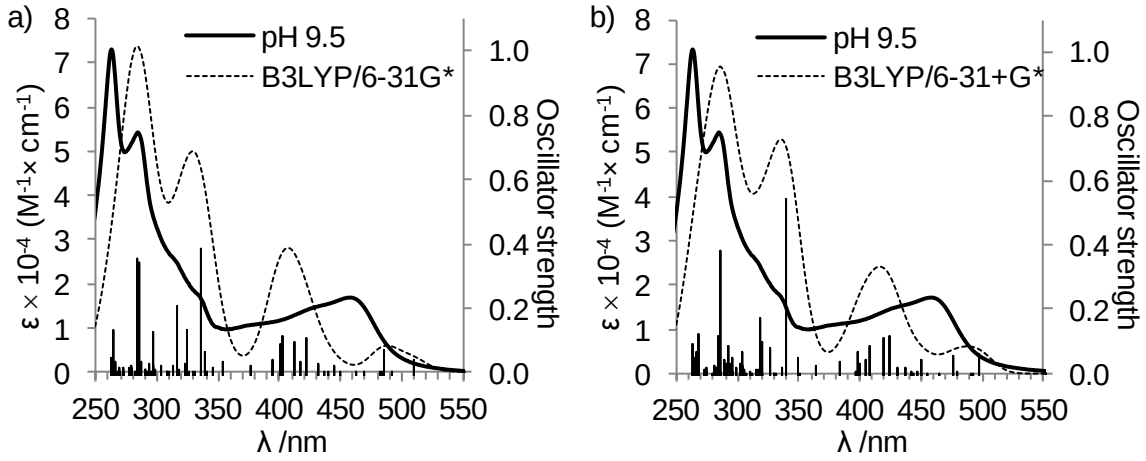

Figure A59. Absorption spectrum of $[Ru(phen)_2(iip)]^{2+}$ in pH 9.5 phosphate buffer solution (solid line) and computed PCM-TD-DFT vertical excitation energies (Nstates = 75) using the basis set 6-31G* (a) and 6-31+G* (b). The dashed line represents a Gaussian convolution of the vertical excitation energies.

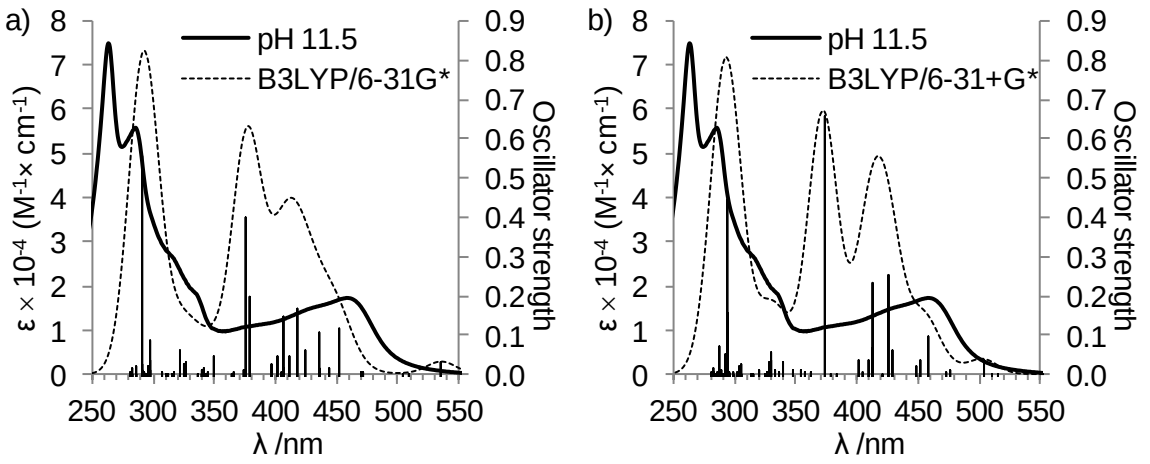

Figure A60. Absorption spectrum of $[Ru(phen)_2(iip)]^{2+}$ in pH 11.5 phosphate buffer solution (solid line) and computed PCM-TD-DFT vertical excitation energies (Nstates = 75) using the basis set 6-31G* (a) and 6-31+G* (b). The dashed line represents a Gaussian convolution of the vertical excitation energies.

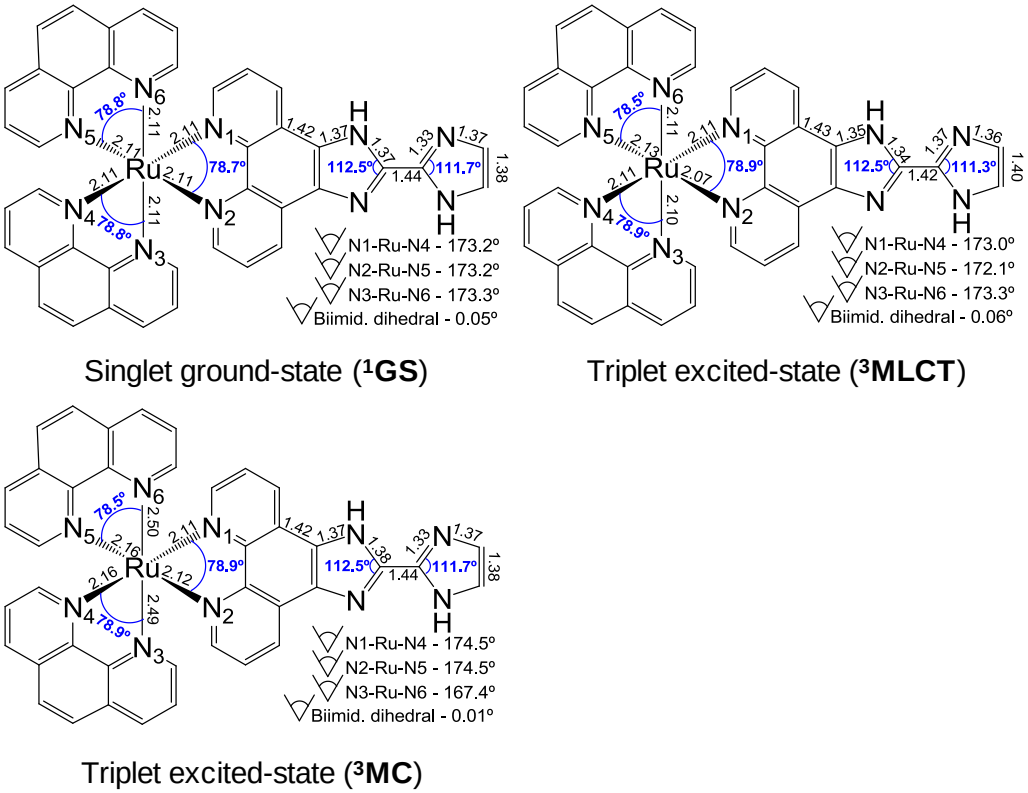

Figure A61. Geometrical features of the singlet ground state (^{1}GS), excited metal-to-ligand charge transfer triplet state (^{3}MLCT) and excited metal-centred triplet state (^{3}MC) of $[Ru(phen)_2(iip)]^{2+}$. Optimizations in gas phase using the computational protocol B3LYP/6-31G*.

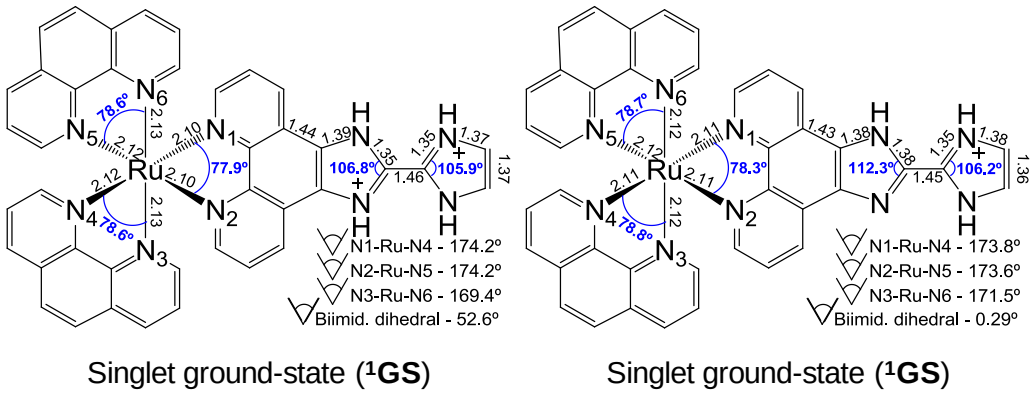

Singlet ground-state (**^{1}GS**) Singlet ground-state (**^{1}GS**)

Figure A62. Geometrical features of the singlet ground state (^{1}GS) of the totally protonated and monoprotonated $[Ru(phen)_2(iip)]^{2+}$. Optimizations in gas phase using the computational protocol B3LYP/6-31G*.

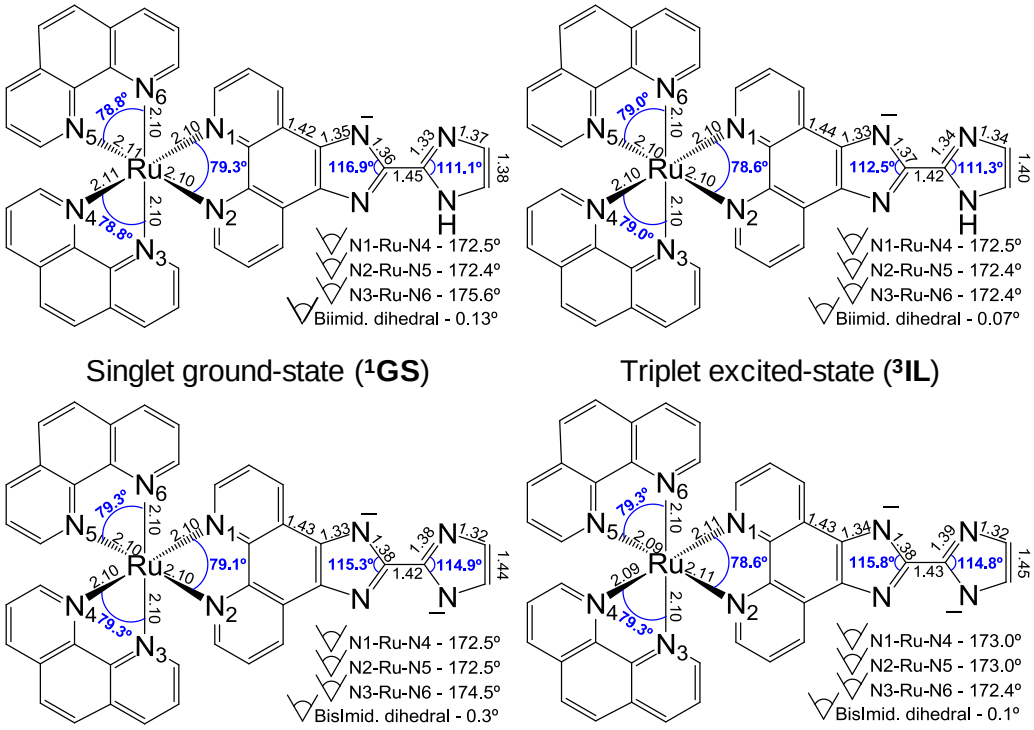

Singlet ground-state (**^{1}GS**) Triplet excited-state (**^{3}IL**)

Singlet ground-state (**^{1}GS**) Triplet excited-state (**^{3}LLCT**)

Figure A63. Geometrical features of the singlet ground state (^{1}GS) and lowest triplet excited state of the totally deprotonated (bottom) and monodeprotonated (top) species of $[Ru(phen)_2(iip)]^{2+}$. Optimizations in gas phase using the computational protocol B3LYP/6-31G*.

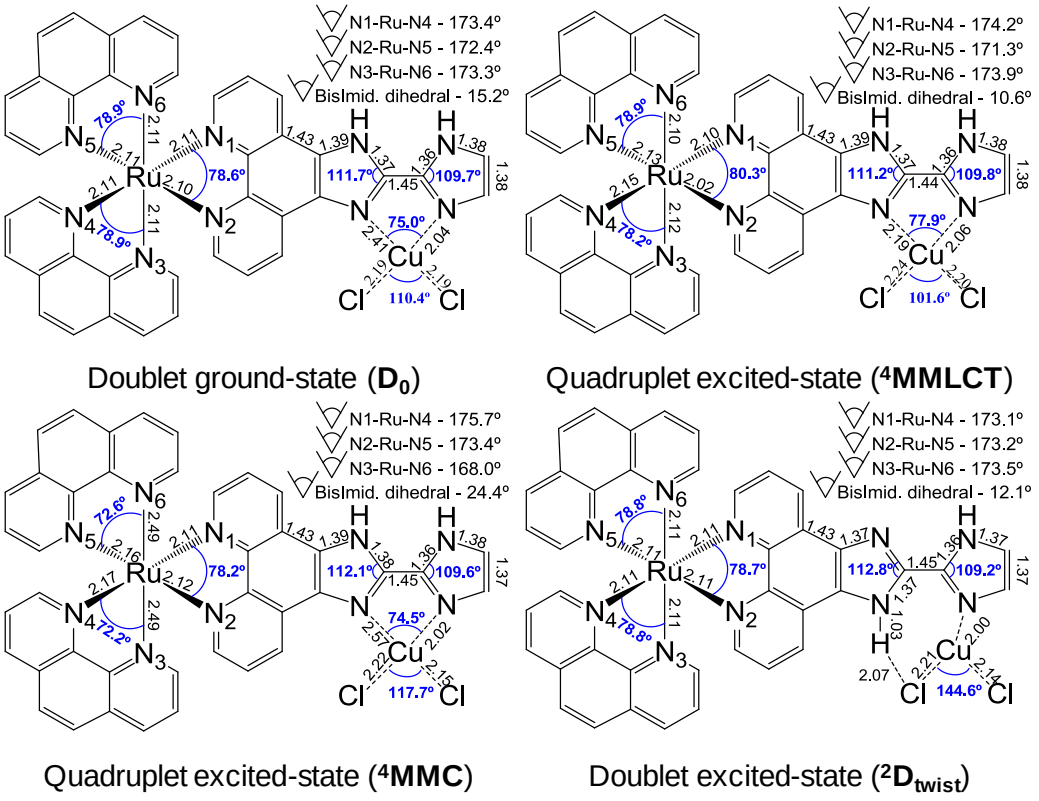

Figure A64. Geometrical features of the relevant states for the supramolecular compound $[Ru(phen)_2(iip)]^{2+}$-$CuCl_2$. Optimizations in gas phase using the computational protocol B3LYP/6-31G*.

6.2.2. $[Ru(phen)_2(hmip)]^{2+}$

Table S10. Major computed PCM-TD-DFT vertical excitation energies ΔE at B3LYP/6-31G*//B3LYP/6-31G* level for the global minimum **GM** isomer of $[Ru(phen)_2(hmip)]^{2+}$ in water. Plot shown in Figure 68a.

Excited state	ΔE /eV (nm)	f[a] /(a.u.)	Orbitals			Coeff.	Assignment[b]			
4	2.74 (452)	23	HOMO	→	LUMO	0.56	π_{hmip}	→	π*	(LLCT; IL)[c]
			HOMO-2	→	LUMO	0.34	d_{xz}; d_{xy}	→	π*	(MLCT)[d]
17	3.14 (395)	31	HOMO	→	LUMO+5	0.40	π_{hmip}	→	π_{hmip}*	(IL)
			HOMO-3	→	LUMO+3	0.39	$d_{x^2-y^2}$	→	d_{z^2}	(MC)[e]
			HOMO-1	→	LUMO+5	0.35	$d_{x^2-y^2}$	→	π_{hmip}*	(MLCT)
26	3.56 (348)	46	HOMO	→	LUMO+6	0.68	π_{hmip}	→	π_{hmip}*	(IL)
43	4.22 (294)	32	HOMO-4	→	LUMO+6	0.39	π_{hmip}	→	π_{hmip}*	(IL)
			HOMO-2	→	LUMO+7	0.28	d_{xz}; d_{xy}	→	π_{phen}*	(MLCT)
			HOMO	→	LUMO+7	0.24	π_{hmip}	→	π_{phen}*	(LLCT)
56	4.39 (283)	21	HOMO-7	→	LUMO+1	0.50	π_{hmip}	→	d_{xz}; d_{xy}	(LMCT)[f]
61	4.47 (277)	52	HOMO-7	→	LUMO+3	0.31	π_{hmip}	→	d_{z^2}	(LMCT)
			HOMO-6	→	LUMO+5	0.28	π_{phen}	→	π_{hmip}*	(LLCT)
			HOMO	→	LUMO+9	0.27	π_{hmip}	→	π_{hmip}*	(IL)
			HOMO-7	→	LUMO+5	0.25	π_{hmip}	→	π_{hmip}*	(IL)
78	4.78 (259)	45	HOMO-9	→	LUMO+2	0.45	π_{phen}	→	$d_{x^2-y^2}$	(LMCT)
79	4.83 (257)	100	HOMO-8	→	LUMO+2	0.35	π_{phen}	→	$d_{x^2-y^2}$	(LMCT)
			HOMO-9	→	LUMO+1	0.26	π_{phen}	→	d_{xz}; d_{xy}	(LMCT)
			HOMO-10	→	LUMO	0.24	π_{hmip}	→	π*	(LLCT; IL)
			HOMO-5	→	LUMO+3	0.22	π_{phen}	→	d_{z^2}	(LMCT)
80	4.84 (256)	52	HOMO-10	→	LUMO	0.51	π_{hmip}	→	π*	(LLCT; IL))
114	5.35 (232)	26	HOMO-4	→	LUMO+9	0.52	π_{hmip}	→	π_{hmip}*	(IL)
			HOMO	→	LUMO+16	0.30	π_{hmip}	→	π_{hmip}*	(IL)

[a] Oscillator strength intensities are shown in percentage

[b] π_{hmip} – orbital centred at the hmip ligand; π_{phen} – orbitals centred at the phenanthroline ligands; π – orbital centred at the phen moiety of the three ligands

[c] Ligand-to-ligand charge transfer and Intra-ligand

[d] Metal-to-ligand charge transfer

[e] Metal-centred

[f] Ligand-to-metal charge transfer

Table S11. Major computed PCM-TD-DFT vertical excitation energies ΔE at B3LYP/6-31G*//B3LYP/6-31G* level for the local minimum **LM** isomer of $[Ru(phen)_2(hmip)]^{2+}$ in water. Plot shown in Figure 68b.

Excited state	ΔE /eV (nm)	f[a] /(a.u.)	Orbitals			Coeff.	Assignment[b]			
7	2.86 (434)	26	HOMO	→	LUMO+1	0.41	π_{hmip}	→	d_{xz}; d_{xy}	(LMCT)[c]
			HOMO-2	→	LUMO+1	0.34	d_{xz}; d_{xy}	→	d_{xz}; d_{xy}	(MC)[d]
			HOMO-3	→	LUMO+2	0.28	$d_{x^2-y^2}$	→	$d_{x^2-y^2}$	(MC)
17	3.18 (389)	23	HOMO-1	→	LUMO+5	0.58	d_{z^2}	→	π_{hmip}*	(MLCT)[e]
31	3.71 (334)	39	HOMO	→	LUMO+6	0.50	π_{hmip}	→	π_{hmip}*	(IL)[f]
			HOMO-4	→	LUMO+3	0.31	π_{hmip}	→	π_{phen}*	(LLCT)[g]
33	3.78 (328)	23	HOMO-4	→	LUMO+5	0.45	π_{hmip}	→	π_{hmip}*	(IL)
			HOMO-1	→	LUMO+6	0.38	d_{z^2}	→	π_{hmip}*	(MLCT)
42	4.20 (295)	70	HOMO-4	→	LUMO+6	0.61	π_{hmip}	→	π_{hmip}*	(IL)
54	4.34 (285)	30	HOMO-7	→	LUMO+1	0.54	$d_{x^2-y^2}$	→	d_{xz}; d_{xy}	(MC)
63	4.50 (276)	69	HOMO-5	→	LUMO+5	0.48	π_{hmip}	→	π_{hmip}*	(IL)
77	4.78 (259)	48	HOMO-9	→	LUMO+2	0.40	π_{phen}	→	$d_{x^2-y^2}$	(LMCT)
			HOMO-6	→	LUMO+4	0.24	π_{phen}	→	π_{phen}*	(IL)
79	4.83 (257)	100	HOMO-8	→	LUMO+2	0.30	π_{phen}	→	$d_{x^2-y^2}$	(LMCT)
			HOMO-1	→	LUMO+9	0.29	d_{z^2}	→	π_{hmip}*	(MLCT)
80	4.84 (256)	78	HOMO-10	→	LUMO	0.41	π_{hmip}	→	π*	(LLCT; IL)

[a] Oscillator strength intensities are shown in percentage

[b] π_{hmip} – orbital centred at the hmip ligand; π_{phen} – orbitals centred at the phenanthroline ligands; π – orbital centred at the phen moiety of the three ligands

[c] Ligand-to-metal charge transfer

[d] Metal-centred

[e] Metal-to-ligand charge transfer

[f] Intra-ligand

[g] Ligand-to-ligand charge transfer

Table S12. Major computed PCM-TD-DFT vertical excitation energies ΔE at B3LYP/6-31G*//B3LYP/6-31G* level for the deprotonated species of $[Ru(phen)_2(hmip)]^{2+}$ in water. Plot shown in Figure 70.

Excited state	ΔE /eV (nm)	f[a] /(a.u.)	Orbitals			Coeff.	Assignment[b]			
21	2.79 (445)	100	HOMO	→	LUMO+8	0.54	π_{hmip}	→	π_{hmip}^*	(IL)[c]
			HOMO-4	→	LUMO+1	0.32	d_{yz}	→	$d_{x^2-y^2}$	(MC)[d]
22	2.81 (441)	38	HOMO-3	→	LUMO+2	0.49	d_{z^2}	→	π_{phen}^*	(MLCT)[e]
			HOMO	→	LUMO+8	0.42	π_{hmip}	→	π_{hmip}^*	(IL)
48	3.73 (332)	45	HOMO	→	LUMO+14	0.49	π_{hmip}	→	π_{hmip}^*	(IL)
84	4.39 (283)	41	HOMO-4	→	LUMO+7	0.36	d_{yz}	→	π_{phen}^*	(MLCT)
85	4.41 (281)	72	HOMO-6	→	LUMO+5	0.42	π_{hmip}	→	π_{hmip}^*	(IL)
			HOMO-7	→	LUMO+4	-0.24	π_{hmip}	→	π_{hmip}^*	(IL)
114	4.75 (261)	55	HOMO-13	→	LUMO+1	0.27	π_{phen}	→	$d_{x^2-y^2}$	(LMCT)[f]
			HOMO-9	→	LUMO+3	-0.22	π_{phen}	→	π_{phen}^*	(IL)
			HOMO-13	→	LUMO+3	-0.21	π_{phen}	→	π_{phen}^*	(IL)
119	4.79 (259)	45	HOMO-11	→	LUMO+4	0.35	π_{hmip}	→	π_{hmip}^*	(IL)
			HOMO-7	→	LUMO+5	-0.21	π_{hmip}	→	π_{hmip}^*	(IL)
			HOMO-14	→	LUMO+4	-0.21	π_{hmip}	→	π_{hmip}^*	(IL)
22	2.81 (441)	38	HOMO-3	→	LUMO+2	0.49	d_{z^2}	→	π_{phen}^*	(MLCT)
			HOMO	→	LUMO+8	0.42	π_{hmip}	→	π_{hmip}^*	(IL)
11	2.54 (489)	31	HOMO	→	LUMO+6	0.69	π_{hmip}	→	π_{phen}^*	(LLCT)[g]
79	4.28 (290)	30	HOMO-7	→	LUMO+4	0.56	π_{hmip}	→	π_{hmip}^*	(IL)

[a] Oscillator strength intensities are shown in percentage

[b] π_{hmip} – orbital centred at the hmip ligand; π_{phen} – orbitals centred at the phenanthroline ligands

[c] Intra-ligand

[d] Metal-centred

[e] Metal-to-ligand charge transfer

[f] Ligand-to-metal charge transfer

[g] Ligand-to-ligand charge transfer

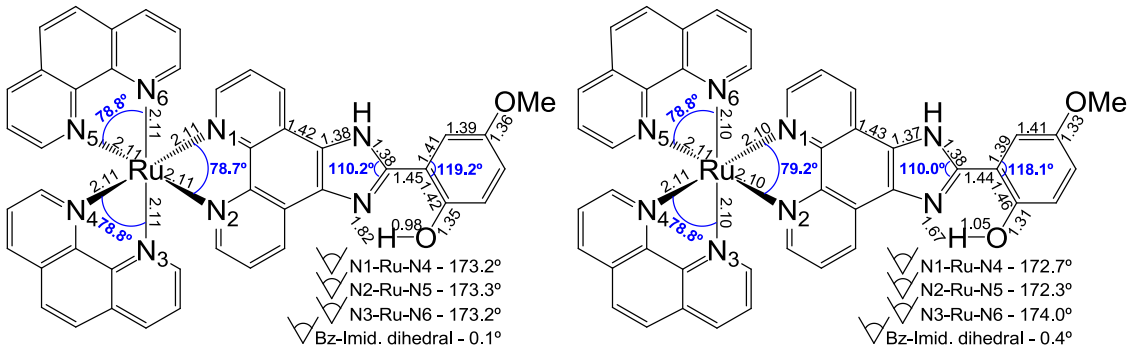

Singlet ground-state (**^{1}GS**) Triplet excited-state (**^{3}IL**)

Figure A65. Geometrical features of both singlet ground state (^{1}GS) and triplet excited state (^{3}IL) of $[Ru(phen)_2(hmip)]^{2+}$. Optimizations in gas phase using the computational protocol B3LYP/6-31G*.

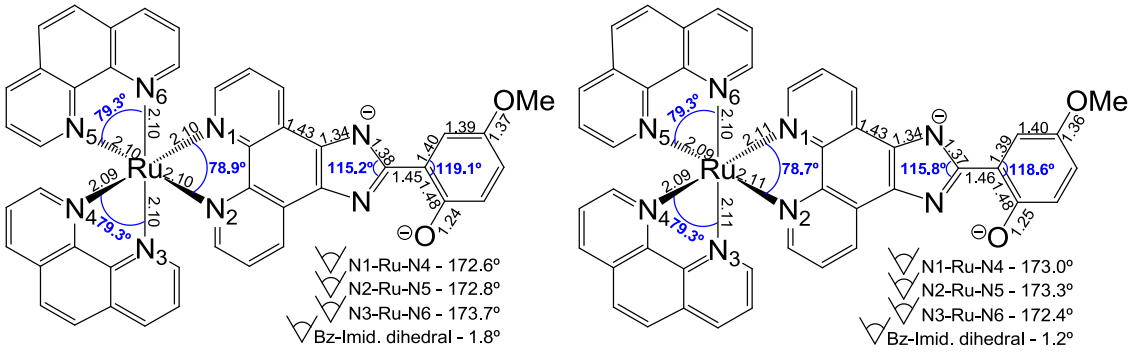

Singlet ground-state (**^{1}GS**) Triplet excited-state (**^{3}LLCT**)

Figure A66. Geometrical features of both singlet ground state (^{1}GS) and triplet excited state (^{3}LLCT) of the deprotonated form of $[Ru(phen)_2(hmip)]^{2+}$. Optimizations in gas phase using the computational protocol B3LYP/6-31G*.

6.2.3. $[Ru(phen)_2(haip)]^{2+}$

Table S13. Major computed PCM-TD-DFT vertical excitation energies ΔE at B3LYP/6-31G*//B3LYP/6-31G* level for the global minimum **GM** isomer of $[Ru(phen)_2(haip)]^{2+}$ in water. Plot shown in Figure 73a.

Excited state	ΔE /eV (nm)	f[a] /(a.u.)	Orbitals			Coeff.	Assignment[b]			
7	2.88 (430)	23	HOMO-1	→	LUMO+1	0.51	d_{xz}; d_{xy}	→	π_{haip}*	(MLCT)[c]
			HOMO-2	→	LUMO+2	-0.35	d_{yz}	→	$d_{x^2-y^2}$	(MC)[d]
28	3.80 (326)	37	HOMO-1	→	LUMO+6	0.61	d_{xz}; d_{xy}	→	π_{haip}*	(MLCT)
31	3.93 (315)	26	HOMO-3	→	LUMO+6	0.37	d_{xz}; d_{xy}	→	π_{haip}*	(MLCT)
			HOMO-1	→	LUMO+7	-0.30	d_{xz}; d_{xy}	→	π_{haip}*	(MLCT)
			HOMO-3	→	LUMO+7	0.28	d_{xz}; d_{xy}	→	π_{haip}*	(MLCT)
			HOMO-4	→	LUMO	0.28	π_{haip}	→	π_{haip}*	(IL)[e]
35	4.04 (307)	25	HOMO-1	→	LUMO+7	0.46	d_{xz}; d_{xy}	→	π_{haip}*	(MLCT)
			HOMO-3	→	LUMO+6	0.42	d_{xz}; d_{xy}	→	π_{haip}*	(MLCT)
65	4.48 (277)	28	HOMO-8	→	LUMO+5	0.33	π_{haip}	→	π_{haip}*	(IL)
			HOMO-6	→	LUMO+5	0.32	π_{phen}	→	π_{haip}*	(LLCT)[f]
			HOMO-8	→	LUMO+3	-0.25	π_{haip}	→	π_{phen}*	(LLCT)
78	4.67 (265)	64	HOMO-4	→	LUMO+6	0.41	π_{haip}	→	π_{haip}*	(IL)
79	4.68 (265)	26	HOMO-9	→	LUMO+3	0.58	π_{phen}	→	π_{phen}*	(IL)
82	4.71 (263)	26	HOMO	→	LUMO+10	0.49	d_{z^2}	→	π_{haip}*	(MLCT)
			HOMO-4	→	LUMO+6	-0.32	π_{haip}	→	π_{haip}*	(IL)
87	4.79 (259)	50	HOMO-10	→	LUMO+2	0.45	π_{phen}	→	$d_{x^2-y^2}$	(LMCT)[g]
88	4.82 (257)	100	HOMO-9	→	LUMO+2	0.36	π_{phen}	→	$d_{x^2-y^2}$	(LMCT)
			HOMO-10	→	LUMO+1	0.28	π_{phen}	→	π_{haip}*	(LLCT)

[a] Oscillator strength intensities are shown in percentage

[b] π_{hmip} – orbital centred at the hmip ligand; π_{phen} – orbitals centred at the phenanthroline ligands

[c] Metal-to-ligand charge transfer

[d] Metal-centred

[e] Intra-Ligand

[f] Ligand-to-ligand charge transfer

[g] Ligand-to-metal charge transfer

Table S14. Major computed PCM-TD-DFT vertical excitation energies ΔE at B3LYP/6-31G*//B3LYP/6-31G* level for the local minimum **LM** isomer of $[Ru(phen)_2(haip)]^{2+}$ in water. Plot shown in Figure 73b.

Excited state	ΔE /eV (nm)	f[a] /(a.u.)	Orbitals			Coeff.	Assignment[b]			
7	2.89 (430)	34	HOMO-1	→	LUMO+1	0.51	d_{xz}; d_{xy}	→	π_{haip}*	(MLCT)[c]
			HOMO-2	→	LUMO+2	-0.38	d_{yz}	→	π_{phen}*	(MLCT)
28	3.82 (324)	42	HOMO-1	→	LUMO+6	0.60	d_{xz}; d_{xy}	→	π_{haip}*	(MLCT)
34	4.03 (307)	73	HOMO-3	→	LUMO+6	0.55	d_{xz}; d_{xy}	→	π_{haip}*	(MLCT)
65	4.48 (277)	31	HOMO-4	→	LUMO+5	0.35	π_{haip}	→	π_{haip}*	(IL)[d]
			HOMO-5	→	LUMO+5	-0.30	π	→	π_{haip}*	(IL; LLCT)[e]
			HOMO-8	→	LUMO+3	-0.23	π	→	π_{phen}*	(IL; LLCT)
68	4.52 (275)	37	HOMO-4	→	LUMO+5	0.44	π_{haip}	→	π_{haip}*	(IL)
			HOMO-5	→	LUMO+5	0.29	π	→	π_{haip}*	(IL; LLCT)
77	4.68 (265)	17	HOMO-9	→	LUMO+3	0.56	π_{phen}	→	π_{phen}*	(IL)
81	4.74 (261)	32	HOMO-4	→	LUMO+6	0.52	π_{haip}	→	π_{haip}*	(IL)
87	4.79 (259)	64	HOMO-10	→	LUMO+2	0.44	π_{phen}	→	π_{phen}*	(IL)
88	4.81 (258)	100	HOMO-9	→	LUMO+2	0.33	π_{phen}	→	π_{phen}*	(IL)
			HOMO-3	→	LUMO+9	0.27	d_{xz}; d_{xy}	→	π_{phen}*	(MLCT)
			HOMO-10	→	LUMO+1	0.24	π_{phen}	→	π_{haip}*	(LLCT)
90	4.88 (254)	38	HOMO-3	→	LUMO+9	0.53	d_{xz}; d_{xy}	→	π_{phen}*	(MLCT)

[a] Oscillator strength intensities are shown in percentage

[b] π_{hmip} – orbital centred at the hmip ligand; π_{phen} – orbitals centred at the phenanthroline ligands; π – orbital centred at the three ligands

[c] Metal-to-ligand charge transfer

[d] Intra-Ligand

[e] Ligand-to-ligand charge transfer

Table S15. Major computed PCM-TD-DFT vertical excitation energies ΔE at B3LYP/6-31G*//B3LYP/6-31G* level for the mono-deprotonated species of $[Ru(phen)_2(haip)]^{2+}$ in water. Plot shown in Figure 73a.

Excited state	ΔE /eV (nm)	f[a] /(a.u.)	Orbitals			Coeff.	Assignment[b]			
16	3.09 (402)	19	HOMO-2	→	LUMO+2	0.62	d_{yz}	→	π_{phen}*	(MLCT)[c]
25	3.62 (343)	17	HOMO-2	→	LUMO+5	0.64	d_{yz}	→	π_{haip}*	(MLCT)
26	3.69 (336)	100	HOMO	→	LUMO+7	0.65	π_{haip}	→	π_{haip}*	(IL)[d]
32	3.86 (321)	19	HOMO-5	→	LUMO+4	0.39	π_{haip}	→	π_{haip}*	(IL)
			HOMO-5	→	LUMO+3	0.32	π_{haip}	→	π_{phen}*	(LLCT)[e]
			HOMO-1	→	LUMO+7	0.29	d_{z^2}	→	π_{haip}*	(MLCT)
56	4.31 (288)	68	HOMO-5	→	LUMO+5	0.50	π_{haip}	→	π_{haip}*	(IL)
78	4.63 (268)	87	HOMO-4	→	LUMO+6	0.51	π_{haip}	→	π_{haip}*	(IL)
80	4.68 (265)	23	HOMO-12	→	LUMO+1	0.46	π_{phen}	→	$d_{x^2-y^2}$	(LMCT)[f]
92	4.78 (259)	18	HOMO-9	→	LUMO+1	0.31	π_{haip}	→	$d_{x^2-y^2}$	(LMCT)
			HOMO-11	→	LUMO+1	-0.31	π_{haip}	→	$d_{x^2-y^2}$	(LMCT)
97	4.84 (256)	75	HOMO-9	→	LUMO+2	0.34	π_{haip}	→	π_{phen}*	(LLCT)
			HOMO-11	→	LUMO+2	-0.25	π_{haip}	→	π_{phen}*	(LLCT)
			HOMO-11	→	LUMO+1	-0.21	π_{haip}	→	$d_{x^2-y^2}$	(LMCT)
101	4.90 (253)	20	HOMO-12	→	LUMO	0.40	π_{phen}	→	π*	(LLCT, IL)
			HOMO-13	→	LUMO	-0.24	π_{haip}	→	π*	(LLCT, IL)

[a] Oscillator strength intensities are shown in percentage

[b] π_{hmip} – orbital centred at the hmip ligand; π_{phen} – orbitals centred at the phenanthroline ligands; π – orbital centred at the three ligands

[c] Metal-to-ligand charge transfer

[d] Intra-Ligand

[e] Ligand-to-ligand charge transfer

[f] Ligand-to-metal charge transfer

Table S16. Major computed PCM-TD-DFT vertical excitation energies ΔE at B3LYP/6-31G*//B3LYP/6-31G* level for the totally deprotonated species of $[Ru(phen)_2(haip)]^{2+}$ in water. Plot shown in Figure 75.

Excited state	ΔE /eV (nm)	f[a] /(a.u.)	Orbitals			Coeff.	Assignment[b]			
18	2.95 (420)	48	HOMO-1	→	LUMO+4	0.33	π_{haip}	→	π_{haip}^*	(IL)[c]
			HOMO-3	→	LUMO+2	0.27	d_{z^2}	→	π_{phen}^*	(MLCT)[d]
			HOMO-1	→	LUMO+3	-0.26	π_{haip}	→	π_{phen}^*	(LLCT)[e]
			HOMO-4	→	LUMO+1	0.25	d_{yz}	→	$d_{x^2-y^2}$	(MC)[f]
21	3.03 (409)	84	HOMO	→	LUMO+6	0.53	π_{haip}	→	π_{phen}^*	(LLCT)
32	3.26 (380)	59	HOMO	→	LUMO+8	0.58	π_{haip}	→	π_{haip}^*	(IL)
62	4.13 (300)	34	HOMO	→	LUMO+15	0.39	π_{haip}	→	π_{haip}^*	(IL)
			HOMO-6	→	LUMO+5	-0.33	π_{haip}	→	π_{haip}^*	(IL)
94	4.49 (276)	78	HOMO-1	→	LUMO+9	0.49	π_{haip}	→	π_{haip}^*	(IL)
			HOMO-4	→	LUMO+14	0.24	d_{yz}	→	d_{yz}, $d_{x^2-y^2}$	(MC)
95	4.50 (276)	33	HOMO-1	→	LUMO+9	0.38	π_{haip}	→	π_{haip}^*	(IL)
			HOMO-4	→	LUMO+14	-0.33	d_{yz}	→	d_{yz}, $d_{x^2-y^2}$	(MC)
108	4.68 (265)	27	HOMO-12	→	LUMO+2	0.58	π_{phen}	→	π_{phen}^*	(IL)
117	4.75 (261)	56	HOMO-14	→	LUMO+1	0.32	π_{haip}	→	$d_{x^2-y^2}$	(LMCT)[g]
			HOMO-13	→	LUMO+1	-0.30	π_{phen}	→	$d_{x^2-y^2}$	(LMCT)
119	4.80 (259)	100	HOMO-12	→	LUMO+1	0.30	π_{phen}	→	$d_{x^2-y^2}$	(LMCT)
			HOMO-13	→	LUMO+3	-0.26	π_{phen}	→	π_{phen}^*	(IL)
			HOMO-13	→	LUMO+4	-0.25	π_{phen}	→	π_{haip}^*	(LLCT)
130	4.93 (251)	36	HOMO-1	→	LUMO+10	0.50	π_{haip}	→	π_{phen}^*	(LLCT)
			HOMO-5	→	LUMO+10	0.39	d_{xz}	→	π_{phen}^*	(MLCT)

[a] Oscillator strength intensities are shown in percentage

[b] π_{hmip} – orbital centred at the hmip ligand; π_{phen} – orbitals centred at the phenanthroline ligands

[c] Intra-Ligand

[d] Metal-to-ligand charge transfer

[e] Ligand-to-ligand charge transfer

[f] Metal centred

[g] Ligand-to-metal charge transfer

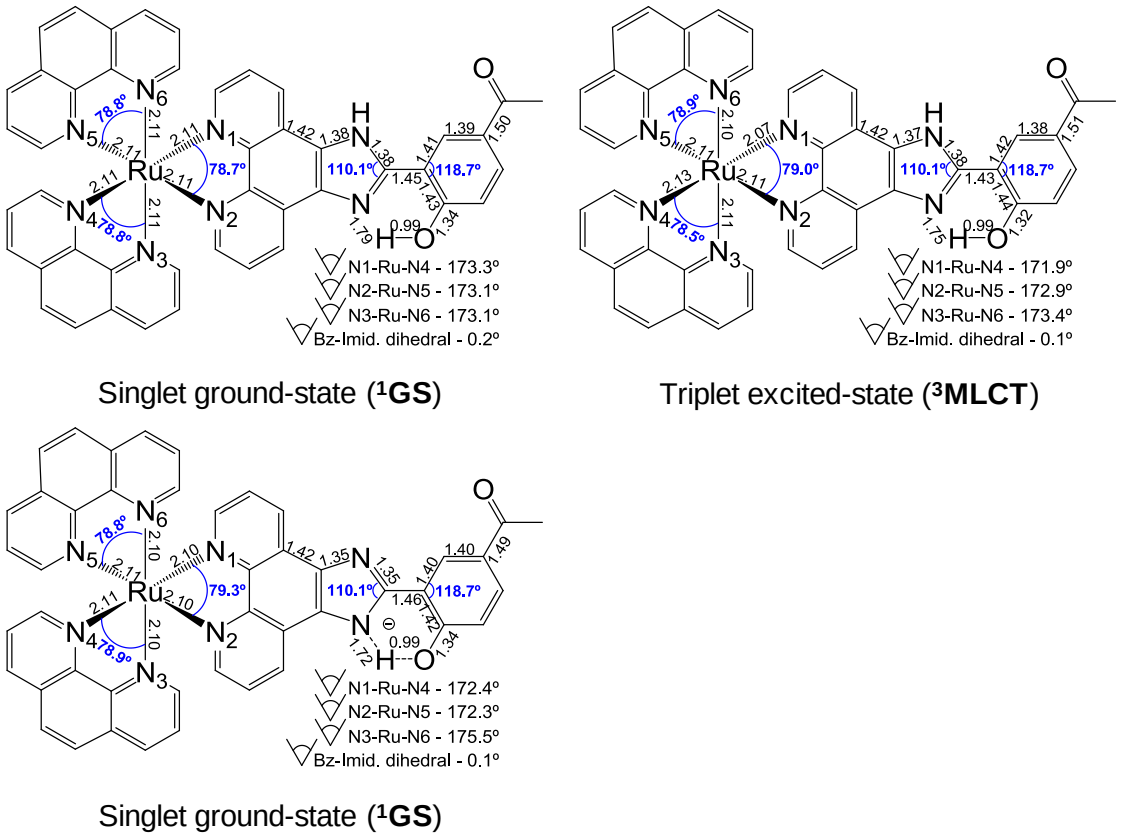

Figure A67. Geometrical features of the singlet ground state (^{1}GS) of the neutral and monodeprotonated species as well as the triplet excited state (^{3}MLCT) of $[Ru(phen)_2(haip)]^{2+}$. Optimization in gas phase using the computational protocol B3LYP/6-31G*.

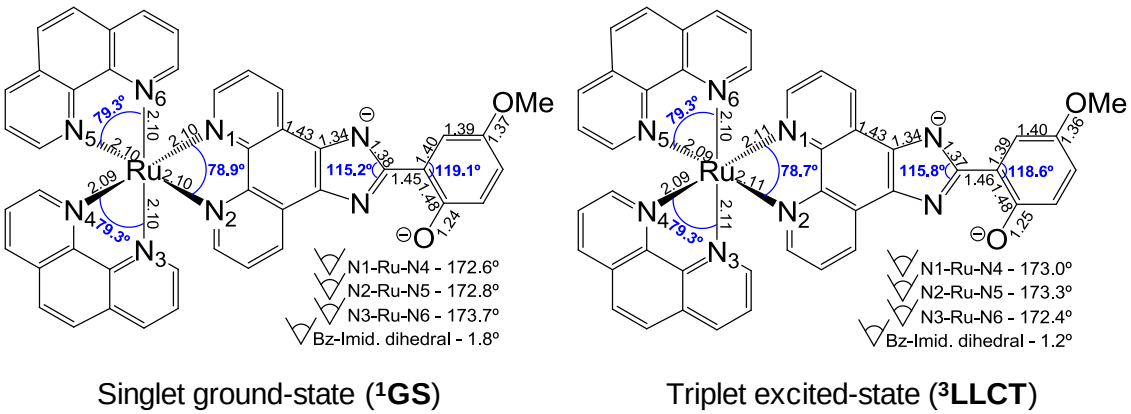

Figure A68. Geometrical features of both singlet ground state (^{1}GS) and triplet excited state (^{3}LLCT) of the deprotonated form of $[Ru(phen)_2(haip)]^{2+}$. Optimizations in gas phase using the computational protocol B3LYP/6-31G*.

6.2.4. $[Ru(phen)_2(bpytym)]^{2+}$

Table S17. Major computed PCM-TD-DFT vertical excitation energies ΔE at B3LYP/6-31G*//B3LYP/6-31G* level for $[Ru(phen)_2(bpytym)]^{2+}$ in water. Plot shown in Figure 77.

Excited state	ΔE /eV (nm)	f[a] /(a.u.)	Orbitals			Coeff.	Assignment[b]			
6	2.82 (440)	14	HOMO-2	→	LUMO	0.58	d_{yz}	→	π_{phen}^*	(MLCT)[c]
9	2.89 (429)	37	HOMO-1	→	LUMO+2	0.54	d_{xz}	→	π_{bpytym}^*	(MLCT)
10	2.92 (425)	10	HOMO	→	LUMO+4	0.58	d_{z^2}	→	π_{phen}^*	(MLCT)
11	3.00 (414)	17	HOMO-1	→	LUMO+3	0.64	d_{xz}	→	π_{phen}^*	(MLCT)
21	3.79 (327)	18	HOMO-1	→	LUMO+5	0.46	d_{xz}	→	π_{bpytym}^*	(MLCT)
			HOMO	→	LUMO+6	-0.39	d_{z^2}	→	π_{bpytym}^*	(MLCT)
			HOMO-2	→	LUMO	0.58	d_{yz}	→	π_{phen}^*	(MLCT)
26	3.88 (319)	15	HOMO-2	→	LUMO+6	0.63	d_{yz}	→	π_{bpytym}^*	(MLCT)
46	4.28 (290)	47	HOMO-7	→	LUMO	0.44	π_{bpytym}	→	π_{phen}^*	(LLCT)[d]
53	4.38 (283)	23	HOMO-7	→	LUMO+2	0.46	π_{bpytym}	→	π_{bpytym}^*	(IL)[e]
70	4.58 (271)	21	HOMO-9	→	LUMO+2	0.60	π_{bpytym}	→	π_{bpytym}^*	(IL)
73	4.61 (269)	26	HOMO-8	→	LUMO+2	0.52	π_{bpytym}	→	π_{bpytym}^*	(IL)
78	4.69 (264)	15	HOMO-11	→	LUMO+2	0.44	π	→	π_{bpytym}^*	(LLCT; IL)
			HOMO-9	→	LUMO+4	-0.40	π_{bpytym}	→	π_{phen}^*	(LLCT)
85	4.78 (259)	57	HOMO-10	→	LUMO+1	0.45	π_{phen}	→	$d_{x^2-y^2}$	(LMCT)[f]
86	4.81 (258)	11	HOMO-11	→	LUMO+3	0.46	π	→	π_{phen}^*	(LLCT; IL)
89	4.83 (257)	100	HOMO-11	→	LUMO+1	0.30	π	→	$d_{x^2-y^2}$	(LMCT)
			HOMO-10	→	LUMO	-0.27	π_{phen}	→	π_{phen}^*	(IL)

[a] Oscillator strength intensities are shown in percentage

[b] π_{bpytym} – orbital centred at the bpytym ligand; π_{phen} – orbitals centred at the phenanthroline ligands; π – orbital centred at the three ligands

[c] Metal-to-ligand charge transfer

[d] Ligand-to-ligand charge transfer

[e] Intra-Ligand

[f] Ligand-to-metal charge transfer

Table S18. Major computed PCM-TD-DFT vertical excitation energies ΔE at B3LYP/6-31G*//B3LYP/6-31G* level for $[Ru(phen)_2(bpytym)]^{2+}$-Hg(II) in water. Plot shown in Figure 79a.

Excited state	ΔE /eV (nm)	f[a] /(a.u.)	Orbitals			Coeff.	Assignment[b]			
6	2.83 (439)	11	HOMO-2	→	LUMO	0.56	d_{yz}	→	π_{phen}*	(MLCT)[c]
8	2.89 (429)	15	HOMO-1	→	LUMO+2	0.43	d_{xz}	→	π_{bpytym}*	(MLCT)
			HOMO-2	→	LUMO+1	-0.34	d_{yz}	→	$d_{x^2-y^2}$	(MC)[d]
11	3.00 (413)	11	HOMO-1	→	LUMO+3	0.57	d_{xz}	→	π_{phen}*	(MLCT)
42	4.23 (293)	13	HOMO-6	→	LUMO+1	0.36	π_{phen}	→	$d_{x^2-y^2}$	(LMCT)[e]
			HOMO-7	→	LUMO	0.23	π_{bpytym}	→	π_{phen}*	(LLCT)[f]
			HOMO-6	→	LUMO+3	-0.21	π_{phen}	→	π_{phen}*	(IL)[g]
44	4.25 (292)	17	HOMO-7	→	LUMO	0.34	π_{bpytym}	→	π_{phen}*	(LLCT)
51	4.36 (285)	11	HOMO-7	→	LUMO+1	0.31	π_{bpytym}	→	$d_{x^2-y^2}$	(LMCT)
			HOMO-7	→	LUMO+2	-0.31	π_{bpytym}	→	π*	(LLCT, IL)
			HOMO-1	→	LUMO+10	-0.29	d_{xz}	→	π_{phen}*	(MLCT)
68	4.56 (272)	14	HOMO-9	→	LUMO+2	0.51	π_{bpytym}	→	π*	(LLCT, IL)
75	4.63 (268)	10	HOMO-9	→	LUMO+3	0.41	π_{bpytym}	→	π_{phen}*	(LLCT)
91	4.78 (259)	37	HOMO-12	→	LUMO+2	0.28	π_{phen}	→	π*	(LLCT, IL)
			HOMO-12	→	LUMO+1	0.26	π_{phen}	→	$d_{x^2-y^2}$	(LMCT)
			HOMO-5	→	LUMO+4	-0.24	π_{phen}	→	π_{phen}*	(IL)
94	4.82 (257)	12	HOMO-4	→	LUMO+7	0.59	π_{bpytym}	→	π_{bpytym}*	(IL)
96	4.83 (257)	100	HOMO-4	→	LUMO+7	0.26	π_{bpytym}	→	π_{bpytym}*	(IL)
			HOMO-12	→	LUMO	-0.25	π_{phen}	→	π_{phen}*	(IL)
			HOMO-13	→	LUMO+1	0.24	π_{bpytym}	→	$d_{x^2-y^2}$	(LMCT)
110	4.94 (251)	21	HOMO-1	→	LUMO+12	0.44	d_{xz}	→	π_{bpytym}*	(MLCT)
121	5.03 (246)	10	HOMO-6	→	LUMO+5	0.36	π_{phen}	→	π_{bpytym}*	(LLCT)
123	5.04 (246)	22	HOMO-5	→	LUMO+5	0.49	π_{phen}	→	π_{bpytym}*	(LLCT)

[a] Oscillator strength intensities are shown in percentage

[b] π_{bpytym} – orbital centred at the bpytym ligand; π_{phen} – orbitals centred at the phenanthroline ligands; π – orbital centred at the three ligands

[c] Metal-to-ligand charge transfer

[d] Metal centred

[e] Ligand-to-metal charge transfer

[f] Ligand-to-ligand charge transfer

[g] Intra-Ligand

Table S19. First 5 computed PCM-TD-DFT vertical excitation energies (ΔE) at B3LYP/6-31G*//B3LYP/6-31G* level and corresponding assignment for the optimized triplet of the supramolecular complex 1:1 $[Ru(phen)_2(bpytym)]^{2+}$-Hg(II) in water.

Excited state	ΔE /eV (nm)	Coeff.	Assignment[a]			
T_1	2.11 (587)	0.54	Ru d_{yz}	→	π_{phen}*	(MLCT)[b]
T_2	2.22 (558)	0.49	Ru d_{yz}	→	π_{phen}*	(MLCT)
T_3	2.28 (543)	0.44	Ru $d_{x^2-y^2}$	→	π_{phen}*	(MLCT)
T_4	2.39 (519)	0.47	Ru d_{xz}	→	π_{phen}*	(MLCT)
T_5	2.43 (510)	0.58	Ru d_{xz}	→	π_{phen}*	(MLCT)

[a] π_{phen} – orbitals centred at the phen ligands

[b] Metal-to-ligand charge transfer

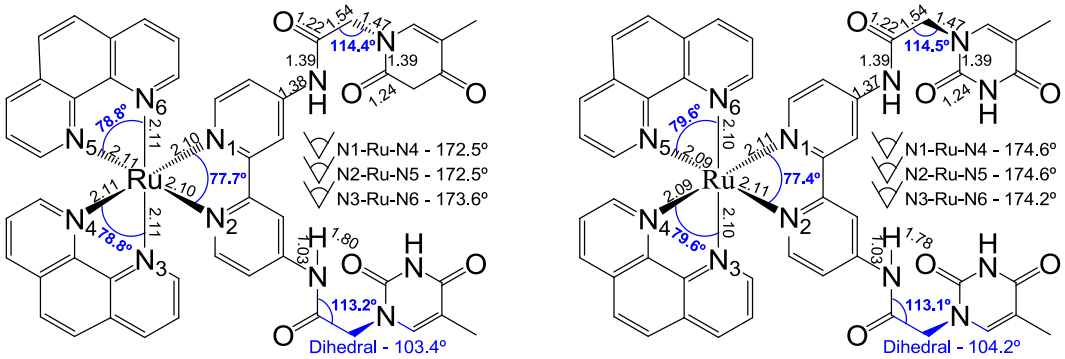

Singlet ground-state (**^{1}GS**) Triplet ground-state (**^{3}MLCT**)

Figure A69. Geometrical features of both singlet ground state (^{1}GS) and triplet excited state (^{3}MLCT) of $[Ru(phen)_2(bpytym)]^{2+}$. Optimizations in gas phase using the computational protocol B3LYP/6-31G*.

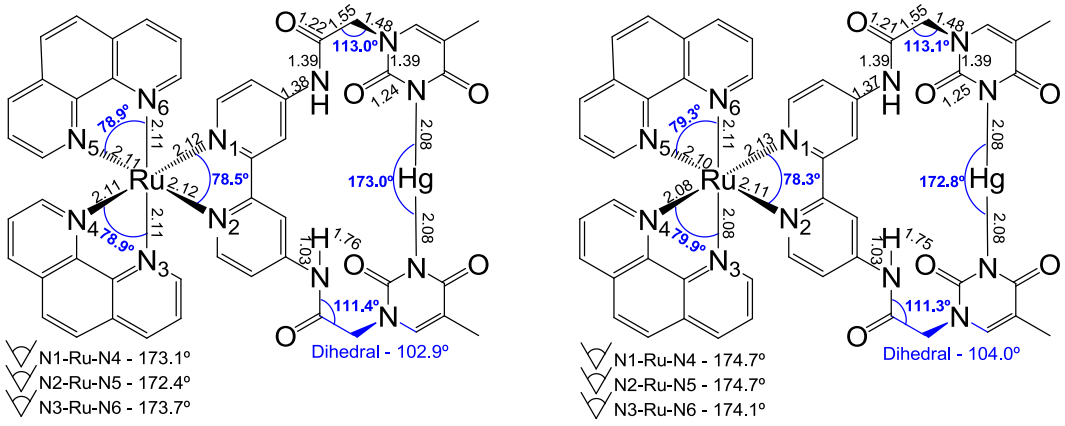

Singlet ground-state (**^{1}GS**) Triplet ground-state (**^{3}MLCT**)

Figure A70. Geometrical features of both singlet ground state (^{1}GS) and triplet excited state (^{3}MLCT) of $[Ru(phen)_2(bpytym)]^{2+}$-Hg(II). Optimizations in gas phase using the computational protocol B3LYP/6-31G*.

UNIVERSIDAD COMPLUTENSE DE MADRID

FACULTAD DE CIENCIAS QUÍMICAS